QA: QA

ANL-EBS-MD-000027 REV 03

September 2004

NOTICE OF OPEN CHANGED DOCUMENTS - THIS DOCUMENT IS IMPACTED BY THE LISTED CHANGE DOCUMENTS AND CANNOT BE USED WITHOUT THEM.

---

1) ACN-001, DATED 04/18/2005
2) ACN-002, DATED 11/28/2005
3) ACN-003, DATED 07/28/2006

THIS DOCUMENT IS IMPACTED BY THE FOLLOWING ERD(S), WHICH SHOULD BE REVIEWED PRIOR TO IT USE:

1) ANL-EBS-MD-000027 ERD 01
ACCESSION #LLR.20080311.0066

Prepared for:
U.S. Department of Energy
Office of Civilian Radioactive Waste Management
Office of Repository Development
1551 Hillshire Drive
Las Vegas, Nevada 89134-6321

Prepared by:
Bechtel SAIC Company, LLC
1180 Town Center Drive
Las Vegas, Nevada 89144

Under Contract Number
DE-AC28-01RW12101

DISCLAIMER

This report was prepared as an account of work sponsored by an agency of the United States Government. Neither the United States Government nor any agency thereof, nor any of their employees, nor any of their contractors, subcontractors or their employees, makes any warranty, express or implied, or assumes any legal liability or responsibility for the accuracy, completeness, or any third party's use or the results of such use of any information, apparatus, product, or process disclosed, or represents that its use would not infringe privately owned rights. Reference herein to any specific commercial product, process, or service by trade name, trademark, manufacturer, or otherwise, does not necessarily constitute or imply its endorsement, recommendation, or favoring by the United States Government or any agency thereof or its contractors or subcontractors. The views and opinions of authors expressed herein do not necessarily state or reflect those of the United States Government or any agency thereof.

QA: QA

Drift Degradation Analysis

ANL-EBS-MD-000027 REV 03

September 2004

OCRWM	MODEL SIGNATURE PAGE/CHANGE HISTORY	Page iii 1. Total Pages: 976

2. Type of Mathematical Model

☒ Process Model ☐ Abstraction Model ☐ System Model

Describe Intended Use of Model

The models and associated analyses documented in this report provide drift degradation input, including rockfall data, for various calculations, models, and analyses. The users of the output data provided in this document include the Specialty Analyses & Waste Package Design Department, the Total System Performance Assessment Department, the Disruptive Events Department, the Ambient and Thermal Drift Seepage Department, the Subsurface Department, and the Preclosure Safety Analysis Department.

3. Title

Drift Degradation Analysis

4. DI (including Rev. No., if applicable):

ANL-EBS-MD-000027 REV 03

5. Total Appendices	6. No. of Pages in Each Appendix
25	A-14, B-10, C-30, D-28, E-58, F-18, G-6, H-8, I-10, J-8, K-14, L-4, M-8, N-26, O-46, P-34, Q-16, R-22, S-64, T-16, U-8, V-10, W-8, X-10, Y-18

	Printed Name	Signature	Date
7. Originator	Dwayne C. Kicker (lead)		9/16/04
8. Independent Technical Reviewer	Robert L. Howard		16 SEP 04
9. Checker	Junghun Leem (lead)		9/16/04
10. QER	Judith E. Gebhart		9/16/04
11. Responsible Manager/Lead	Mark P. Board		9/16/04
12. Responsible Manager	Mark P. Board		9/16/04

13. Remarks

The preparer and checker for each section in this report are identified as follows:

Section or Appendix	Preparer	Checker
1	Dwayne Kicker, Mark Board	Junghun Leem
2, 3, 5, 6.1	Dwayne Kicker	Junghun Leem
4, 9, O	Dwayne Kicker	David Tang
6.2, C, M, Q	Junghun Leem	Ming Lin
6.3, 6.4	Ming Lin	Junghun Leem
6.5 through 6.8, 8, B, F, O, S, T	Dwayne Kicker	Junghun Leem
7	Mark Board	Junghun Leem
A	Dwayne Kicker, Ming Lin	Junghun Leem
E	Dwayne Kicker, Mark Board	David Tang
D, G, H, I, J, K, L, N, P, R, U, V, W, Y	Ming Lin	Junghun Leem
X	Ming Lin	David Tang

Robert Lung (USBR) and Michael Fahy (USGS) provided technical support in the development of Section 6.1 and Appendix B. David Buesch (USGS) provided technical support in the development of Section 6.1, Appendices O and T.

(Continued on next page)

13. Remarks

(Continued from previous page)

Branko Damjanac (Itasca) provided technical support in the development of Sections 6.3, 6.4, 7, Appendices S, U, V, W, and Y.
Carlos Carranza-Torres (Itasca) provided technical support in the development of Section 6.2 and Appendix C.
David Potyondy (Itasca) provided technical support in the development of Section 7.6 and Appendix S.
John Kemeny (Univ. of Arizona) provided technical support in the development of Appendix D.

Change History

14. Revision No.	15. Description of Change
REV 00	Initial issue.
REV 00 ICN 1	The technical product cover sheet was changed to indicate that this document reports the development and use of a model. Section 6.5 on model validation was added. The report was changed to include results for 75º-azimuth emplacement drifts and to provide additional results for emplacement drifts with no backfill. The Document Input Reference System (DIRS) information was removed from document and made part of the records package. The numbering of the attachments has been changed to reflect removal of the DIRS information. Attachment VI is now Attachment I. Table 2 was modified. The description of the use of software routines in Section 3 was changed. The data in Tables 14, 15, 20, 21, 23, 24, and Figure 17 were corrected. Additional attachments were added to document the field observation of key blocks in the Cross-Drift, and to document natural analogues for the seismic effect on rock fall.
REV 01	The Tptpln fracture geometry inputs to DRKBA were revised to be consistent with the developed fracture geometry data in ANL-EBS-GE-000006. Output information for the Tptpln was revised throughout the report. The data and information presented in the supporting calculation, CAL-EBS-MD-000010 REV 00, has been updated and merged with this report. Therefore, this revision supersedes calculation CAL-EBS-MD-000010 REV 00. Additional seismic analyses have been included in Attachment V. Information supporting the analysis of drift degradation features, events, and processes (FEPS) has been added in Section 6.6. Information supporting the resolution of applicable Nuclear Regulatory Commission (NRC) key technical issues has been added in Section 6.7. A brief discussion of the impacts of the small-trace length fracture data on drift degradation has been added in Section 7.2. Attachments VIII through XI were added to include the information that was previously provided in calculation CAL-EBS-MD-000010 REV 00 (note that data for the Tptpln unit has been updated in these attachments). Drift profile figures were moved from Section 6.4.3 to Attachment XII. The calculation of mean input data based on source DTNs identified in Section 4.1 was added as documented in Attachment XIII. An assessment of the joint plane representation in the DRKBA rock fall model was added in Attachment XIV to provide additional bases for Assumption 5.1.
REV 01 ICN 1	Assumption 5.6 has been revised resulting in the removal of TBV-4408 from the input status of DTN: MO0003SEPSDARS.002, which provides the basis for ground motion parameters. Section 7.3 of the previous version of this document has been omitted, and Section 7.4 has been renumbered as Section 7.3 in this document. Additional documentation of the use of exempt software has been provided in response to Deficiency Report LVMO-00-D-039 (DR 39), as described in a stand alone DR 39 package (Kicker 2001). This documentation includes minor changes to Section 3.2 and Attachments I, II, and XI (note: the information on the CDs included with Attachment II has not changed). Also, Attachments XV through XVIII were added to provide additional information on the use of commercial software consistent with the requirements of AP3.10Q, Attachment I, and Section 3. (Continued on next page)

Change History

14. Revision No.	15. Description of Change
REV 01 ICN 1	(Continued from previous page) Attachment VIII of this technical product contains documentation of a single-use software macro (Volume_cal V1.1) that was qualified under procedure AP-SI.1Q, Software Management, prior to the release of Revision 3 of said procedure. This macro has not changed with the development of this ICN, nor has the macro been used to develop additional quality affecting information. However, an error in the listing of the macro source code (Figure VIII-1) was corrected in this ICN. The changes in this ICN are indicated by change bars in the right margin.
REV 02	This document has been completely revised to include additional approaches for analyzing seismic, thermal, and time-dependent effects on drift degradation. Since this revision is an extensive modification to the model and analysis documentation, the specific changes have not been tracked. The primary changes include the following: 1. A nonlithophysal rockfall model was developed using the three-dimensional discontinuum code, 3DEC. 2. A lithophysal rockfall model was developed using the two-dimensional discontinuum code, UDEC. 3. Site-specific ground motion time histories appropriate for both the preclosure and postclosure time periods have been included in the rockfall models. 4. Thermal stresses have been calculated and included in the rockfall models. 5. Model validation activities have been added for validating the mechanical material models for both lithophysal and nonlithophysal rocks, and for validating the implementation of these material models in general numerical modeling schemes. The changes included in this revision correct the errors identified in Technical Error Report TER-02-0036.
REV 03	This document has been completely revised to include additional details for FracMan fracture modeling and new seismic ground motion data. Time-dependent strength analyses have also been included based on static-fatigue test data for tuff. Since this revision is an extensive modification to the model and analysis documentation, the specific changes have not been tracked. The primary changes include the following: 1. Updated format, including renumbered pages, figures, and tables; and changing Attachments to Appendices. 2. Minor editorial corrections. 3. Updated superseded DTNs and references. 4. Updated impact analyses on thermal properties in response to superseded DTN (Appendix Q). 5. Updated FracMan fracture modeling in Section 6.1.6. 6. Added rockfall analyses to include ground motions with 1×10^{-4} and 1×10^{-5} annual probabilities of exceedance (Sections 6.3 and 6.4). 7. Added time-dependent strength analyses in Section 6.4.2 and Appendix S. (Continued on next page)

Change History

14. Revision No.	15. Description of Change
REV 03	(Continued from previous page) 8. Added rockfall modeling with a consideration of spatial variation of rock mass strength throughout the model region (Appendix S, Section S4). 9. Added discussion of limitations and uncertainties of the static-fatigue and long-term strength data used in the predictions of time-dependent behavior of emplacement drift excavations in Section 6.5. 10. Added an assessment of the sufficiency of the number of 3DEC simulations to represent the rockfall characteristics (Appendix K). 11. Added an assessment of spatial variation of lithophysal porosity in Appendix T. 12. Added a discussion of the methodology and verification of the interchange of output from the NUFT thermal calculation to the UDEC rockfall model (Appendix U). 13. Added details for the calculation of bulking of broken rock and the impact of stress arching in the broken rock above the drip shield (Appendix V). 14. Added details for boundary conditions in the thermal-mechanical model (Appendix W). 15. Added a listing of site-specific ground motion parameters (Appendix X). 16. Added validation of the UDEC drip shield model (Appendix Y). This revision corrects the errors identified in REV 02 Errata 001.

EXECUTIVE SUMMARY

Degradation of underground openings as a function of time is a natural and expected occurrence for any subsurface excavation. Over time, changes occur to both the stress condition and the strength of the rock mass due to several interacting factors. Once the factors contributing to degradation are characterized, the effects of drift degradation can typically be mitigated through appropriate design and maintenance of the ground support system. However, for the emplacement drifts of the geologic repository at Yucca Mountain, it is necessary to characterize drift degradation over a 10,000-year period, which is well beyond the functional period of the ground support system. This document provides an analysis of the amount of drift degradation anticipated in repository emplacement drifts for discrete events and time increments extending throughout the 10,000-year regulatory period for postclosure performance. This revision of the drift degradation analysis was developed to support the license application and fulfill specific agreement items between the U.S. Nuclear Regulatory Commission (NRC) and the U.S. Department of Energy (DOE).

The earlier versions of *Drift Degradation Analysis* (BSC 2001 [DIRS 156304]) relied primarily on the DRKBA numerical code, which provides for a probabilistic key-block assessment based on realistic fracture patterns determined from field mapping in the Exploratory Studies Facility (ESF) at Yucca Mountain. A key block is defined as a critical block in the surrounding rock mass of an excavation, which is removable and oriented in an unsafe manner such that it is likely to move into an opening unless support is provided. However, the use of the DRKBA code to determine potential rockfall data at the repository horizon during the postclosure period has several limitations:

- The DRKBA code cannot explicitly apply dynamic loads due to seismic ground motion.
- The DRKBA code cannot explicitly apply loads due to thermal stress.
- The DRKBA code, which determines structurally controlled key-block failure, is not applicable for stress-controlled failure in the lithophysal units.

To address these limitations, additional numerical codes have been included that can explicitly apply seismic and thermal loads, providing significant improvements to the analysis of drift degradation and extending the validity of drift degradation models.

KEY COMPONENTS OF REPOSITORY ROCKFALL MODELING

Rock Mass Characterization–The repository horizon is located in both lithophysal (lower lithophysal [Tptpll] and upper lithophysal [Tptpul] zones) and nonlithophysal (middle nonlithophysal [Tptpmn] and lower nonlithophysal [Tptpln] zones) rock units in the Topopah Spring Tuff. These two rock types are expected to have fundamentally different modes of failure under static and dynamic loading, and require different analysis methods. The nonlithophysal rocks, which comprise roughly 15 percent of the emplacement area, are hard, strong; jointed rock masses; whereas the lithophysal rocks, which comprise approximately 85 percent of the emplacement area, are relatively more deformable with lower compressive strength.

The geologic structure and rock strength defines the failure mode in the Tptpmn. The failure mode in the Tptpmn is due to gravity drop of rock blocks resulting from stress-induced yield in either the intact rock or the joint surfaces. The analysis of the failure mechanism is complicated somewhat by the fact that the jointing in the Tptpmn is of relatively short continuous trace length and is discontinuous in nature, thus forming fewer kinematically removable blocks. This type of jointing results in an inherently stronger rock mass as opposed to typical "blocky" rock masses where the block structure is well defined by multiple, continuous joint sets.

The Tptpll is characterized by about 10 to 30 percent lithophysal cavities by volume. This unit has abundant small-scale fractures between lithophysae that result in the relatively weaker nature of the material. Rock mass failure in the Tptpll is controlled by the transient ground motion induced stress concentrations that occur around the excavation. The mode of failure is primarily via tension from rarefaction of vertically traveling compression waves.

Seismic Ground Motion–Site-specific ground motions have been determined based on results from a probabilistic seismic hazard analysis. For a suite of ground motion measures, the probabilistic seismic hazard analysis determined the annual probability that various levels of ground motion would be exceeded. For an annual probability of exceedance of interest, a site response model modifies the ground motion from the probabilistic seismic hazard analysis by taking into account the effect of local site materials. Peak ground velocity determined from the site response model is used to develop seismic time histories (typically fifteen three-component sets) for postclosure rockfall analysis. The time histories are developed such that observed randomness among time histories, for a given peak ground velocity, is maintained. The time histories thus appropriately reflect variability in ground motion estimation for Yucca Mountain.

Thermal Stress–Once the waste packages are placed within the emplacement drifts, heat will be released as a part of the process of the radioactive materials in the waste packages becoming less radioactive over time. This heat will transfer to the rock mass and thermally induced stresses will be generated by thermal expansion of the rock mass. Thermal stresses at any location depend on the proximity and timing of waste emplacement, the amount of heat generated, the age of the waste, packaging and emplacement configuration, ventilation of the emplacement drifts, and the thermal-mechanical properties of the rock mass. Thermal stresses are time-dependent and are calculated over the 10,000-year regulatory period for postclosure performance.

Time-Dependent Degradation of Rock Strength–The rock mass surrounding the emplacement drifts may undergo over-stressing from thermal heating or time-dependent damage associated with static fatigue resulting from stress corrosion mechanisms. This damaged material may result in a slow unraveling (lithophysal rock) or block fallout (nonlithophysal rock). In the nonlithophysal rocks, static fatigue failure of roughness along fracture surfaces is possible and could result in gravitationally induced block failures. Static fatigue of hard rocks typically is associated with stress levels on the order of 80 percent or greater of the uniaxial compressive strength. This means that fatigue failure would presumably initiate along asperities on fracture surfaces, reducing their effective friction angle. In the case of the lithophysal rocks, the compressive stress concentrations along the immediate rib springline of the emplacement drifts will be near the uniaxial compressive strength so static fatigue failure is a distinct possibility.

ROCKFALL MODELING OF NONLITHOPHYSAL TUFF

A nonlithophysal rockfall model was developed using the three-dimensional discontinuum code, 3DEC. This model includes the development of fracture patterns generated from multiple sampling from a synthetic rock mass volume that contains a realistic fracture population based on field mapping data. Site-specific ground motion time histories appropriate for both the preclosure and postclosure time periods, are included in the model.

Degradation in the nonlithophysal units is primarily controlled by geologic structure. Preclosure ground motion results in minor drift damage due to rockfall. It should be noted that the results presented in this report are based on unsupported drift openings. The rockfall estimate during the preclosure period should be conservative, because the rockfall models do not consider ground support, while ground support will in fact be included to prevent rockfall. Postclosure ground motion results in varying extent of drift damage due to rockfall, with localized areas of rock failure sufficient to cover the drip shield.

Thermal-mechanical analyses were conducted using both a base case set of thermal properties and a sensitivity case considering the values for thermal conductivity and specific heat one standard deviation smaller than the mean. The transient temperature field around the repository was calculated using 90- and 70-percent ventilation heat removal efficiencies. There was minimal rockfall predicted at any time for the thermal only scenario (i.e., no seismic loading) for the cases analyzed. When thermal stresses were considered in combination with the stresses resulting from postclosure seismic ground motion, it is clearly shown that thermal loading significantly reduces the amount of rockfall.

Drift stability due to the effect of time-dependent rock joint degradation is assessed based on a reduction of joint cohesion and friction angle. The reduced joint strength parameters are estimated to be in the range of the residual state with joint cohesion reduced to zero and the joint friction angle reduced to 30 degrees. Dilation angle is also reduced to zero considering that the asperities on fracture surfaces had been sheared off. The degraded joint strength and dilational properties were applied for several selected cases, including the worst cases (cases with the most rockfall), the typical case, and the no rockfall case observed with postclosure seismic ground motion. While a slight increase in rockfall is predicted for the degradated state, joint strength degradation has a minor impact on drift stability.

ROCKFALL MODELING OF LITHOPHYSAL TUFF

A lithophysal rockfall model was developed using the two-dimensional discontinuum code, UDEC. In this model, the rock mass is represented as an assembly of polygonal, elastic blocks in which the bond strength of the blocks is calibrated such that the overall mechanical behavior of the mass is consistent with the material model developed for the lithophysal rock. The lithophysal rockfall model allows for the formation of fractures between blocks (i.e., the formation of internal fracturing), separation, and instability (under action of gravity) of the rock mass around the drift. Site-specific ground motion time histories appropriate for both the preclosure and postclosure periods, are included in the model. Thermal-mechanical analyses were conducted using both a base case set of thermal properties and a sensitivity case considering the values for thermal conductivity and specific heat one standard deviation smaller

than the mean. The transient temperature field around the repository was calculated using 90- and 70-percent ventilation heat removal efficiencies. The analysis was done for five categories of rock mass qualities, which represents the variability in lithophysal rock mechanical properties expected on the repository level. The lowest quality categories (1 and 2) represent the rock mass with 20 percent or greater lithophysal porosity, and make up less than about 10 percent of the repository host rock. Category 1, which represents the lowest quality/highest porosity rock, makes up less than 5 percent of the rock mass and thus represents localized conditions of high porosity rock found primarily near the top of the Tptpll. Categories 3, 4, and 5, which are representative of the rock mass with approximately 10 to 20 percent lithophysal porosity, are of higher geomechanical quality. Category 3, which represents rock with lithophysal porosity of approximately 15 to 20 percent, represents a typical rock quality condition.

Preclosure degradation in the lithophysal units is primarily controlled by stress conditions. The analyses show that the drifts are stable after excavation with fracturing extending to a maximum depth of less than 0.5 m in the drift walls for the poorest quality rock. No significant rockfall is predicted, due to heating, for any of the five rock mass categories irrespective of the considered ventilation efficiency (70 or 90 percent) and the selection of rock mass thermal properties. There is also no significant rockfall due to preclosure ground motion for rock mass Categories 1 through 5. A relatively minor amount of rockfall is predicted for preclosure seismic loading for the lowest quality, Category 1 rock mass. Little or no rockfall is predicted for other rock qualities for preclosure ground motions. Again, it should be noted that the modeled rockfall in the Tptpll is based on unsupported drift openings. The absence of ground support in the lithophysal rockfall model leads to a conservative rockfall estimate during the preclosure period, because the preclosure ground support will be designed to prevent rockfall.

The analyses of the available static fatigue data indicate that an approximate 40 percent reduction in cohesive strength occurs over a 20,000-year period. The nominal case for drift degradation (i.e., considering thermal and time-dependent effects, but excluding seismic effects) results in only partial collapse of the emplacement drifts at 20,000 years. The lower bound rock mass quality is represented as rock mass Category 2, which is considered to be less than 10 percent of the rock mass. A combination of the thermally induced stresses with time-dependent strength degradation results in time-dependent fracturing and a deterioration of the emplacement drift walls for Category 2, however, the drip shield is not expected to be covered during the postclosure period. As rock mass quality increases to categories 3 to 5, rockfall becomes less in volume with little change in drift profile. Coupling preclosure seismic ground motion with both time-dependent strength degradation and thermal load causes additional, but not significant, rockfall as a result of shaking down already loose, broken ground. Thus, the nominal scenario considers negligible drift degradation occurs over the postclosure period.

Postclosure ground motions cause drift collapse irrespective of rock mass quality or particular case of ground motion. The extreme conditions of drift deterioration due to rock mass strength degradation were analyzed. Cohesive strength (cohesion and tensile strength) was gradually reduced to zero and resulting rockfall was monitored. The model was set to achieve conservative conditions of bulking of the caved rock mass (i.e., such that larger vertical pressures are imposed). The resulting average vertical pressures of the rock on the drip shield are, with few exceptions, in the range between 150 kN/m^2 and 200 kN/m^2. The vertical and lateral pressures

associated with complete collapse of the emplacement drifts are conservatively used as input loading parameters for the design of the drip shield.

RESOLUTION OF KEY TECHNICAL ISSUES REGARDING ROCKFALL

The drift degradation models and analyses documented in this report address the requirements of NRC/DOE agreement items regarding rockfall and related issues to support the resolution of NRC's key technical issue (KTI) on Repository Design and Thermal-Mechanical Effects.

INTENTIONALLY LEFT BLANK

CONTENTS

Page

CONTENTS (Continued)

Page

CONTENTS (Continued)

Page

CONTENTS (Continued)

Page

CONTENTS (Continued)

Page

CONTENTS (Continued)

Page

CONTENTS (Continued)

Page

INTENTIONALLY LEFT BLANK

FIGURES

Page

FIGURES (Continued)

Page

FIGURES (Continued)

Page

FIGURES (Continued)

Page

FIGURES (Continued)

Page

FIGURES (Continued)

Page

FIGURES (Continued)

Page

FIGURES (Continued)

Page

FIGURES (Continued)

Page

FIGURES (Continued)

Page

FIGURES (Continued)

Page

FIGURES (Continued)

Page

FIGURES (Continued)

Page

FIGURES (Continued)

Page

FIGURES (Continued)

Page

FIGURES (Continued)

Page

FIGURES (Continued)

Page

FIGURES (Continued)

Page

FIGURES (Continued)

Page

FIGURES (Continued)

Page

FIGURES (Continued)

Page

FIGURES (Continued)

Page

FIGURES (Continued)

Page

FIGURES (Continued)

Page

TABLES

Page

TABLES (Continued)

Page

TABLES (Continued)

Page

TABLES (Continued)

Page

TABLES (Continued)

Page

TABLES (Continued)

Page

TABLES (Continued)

Page

INTENTIONALLY LEFT BLANK

ACRONYMS AND ABBREVIATIONS

ACRONYMS

BSC	Bechtel SAIC Company, LLC
DOE	U.S. Department of Energy
DRKBA	Discrete Region Key Block Analysis
DTN	data tracking number
EBS	engineered barrier system
ECRB	Enhanced Characterization of the Repository Block
ESF	Exploratory Studies Facility
FEPs	features, events, and processes
GSI	geological strength index
ICN	Interim Change Notice
KTI	key technical issue
LdB	Lac du Bonnet granite
LDTH	line-averaged heat source, drift scale, thermohydrologic
NRC	U.S. Nuclear Regulatory Commission
PFC	Particle Flow Code
PGV	peak ground velocity
RMR	rock mass rating
RQD	rock quality designation
TSPA-LA	Total System Performance Assessment for the License Application
UCS	unconfined compressive strength
YMP	Yucca Mountain Project

ABBREVIATIONS

CHn1	Calico Hills and Lower Paintbrush non-welded
CHn2	Calico Hills and Lower Paintbrush non-welded
TCw	Tiva Canyon welded
Tptpll	Topopah Spring Tuff crystal poor lower lithophysal
Tptpln	Topopah Spring Tuff crystal poor lower nonlithophysal
Tptpmn	Topopah Spring Tuff crystal poor middle nonlithophysal

ACRONYMS AND ABBREVIATIONS (Continued)

Tptpul	Topopah Spring Tuff crystal poor upper lithophysal
TSw1	Topopah Spring welded, lithophysal-rich
TSw2	Topopah Spring welded, lithophysal-poor
TSw3	Topopah Spring welded, vitrophyre

1. PURPOSE

The purpose of this report is to document the scientific analysis and modeling of the behavior of the rock mass surrounding the emplacement drifts of the geologic repository at Yucca Mountain. Drift degradation has the potential to affect drip shield integrity, waste package integrity, and thermal-hydrologic environments within drifts. The results of this modeling and analysis activity provide:

- Data on rockfall (size distribution, velocity, impact energy and impact location) in response to the combined effects of in situ, thermal and seismic loading to support structural analyses of the ground support system, the drip shield, and waste package.

- Transient change in drift profile (size and shape) due to combined in situ, thermal and seismic loading and due to nominal time-dependent change in rock mechanical properties, which supports analyses of groundwater seepage into the emplacement drift during the period of compliance for postclosure performance.

- Quasi-static load distribution to the drip shield from accumulated rubble for structural analysis of drip shield stability.

- Support for the assessment of in-drift temperature and humidity resulting from the presence of rubble within the emplacement drift.

Figure 1-1 is a schematic that depicts the required inputs supporting the drift degradation analysis along with the primary users of the results of this study. In addition to acquired data from field mapping (i.e., fracture geometry) and laboratory testing (i.e., rock strength properties), the following analysis and modeling reports provide developed data inputs for this report:

- *Geologic Framework Model (GFM2000)* (BSC 2004 [DIRS 170029])

- *Development of Earthquake Ground Motion Input for Preclosure Seismic Design and Postclosure Performance Assessment of a Geologic Repository at Yucca Mountain, NV* (BSC 2004 [DIRS 170027])

- *Multiscale Thermohydrologic Model* (BSC 2004 [DIRS 169565])

- *Thermal Conductivity of the Potential Repository Horizon* (BSC 2004 [DIRS 169854])

- *Thermal Conductivity of Non-Repository Lithostratigraphic Layers* (BSC 2004 [DIRS 170033])

- *Heat Capacity and Thermal Expansion Coefficients Analysis Report* (BSC 2003 [DIRS 164670])

- *Sampling of Stochastic Input Parameters for Rockfall Calculations and for Structural Response Calculations Under Vibratory Ground Motion* (BSC 2004 [DIRS 169999]).

The outputs from the drift degradation analysis support scientific analyses, models, and design calculations, including the following:

- *Abstraction of Drift Seepage*
- *Seismic Consequence Abstraction*
- *Structural Stability of a Drip Shield Under Quasi-Static Pressure*
- *Drip Shield Structural Response to Rock Fall*.

This report has been developed in accordance with *Technical Work Plan for: Regulatory Integration Modeling of Drift Degradation, Waste Package and Drip Shield Vibratory Motion and Seismic Consequences* (BSC 2004 [DIRS 171520]). The drift degradation analysis includes the development and validation of rockfall models that approximate phenomenon associated with various components of rock mass behavior anticipated within the repository horizon. Two drift degradation rockfall models have been developed: the rockfall model for nonlithophysal rock and the rockfall model for lithophysal rock. These models reflect the two distinct types of tuffaceous rock at Yucca Mountain. The output of this modeling and analysis activity documents the expected drift deterioration for drifts constructed in accordance with the repository layout configuration (BSC 2004 [DIRS 164519]).

1.1 BACKGROUND

Information on the Geologic Setting and Repository Subsurface Design–The repository site at Yucca Mountain is located approximately 300 m below ground surface within the Topopah Spring formation—a densely welded, laterally-expansive tuff unit comprised of a number of subunits that dip gently from west to east (BSC 2004 [DIRS 170029], Section 6.5.1.4). These subunits can be divided into two broad physical and mechanical categories: nonlithophysal and lithophysal[1] welded tuffs. The basic matrix material of these two subunits is similar in most respects (mineralogical, textural, mechanical properties). However, due to varying cooling histories and as a result of position within the flow, they are, structurally (and therefore thermomechanically), significantly different in character. The nonlithophysal rocks (the middle and lower nonlithophysal units) are hard, strong, fine-grained and fractured volcanic rocks whose mechanical behavior is strongly controlled by the geometry and surface characteristics of its fracturing. The lithophysal rocks (the upper and lower lithophysal units) are composed of the same strong, hard matrix material, but have porosity in the form of lithophysal cavities ranging from about 10 percent to 30 percent by volume. The presence of these cavities results in significantly different mechanical behavior (i.e., in the deformability and strength) of the rock mass.

[1] Lithophysae–A hollow, bubble like cavity in a volcanic rock that is surrounded by a porous rim formed by fine-grained alkali feldspar, quartz, and other minerals. Lithophysae are typically a few centimeters to a few decimeters in diameter; however, they can be as small as 1 mm in diameter or less to as large as 1 m or more in diameter (BSC 2003 [DIRS 166660]).

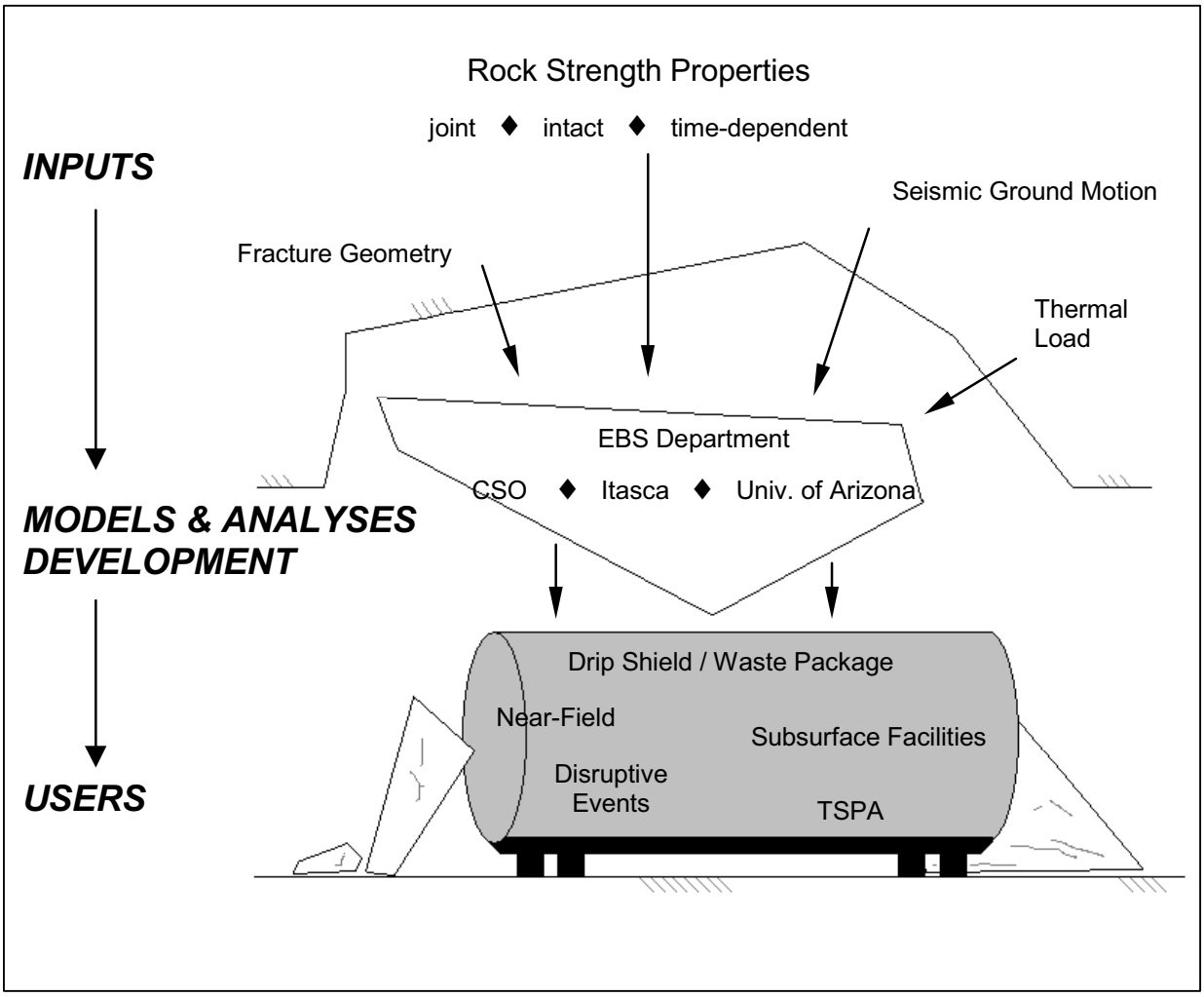

Figure 1-1. Drift Degradation Analysis

The proposed repository layout and the Topopah Spring Tuff subunits within which the excavations are located are shown in Figure 1-2. The repository consists of a series of emplacement panels that are accessed via ramps and access mains from the ground surface. The emplacement drifts are circular in the cross-section with a diameter of 5.5 m (BSC 2003 [DIRS 165572], Table 8), and driven at 81-m spacing (Williams 2002 [DIRS 159916]). This layout results in approximately 85 percent of the emplacement area to be within the lithophysal rocks, and about 15 percent within the nonlithophysal units (BSC 2003 [DIRS 165572], Table II-2).

Waste packages will be delivered to the emplacement drift from the surface facilities on steel pallets. The waste package assembly will be placed, using remote handling equipment, on a steel framework and crushed tuff drift invert at a nominal 10 cm end-to-end spacing. The nominal waste package heat output and spacing result in a maximum thermal loading density of 1.45 kW/m of drift length (BSC 2004 [DIRS 167369]). The waste packages will be ventilated for a minimum of 50 years using forced ventilation air at a nominal delivery rate of 15 m^3/sec per emplacement drift (BSC 2004 [DIRS 169862], Section 4.1.10). This ventilation air removes

approximately 80 to 90 percent of the heat generated by the waste packages along the typical 600-m nominal emplacement drift length (BSC 2004 [DIRS 169862], Section 6.6, Figure 6-7) during the ventilation period, with resulting drift wall temperatures being approximately 80°C (BSC 2004 [DIRS 169862], Section 6.6, Figure 6-5). Closure of the repository is considered to occur within 100 years after emplacement of the first waste package. Closure involves placing drip shields in a continuous covering over the waste packages, backfilling of the access drifts, and cessation of forced ventilation. Drift wall temperatures will rapidly rise, reaching a maximum at approximately 160°C about 20 years after closure, followed by a slow decay over time. The drift wall temperature will remain above 100°C for approximately 1,000 years (see Section 6.2, Figure 6-25).

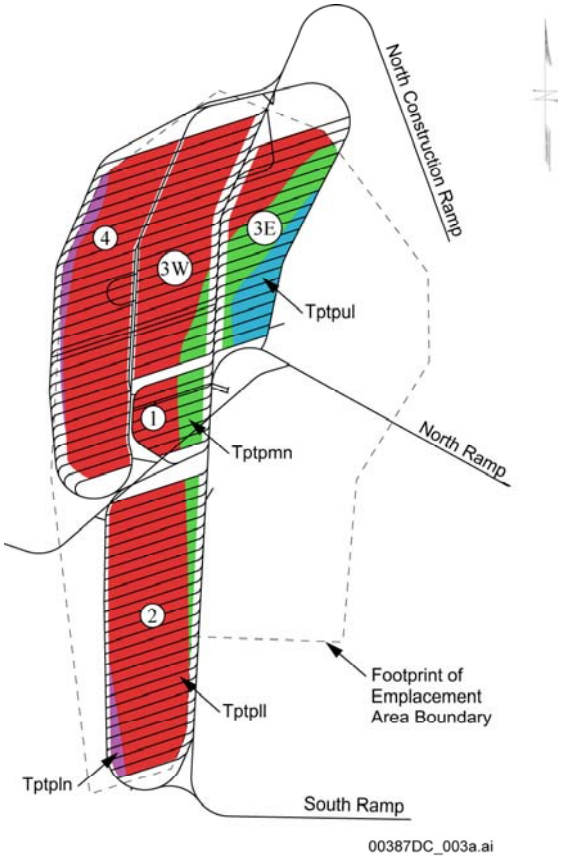

Source: *Underground Layout Configuration* (BSC 2003 [DIRS 165572], Figure II-2).

NOTE: Numbered labels refer to emplacement panel numbers (BSC 2003 [DIRS 165572], Section 8.1).

Figure 1-2. Proposed Repository Layout in Plan View Showing Intersections of Geologic Sub-units With Emplacement Drifts

Preclosure and Postclosure Periods and Objectives of Mechanical Degradation Analyses– Ground support will be functional and maintained during the preclosure period. After closure, the ground support will corrode and lose its function over the period of perhaps tens to hundreds of additional years. Thus, the emplacement drifts will essentially be unsupported through a greater part of the postclosure period.

During the postclosure period, the emplacement drifts will be subjected to the following loading conditions (Figure 1-3):

- In situ gravitational stress state
- Transient thermally induced stresses due to expansion of the rock mass[2]
- Seismic stresses due to potential earthquake shaking.

In addition, the rock mass strength, particularly in lithophysal rock, will exhibit a degree of time-dependency as a result of typical stress corrosion mechanisms[3]. The impact of these in situ and induced stress components is the potential for rock mass yield in the immediate region around the tunnels and some degree of rockfall. The rockfall has potential performance impacts on the following systems:

- Mechanical degradation effects on engineered barriers

  – Effects include possible rock particle impacts and dynamic loading of the drip shield, either under gravitational or earthquake-induced accelerations. The dynamic loading from rock impact derived from this document provides input to *Drip Shield Structural Response to* Rock *Fall*, which is a calculation providing a structural damage assessment due to rockfall impacts.

  – Quasi-static loading and contact from rock particles resting on the drip shield following rockfall. The quasi-static loading from rubble derived from a degraded emplacement drift presented in this document provides input to *Structural Stability of a Drip Shield Under Quasi-Static Pressure*, which is a calculation providing a structural stability assessment of the drip shield under rubble loading.

- Mechanical degradation effects on in-drift environment

  – Rockfall of sufficient volume could result in an "insulating" blanket surrounding the drip shield (and waste package), impairing heat transfer to the rock mass, and increasing waste package temperatures. The importance of this effect on heat transfer is dependent on the timing of the rockfall. For example, if significant amounts of rockfall occur relatively early in the postclosure period when the waste package is still outputting significant heat energy, then there will be a greater impact on waste package temperature. Conversely, if significant rockfall occurs in later periods of the postclosure period when the waste package has lost most of its energy, then there will be a less significant impact on temperature distributions. Additionally, rock particles within the drift can potentially alter the in-drift humidity environment and, therefore, need to be accounted for in drip shield and waste package corrosion. The impact of a complete collapse of an emplacement drift at various times in the postclosure period

[2] A large portion of the thermally induced strains and stress are recoverable as the rock mass cools over time.
[3] "Stress Corrosion" is a term used for time-dependent, sub-critical crack growth that occurs when existing material flaws in the rock are subjected to stresses that are near the failure state of the material. This process, which occurs at a more rapid rate in the presence of moisture, may result in damage and yield at applied stresses that are less than the short-term strength. Corrosion here does not refer to corrosion of metals.

on in-drift temperature and humidity is analyzed in *Multiscale Thermohydrologic Model* (BSC 2004 [DIRS 169565]).

- Mechanical degradation effects on seepage of groundwater into the drift
  - Drift degradation could result in temporal changes to the size and shape of the emplacement drifts, as well as impact to the capillary flow barrier provided by the drift itself. These effects could alter the seepage flow to the drift. Impacts of seepage are accounted for in the seismic scenario class and are described in *Seismic Consequence Abstraction* and in *Abstraction of Drift Seepage*.

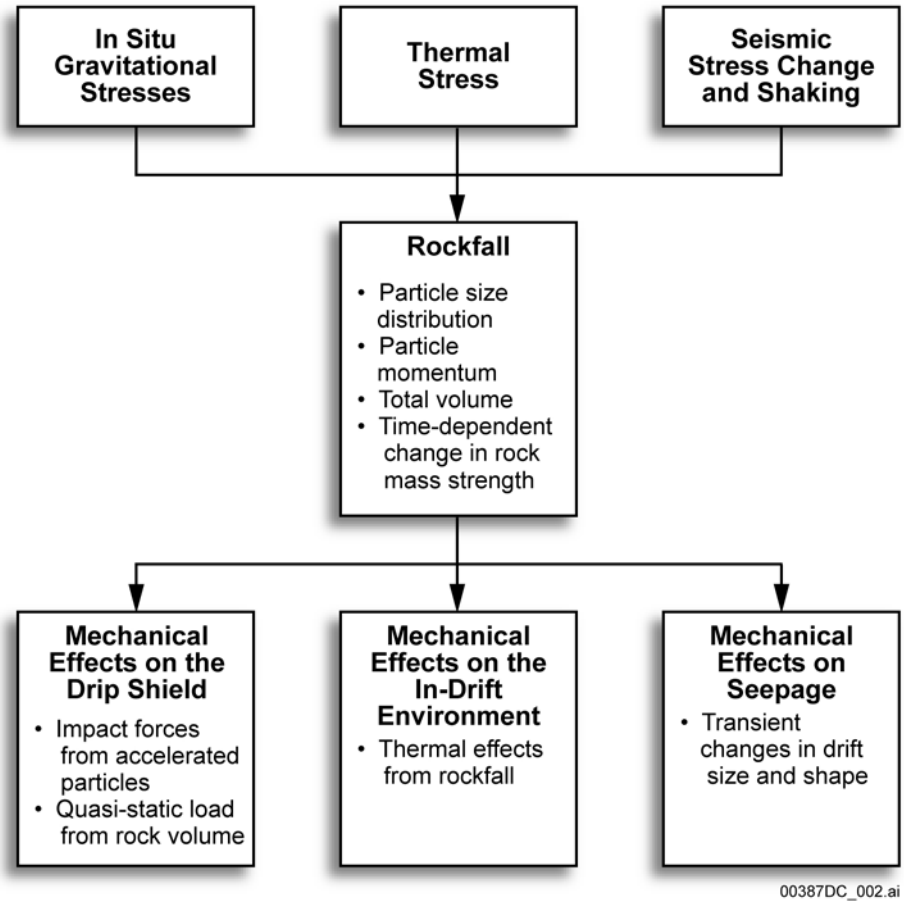

Figure 1-3. Potential Postclosure Performance Impacts of Rockfall on Engineered Barriers, In-Drift Environment, and Groundwater Seepage into Drifts

The primary objectives of the drift degradation analyses discussed in this analysis and model report are to provide postclosure estimates of the temporal development of both rockfall and drift dimension changes, which are input to the seismic consequences and drift seepage abstractions for eventual inclusion into the total system performance assessment (TSPA) modeling.

Summary of Approach to Addressing Mechanical Degradation Issues–The approach to addressing the mechanical degradation issues described above was presented in *Resolution*

Strategy for Geomechanically-Related Repository Design and Thermal-Mechanical Effects (RDTME) (Board 2003 [DIRS 165036]). A basic factor in the approach described in that report is that the repository host rock mass may be subdivided into two general thermomechanical units: lithophysal and nonlithophysal rocks, as was described previously. This subdivision is made as the mechanical properties and behavior of these units are distinctly different, and, thus, the response requires different testing and modeling strategies. In the case of the nonlithophysal subunit, the rock mass response is largely controlled by the fracturing; whereas, in the lithophysal rock, the mechanical response is highly dependent on the lithophysal porosity and its variability. It is recognized that, due to the impact of the geologic structure on the rock mass performance, detailed geotechnical characterization is required as a basic building block in formulating the rock mass properties, applicable modeling techniques, and analysis procedures.

The approach (Figure 1-4), which forms the basis of the analyses presented in this report, involves the progressive development of a knowledge of the mechanical behavior of lithophysal and nonlithophysal rock through:

- Detailed geotechnical characterization of the rock structure, laboratory, and field testing and estimation of rock mass properties
- Development and validation of numerical modeling tools for estimation of mechanical degradation processes
- Performance analyses of mechanical degradation in response to in situ, thermal, and seismic loading.

This report presents data and analyses in these three broad areas:

- Geological characterization of the lithophysal and nonlithophysal rock mass and development of rock mass properties and their variability
  - Description and analysis of the variability of rock mass fracturing and lithophysae characteristics obtained from field mapping in the ESF and Enhanced Characterization of the Repository Block (ECRB) Cross-Drift (Sections 6.1 and Appendix B describe fracture characteristics, and Sections 7.3 and Appendix O describe lithophysal characteristics)
  - Laboratory and in situ testing database of thermal-mechanical and time-dependent material properties for the intact rock matrix, lithophysal rock, and fractures (Section 4 and Appendix E describe the rock properties database)
  - Estimation of the effect of geologic structure (fractures and lithophysae) and its variability on rock mass properties (Section 7.3 and Appendix E)

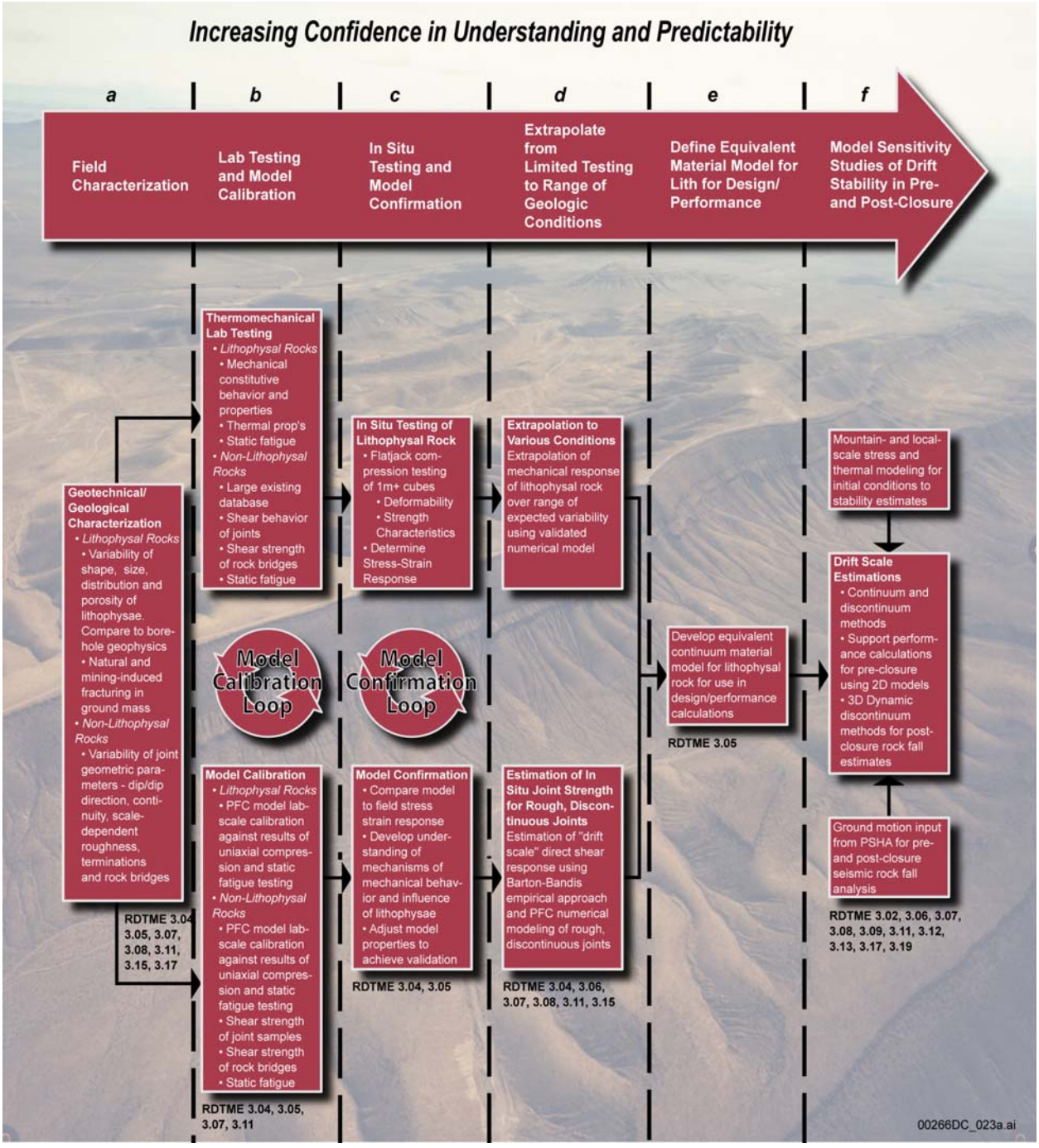

NOTE: Process starts with compilation and analysis of basic geotechnical mapping, followed by laboratory and field testing and model validation to develop rock mass property estimates for design and performance sensitivity studies.

Figure 1-4. General Approach to Resolution of the Repository Design and Thermal-Mechanical Effects KTIs

- Development and validation of numerical modeling tools

  – Determination or development of appropriate models for sensitivity studies of excavation stability and rockfall under gravitational, thermal, and seismic loading as well as time-dependent strength changes (Sections 6.3, 6.4, 7, and Appendices S, T, U, W, and Y). Specific issues related to selection of appropriate modeling techniques addressed in these sections of the report include:

    -- Continuum versus discontinuum modeling
    -- Two versus three-dimensional models
    -- Appropriate initial and boundary conditions
    -- Inclusion of time-dependency in the models

- Mechanical degradation performance analyses and feeds of model output to engineered barrier system and drift seepage abstractions to the TSPA model

  – Stability analysis and rockfall estimates for nonlithophysal and lithophysal subunits under the action of in situ, thermal, and seismic loading (Section 6)

  – Assessment of long-term stability and rockfall in tunnels subject to time-dependent rock mass strength degradation and in situ, thermal, and seismic loading (Appendix S).

1.2 OBJECTIVES

The specific objectives of the drift degradation analysis are to:

- Provide validated modeling methods that adequately represent:

  – The mechanical response of the rock mass structure (fractures and lithophysae) surrounding the emplacement drift

  – The applied in situ, thermal, and seismic loading conditions and time-dependent rock strength degradation mechanisms.

- Provide a statistical description of block sizes and rockfall volume resulting from stress-induced rockfall around the emplacement drifts for the lithologic units of the repository host horizon.

- Provide dynamic and static load distributions to the drip shield resulting from rockfall and rubble accumulation in the emplacement drifts

- Estimate transient changes in emplacement drift profiles resulting from in situ, thermal, and seismic stressing and time-dependent rock strength degradation.

1.3 SCOPE OF MODEL DOCUMENTATION

Activities documented in this report involve developing models, using analytical methods, and performing calculations and statistical analyses to determine the expected quantities, locations, size distributions, and frequencies of rockfall, based on the repository layout configuration (BSC 2004 [DIRS 164519]). Drift profiles, including the predicted deterioration as a result of rockfall, have been determined. This analysis has examined unsupported drifts with no backfill, and applied static, thermal, and seismic loading conditions.

The scope of model documentation required for analyzing the degradation anticipated in the repository emplacement drifts includes the following activities:

- Conduct a thermal-mechanical assessment of the repository block at Yucca Mountain to determine thermal stress inputs to the drift degradation models.
- Conduct a fracture degradation assessment to account for long-term strength degradation. This assessment provides strength degradation inputs to the drift degradation models.
- Develop a drift degradation structural model for nonlithophysal rock that includes thermal and seismic loading.
- Develop a drift degradation lithophysal model that includes thermal and seismic loading.

Revision 1 ICN 1 of this analysis (BSC 2001 [DIRS 156304]) considered various emplacement drift orientations, with the drift azimuth varied in appropriate increments to examine the effect of orientation on key block size and frequency. The results from this drift orientation study have not been included in this revision, and only the current emplacement drift orientation (BSC 2004 [DIRS 164519]) has been considered in this report.

1.4 ANALYSIS/MODEL APPLICABILITY AND LIMITATIONS

The drift degradation results with seismic and thermal consideration, including the drift profiles, are applicable for 5.5-m-diameter emplacement drifts oriented at an azimuth of 72º in accordance with the repository underground layout configuration (BSC 2004 [DIRS 164519]; BSC 2004 [DIRS 168489]; BSC 2003 [DIRS 165572]). The model results presented in this report are applicable to the lithophysal and nonlithophysal rock units of the repository host horizon. Uncertainties associated with the data available for model development are described in Section 6.5. The rockfall models presented in this report are valid for conditions anticipated within the repository over the 10,000-year regulatory period for both preclosure and postclosure performance, including increased loads due to seismic ground motion and thermal stress, and decreased rock strength due to time-dependent strength degradation.

2. QUALITY ASSURANCE

This analysis and modeling report and the supporting modeling activities are subject to the Office of Civilian Radioactive Waste Management quality assurance program, as indicated in *Technical Work Plan for: Regulatory Integration Modeling of Drift Degradation, Waste Package and Drip Shield Vibratory Motion and Seismic Consequences* (BSC 2004 [DIRS 171520], Section 8). Approved QA procedures identified in the technical work plan (BSC 2004 [DIRS 171520], Section 4) have been used to conduct and document the activities described in this analysis and model report. The technical work plan also identifies the methods used to control the electronic management of data (BSC 2004 [DIRS 171520], Section 8) during modeling and documentation activities.

To ensure accuracy and completeness of the information generated by this report, access to the information on the personal computer used to develop this report is controlled with password protection. The personal computer files are stored on a network drive that is backed up daily per Yucca Mountain Project (YMP) standards. Upon completion of this work, the files are transferred to a suitable media, appropriately labeled, and verified by examining the file listing. Visual checks are conducted on printouts. The electronic files generated by this report are transmitted to Document Control for transfer to the Records Processing Center. During the checking process, accuracy and completeness of the data retrieved and reported in this document is verified against the information placed in the Records Processing Center and YMP information databases, as applicable.

This model report examines the properties of natural or engineered barriers that are classified in the *Q-List* (BSC 2004 [DIRS 168361]) as "Safety Category" because they are important to waste isolation, as defined in AP-2.22Q, *Classification Analyses and Maintenance of the Q-List*. It contributes to the analysis and modeling data used to support performance assessment. The conclusions of this model report do not affect the proposed repository design or engineered features important to safety, as defined in AP-2.22Q.

INTENTIONALLY LEFT BLANK

3. USE OF SOFTWARE

3.1 QUALIFIED COMPUTER SOFTWARE

All controlled and baselined software used in the development of the drift degradation analysis is identified in Table 3-1, including the software tracking number, version, operating environment, and range of use. Table 3-1 also includes a discussion of why the software was selected and describes any limitations on outputs from the software. The software documented in this section is appropriate for the applications used in this drift degradation analysis, and is consistent with its intended use. Each software item was obtained from Software Configuration Management in accordance with LP-SI.11Q-BSC. All software was used only within the range of its validation as specified in the software qualification documentation, in accordance with LP-SI.11Q-BSC. The input and output files for each software item used in this analysis have been submitted to the Technical Data Management System as noted in Appendix A.

Table 3-1. List of Qualified Software Supporting the Drift Degradation Analysis

Software Title/Version	Software Tracking Number	Operating Environment (Platform/Operating System)	Brief Description of Software (Range of Use/Selection/Limitations)
UDEC V3.1 (BSC 2002 [DIRS 161949])	10173-3.1-00	PC/Windows 2000	UDEC was used to analyze the seismic and thermal effects on block movement in the lithophysal rock units (Section 6.4). UDEC was selected for its capability of modeling block slip and block separation in plane strain condition. Also, it is capable of thermal and dynamic simulation. There are no known limitations on outputs.
3DEC V2.01 (BSC 2002 [DIRS 161930])	10025-2.01-00	PC/Windows 2000	3DEC was used to analyze the seismic and thermal effects on block movement in the nonlithophysal rock units (Section 6.3). 3DEC was selected for its capability of modeling of wedge type of rockfall with consideration of block slip and block separation in three-dimensional space. Also, it is capable of thermal and dynamic simulation. There are no known limitations on outputs.
FLAC V4.0 (BSC 2002 [DIRS 161953])	10167-4.0-00	PC/Windows 2000	FLAC was used in the thermal-mechanical calculation to define the distribution of stresses around the drifts due to the progressive heating of the repository area (Section 6.2). FLAC was selected as an efficient code to run thermal-mechanical analysis. There are no known limitations on outputs.
FLAC3D V2.1 (BSC 2002 [DIRS 161947])	10502-2.1-00	PC/Windows 2000	FLAC3D was used in the thermal-mechanical calculation to define the distribution of stresses around the drifts due to the progressive heating of the repository area (Appendix C). FLAC3D was selected as an efficient code to run thermal-mechanical analysis for the regional scale and drift scale. There are no known limitations on outputs.

Table 3-1. List of Qualified Software Supporting the Drift Degradation Analysis (Continued)

Software Title/Version	Software Tracking Number	Operating Environment (Platform/Operating System)	Brief Description of Software (Range of Use/Selection/Limitations)
PFC2D V2.0 (BSC 2002 [DIRS 161950])	10828-2.0-00	PC/Windows 2000	PFC2D was used to characterize rock mass behavior, including the analysis of long-term strength degradation (Section 7 and Appendix S). PFC2D was selected for its capability of modeling behaviors of a rock material by combining behaviors of individual grain particles to simulate complicated non-linear deformation of a rock material including long-term mechanical strength degradation and rock mass deformation with voids. There are no known limitations on outputs from PFC2D.
PFC2D V2.0 (BSC 2004 [DIRS 169930])	10828-2.0-01	PC/Windows 2000	This version of PFC2D was used to run impact analyses to confirm the initial PFC2D results (using software tracking number 10828-2.0-00), as documented in Appendix Q. The initial PFC2D software qualification did not specifically identify the library of support functions (known as Fish functions) that are used within the code. This new version (software tracking number 10828-2.0-01) specifically qualifies FishTank 041b, which is the library of Fish functions included within the code. The impact assessments in Appendix Q confirm that the results are identical using either the initial or new version of PFC2D.
PFC3D V2.0 (BSC 2002 [DIRS 160612])	10830-2.0-00	PC/Windows 2000	PFC3D was used to characterize rock mass behavior, including the analysis of long-term strength degradation (Section 7 and Appendix S). PFC3D was selected for its capability of modeling behaviors of a rock material by combining behaviors of individual grain particles to simulate complicated non-linear deformation of a rock material including long-term mechanical strength degradation and rock mass deformation with voids. There are no known limitations on outputs from PFC3D.
PFC3D V2.0 (BSC 2004 [DIRS 169931])	10830-2.0-01	PC/Windows 2000	This version of PFC3D was used to run impact analyses to confirm the initial PFC3D results (using software tracking number 10830-2.0-00), as documented in Appendix Q. The initial PFC3D software qualification did not specifically identify the library of support functions (known as Fish functions) that are used within the code. This new version (software tracking number 10830-2.0-01) specifically qualifies FishTank 041b, which is the library of Fish functions included within the code. The impact assessments in Appendix Q confirm that the results are identical using either the initial or new version of PFC3D.

Table 3-1. List of Qualified Software Supporting the Drift Degradation Analysis (Continued)

Software Title/Version	Software Tracking Number	Operating Environment (Platform/Operating System)	Brief Description of Software (Range of Use/Selection/Limitations)
DRKBA Version 3.31 (BSC 2002 [DIRS 161946])	10071-3.31-00	PC/Windows 2000	DRKBA was used to analyze block development and failure in the nonlithophysal rock units (Appendix D). DRKBA was selected to assess the impact of small-scale fractures on rockfall because it has an efficient key-block simulation algorithm. DRKBA was also selected as an alternative numerical code to verify the results from 3DEC. DRKBA does not directly apply seismic and thermal loads, and therefore was not selected as the primary code for rockfall analyses.
FracMan V2.512 (USGS 1999 [DIRS 160577])	10114-2.511-00	PC/Windows NT	FracMan was used to replicate the fracture geometry observed in the ESF to develop a representative volume of jointed rock mass (Section 6.1.6). FracMan was selected for its capability of discrete fracture data analysis, geologic fracture network construction, spatial analysis, and visualization. There are no known limitations on outputs.
NUFT V3.0s (LLNL 2002 [DIRS 157280])	10088-3.0s-01	SUN/SUN O.S. 5.7	NUFT was used to simulate heat transfer around the emplacement drift (Section 6.2). NUFT was selected for its capability of modeling thermal-hydrology of an unsaturated zone including subsurface heat and fluid flow. There are no known limitations on outputs from NUFT.
EarthVision V.5.1 (Dynamic Graphics 2000 [DIRS 167994])	10174-5.1-00	SGI/IRIX 6.5	EarthVision was used to extract stratigraphic unit thickness and cross-sections from the Geological Framework Model (GFM2000) (Appendix M). EarthVision was selected for its capability of extracting specific data from GFM2000 and presenting the data in a common graphical format. EarthVision was not used to perform data manipulation in this report. There are no known limitations on outputs based on the range of use in this report.
UNWEDGE V2.3 (CRWMS M&O 1998 [DIRS 145366])	30053 V2.3	PC/DOS Emulation	UNWEDGE was used as a reference-only example of a deterministic method for key-block analysis (Appendix D). UNWEDGE was selected for its common usage on static block analysis for the geotechnical and mining industries. There are no known limitations on outputs.
Clustran V.1.1 (BSC 2004 [DIRS 169203])	11162-1.1-00	PC/Windows 2000	Clustran was used to analyze fracture data in Section 6.1.6. Clustran was selected for its common usage on fracture orientation analysis for the geotechnical and mining industries. There are no known limitations on outputs.

Table 3-1. List of Qualified Software Supporting the Drift Degradation Analysis (Continued)

Software Title/Version	Software Tracking Number	Operating Environment (Platform/Operating System)	Brief Description of Software (Range of Use/Selection/Limitations)
Read DXF V.1.0 (BSC 2004 [DIRS 169204])	11159-1.0-00	PC/Windows 2000	Read DXF was used to read fracture data files in DXF format and extract polyline data with associated strike/dip tags for input into FracMan (Section 6.1.6). Read DXF was specifically developed to extract fracture data from full periphery geologic maps to facilitate the comparison of field fracture data to synthetic FracMan fracture data. There are no known limitations on outputs.

3.2 OTHER SOFTWARE

In addition to the above listed items, the standard functions of commercial off-the-shelf software, including both Microsoft Excel 97 SR-2 and Mathcad 2001i Professional, were used. These software items were used to perform support calculation activities as described in Section 6.3, Section 6.4, and associated Appendices. Appendix A provides a listing of the calculation files (Table A-1), including the location in this report where specific details of the calculation can be found. Microsoft Excel was used to calculate joint cohesion degradation, excavation orientation inputs, joint description input, and mean rock property values. Additionally, Microsoft Excel was used to process and summarize rockfall data and to provide graphical presentation of the block size distribution data. Mathcad was used to calculate joint cohesion degradation, joint description input parameters, and rock property values. Microsoft Excel 97 SR-2 and Mathcad 2001i Professional are exempted software applications in accordance with LP-SI.11Q-BSC, Section 2.1.

Appendices D, E, I, J, K, L, O, and T have been provided with this report to document the use of standard functions of commercial off-the-shelf software in sufficient detail to allow independent repetition of the software in accordance with AP-SIII.10Q, Attachment 2. Specifically, these Appendices provide:

- The formula or algorithm used
- A listing of the inputs to the formula or algorithm
- A listing of the outputs from the formula or algorithm
- Narrative to describe the calculation(s).

These Appendices document the following calculations:

- Calculation of joint parameter inputs to DRKBA (Appendix D)
- Calculation of joint cohesion reduction for thermal and time-dependent effects in DRKBA analyses (Appendix D)
- Calculation of the plane equations to describe the excavation opening as input to DRKBA (Appendix D)

- Calculation of rock property values (Appendix E)
- Random selection of 3DEC modeling region (Appendix J)
- Study of the sufficiency of the number of 3DEC simulations to represent the rockfall characteristics (Appendix K)
- Conversion of FracMan fracture output to 3DEC input (Appendix L)
- Calculation of descriptive statistics of lithophysal abundance and characteristics (Appendix O)
- Projection of lithophysal cavity porosity to a vertical cross section (Appendix T)
- Calculation of Power Spectral Density and summary of ground motion parameters (Appendix X)

DIPS Version 4.03 (CRWMS M&O 1997 [DIRS 149839]) was used solely for graphical presentation of fracture data in Sections 6.1, 6.3, and Appendix B, and is an exempted software application in accordance with LP-SI.11Q-BSC, Section 2.1.

INTENTIONALLY LEFT BLANK

4. INPUTS

4.1 DIRECT INPUT

The geotechnical parameters used as direct input for drift degradation analyses include data and information collected either by field mapping or by laboratory testing. Input data include

- Joint geometry
- Joint mechanical properties
- Intact rock physical and mechanical properties
- Rock mass mechanical properties
- Seismic ground motion
- Rock thermal properties
- Repository layout information.

These data and parameters are summarized in Table 4-1 and described below. Uncertainties in input data and parameters are discussed in Section 6.5.

4.1.1 Fracture Geometry Data

The development of fracture geometry parameters is based on mapping data collected from the ESF, including the main loop (which is composed of the North Ramp, Main Drift, South Ramp) and the ECRB Cross-Drift. Qualified joint mapping data in the ESF were collected from the following lithologic units: the Topopah Spring Tuff crystal poor upper lithophysal zone (Tptpul), the Topopah Spring Tuff crystal poor middle nonlithophysal zone (Tptpmn), the Topopah Spring Tuff crystal poor lower lithophysal zone (Tptpll), and the Topopah Spring Tuff crystal poor lower nonlithophysal zone (Tptpln).

Mapping data from the ESF being used in the analysis include both U.S. Geological Survey/U.S. Bureau of Reclamation full periphery geologic maps and the detailed line survey. Source data tracking numbers (DTNs) for the full periphery geologic maps and the detailed line survey data are listed in Table 4-1.

Table 4-1. Input Data and Parameters for the Drift Degradation Analysis

Parameter		Value	Range	Source/*Supporting Information* [a]	Application
Fracture geometry	Fracture type – from detailed line survey (Location, Strike, Dip, Length)	See files *Tptpmn DLS pole plot.xls* and *Tptpll cu# & rad dist plots.xls* in FracMan Inputs & Outputs (Appendix A) Data summary provided by Table 6-2 (Tptpmn); Appendix B, Table B-1 (Tptpll)	See files *Tptpmn DLS pole plot.xls* and *Tptpll cu# & rad dist plots.xls* in FracMan Inputs & Outputs (Appendix A) Data summary provided by Table 6-2 (Tptpmn); Appendix B, Table B-1 (Tptpll)	GS971108314224.025 DIRS 106025] GS960708314224.008 DIRS 105617] GS000608314224.004 [DIRS 152573] GS960708314224.010 [DIRS 106031] GS960908314224.014 [DIRS 106033] GS970208314224.003 [DIRS 106048] GS970808314224.010 [DIRS 106050] GS971108314224.028 [DIRS 106047] GS990408314224.001 [DIRS 108396] GS990408314224.002 [DIRS 105625]	Rockfall Model for Nonlithophysal Rock (Sections 6.1.6, 6.3.1.2.2, Appendix D) Rockfall Model for Lithophysal Rock (Section 6.4.3, Appendix B)
	Fracture type – from full periphery geologic map	Full periphery geologic maps provided by the source DTNs Data summary provided by Table 6-2 (Tptpmn); Appendix B, Table B-1 (Tptpll)	Full periphery geologic maps provided by the source DTNs Data summary provided by Table 6-2 (Tptpmn); Appendix B, Table B-1 (Tptpll)	GS960908314224.020 [DIRS 106059] GS000608314224.006 [DIRS 152572] GS960908314224.015 [DIRS 108372] GS960908314224.016 [DIRS 107373] GS960908314224.017 [DIRS 108376] GS970108314224.002 [DIRS 107490] GS990408314224.004 [DIRS 108405] GS990408314224.005 [DIRS 108408] GS990408314224.006 [DIRS 108409]	
Small-scale fracture geometry	Fracture type – from detailed line survey (Location, Strike, Dip, Length)	See Appendix A, calculation file, *small trace filtering.xls* Data summary provided by Table 6-37 and Figure 6-105	See Appendix A, calculation file, *small trace filtering.xls* Data summary provided by Table 6-37 and Figure 6-105	GS040108314224.001 [DIRS 169591]	Rockfall Model for Nonlithophysal Rock (Sections 6.1.4.1, 6.3.3)

Table 4-1. Input Data and Parameters for the Drift Degradation Analysis (Continued)

Parameter			Value	Range	Source/*Supporting Information* [a]	Application
Fracture strength	Rotary shear tests	Joint normal stress, σ (MPa); Joint peak shear stress, τ_p (MPa); Joint dilation (deg)	See Appendix E, Table E-3	See Appendix E, Table E-3	SNL02112293001.003 [DIRS 108412], Olsson and Brown 1997 [DIRS 106453]; SNL02112293001.005 [DIRS 108413], SNL 1996 [DIRS 165408]; SNL02112293001.007 [DIRS 108414], SNL 1996 [DIRS 165410]	Rockfall Model for Nonlithophysal Rock (Section 6.3.1.1, 6.3.1.6.2; Appendix E, Section E2)
		Joint normal stiffness, K_n (MPa/mm); Joint shear stiffness, K_s (MPa/mm)	See Appendix E, Table E-4	See Appendix E, Table E-4		
	Direct shear tests	Joint cohesion (MPa); Joint friction angle (deg); Joint dilation (deg); Joint shear stiffness, K_s (MPa/mm)	See Appendix E, Table E-5	See Appendix E, Table E-5	BSC 2003 [DIRS 166660], Tables 8-47 and 8-52	Rockfall Model for Nonlithophysal Rock (Section 6.3.1.6.2; Appendix E, Section E2)

Table 4-1. Input Data and Parameters for the Drift Degradation Analysis (Continued)

Parameter		Value	Range	Source/*Supporting Information* [a]	Application
Intact rock strength for nonlithophysal rock	Young's modulus (GPa); Poisson's ratio	See Appendix E, Table E-6	See Appendix E, Table E-6	MO0402DQRIRPPR.003 [DIRS 168901]	Rockfall Model for Nonlithophysal Rock (Section 6.3.1.1; Appendix E, Section E3)
	Tensile strength (MPa)	See Appendix E, Table E-7	See Appendix E, Table E-7	MO0401DQRIRPTS.003 [DIRS 168905]	
	Ultimate differential strength (MPa) (also referred to as compressive strength, intact rock triaxial compressive strength, or intact rock uniaxial compressive strength); Confining pressure, σ_3 (MPa)	See Appendix E, Table E-8	See Appendix E, Table E-8	MO0311RCKPRPCS.003 [DIRS 166073]	
Rock mass strength for lithophysal rock	Compressive strength (MPa) (also referred to as ultimate differential strength, intact rock triaxial compressive strength, or intact rock uniaxial compressive strength); Young's modulus (GPa); Poisson's ratio	See Appendix E, Table E-9	See Appendix E, Table E-9	SN0208L0207502.001 [DIRS 161871] SN0211L0207502.002 [DIRS 161872] MO0311RCKPRPCS.003 [DIRS 166073]	Rockfall Model for Lithophysal Rock (Section 6.4.1.2; Appendix E, Section E4.1)
	Long-term strength (static fatigue)	See Appendix S, Table S-1, Figure S-1, Figure S-2	See Appendix S, Table S-1, Figure S-1, Figure S-2	Martin et al. (1997a [DIRS 165960]) [b] Schmidtke and Lajtai (1985 [DIRS 164774]) [b] Lau et al. (2000 [DIRS 164769]) [b]	Rockfall Model for Lithophysal Rock (Section 6.4.2.4; Appendix S, Section S2

Table 4-1. Input Data and Parameters for the Drift Degradation Analysis (Continued)

Parameter			Value	Range	Source/*Supporting Information* [a]	Application
Rock mass strength for thermal-mechanical units	Q system input parameters from tunnel mapping in the ESF	Rock quality designation (RQD), J_n, J_r, J_a	See Appendix A, calculation file, *rock mass strength v2.xls*, worksheet "Spatial Data"	See Appendix A, calculation file, *rock mass strength v2.xls*, worksheet "Spatial Data"	GS950508314224.003 [DIRS 107488], *Singleton 1995 [DIRS 107044]*; GS000608314224.005 [DIRS 166002], *USGS 1996 [DIRS 169024]*; GS960408314224.001 [DIRS 168135], *USGS 1996 [DIRS 169025]*; GS960408314224.003 [DIRS 168136], *USGS 1996 [DIRS 169026]*; GS960708314224.009 [DIRS 168137], *USGS 1996 [DIRS 169027]*; GS000608314224.006 [DIRS 152572], *USGS 1996 [DIRS 169029]*; GS960908314224.015 [DIRS 108372], *USGS 1996 [DIRS 169030], and USGS 1996 [DIRS 169031]*; GS960908314224.016 [DIRS 108373], *USGS 1996 [DIRS 169032], and USGS 1996 [DIRS 169033]*; GS960908314224.017 [DIRS 108376], *USGS 1996 [DIRS 169034]*; GS970108314224.002 [DIRS 107490], *USGS 1996 [DIRS 169035]*; GS970208314224.004 [DIRS 107492], *USGS 1997 [DIRS 169036]*; GS970808314224.009 [DIRS 107494], *USGS 1997 [DIRS 169037]*; GS970808314224.011 [DIRS 107495], *USGS 1997 [DIRS 169038]*; GS970808314224.013 [DIRS 107497], *USGS 1997 [DIRS 169039]*; GS990408314224.003 [DIRS 108404], *USGS 1999 [DIRS 169018]*; GS990408314224.004 [DIRS 108405], *USGS 1999 [DIRS 169019]*; GS990408314224.005 [DIRS 108408], *USGS 1999 [DIRS 169020]*; GS990408314224.006 [DIRS 108409], *USGS 1999 [DIRS 169021]*	Thermal-Mechanical Calculation (Section 6.2; Appendix C; Appendix E, Section E4.3)

Table 4-1. Input Data and Parameters for the Drift Degradation Analysis (Continued)

Parameter			Value	Range	Source/*Supporting Information* [a]	Application
Rock mass strength for thermal-mechanical units	Intact unconfined compressive strength for thermal-mechanical units, σ_{ci} (MPa) (also referred to as intact rock uniaxial compressive strength or ultimate differential strength)		See Appendix A, calculation file, *rock mass strength v2.xls*, worksheet "Intact Strength"	See Appendix A, calculation file, *rock mass strength v2.xls*, worksheet "Intact Strength"	MO0311RCKPRPCS.003 [DIRS 166073] SNL02030193001.001 [DIRS 120572] SN0306L0207502.008 [DIRS 165015]	Thermal-Mechanical Calculation (Section 6.2; Appendix C; Appendix E, Section E4.3)
	Intact Poisson's ratio for thermal-mechanical units; Intact Young's modulus for thermal-mechanical units (GPa)		See Appendix A, calculation file, *rock mass strength v2.xls*, worksheet "Intact Strength"	See Appendix A, calculation file, *rock mass strength v2.xls*, worksheet "Intact Strength"	MO0402DQRIRPPR.003 [DIRS 168901]] SN0306L0207502.008 [DIRS 165015]	
Rock mass strength in the Heated Drift	Q system input parameters from tunnel mapping in the Heated Drift	RQD, J_n, J_r, J_a	See Appendix E, Table E-13	See Appendix E, Table E-13	GS970608314224.007 [DIRS 158430], USGS 1997 [DIRS 169040]	Rockfall Model for Nonlithophysal Rock (Section 6.3.1.6.4; Appendix E, Section E4.2)
	Ultimate differential strength (MPa) (also referred to as compressive strength, intact rock triaxial compressive strength, or intact rock uniaxial compressive strength)		See Appendix E, Table E-14	See Appendix E, Table E-14	MO0311RCKPRPCS.003 [DIRS 166073]	
	material constant for intact rock, m_i		33.87	—	BSC 2003 [DIRS 166660], Table 8-39	
Block strength for nonlithophysal rock	Uniaxial compressive strength $(\sigma_{ax})_u$ (MPa) (also referred to as intact rock uniaxial compressive strength or ultimate differential strength)		See Appendix E, Table E-17	See Appendix E, Table E-17	MO0311RCKPRPCS.003 [DIRS 166073]	Rockfall Model for Nonlithophysal Rock (Section 6.3.1.6.4; Appendix E, Section E4.4)

Table 4-1. Input Data and Parameters for the Drift Degradation Analysis (Continued)

Parameter		Value	Range	Source/*Supporting Information* [a]	Application
Thermal conductivity (W/m°C)		See Appendix E, Table E-18	See Appendix E, Table E-18	SN0303T0503102.008 [DIRS 162401], *BSC 2004 [DIRS 170033]*; SN0404T0503102.011 [DIRS 169129], *BSC 2004 [DIRS 169854]*	Thermal-Mechanical Calculation (Section 6.2; Appendix C; Appendix E, Section E5)
Rock specific heat (J/kg°C)		See Appendix E, Table E-19	See Appendix E, Table E-19	SN0307T0510902.003 [DIRS 164196]	
Thermal expansion coefficient (/°C)		See Appendix E, Table E-20	See Appendix E, Table E-20	SNL01B05059301.006 [DIRS 129168]	
Initial heat load (kW/m)		1.45 kW/m	—	BSC 2004 [DIRS 167369]	
Rock density	Rock density for thermal-mechanical units	See Appendix E, Table E-1	See Appendix E, Table E-1	SN0303T0503102.008 [DIRS 162401], *BSC 2004 [DIRS 170033]*; SN0404T0503102.011 [DIRS 169129], *BSC 2004 [DIRS 169854]*	Thermal-Mechanical Calculation (Section 6.2; Appendix C; Appendix E, Section E1)
	Rock density at the repository horizon	See Appendix E, Table E-2	See Appendix E, Table E-2	SNL02030193001.027 [DIRS 108410]	Rockfall Model for Nonlithophysal Rock (Section 6.3.1.1; Appendix E, Section E1); Rockfall Model for Lithophysal Rock (Section 6.4)
In situ stress	Intermediate principal stress, σ_2 (MPa) (horizontal)	2.9 MPa N15°E (Direction)	± 0.4 MPa ± 14°	SNF37100195002.001 [DIRS 131356]	Thermal-Mechanical Calculation (Appendix C); Rockfall Model for Nonlithophysal Rock (Section 6.3.1.1); Rockfall Model for Lithophysal Rock (Section 6.4)
	Minor principal stress, σ_3 (MPa) (horizontal)	1.7 MPa N75°W (Direction)	± 0.1 MPa ± 14°		

Table 4-1. Input Data and Parameters for the Drift Degradation Analysis (Continued)

Parameter		Value	Range	Source/*Supporting Information* [a]	Application
Regional geology - stratigraphic thickness		See Appendix E, Tables E-1, E-18, E-19	—	MO0012MWDGFM02.002 [DIRS 153777]	Thermal-Mechanical Calculation (Appendix C; Appendix E, Sections E1 and E5)
Repository layout		See Appendix C, Sections C2 and C3	See Appendix C, Sections C2 and C3	BSC 2004 [DIRS 164519], BSC 2003 [DIRS 165572]	Thermal-Mechanical Calculation (Appendix C)
Emplacement drift orientation		72° drift azimuth	—	BSC 2004 [DIRS 164519], BSC 2003 [DIRS 165572]	Rockfall Model for Nonlithophysal Rock (Section 6.3.1.1) Rockfall Model for Lithophysal Rock (Section 6.4.2.2, Appendix Y)
Emplacement drift diameter (m)		5.5 m	—	BSC 2004 [DIRS 168489]	
Drip shield, waste package, and invert geometry		See Appendix Y, Table Y-1; Appendix A, calculation file, *impact velocity bounding cal for preclosure rockfall rev1.mcd*	—	BSC 2004 [DIRS 169220], BSC 2004 [DIRS 168489], BSC 2004 [DIRS 169472], BSC 2004 [DIRS 169503]	
Seismic ground motion	5×10^{-4} per year	See Section 6.3.1.2.1 (Tables 6-5, 6-6, 6-7; Figure 6-36), Appendix X	See Section 6.3.1.2.1 (Tables 6-5, 6-6, 6-7; Figure 6-36), Appendix X	MO0407TMHIS104.003 [DIRS 170599]	Rockfall Model for Nonlithophysal Rock (Section 6.3.1.2, Appendix X) Rockfall Model for Lithophysal Rock (Section 6.4.2.2)
	1×10^{-4} per year			MO0306SDSAVDTH.000 [DIRS 164033]	
	1×10^{-5} per year			MO0402AVDTM105.001 [DIRS 168890]	
	1×10^{-6} per year [c]			MO0403AVDSC106.001 [DIRS 168891] MO0301TMHIS106.001 [DIRS 161868];	
	1×10^{-7} per year			MO0403AVTMH107.003 [DIRS 168892]	

Table 4-1. Input Data and Parameters for the Drift Degradation Analysis (Continued)

Parameter	Value	Range	Source/*Supporting Information* [a]	Application
Sampling of Stochastic Input Parameters	See Section 6.3.1.2.2 (Table 6-8) and Section 6.4.2.2 (Table 6-44)	See Section 6.3.1.2.2 (Table 6-8) and Section 6.4.2.2 (Table 6-44)	MO0301SPASIP27.004 [DIRS 161869]	Rockfall Model for Nonlithophysal Rock (Section 6.3.1.2) Rockfall Model for Lithophysal Rock (Section 6.4.2.2)
Lithophysal abundance	See Appendix O	See Appendix O	GS021008314224.002 [DIRS 161910] GS040608314224.001 [DIRS 171367]	Rockfall Model for Lithophysal Rock (Section 6.4)

[a] The italicized supplemental references listed along with the source DTNs provide either summary or supporting information that is linked to the source DTN, and provide direct input for this analysis and model report.

[b] Long-term strength data are provided by outside sources and qualified for use in this report (Appendix S, Section S2.1.2) in accordance with the requirements of AP-SIII.10Q, Section 5.2.

[c] Note that two sets of 1×10^{-6} time histories are provided. The difference in these sets is described in DTN: MO0403AVDSC106.001 [DIRS 168891], file *10-6 TH memo.doc*. The original set (i.e., DTN: MO0301TMHIS106.001 [DIRS 161868]) is used in Section 6.4.2.2. Since this ground motion results in complete drift collapse for lithophysal rock, it was not necessary to repeat the analyses using the revised set (i.e., DTN: MO0403AVDSC106.001 [DIRS 168891].

DRKBA Fracture Geometry Inputs–Studies by the U.S. Geological Survey/U.S. Bureau of Reclamation have generated data on "small-scale" fractures with trace lengths less than 1 m (DTN: GS040108314224.001 [DIRS 169591]). These data were collected at six locations in the Tptpmn (2 locations), Tptpll (3 locations), and Tptpln (1 location). These data are used in this analysis to provide an assessment of the impact of the small trace length fracture data on rockfall development (Section 6.3.3).

3DEC Fracture Geometry Inputs–The 3DEC software uses source fracture geometry inputs provided in Table 4-1. These inputs are then developed to produce a 100-m x 100-m x 100-m rock mass volume that contains a three-dimensional generation of fracture data derived from the field mapping data using a Poisson process (Section 6.1.6). Fractures are generated within this volume as circular disks with their size, dip, and dip direction determined based on field data. The location of each fracture plane within the three dimensional space is also provided. Details for sampling within this rock mass volume to select fracture patterns for 3DEC modeling are provided in Section 6.3.1.2.2.

4.1.2 Fracture Mechanical Properties Data

Fracture strength is characterized by cohesion, friction angle, dilation, and stiffness. Joint cohesion (C_j) and friction angle (ϕ_j) values were developed in Appendix E based on laboratory shear strength test data from core specimens (see Appendix E, Table E-3). Mean value and standard deviation are required as the inputs for the DRKBA and 3DEC structural analyses. The calculation of mean values in Appendix E (Section E2) is consistent with *Yucca Mountain Site Geotechnical Report* (CRWMS M&O 1997 [DIRS 103564], p. 5-143). Joint stiffness values (K_n and K_s) are required as inputs for 3DEC, and are documented in Appendix E (Table E-4) based on laboratory shear strength test data from core specimens. Joint dilation data are provided based on the laboratory shear strength test data from core specimens (see Appendix E, Table E-3). Note that for 3DEC analyses, dilation was conservatively selected to be zero, resulting in a higher estimation of rockfall (see Section 6.3.1.1).

4.1.3 Intact Rock Physical and Mechanical Properties Data

The mean rock density value used in rockfall modeling (Sections 6.3 and 6.4) was calculated based on data from laboratory tests performed on rock cores from the North Ramp geotechnical and the systematic drilling boreholes (see Appendix E, Table E-2). The saturated bulk density (ρ) of 2.41 g/cc (see Appendix E, Table E-2) for the Tptpln unit was used in each of the rockfall models in this analysis. This value is in agreement with the mean Tptpln saturated bulk density reported in the *Yucca Mountain Site Geotechnical Report* (CRWMS M&O 1997 [DIRS 103564], p. 5-26). That document also indicates that the mean density for the Tptpln unit is the highest mean value compared to other units of the repository horizon (i.e., the Tptpul, Tptpmn, Tptpll, and Tptpln) (CRWMS M&O 1997 [DIRS 103564], pp. 5-25 and 5-26). The use of the mean density for the Tptpln unit to represent the density of the rock units in this analysis results in a larger mass of rock blocks, and is, therefore, conservative. The thermal-mechanical calculation (Section 6.2) uses density inputs grouped according to thermal-mechanical units. The calculation of mean density values for each thermal-mechanical unit is also documented in Appendix E (Table E-1).

Mean elastic rock properties from the TSw2 thermal-mechanical unit, including a Young's modulus (E) of 33.6 GPa and a Poisson's ratio (ν) of 0.20, were used in this analysis for modeling nonlithophysal rock as calculated in Appendix E (Table E-6). Elastic rock properties were determined from laboratory tests performed on rock cores from the North Ramp geotechnical and the systematic drilling boreholes. The calculation of mean values in Appendix E is consistent with *Yucca Mountain Site Geotechnical Report* (CRWMS M&O 1997 [DIRS 103564], pp. 5-88 and 5-96). Intact bulk modulus (K) and intact shear modulus (G) for nonlithophysal rock were calculated based on the mean values of E and ν using Equations E-2 and E-3, respectively, as documented in Appendix E (Section E3).

Tensile strength data for the TSw2 thermal-mechanical unit were obtained from indirect tensile strength tests performed by the Brazilian Test method using core specimens (Appendix E, Table E-7). The mean tensile strength from this data is 8.9 MPa.

Triaxial strength data (see Appendix E, Table E-8) are used to calculate intact cohesion and friction angle of the nonlithophysal rocks. The calculation of cohesion and friction angle is documented in Appendix E, resulting in a cohesion of 36 MPa and a friction angle of 50 degrees.

4.1.4 Rock Mass Properties Data

4.1.4.1 Strength of Lithophysal Rock

Mechanical properties for lithophysal rock were determined based on available laboratory testing data on large rock cores from drilling in the ECRB Cross-Drift and Busted Butte (Appendix E, Section E4.1.3 and Table E-9). Values of cohesion (C), bulk modulus (K), and shear modulus (G) for lithophysal rock were calculated based on values of unconfined compressive strength (σ_c), Young's modulus (E), and Poisson's ratio (ν) as documented in Appendix E (Section E4.1).

4.1.4.2 Rock Mass Elastic Properties for Thermal-Mechanical Units

The rock mass properties data used in this report include modulus of deformation and Poisson's ratio for each of the thermal-mechanical units (see Appendix E, Table E-16). The rock mass properties data were calculated based on the intact rock data from laboratory testing and the Q system input parameters from tunnel mapping in the ESF identified in Table 4-1. Note that Q system parameters J_n, J_r, and J_a are provided by the supplemental sources cited in Table 4-1 (see *italicized* references in Table 4-1). Since the verified source DTNs providing the Q values have been calculated using the parameters J_n, J_r, and J_a, the supplemental sources providing the Q system data are also qualified and verified.

The rock mass modulus of deformation data is provided for five rock mass categories representing the range of rock mass conditions encountered in ESF tunnels. The five rock mass categories correspond to 5 percent, 20 percent, 40 percent, 70 percent, and 90 percent probabilities of occurrence, and are provided to be consistent with geotechnical design analyses (BSC 2004 [DIRS 170292], Section 3.1.4). Mid-range values corresponding to a 40 percent probability of occurrence were used in this analysis, which provides an approximate estimate of the mean value. This data is appropriate for its use in the thermal-mechanical calculation (Section 6.2), which provides an assessment of the regional stresses anticipated within the rock

mass. Poisson's ratio for the rock mass was determined to be equal to the Poisson's ratio from intact laboratory tests based on recent field testing (see Appendix E, Table E-16).

4.1.4.3 Rock Mass Properties for the Heated Drift in the ESF

Rock mass properties for the Heated Drift are calculated using the Hoek-Brown failure criterion (Hoek et al. 2002 [DIRS 162204]) as documented in Appendix E (Section E4.2). The inputs needed include rock mass classification data using the Q system as provided in Appendix E (Table E-13). Additionally, intact unconfined compressive strength (σ_{ci}) is required input for the Hoek-Brown method (Table E-14). The calculated rock mass properties using these data are provided in Appendix E (Table E-15).

4.1.4.4 Block Strength of Nonlithophysal Rock

The strength of large-scale intact rock block material (i.e., between joints) for nonlithophysal rock is calculated based on available size-effect laboratory compression test data from Price (1986 [DIRS 106589]). The size-effect data are presented in Appendix E (Table E-17). The approach for extrapolating this data to the block scale is documented in Appendix E (Section E4.4).

4.1.5 Seismic Ground Motion Data

Seismic ground motion time history data were provided for the following hazard levels: 5×10^{-4} per year, 1×10^{-4} per year, 1×10^{-6} per year, and 1×10^{-7} per year. DTNs for each of these ground motion levels are listed in Table 4-1. The ground motion data for the postclosure ground motion levels (i.e., 1×10^{-6} and 1×10^{-7}) each include 15 sets (three components) of time histories at the repository horizon. The sets were developed by scaling recorded motions such that their integrated peak particle velocities match expected point repository horizon particle velocities for the hazard level under consideration. Additionally, a desirable feature of the 15 sets is a magnitude distribution reflective of the horizontal component peak particle velocity deaggregation. This ensures a reasonable and defensible distribution of spectral shapes and time history durations. Conditioning on expected peak particle velocity alone was considered desirable as damage to underground structures is most strongly correlated with this point measurement, recognizing that underground (at-depth) spectral shapes are generally not identical to surficial or outcrop spectral shapes due to the effects of down going wave fields (BSC 2004 [DIRS 170027], Section 6.3.2).

The ground motion data for preclosure annual exceedance probabilities (i.e., 5×10^{-4} and 1×10^{-4}) consist of a single three-component set of time histories. These sets were developed such that the response spectra of the time histories match the design response spectra for the hazard level at the repository horizon.

4.1.6 Rock Thermal Properties Data

A regional thermal-mechanical calculation has been developed as part of this drift degradation analysis (Section 6.2), and uses the following thermal properties data (see Table 4-1 and Appendix E, Section E5 for parameter values and source DTNs):

- Thermal conductivity (W/m°K)
- Rock specific heat (J/kg°K)
- Thermal expansion (/°C)
- Heat decay curve.

4.1.7 Repository Layout Information

Repository layout information (Table 4-1), including emplacement drift diameter and azimuth, is provided by repository design and performance assessment information exchange drawings (BSC 2004 [DIRS 164519]; BSC 2004 [DIRS 168489]) and *Underground Layout Configuration* (BSC 2003 [DIRS 165572], Sections 5.1.4 and 8.7).

4.1.8 Matrix and Fracture Hydrologic Properties Data

A temperature-history calculation has been developed as part of this analysis (Section 6.2) based on a two-dimensional drift scale thermohydrologic model from *Multiscale Thermohydrologic Model* (BSC 2004 [DIRS 169565]) and DTN: LL030808623122.036 [DIRS 165790]. Matrix and fracture hydrologic properties data used in the calculation are provided in DTN: LL030808623122.036 [DIRS 165790] as a part of the NUFT input files (i.e., file *dkm-afc-1Dds-mc-mi-04*). Summaries of the matrix and fracture hydrologic properties data are also available in DTN: LB0205REVUZPRP.001 [DIRS 159525] and DTN: LB0208UZDSCPMI.002 [DIRS 161243].

4.1.9 In Situ Stress Data

In situ stress data were determined by hydraulic fracturing in a borehole located in the Tptpmn unit in the Thermal Test Facility in the ESF (DTN: SNF37100195002.001 [DIRS 131356]; CRWMS M&O 1997 [DIRS 147458], pp. 15, 19, and 20). The in situ stress measurements included a series of five hydraulic fracturing tests, resulting in an estimate of the state of stress in the ESF as shown in Table 4-1. The vertical stress shown in Table 4-1 was calculated based on the depth of cover in the Thermal Test Facility at the test borehole location. The in situ stress for each emplacement drift will vary depending on the cover depth on top of the drift. The approximated values assigned for the in situ stress for the rockfall modeling activities in Sections 6.3 and 6.4 are adequate and insensitive to the results judging the magnitude of the induced seismic and thermal stress.

4.2 CRITERIA

This model report addresses acceptance criteria from Sections 2.2.1.3.1.3 and 2.2.1.3.2.3 of *Yucca Mountain Review Plan, Final Report* (NRC 2003 [DIRS 163274]) regarding the degradation of engineered barriers and the mechanical disruption of engineered barriers.

Acceptance criteria from the *Yucca Mountain Review Plan* include the following:

- AC1: System description and model integration are adequate
- AC2: Data are sufficient for model justification
- AC3: Data uncertainty is characterized and propagated through the model abstraction
- AC4: Model uncertainty is characterized and propagated through the model abstraction
- AC5: Model abstraction output is supported by objective comparison.

The *Yucca Mountain Review Plan* criteria are based on meeting the requirements of 10 CFR 63.114(a)–(c) and (e)–(g), relating to the degradation and mechanical disruption of engineered barriers model abstractions. A mapping between the Acceptance Criteria and subcriteria and where they are addressed in this document is provided in Section 8.2 (see Table 8-1).

Similarly, the *Project Requirements Document* (Canori and Leitner 2003 [DIRS 166275], Table 2-3) expresses these requirements as follows:

- PRD-002/T-014 "Performance Objectives for the Geologic Repository After Permanent Closure" (traceable to 10 CFR 63.113)

- PRD-002/T-015 "Requirements for Performance Assessment" (traceable to 10 CFR 63.114)

This report was therefore prepared to comply with subparts of the NRC high-level waste rule, 10 CFR Part 63. Relevant requirements for performance assessment from Section 114 of that document are:

> Any performance assessment used to demonstrate compliance with Sec. 63.113 must: (a) Include data related to the geology, hydrology, and geochemistry ... used to define parameters and conceptual models used in the assessment. (b) Account for uncertainties and variabilities in parameter values and provide for the technical basis for parameter ranges, probability distributions, or bounding values used in the performance assessment. ... (g) Provide the technical basis for models used in the performance assessment such as comparisons made with outputs of detailed process-level models and/or empirical observations (e.g., laboratory testing, field investigations, and natural analogs).

4.3 CODES, STANDARDS, AND REGULATIONS

There are no codes and standards applicable to this drift degradation analysis. The regulation that is applicable to the development of this document is 10 CFR Part 63 [DIRS 156605], specifically 10 CFR 63.113 and 10 CFR 63.114.

5. ASSUMPTIONS

The following assumptions have been used in this drift degradation analysis.

5.1 THERMAL-MECHANICAL CALCULATION

5.1.1 Simultaneous Emplacement

Assumption: The thermal-mechanical calculation in this report assumes that generation of heat from the waste packages occurs simultaneously throughout the repository. The entire repository begins heating at the same time because sequential emplacement of waste packages has not been considered.

Basis: This assumption is necessary because design information is available only for the emplacement drift layout (BSC 2004 [DIRS 164519]), and not for the emplacement schedule.

Confirmation Status: This assumption does not require further confirmation, because results from the thermal-mechanical calculation should be the most conservative based on this assumption (i.e., the assumption produces increased heat and greater stresses in the rock mass). Sequential emplacement may cause an additional internal stress between the emplacement drifts and the remaining drifts. This internal stress will be insignificant during the preclosure period, because the majority of the heat load will be removed from the emplacement drifts due to ventilation (Section 5.1.2). The effects of the internal stress are expected to be minor during the postclosure period, because the waste packages will cool down significantly during the preclosure period, and the repository temperature is expected to be homogenized due to heat conduction between the drifts during the preclosure period. A range of temperatures has been considered in the rockfall analyses presented in this report (Sections 6.3.1.3 and 6.4.2.3), and the rockfall results are relatively insensitive to the temperature changes evaluated.

Use in the Analysis/Model: This assumption is used in the thermal-mechanical calculation of regional (repository-scale) and local (drift scale) temperature and thermal stress (Sections 6.2, 6.3.1, and 6.4.2; Appendix C).

5.1.2 Ventilation Heat Removal Ratio

Assumption: During the ventilated preclosure period, 90 percent of the decay heat output is removed from the emplacement drift system.

Basis: The basis of this assumption is provided from the ventilation model supporting a license application (BSC 2004 [DIRS 169862]), which has integrated heat removal ratios (averaged spatially and temporally) of 88 percent and 90 percent for the 50-year preclosure ventilation period and 600-m long drifts (MO0306MWDASLCV.001 [DIRS 165695] and MO0306MWDALAFV.000 [DIRS 163961], respectively).

Confirmation Status: No further confirmation is needed for this assumption because sensitivity calculation regarding the heat removal ratio was conducted covering the heat removal ratio down to 70 percent (Section 6.2). The calculation showed that the results of rockfall analyses are not sensitive to heat removal ratio over this range. Heat removal ratio that is a function of time and

distance from the drift inlet was considered in an impact analyses (Appendix Q). The impact analyses also showed that the results of rockfall analyses are not sensitive to the heat removal ratio.

Use in the Analysis/Model: This assumption is used in the preclosure thermal-mechanical calculations except the ventilation sensitivity calculation (Sections 6.2, 6.3.1, and 6.4.2; Appendix C). Because of this assumption it is accurate to model the preclosure period by simply reducing the decay heat output to 10 percent of its non-ventilated rate.

5.1.3 Thermal Expansion

Assumption: Thermal expansion values used in the underlying layers (CHn1 and CHn2) under the repository units (TSw2) are assumed to be equal to those for the repository layers.

Basis: This assumption is necessary because the test data from core samples are limited.

Confirmation Status: This assumption does not require further confirmation because temperature increase in the underlying layers is insignificant and thermally induced stresses are negligible.

Use in the Analysis/Model: This assumption is used in the thermal-mechanical calculations throughout the report (Sections 6.3.1 and 6.4.2; Appendix C).

5.2 ROCKFALL MODELING

5.2.1 Joint Position Parameter in DRKBA

Assumption: The positioning parameter required as joint parameter input is assumed to be the offset measured from the center of the trace length to the scan line of the detailed line survey.

Basis: This is the best available way to represent the positioning parameter because the determination of the true positioning parameter requires the three dimensional information of the joint plane that is not available.

Confirmation Status: This assumption does not require further confirmation. This approach is considered conservative because the offset measured from the one-dimensional scan line is smaller than the true offset in three-dimensional space (the probability of forming a key block is higher with a smaller offset value). The DRKBA rockfall results are used for confirmation only. This assumption does not impact the rockfall output documented in this report.

Use in the Analysis/Model: This assumption is used in Section 6.3.3 and Appendix D.

5.2.2 Block Size Distribution for Potential Rockfall in Lithophysal Units

Assumption: Block size distribution is assumed as a function of inter-lithophysal fracture density and lithophysae spacing.

Basis: This assumption is needed because the size of rock particles that are created from the lithophysal rocks is estimated from geologic and empirical evidence.

Confirmation Status: This assumption does not require further confirmation. The relatively abundant uniformly distributed lithophysae combined with fracturing fabric provide natural breaking surfaces. Observation in the ECRB Cross-Drift for block sizes on the order of a few inches in diameter supports this assumption (Appendix O).

Use in the Analysis/Model: This assumption is used in Section 6.4.

INTENTIONALLY LEFT BLANK

6. MODEL DISCUSSION AND ANALYSIS RESULTS

This section documents the models and analyses conducted to predict the postclosure drift degradation resulting from thermally induced stresses, seismically induced rockfall, and possible time-dependent static fatigue mechanisms.

The potential exists for rockfall to occur as a result of shaking induced by earthquakes. The models and analyses described in this section quantify possible seismically induced rockfall over the 10,000-year regulatory postclosure period. Geologic mapping is used to define a "synthetic" or representative rock mass that is sampled randomly to create possible rock masses in which the tunnel is simulated. Numerical models (two- or three-dimensional, depending on the lithology in question), with input geometry and properties based on the geologic variability, are used to make rockfall estimates for ground motion levels whose amplitude is based on the probability of occurrence in terms of annual exceedance frequency. For each annual exceedance frequency, a number of probabilistically based, site-specific ground motions have been developed and used to provide the transient boundary conditions to the models. The resulting rockfall, in terms of the tonnage of the maximum size rock particle, total tonnage for a given simulated length of tunnel, and the velocity of rock particles, has been determined.

The rock mass surrounding the excavations may undergo damage from thermally induced stresses or time-dependent damage associated with static fatigue resulting from stress corrosion mechanisms. This damaged material may result in a slow unraveling (Tptpll) or block fallout (Tptpmn) mode of failure with some extent of drift filling. The effect of thermal stress on rock failure extent has been examined using the numerical techniques discussed in the subsequent sections.

Time-dependent degradation (i.e., rockfall from a tunnel or other unsupported excavation over long time periods) is not currently well understood, particularly in hard, strong rocks. It is expected that time-related rockfall will be more prominent in heavily fractured rocks such as the Tptpll, and will be related to the ratio of induced stress to rock mass strength. The analyses presented in this section provide a reasonable estimate of the propensity for yield and rockfall as a function of the induced stress levels and time.

Ground support is not considered in the rockfall models presented in this report. The rock blocks predicted in this model report are, therefore, blocks that fail in an unsupported opening. This modeling approach leads to a conservative prediction of blocks for the preclosure period (i.e., more blocks will be predicted to fail in the model than would otherwise be supported and remain stable with ground support). During the postclosure period, ground support will degrade and eventually fail. Not including ground support in the rockfall models is realistic for the postclosure period.

All direct inputs used to develop the rockfall models are listed in Table 4-1. Corroborating/ supporting data, models, and product output that are used to develop the rockfall models include the following:

- Rock mass characteristics of the repository horizon (Section 6.1)
  - Albin et al. 1997 [DIRS 101367]

  - Barton et al. 1974 [DIRS 101541]
  - Bieniawski 1989 [DIRS 101715]
  - Broxton et al. 1993 [DIRS 107386]
  - Buesch 2003 [DIRS 162271]
  - Buesch 2003 [DIRS 163729]
  - Buesch and Spengler 1998 [DIRS 101433]
  - Buesch et al. 1996 [DIRS 100106]
  - Byers et al. 1976 [DIRS 104639]
  - Christiansen et al. 1977 [DIRS 157236]
  - CRWMS M&O 1999 [DIRS 108441]
  - Day et al. 1998 [DIRS 100027]
  - Dershowitz and Herda (1992 [DIRS 104893]
  - Flint 1998 [DIRS 100033]
  - Gibson et al. 1990 [DIRS 157245]
  - Goodman and Shi 1985 [DIRS 150094]
  - Hoek 2000 [DIRS 160705]
  - Lipman et al. 1966 [DIRS 100773]
  - Mongano et al. 1999 [DIRS 149850]
  - Munsell Color Company 1994 [DIRS 106399]
  - Ortiz et al. 1985 [DIRS 101280]
  - Peterman and Cloke 2002 [DIRS 162576]
  - Sawyer et al. 1994 [DIRS 100075]
  - Schuraytz et al. 1989 [DIRS 107248]
  - Scott 1990 [DIRS 106751]
  - Scott and Bonk 1984 [DIRS 104181]
  - Terzaghi 1966 [DIRS 105805]

- Thermal-mechanical calculation (Section 6.2)
  - BSC 2003 [DIRS 164670]
  - BSC 2004 [DIRS 169565]
  - Itasca Consulting Group 2002 [DIRS 160331]

- Rockfall in the nonlithophysal units (Section 6.3)
  - Albin et al. 1997 [DIRS 101367]
  - BSC 2003 [DIRS 166183]
  - BSC 2003 DIRS [166660]
  - Buesch and Lung 2003 [DIRS 170297]
  - Carlos et al. 1995 [DIRS 101326]
  - CRWMS M&O 1998 [DIRS 102679]
  - Duan 2003 [DIRS 163586]
  - Goodman 1980 [DIRS 101966]
  - Itasca Consulting Group 2002 [DIRS 160331]

- Rockfall in the lithophysal units (Section 6.4)
  - Bauer et al. 1991 [DIRS 161775]
  - Bieniawski 1989 [DIRS 101715]
  - Brace et al. 1966 [DIRS 101990]
  - Brekke et al. 1999 [DIRS 119404]
  - Brown 2003 [DIRS 169527]
  - BSC 2003 [DIRS 166660]
  - BSC 2004 [DIRS 169131]
  - BSC 2004 [DIRS 169183]
  - BSC 2004 [DIRS 168993]
  - BSC 2004 [DIRS 169999]
  - BSC 2004 [DIRS 169565]
  - Byrne et al. 1990 [DIRS 168921]
  - Charles 1959 [DIRS 170308]
  - Duncan et al. 1980 [DIRS 161776]
  - Fruchtbaum 1988 [DIRS 161774]
  - Goodman 1980 [DIRS 101966]
  - Hoek 2000 [DIRS 160705]
  - Hoek and Brown 1982 [DIRS 120981]
  - Itasca Consulting Group 2002 [DIRS 160331]
  - Lefebvre et al. 1976 [DIRS 168919]
  - Martin 1972 [DIRS 169721]
  - Martin and Durham 1975 [DIRS 170301]
  - MRD 1995 [DIRS 169719]
  - Newmark 1965 [DIRS 169515]
  - Potyondy and Cundall 2001 [DIRS 156895]
  - Scholz 1972 [DIRS 169724]
  - SN0406L0212303.002 [DIRS 170289]
  - Terzaghi 1943 [DIRS 162180]
  - Wiederhorn 1968 [DIRS 170309]

- Uncertainties and Limitations (Section 6.5)
  - Potyondy 2003 [DIRS 165550]

- Drift Degradation FEPs (Section 6.6)
  - Freeze et al. 2001 [DIRS 154365]
  - MO0407SEPFEPLA.000 [DIRS 170760]

- Documentation of Alternative Conceptual Models (Section 6.7)
  - Chen 1987 [DIRS 101800]
  - CRWMS M&O 1998 [DIRS 102723]
  - Hudson and Priest 1979 DIRS 104915]

- Resolution of key technical issues (Section 6.8)
  - BSC 2003 [DIRS 166660]
  - NRC 2002 [DIRS 159538]
  - Reamer and Williams 2001 [DIRS 154348]

6.1 ROCK MASS CHARACTERISTICS OF REPOSITORY HOST HORIZON

The purpose of this section is to provide a background discussion of rock mass characteristics that are important in understanding fundamental rock mass behavior. Specific rock mass parameters that are input to the rockfall models developed in this report are identified in Sections 6.3 and 6.4. Two systems of stratigraphic nomenclature are used in this report: thermal-mechanical (Ortiz et al. 1985 [DIRS 101280]) and lithostratigraphic (Buesch et al. 1996 [DIRS 100106]). Correlation between these two systems is provided in Figure 6-1.

6.1.1 Regional Geology

Yucca Mountain lies in southern Nevada, in the Great Basin, which is part of the Basin and Range structural/physiographic province. In the Yucca Mountain area, pre-Tertiary rocks (consisting of a thick sequence of Proterozoic and Paleozoic sedimentary rocks) underlie approximately 1,000 to 3,000 m of Miocene volcanic rocks (Gibson et al. 1990 [DIRS 157245]).

The Miocene volcanic sequence exposed at Yucca Mountain includes units of the Paintbrush and Timber Mountain Groups (Sawyer et al. 1994 [DIRS 100075]) and the entire section dips 5 to 10 degrees east (Day et al. 1998 [DIRS 100027]). The Paintbrush Group consists of pyroclastic rocks and lavas that originate from the Claim Canyon caldera (approximately 6 km north of the study area) and are from 12.7 to 12.8 million years old (Byers et al. 1976 [DIRS 104639]; Sawyer et al. 1994 [DIRS 100075]). The Paintbrush Group includes a sequence of four formations: the Tiva Canyon, Yucca Mountain, Pah Canyon, and Topopah Spring Tuffs, each of which consist primarily of large-volume, pyroclastic-flow deposits with minor amounts of pyroclastic-fall deposits (Byers et al. 1976 [DIRS 104639]; Christiansen et al. 1977 [DIRS 157236]; Broxton et al. 1993 [DIRS 107386]; Buesch et al. 1996 [DIRS 100106]) (Figure 6-1). At Yucca Mountain, two of these formations, the Topopah Spring and Tiva Canyon Tuffs, are voluminous, mostly densely welded, compositionally zoned, outflow sheet, pyroclastic-flow deposits (also referred to as ignimbrites) that grade upward from rhyolite composition to quartz latite composition (Lipman et al. 1966 [DIRS 100773]; Byers et al. 1976 [DIRS 104639]; Schuraytz et al. 1989 [DIRS 107248]). The formations of the Paintbrush Group are interbedded with bedded tuffs, which consist of thinner pyroclastic-flow and pyroclastic-fall deposits, and, locally, a few lava flows (Byers et al. 1976 [DIRS 104639]; Christiansen et al. 1977 [DIRS 157236]; Broxton et al. 1993 [DIRS 107386]; Buesch et al. 1996 [DIRS 100106]; Day et al. 1998 [DIRS 100027]). The 11.45 to 11.6 million year old rocks of the Timber Mountain Group were erupted from Timber Mountain caldera complex and consist of the Ammonia Tanks and Rainer Mesa Tuffs (Sawyer et al. 1994 [DIRS 100075]) and interbedded tuffaceous rocks and lava flows.

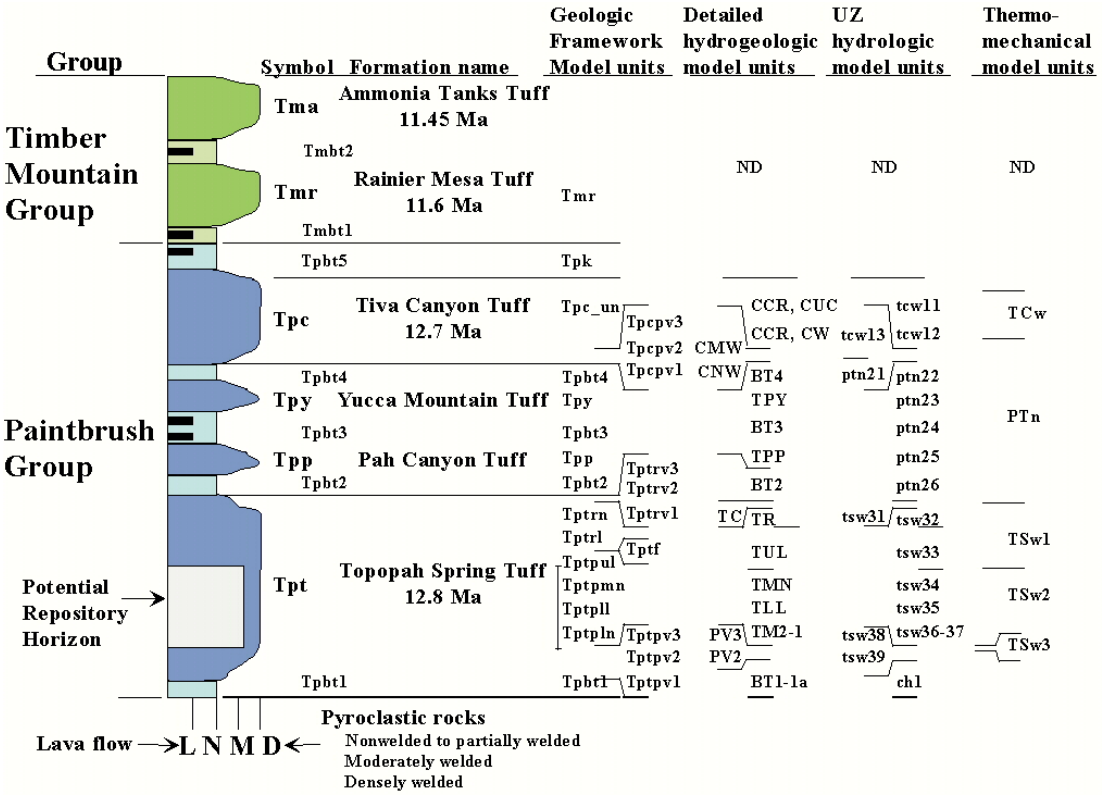

Figure 6-1. Simplified Lithostratigraphic Column of Paintbrush Group and the Rock Units that Form the Repository Host Horizon

The central block of Yucca Mountain is bounded by the Yucca Wash to the north, by the Solitario Canyon fault to the west, and the Bow Ridge fault to the east (Figure 6-2). Alluvium-filled structural valleys, consisting mostly of alluvial fan deposits (fluvial and colluvial sediments) and some thin eolian deposits, lie adjacent to the Bow Ridge and Solitario Canyon faults on the east and west sides, respectively. The Yucca Mountain area is cut by steeply dipping, north–south-striking normal faults, which separate the Tertiary volcanic rocks into blocks one to four km wide (Scott 1990 [DIRS 106751]; Day et al. 1998 [DIRS 100027]). The Solitario Canyon and Ghost Dance faults dip steeply toward the west, and displacement, amount of brecciation, and number of associated splays vary considerably along their trace (Scott and Bonk 1984 [DIRS 104181]; Day et al. 1998 [DIRS 100027]). The Solitario Canyon fault has normal down-to-the-west displacement of about 260 m in the vicinity of the repository block (Mongano et al. 1999 [DIRS 149850], p. 60). The Ghost Dance fault is in the central part the repository block and is a generally north-striking normal fault zone, with down to the west displacement. The Sundance fault is located in the north-central portion of the repository block. It is a northwest-striking, east-dipping normal fault with a maximum cumulative down-to-the-northeast displacement of 6 to 11 m (Day et al. 1998 [DIRS 100027]). Numerous smaller faults and fault zones are present throughout the repository block, generally north-trending with offsets less than 5 m (Mongano et al. 1999 [DIRS 149850]).

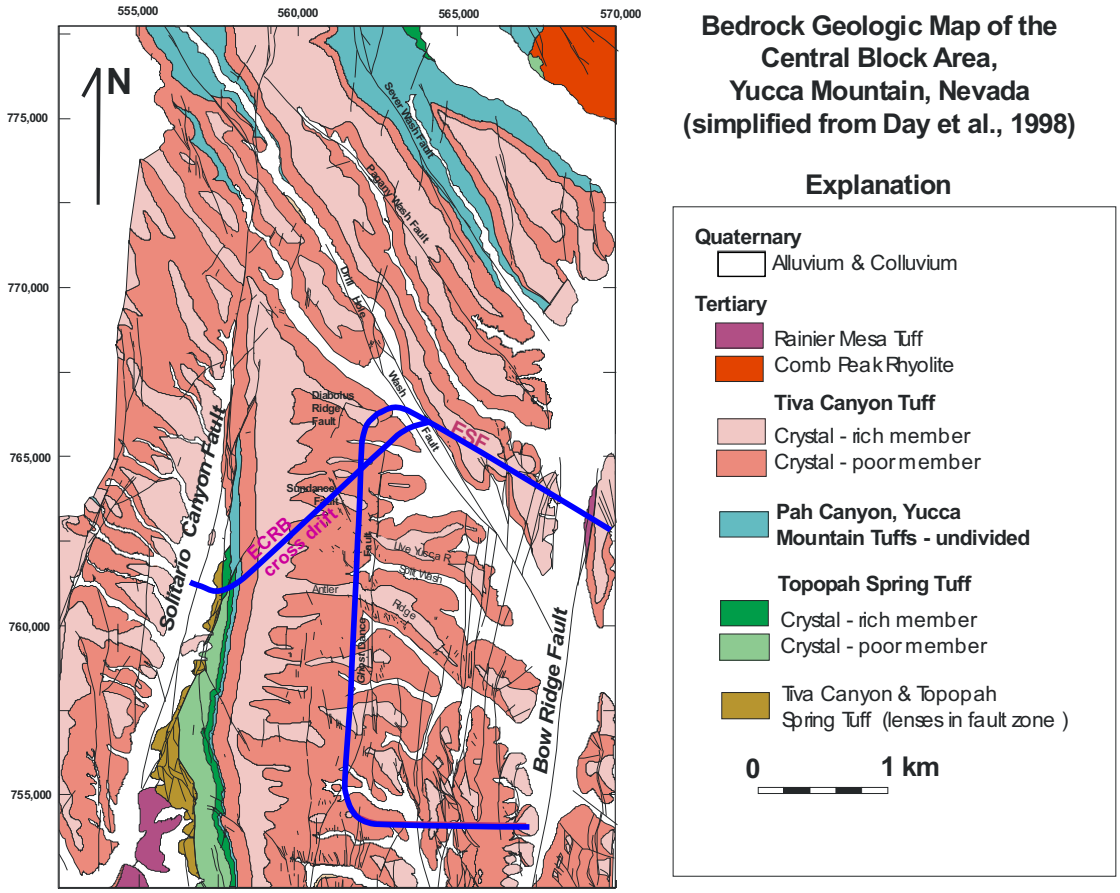

Source: Day et al. 1998 [DIRS 100027].

Figure 6-2. Geology of the Central Block at Yucca Mountain and Location of the ESF, Including the ECRB Cross-Drift

6.1.2 Lithostratigraphy at the Repository Horizon

All of the rocks of the repository host horizon lie within the Topopah Spring Tuff—specifically within the crystal-poor member—and geochemically these rocks have a very uniform composition of rhyolite (Peterman and Cloke 2002 [DIRS 162576]). The repository host horizon includes rocks from the lower part of the upper lithophysal zone (Tptpul) of the TSw1 thermal-mechanical unit and the TSw2 thermal-mechanical unit, including the middle nonlithophysal zone (Tptpmn), the lower lithophysal zone (Tptpll), and the lower nonlithophysal zone (Tptpln) (Figure 6-1). These lithostratigraphic units are described in this section and are based on Mongano et al. (1999 [DIRS 149850]) unless otherwise indicated.

In the densely welded and crystallized rocks of the Topopah Spring Tuff, the zones and many of the subzones are identified on the basis of the abundance, size, and distribution (or lack thereof) of lithophysae, which are cavities in the rock formed during welding from the accumulation of the vapor phase. Lithophysae, spots (which are similar to the rims on lithophysae, but there is no cavity), and many fractures have similar characteristics, such as rims, borders, and possibly vapor-phase mineral coatings (Figure 6-3).

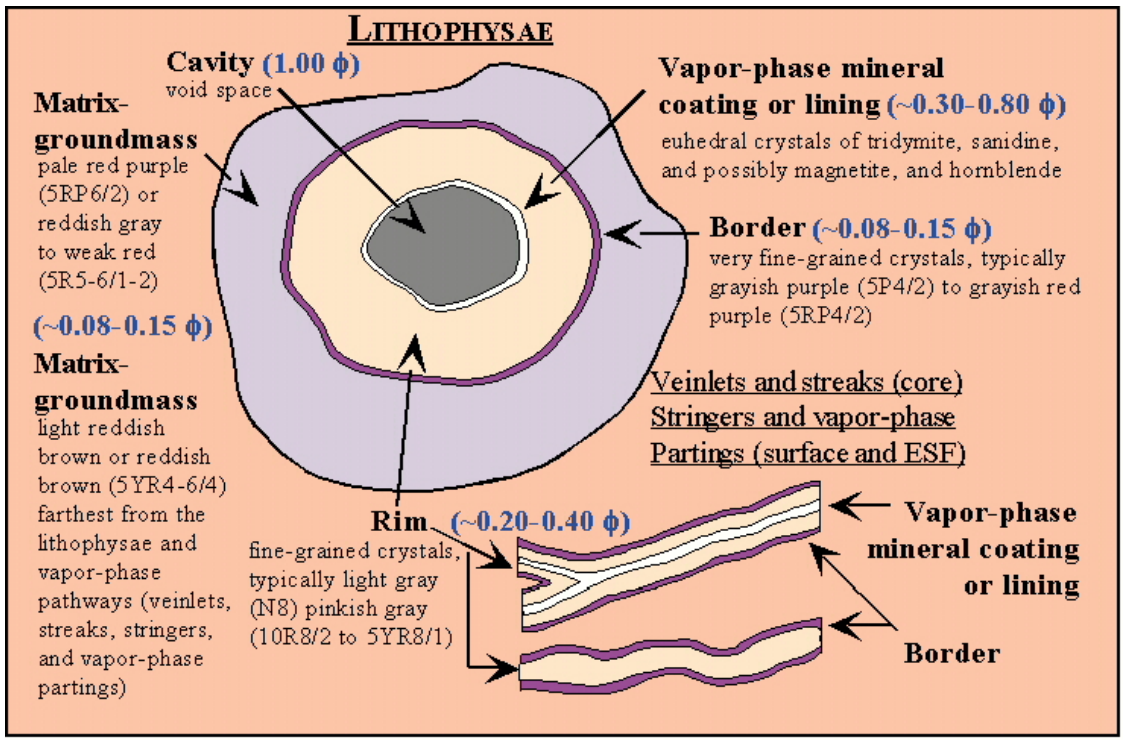

NOTE: Porosity values for the matrix-groundmass are by Flint (1998 [DIRS 100033]), and the values for rims, borders, and vapor-phase mineral coatings are estimates by Buesch (2003 [DIRS 162271]). The nomenclature for color (e.g., pale red purple is 5RP6/2), is based on soil color charts (Munsell Color Company 1994 [DIRS 106399]).

Figure 6-3. Lithostratigraphic Features Related to Lithophysae and Fractures

Tptpul–The Tptpul is exposed in both the ESF main loop and ECRB Cross-Drift. In the ESF main loop, the upper lithophysal zone is exposed from Stations 17+97 to 27+20, 63+08 to 64+55, 67+91 to 68+47, and 71+68 to 73+02. The ECRB Cross-Drift begins in the upper central portion of the zone and it exposes rocks of the middle and lower portions of the zone from Stations 0+00 to 10+15. The upper portion of the upper lithophysal zone is also exposed in the hanging wall of the eastern strand of the Solitario Canyon fault zone from Stations 25+90 to 26+57.5. The unit is densely welded, crystallized, lithophysal, and has various amounts of vapor-phase corrosion and mineralization. The rock contains 1 to 5 percent crystal fragments, 0 to 5 percent lithic fragments, 0 to 15 percent pumice fragments, 3 to 60 percent lithophysae, and 40 to 92 percent matrix-groundmass. The matrix-groundmass is a variable mix of pale to grayish red-purple (5RP5-7/1-2 to 5RP4/2), light brown (5YR6/3-4) to pale reddish brown (10R5/4), and pale red (5-10R6/2) crystallized material. The matrix-groundmass contains 3 to 50 percent white to very light gray (N-9 to N6) to grayish pink (5-10R8/2-1) spots, veinlets, streaks, rims on fractures, stringers, and vapor-phase partings of crystallized materials.

Tptpmn–The Tptpmn is exposed in both the ESF main loop and ECRB Cross-Drift. The ESF main loop is excavated in the middle nonlithophysal zone from Stations 27+21 to 57+29, 58+78 to 63+08, and from 70+58 to 71+68. The middle nonlithophysal zone contains an intensely fractured zone exposed in the ESF main loop from Stations 42+00 to 51+50 (Albin et al. 1997 [DIRS 101367]). This intensely fractured zone has been treated separately in the analyses

presented in this report. The ECRB Cross-Drift exposes the middle nonlithophysal zone from Stations 10+15 to 14+44. In general, the rocks are densely welded, crystallized, and have various amounts of vapor-phase corrosion and mineralization. The rock contains 1 to 2 percent crystal fragments, 1 to 5 percent lithic fragments, 1 to 15 percent pumice fragments, 0 to 3 percent lithophysae, and 76 to 97 percent matrix-groundmass. The matrix-groundmass has two main colors that appear to result from variations in the types of crystallization, but locally there are gradations between these two types that form a heterogeneous mix of colors and crystallization products. One type of rock is a mix of grayish orange-pink (5YR7/2), grayish red (5R4/2), and grayish red-purple (5RP4-5/2) that locally has small veinlets and stringers. The other type of rock is pale brown (5YR6/2), light brown (5YR6/3-4), and moderate brown (5YR4/3), grayish brown (5YR6/1), or pale red (5-10R6/2). The matrix-groundmass contains 0 to 25 percent, white (N9), very light gray (N8), and light gray (N7) to grayish pink (5R8/2) spots, veinlets, streaks, rims on fractures, stringers, and vapor-phase partings of crystallized materials. Smooth, high-angle fractures are typical of the zone, but it also contains some low-angle, continuous shears and cooling joints. Another feature characteristic of the Tptpmn is the presence of concentrations of vapor-phase minerals along vapor-phase partings and these features appear as low-angle continuous partings subparallel to the dip of the unit. The lithophysae-bearing subzone (Tptpmn2) described by Buesch et al. (1996 [DIRS 100106]) occurs in the ECRB Cross-Drift and has 1 to 3 percent lithophysae (Mongano et al. 1999 [DIRS 149850]), but this subzone does not occur in the Main Drift of the ESF (Mongano et al. 1999; Buesch and Spengler 1998 [DIRS 101433]).

Tptpll–The Tptpll is exposed in both the ESF main loop and ECRB Cross-Drift. The ESF main loop exposes the uppermost few meters of the lower lithophysal zone from Stations 57+29 to 58+78. The lower lithophysal zone is exposed along the ECRB Cross-Drift from Stations 14+44 to 23+26. The rocks are densely welded, crystallized, lithophysal, and have various amounts of vapor-phase corrosion and mineralization. The rocks are composed of 1 to 2 percent crystal fragments, 1 to 5 percent lithic fragments (locally 12 to 15 percent), 0 to 7 percent pumice fragments (locally 10 to 35 percent), 5 to 30 percent lithophysae (locally 1 to 5 percent), and 56 to 93 percent matrix-groundmass. The matrix-groundmass is a mottled mix of pale red (5R6/2, 5R5/2, 10R6/2-3) and pale to light brown (5YR6/2; 5YR6/3; 5YR6/4), and moderate brown (5YR4-5/4) with variable amounts of pale to grayish red-purple (5RP5-7/1-2 to 5RP4/2), and locally it is dusky yellowish brown (10YR3/2). The matrix-groundmass contains 3 to 20 percent (locally 15 to 40 percent) grayish orange-pink (5YR7/2) or pinkish gray (5R8/2; 10R8/2) to light or very light gray (N7; N8) spots, veinlets, streaks, rims on fractures, stringers, and vapor-phase partings of crystallized materials. Lithophysae vary in size from a few centimeters to greater than 1 m in diameter.

Tptpln–The Tptpln is not exposed in the ESF main loop, but is exposed in the ECRB Cross-Drift from Stations 23+26 to 25+85. The rocks are densely welded, crystallized pyroclastic-flow material and typically are composed of 1 to 2 percent crystal fragments, 3 to 7 percent lithic fragments, 3 to 20 percent pumice fragments, 0 to 5 percent lithophysae, and 66 to 93 percent matrix-groundmass. Rocks of the lower nonlithophysal zone vary from a heterogeneous mix of grayish red and grayish orange pink (5YR7/2) matrix-groundmass to comparatively homogeneous pale red, light brown, pale brown, or grayish brown (5YR6/4) matrix-groundmass. Veinlets, streaks, and stringers form a minor component of the rock in some portions of the unit. In proximity to the Solitario Canyon fault zone, the unit is brecciated and

altered. In this area, the breccia matrix varies from moderate reddish brown to grayish orange pink. Some breccia clasts adjacent to the fault plane are very light gray.

6.1.3 Geotechnical Characterization

Geotechnical data were collected based on two empirical rock mass classification systems: the Norwegian Geotechnical Institute rock quality system (Q system) (Barton et al. 1974 [DIRS 101541]) and the Geomechanics Rock Mass Rating (RMR) system (Bieniawski 1989 [DIRS 101715]). Ratings are assigned to a 5-m length of tunnel using both rock classification systems. The use of this relatively short rating length may have the disadvantage of introducing variations in some evaluated parameters, which may be expected to be stable, yet it has the advantage of capturing expected variations in more unstable parameters. For example, using the Q system, the number of joint sets could be considered constant over a long reach of tunnel. Using a 5-m rating length permits evaluation of the actual occurrence of a particular joint set; therefore, the rating value for the number of joint sets may vary within a 10-m reach of tunnel. On the other hand, the 5-m rating length permits a description of the changes in fracture frequency represented by the rock quality designation (RQD). Overall, the 5-m rating length emphasizes changes in rock quality from one length to the next. When longer reaches of the tunnel or various stratigraphic units are compared, differences in the trends of the 5-m ratings and differences in the average ratings are meaningful. The geotechnical characterization of lithostratigraphic units is described in this section and is based on Mongano et al. (1999 [DIRS 149850]). It must be recognized that application of geotechnical characterization methods and determination of rock "quality" is problematic in lithophysal rocks since these classification systems are based on the presence of fractures as the primary structural features and have no provision for lithophysal cavities. Therefore, it was considered that the RQD rating accounts for the presence of lithophysal cavities. The difficulty inherent in correspondence of RQD based on cross-cutting fractures and RQD based on isolated cavities in a solid rock matrix tends to downplay the utility of rock mass classifications in lithophysal rock.

Tptpul–The Tptpul (Stations 0+00 to 10+15 and Stations 23+26 to 25+85), the longest reach of the ECRB Cross-Drift, has the lowest RQD rating (36 [poor]), yet the highest Q system rating (14 good). The Tptpul RMR value (57 fair) equals the RMR value of the Tptpll and its lithophysae content ranges from 10 to 40 percent by volume. These cavities average 10 cm in diameter. Fractures are difficult to distinguish, with an average of only one joint set. No key blocks are expected to form within this unit; however, there are occasionally some horizontal cooling joints. It has 11 faults, 1 fault zone, and 25 shears or shear zones.

Tptpmn–The Tptpmn (Stations 10+15 to 14+44) has a mean horizontal RQD rating of 60 (fair) including lithophysae, and 62 (fair) excluding lithophysae. The tunnel-calculated Q rating is 12.7 (good). The RMR system rates the Tptpmn and the Tptpln as the highest, with a rating of 60 (fair). The unit is generally characterized by less than 3 percent lithophysae by volume. The Tptpmn has 430 m of exposure in the ECRB Cross-Drift and has the least amount of fault/shear activity with a total of 1 fault zone, 6 faults, and 13 shears. It has an average of three to three+ random joint sets. The horizontal joint sets, or vapor-phase partings, cause the formation of key blocks at Stations 10+80 to 11+55 and Stations 13+10 to 13+15.

Tptpll–The Tptpll (Stations 14+44 to 23+26) has a horizontal RQD rating of 42 (poor). Its tunnel-calculated Q rating is 7.9 (fair), the lowest in the ECRB Cross-Drift. The RMR system estimates this unit at 57 (fair). The Tptpll is generally characterized by lithophysae of 5 to 30 percent by volume and that range in size from 5 to 130 cm. The larger lithophysal cavities tend to be irregular or ellipsoidal features that exhibit prismatic fracturing. The unit has an average of two+ random joint sets; however, no key-block problems are apparent. The Tptpll has 4 faults and 30 shears exposed in 882 m of rated tunnel.

Tptpln–The Tptpln (Stations 23+26 to 25+85) has the best horizontal RQD ratings: 62 (fair) including lithophysae, and 67 (fair) excluding the lithophysal cavities. Its tunnel-calculated Q rating is 12.3 (good). The RMR system rates this unit at 60 (fair). This unit is characterized by generally less than 3 percent lithophysal cavities by volume. The Tptpln has an average of three joint sets, with no significant key-block occurrences, and has 6 faults and 36 shear or shear zones.

6.1.4 Discussion of Engineering Characteristics of Rock Mass Important to Geomechanical Performance

The structure of the rock mass plays an important role in defining the structural response of the repository to thermal and mechanical loading. In particular, the fracture geometry and properties and the amount of lithophysal porosity are the primary geologic structures of importance. Extensive geotechnical mapping of fractures has been performed in the entire ESF main loop and the ECRB Cross-Drift (CRWMS M&O 1998 [DIRS 102679]; Mongano et al. 1999 [DIRS 149850]). Figure 6-4 shows a schematic of the Topopah Spring Tuff illustrating the general occurrence of fracturing and lithophysae in the various zones of the formation. The occurrence of fractures and lithophysae are roughly inversely proportional. This is illustrated schematically in Figure 6-4 and demonstrated quantitatively in Figure 6-5, where the fracture density (fractures with trace length greater than 1 m), determined from detailed line mapping (i.e., the detailed line survey), and the approximate percentage of lithophysal porosity in the ECRB Cross-Drift are shown. The density of fractures with trace length greater than 1 m is significantly larger in the Tptpmn and Tptpln (20-35 fractures/10 m), as compared to five fractures/10 m or less in the Tptpul and Tptpll.

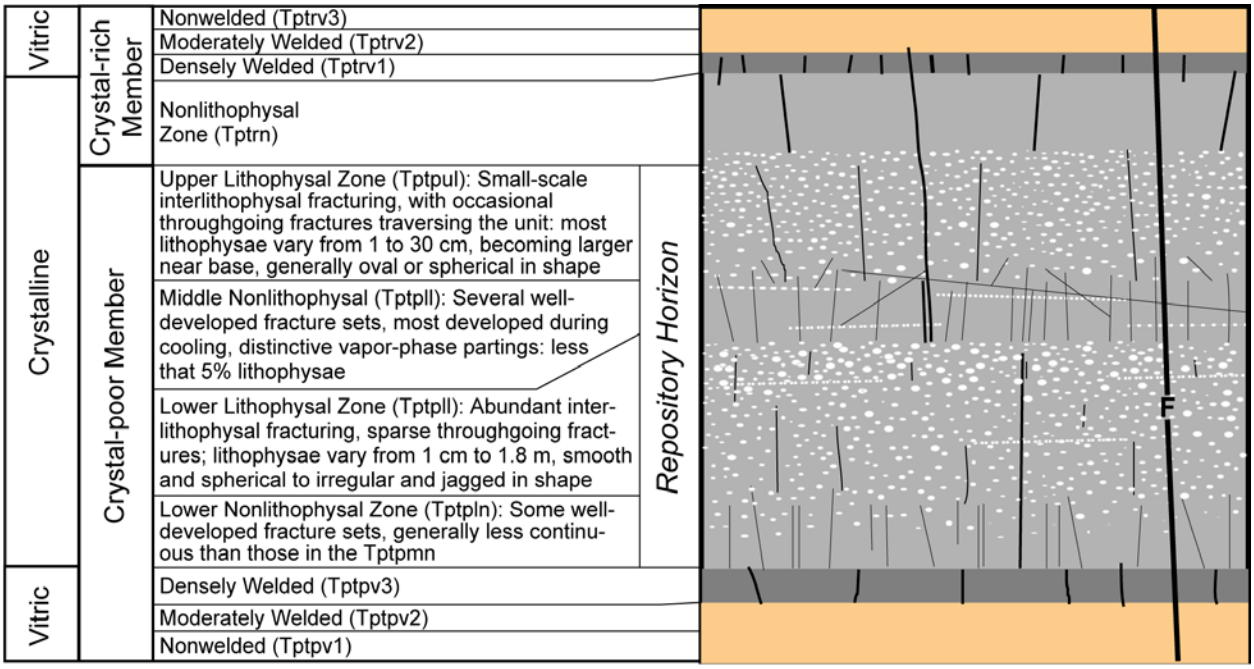

Diagrammatic Cross Section of the Topopah Spring Tuff Illustrating Relative Discontinuity Densities and Orientations: This figure indicates how fractures, faults, and lithophysae are typically distributed through the ignimbrite.

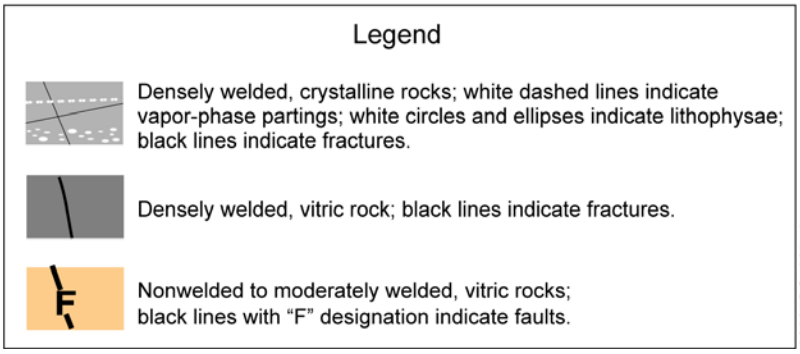

Source: Buesch et al. 1996 [DIRS 100106], Appendix 2; Mongano et al. 1999 [DIRS 149850], pp. 12 to 43.

Figure 6-4. Schematic Illustration of the Structure of the Topopah Spring Tuff

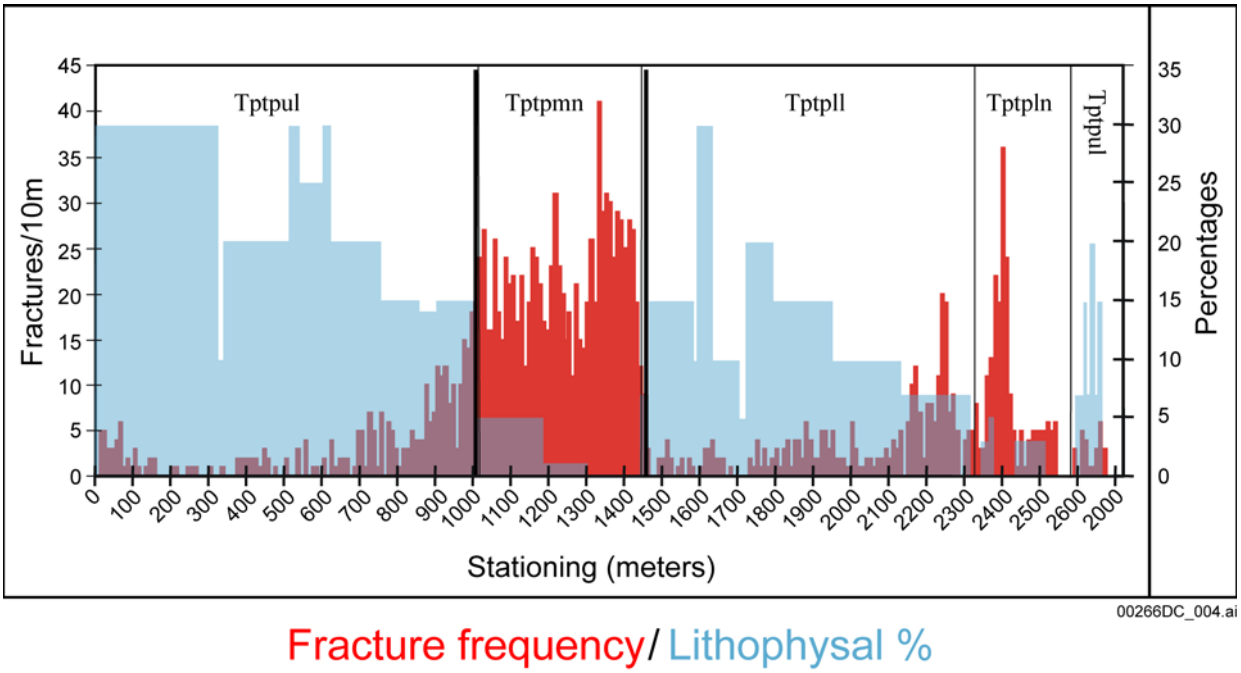

Source: Mongano et al. 1999 [DIRS 149850], Figure 13.

Figure 6-5. Fractures and Lithophysal Abundance in the ECRB Cross-Drift from Stations 0+00 to 27+00

6.1.4.1 Fracturing

The discussion of fracturing presented in this section is based on Mongano et al. (1999 [DIRS 149850]). Full periphery geologic mapping and detailed line surveys (consisting of a description of orientation, trace length, small and large scale roughness, and end terminations for fractures with trace lengths of greater than or equal to 1 m) were performed in the drifts. The database consists of over 35,000 entries and is recorded on CAD drawings as well as spreadsheets. There are, in general, four sets of fractures in the Tptpmn with the characteristics identified in Table 6-1.

The fractures have relatively short continuous trace lengths (Figure 6-6), with ends often terminating either against other fractures or in solid rock, leaving a solid rock "bridge" between joint tracks. Full periphery geologic maps that logged the fracture traces with lengths greater than 1 m were created behind the tunnel boring machine as the ESF main loop and the ECRB Cross-Drift were driven. A typical full periphery geologic fracture map is shown in Figure 6-7. Figure 6-8 provides a photograph typical of the wall of the ECRB Cross-Drift within the Tptpmn, and shows the discontinuous nature of the fractures in each joint set. The fracture traces were painted during the detailed line mapping (Figure 6-8). Each fracture termination was logged as being against another fracture, within solid rock, or continuous. The photo shows the common occurrence of fractures that terminate in solid rock (T-junctions) as opposed to continuous structures (arrowheads). The sub-vertical fractures, in particular, often have curved surfaces with large-amplitude (dozens of centimeters) asperities and wavelength of meters. Fractures sometimes terminate in solid rock with discontinuous interconnection to adjacent joint tracks (i.e., a rock "bridge") or terminate against other joints.

Table 6-1. General Characteristics of Fracture Sets in the Middle Nonlithophysal Unit

Set	Mean Azimuth/Dip	Median Spacing (m)	Median Trace Length (m)	Comment
1	120/84	0.48	3.3	Rough to smooth, planar
2	215/88	1.08	2.8	Smooth but curved
3	302/38	3.40	3.7	Random fractures with generally flat to moderate dip
4	329/14	2.46	3.5	Vapor-phase partings, rough, cohesive with coating minerals, planar

Source: Median spacing and trace length are from tunnel mapping data (see Table 6-2).

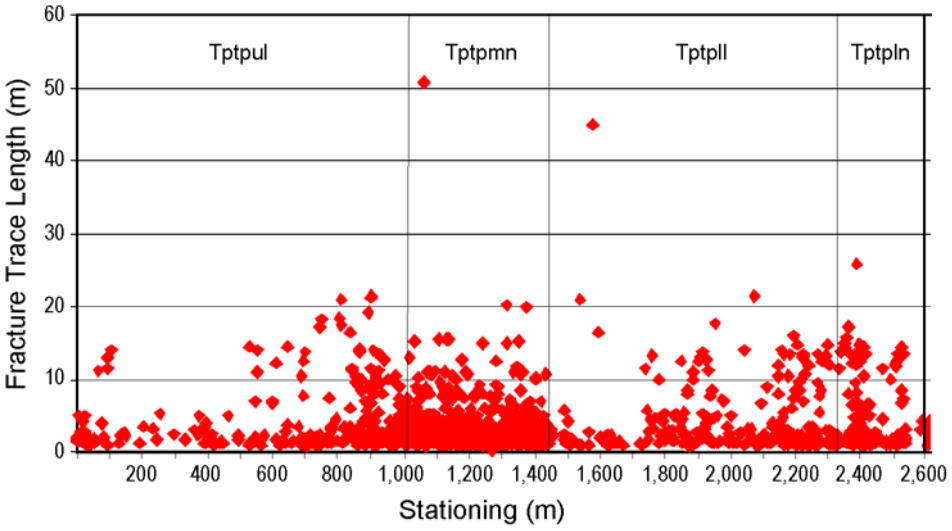

Source: Mongano et al. 1999 [DIRS 149850], Figure 14.

Figure 6-6. Fracture Trace Length from Detailed Line Surveys as a Function of Stationing Along the ECRB Cross-Drift

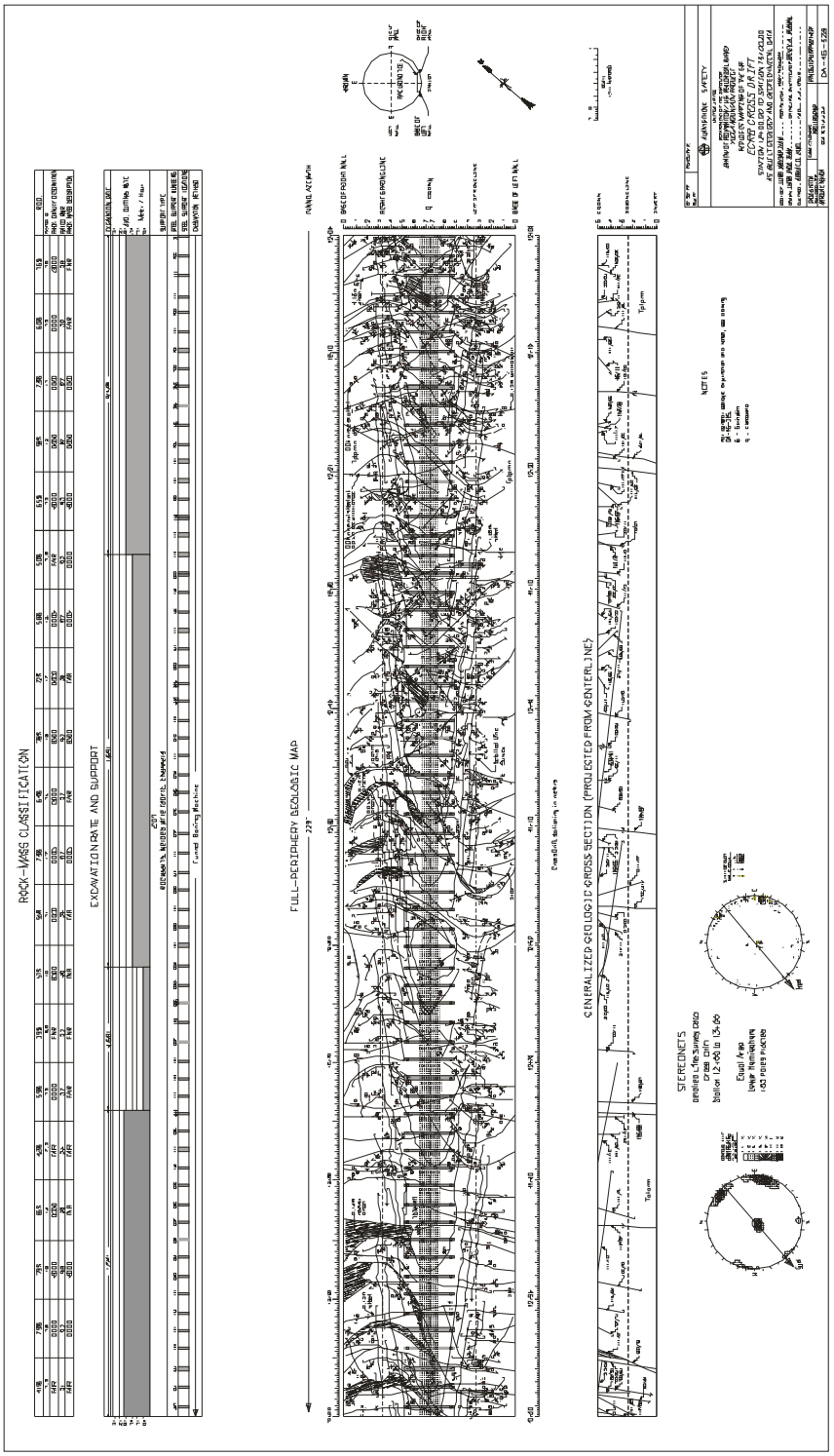

Source: DTN: GS990408314224.004 [DIRS 108405].

NOTE: The purpose of this figure is to illustrate the geologic structure contained on a full periphery geologic map. The annotated information on this figure is not intended to be legible. An enlarged, legible map is available through the source DTN.

Figure 6-7. Illustrative Example of a Full Periphery Geologic Map from the ESF, Tptpmn

00266DC_007.ai

NOTE: T-junctions on fractures indicate terminations; arrowheads show continuous features.

Figure 6-8. Fractures in Wall of the ECRB Cross-Drift in the Tptpmn

The sub-horizontal vapor-phase partings (Figure 6-9) are relatively continuous structures seen throughout the Tptpmn. These continuous, but anastomosing fractures are sub-parallel to the dip of the rock unit, and are filled with concentrations of vapor-phase minerals (primarily tridymite and cristobalite). The surfaces are rough on a small scale and, as a result of the mineral filling, they have cohesion (unlike the sub-vertical fractures).

The nature of the fracture geometry is extremely important to estimates of the stability of the rock mass, particularly under seismic shaking, as well as to estimates of the support function and level of required ground support. Most rock mass classification schemes are based on experience of rock masses with continuous joint sets that create regular, blocky masses (e.g., Hoek 2000 [DIRS 160705]). In the Tptpmn, the relatively short trace lengths and non-persistent joints create relatively few kinematically removable blocks. This sparseness is evidenced by the fact that only a very small number of rock blocks have actually been removed in the ECRB Cross-Drift. Those blocks removed actually occurred under the action of the tunnel boring machine or were scaled out of the back and walls.

Short-length fractures (less than 1-m trace length), coupled with the lithophysae, are the most important features that govern stability in the Tptpll because they impact the rock mass strength as described in Appendix E (Section E4). Whereas the Tptpul tends to have some small-scale fractures in the matrix-groundmass between lithophysae, and a few that intersect lithophysae (Figure 6-10a), the Tptpll has abundant fractures. Figure 6-10b, from the upper portion of the Tptpll, shows the intensive fracturing of the matrix-groundmass between lithophysae, several “circum-lithophysal” fractures (fractures that formed around or parallel to the margins of lithophysae), and very few fractures that actually intersect the lithophysae. The fractures, which exist throughout the Tptpll, have a primary vertical orientation, and have lateral spacing of a few centimeters.

Small-scale fracture traverses in the Tptpll confirm the close spacing and short trace lengths of fractures in this zone. The intensity and short trace lengths of fractures in this zone create a texture that severely limits the potential block size in this zone. By comparing the detailed line survey (fracture greater than 1m) and the small-scale surveys, this intensity is clearly due to small-scale fractures (less than 1m trace length). The detailed line survey sampled almost 880 m of tunnel in the ECRB Cross-Drift. There are 300 fractures recorded over this run of tunnel that have a trace length greater than 1 m. The small-scale survey in the Tptpll can be combined into 18 m of horizontal sampling. There are 376 fractures recorded over this 18 m of sampling.

In some cases, it is difficult to distinguish whether these fractures have been disturbed by mining or induced by in situ stresses, or whether they are newly created by mining along a weakness fabric in the rock. However, it is clear that the middle portion of the Tptpll has a ubiquitous fracture fabric that is most evident when large diameter core is removed from boreholes (see Figure 7-1a). The core, although competent, has numerous fractured surfaces that break into small blocks when stressed. Lithophysae and occasional horizontal fractures tend to create blocks with dimensions on the order of about 10 cm or less on a side. Thin section analyses of the fracturing in the Tptpll and the Tptpmn show rims on many of the fracture surfaces within the rock mass away from the tunnel wall, indicating there are numerous natural fractures (i.e., not mining-induced) and were formed during the cooling process (Buesch 2003 [DIRS 163729]).

00266DC_008.ai

Figure 6-9. Low-Angle Vapor-Phase Partings in Nonlithophysal Units in the ESF

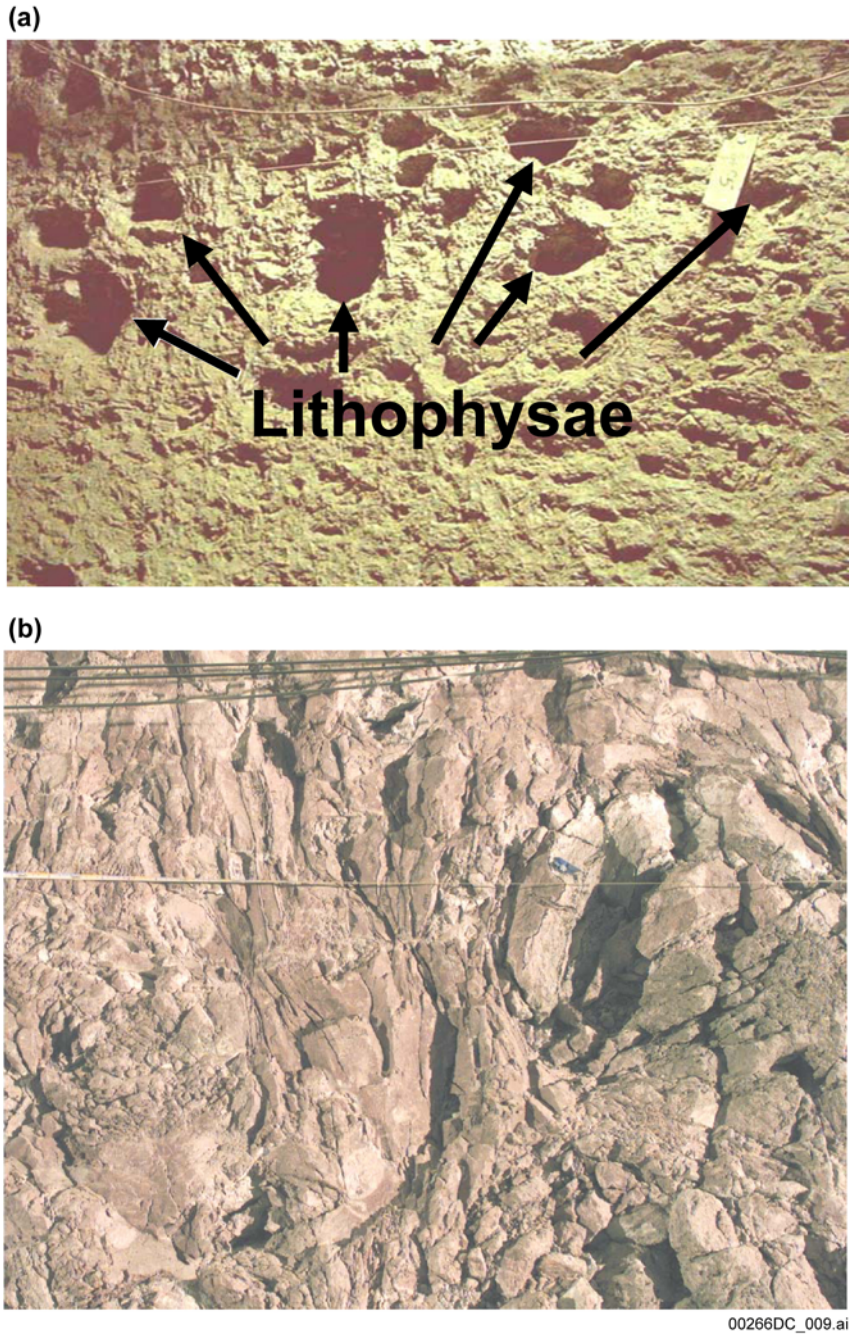

NOTE: The Tptpul (a) is characterized by a relatively few fractures in the matrix-groundmass between lithophysae whereas the Tptpll (b) has abundant, natural, short-length fractures in the matrix-groundmass, some of which intersect or connect lithophysae. Spacing of the fractures in the Tptpll is generally less than 5 cm.

Figure 6-10. Comparison of Lithophysae and Fracturing in the Tptpul and Tptpll

6.1.4.2 Lithophysae

Although the character of the lithophysae varies between the Tptpul and Tptpll as shown in Figure 6-10, the mineralogy of the matrix material within both of these units is generally the

same as in the nonlithophysal units, based on the rock unit descriptions provided by Mongano et al. (1999 [DIRS 149850]).

Compositionally and mineralogically the rocks in lithophysal and nonlithophysal zones are similar, but there can be variations in the amounts of quartz, cristobalite, and tridymite; however, the main difference is in the abundance of lithophysae and features formed by crystallization in the presence of the vapor phase (rims, spots, etc.). The upper and lower lithophysal zones share many characteristics, but there are also numerous distinctions (Mongano et al. 1999 [DIRS 149850]), and these general characteristics are as follows.

The lithophysae in the Tptpul:

- Tend to be smaller (roughly 1 to 10 cm in diameter) compared to the Tptpll
- Are more uniform in size and distribution within the unit compared to the Tptpll
- Vary in infilling and rim thicknesses
- Have a volume percentage that varies consistently with stratigraphic position
- Are stratigraphically predictable.

The lithophysae in the Tptpll:

- Are highly variable in size, from less than 1 cm to 1.8 m in size
- Have shapes that are highly variable and are described as simple (elliptical cross-sections and spherical to ellipsoidal shapes), irregular, cuspate, merged (two or more lithophysae joined into one large one), and extension-crack lithophysae
- Have infilling and rim thickness that vary greatly with vertical and horizontal spacing
- Have volume percentages that vary consistently with stratigraphic position
- Are stratigraphically predictable.

With the large amount of the repository located in the lower lithophysal zone, a detailed study of the lithostratigraphic features in the lower lithophysal zone exposed in the ECRB Cross-Drift has been completed (DTNs: GS021008314224.002 [DIRS 161910] and GS040608314224.001 [DIRS 171367]). The data package documents the distributions of size, shape, and abundance of lithophysal cavities, rims, spots, and lithic clasts, and these data can be displayed and analyzed as local variations, along the tunnel (a critical type of variation), and as values for the total zone. A detailed description of lithophysal abundance and lithophysal characteristics is provided in Appendix O.

In addition to the along-the-tunnel variation in the abundance of features such as lithophysae, there are variations in the sizes, shapes, and distances between features. These types of variations are most easily observed with panel map data (Figure 6-11). Locations of the panel maps were positioned to capture representative variations in the rocks along the tunnel. Additional details on the development of these panel maps are provided in Appendix O.

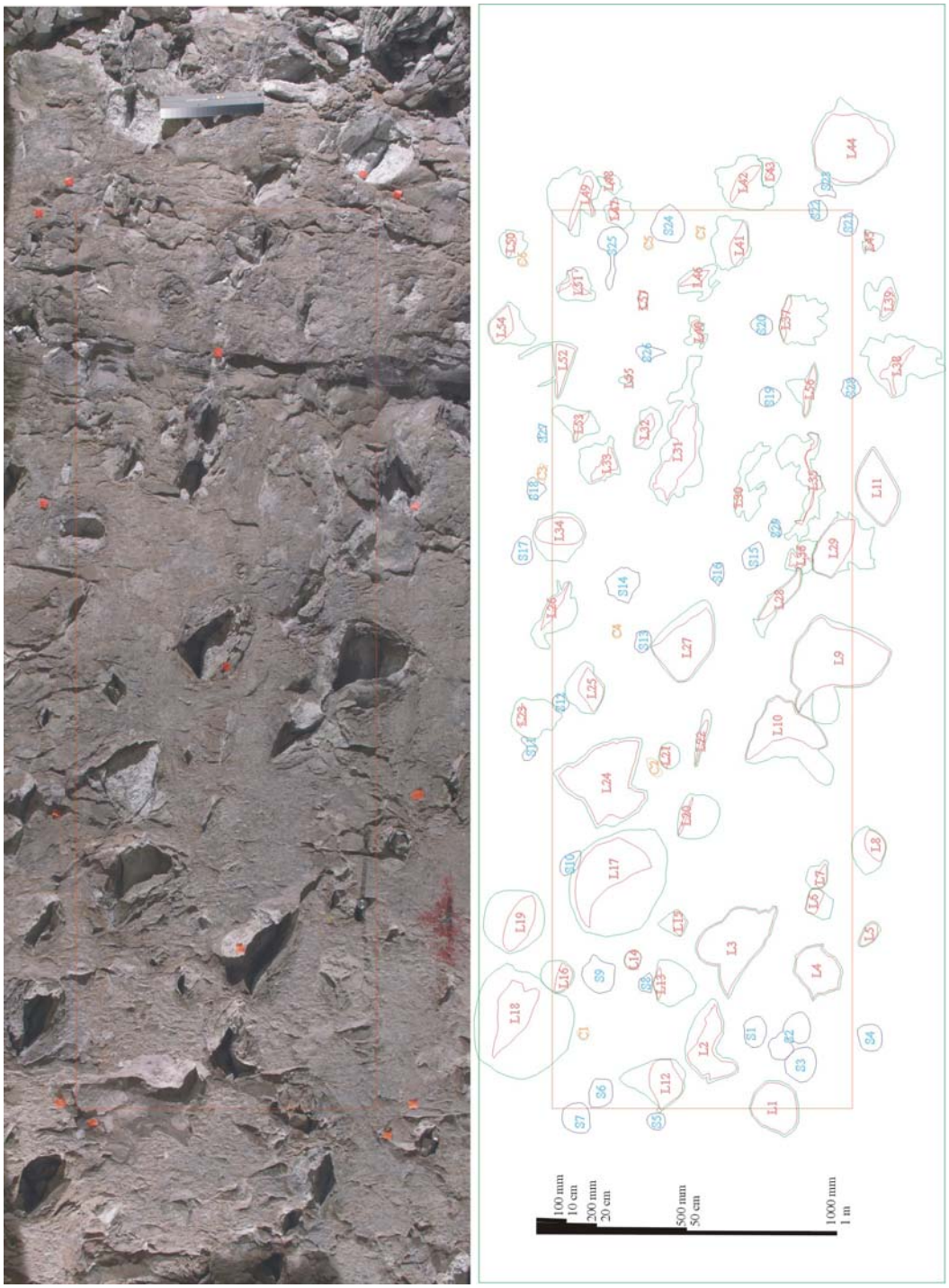

NOTE: Lithophysae have red "L" identifiers with cavities outlined in red and rims in green. Spots have blue "S" identifiers with cyan outlines. Lithic clasts have orange "C" identifiers with gold outlines.

Figure 6-11. Lithophysae, Spots, and Clasts of Tptpll in Panel Map 1493 Located on the Right Rib from Stations 14+93 to 14+96

Using the approach described in Appendix O, the total porosity of the component features of the lithophysal rock mass (i.e., the porosity of the lithophysal cavities, rims, and spots) has been calculated. The porosity variation along the ECRB Cross-Drift is shown in Figure 6-12, with total porosity typically ranging from 20 to 35 percent.

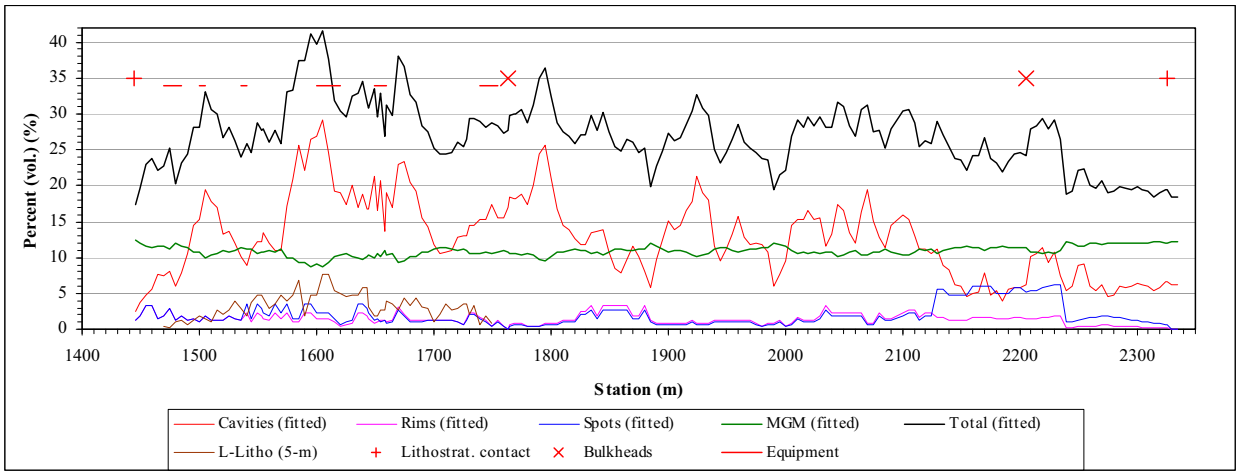

a. Porosity Along the Tunnel Displayed in Five Components (Excluding the 5-m Averaged Large-Lithophysae).

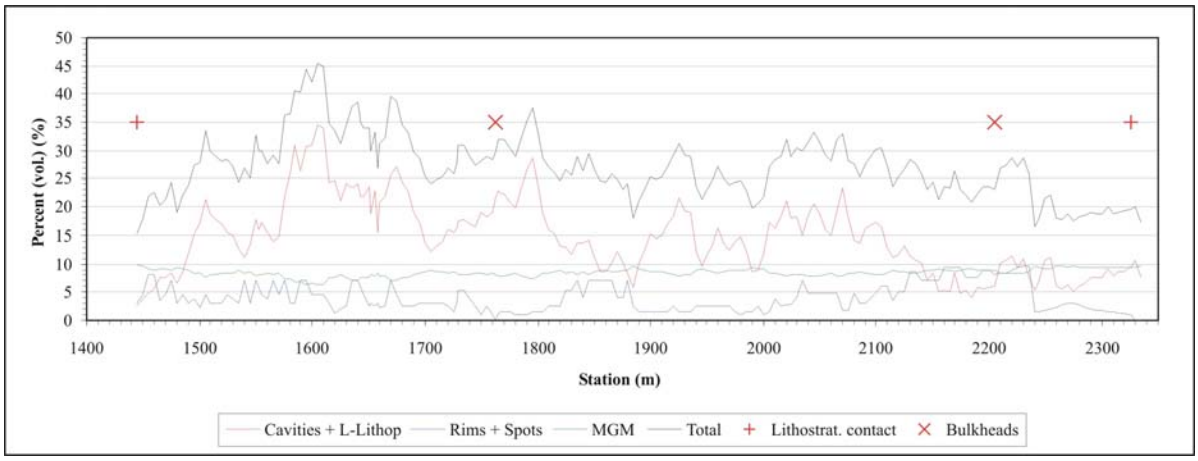

b. Porosity Along the Tunnel Displayed in Three Components (Lithophysal Cavities and Large-Lithophysae Inventory are Combined, and Rims and Spots are Combined).

NOTE: Source file provided in DTN: MO0408MWDDDMIO.002, file *Drift Deg AMR AF T-A-P Fit V1.xls*.

Figure 6-12. Calculated Porosity of Lithophysal Cavities, Rims, Spots, Matrix-Groundmass, and the Total Porosity in the Tptpll Exposed Along the ECRB Cross-Drift

6.1.5 Field Observation of Key Blocks

Key blocks are critical blocks in the surrounding rock mass of an excavation which are kinematically removable and oriented in an unsafe manner so that they are likely to move into an opening unless support is provided (Goodman and Shi 1985 [DIRS 150094], pp. 98 and 99). The failure of a key block opens up the excavation surface for further potential failures by subsequent blocks. Key blocks are formed by the intersection of three or more planes of structural discontinuities as shown in Figure 6-13. Key blocks in the 5-m diameter ECRB Cross-Drift are first evident in the crown at about Station 10+50 in the Tptpmn unit (note that metric stationing is used throughout the ESF; i.e., Station 10+50 is located 1050 m from the start of the tunnel). Most of the key blocks in this region are of minor size and typically fall immediately after excavation prior to ground support installation. Key blocks are possible in this area because of the increased presence of the plane of weakness (i.e., a vapor-phase parting) in the near horizontal orientation that intersects with two opposing near-vertical joint planes. Fallout from these key blocks during excavation is typical of the rock in the middle nonlithophysal zone (Tptpmn) of the TSw2 thermal-mechanical unit. The largest resultant void is possibly 0.5 cubic meters at approximately Station 11+55 as shown in Figure 6-14. No unstable key blocks were observed in the field. Documentation of key blocks observed in the ECRB Cross-Drift is provided in Appendix F.

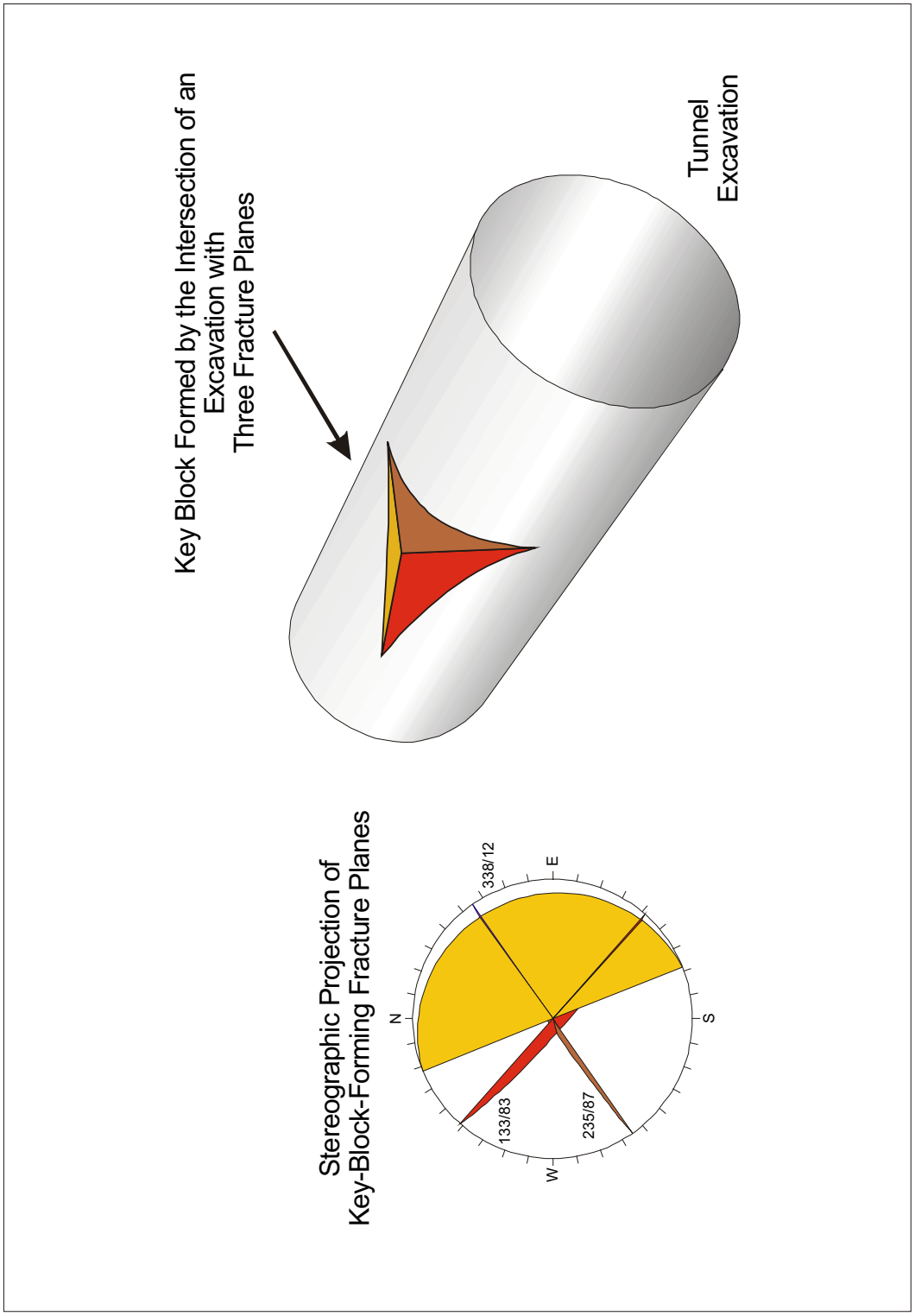

Figure 6-13. Illustration of a Typical Key Block and Associated Fracture Planes

Figure 6-14. Evidence of Key-Block Occurrence in the ECRB Cross-Drift, Station 11+55

While ground support monitoring in the ESF main loop has provided long-term evidence indicating stable rock support performance, there are several sections in the ESF where raveling and block fallout have occurred. These typically corresponded to the 3.01X areas, and most often occurred in fault zones and in the TCw and TSw2 thermal-mechanical units. The 3.01X areas refer to sections of the ESF main loop that were constructed under Section 3.01X of the subsurface general construction specification (BSC 2002 [DIRS 161707], p. 17). The specification indicates that special actions may be necessary to continue excavation in the event

that adverse ground conditions prevent normal tunnel boring machine operations. The location of 3.01X areas is provided by *South Ramp 3.01.X Area Ground Support Analysis* (CRWMS M&O 1999 [DIRS 108441], Section 1). A typical opening profile in a 3.01X area is shown in Figure 6-15. This profile is indicative of the worst case ground conditions in the Tptpmn lithologic unit of the ESF main loop.

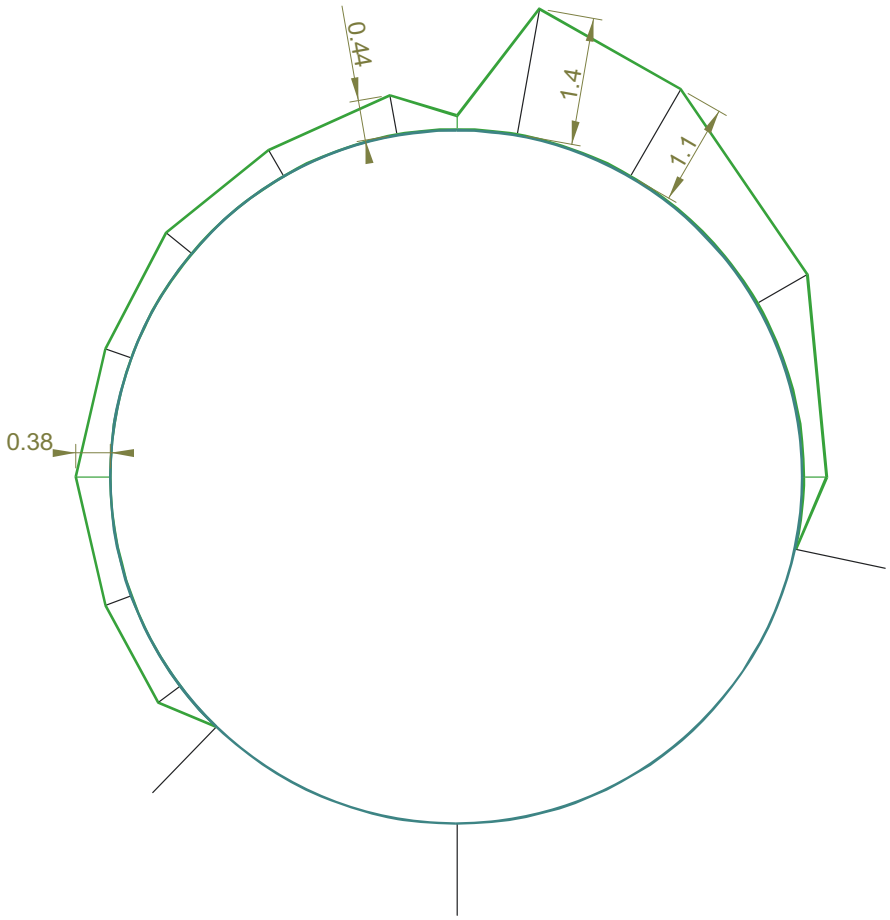

Source: CRWMS M&O 1999 [DIRS 108441], p. 29.

NOTE: Dimensions are in meters.

Figure 6-15. Opening Profile at ESF Main Loop Station 60+24.70 (Steel Set #1272, Tptpmn Lithostratigraphic Unit) Based on Field Survey Data

6.1.6 Generation of Representative Rock Volumes Using FracMan

6.1.6.1 Background

Analysis of seismic response and rockfall in emplacement drifts in fractured, nonlithophysal rock is, in general, a three-dimensional problem requiring the rock mass to be represented as an explicitly fractured assemblage. To achieve this objective, the 3DEC three-dimensional discontinuum program (see Section 6.3.1) is used to model the mechanical response of a rock block assemblage subjected to in situ, thermal, and seismic loads. The 3DEC program allows direct input of the fracture geometry in creation of a "synthetic" rock mass composed of an

assemblage of blocks within which emplacement drifts may be simulated. The details of the 3DEC model are described in Section 6.3.1.1.

The blocks of nonlithophysal rock are significantly stronger than the in situ and thermally induced stresses, and thus the problem of modeling this material is essentially one of elastic blocks separated by fracture surfaces. Therefore, in modeling of the stability of the tunnels and the rockfall that may occur from the applied load, the fracture geometry and surface properties become of primary importance. A methodology for defining statistically representative fractures is therefore required as an input to the 3DEC program for development of the rock block structure. In particular, the input fracture geometry must provide an adequate representation of the orientation, length (area), spacing and continuity of fractures and their variability, as this controls the size and number of kinematically removable blocks that surround the tunnel. Additionally, the surface characteristics, including roughness, planarity, and alteration/infilling define the shearing and tensile resistance of the fractures under load. In the following section, the generation of a statistically representative network of fractures for describing the repository host horizon subunits is described. In particular, the fracturing within the Tptpmn unit is given since this unit represents the largest emplacement area of nonlithophysal rock.

6.1.6.2 FracMan Program Approach to Fracture Geometry Analysis

The development of a stochastically defined fracture system, representative of the host horizon rock mass is accomplished using the FracMan program (USGS 1999 [DIRS 160577]). FracMan is a special-purpose fracture-analysis tool that was developed for the creation of synthetic fracture representations for use in hydrologic modeling, reservoir engineering, and rock mechanics applications. It has been used for preliminary hydrologic modeling of Yucca Mountain (Anna 1998 [DIRS 144421] and Anna 1998 [DIRS 138501]) for estimation of rock mass permeability.

The existing fracture mapping database (see fracture geometry data in Table 4-1) provides the basic input to the FracMan program, which develops sets of planar, circular fractures whose geometric parameters conform to the statistical variability of the geometric characteristics of the input data. Statistical models are fitted to the various geometric characteristics of each fracture set in the database, followed by generation of representative fracture sets. These representative fractures are then back-checked against the statistical variability and geologic realism of the original sets (i.e., field data) to achieve an acceptable facsimile. The FracMan simulations are not intended to replicate actual field conditions but to create a reasonable facsimile of these conditions based on the observed data.

The use of the FracMan program for providing a calibrated set of fractures representative of the repository host horizon is considered to be a scientific analysis governed by procedure AP-SIII.9Q. The definition of a scientific analysis in this procedure is (pg. 6):

> *A documented study that 1) defines, calculates, or investigates scientific phenomena or parameters; 2) evaluates performance of components or aspects of the overall geologic repository; or 3) solves a mathematical problem by formula, algorithm, or other numerical method. A scientific analysis may involve numerical manipulations that are not part of a previously developed and*

validated mathematical model (per AP-SIII.10Q,, Models) if the choice of method is evident from standard scientific practice, approach, or method.

Use of FracMan as a scientific analysis is justified based on the following considerations:

- FracMan is used to investigate and evaluate the stochastic variability of fracture geometry only. FracMan is not used to model a physical process (e.g., rockfall) that involves prediction or extrapolation of physical response.

- FracMan is used only to provide a reasonable facsimile of the occurrence and variability of fracturing in the Tptpmn and Tptpll units. To provide this facsimile, the model is calibrated against the existing field data in such a way that the statistical variability of the dip, dip direction, spacing (intensity) and trace length can be verified to be quantitatively similar.

- The FracMan analysis is not used for extrapolation purposes, but only to provide a calibrated representation of the fracture geometry represented by the database from which it is derived. This database is obtained from detailed line survey and full periphery geologic mapping in the ESF and ECRB Cross-Drift. The ESF provides a North-South sampling over a substantial length of the Tptpmn along the eastern boundary of panels 1 and 2 of the proposed repository, and the ECRB Cross-Drift cuts across all repository host horizon units on a NE-SE azimuth through the center of the repository (see Figure 1-2). It is considered that this total sampling reasonably represents the range of fracture geometries with trace lengths of 1 m or longer, to be expected within the repository and the Tptpmn in particular. Therefore, the FracMan representation, calibrated to the complete fracture database provides a similar representation of the fracture variability in the Tptpmn in particular. In this manner, FracMan is not used to extrapolate fracture geometry to new regions since it is implicit in this approach that the fracture database provides a reasonable representation of the fracture variability throughout the repository host horizon.

- FracMan is a fracture geometry simulation program that is commonly used in industrial and scientific practice.

Based on these considerations, model validation, as described in procedure AP-SIII.10Q, Models, is not required for the fracture simulation analysis described in this section.

The FracMan simulations consist of development of cubical regions of fractures, 100-meter on-a-side, representing the Tptpmn and Tptpll lithostratigraphic zones of the repository horizon. The regions are populated with simulated fracture networks to represent the rock mass of the respective zones. Data from the detailed line survey and full periphery geologic mapping are used as a basis for constructing the representative fracture networks in these regions. As previously discussed, these data consist of fractures with trace lengths of one meter or greater. Each fracture is described by its centroid coordinate, dip, dip direction, and radius. These geometric properties are used as input to the 3DEC program for development of a block geometry within which emplacement drifts can be randomly excavated. Development of the Tptpmn FracMan cube is described in this section to represent the modeling approach used for

nonlithophysal rock. Details for the analysis of the Tptpll long-fracture network, which represents the lithophysal rock within the repository, are provided in Appendix B.

6.1.6.3 Fracture Studies in the ESF and ECRB Cross-Drift

6.1.6.3.1 Data Sources

There are two primary data sources for subsurface fractures within the repository horizon at Yucca Mountain: the detailed line survey and the full-periphery geologic mapping (Beason et al. 1996 [DIRS 101191]; Barr et al. 1996 [DIRS 100029]; Albin et al. 1997 [DIRS 101367]; Eatman et al. 1997 [DIRS 101219], Mongano et al. 1999 [DIRS 149850]). The detailed line survey presents a detailed inventory of fractures and fracture attributes as measured in the ESF and ECRB Cross-Drift. The survey was conducted using a traverse located 0.9 m below the right-rib springline in the ESF (Albin et al. 1997 [DIRS 101367], p. 10; Eatman et al. 1997 [DIRS 101219], p. 8) and at the left-rib springline in the ECRB Cross-Drift (Mongano et al. 1999 [DIRS 149850], p. 9). Data collected by the detailed line survey included information on fracture location (i.e., station), orientation, trace length, width, roughness, among others. The full periphery geologic mapping presents a "rolled-out" record of geologic conditions encountered during tunnel excavation activities. The maps are hinged at the crownline and unrolled to produce flat maps of the tunnel periphery at 100-m intervals. The maps record lithostratigraphic contacts and structural discontinuities (i.e., fractures, faults, and shears) with trace lengths longer than 1 m, as well as engineered features (e.g., rock bolts, steel sets, and installed lagging).

As previously discussed, both the detailed line survey and the full periphery geologic map methods exhibit an inherent sampling bias in that fractures approaching the orientation of the survey line will be underrepresented. Various methods exist for evaluating this bias. The Terzaghi correction (Terzaghi 1966) is a commonly used method to evaluate this directional bias in these types of linear surveys. However, the need for bias correction is avoided in the FracMan model, because the simulations are constructed to reproduce the statistical variability of the field data. As a result the output from a FracMan detailed line survey, similarly oriented to a comparable ESF detailed line survey, will automatically recreate the same bias as exists in the field data, confirming the accurate reproduction of field conditions in the FracMan simulations. In other words the same bias encountered in collecting the observed data is sampled in the synthetic data allowing a valid comparison without necessitating bias correction for the observed fractures. For this reason there is no requirement to apply corrections to evaluate bias. Comparisons of simulated detailed line surveys to the actual field surveys are presented in Section 6.1.6.4.

6.1.6.3.2 Representativeness of ESF and ECRB Cross-Drift Data of the Tptpmn Across the Repository Emplacement Area

Fracture data from the existing ESF and ECRB Cross-Drift excavations has been used for developing the FracMan analysis. Although the excavations traverse a large portion of the subsurface area being considered for the repository, they do not extend to the limits of the proposed repository area (Figure 1-2). To investigate changes in the geometry and character of fractures outside the existing excavations, studies of fractures were implemented in surface exposures of Topopah Spring Tuff at various locations around Yucca Mountain. These studies

examined the significant outcrops of the repository host horizon in the vicinity of the site. These areas included Solitario Canyon (west of the proposed repository area), WT-11 wash (south of the site), Windy Wash (northwest of the site), and Yucca Wash (north of the site).

In each of these areas, the purpose of the data collection was to determine how fracture orientation might vary with distance from the repository area. Orientation data was collected, along with some fracture characteristics and notes, from the four zones in the repository host horizon (i.e., the Tptpul, Tptpmn, Tptpll, and Tptpln). The bulk of the data was collected in the Tptpmn, as this unit is the most erosion resistant. Comparing the fracturing in the Tptpmn from around the periphery of the site allows a relatively easy evaluation of the changes in fracture orientation. Useable outcrops of the other zones – Tptpul, Tptpll, and Tptpln – are sparse in the Yucca Mountain area.

Note that fracture orientation data is only a portion of the fracture data used to develop fracture sets in the FracMan analysis. The analysis has used a hierarchical approach to develop the fracture geometry in FracMan. This approach starts with fracture length, based on the consideration that the long fractures formed first, shorter fractures thereafter. An orientational analysis was then done of the different length fractures to determine the orientation of the fracture sets. Fracture length however, is not easily collected on a systematic basis at outcrop, so a comparison of orientations has been used here for simplicity.

Data from the various Tptpmn outcrops around the Yucca Mountain area show remarkable consistency in fracture orientation. Measurements from the Tptpmn in Solitario Canyon, even far south of the repository area show essentially identical fracture orientations to those observed in the ESF and ECRB Cross-Drift (DTN: GS020908314224.001 [DIRS 171038]). Data from the far southern outcrops in WT-11 Wash show a slight rotation of fractures in that area in comparison with those farther north (along Solitario Canyon). Fractures along the Solitario Canyon fault show similar orientations to those collected in the ESF and ECRB Cross-Drift. Fractures in Windy Wash (DTN: GS040308314224.002 [DIRS 171039]), northwest of the proposed repository, also show similar orientations to those in the underground. These data from widely dispersed locales indicate that fracturing in the Tptpmn is similar across the repository site, and that variations observed underground (such as the intensely fractured zone) generally bound the variations observed in outcrop.

It has been long understood that the fractures at Yucca Mountain and in particular the fractures in the repository host horizon are stratabound (Mongano et al. 1999 [DIRS 149850]). Data from the ECRB Cross-Drift show that fracture orientation in the nonlithophysal Tptpmn and Tptpln are similar in orientation (Mongano et al. 1999 [DIRS 149850]). While not identical, the orientation, frequency, and infilling were found to be quite similar in the two nonlithophysal units. Using the relative frequency and orientation differences seen between the lithophysal and nonlithophysal zones in the ESF Main Drift, South Ramp, and ECRB Cross-Drift, a general understanding can be developed of the density and character of fractures in the lithophysal units as compared to the over- and underlying nonlithophysal zones. Outcrops in Windy Wash, Solitario Canyon, and WT-11 Wash (near Iron Ridge) display similar relationships between lithophysal and nonlithophysal zones. Fracture densities and orientations in Tptpmn outcrops at all locations (except at Prow Pass and Yucca Wash) display 3 to 4 closely spaced sets of fractures, a significant percentage of which are cooling joints. Where the contacts with the

adjacent lithophysal units are exposed, the fracture characteristics change. This change across lithostratigraphic boundaries has been observed at the locations where the rock is exposed. The most dramatic of these exposures are underground such as the Tptpmn/Tptpll contact at station 14+44 in the ECRB Cross-Drift (Mongano et al. 1999 [DIRS 149850]) and the same contact at the southern end of the Main Drift at station 57+29 (Eatman et al. 1997 [DIRS 101219]). At both these locations, the fracture sets that are clearly exposed in the base of the Tptpmn terminate within 1 to 2 m of penetrating into the underlying lithophysal rock of the Tptpll. Similar changes are observed at the Tptpul/Tptpmn and the Tptpll/Tptpln contacts. In each case, the transition from lithophysal to nonlithophysal rock results in a significant increase in long, recognizable fractures. This same relationship is also clearly exposed in surface outcrops. Wherever the contact is visible between lithophysal and nonlithophysal zones, fracture attributes display consistent differences at such contacts (see Figure 6-4).

Fractures in the Yucca Wash area are the only exception to the uniformity of fractures around Yucca Mountain. The area where most of the fractures were measured was west of where the Solitario Canyon fault enters the Yucca Wash drainage. The lithostratigraphic zones of the Topopah Spring Tuff in this area differ considerably in thickness and characteristics from the rest of the mountain (DTN: MO0012MWDGFM02.002 [DIRS 153777]). This change in lithostratigraphy may result from thickness increases in the underlying Calico Hills, specifically the presence of lava flows that extend to the southeast. The rocks in the repository host horizon at this locale differ from the rest of the mountain such that Day et al. (1998 [DIRS 100027]) mapped this area breaking out only the crystal-rich/crystal-poor members, rather than the zones recognized elsewhere. This change causes the fractures in this region to have significantly different orientations and characteristics from those observed elsewhere at Yucca Mountain, and represents the boundary of where present fracture analyses can be used with confidence.

6.1.6.4 Construction Techniques used in Generating the FracMan Simulations

6.1.6.4.1 Hierarchy of Fracture Formation in the Topopah Spring Tuff

Fractures in the densely welded and crystallized tuffs at Yucca Mountain, for example the lithophysal and nonlithophysal zones of the Topopah Spring Tuff, can be divided into two petrogenetic groups: those associated with cooling processes, and those associated with tectonic processes. Because the timing of fracture formation determines the geometry of the fracture network (i.e., trace length and truncations), and thus the size and position of potential rock blocks, it is important to understand the general sequence of fracture formation based on these processes.

All fractures have been described on the basis of geometric relations (strike, dip, trace length, planarity, truncations, etc.) and features such as tubular structures, rims (the light gray crystallized area along the edge of the fracture that is similar to what surrounds lithophysal cavities), and mineral or material filling of the fractures. Tubular structures, rims, and vapor-phase mineralization are indicative of features that formed very early in the cooling history of the deposit (possibly during the first 100 years), and are characteristic of cooling joints (Buesch and Spengler 1998 [DIRS 101433]; Buesch et al. 1999 [DIRS 165483]). Early-formed and even late-formed cooling fractures (referred to as Type 1 and Type 2 fractures in Buesch et al. 1999 [DIRS 165483]) typically have long trace lengths, are the fractures into which shorter

trace-length fractures typically truncate, and form the initial geometric framework for the fracture network. Included in these cooling fractures are (1) vapor-phase partings, which are characteristically long, anastomosing to planar, low-angle discontinuities (i.e., dips less than 20°), and (2) typically long, smooth (i.e., planar), high-angle (i.e., steeply dipping) fractures. As cooling progressed, shorter trace-length fractures formed, which typically truncate into the earlier formed and longer fractures. These smaller fractures can have any orientation (shallowly, moderately, or steeply dipping), but typically have similar orientations as the longer fractures, and may or may not have rims or vapor-phase mineralization. After the rocks had cooled, and in the 12.8 million years since the time of cooling, some fractures, shears (discontinuities with less than 0.1 m of separation), and faults formed as a result of structural tilting and faulting of the mountain. These post-cooling fractures typically have shorter trace lengths and are not as smooth (i.e., are rougher) as cooling fractures. Many shears appear to be reactivated cooling joints or an integration of cooling joints, although some might have formed in conjunction with development of the fracture itself. Some faults can be fairly simple and somewhat planar discontinuities, but many are an integration of short-trace-length fractures to form irregular and rough discontinuities, and some are complex zones of deformation (Mongano et al. 1999 [DIRS 149850]). Many faults and shears, especially those with separations of less than four meters, have similar strikes and dips to the fractures (Mongano et al. 1999 [DIRS 149850]).

6.1.6.4.2 Hierarchical Construction of Fractures in the FracMan Model

Construction of the FracMan network starts with the low-angle vapor phase features. Because these features form first in the cooling process their truncation by other features is minimal. The truncation probability value (i.e., the probability that a fracture that intersects another fracture will be terminated against that fracture) for these features used in FracMan is set to 0 percent as qualitatively estimated from fracture terminations from the full periphery geologic maps. To continue the construction of the FracMan network, the remaining fractures, having a dip greater than 20 degrees are separated into two classes. The first class includes those fractures that formed about the same time as the vapor-phase partings. These fractures are referred to as cooling joints and have long trace lengths with some truncation occurring against the vapor-phase partings and themselves. A truncated power law distribution is used for these features. A large max/min fracture length is used along with a termination probability value of 15 percent, again based on qualitative examination of the terminations in the full periphery geologic maps. The second class includes the fractures that have a shorter trace length. The length distribution can be separated into two populations; those with trace length below 7 to 8 meters (“short” trace length) and those with trace length greater than 7 to 8 m (“long” trace length fractures). This separation is based on a break in slope of the trace length frequency as shown in Figure 6-16. These fractures are considered to be later cooling and tectonic fractures. These fractures are generated into a network comprised of vapor-phase partings and long high-angle cooling fractures and are truncated more severely than the earlier fractures. A shorter max/min fracture length is used along with a termination probability value of 10 percent (as qualitatively estimated from full periphery geologic maps).

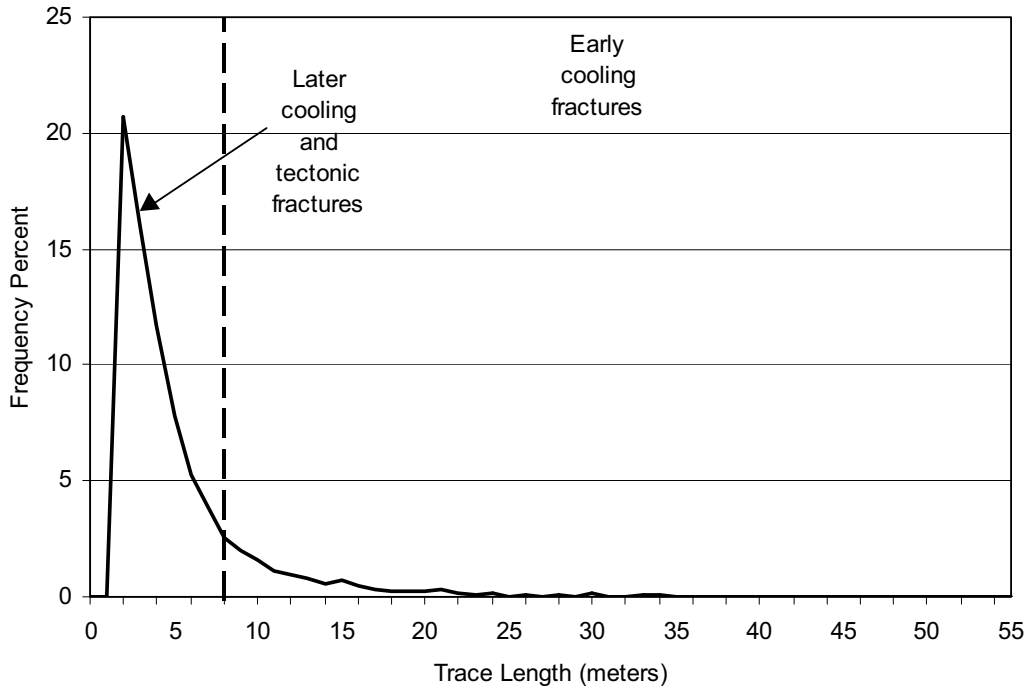

Figure 6-16. Trace Length Distribution of the Tptpmn Fractures with Dips > 20°

Based on the observed data, four fracture sets are defined in the Tptpmn. The great circles for these sets are displayed in Figure 6-17. The fracture analysis of the Tptpmn begins with defining the first forming discontinuities. Based on a hierarchical distribution of discontinuities, the first forming features are the low angle (less than 20 degrees) vapor-phase partings and the long high-angle fractures.

The hierarchical or sequential method of construction is significantly different from a construction with sets solely identified on the basis of orientation. Observations of mineralization and truncation relations (Mongano et al. 1999 [DIRS 149850]) suggest that the current sequential construction is more appropriate to generate a representative rock volume since short fractures truncate against longer fractures. This construction does not create a replicate of the actual fracture geometries observed in the limited sampling afforded by the detailed line surveys and the full periphery geologic maps. The objective is to provide a generalized, representative fracture network for evaluation of the Tptpmn rock mass as a whole. The output from FracMan is a fracture network whose geometry is conditioned from evaluation of the detailed line survey and full periphery geologic map data. Special geologic features are not represented in this effort. For example, in a given segment of tunnel mapping there may be a small section that shows an increased amount of fractures from a given set. The developer may decide to represent this zone by developing a specific distribution for this occurrence[1]. However,

[1]A zone within the Tptpmn that was given specific treatment and not included in the general fracture characteristics for FracMan development is the "intensely fractured zone". The intensely fractured zone, a 1000-m zone with anomalously high Set 1 fracture frequency (i.e., the mean and median joint spacing for the predominant Set 1 fractures were calculated to be 0.24 m and 0.12 m, respectively), is not modeled with FracMan, but is treated as an anomalous zone of ubiquitous fracturing with the Set 1 orientation as described in Section 6.3.2.

for this report an average geometry is used to describe the simulation because the fracture network developed does not represent a specific section of the mapped area, but is representative of the general condition of the rock mass. Zones that display anomalous geometries in each lithostratigraphic unit are averaged into the simulation when the decision is made that adding this input helps represent the rock mass correctly (in an overall sense) with the data that is available. Because this output is not a replicate, a single constant fracture intensity is imposed for each set in each lithostratigraphic unit.

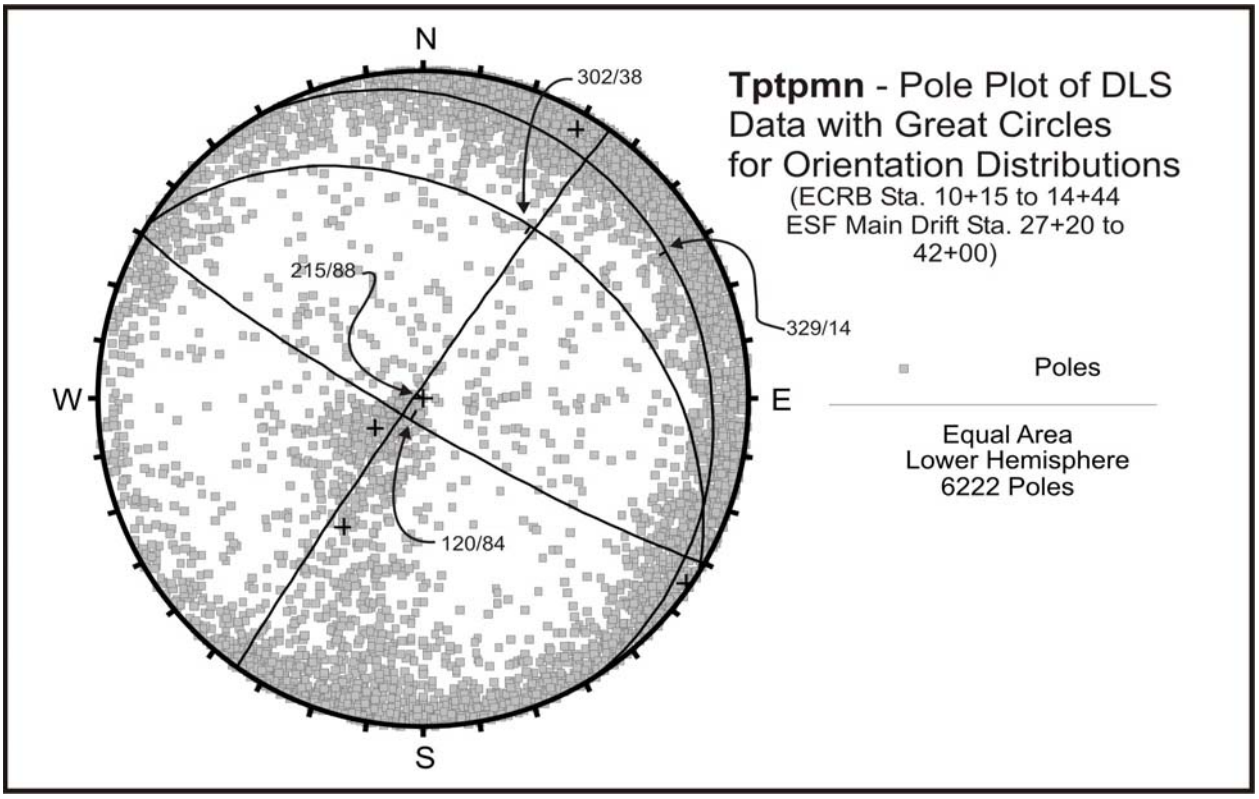

Source: DTN: GS971108314224.025 [DIRS 106025]; GS000608314224.004 [DIRS 152573] GS960708314224.008 [DIRS 105617]; GS960708314224.010 [DIRS 106031]; GS990408314224.001 [DIRS 108396].

NOTE: Data from the intensely fractured zone are not included in this pole plot. Orientations are given in strike and dip of mean poles.

Figure 6-17. Pole Plot of Tptpmn Detailed Line Survey Data from the ESF Main Loop and ECRB Cross-Drift

6.1.6.4.3 Fracture Trace Length

Correct fracture size (trace length and area) is critical to the construction of a representative network. Unfortunately, the radius of a fracture cannot be measured from sampling of the fracture network along the surface of a tunnel. If the fractures are considered circular disks, the centers of those disks do not have to coincide with the sampling surface. The observed trace length is then typically not the disk diameter because the centers of the fracture disks do not coincide with the sample surface. In a tunnel surface sampling, observed trace length could be longer or shorter depending on the position of the center of the fracture.

To get an intuitive feel for the radius distribution and how it relates to the observed trace length distribution consider a single fracture of radius R oriented perpendicular to the sampling plane. If the fracture intersects the plane, the observed trace length can vary from 0.0 to 2.0R.

The trace length, T, is a function of the distance from the sampling plane, z, and the fracture radius, R, and is defined based on standard geometric relationships (see Figure D-11):

$$T=2\ (R^2-z^2)^{0.5} \qquad \text{(Eq. 6-1)}$$

The mean observed trace length T_m is then

$$T_m = \frac{1}{R}\int_0^R 2(R^2 - z^2)^{0.5}\,dz \qquad \text{(Eq. 6-2)}$$

$$T_m = \pi R/2 \text{ or } R = T_m\, 2/\pi \qquad \text{(Eq. 6-3)}$$

indicating that the mean fracture radius is about 2/3 of the mean trace length observed.

This means that the expected distribution of trace lengths is equal to the distribution of the intersecting fractures times a constant factor $\pi/2$. In a log-log plot, multiplication of a power law by a constant does not change the slope, so that the scaling exponent of trace lengths is the same as the scaling exponent of the radius distribution of intersecting fractures.

The radii distributions are compared to a distribution formed from the trace lengths observed multiplied by two-thirds to adjust the trace lengths to approximate radii. This is not a perfect adjustment because the dip of the fractures as well as their persistence will influence the number "two-thirds." The trace lengths are observed with a sampling surface or detailed line survey. Additional effects may be present when comparing the radii in the 100-m cube synthetic fracture region generated by FracMan with the surface or line sampling. Individual plots of these distributions are included in each of the following sections for the lithostratigraphic units. Overall, the fits are good to excellent.

After the sequence of formation is defined and the length distribution selected, orientation is evaluated to further subdivide the fractures into sets based on analysis of stereonet pole plots. Fractures with a dip greater than 20 degrees are used for this analysis because the orientations of the longer fractures and the shorter fractures are coincident. Once this is accomplished, the actual inputs for FracMan are developed.

6.1.6.4.4 Fracture Geometry

The following is a brief description of the inputs required to begin the generation of simulated fracture geometries. The fracture geometry data for each lithostratigraphic unit are converted to the parameters needed for FracMan. The input values for the FracMan model of each lithostratigraphic unit are derived from the detailed line survey data and used to develop an input data form. The FracMan input sheet for the Tptpmn is shown in Figure 6-18. Sets are based on

FracMan/FracWorks

Project Tptpmn Task Drift Degradation Date 03/04 Modeler Lung-Fahy

Seed #: 1 Fracmeter Unit: 50 Truncation mode Region View Center 0,0,0

Direction _____ Scale _____ % displayed 100 Orientation = Pole or Dip Pole # frac sides 6

Frac. Set	Model Type	Generation Region & Dimension	Orientation Trend, Plunge	Dist. Type	K or K1/K2 dispersion	Size Eqv. Radius	Dist. Type	Mean SD	Max. Min.	Elongation	Aspect Ratio	Termin. %	Intensity
S1s	BART	100x100x100	035/06	BiBing	-39.5/-4.5	1.00	TPow (3.5)		8/1	NA	NA	10	0.40
S2s	BART	100x100x100	124/04	BiBing	-11.8/-6.2	1.00	TPow (3.5)		8/1	NA	NA	10	0.30
S3s	BART	100x100x100	209/47	BiBing	-72.6/-8.8	1.00	TPow (3.5)		8/1	NA	NA	10	0.10
VPP	Baecher	100x100x100	237/82	Fisher	05	1.00	Power (3.5)		NA	NA	NA	0	0.16
S1l	BART	100x100x100	035/06	BiBing	-39.5/-4.5	1.00	TPow (3.5)		50/4	NA	NA	15	0.2
S2l	BART	100x100x100	124/04	BiBing	-11.8/-6.2	1.00	TPow (3.5)		50/4	NA	NA	15	0.2
S3l	BART	100x100x100	209/47	BiBing	-72.6/-8.8	1.00	TPow (3.5)		50/4	NA	NA	15	0.15

NN factor _____ NN export: _____ WZ inten: _____ WZ parall: _____ WZ large: _____ WZ close _____ Frac Dim (LL,FB)(.5-5.) _____

Zone Thick _____ Fracs _____ # iterations _____ Frac Dim (POCS) _____ Ampl Shaper Fac (POCS) _____ Box Frac Dim _____ Spherical/ Exp _____

Variogram _____ Semivariogram Sill _____ Corr Length _____

_____.FDT (Binary. Cannot port to non DOS computers. Cannot be edited in standard word processing.)

_____.BAB (Babylonian ASCII version of FDT. Only fracture data stored. Can be ported to non DOS computers. No standard word processing.)

_____.DCM (Standard ASCII version of FDT. Only fracture data stored. Can be ported to most computers. Can be edited by standard word processing. Large files.)

_____.SAM (ASCII) _____ .ORS (ASCII) _____.PCS (ASCII, for conditioned data)

_____.F2D (ASCII, fracture trace data)

NOTE: See Figure 6-17 for detailed line survey source DTNs. The parameter, “K or K1/K2 dispersion” is determined using CLUSTRAN (with the exception of VPP, or vapor-phase parting, which is determined visually by comparing simulated stereonets to observed stereonets). The parameter, “Size Eqv. Radius” is the mean radius (m). The power law distribution is used for the parameter, “Dist. Type.” The power law is selected because the fracture process generally follows power law physics, such that the number of fractures greater than a given length (x) is proportional to 1/x raised to the power law exponent. The parameter, “Intensity” is selected to maintain the proportion of fractures in each set.

Figure 6-18. FracMan Input Sheet for the Tptpmn

length in a hierarchical model. A truncated power law is used because the short and long fractures are defined for a given window of trace length (Figure 6-16). Vapor-phase partings are not subjected to a truncated power law distribution, because they are first-occurring features with a long trace length. The other sets are developed using "Baecher Revised Terminations" model type in order to simulate the truncation probability.

Based on the long fractures, the trend and plunge of the poles are used to set the mean orientations for each of the sets. CLUSTRAN (Shanley and Mahtab 1974 [DIRS 169199]), a structural geology statistical software application, is used to determine both mean pole values and dispersion of fractures around the mean. CLUSTRAN is a computer program that analyzes fracture data using stereographic projection techniques. Stereographic projection involves the projection of points from a spherical surface (typically the lower hemisphere of the surface) to a planar surface (the stereographic plot surface). The purpose of the CLUSTRAN program is to plot and analyze the orientations of fracture directional data sets for the purpose of identification and analysis of clusters of poles from which sets and their dispersion can be identified. Conventional identification of fracture sets involves plotting of the fracture poles onto a stereographic net, followed by contouring of the poles and use of the concentrations of data to identify clusters that indicate numbers of sets and directional trends. The use of CLUSTRAN eliminates the conventional visual interpretation of data, presenting a more objective interpretation through evaluation of set clusters and dispersion directly using statistical evaluation techniques.

CLUSTRAN statistically analyzes the identified longer fractures for non-randomness. The program locates clustered subsets of the data by using an algorithm described by Shanley and Mahtab 1974 [DIRS 169199]). This algorithm uses an iterative process to identify the statistically optimal data clusters. In the algorithm, dense points (those data points that have at least n neighbors within a cluster radius R) are first identified. The remaining non-dense points are then allocated to the nearest dense point. Finally, the dense points are grouped into clusters by chaining them together by segments of length R or less. In the original algorithm developed by Shanley and Mahtab (1974 [DIRS 169199], p. 2), both variables R and n had to be selected by the user. In CLUSTRAN, the integer n is calculated from a Poisson statistical model such that the probability of n points occurring within the radius R by chance alone is no more than 5 percent. Because a data set can be clustered many different ways depending on the cluster radius, Shanley and Mahtab (1974 [DIRS 169199], p. 3) developed an objective function, $F(P)$, as a tool for selecting the best clustering of the data set. This function is the sum of the within-cluster distances squared with the between-cluster distances squared. The best partition, and best value of R, occurs where the $F(P)$ is minimum. This condition means that the distances have been minimized by trading off within-cluster distances with between-cluster distances. Thus, the CLUSTRAN cluster analysis process is iterative. The user selects a trial value for the cluster radius, R. CLUSTRAN identifies the clusters based on this R and evaluates for the objective function, $F(P)$. Other values of R are tried over a broad range until the lowest objective function value is found. CLUSTRAN will evaluate the iterative runs and select the correct R to use based on the lowest $F(P)$ value.

Once clusters have been identified from the data set, CLUSTRAN carries out statistical analysis on each cluster. First, moment-of-inertia analysis is carried out. This analysis treats each data point as a point of mass on a unit hemisphere. The maximum moment-of-inertia goes through

the center of the cluster, the intermediate moment parallels the long axis, and the minimum moment is perpendicular to the long axis. The Bingham probability distribution is applicable to moment-of-inertia analysis (DOE 2004 [DIRS 170474]). It provides two concentration parameters, *K1* and *K2*, that describe the shape and concentration of the data set. Then, using the output from the Bingham distribution, the test for circular symmetry is performed to yield bipolar and girdle test statistics.

If the distribution is symmetric according to these previous tests, then additional tests are performed. The Dimroth-Watson distribution (the circularly symmetric form of the Bingham distribution) yields a concentration parameter to describe the data cluster (DOE 2004 [DIRS 170474]). If the concentration parameter is near zero the distribution is random, whereas if the concentration parameter is large, the points are concentrated. Further, if the parameter is less than zero the distribution is symmetric bipolar, and if the parameter is greater than zero the distribution is a symmetric girdle.

If the cluster is symmetric and bipolar, the vector mean and associated Fisher statistics are also calculated. The Fisher distribution (equivalent to a normal distribution in univariate statistics) does not apply to moment-of-inertia analyses, but to vector analyses (DOE 2004 [DIRS 170474]). It is also strictly applicable to the polar distribution, but bipolar distribution may be treated by using the axis ends nearest each other. The Fisher mean is the vector sum of the directions, where each fracture pole direction is treated as a unit vector. These parameters, mean orientation and dispersion, are "inputs" into the FracMan code. Just as one would set the variance of a univariate parameter, distributions of structural geology vectors are described by a mean orientation and a dispersion about the mean direction.

Several comparisons are made to confirm that the results of the FracMan output are producing a simulated fracture geometry that resembles the actual rock mass. Comparison is made between the detailed line survey data pole plots and the FracMan data pole plots. Correct selection of the mean orientation as well as the correct dispersion, *K*, is key to obtaining an acceptable distribution of poles on the stereonet. The results of this comparison are presented in the following section for the Tptpmn. Stereonets generated by the FracMan realization and stereonets from the observed detailed line survey data show reasonable comparisons for both the mean orientation and dispersion about the mean (Figure 6-19). There are several methodologies to modeling the dispersion of real fracture data. One is to completely encompass the full range of observed data. When fitting the dispersion in this style the dispersion factor is small, typically less than 20 for a Fisher *K* value. However the range of variability is large. An alternative method focuses on a tighter description of the observed data, considering that the extent of the observed data is below the level of significance for data on the stereonet. For example, with 100 data points, a 1 percent count circle needs to have encompassed approximately four data points in order for the level of significance to be distinguishable from a random data set. There are no random sets in nature so we wish to depict sets that meet the nonrandomness criteria. A larger *K* value will accomplish this. Larger *K* values depict a smaller dispersion about the mean orientation. This is the style of fit used for these analyses.

Comparison of the observed to synthetic fracture geometry for each set is given qualitatively in the stereonet plots of poles given in Figure 6-19 and quantitatively in Table 6-2. The criteria for adequate agreement of the fracture geometry from observed to synthetic models are: 1) that the

mean orientation is adequately estimated, and 2) that a large portion of the observed data dispersion is encompassed but not every pole. Analysis of data on the stereonet requires that sets are identified from data that are significantly different from a uniform distribution on the stereonet. The outer portions of a distribution are similar to the tail of a univariate distribution. The goal was to simulate the main portion of the distribution and not the tail of the distribution. Therefore, the synthetic data pole plots are more tightly clustered than the observed pole plots for this reason (Figure 6-19).

The goal of the orientation comparison is, therefore, to represent the major sets with reasonable conformance to the observed mean orientations and the observed spread or dispersion about the mean. Not every fracture observed will be represented in the FracMan realizations since the synthetic model represents a reasonable facsimile of the rock mass, but not a replicate.

More fractures will be displayed in the 100-m on a side FracMan cube than are observed in the detailed line survey data. The detailed line survey data samples a small surface area compared to full periphery geologic mapping and considerably fewer fractures are observed than are present in the 100-m cube. The primary comparison to make between the rock mass geometry and the FracMan geometry is to compare full periphery geologic maps. The FracMan geometry allows for the same kind of sampling as the original data. For each of the following sections a direct comparison is presented to confirm that the FracMan geometry resembles the observed geometry. Intensity controls the number of fractures and the check for intensities relies on the comparison of FracMan full periphery geologic maps to the observed full periphery geologic maps for validation. If the intensity from the FracMan full periphery geologic maps and the observed full periphery geologic maps are similar and trace length comparisons are good, the validation is considered satisfactory.

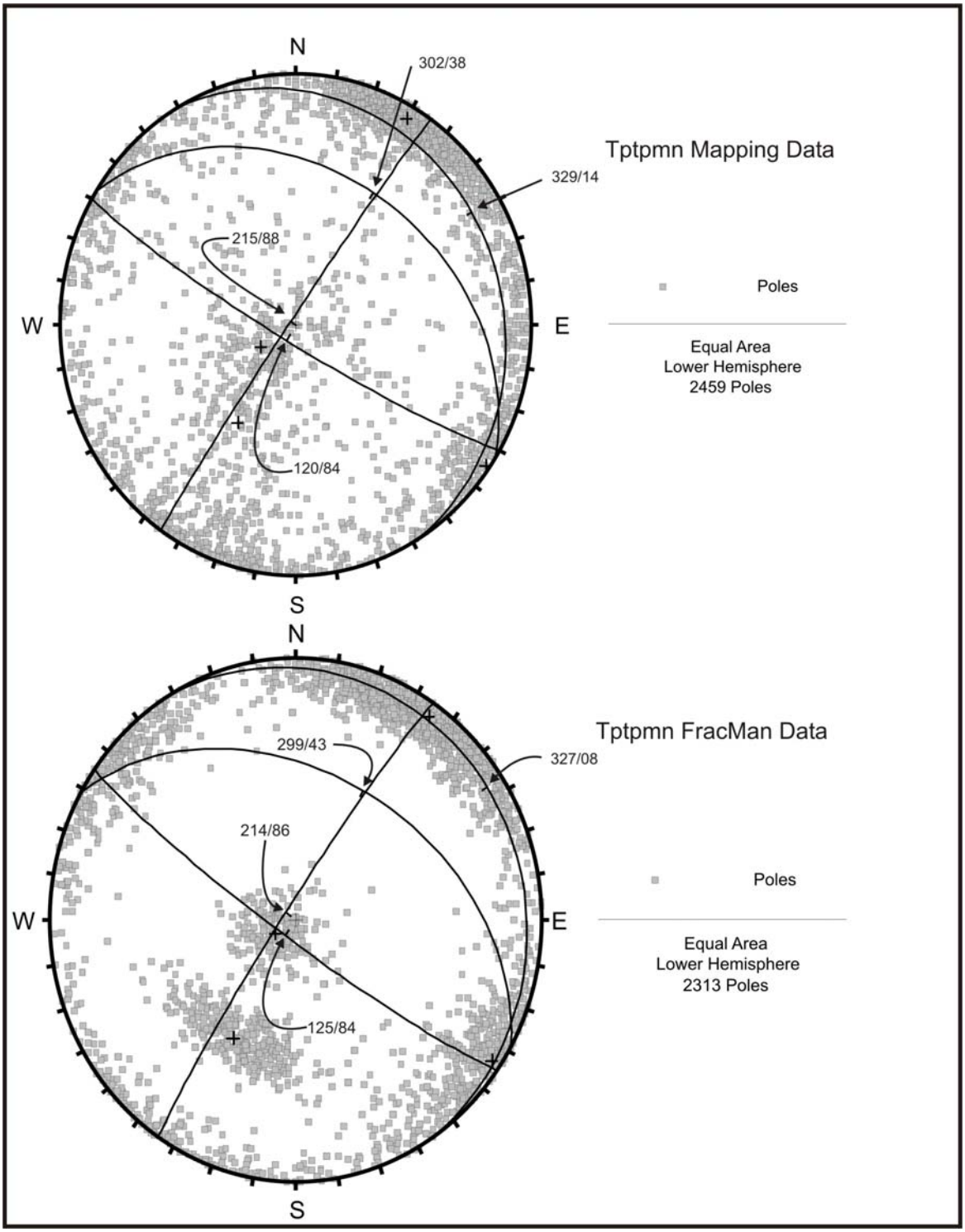

NOTE: The Tptpmn FracMan data include 15 samples, or "excavations", extracted from the FracMan cube at random locations resulting in 2313 fractures. The Tptpmn mapping data was selected by sampling the full periphery geologic maps until a similar number of fractures could be compared to the FracMan data. The source DTNs for the full periphery geologic map are: GS960908314224.020, GS000608314224.006, GS960908314224.015, GS960908314224.016.

Figure 6-19. Comparison of the Observed Tptpmn Fracture Poles to the FracMan Fracture Poles

Table 6-2. Comparison of Data from Underground Mapping and FracMan for the Tptpmn

Set Number	Observed Orientation Strike/Dip (Trend/Plunge)	FracMan Orientation (Strike/Dip)	Inter-Fracture Median Distance (m)		Trace Length Median from Full Periphery Geologic Maps (m)	Trace Length Median from FracMan (m)
			Observed	FracMan		
Set 1	120/84 (030/06)	125/84	0.48	0.79	3.3	2.8
Set 2	215/88 (125/02)	214/86	1.08	1.29	2.8	3.1
Set 3	302/38 (212/52)	299/43	3.40	3.16	3.7	3.6
Vapor-Phase Parting	329/14 (239/76)	327/08	2.46	1.48	3.5	3.4

Source: DTNs for tunnel mapping include: GS960908314224.020 [DIRS 106059]; GS000608314224.006 [DIRS 152572]; GS960908314224.015 [DIRS 108372]; GS960908314224.016 [DIRS 108373]; GS971108314224.025 [DIRS 106025]; GS960708314224.008 [DIRS 105617]; GS000608314224.004 [DIRS 152573]; GS960708314224.010 [DIRS 106031]; GS960908314224.014 [DIRS 106033]; GS970208314224.003 [DIRS 106048]; GS970808314224.010 [DIRS 106050]; and GS971108314224.028 [DIRS 106047].

NOTE: Trace length medians are taken from a compilation of tunnel mapping and synthetic tunnel samples from FracMan (see Figure 6-23 for the trace-length distribution).

6.1.6.4.5 Fracture Intensity

A number of fracture intensity (e.g., the relationship of fracture spacing, orientation and areal extent within a rock mass) measures are typically used for quantification of field measurements. These include (Dershowitz and Herda 1992 [DIRS 104893]):

- P_{10}[2] – the number of fractures/length of a scanline
- P_{21} – the length of fracture traces/area of exposure from a full periphery map
- P_{32} – area of fractures/volume of the rock mass

Thus, P_{10} represents a linear measurement of fracture intensity, P_{21} an areal measurement and P_{32} is a volumetric measure. The first two measures of intensity can be made from available detailed line surveys and full periphery geologic maps. The P_{32} measure is the most accurate measure of fracture intensity, but must be estimated since it is impossible in practice to provide a volumetric measurement since sampling is via a line or tunnel surface mapping.

The general relationship between the fracture intensity P_{32} and the mean fracture spacing, S, along a line is given by Dershowitz and Herda (1992):

$$P_{32} = C/S = C\,P_{10} \qquad \text{(Eq. 6-4)}$$

where C is a constant that depends on the orientation distribution of the fractures. Dershowitz and Herda (1992, p. 763) suggested a range of expected values for C between 1.0 and 3.0 and a value of 2.0 for a uniform distribution of orientations.

[2] The term P stands for persistence.

Equation 6-4 has been derived for the simplified case where the orientation distribution is constant. For different orientation distributions, the equation becomes inaccurate for large variations about the mean pole orientation. In the general case, the P_{32} value can be expressed as:

$$P_{32} = \frac{C}{d \cdot \left(\frac{1}{\int_0^{\pi} \sin(\theta)\, f(\theta)\, d\theta} \right)} \qquad \text{(Eq. 6-5)}$$

where d is the inter-fracture distance along a line, and $f(\theta)$ is the orientation probability density function.

In this report, the FracMan model uses a constant P_{32} for each set of fractures, which is based on the consideration that there is no spatial heterogeneity in intensity. There are a few discrete changes in intensity observed in the detailed line survey and full periphery geologic map data, but for the most part, the "average" intensity is constant as depicted by a linear cumulative fracture number versus stationing plot for each of the lithostratigraphic units. As shown in Figure 6-20, a plot of the cumulative number of fractures versus distance along the ESF for the Tptpmn is given based on detailed line survey data. This data shows that a roughly linear relationship exists between fracture frequency and distance for the Tptpmn within the ESF at a slope of approximately 2 fractures per meter. A distinct break in slope occurs over a 1000-m section termed the "intensely fractured zone" in which the fracture frequency roughly doubles. This zone is considered to be anomalous as it is not observed in any other locations in the underground excavations, and is excluded from FracMan. Modeling studies (see Section 6.3.2.1) examine stability of the intensely fractured zone using continuum-based modeling methods. The linear character of the cumulative fracture frequency plot demonstrates that little spatial heterogeneity of the fracture intensity exists in the Tptpmn overall.

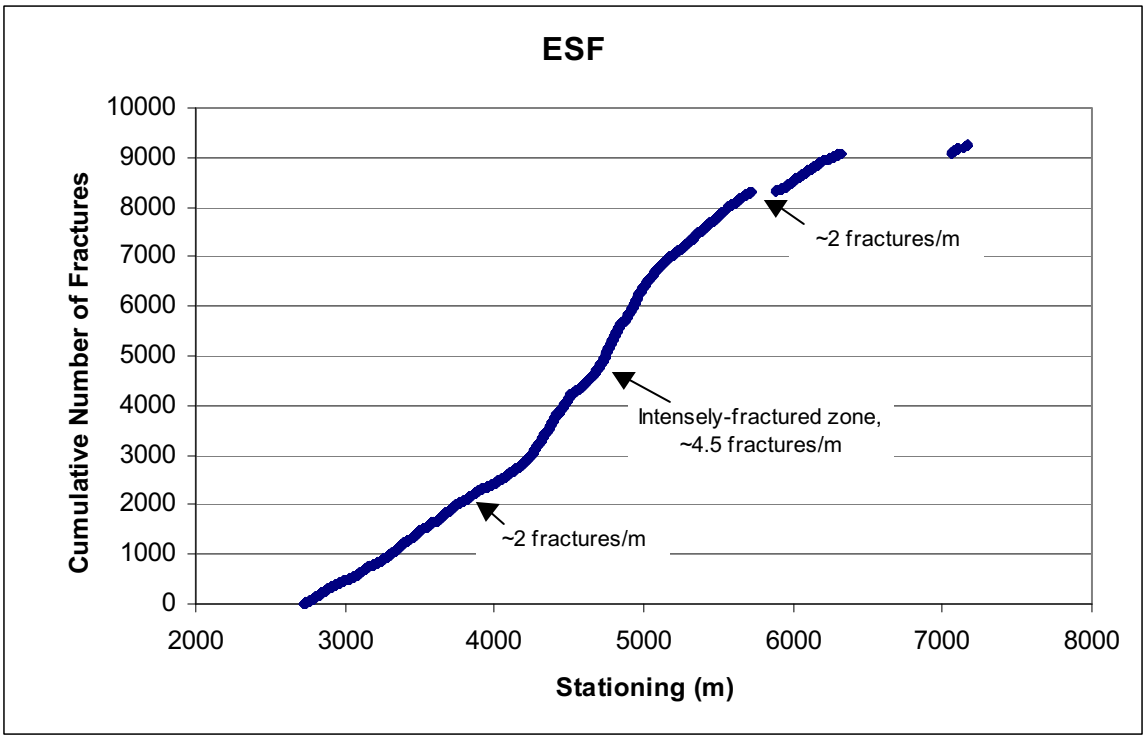

NOTE: The fracture frequency shows a break in slope from approximately 2 fractures per meter to over 4 fractures per meter over an approximately 1000-m section of the ESF. This region is termed the "intensely fractured zone" and is not observed in the ECRB Cross-Drift.

Figure 6-20. Cumulative Number of Fractures Versus Stationing for Detailed Line Surveys Along the ESF

6.1.6.4.6 Comparison of FracMan Synthetic Fracture Geometry and Field Data

Comparison of the FracMan-generated synthetic fracture geometry to the field fracture data is performed both qualitatively and quantitatively. From a qualitative standpoint, the FracMan program is used to create equivalent full periphery geologic maps by creation of virtual tunnels parallel to the ESF within the FracMan synthetic rock mass. Visual comparison is made between the FracMan and field full periphery maps are performed to ensure that the model produces the primary structural features evident in the field data. Quantitative comparisons of fracture trace length, spacing and orientation are made by comparison of the statistical distributions.

Qualitative Comparison–To insure that the synthetic fracture network is not only statistically representative, a qualitative comparison of random full periphery geologic maps from the ESF and FracMan synthetic full periphery geologic maps created at the same orientation are visually compared (Figure 6-21). This is a direct comparison between actual full periphery geologic maps from the ESF to synthetic full periphery geologic maps from FracMan. The comparison is made to evaluate the general fracture intensity and length with the same biases inherent in the field full periphery geologic mapping. Based on the professional expertise and experience of project geologists, the FracMan full periphery geologic maps are acceptably conditioned to be visually similar to observed full periphery geologic mapping.

Quantitative Comparison–The detailed line survey data and full periphery geologic maps are used to condition FracMan to develop representative fracture trace lengths and inter-fracture distance. The same comparisons of the mapping data and FracMan output apply to this realization. Table 6-2 provides a quantitative comparison of the orientation of the sets and trace lengths from the full periphery geologic maps and samples from FracMan. Intensity (inter-fracture distance) from FracMan and inter-fracture distance from the detailed line surveys is also compared. Because no line surveys were conducted on the full periphery geologic maps, detailed line survey data were used for generating inter-fracture distance data, which was compared to 1 m diameter (synthetic) boreholes randomly drilled in the same orientation in the FracMan rock mass. By sampling the FracMan rock mass in the same orientation as the detailed line survey data, the need for a correction to either data set is eliminated. Distribution comparisons of inter-fracture distance from both FracMan and detailed line survey data are shown in Figure 6-22, show a reasonable comparison, both in the univariate statistical mean as well as the general shape of the distributions.

The comparison in Figure 6-23 confirms that a reasonable conformance exists between the trace length distribution from FracMan and the observed trace length distribution. To develop a true comparison of trace length between the observed and the synthetic data, length data from observed and synthetic full periphery geologic maps are compared. As with the inter-fracture distance comparisons, the full periphery geologic maps from FracMan are sampled on the same orientation as the observed data to eliminated the need to correct either data set. The orientation comparison was previously presented in Figure 6-19.

In summary, a FracMan fracture region was constructed which is calibrated to the observed data for orientation and its dispersion, size and its distribution, and intensity (as measured by interfracture distance) and its distribution on a set by set basis. In addition, any biases due to sampling were effectively removed by using the same sampling style as the observed data collection when comparing the synthetic and the observed data sets.

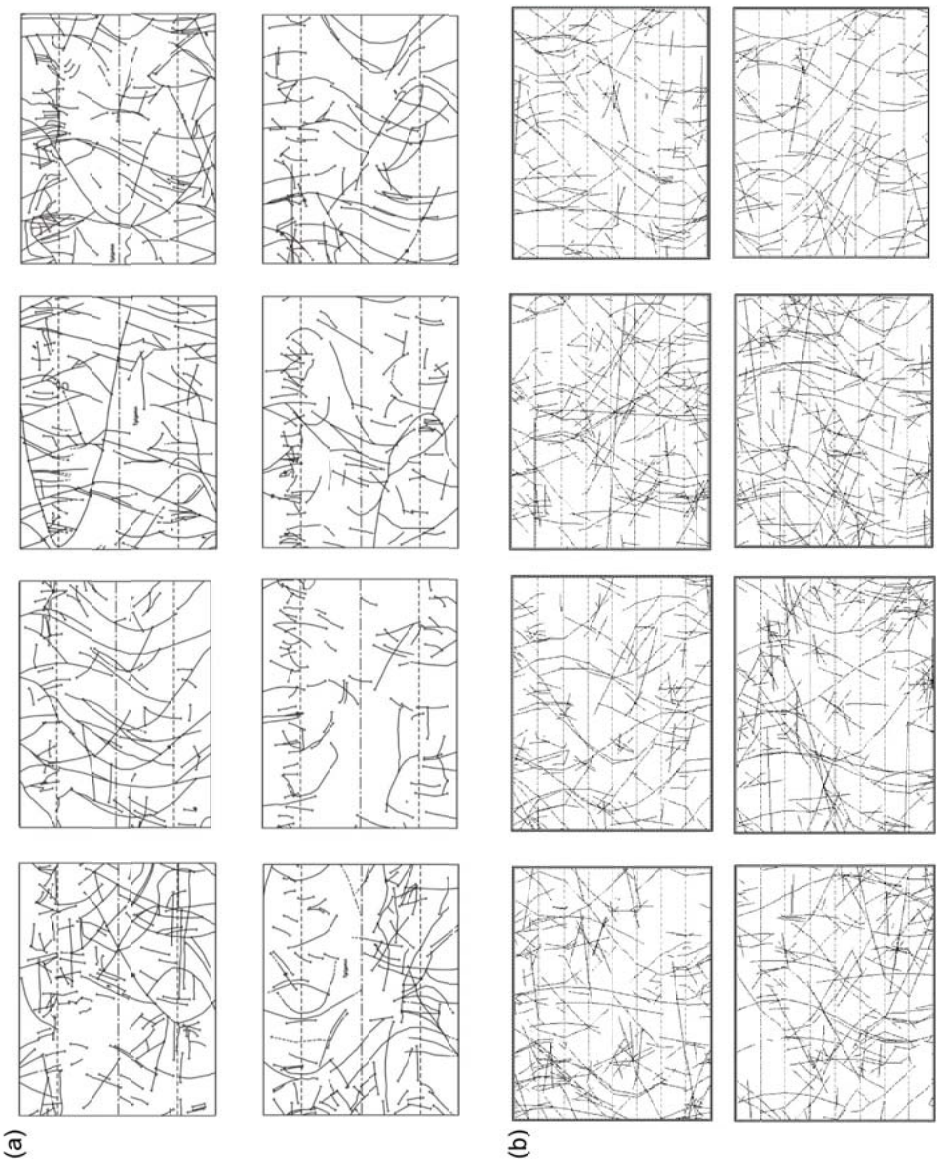

Source: DTNs: GS990408314224.004 [DIRS 108405]; GS000608314224.006 [DIRS 152572]; GS960908314224.015 [DIRS 108372]; GS960908314224.016 [DIRS 108373]; GS960908314224.017 [DIRS 108376]; GS970108314224.002 [DIRS 107490].

NOTE: The purpose of this figure is to illustrate the geologic structure contained on a full periphery geologic map. The annotated information on this figure is not intended to be legible.

Figure 6-21. Comparison of (a) Full Periphery Geologic Maps from the Tptpmn in the ESF (b) with Simulated Full Periphery Geologic Maps from the FracMan Cube

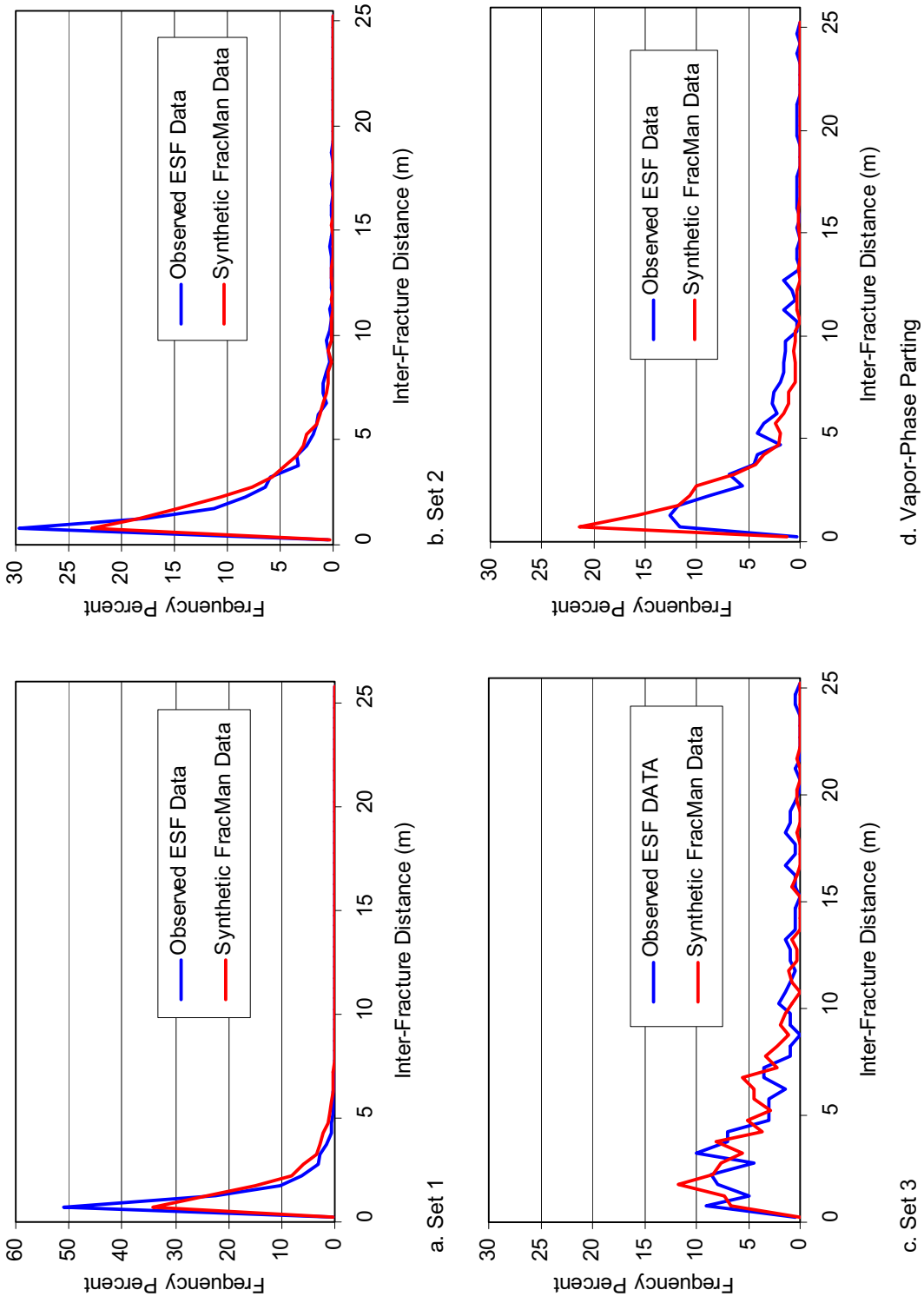

Source: DTNs for the detailed line survey data include GS971108314224.025 [DIRS 106025]; GS960708314224.008 [DIRS 105617]; GS000608314224.004 [DIRS 152573]; GS960708314224.010 [DIRS 106031]; GS960908314224.014 [DIRS 106033]; GS970208314224.003 [DIRS 106048]; GS970808314224.010 [DIRS 106050]; GS971108314224.028 [DIRS 106047].

Figure 6-22. Distribution Comparisons of Inter-Fracture Distance

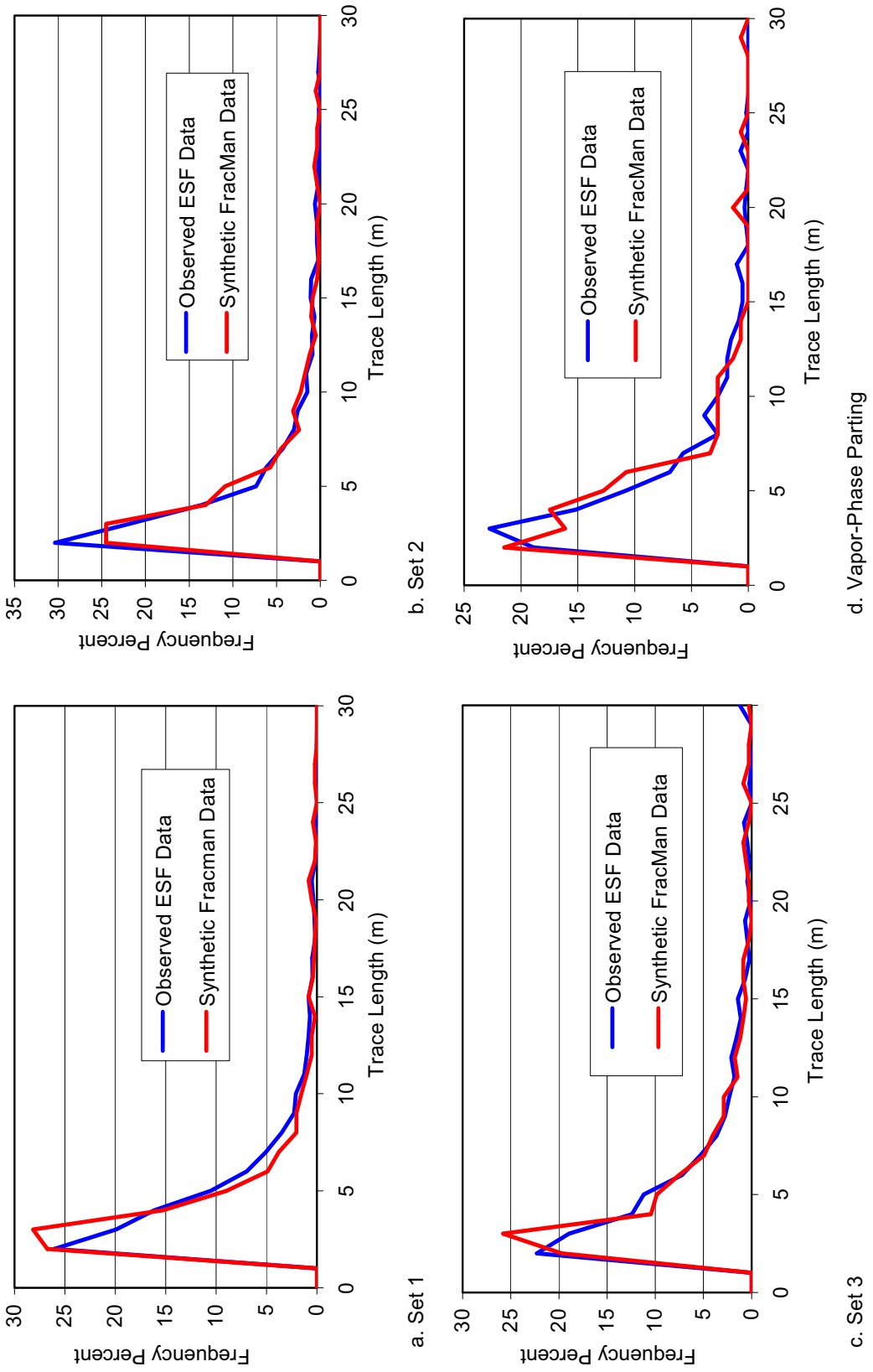

Source: The source DTNs for the full periphery geologic map are: GS960908314224.020, GS000608314224.006, GS960908314224.015, GS960908314224.016.

Figure 6-23. Comparison of Sampled Fracture Trace Lengths from the FracMan Cube and Full Periphery Geologic Maps from the ESF for the Tptpmn

6.2 THERMAL-MECHANICAL CALCULATION

Coupled thermal-mechanical processes in the rock mass surrounding the geologic repository at Yucca Mountain are examined in this section. This thermal-mechanical calculation investigates the temperature history throughout the preclosure and postclosure periods of the repository, and stress changes, $\Delta\sigma_{ij}$, due to temperature change, according to the following relation (Itasca Consulting Group 2002 [DIRS 160331], Manuals/3DEC/Optional Features/Section 1: Thermal Option, Section 1.2.3):

$$\Delta\sigma_{ij} = \delta_{ij} 3K\alpha\Delta T \quad \text{(Eq. 6-6)}$$

where δ_{ij} is the Kronecker δ (unit matrix), α is the coefficient of thermal expansion ($°C^{-1}$), K is the bulk modulus (Pa), and ΔT is the change in temperature (°C). The coupled thermal-mechanical calculation was conducted by two sets of calculations: the drift scale (described in this section) and the coupled regional and drift scale calculations (described in Appendix C).

The drift scale thermal-mechanical calculation consists of the temperature history (thermal) calculation and the thermal stress (mechanical) calculation. The thermal part of the drift scale calculation was performed by the NUFT thermohydrology software simulating two-dimensional drift scale thermal-hydrologic behavior. The temperature history results from the NUFT code were imported to the UDEC discrete-element software and the FLAC finite-difference software to calculate the thermal stress around the emplacement drift (see Appendix U). UDEC and 3DEC (the three-dimensional equivalent of UDEC) were used to model the effects of the thermal stress and to conduct a rockfall analysis associated with the previous thermal stress calculation. Details of the thermal stress calculation and the rockfall analysis for nonlithophysal and lithophysal units are presented in Sections 6.3.1.3 and 6.4.1.2, respectively.

The drift scale calculations (both thermal and mechanical) consider an infinite extent (perpendicular and in the direction of the drifts) of the repository; consequently, they are two-dimensional (a single drift included in the calculation), with a symmetry boundary condition on a plane halfway between the emplacement drifts[3]. The coupled regional and drift scale thermal-mechanical calculation (Appendix C) was planned and conducted to support this drift scale calculation by assessing repository-scale effects, including edge effects and the effects of finite repository size and depth on predicted temperatures and stresses. These calculations are three-dimensional, and analysis was carried out in two steps. First, the regional scale thermal-mechanical calculation was used to determine temperature and stress changes on the scale of the entire mountain. In the next step, the drift scale thermal-mechanical analysis was performed such that boundary conditions for temperature and stress fields (functions of time) were determined from the regional scale calculation. Thus, this calculation did not use any simplifying assumptions (e.g., infinite extent of the repository) for the boundary conditions. Both components of the regional and drift scale thermal-mechanical calculations were performed using FLAC3D. Because the goal of the calculation was to support the drift scale calculation, details of the calculation and results are presented in Appendix C. A comparison of temperatures

[3] The symmetry boundary condition results in zero displacements perpendicular to the boundary and zero heat flux across the boundary.

and stresses as calculated by the drift scale and the coupled regional and drift scale calculations is presented at the end of this section.

The thermal part of the drift scale calculation was performed by the NUFT thermohydrology software, applying a two-dimensional line-averaged heat source, drift scale, thermohydrologic (LDTH) sub-model, which is described in *Multiscale Thermohydrologic Model* (BSC 2004 [DIRS 169565]). The LDTH sub-model is a part of the multiscale thermohydrologic model that is created by the NUFT software. The LDTH sub-model accounts for hydrologic effects in the rock mass, and conductive and radioactive heat transfer mechanisms around the drift. Effects of the preclosure forced ventilation are accounted for by removing a percentage of the heat given off by the waste package (Section 5.1.2). A non-backfilled and mean infiltration version of the LDTH sub-model L2C3 (coordinates: E170731, N234973) was selected and extracted among the 31 LDTH sub-models. The L2C3 LDTH sub-model is used to compute temperature history of the emplacement drift and surrounding areas throughout the preclosure and postclosure periods.

The L2C3 LDTH sub-model location selected has the following characteristics of interest:

- Approximately the geometric center of the license application reference repository layout (BSC 2004 [DIRS 164519]).
- The repository horizon is located approximately 281 m below the ground surface and 327 m above the water table. This elevation puts the repository horizon at approximately 1057 m above sea level.
- The repository horizon is located in the Tptpll with approximately 34 m of Tptpll above the repository horizon and 68 m of Tptpll below the repository horizon.
- The mean infiltration conditions have surface infiltration rates of 12.0 mm/year during the first 600 years of emplacement (present day climate), 40.8 mm/year from 600 years to 2000 years (monsoonal climate), and 63.2 mm/year from 2,000 years on (glacial transition climate).
- The ground surface temperature is fixed at 16.9°C, and the water table temperature is fixed at 29.2°C.

In addition to the LDTH sub-model, updated thermal and hydrologic properties were used for the repository and non-repository rock units. The thermal and hydrologic properties are presented in Section 4.1.6 and 4.1.8, respectively. Details of the data preparation for input files of the LDTH sub-model are described in *Multiscale Thermohydrologic Model* (BSC 2004 [DIRS 169565]).

Three major cases of the drift scale thermal calculation were carried out, including:

- Case 1: Base case calculation with 1.45 kW/m initial heat load and 50 years preclosure ventilation (90 percent heat removal ratio, Section 5.1).
- Case 2: Sensitivity calculation for thermal properties of repository rock material (Tptpll) with 1.45 kW/m initial heat load, 50 years preclosure ventilation, and 90 percent

heat removal ratio. Values of thermal conductivity and specific heat one standard deviation less than the mean values were used:

- Thermal Conductivity (DTN: SN0404T0503102.011 [DIRS 169129]): 1.64 W/m-K (= 1.89 W/m-K – one standard deviation [0.25 W/m-K]) for wet conditions and 1.03 W/m-K (= 1.28 W/m-K – one standard deviation [0.25 W/m-K]) for dry conditions.

- Heat Capacity: 811 J/kg-K (= 954 J/kg-K – one standard deviation [143 J/kg-K]).

- Case 3: Sensitivity calculation for heat removal ratio. 70 percent heat removal ratio was used for the preclosure ventilation (Section 5.1).

The LDTH sub-model that was used in the thermal-mechanical analysis presented in this document has been superseded by a new LDTH sub-model (DTN: LL030808623122.036 [DIRS 165790]). The new LDTH sub-model updated several input parameters including rock mass thermal property data and preclosure ventilation efficiency data. The heat capacity data used in the thermal analyses were preliminary and have been superseded by *Heat Capacity and Thermal Expansion Coefficients Analysis Report* (BSC 2003 [DIRS 164670], Table 6-5) and DTN: SN0307T0510902.003 [DIRS 164196] (see Appendix E, Table E-16). In this document, heat capacity values for the range of $T \leq 95°C$ only were utilized for the thermal calculations using the LDTH sub-model (Table E-16). Because consideration of latent heat effects above the boiling point is built into the NUFT code, the high heat capacity value at the temperature range of 95 to 114°C (Table E-16) were not used in the thermal calculations in this document. The new LDTH sub-model uses a drift location-dependent and time-dependent heat removal ratio (DTN: MO0306MWDALAFV.000 [DIRS 163961]) instead of a constant heat removal ratio (Section 5.1.2) as was assumed in the rock mass temperature calculations performed in this document. This new logic considers that ventilation air will have a varying heat removal capacity as it travels from the entrance to the exit of an emplacement drift. The heat removal capacity will also vary as a function of time as both the waste package power output and rock mass temperature change (BSC 2004 [DIRS 169862]). These changes could potentially cause a significant difference in drift wall temperature during the preclosure period. Further details of the new LDTH sub-model can be found in *Multiscale Thermohydrologic Model* (BSC 2004 [DIRS 169565]).

Impact analyses were conducted regarding the new LDTH sub-model and are presented in Appendix Q (Section Q2). The impact analyses show that the use of the new LDTH sub-model primarily impacts preclosure temperature. The impact on the prediction of rock mass stress and drift degradation is insignificant.

Decay curves of the linear heat load used in the calculation cases are presented in Figure 6-24. The original linear heat decay curve (no ventilation) was obtained from *D&E/PA/C IED Subsurface Facilities* (BSC 2004 [DIRS 167369]). Ninety percent of the constant ventilation heat removal ratio (Section 5.1) was applied for Cases 1 and 2, while 70 percent of constant heat removal ratio (Section 5.1) was used in Case 3.

Temperature histories at the drift crown for the cases of the drift scale thermal calculations are presented in Figure 6-25. The results exhibited the temperature increase from base case (Case 1) to sensitivity calculations (Cases 2 and 3). In particular, Case 3 showed a significant temperature increase at the preclosure period. The peak temperate for Case 1 was 138°C at around 75 years, while Cases 2 and 3 were 161°C and 153°C at around 75 years, respectively.

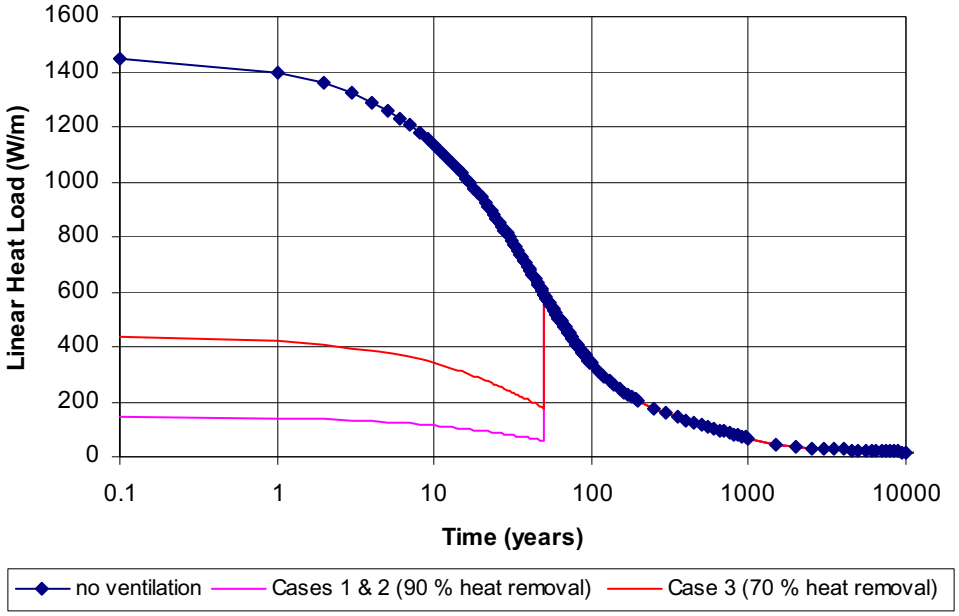

Source File: DTN: MO0408MWDDDMIO.002, file *Heat_Decay_Cal_LA1450.xls.*

NOTE: The no ventilation curve is from BSC 2004 [DIRS 167369]. Cases 1 and 2 use the 90 percent heat removal curve while Case 3 uses the 70 percent heat removal curve.

Figure 6-24. Heat Decay Curves for Thermal Calculations

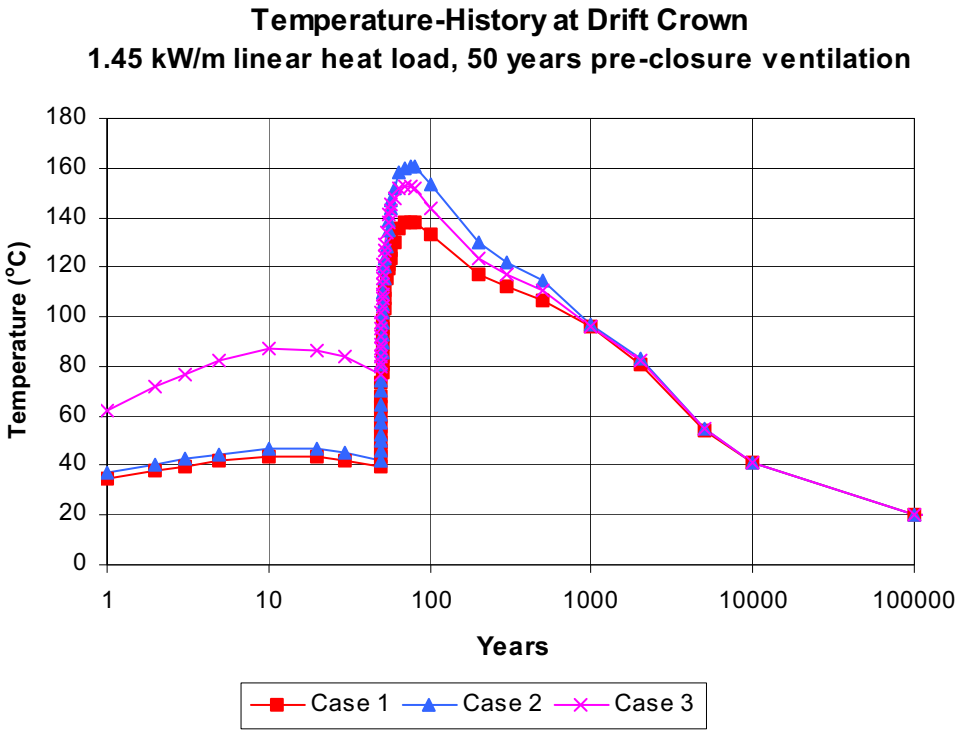

Source File: DTN: MO0408MWDDDMIO.002, file *LA1450_NUFT_Temp_crss-sctn3.xls.*

Figure 6-25. Temperature History at the Drift Crown Due to the Linear Heat Load Presented in Figure 6-24

A comparison of temperature histories in the drift crown for Case 1, as determined in the drift scale calculation (NUFT) and the coupled regional and drift scale calculations (FLAC3D) for the conditions in the middle of the repository, is shown in Figure 6-26. The agreement between histories is quite good. With the exception of the state at 10,000 years after waste emplacement, the temperature differences between the two calculations are less than 10°C.

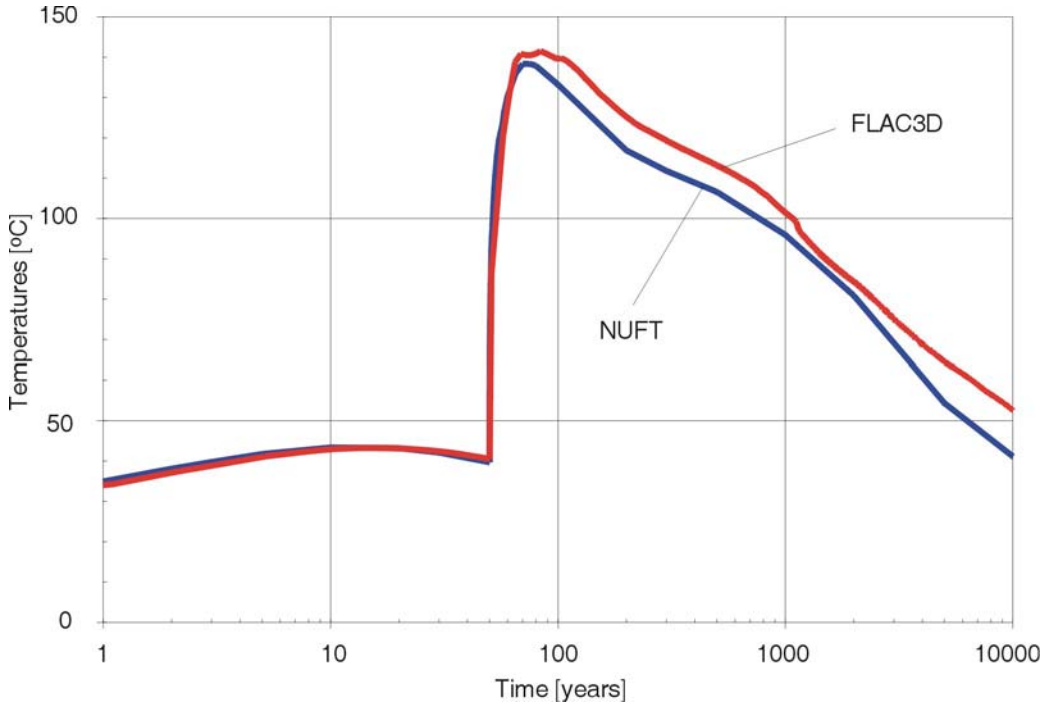

Source File: DTN: MO0408MWDDDMIO.002, FLAC 3D Inputs & Outputs\TM model.

Figure 6-26. Comparison of Temperature Histories at Tunnel Crown for Case 1 Calculated Using NUFT and FLAC3D

Stresses in the drift wall and crown for conditions in the middle of the repository, as predicted by two calculations (drift scale [NUFT-FLAC] and coupled regional and drift scale [FLAC3D]), are shown for 10 years, 100 years, and 1,000 years after waste emplacement in Figures 6-27, 28, and 29, respectively. NUFT-FLAC results are presented from the calculation for lithophysal rock mass Category 4 (discussed in Section 6.4), which has the same Young's modulus as the value used in the coupled regional and drift scale calculation. Agreement of the tangential stresses in the crown is excellent at the three times presented. As expected, the two-dimensional calculation (NUFT-FLAC) predicts a slightly higher tangential stress in the crown after 1,000 years of heating. The most significant difference between the two calculations is the vertical stress after 100 and 1,000 years. The coupled regional and drift scale calculations (FLAC3D) show an increase in the vertical stress (in the wall after 100 years and 1,000 years, but also throughout the repository horizon after 1,000 years) because of the effect of the finite repository size and elastic restoring stresses caused by the heat-induced deformation. This effect could not be accounted for in the drift scale calculation in which the average vertical stress is determined by the weight of the overburden. The drift scale calculation stress predictions are justified for use in the analysis of drift degradation, because the increase in the vertical stress in the wall (not accounted for in the two-dimensional calculation) is not significant.

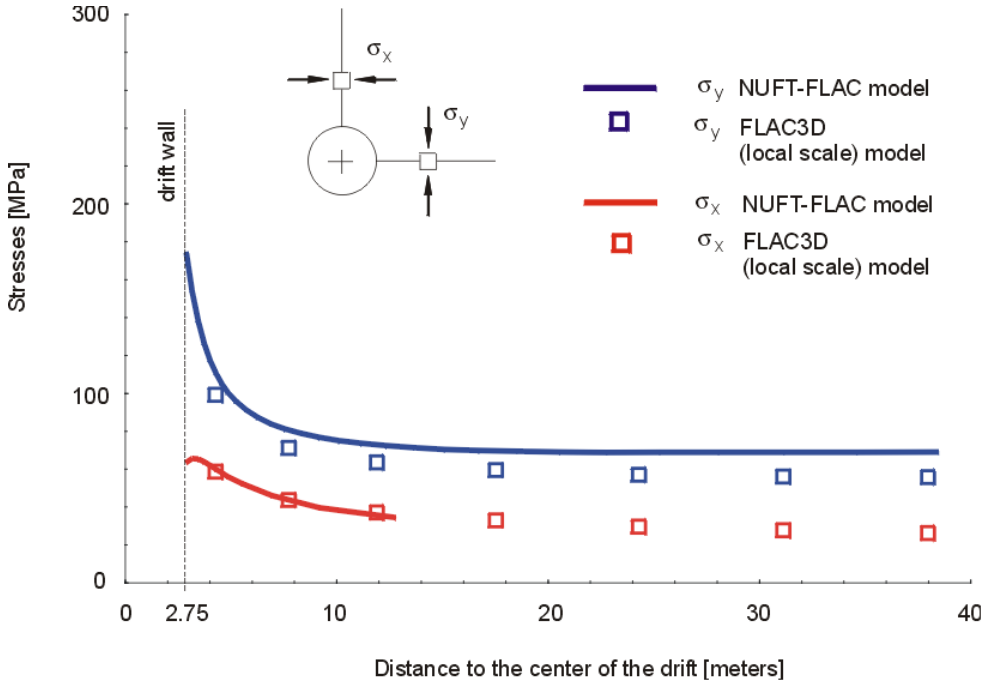

Source File: DTN: MO0408MWDDDMIO.002, FLAC 3D Inputs & Outputs\TM model.

Figure 6-27. Comparison of Stresses Around the Drift Between the NUFT-FLAC and FLAC3D Predictions After 10 Years of Heating

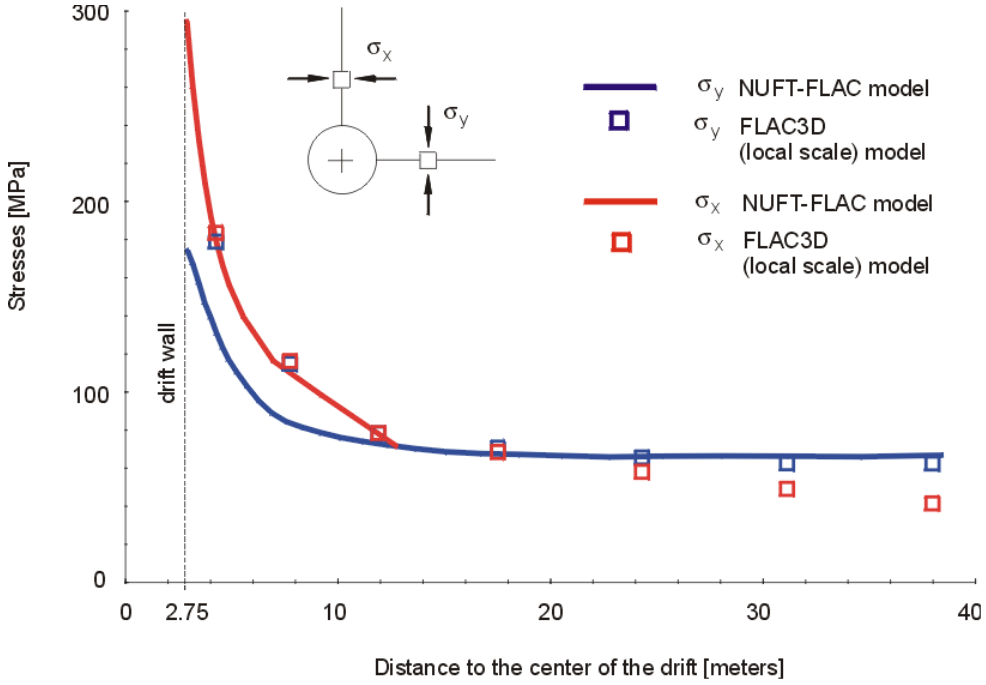

Source File: DTN: MO0408MWDDDMIO.002, FLAC 3D Inputs & Outputs\TM model.

Figure 6-28. Comparison of Stresses Around the Drift Between the FLAC and FLAC3D Predictions After 100 Years of Heating

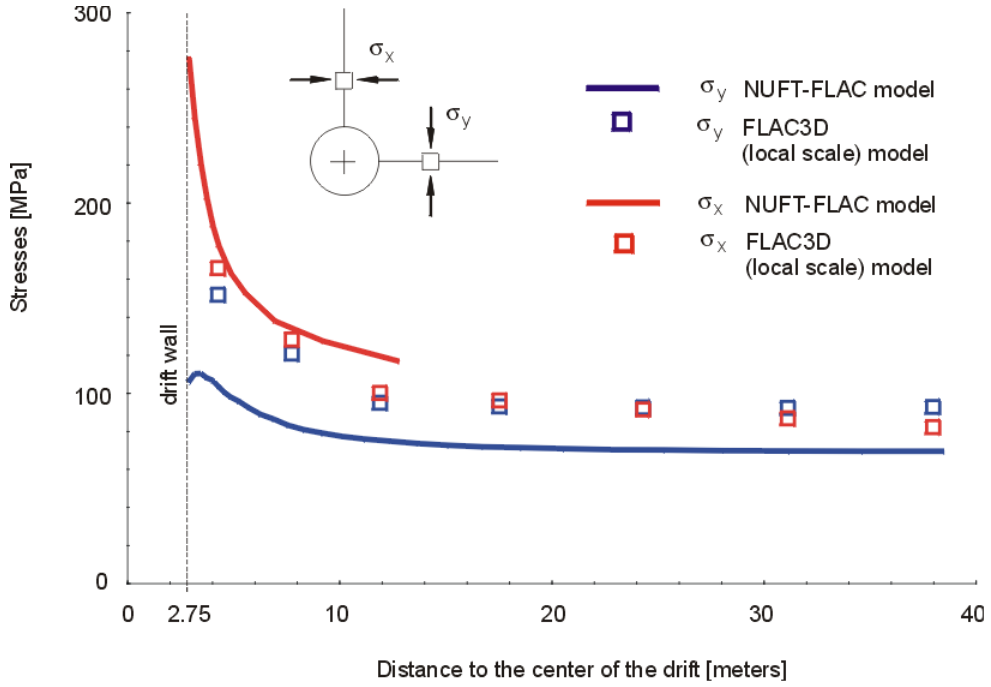

Source File: DTN: MO0408MWDDDMIO.002, FLAC 3D Inputs & Outputs\TM model.

Figure 6-29. Comparison of Stresses Around the Drift Between the NUFT-FLAC and FLAC3D Predictions After 1,000 Years of Heating

The drift stability analysis presented in this report was carried out for temperature and stress conditions in the middle of the repository. However, the temperatures and stresses for the conditions at the edge of the repository are investigated using the coupled regional and drift scale (FLAC3D) calculations (the actual location considered and other details are described in Appendix C). The temperature history from the coupled calculations for the edge of the repository, compared with the NUFT results for the center of the repository, are shown in Figure 6-30. As expected, the temperatures at the edge of the repository will be smaller than temperatures in the middle of the repository.

The stress profiles around the emplacement drift located at the edge of the repository—10, 100 and 1,000 years after waste emplacement—are shown in Figures 6-31 through 6-33. Stresses at the edge of the repository are, in general, smaller than in the middle of the repository. Smaller vertical stress at the repository edge is due to smaller overburden. However, the most significant difference between stress conditions at the edge and in the middle is in the horizontal stress 1,000 years after waste emplacement. The horizontal stress is approximately 5 MPa smaller at the edge compared to the middle of the repository (Figure 6-32). After a heating time when the drifts start to thermally interact with each other, conditions of almost complete confinement (idealized in two-dimensional models by symmetry conditions on the plane half-way between the drifts) exist in the middle of the repository, leading to increased horizontal stresses. The confinement and temperatures at the edge are smaller (than in the middle of the repository) resulting in smaller horizontal stresses. It appears from these results that limiting the drift degradation analysis to thermally induced stresses in the middle of the repository is justified.

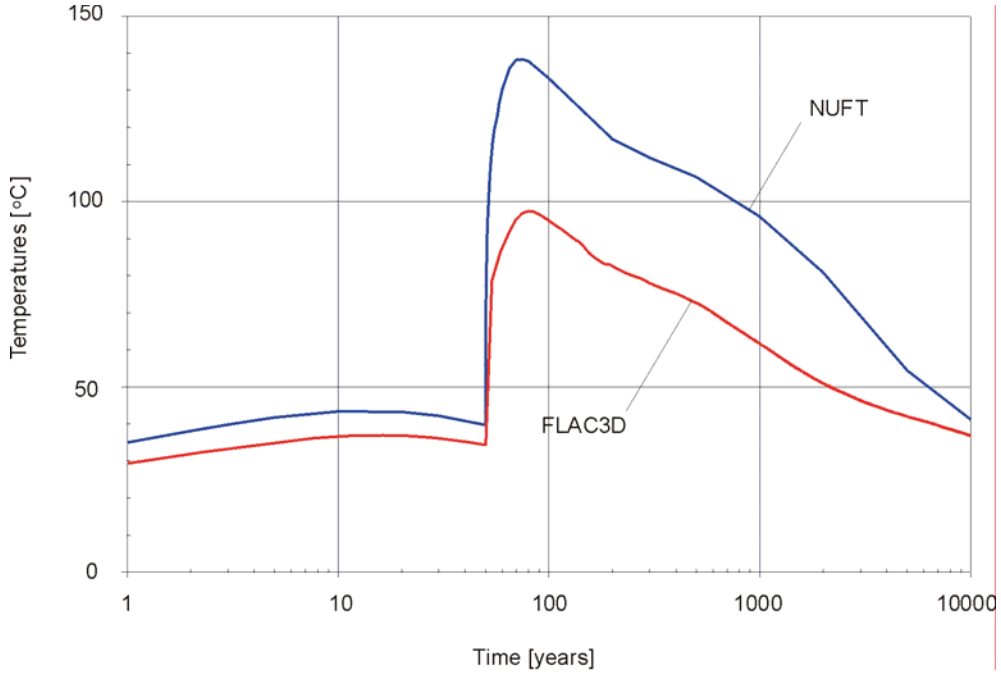

Source File: DTN: MO0408MWDDDMIO.002, FLAC 3D Inputs & Outputs\TM model.

Figure 6-30. Comparison of Temperature Histories at Tunnel Crown for Case 1 Calculated Using NUFT (at the Center of the Repository) and FLAC3D (for the Edge of the Repository)

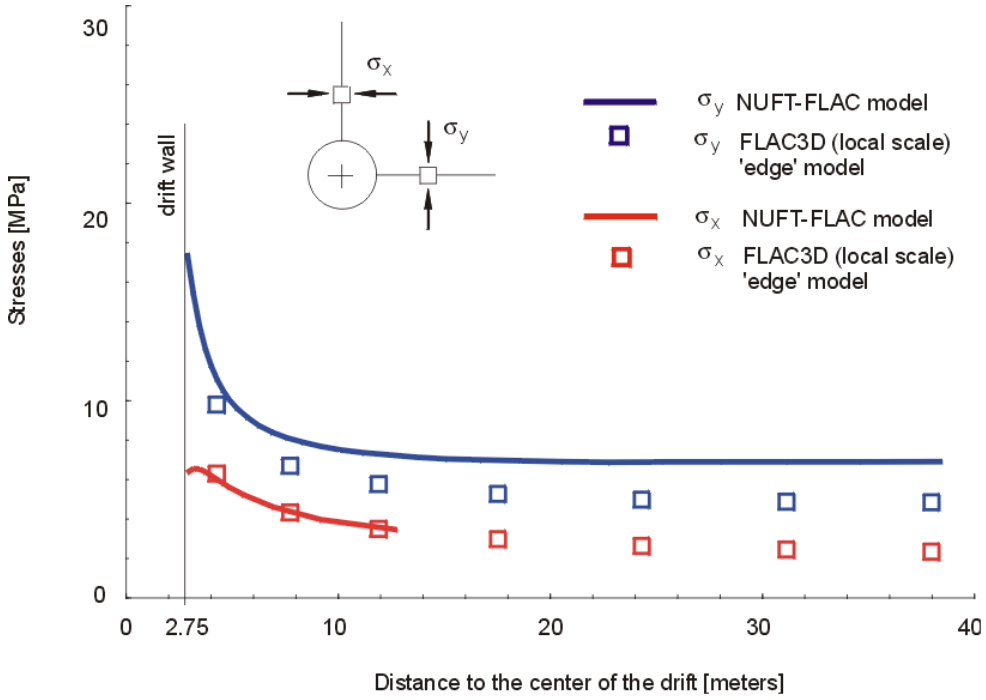

Source File: DTN: MO0408MWDDDMIO.002, FLAC 3D Inputs & Outputs\TM model.

Figure 6-31. Comparison of Stresses Around the Drift Between the NUFT-FLAC and FLAC3D Calculations for Edge of the Repository After 10 Years of Heating

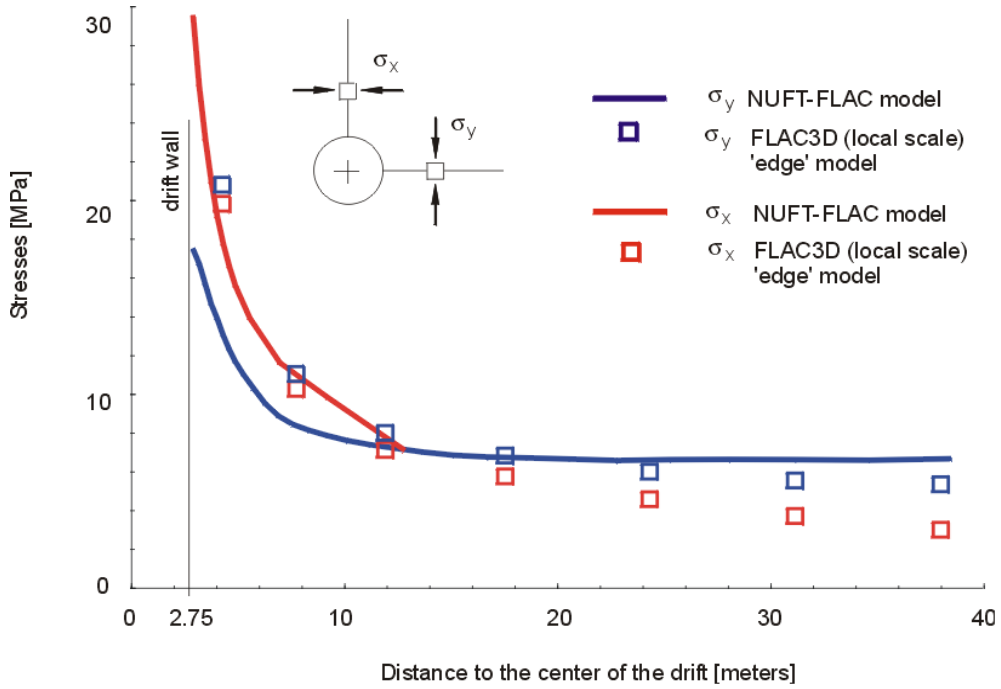

Source File: DTN: MO0408MWDDDMIO.002, FLAC 3D Inputs & Outputs\TM model.

Figure 6-32. Comparison of Stresses Around the Drift Between the NUFT-FLAC and FLAC3D Calculations for Edge of the Repository After 100 Years of Heating

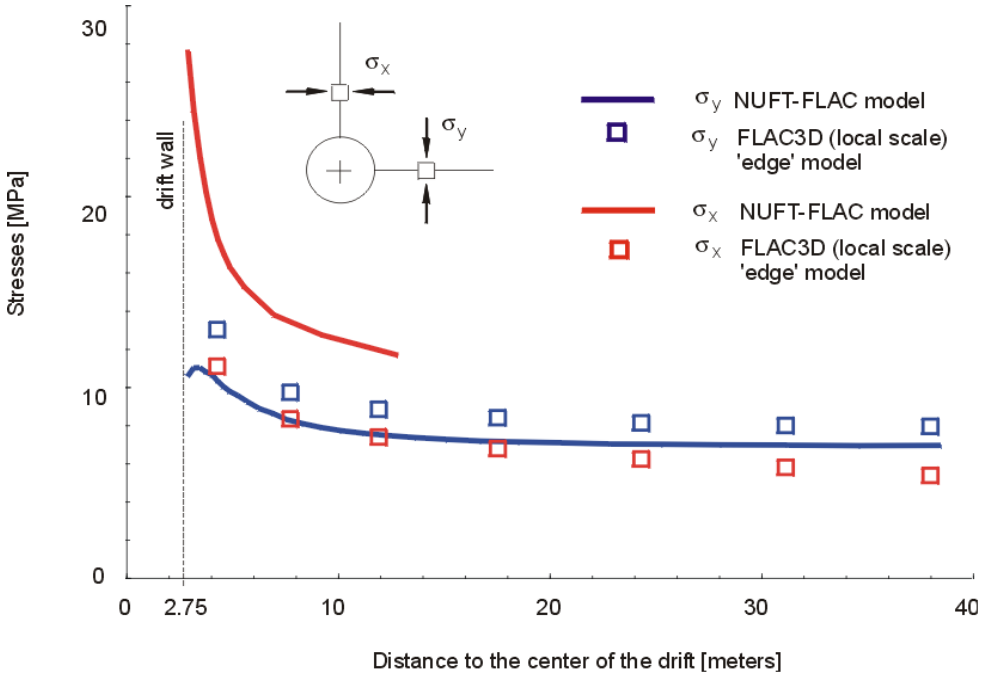

Source File: DTN: MO0408MWDDDMIO.002, FLAC 3D Inputs & Outputs\TM model.

Figure 6-33. Comparison of Stresses Around the Drift Between the NUFT-FLAC and FLAC3D Calculations for Edge of the Repository After 1,000 Years of Heating

6.3 ROCKFALL IN THE NONLITHOPHYSAL UNITS

The assessment of rockfall in the nonlithophysal units is primarily based on a three-dimensional discontinuum analysis (3DEC analysis). This analysis is adequate for the wedge-type failure in a jointed rock mass, which has been validated in Section 7.7. A description of this set of analyses and a presentation of the results are provided in Section 6.3.1. An intensely fractured zone was observed in the ESF main loop between Stations 42+00 and 51+50 (Albin et al. 1997 [DIRS 101367], p. 58). A 3DEC analysis is not suited for such highly fractured rock. Therefore, a three-dimensional continuum analysis with a ubiquitous joint model (FLAC3D analysis) was adopted to account for the effect of the highly fractured and anisotropic behavior of the rock mass in this limited zone as described in Section 6.3.2. The aforementioned analyses consider only fractures with trace lengths greater than 1 m. The impact of small-scale fractures (less than 1-m trace length) for block forming is assessed using the key-block code DRKBA. A comparison of the results for including and excluding the small-scale fractures is provided in Section 6.3.3. The drift profile predictions considering wedge-type failure are provided in Section 6.3.4.

It should be noted that in previous versions of this document (BSC 2001 [DIRS 156304]), rockfall in the nonlithophysal units was based on a Discrete Region Key Block Analysis (DRKBA). In this report, DRKBA analyses primarily provide a confirmatory role in the assessment of drift degradation. DRKBA analyses are documented in Appendix D.

6.3.1 Three-Dimensional Discontinuum Analysis of Jointed Rock Mass for Wedge-Type Rockfall

The three-dimensional discontinuum analysis is used for simulation of the mechanical behavior of the jointed rock mass in the nonlithophysal units for loading conditions with which stability response will be controlled by the fractures. 3DEC was selected for its capability of simulating fractured rock masses under both thermal and seismic loadings. The fractured rock mass is represented as a number of intact rock blocks that are separated by interface planes whose mechanical behavior is represented by a standard Coulomb slip criterion. The intact blocks are subdivided into tetrahedral finite difference zones and can be assigned suitable mechanical constitutive law (Itasca Consulting Group 2002 [DIRS 160331]). Due to the high intact rock strength in the nonlithophysal units, rock blocks are considered to behave elastically.

It is important in the 3DEC analysis to include field fracture geometric data for modeling the nonlithophysal units. Because the fractures within the Tptpmn may be non-persistent in nature (with median trace lengths of approximately 3 m [see Table 6-2], which is smaller than the diameter of the tunnel), many fractures are of insufficient length to form a regular block. The fracture geometries used as input to 3DEC are derived from FracMan simulations as discussed in Section 6.1.6. Modifications to the 3DEC program have been made to accommodate the FracMan output; namely, the discontinuous nature of the fractures. In versions of the 3DEC program developed prior to the use described here, fractures are modeled as continuous in nature and thus it was impossible to have a fracture that ends in solid rock. The program was modified to provide the capability to allow contact points along a fracture trace to be assigned a particular material property. In other words, portions of a fracture plane could be assigned a standard Coulomb slip behavior, whereas others could be bonded to the opposing surface with the

strength of the adjacent rock blocks, thereby creating fractures that have rock "bridges" along their surface. In this case, the rock bridge acts as a strong location along the fracture surface, but can still fail in shear or tension if the stresses so dictate. In this manner, it is possible to represent a discontinuous fracture system, but one in which breakage of solid rock can occur.

Other enhancements added to 3DEC for rockfall modeling include:

- Implementation of the "free field" boundary to provide a "quiet" or "non-reflecting" boundary for dynamic analysis with superposition of the P and S wave motions
- Partial density scaling for dynamic analysis.

Descriptions for these enhancements are provided in Appendix H.

For each simulated fracture, the FracMan program provides the centroid, radius (fractures are considered to be circular), dip and dip direction for input to 3DEC which then generates the fracture by cutting the block(s) in which the fracture lies. The coordinate systems adopted in FracMan and 3DEC are different; requiring a conversion of the outputs from FracMan to inputs in 3DEC (Appendix L). To account for the stochastic nature of the jointed medium, a total of 50 fracture geometries were selected by generating random tunnel centroid locations within the 100-m-cube simulated FracMan rock mass. A representative tunnel volume, approximately two tunnel diameters around the tunnel centroid and 25 m in length, is created at each of these locations to contain fractures generated in FracMan. This volume is considered sufficient to contain the limits of damaged rock, and of sufficient length (approximately five times the tunnel diameter and about 10 times the median trace lengths) to provide a representative volume of rockfall (see Figure 6-34 for 3DEC model region).

The combination of computer runs considering fracture geometry, seismic ground motion, material properties variation, and thermal loading scenario are immense. In order to complete the task in a timely fashion, several techniques were used to speed up the calculation. These techniques are described in Appendix H.

6.3.1.1 3DEC Model Set Up

Figure 6-34 shows the base case 3DEC model geometry with fracture modeling region #38. The model is slightly larger than a 25-m x 25-m x 25-m cube with the 5.5-m diameter tunnel oriented at 75 degrees azimuth[4]. The region with detailed fractures imported from FracMan is one tunnel diameter at the side of the tunnel and two diameters on top of the tunnel. Three cross-section views are included in Figure 6-34 to illustrate the fractures and blocks around the excavation. That portion of the rock mass that does not form blocks is shown with a green color, while distinct blocks are identified as areas with different colors. Some of the fractures shown in the cross-section views are artificial, i.e., they were generated during the block cutting process or to facilitate mesh generation. A detailed description of mesh generation with artificial fractures is

[4] The emplacement drift azimuth of 72º (see Table 4-1) was modeled in this document with drifts trending 75º. This 3-degree difference between the modeled and actual drift alignment is acceptable given the variability of joint set orientations captured in the model (see Section 6.1.6). The 3-degree difference does not significantly effect the results from this analysis.

provided in the 3DEC manual (Itasca Consulting Group 2002 [DIRS 160331]). The dimension of the model is selected to optimize the time required for analysis and the ability of the model to predict rockfall accurately. Sensitivity of the model dimension to the outcome of rockfall prediction is provided in Section 6.3.1.6. The drip shield is represented as a stiff, rectangular block fixed to the invert of the drift, based on a simplified drip shield geometry (BSC 2004 [DIRS 169220]). The drip shield block is placed to collect information on the locations and relative velocities of the rockfall impact.

Input properties for the distinct block 3DEC model involve both the fracture and block (intact) properties. Table 6-3 lists the base case properties used in 3DEC. The selected input properties were derived as the best estimates at the time of analysis. These values may have slight deviation from the statistics mean or median presented in Appendix E. Sensitivity analyses on these input parameters to the outcome of rockfall prediction were conducted and the results are presented in Section 6.3.1.6.

A linear elastic model is used for the block material, whereas Coulomb slip criterion is used to present joint mechanical behavior. A linear elastic model is used as the intact block constitutive model for the 3DEC analysis. This approach is used to obtain a conservative (i.e., increased) estimate of the block volume. Breaking and spalling of the rock inside the blocks are expected considering the large amplitude of seismic waves for postclosure ground motions. This mechanism is addressed in Section 6.3.1.6 with a two-dimensional discontinuum model representing the rock mass (UDEC analysis). Although the shallow-dipping vapor-phase parting consists of higher cohesive material, a single set of joint mechanical properties are used for the joint sets for conservatism (i.e., more rockfall will be produced). Coulomb slip criterion is also used for the intact bridges between adjacent fractures, as the intact cohesion and friction is assigned for the bridge strength. Sensitivity analyses of the joint strength properties, dilation angle, and joint stiffness were conducted to evaluate their impact to rockfall, the range of properties, and their impacts to the analysis results are presented in Section 6.3.1.6.

The initial state of stress was included at the model consolidation stage. From the in situ stress measurement using the hydraulic fracturing technique (DTN: SNF37100195002.001 [DIRS 131356]), the horizontal components of in situ stress are provided: maximum 2.9 MPa acting N15°E and minimum 1.7 MPa acting N105°E (Table 4-1). The vertical component of in situ stress was calculated based on the weight of the overburden at the depth of the test from the surface. First, the coordinates of borehole ESF-AOD-HDRFR#1 (i.e., the hydraulic fracturing test borehole) were estimated based on the layout of the ESF and the Thermal Test Facility, starting from known coordinates at Main Drift Station 28+04 (BSC 2003 [DIRS 165572], Figure 3; CRWMS M&O 1997 [DIRS 147458], MOL.19970717.0008, Appendix 6). The estimated coordinates of the borehole ESF-AOD-HDRFR#1 are NS 234025 and WE 171440. Next, the overburden stratigraphic unit thickness at the borehole location was extracted from DTN: MO0012MWDGFM02.002 [DIRS 153777] using EarthVison (see Appendix M for input/output details and Table M-1 for the overburden unit thickness). The overburden unit thickness and the mean unit densities in Table E-1 are used to calculate an overburden load of 4.7 MPa at the depth of the test (Table M-1). The calculated vertical stress is in agreement with the initially estimated vertical stress at the location of the hydraulic fracturing test (CRWMS M&O 1997 [DIRS 147458], MOL.19970717.0008, Table 4). Therefore, the direction of the intermediate principal stress is N15°E with a ratio to major principal stress

of 0.617 (= 2.9 MPa ÷ 4.7 MPa), whereas the direction of the minor principal stress is N105°E with a ratio to major principal stress of 0.361 (= 1.7 MPa ÷ 4.7 MPa).

The vertical component of in situ stress (the major principal stress) is approximated as 7 MPa considering an overburden depth of 300 m (BSC 2003 [DIRS 166183], Section 4.2.1) and an overburden density of 2.41 g/cc (Section 4.1.3) (i.e., vertical stress = 300 m × 9.81 m/sec^2 × 2.41 g/cc ≈ 7 MPa). The horizontal components of in situ stress (the minor and intermediate principal stresses) are simplified to be 3.5 MPa based on an average horizontal-to-vertical stress ratio of 0.5 (i.e., the average of 0.617 and 0.361 as described above). The in situ stress for each emplacement drift will vary depending on the cover depth on top of the drift. The approximated values assigned for the in situ stress are adequate and insensitive to the results judging the magnitude of the induced seismic and thermal stress.

The boundary conditions for various stages of the analysis are presented in Table 6-4. At the initial consolidation stage and the later thermal loading period, fixed velocity boundaries were used to ensure the boundary effect does not affect the stress distribution around the opening. For the seismic analysis, non-reflecting boundaries are used for both the top and bottom of the model, whereas free-field boundaries are imposed at the perimeter of the model as shown in Figure 6-35. The free-field boundaries ensure that plane waves propagating upward suffer no distortion at the boundary. A description of the free-field boundary is provided in Appendix H. Dynamic loading was applied at the bottom of the model as a prescribed stress boundary, and propagated vertically upwards. The conversion of the ground motion velocity to input seismic stress is discussed in Section 6.4.2.2 (Equation 6-7).

6.3.1.2 Seismic Consideration in Nonlithophysal Units

6.3.1.2.1 Site Specific Ground Motions

Site-specific ground motions for five levels of annual probability of exceedance, 5×10^{-4}, 1×10^{-4}, 1×10^{-5}, 1×10^{-6}, and 1×10^{-7}, are included in this study (see Table 4-1 for source DTNs). Development of the ground motion time histories following use of a probabilistic seismic hazard analysis and Yucca Mountain site response model can be found in BSC 2004 [DIRS 170027]. The 5×10^{-4} and 1×10^{-4} ground motions are for preclosure consideration, while the 1×10^{-5}, 1×10^{-6} and 1×10^{-7} ground motions are for postclosure. The preclosure ground motion levels are provided in this section for comparison to the postclosure levels. For higher-frequency spectral accelerations (5 to 10 Hz) and an annual exceedance probability of 5×10^{-4}, results of the probabilistic seismic hazard analysis for Yucca Mountain indicate the ground motion hazard derives primarily from earthquakes in the magnitude range of 5.0 to 6.5 occurring at distances less than 15 km from the site. For lower-frequency spectral accelerations (1 to 2 Hz) at the same annual exceedance probability, the hazard shows, in addition to nearby sources, a significant contribution from earthquakes in the magnitude range of 7.0 to 8.0 occurring at an epicentral distance of about 50 km. For annual exceedance probabilities of 1×10^{-6} and 1×10^{-7}, nearby earthquakes in the magnitude range 5.5 to 7.0 are the dominant sources contributing to ground motion hazard at both higher and lower spectral acceleration frequency ranges.

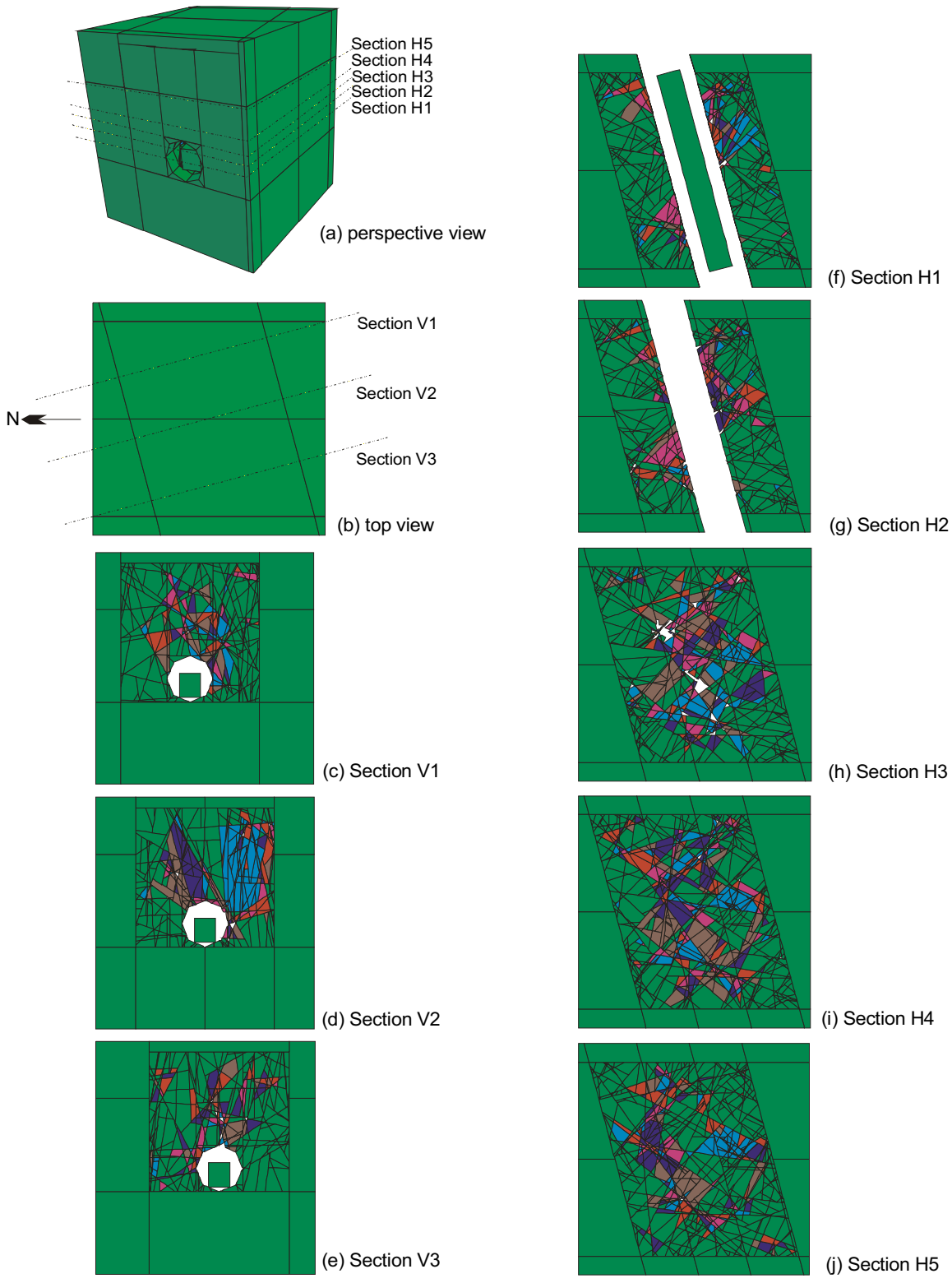

Figure 6-34. 3DEC Model Geometry and Cross-Sections

Table 6-3. Base Case Material Properties for 3DEC Analysis

Parameter		Value
Joint strength properties	Joint cohesion (MPa)	0.1
	Joint friction (deg)	41
	Joint dilation (deg)	0
	Joint normal stiffness, K_n (MPa/m)	5.0E+04
	Joint shear stiffness, K_s (MPa/m)	5.0E+04
Intact rock deformation properties	Young's Modulus (GPa)	33.03
	Poisson's ratio	0.21
	Bulk modulus (GPa)	19.2
	Shear modulus (GPa)	13.6
Intact bridge strength properties	Cohesion (MPa)	47.2
	Friction angle (deg)	42
	Tensile strength (MPa)	11.56

NOTE: The selected input properties were derived as the best estimates at the time of analysis. These values may have slight deviation from the statistics mean or median presented in Appendix E. Sensitivity analyses on these input parameters to the outcome of rockfall prediction were conducted and the results are presented in Section 6.3.1.6.

Table 6-4. Boundary Conditions for 3DEC Analysis

Boundary	Initial Consolidation and Excavation Stage	Thermal Analysis Stage	Dynamic Analysis Stage
Lateral	Fixed at the direction normal to the face	Fixed at the direction normal to the face	Free-Field boundary
Bottom	Fixed at the vertical direction	Fixed at the vertical direction	Non-reflecting boundary
Top	Fixed at the vertical direction	Fixed at the vertical direction	Non-reflecting boundary

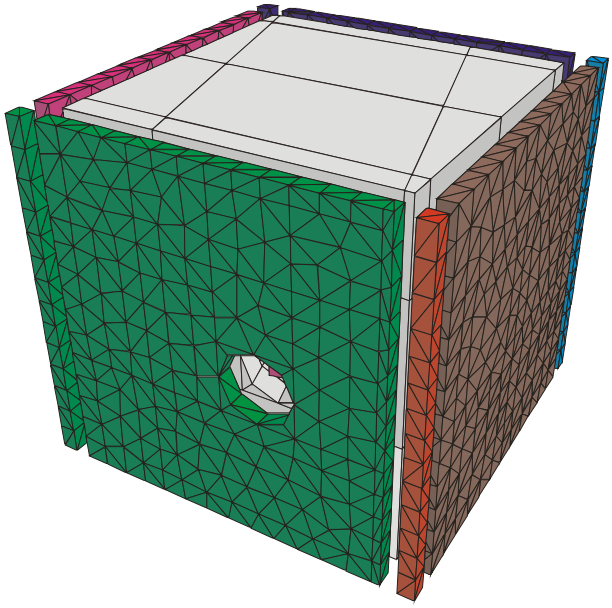

(a) Free-Field Boundaries
(Perspective View)

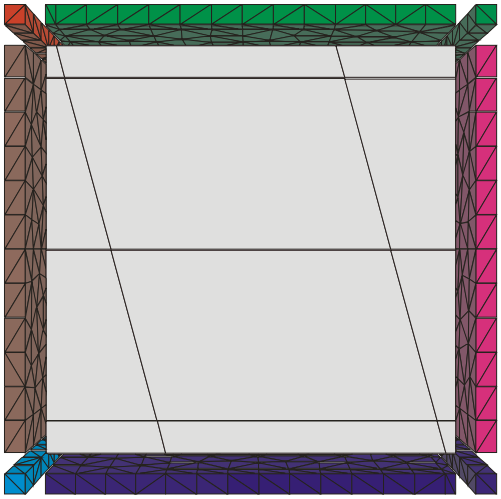

(b) Free-Field Boundaries
(Top View)

Figure 6-35. Illustration of Free-Field Boundaries in 3DEC Model

A total of 15 sets of Point B ground motions (i.e., ground motions developed at repository horizon) were selected for each annual postclosure hazard level. The multiple sets ensure a reasonable distribution of spectral shapes and time history durations. For each set of ground motions, two horizontal components (H1 and H2) and one vertical component (V) of acceleration, velocity, and displacement are supplied. Figure 6-36 shows the H1 velocity time history for four annual hazard levels. Only one ground motion was provided for the preclosure hazard levels because of the deterministic-based approach for preclosure consideration. The

amplitude of the peak ground acceleration, velocity, and displacement, and the seismic induced far field stress for one of the ground motion sets from each hazard level, are provided in Table 6-5. The induced stresses are calculated based on the intact material properties for nonlithophysal rock. This table is used to demonstrate the typical ground motion parameters for the three hazard levels considered. It is apparent that the preclosure ground motions have lower amplitude vibrations and, hence, lower induced stresses compared with the postclosure ground motions.

The peak values for each ground motion set provided for postclosure hazard level varies significantly and can be highly conservative, particularly for the 1×10^{-6} and 1×10^{-7} probability levels as summarized in Table 6-5 (see Appendix X for a complete listing of ground motion parameters). Arias intensity (an estimate of energy delivered to structures) for each set of ground motions is listed in Table 6-6. A large variation of energy within the same hazard level is observed. The 15 sets of ground motions were combined with fracture patterns for probabilistic analysis. The combining of ground motion and fracture patterns is described in Section 6.3.1.2.2.

Although not taken into account in the base-case calculations provided in this document, a study addressing the conservative, and potential physically-unrealizable peak ground velocities associated with these low hazard levels has been developed (BSC 2004 [DIRS 170137]). Geologic evidence gained from panel mapping of lithophysae and fractures in the Tptpll (Appendix O) has shown that the rock mass has not been subjected to shear strain levels sufficient to result in fracture between lithophysal cavities since the rock mass was deposited and cooled (the existing fractures can be shown to have occurred as a result of cooling). As shown by the large-core laboratory testing (Appendix E), this strain level is approximately 0.1 to 0.35 percent. Therefore, in the approximately 12.8 million years since the Topopah Spring Tuff was deposited, an earthquake sufficient to produce a peak shear strain of this level has not occurred. Since peak ground velocity (PGV) can be directly related to strain, these observations can provide an indication of the maximum PGV that has occurred in this time period. The peak ground velocity study (BSC 2004 [DIRS 170137]) has subsequently been used to develop a conservative estimate that the horizontal PGV varies as a uniform distribution with lower and upper limits of 1.5 and 5 m/sec which, in turn, has been used to develop a modified hazard curve (the relationship between PGV and annual exceedance probability).

The base-case modeling performed in this document *does not* limit the highly conservative PGV values generated from the site response model, and thus the estimates of rockfall and drift damage generated by the postclosure ground motions (e.g., 1×10^{-5}, 1×10^{-6} and 1×10^{-7}) are correspondingly conservative. However, the abstraction of damage to Engineered Barrier System components for the seismic scenario, presented in the *Seismic Consequence Abstraction* (BSC 2004 [DIRS 169183]), is based on relating damage (e.g., area of stress corrosion cracking on drip shield or waste package) to PGV, and, in turn, to probability based on the hazard curve. The seismic consequence abstraction uses the hazard curve, modified by bounding PGV limits, to define damage.

Table 6-5. Peak Ground Motion Parameters

Annual Hazard Level	Ground Motion Component	Peak Acceleration (g)	Peak Velocity (cm/sec)	Peak Displacement (cm)	Seismic Induced Stress Corresponding to Peak Velocity (MPa)
5×10^{-4}	H1	0.19	19.00	12.86	1.09
	H2	0.18	17.72	12.37	1.02
	V	0.22	17.73	11.34	1.68
1×10^{-4}	H1	0.39	38.38	44.44	2.20
	H2	0.37	43.78	45.30	2.51
	V	0.47	47.51	31.73	4.50
1×10^{-5} Ground Motion Set 1	H1	2.77	104.58	20.06	6.00
	H2	2.50	83.31	14.37	4.78
	V	2.63	70.88	13.00	6.71
1×10^{-6} Ground Motion Set 1	H1	7.42	244.14	16.76	14.009
	H2	6.74	195.41	26.78	11.21
	V	4.90	111.29	13.75	10.54
1×10^{-7} Ground Motion Set 1	H1	16.28	535.26	58.68	30.0
	H2	14.79	428.42	58.72	24.57
	V	13.15	298.44	36.86	28.25

Source: DTNs: MO0407TMHIS104.003 [DIRS 170599]; MO0306SDSAVDTH.000 [DIRS 164033]; MO0402AVDTM105.001 [DIRS 168890]; MO0403AVDSC106.001 [DIRS 168891]; MO0403AVTMH107.003 [DIRS 168892].

NOTES: Native data files (available as ASCII text files) containing the acceleration, velocity, and displacement time-history data can be downloaded from the source DTNs.

Seismic induced stress (column six) is calculated based on elastic wave equations (Itasca Consulting Group 2002 [DIRS 160331], Manuals/3DEC/Optional Features/Section 2: Dynamic Analysis, Section 2.5).

Peak ground motion parameters for the ground motion sets are provided in Appendix X.

In running the 3DEC seismic simulation, the duration of the seismic time histories was truncated to that portion of the records displaying the majority of the energy. Initially, records were truncated to a duration bracketed by the 5 percent and 95 percent points in the energy buildup as measured by the Arias Intensity. For each three-component set of ground motions, these points were determined for each component (H1, H2, and V) and then the earliest 5 percent point and the latest 95 percent point were used to define the duration for that set of ground motions. Because preliminary analyses showed that rockfall continued in some cases beyond the 95 percent energy buildup point, additional time was added for analyses to ensure that the simulated duration covered the rockfall. Table 6-7 presents the total duration of each set of time histories and the 5 percent and 95 percent points. The sensitivity of rockfall to the duration of seismic ground motion is examined in Section 6.3.1.6.

6.3.1.2.2 Combinations of Ground Motion and Fracture Pattern

Rockfall is part of the seismic scenario calculations in support of the Total System Performance Assessment for the License Application. The analysis results provide inputs to the drip shield structural response calculation for assessment of the structural integrity of drip shields. To ensure that the ultimate performance measure of interest (i.e., damaged surface area of the drip shield) can be tracked to the underlying uncertain inputs in a consistent fashion, a sampling

strategy was developed to include a consistent set of pointers for the sampled parameters (i.e., ground motions and fracture modeling regions in rockfall analysis). A detailed description of the sampling strategy is provided in DTN: MO0301SPASIP27.004 [DIRS 161869].

As described in Section 6.1, a 100-m cube was constructed for providing the fracture network required in 3DEC analysis. A random selection of 105 centroid locations was conducted. These 105 centroid locations combined with the 15 sets of ground motions served as the pointers for sampling. The process of random generation and the coordinate of the centroid locations in the 100-m cube are provided in Appendix J. A simple Latin Hypercube sampling scheme was used for the paring of ground motion and fracture modeling region (DTN: MO0301SPASIP27.004 [DIRS 161869]). Table 6-8 lists the 50 sets of analyses conducted for seismic consideration. The adequacy of 50 sets of 3DEC analyses representing the rockfall characteristics for the non-lithophysal rock is presented in Appendix K.

6.3.1.2.3 Results for Seismic Analysis Subjected to 1×10^{-5} Annual Probability of Exceedance Ground Motions

The results for a complete set of 3DEC analyses, as tabulated in Table 6-8, subjected to the postclosure hazard level of 1×10^{-5} annual probability of exceedance ground motions are presented in this section. Figure 6-37 compares the input ground motion for the first horizontal component (H1, Ground Motion Set 10) with the recorded velocities at the base of the model and at the center of the model. The results confirm the correct wave inputs and proper wave propagation in the 3DEC model. As described in Section 6.3.1.1, a drip shield block anchored at the invert is included in the model to record the information of the locations and relative velocities for the rockfall impact. Figure 6-38 shows a typical block impacting the drip shield in the 3DEC dynamic simulation. Note that fallen blocks are subsequently deleted after impacting the drip shield. The deletion is to facilitate the recording of all possible rockfall on the drip shield. If the blocks are not deleted for the heavy rockfall cases, the drip shield will be covered with fallen rocks so that some of the rockfall at the later part of seismic shaking will not impact the drip shield. The simulation without deletion of the rock block after the impact is presented in Section 6.3.1.6. The results indicate less rockfall impact without the deletion scheme. For certain conditions, the algorithm for accounting and deletion of the blocks may lead to deleting stable blocks with corner and/or edge in the near vicinity of the drift shield at the floor. Blocks are not accounted as rockfall for these conditions.

Time histories of normal and shear stresses for joints close to the opening were recorded during the seismic shaking in the 3DEC model. Figure 6-39 shows normal and shear stress time histories at selected fracture subcontacts taken from 3DEC simulation #16 with ground motion set #11. Peak seismic loading appears to occur at the time of 4 to 6 seconds, consistent with the input ground motion. Information of the subcontacts is provided in Figure 6-40. Subcontact *a* represents the true fracture while subcontacts *b* and *c* are for the rock bridge in between the fracture segments. The stress paths of the fracture subcontacts are plotted against the fracture Coulomb slip criterion and rock bridge shear or tensile strength criterion, as shown in Figure 6-41. The in situ normal and shear stress state along the fracture is also included as the orange square for each subcontact in the figure. The in situ stress state at subcontact *a* is very close to the Coulomb slip criterion. The fracture containing this subcontact has apparently undergone yielding during seismic motions. The stress paths for rock bridges containing

subcontacts *b* and *c* are well under the rock shear or tensile strength criterion and representative of most of the rock mass.

The percentages of the area of joint slip/separation versus the total area of joint planes for the selected cases were calculated as a stability indicator for the fracture system around the opening. A total of 8 cases are presented in Table 6-9. Total joint and bridge areas contained in the model were first calculated. The bridge area is around 20 percent of the total joint area for the selected cases. A large portion of fractures (greater than 70 percent) has undergone shear slip or tensile separation when subjected to 1×10^{-5} ground motions. The percentage of shear and tensile failure is transient during the seismic shaking. Tensile mode can dominate for one instance and then change to shear mode for the next instance. However, shear failure becomes the dominant mode when approaching to the end of shaking. In addition to joint slip/separation, bridge damage percentage was also calculated. The results are presented in Table 6-9. In general, less than 1 percent bridge area is predicted to be damaged by shaking. However, for certain large ground motions (e.g., ground motion #3 for Case 38), higher damage percentage is predicted. Correlation of the bridge damage percentage versus peak ground velocity shows a strong relationship between the two. A detailed discussion on the bridge damage is provided in Section 6.3.1.6.3.

The results of the 50 3DEC simulations are summarized in Table 6-10. Approximately two thirds of the simulations predicted rockfall under seismic shaking. A total of 1,767 blocks have been identified from the analyses. The associated impact parameters for these blocks from the analyses include the following:

- Rock block volume falling on the drip shields (unit in m^3)
- Relative impact velocity of rock block to the drip shields (unit in m/sec)
- Impact location.

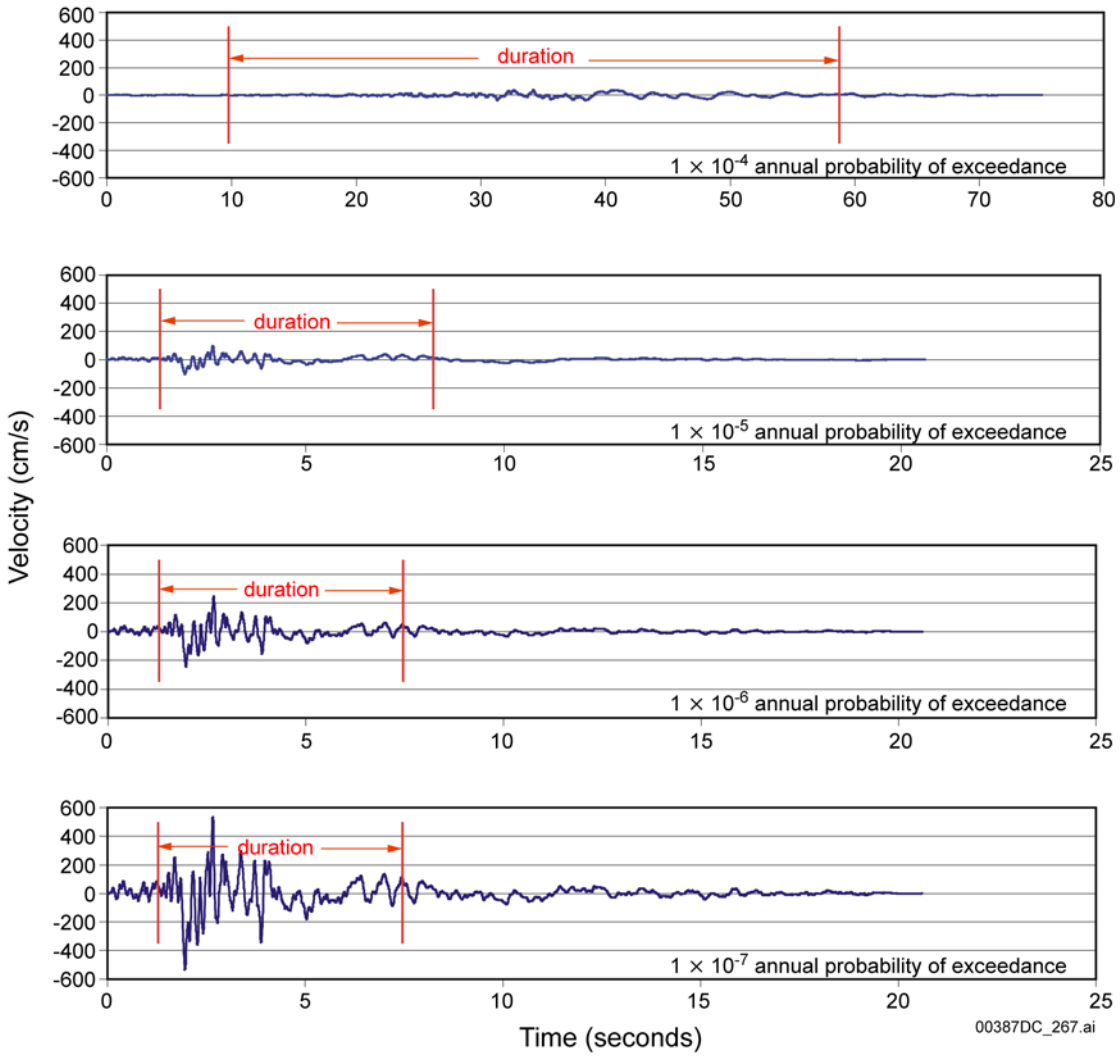

Sources: DTNs: MO0306SDSAVDTH.000 [DIRS 164033]; MO0402AVDTM105.001 [DIRS 168890]; MO0403AVDSC106.001 [DIRS 168891]; and MO0403AVTMH107.003 [DIRS 168892].

NOTES: The 5×10^{-4} time history is not presented due to its small magnitude. Native data files (available as ASCII text files) containing the velocity time-history data can be downloaded from the source DTN.

Figure 6-36. Examples of Ground Velocity Time Histories (H1) with Truncated Duration for Analysis

Table 6-6. Arias Intensity (m/sec) for Each Ground Motion Set

Annual Hazard Level	Ground Motion Set	H1	H2	V	Total Sum
1×10^{-5} Annual Probability of Exceedance	1	33	34	36	103
	2	31	38	123	192
	3	34	48	48	130
	4	12	15	20	48
	5	16	11	13	41
	6	7	5	18	30
	7	4	4	49	57
	8	8	13	16	37
	9	22	52	139	213
	10	9	4	14	26
	11	8	7	15	30
	12	4	4	7	15
	13	9	16	26	51
	14	3	2	7	12
	16	3	2	7	11
1×10^{-6} Annual Probability of Exceedance	1	235	253	114	602
	2	206	250	413	869
	3	120	153	135	408
	4	178	219	141	538
	5	78	52	29	159
	6	69	56	79	204
	7	63	61	467	590
	8	71	109	61	241
	9	169	352	465	986
	10	59	26	57	141
	11	57	45	45	146
	12	58	59	46	163
	13	98	170	123	390
	14	63	73	119	255
	16	23	15	34	72
1×10^{-7} Annual Probability of Exceedance	1	1128	1215	820	3163
	2	989	1202	2972	5163
	3	577	735	971	2283
	4	856	1052	1013	2921
	5	373	252	205	830
	6	331	271	566	1168
	7	303	291	3357	3951
	8	343	524	437	1304
	9	813	1691	3340	5844
	10	282	125	409	816

Table 6-6. Arias Intensity (m/sec) for Each Ground Motion Set (Continued)

Annual Hazard Level	Ground Motion Set	H1	H2	V	Total Sum
1×10^{-7} Annual Probability of Exceedance	11	272	214	321	808
	12	277	284	332	893
	13	469	815	881	2165
	14	302	351	854	1507
	16	112	72	244	428
5×10^{-4} Annual Probability of Exceedance		0.59	0.67	0.46	1.72
1×10^{-4} Annual Probability of Exceedance		4.21	4.51	8.97	17.69

Sources: DTNs: MO0407TMHIS104.003 [DIRS 170599]; MO0306SDSAVDTH.000 [DIRS 164033]; MO0402AVDTM105.001 [DIRS 168890]; MO0403AVDSC106.001 [DIRS 168891]; MO0403AVTMH107.003 [DIRS 168892].

NOTES: A total of 17 sets of ground motions was developed for each postclosure level. Ground motion sets #15 and #17 were not used. The selection of ground motion sets is documented in *Sampling of Stochastic Input Parameters for Rockfall Calculations and for Structural Response Calculations Under Vibratory Ground Motion* (BSC 2004 [DIRS 169999]). Native data files (available as ASCII text files) containing the Arias intensity data can be downloaded from the source DTNs (see file Dur.zip). Arias intensity is the total energy (m/sec) over the full duration (0 to 100 percent energy).

Table 6-7. Seismic Analysis Duration and Complete Time History Duration

Annual Hazard Level	Ground Motion Set	Duration of Time History (sec)	5 % Time (sec)	95 % Time (sec)
1×10^{-5} Annual Probability of Exceedance	Set 1	20.60	1.34	8.22
	Set 2	20.60	0.80	8.58
	Set 3	20.01	1.76	4.62
	Set 4	26.13	1.57	17.90
	Set 5	20.01	1.70	10.27
	Set 6	20.01	2.62	10.73
	Set 7	16.27	3.76	12.17
	Set 8	20.60	1.21	7.48
	Set 9	29.98	0.75	8.83
	Set 10	20.02	1.68	10.26
	Set 11	20.60	2.07	10.93
	Set 12	40.02	2.27	17.53
	Set 13	39.96	2.05	20.33
	Set 14	40.00	5.49	24.85
	Set 16	32.01	3.80	11.63
1×10^{-6} Annual Probability of Exceedance	Set 1	20.60	1.28	7.47
	Set 2	20.60	0.80	7.40
	Set 3	20.01	1.75	4.73
	Set 4	26.13	1.48	17.29
	Set 5	20.01	1.69	8.78
	Set 6	20.01	2.44	10.57
	Set 7	16.27	3.55	12.23
	Set 8	20.60	1.21	6.48

Table 6-7. Seismic Analysis Duration and Complete Time History Duration (Continued)

Annual Hazard Level	Ground Motion Set	Duration of Time History (sec)	5 % Time (sec)	95 % Time (sec)
1×10^{-6} Annual Probability of Exceedance	Set 9	29.98	0.76	8.00
	Set 10	20.02	1.67	9.58
	Set 11	20.60	2.08	10.30
	Set 12	40.02	2.17	15.66
	Set 13	39.96	1.90	19.53
	Set 14	40.00	5.37	23.94
	Set 16	32.01	3.43	10.43
1×10^{-7} Annual Probability of Exceedance	Set 1	20.60	1.28	7.47
	Set 2	20.60	0.80	7.40
	Set 3	20.01	1.75	4.73
	Set 4	26.13	1.48	17.29
	Set 5	20.01	1.69	8.78
	Set 6	20.01	2.44	10.57
	Set 7	16.27	3.55	12.23
	Set 8	20.60	1.21	6.48
	Set 9	29.98	0.76	8.00
	Set 10	20.02	1.67	9.58
	Set 11	20.60	2.08	10.30
	Set 12	40.02	2.17	15.66
	Set 13	39.96	1.90	19.53
	Set 14	40.00	5.37	23.94
	Set 16	32.01	3.43	10.43
5×10^{-4} Annual Probability of Exceedance		40.96	3.46	28.67
1×10^{-4} Annual Probability of Exceedance		75.00	9.78	58.79

Sources: DTNs: MO0407TMHIS104.003 [DIRS 170599]; MO0306SDSAVDTH.000 [DIRS 164033]; MO0402AVDTM105.001 [DIRS 168890]; MO0403AVDSC106.001 [DIRS 168891]; MO0403AVTMH107.003 [DIRS 168892].

NOTES: A total of 17 sets of ground motions was developed for each postclosure level. Ground motion sets #15 and #17 were not used. The selection of ground motion sets is documented in *Sampling of Stochastic Input Parameters for Rockfall Calculations and for Structural Response Calculations Under Vibratory Ground Motion* (BSC 2004 [DIRS 169999]). Native data files (available as ASCII text files) containing time-history duration can be downloaded from the source DTNs (see file *Dur.zip*). Data are extracted from the 5 to 95 percent energy range. The earliest 5 percent point and the latest 95 percent point for each component (H1, H2, and V) are used to define the duration of each ground motion set.

Table 6-8. Combinations of Ground Motion and Fracture Modeling Region of 3DEC Analyses

3DEC Simulation Number	Ground Motion Time History Number	Fracture Pattern
14	7	22
15	11	21
16	11	30
17	16	27
18	14	26
19	13	10
20	5	19
21	10	9
22	5	23
23	12	5
24	3	6
25	3	17
27	6	14
28	7	25
29	13	3
31	16	79
32	12	7
33	1	102
34	16	75
35	11	33
36	5	78
38	3	29
39	5	37
40	6	99
41	16	42
42	6	24
43	4	59
44	9	65
45	10	39
46	6	50
48	16	35
49	5	57
50	9	67
51	10	63
52	9	82
53	12	4
54	1	83
55	12	16
56	3	98
57	14	28

Table 6-8. Combinations of Ground Motion and Fracture Modeling Region of 3DEC Analyses (Continued)

3DEC Simulation Number	Ground Motion Time History Number	Fracture Pattern
58	4	8
59	2	74
60	11	80
61	12	81
62	12	71
63	11	96
64	14	49
65	7	20
66	3	62
67	9	41

Source: DTN: MO0301SPASIP27.004 [DIRS 161869].

NOTES: 3DEC simulation numbers 14 through 29 are from the corresponding realization numbers from the first sampling in the nonlithophysal zone provided by the source DTN.

3DEC simulation numbers 31 through 67 are from the second sampling (realization numbers 1 through 60) in the nonlithophysal zone provided by the source DTN.

Duplicate fracture modeling regions (i.e., synthetic fracture pattern numbers) occurring in both the first and second samplings were not used as part of the base case for rockfall modeling.

Simulation Number 26, 37, and 47 were not used due to numerical difficulties for 3DEC block generation.

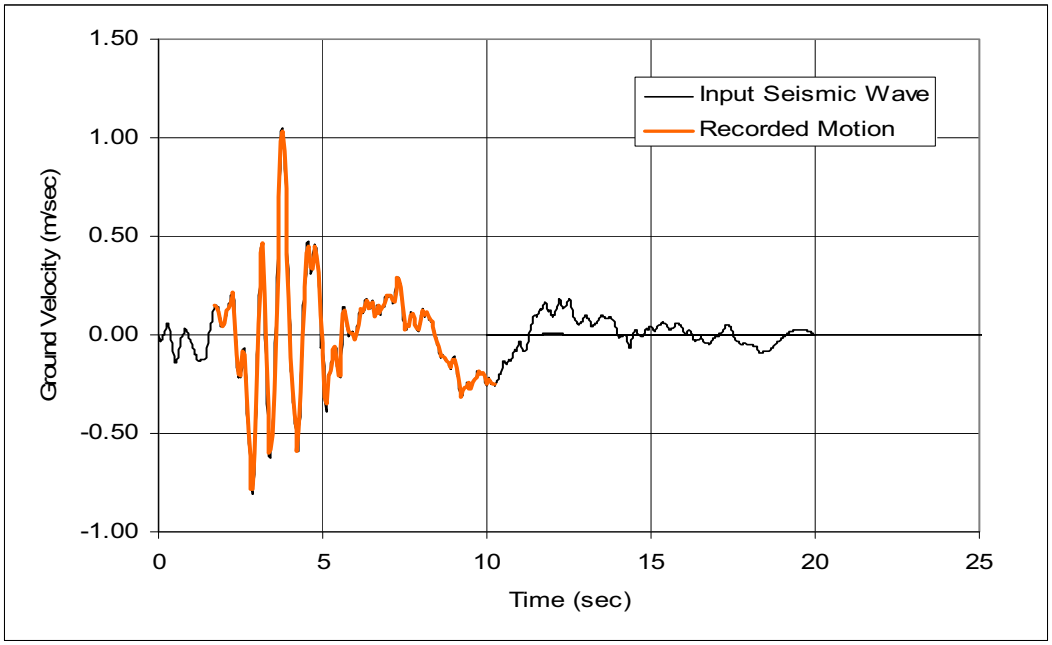

NOTE: The ground motion was recorded at the drip shield block during 3DEC simulation.

Figure 6-37. Comparison of Input Seismic Wave and Recorded Velocities in 3DEC Model (Ground Motion Set 4, H1)

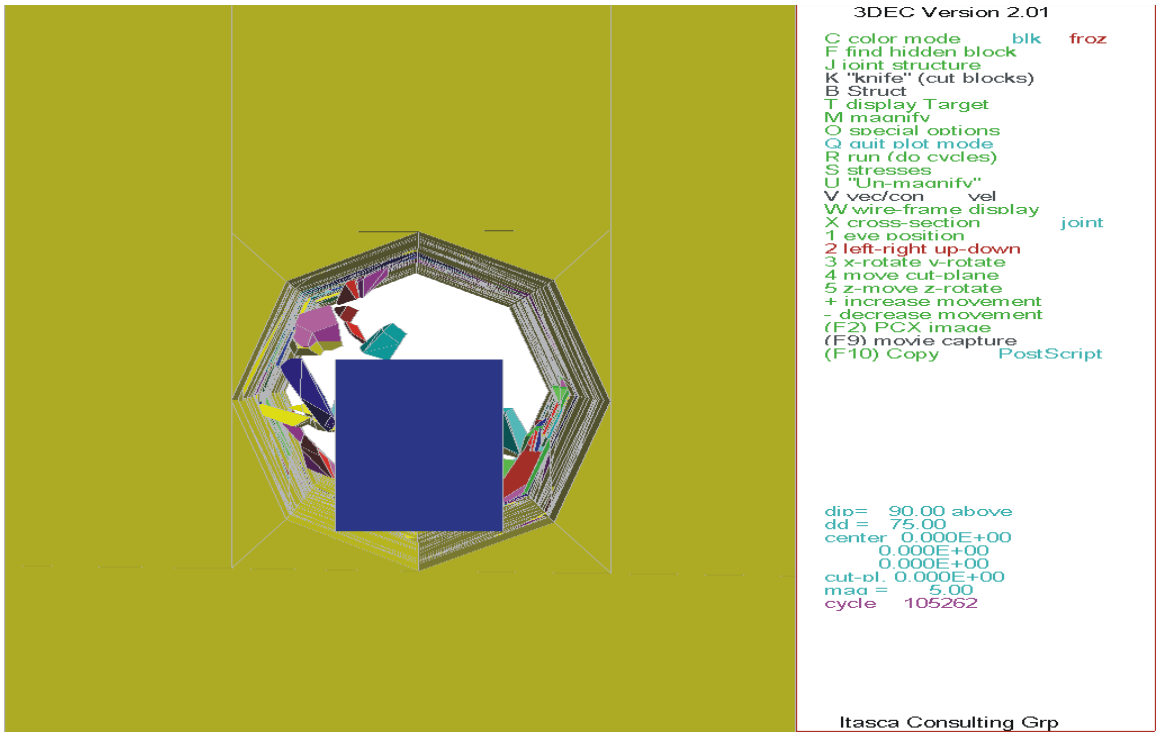

Figure 6-38. Illustration of the Simulation of Rockfall Impact to the Drip Shield 3DEC Simulation #44, 1×10^{-5} Ground Motion # 9, at t = 3.6 sec

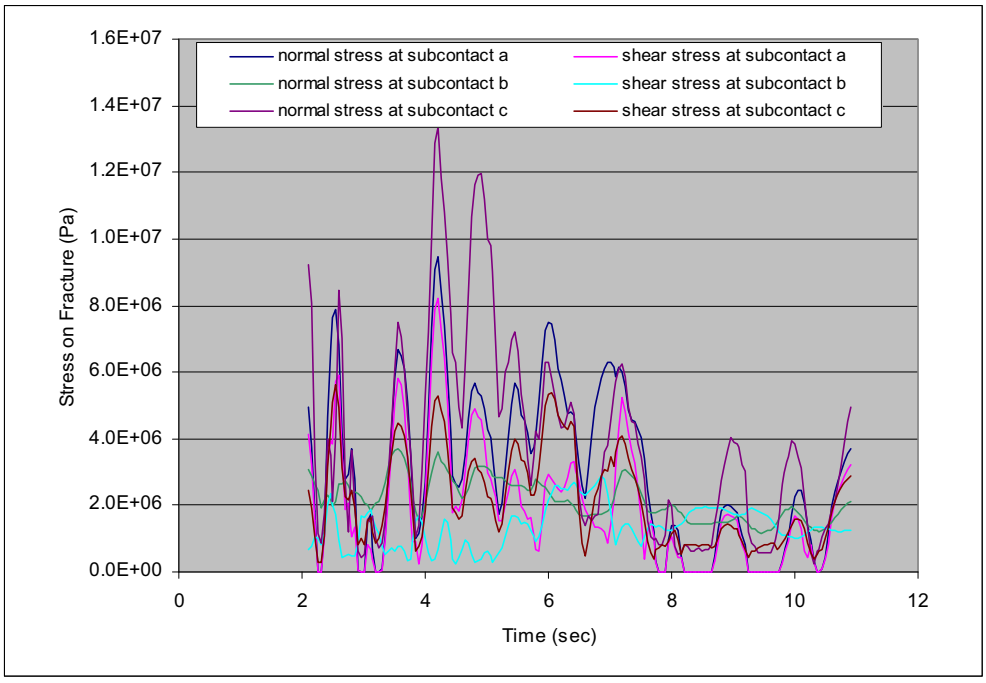

Figure 6-39. Time Histories for Normal and Shear Stress at Selected Fracture Subcontacts for 1×10^{-5} Annual Probability of Exceedance Hazard (Simulation 16, Ground Motion Set 11)

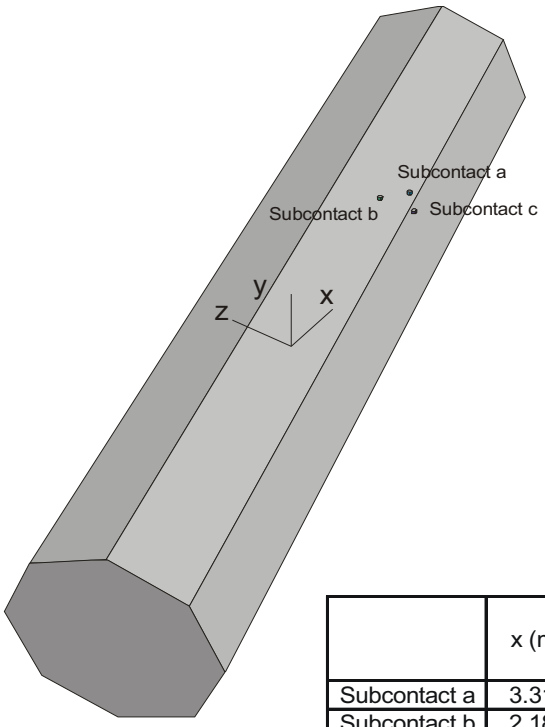

Perspective View

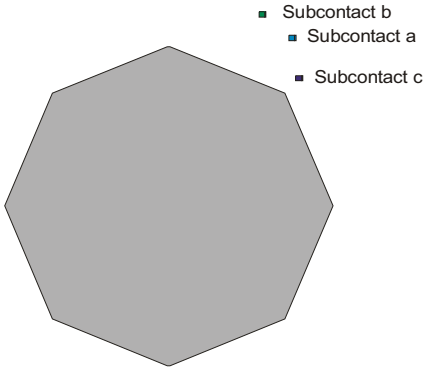

Side View

Subcontact Information

	x (m)	y (m)	z (m)	dip direction (degree)	dip (degree)	contact type
Subcontact a	3.311	2.879	-1.257	305.97	82.36	actual joint
Subcontact b	2.189	3.288	-1.041	54.56	82.7	rock bridge
Subcontact c	3.434	2.19	-1.348	317.73	5.82	rock bridge

Figure 6-40. Information for the Selected Fracture Subcontacts

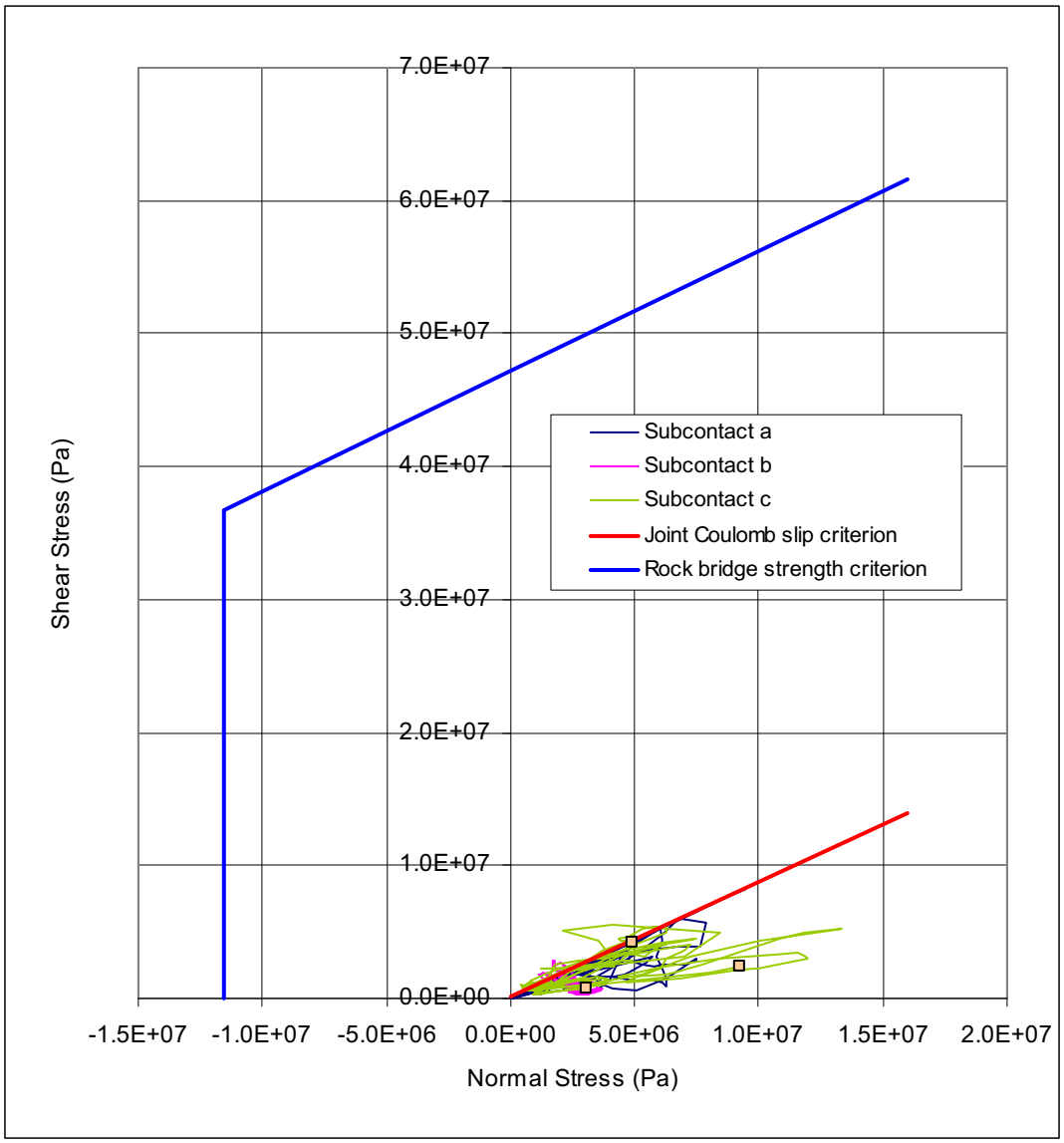

Figure 6-41. Normal and Shear Stress Path at Selected Fracture Subcontacts for 1×10^{-5} Annual Probability of Exceedance Hazard (Simulation 16, Ground Motion Set 11)

Table 6-9. Summary of Joint Slip/Separation and Bridge Damage for 1×10^{-5} Ground Motions for Selected Cases

Parameter	Case 38	Case 40	Case 66	Case 23	Case 48	Case 45	Case 63	Case 31
Total Joint Area (m^2)	4319	4251	2583	3026	4260	4737	1911	3400
Total Bridge Area (m^2)	862	885	592	550	923	1054	425	720
Percentage of Joint Slip/Separation	94.98%	90.94%	96.24%	77.07%	82.09%	70.80%	79.33%	73.59%
Percentage of Bridge Damaged	14.62%	1.00%	10.14%	0.24%	0.06%	0.00%	0.47%	0.06%

Table 6-10. Summary of 3DEC Rockfall Prediction for 1×10^{-5} Annual Probability of Exceedance Hazard

Parameter	Value
Simulations Completed	50
Number of Simulations Predicting No Rockfall	1
Total Number of Rockfall	1767
Total Volume of Rockfall (m^3)	255.4
Total Length of Drift Simulated (m)	1250
Number of Blocks per km	1414
Volume of Rockfall per km (m^3)	204.3

A detailed listing of the impact information for each recorded block is provided in an output DTN of this document (DTN: MO0408MWDDDMIO.002, file *nonlith rockfall characteristics in emplacement drifts with 1e-5 gm.xls*). The impact locations are provided as the coordinates based on the drip shield local coordinate system (Figure 6-42). The distribution of the data for each parameter (i.e., block mass, relative impact velocity, impact angle, impact momentum, and impact energy) is presented using histograms (Figures 6-43 to 6-47). Also included in each histogram plot is the cumulative frequency of occurrence. Due to the gravity effect, most of the rockfall will occur in the range of 48 degrees to 132 degrees as confirmed in Figure 6-45. The impact momentum and impact energy, both functions of block mass and impact velocity, were calculated as the required outputs for drip shield structural response calculation. Summary statistics for these parameters are provided in Table 6-11. The maximum rockfall block mass predicted is 19.07 metric tons with median block size of 0.12 metric tons. The predicted results (Table 6-11) show large variance and high skewness with the exception of impact velocity, as confirmed by the shape of the histograms (Figures 6-43 to 6-47). The block mass, impact angle, impact momentum, and impact energy show the trend of exponential distribution with most of the data concentrated on the low end of the data range. The impact velocity shows a typical bell shape for the normal distribution. The distribution centers around 3 m/sec with a standard deviation of approximately 1.5 m/sec. The relative low impact velocities indicate that block fall-out is mainly due to free fall. Differential acceleration or energy trapping to induce high ejection velocity is not observed.

Table 6-11. Statistic Summary of the Rockfall Impact Parameters, 1×10^{-5} Annual Probability of Exceedance Hazard

Parameter	Block Mass (tonnes)	Relative Impact Velocity (m/sec)	Impact Angle (degree)	Impact Momentum (kg*m/sec)	Impact Energy (Joules)
Mean	0.35	2.69	144.74	964	1814
Median	0.12	2.57	127.13	276	357
Standard Deviation	0.93	1.48	99.69	3789	11430
Skewness	10.03	0.74	0.75	24	32
Range	19.04	9.38	359.74	128809	435077
Minimum	0.02	0.04	0.18	3	0
Maximum	19.07	9.42	359.92	128812	435077
Sum	615.97	NA	NA	1703088	3205138

NA = Not Applicable

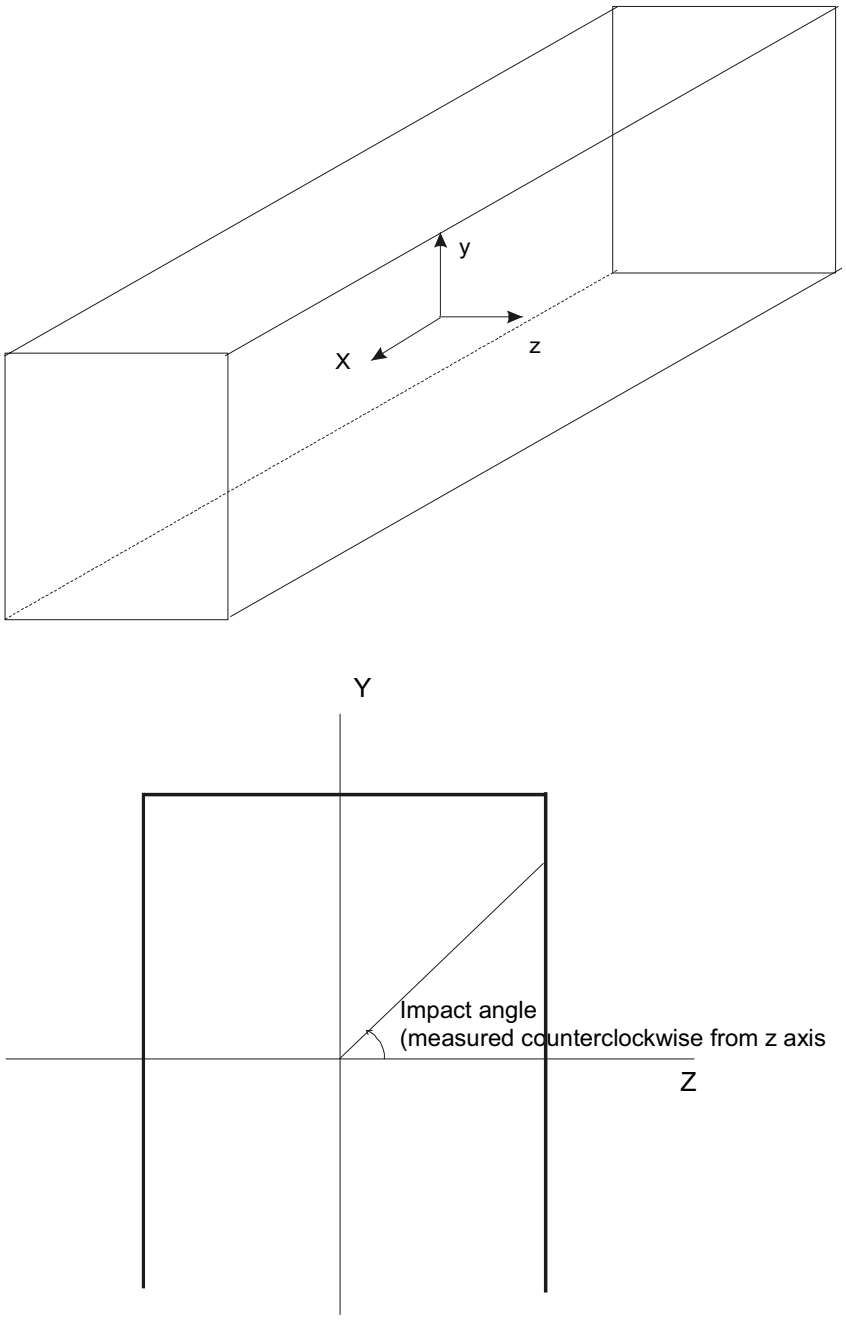

Figure 6-42. Definition of Impact Angle and Drip Shield Block Local Coordinate System

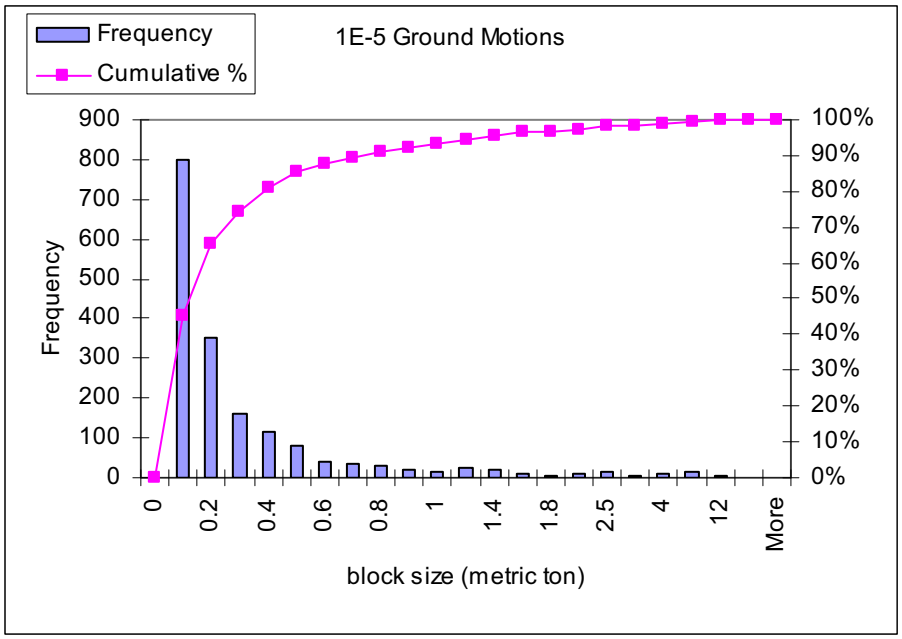

Figure 6-43. Histogram for Block Mass (1×10^{-5} Annual Probability of Exceedance Hazard)

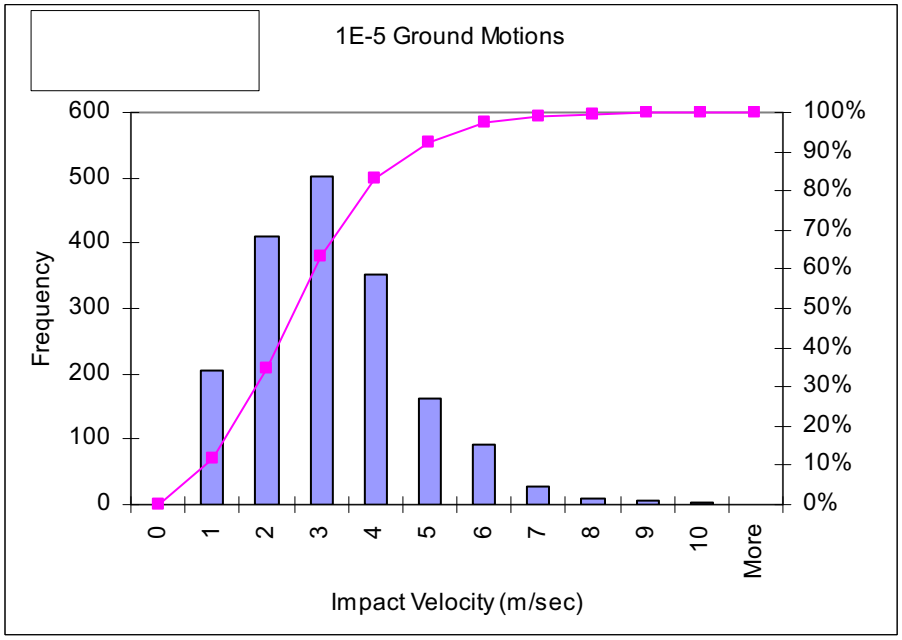

Figure 6-44. Histogram for Relative Impact Velocity (1×10^{-5} Annual Probability of Exceedance Hazard)

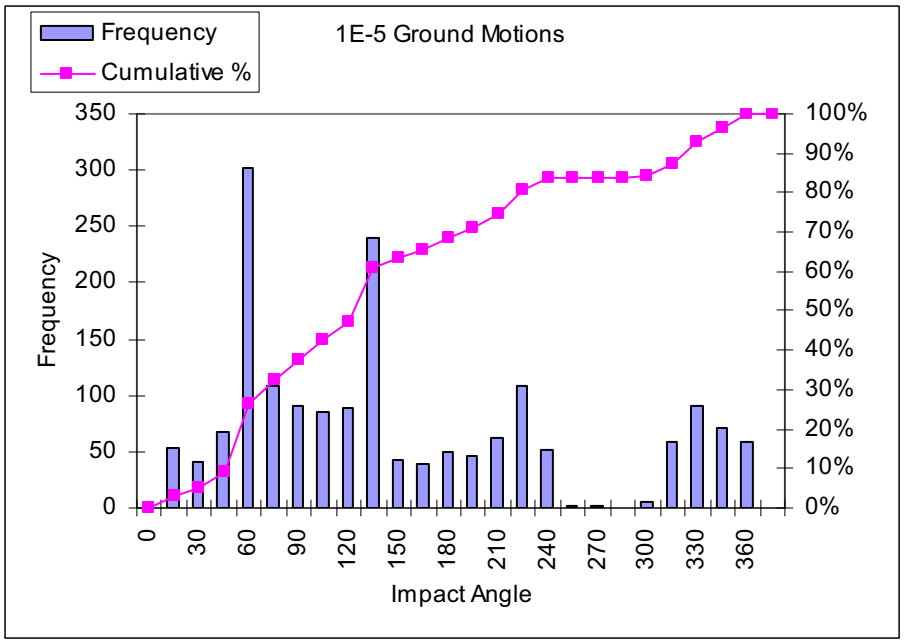

Figure 6-45. Histogram for Impact Angle (1×10^{-5} Annual Probability of Exceedance Hazard)

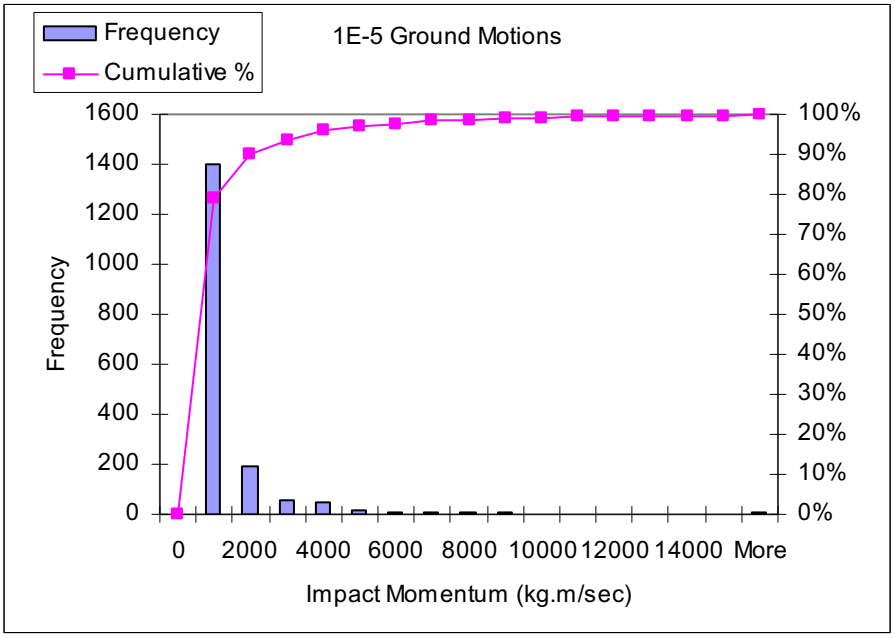

Figure 6-46. Histogram for Impact Momentum (1×10^{-5} Annual Probability of Exceedance Hazard)

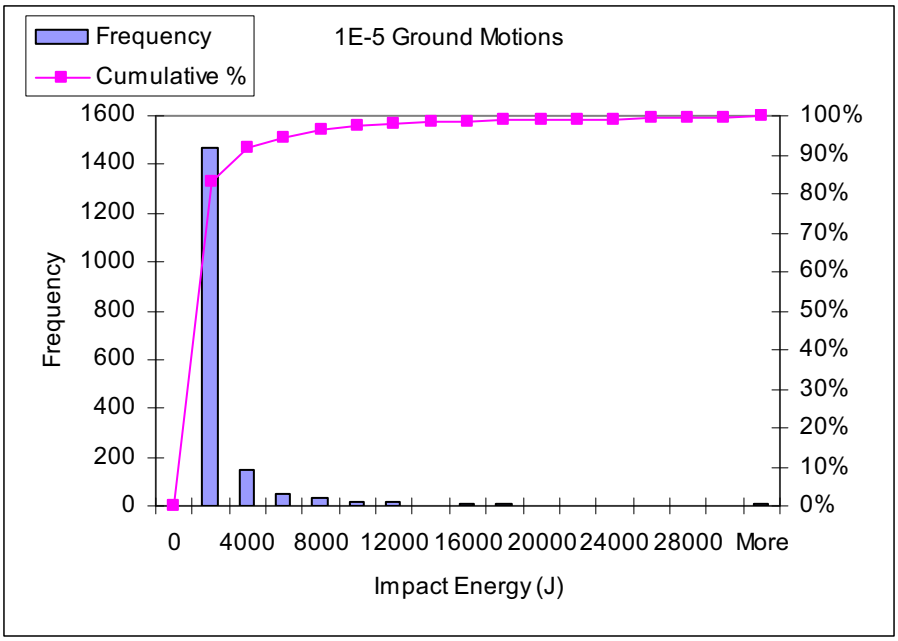

Figure 6-47. Histogram for Impact Energy (1×10^{-5} Annual Probability of Exceedance Hazard)

6.3.1.2.4 Results for Seismic Analysis Subjected to 1×10^{-6} Annual Probability of Exceedance Ground Motions

The results for a complete set of 3DEC analyses subjected to the postclosure hazard level of 1×10^{-6} annual probability of exceedance ground motions are presented in this section. Figure 6-48 compares the input ground motion for the second horizontal component (H2, Ground Motion Set 6) with the recorded velocities at the center of the model. As for the case of 1×10^{-6} annual probability of exceedance hazard, the results confirm the correct wave inputs and proper wave propagation in the 3DEC model.

Figure 6-49 shows a perspective view of blocks impacting drip shield in 3DEC dynamic simulation. Time histories of normal and shear stresses for fractures and rock bridges close to the opening were recorded during the seismic shaking in the 3DEC model. Figure 6-50 shows normal and shear stress time histories at the same selected fracture subcontacts as presented for the 1×10^{-5} annual probability of exceedance ground motions (3DEC simulation #16 with ground motion set #11). Peak normal stress at subcontact *c* reaches approximately 20 MPa at around 4 seconds. Information of the subcontacts is provided in Figure 6-40. The stress paths of the fracture subcontacts are plotted against the fracture Coulomb slip criterion and rock bridge strength criterion, as shown in Figure 6-51. The in situ normal and shear stress state along the fracture is also included as the orange square for each subcontact in the figure. As in the 1×10^{-5} ground motion case, the fracture containing subcontact *a* yielded during seismic motions. The stress paths for rock bridges containing subcontacts *b* and *c* are still under the rock strength criterion when subjected to 1×10^{-6} ground motion.

The percentages of the area of joint slip/separation versus the total area of joint planes for the selected cases were calculated and presented in Table 6-12. The majority of fractures (greater

than 95 percent for most cases) have undergone shear slip or tensile separation when subjected to 1×10^{-6} ground motions. Bridge damage percentages are also presented in Table 6-12. It is predicted that, for the majority of cases, around 5 percent bridge area would be damaged by shaking of 1×10^{-6} ground motions. However, for certain large ground motions (e.g., ground motion #3 for Case 38), higher damage percentage is predicted. Correlation of the bridge damage percentage versus peak ground velocity shows a strong relationship between the two. A detailed discussion on the bridge damage is provided in Section 6.3.1.6.3.

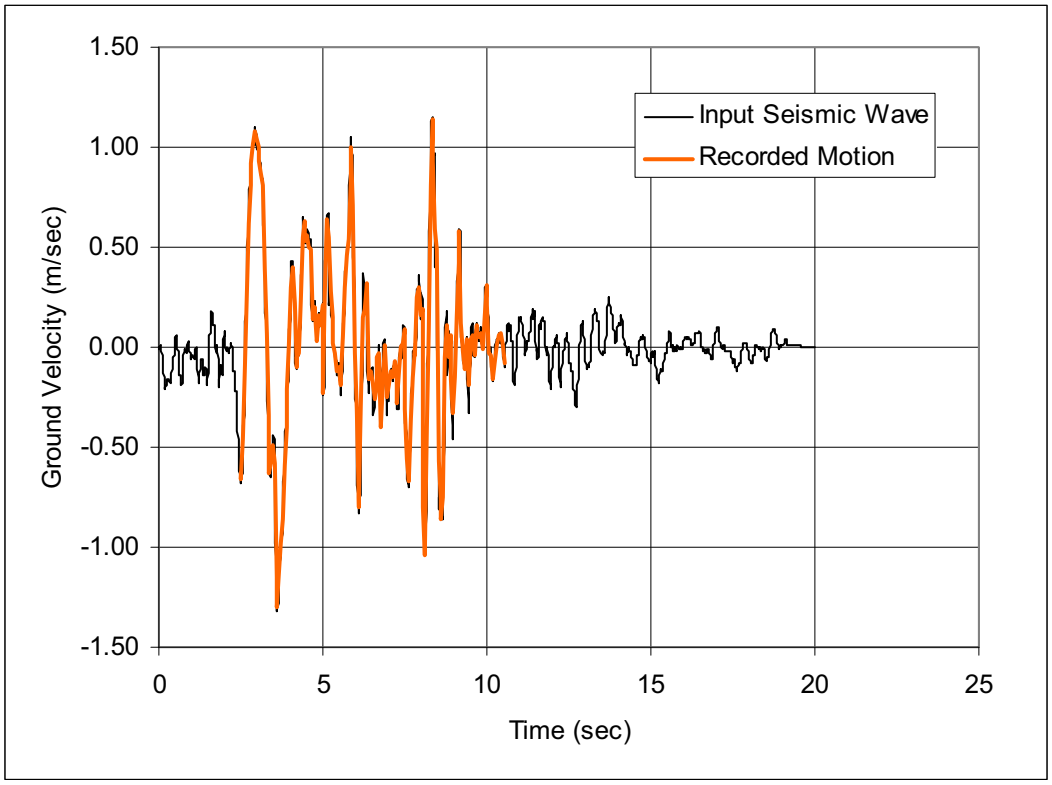

NOTE: The ground motion was recorded at the drip shield block during 3DEC simulation.

Figure 6-48. Comparison of Input Seismic Wave and Recorded Velocities in 3DEC Model for 1×10^{-6} Annual Probability of Exceedance Ground Motion (Ground Motion Set 6, H2)

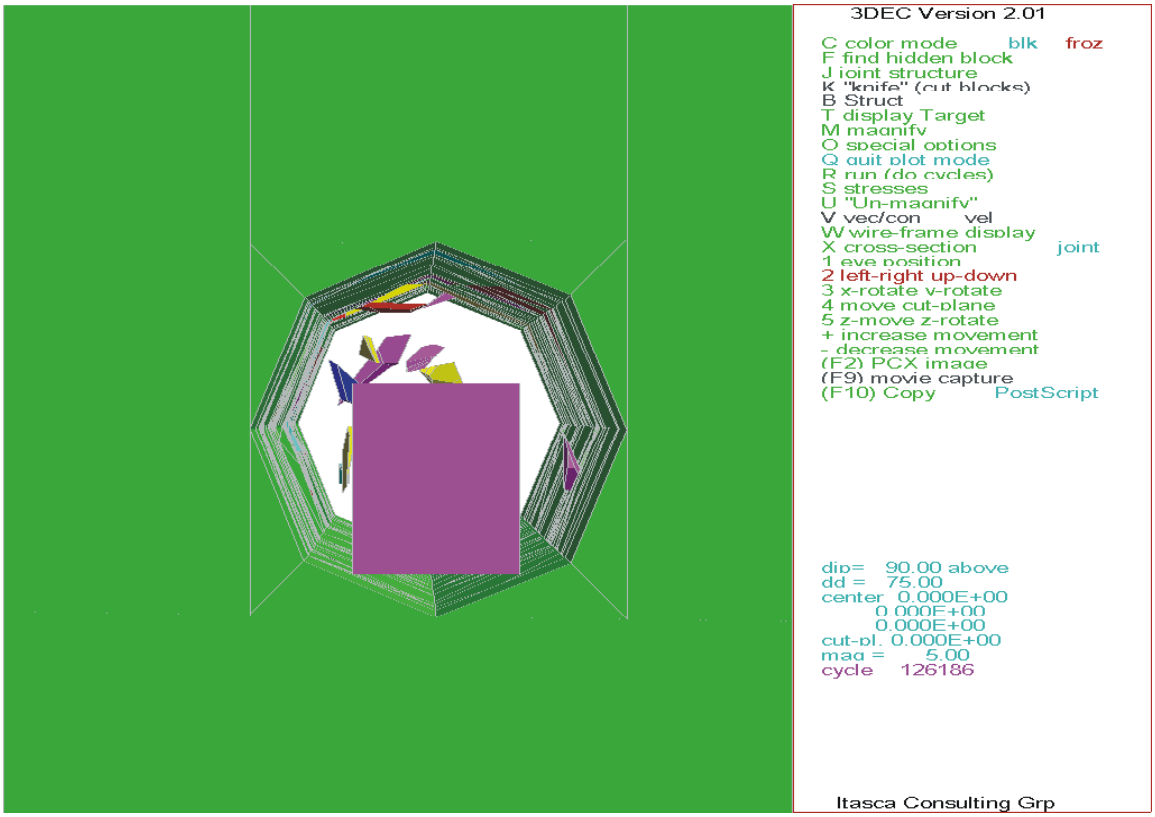

Figure 6-49. Illustration of the Simulation of Rockfall Impact to the Drip Shield (3DEC Simulation # 22, 1×10^{-6} Ground Motion # 5, at t = 5.24 sec) (Simulation 16, Ground Motion Set 11)

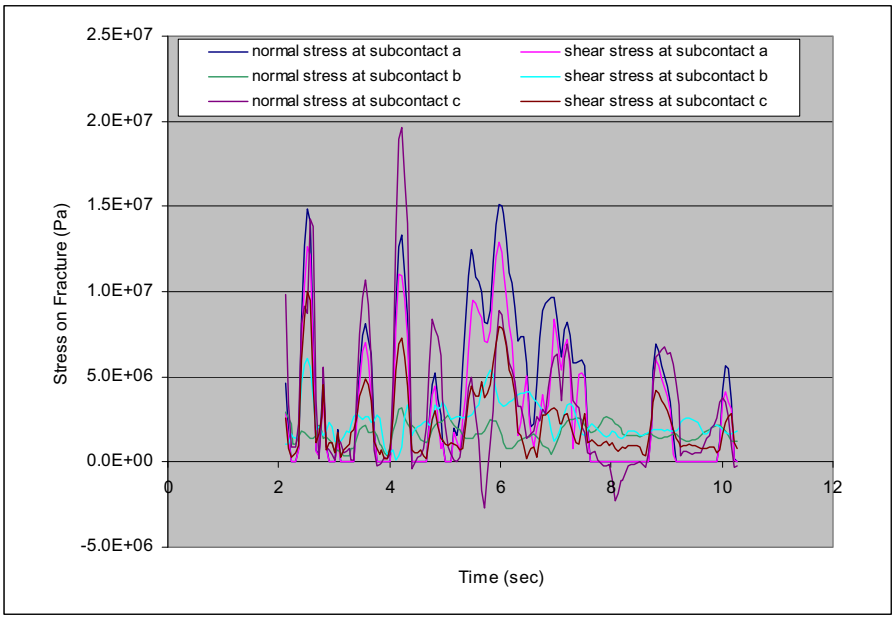

NOTE: Information for the subcontacts is presented in Figure 6-40.

Figure 6-50. Time Histories for Normal and Shear Stress at Selected Fracture Subcontacts for 1×10^{-6} Annual Probability of Exceedance Hazard

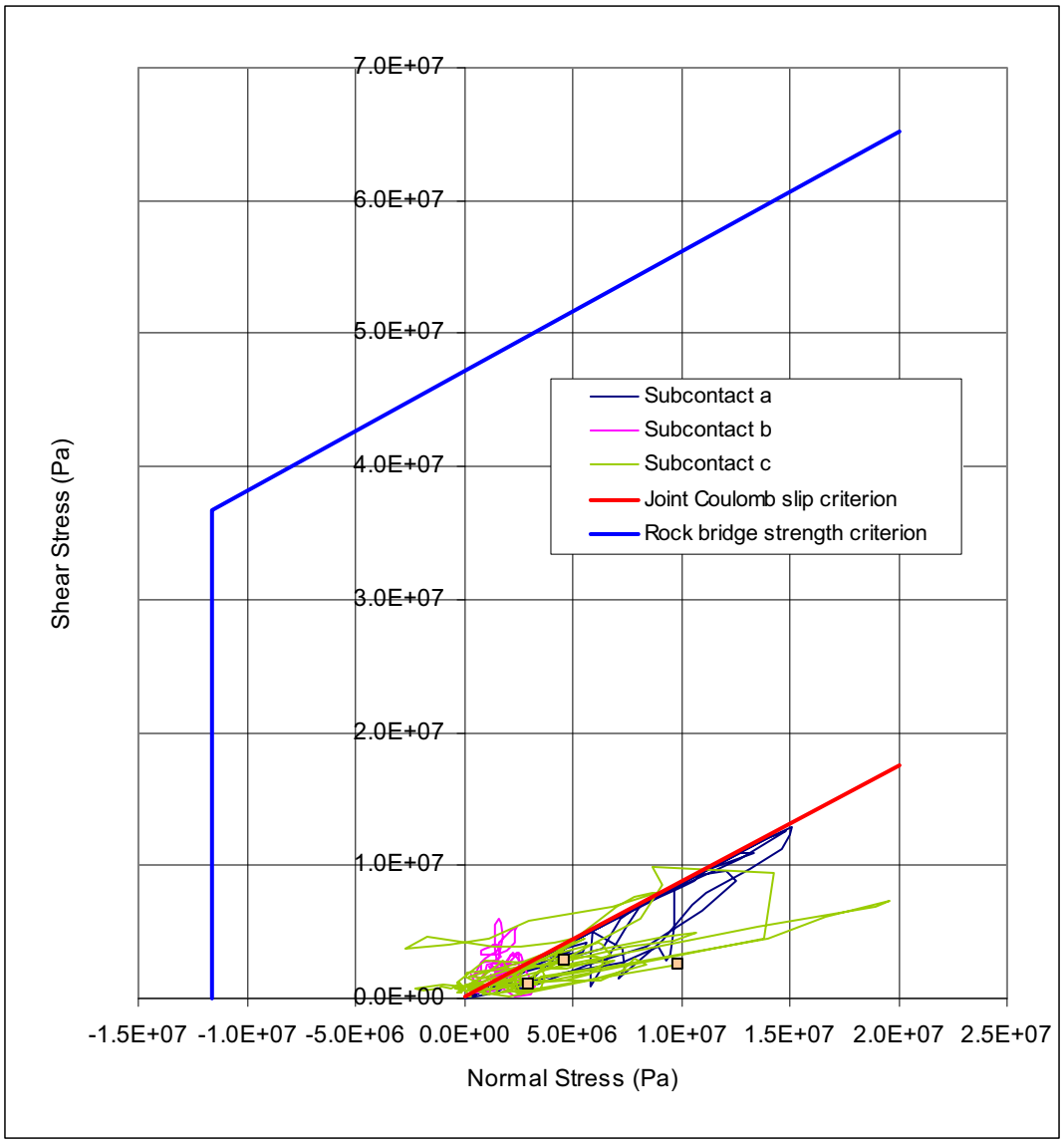

NOTE: Information for the subcontacts is presented in Figure 6-40.

Figure 6-51. Normal and Shear Stress Path at Selected Fracture Subcontacts for 1×10^{-6} Annual Probability of Exceedance Hazard (Simulation 16, Ground Motion Set 11)

The results of the 50 3DEC simulations are summarized in Table 6-13. A total of 2,797 blocks have been identified from the analyses. A detailed listing of the impact information for each recorded block is included in an output DTN of this document (DTN: MO0408MWDDDMIO.002, file *nonlith rockfall characteristics in emplacement drifts with 1e-6 gm.xls*). Summary statistics for these parameters are provided in Table 6-14. The maximum rockfall block mass predicted is 28.22 metric tons. The median block size is 0.13 metric tons, very similar to the value predicted for the 1×10^{-5} annual probability of exceedance hazard. Figures 6-52 to 6-56 present the histograms and the cumulative frequency of occurrence for the five impact parameters. The distribution of each parameter is similar to that for the 1×10^{-5} annual probability of exceedance hazard.

Table 6-12. Summary of Joint Slip/Separation and Bridge Damage for 1×10^{-6} Ground Motions for Selected Cases

Parameter	Case 38	Case 40	Case 66	Case 23	Case 48	Case 45	Case 63	Case 31
Total Joint Area (m^2)	4319	4251	2583	3026	4260	4737	1911	3400
Total Bridge Area (m^2)	862	885	592	550	923	1054	425	720
Percentage of Joint Slip/Separation	93.70%	97.13%	96.36%	97.06%	96.74%	95.33%	95.40%	96.50%
Percentage of Bridge Damaged	32.60%	6.07%	28.89%	4.28%	4.14%	2.66%	2.82%	2.31%

Table 6-13. Summary of 3DEC Rockfall Prediction for 1×10^{-6} Annual Probability of Exceedance Hazard

Parameter	Value
Simulations Completed	50
Total Number of Rockfall	2797
Total Volume of Rockfall (m^3)	497.7
Total Length of Drift Simulated (m)	1250
Number of Blocks per km	2238
Volume of Rockfall per km (m^3)	398.2

Table 6-14. Statistic Summary of the Rockfall Impact Parameters, 1×10^{-6} Annual Probability of Exceedance Hazard

Parameter	Block Mass (tonnes)	Relative Impact Velocity (m/sec)	Impact Angle (degree)	Impact Momentum (kg*m/sec)	Impact Energy (Joules)
Mean	0.43	3.23	136	1217	2350
Median	0.13	2.97	124	377	576
Standard Deviation	1.30	1.74	93	3464	7704
Skewness	11.61	1.06	0.87	11	12
Range	28.19	12.03	359	79001	163657
Minimum	0.02	0.07	0	2	0
Maximum	28.22	12.10	360	79003	163657
Sum	1200.43	NA*	NA*	3403555	6573633

* Not Applicable

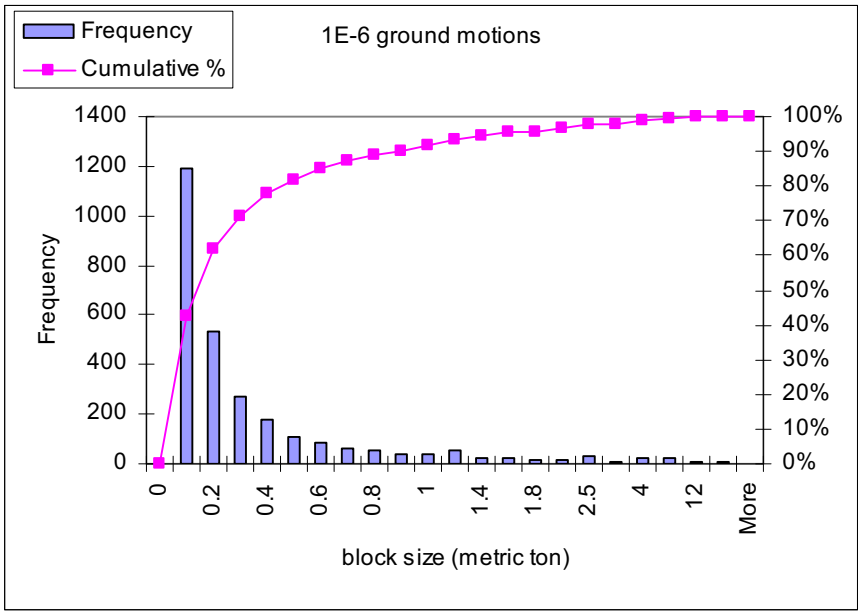

Figure 6-52. Histogram for Block Mass (1×10^{-6} Annual Probability of Exceedance Hazard)

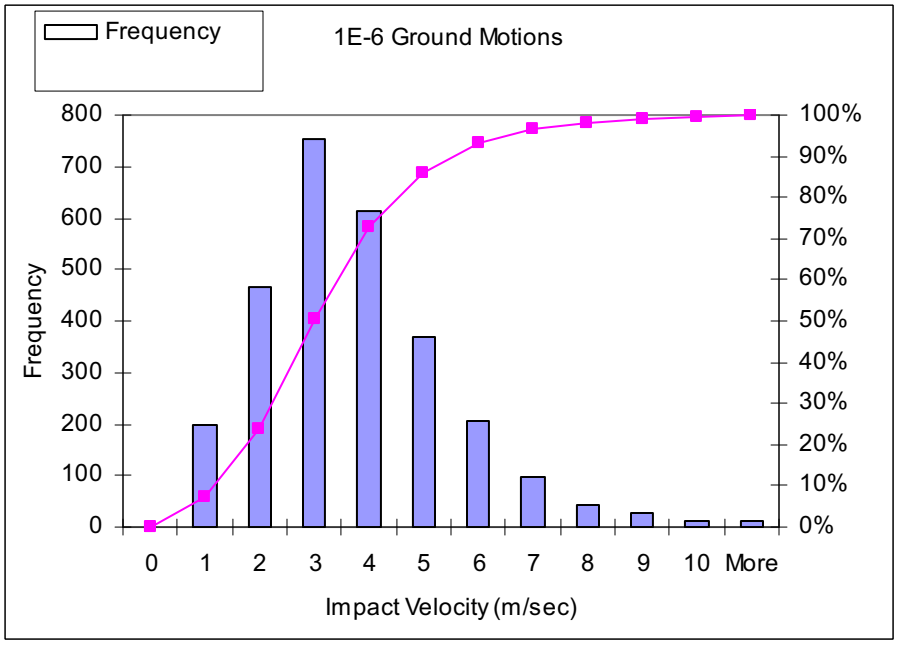

Figure 6-53. Histogram for Relative Impact Velocity (1×10^{-6} Annual Probability of Exceedance Hazard)

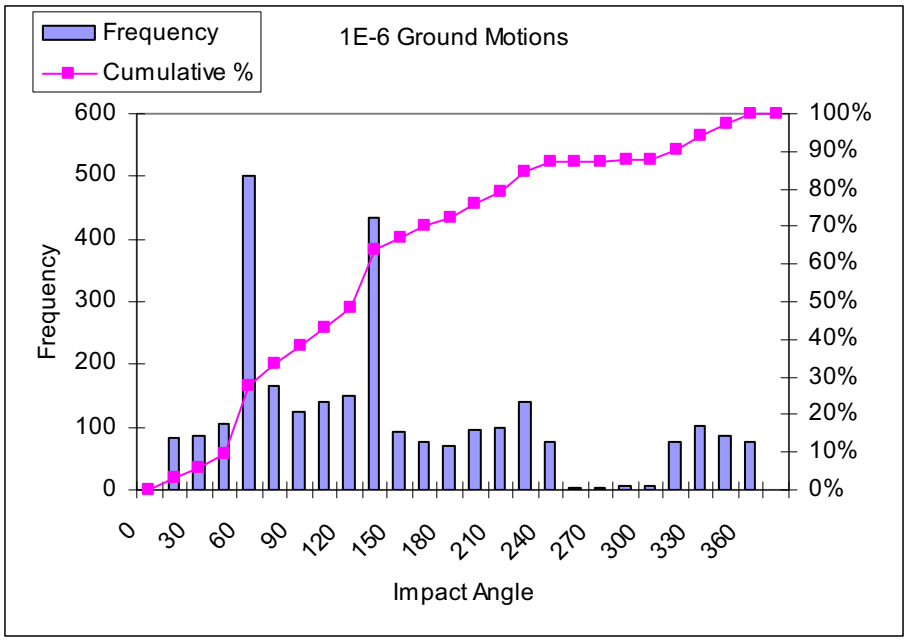

Figure 6-54. Histogram for Impact Angle (1×10^{-6} Annual Probability of Exceedance Hazard)

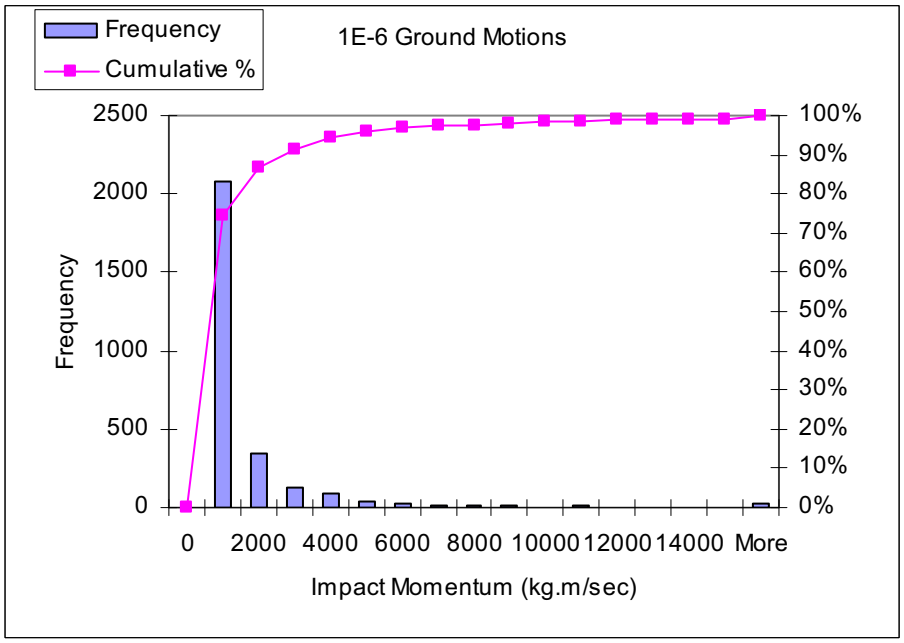

Figure 6-55. Histogram for Impact Momentum (1×10^{-6} Annual Probability of Exceedance Hazard)

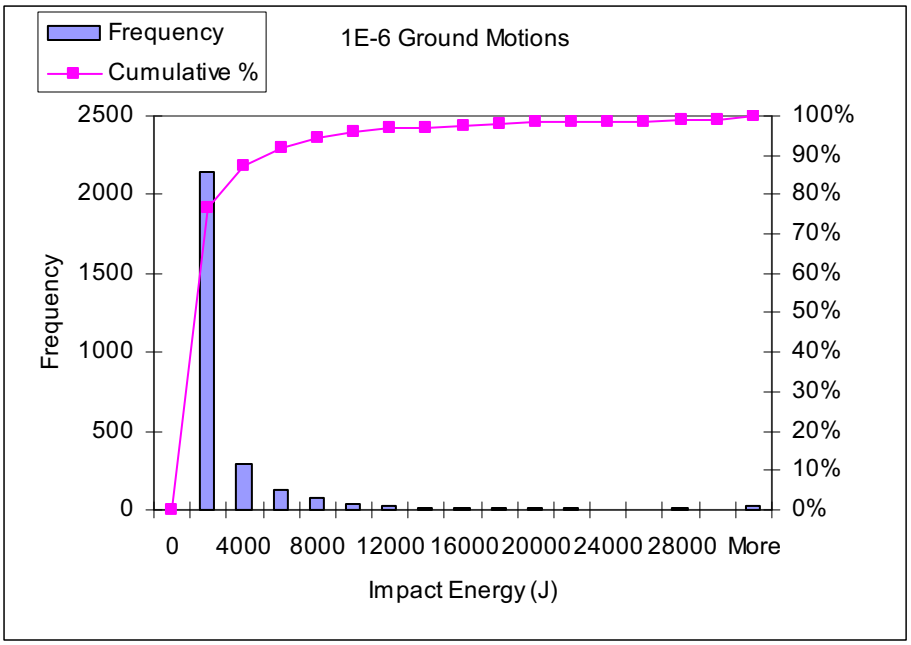

Figure 6-56. Histogram for Impact Energy (1×10^{-6} Annual Probability of Exceedance Hazard)

6.3.1.2.5 Results for Seismic Analysis Subjected to 1×10^{-7} Annual Probability of Exceedance Ground Motions

The results for a complete set of 3DEC analyses subjected to the postclosure hazard level of 1×10^{-7} annual probability of exceedance ground motions are presented in this section. Figure 6-57 compares the input ground motion for the vertical component (V, Ground Motion Set 3) with the recorded velocities at the center of the model. The results confirm the correct wave inputs and proper wave propagation in the 3DEC model.

Figure 6-58 shows a perspective view of blocks impacting the drip shield in the 3DEC dynamic simulation. Extensive rockfall is observed for many simulations for this level of ground motion. Numerical difficulties were encountered for several simulations due to the extremely large inertial force applied to the discontinuum. A total of 44 simulations were completed for this level of ground motion (Simulations 19, 24, 25, 28, 38, and 52 were not completed due to numerical difficulties). The sufficiency of 44 simulations to capture the rockfall characteristics for this level of ground motion is documented in Appendix K.

Time histories of normal and shear stresses for fractures and rock bridges close to the opening were recorded during the seismic shaking in the 3DEC model. Figure 6-59 shows normal and shear stress time histories at the same selected fracture subcontacts as presented for the 1×10^{-5} annual probability of exceedance ground motions (3DEC simulation #16 with ground motion set #11). Peak normal stress at subcontacts *a* and *c* reaches approximately 25 MPa and 30 MPa respectively, while the peak shear stress reaches to 25 MPa (information of the subcontacts is provided in Figure 6-40). The stress paths of the fracture subcontacts are plotted against the fracture Coulomb slip criterion and rock bridge strength criterion, as shown in Figure 6-60. The in situ normal and shear stress state along the fracture is identified as the orange square for each

subcontact in the figure. As with other postclosure level ground motions, the fracture containing subcontact *a* yielded during seismic motions. However, the stress paths for rock bridges containing subcontacts *b* and *c* are under the rock strength criterion when subjected to 1×10^{-7} ground motion.

The percentages of the area of fracture slip/separation versus the total area of joint planes for the selected cases were calculated and presented in Table 6-15. Most of the fractures (greater than 95 percent for most cases) have undergone shear slip or tensile separation when subjected to 1×10^{-7} ground motions. Bridge damage percentages are also presented in Table 6-15. It is predicted that, for the majority of the cases, around 20 percent bridge area would be damaged by shaking of 1×10^{-7} ground motions. However, for certain large ground motions (e.g., ground motion #3 for Case 38), damage percentage goes up to approximately 60 percent. Correlation of the bridge damage percentage versus peak ground velocity shows a strong relationship between the two. A detailed discussion on the bridge damage is provided in Section 6.3.1.6.3.

The results of the 44 3DEC simulations are summarized in Table 6-16. A total of 3,387 blocks have been identified from the analyses. A detailed listing of the impact information for each recorded block is included in an output DTN of this document (DTN: MO0408MWDDDMIO.002, file *nonlith rockfall characteristics in emplacement drifts with 1e-7 gm.xls*). Summary statistics for these parameters are provided in Table 6-17. The maximum rockfall block mass predicted is 28.29 metric tons, which is similar to the prediction for the 1×10^{-6} annual probability of exceedance ground motions. The median block size is 0.15 metric tons, similar to the value predicted for the 1×10^{-5} and 1×10^{-6} annual probability of exceedance hazards. Figures 6-61 to 6-65 present the histograms and the cumulative frequency of occurrence for the five impact parameters.

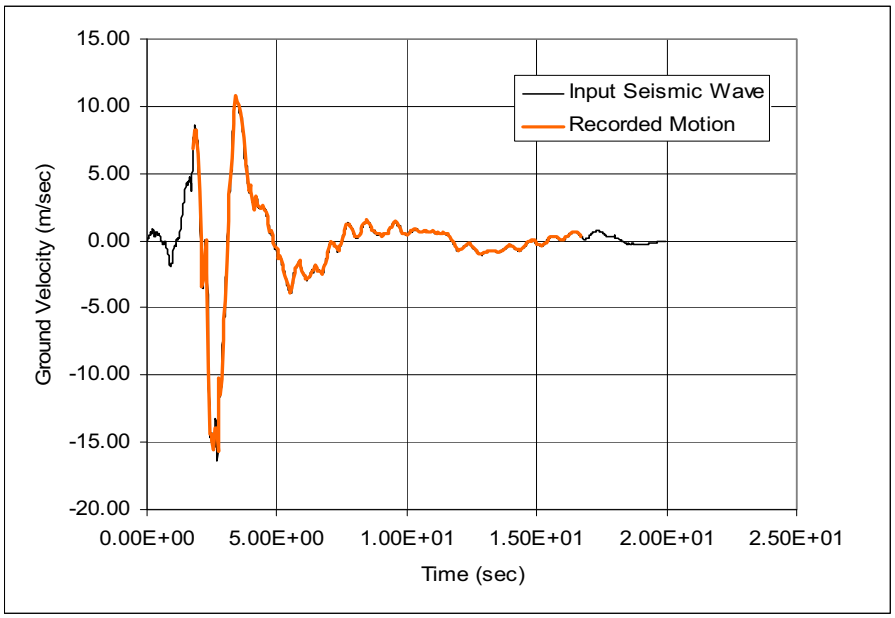

NOTE: The ground motion was recorded at the drip shield block during 3DEC simulation.

Figure 6-57. Comparison of Input Seismic Wave and Recorded Velocities in 3DEC Model for 1×10^{-7} Annual Probability of Exceedance Ground Motion (Ground Motion Set 3, Vertical Motion)

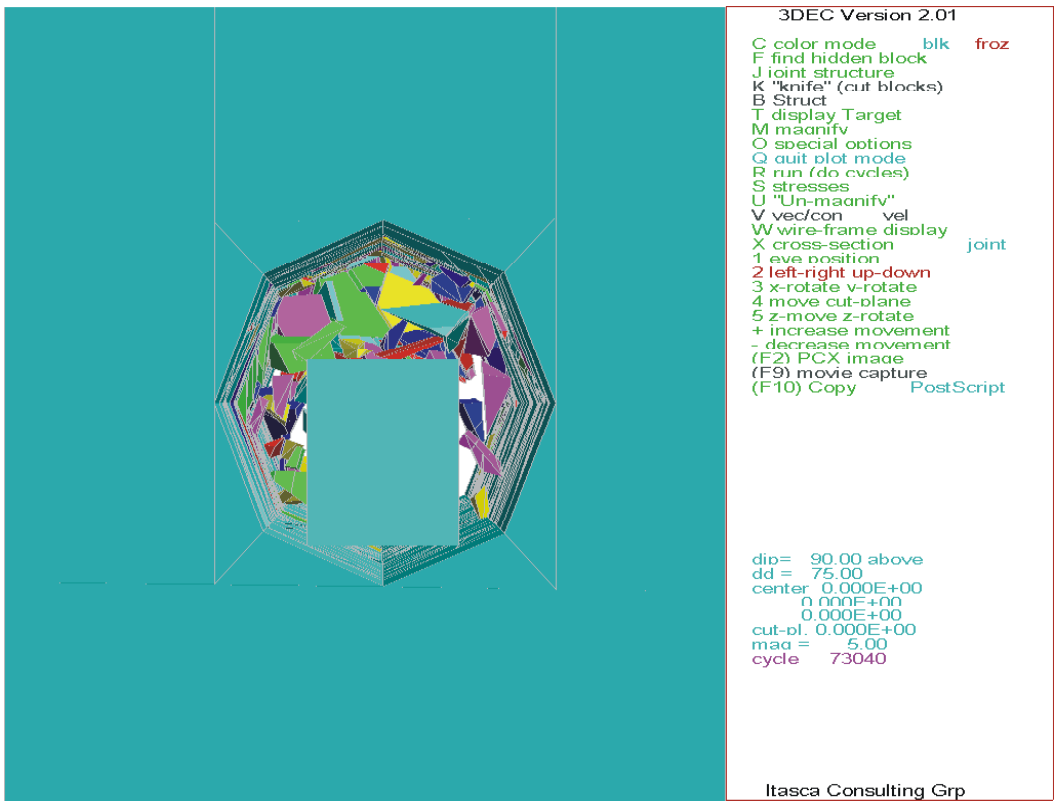

Figure 6-58. Illustration of the Simulation of Rockfall Impact to the Drip Shield (3DEC Simulation # 64, 1×10^{-7} Ground Motion # 14, at t = 7.37 sec)

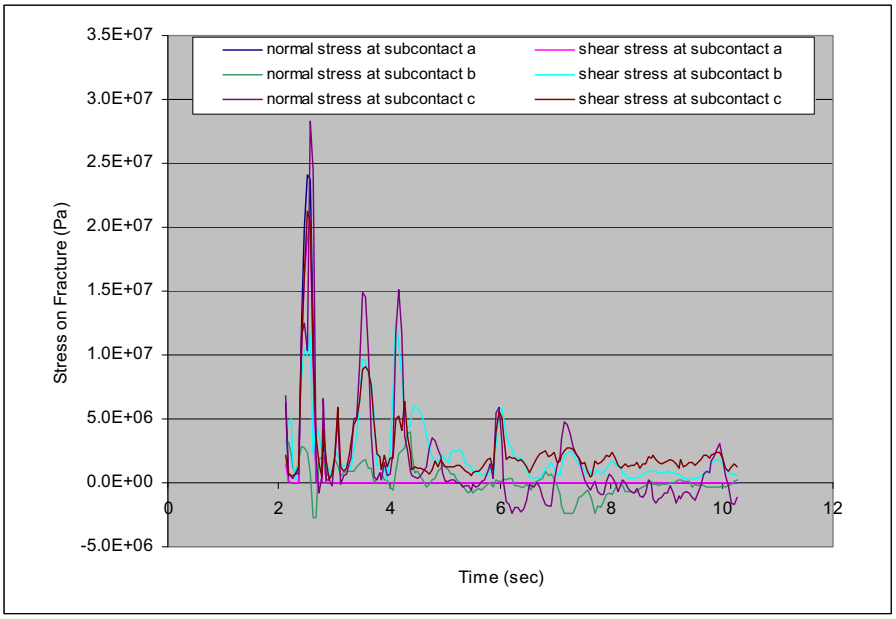

NOTE: Information for the Subcontacts is presented in Figure 6-40.

Figure 6-59. Time Histories for Normal and Shear Stress at Selected Fracture Subcontacts for 1×10^{-7} Annual Probability of Exceedance Hazard (Simulation 16, Ground Motion Set 11)

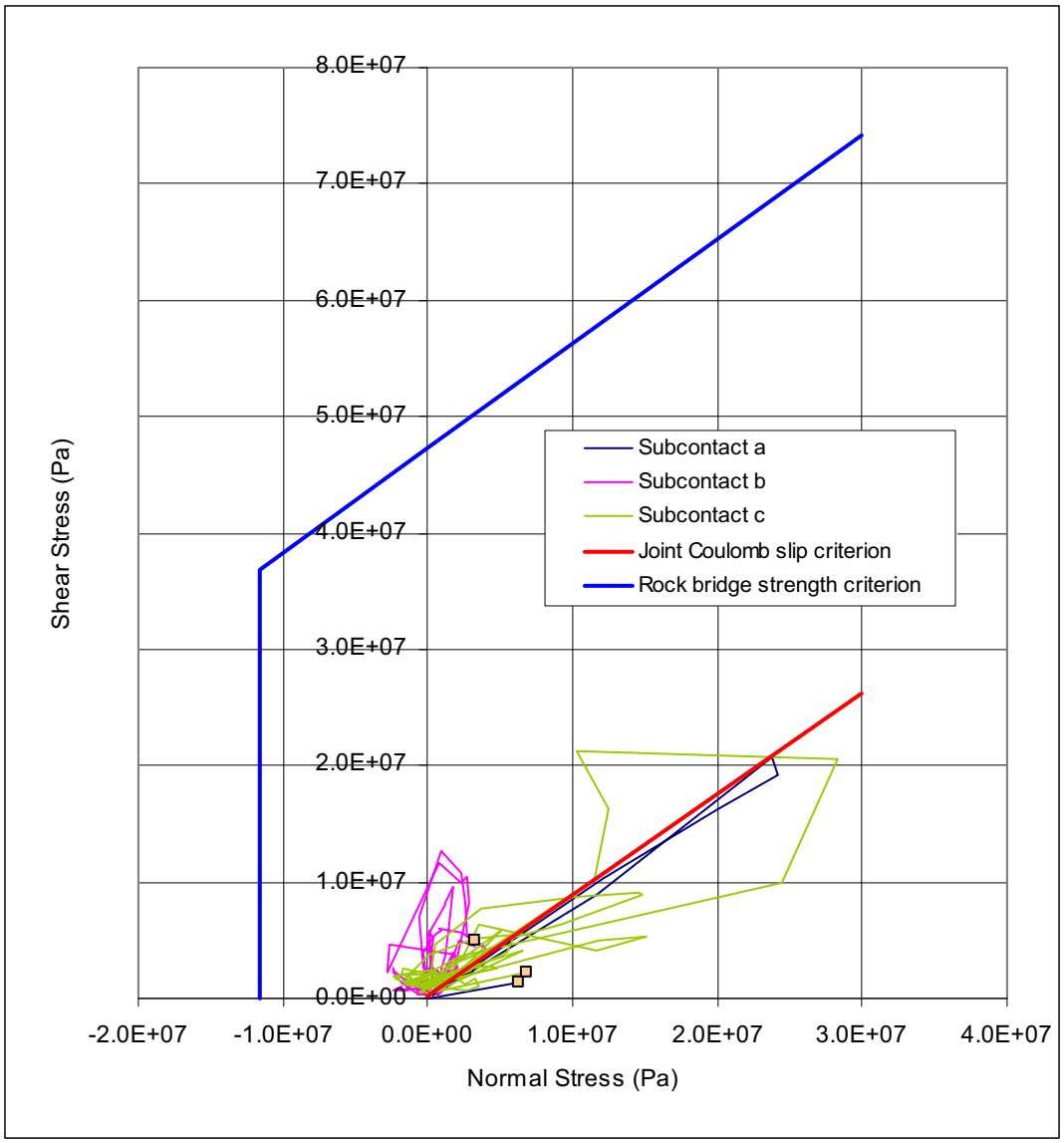

NOTE: Information for the Subcontacts is presented in Figure 6-40.

Figure 6-60. Normal and Shear Stress Path at Selected Fracture Subcontacts for 1×10^{-7} Annual Probability of Exceedance Hazard (Simulation 16, Ground Motion Set 11)

Table 6-15. Summary of Joint Slip/Separation and Bridge Damage for 1×10^{-7} Ground Motions for Selected Cases

Parameter	Case 40	Case 66	Case 23	Case 48	Case 45	Case 63	Case 31
Total Joint Area (m^2)	4251	2583	3026	4260	4737	1911	3400
Total Bridge Area (m^2)	885	592	550	923	1054	425	720
Percentage of Joint Slip/Separation	97.18%	92.26%	97.88%	97.11%	97.91%	98.53%	98.32%
Percentage of Bridge Damaged	27.78%	61.99%	29.07%	21.99%	18.22%	20.47%	16.92%

Table 6-16. Summary of 3DEC Rockfall Prediction for 1×10^{-7} Annual Probability of Exceedance Hazard

Parameter	Value
Simulations Completed	44
Total Number of Rockfall	3387
Total Volume of Rockfall (m^3)	705.2
Total Length of Drift Simulated (m)	1100
Number of Blocks per km	3079
Volume of Rockfall per km (m^3)	641.1

Table 6-17. Statistic Summary of the Rockfall Impact Parameters, 1×10^{-7} Annual Probability of Exceedance Hazard

Parameter	Block Mass (tonnes)	Relative Impact Velocity (m/sec)	Impact Angle (degree)	Impact Momentum (kg*m/sec)	Impact Energy (Joules)
Mean	0.50	4.17	135	1676	4146
Median	0.15	3.78	124	528	1022
Standard Deviation	1.43	2.47	92	5293	16749
Skewness	8.81	1.21	0.94	20	26
Range	28.26	20.90	359	199976	706914
Minimum	0.02	0.04	0	3	0
Maximum	28.29	20.94	359	199979	706914
Sum	1699.57	NA	NA	5677385	14044153

NA = Not Applicable

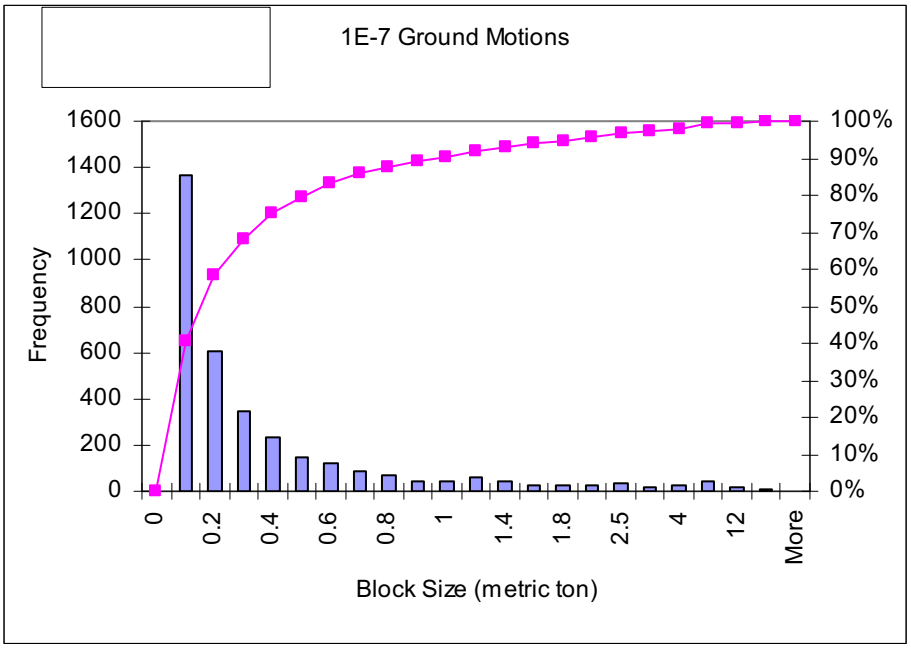

Figure 6-61. Histogram for Block Mass (1×10^{-7} Annual Probability of Exceedance Hazard)

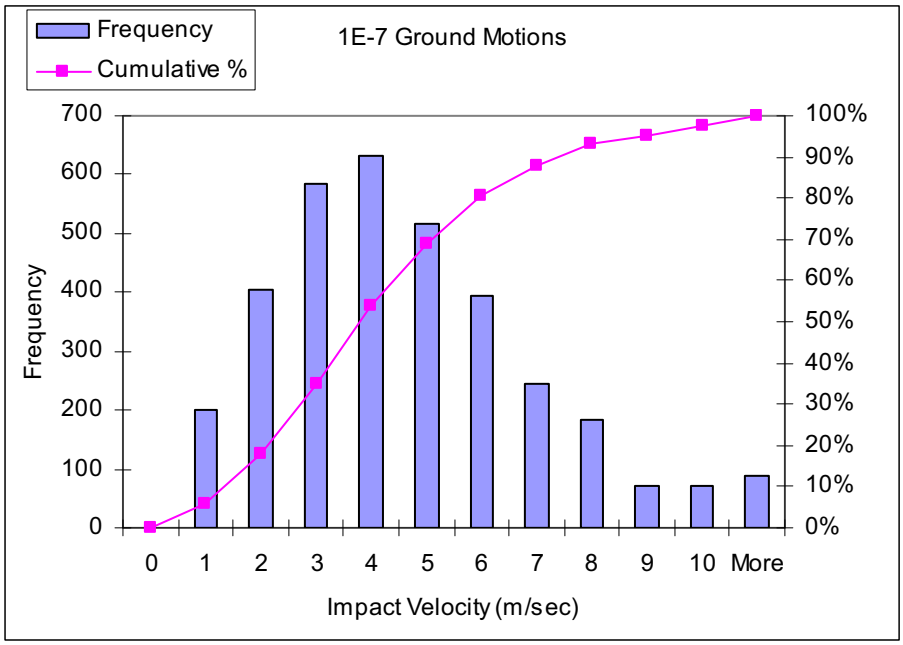

Figure 6-62. Histogram for Relative Impact Velocity (1×10^{-7} Annual Probability of Exceedance Hazard)

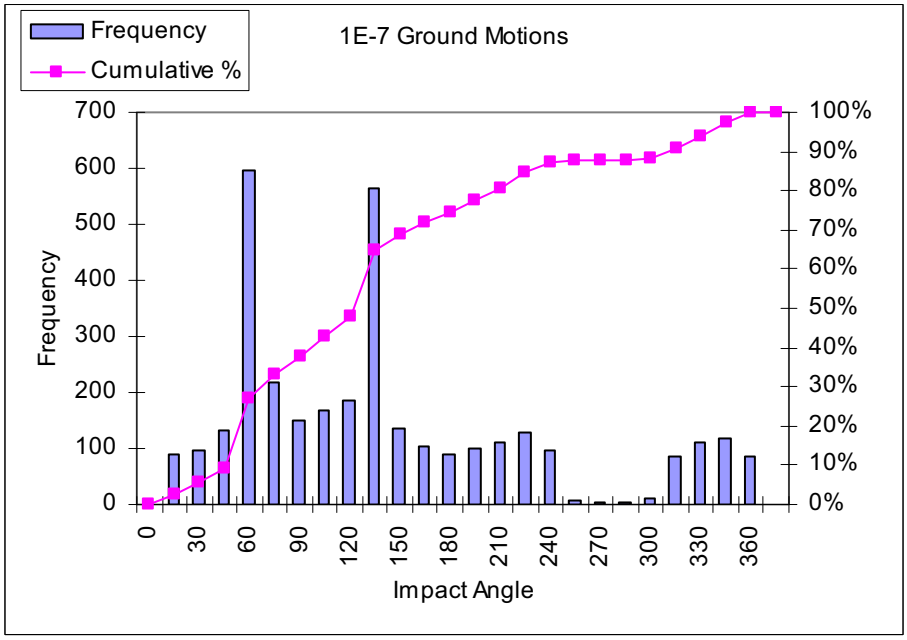

Figure 6-63. Histogram for Impact Angle (1×10^{-7} Annual Probability of Exceedance Hazard)

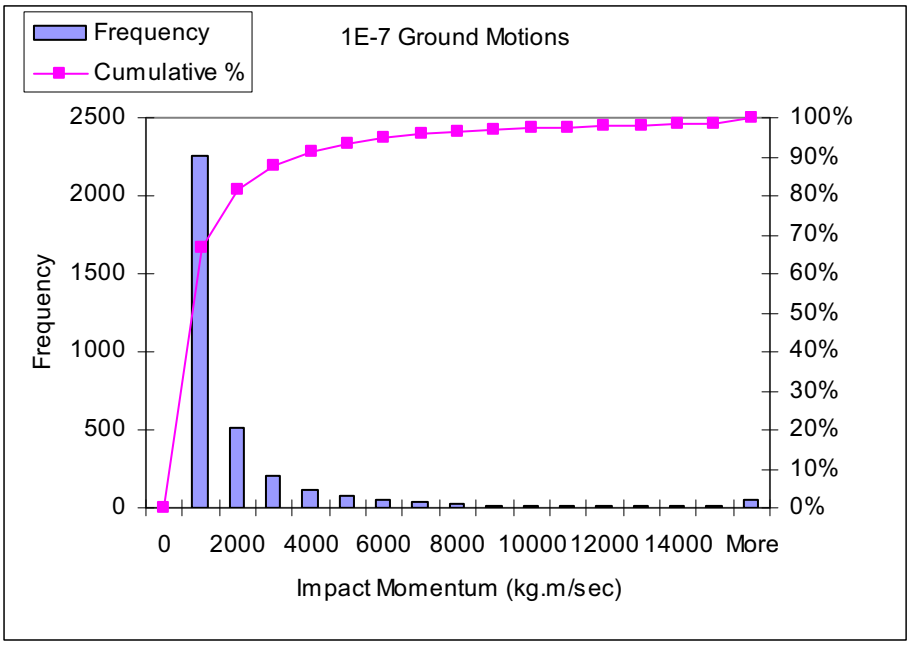

Figure 6-64. Histogram for Impact Momentum (1×10^{-7} Annual Probability of Exceedance Hazard)

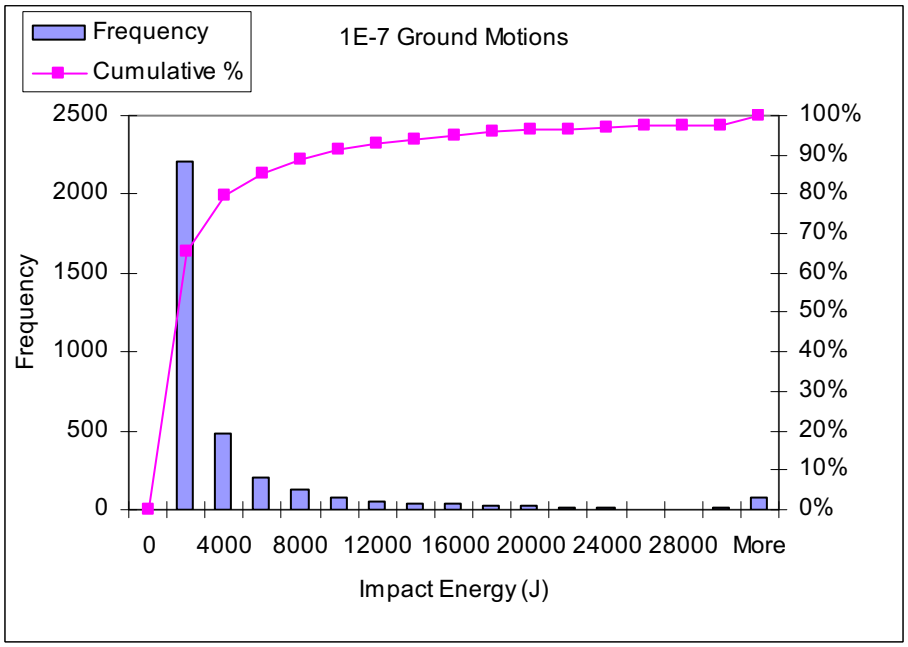

Figure 6-65. Histogram for Impact Energy (1×10^{-7} Annual Probability of Exceedance Hazard)

6.3.1.2.6 Results for Seismic Analysis Subjected to Preclosure Ground Motion

The results for the preclosure hazard level of 1×10^{-4} annual probability of exceedance ground motion are presented in this section. The 5×10^{-4} annual probability of exceedance ground motion was not included due to the relatively small amount of rockfall predicted for the 1×10^{-4} motion. As described in Section 6.3.1.2.1, only a single set of ground motion is considered in the rockfall analysis for preclosure seismic level for the deterministic design approach. Due to the much lower amplitude of ground motion considered for the preclosure hazard level and, hence, much less rockfall hazard anticipated, only 32 simulations were conducted for preclosure cases compared to 50 cases for postclosure. The sufficiency of 32 simulations to capture the rockfall characteristics for the preclosure ground motion is documented in Appendix K.

Figure 6-66 compares the input ground motion for the first horizontal component (H1) with the recorded velocities at the center of the model. The results confirm that the correct wave inputs were used and proper wave propagation occurs in the 3DEC preclosure seismic analyses. Figure 6-67 shows rockfall impacting a drip shield in the 3DEC dynamic simulation. Blocks are small and sporadic in most of the simulations.

Time histories of normal and shear stresses for fractures and rock bridges close to the opening were recorded during the seismic shaking in the 3DEC model. Figure 6-68 shows normal and shear stress time histories at the same selected fracture subcontacts as presented in Figure 6-40. The stress paths of the fracture subcontacts are plotted against the fracture Coulomb slip criterion and rock bridge strength criterion, as shown in Figure 6-69. The in situ normal and shear stress states along the fracture are identified as the orange squares for each subcontact in the figure. As with the postclosure level ground motions, the fracture containing subcontact *a* yielded during seismic motions. However, the stress paths for rock bridges containing subcontacts *b* and *c* are under both the Coulomb slip criterion and the rock strength criterion when subjected to 1×10^{-4} ground motion.

The percentages of the area of fracture slip/separation versus the total area of fracture planes under 1×10^{-4} ground motion for the selected cases were calculated and presented in Table 6-18. Contrary to the postclosure earthquake results, only around 20 percent of total fractures have undergone shear slip or tensile separation when subjected to 1×10^{-4} ground motions. Limited rock bridge damage is observed for this level of ground motion, as presented in Table 6-18.

The results of the 32 3DEC preclosure simulations are summarized in Table 6-19. Approximately half of the simulations predicted rockfall under seismic shaking. A total of 428 blocks were identified from the analyses.

The associated impact parameters due to rockfall on the drip shield are included in an output DTN of this document (DTN: MO0408MWDDDMIO.002, file *nonlith rockfall characteristics in emplacement drifts with 1e-4 gm.xls*). Summary statistics for these parameters are provided in Table 6-20. The maximum rockfall block mass predicted for preclosure case is 2.72 metric tons with a median block size of 0.10 metric ton. Most of the estimated parameters are considerably smaller than predicted for postclosure cases. Figures 6-70 to 6-74 present the histograms and the cumulative frequency of occurrence for the five parameters. The relatively low impact

velocities, as shown in Figure 6-71, indicate that block fall-out is mainly due to free fall. Differential acceleration or energy trapping to induce high ejection velocity is not observed.

The bounding impact velocity for preclosure rockfall is required for characterization of credible rockfalls of the preclosure period (BSC 2004 [DIRS 168508]). Calculation of the bounding velocity is based on the drop height of the fallen rock at one drift diameter above the drift crown. The approach is based on the observation of drift profiles at areas with rockfall in 3DEC simulations. Detailed description of the bounding calculation is provided in file, *impact velocity bounding calculation for preclosure rockfall rev1.mcd*, listed in Appendix A (Table A-1). The bounding impact velocity is calculated to be 14 m/sec, which is approximately two times the maximum impact velocity listed in Table 6-20.

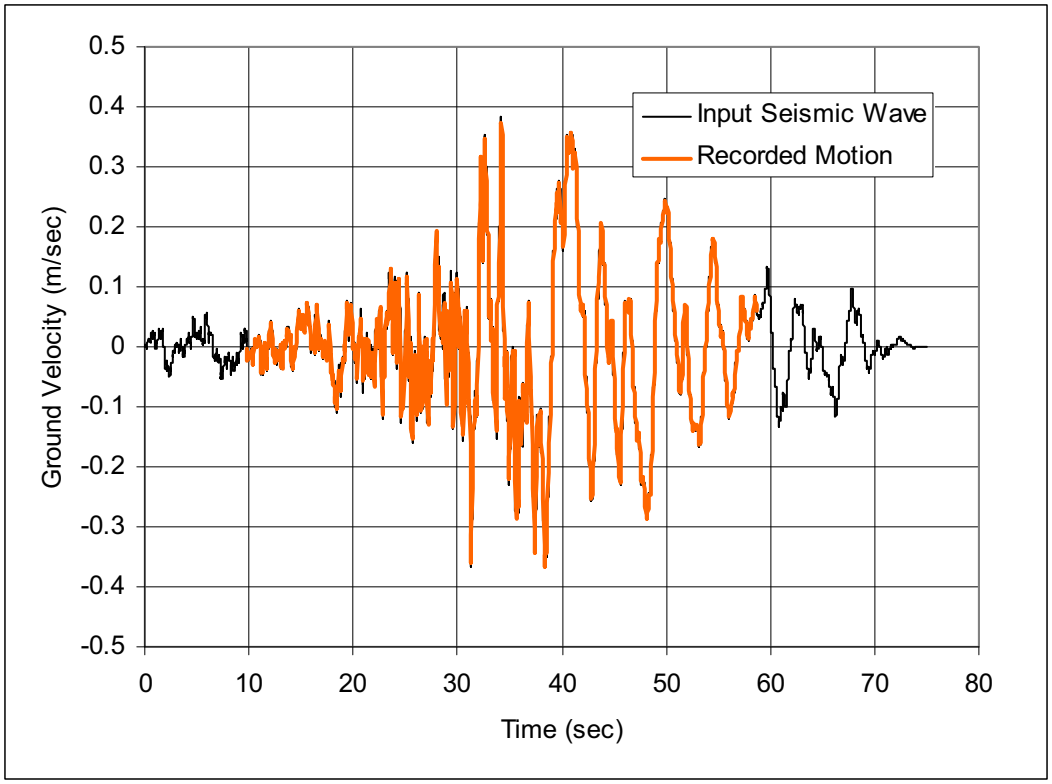

Figure 6-66. Comparison of Input Seismic Wave and Recorded Velocities in 3DEC Model for 1×10^{-4} Annual Probability of Exceedance Ground Motion (H1)

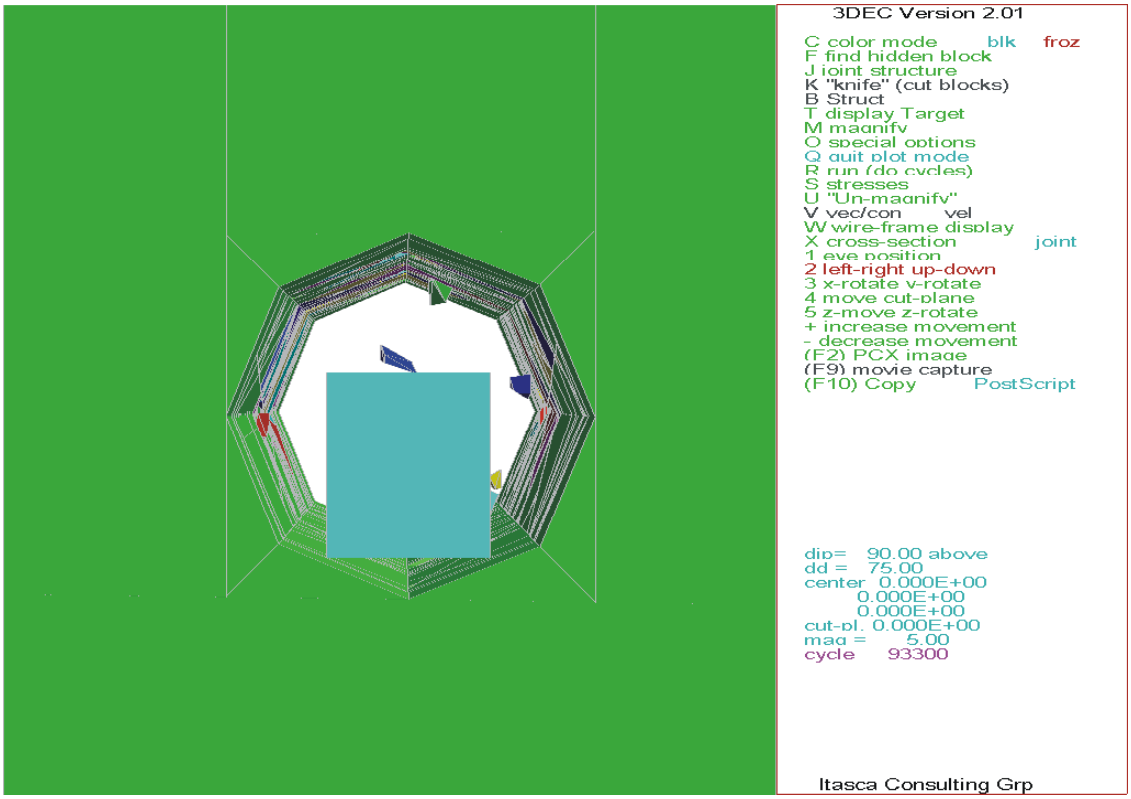

NOTE: The ground motion was recorded at the drip shield block during 3DEC simulation.

Figure 6-67. Illustration of the Simulation of Rockfall Impact to the Drip Shield (3DEC Simulation for 1×10^{-4} Preclosure Run 21, at t = 32.5 sec)

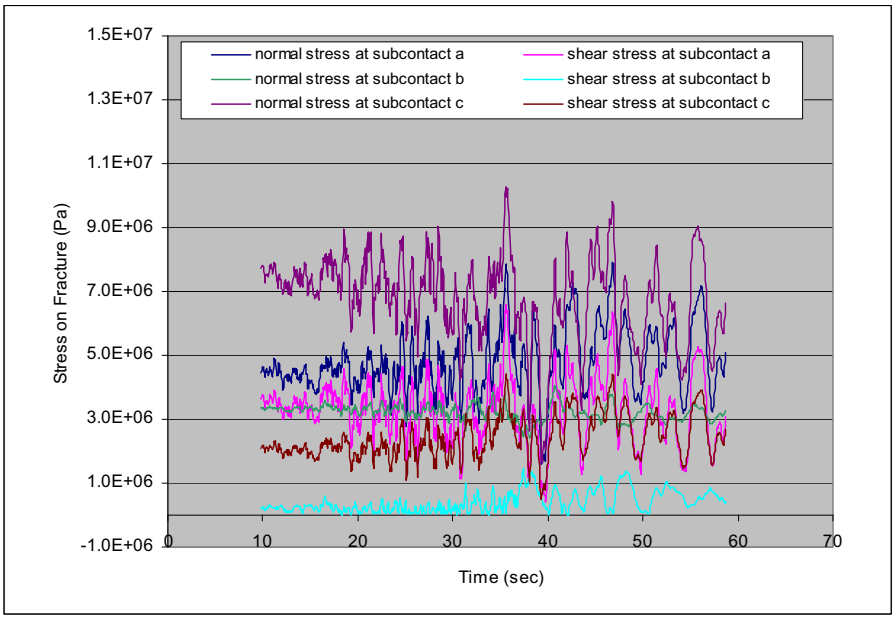

NOTE: Subcontact Information is presented in Figure 6-40.

Figure 6-68. Time Histories for Normal and Shear Stress at Selected Fracture Subcontact for 1×10^{-4} Annual Probability of Exceedance Hazard (Simulation 16)

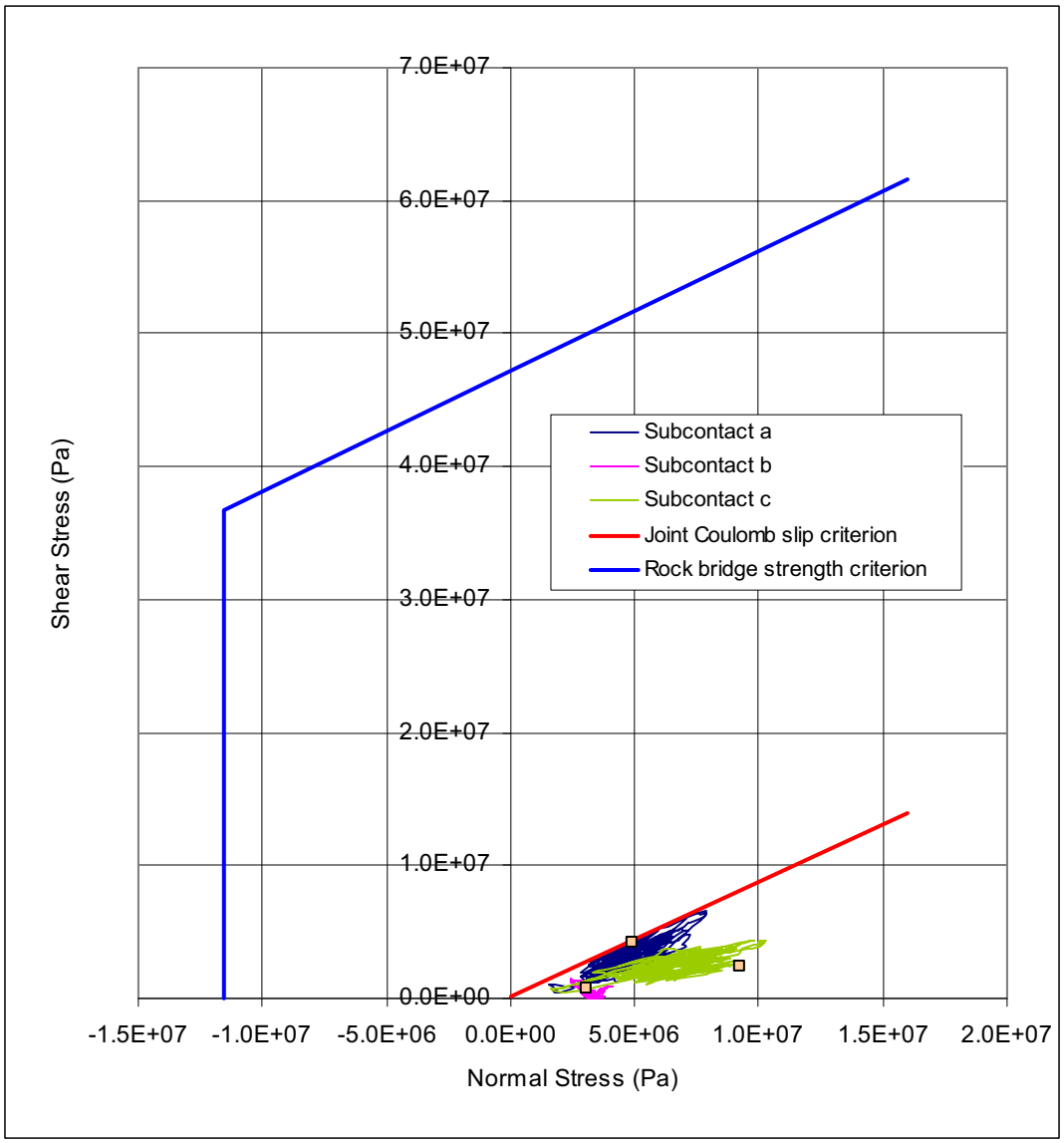

NOTE: Subcontact Information is presented in Figure 6-40.

Figure 6-69. Normal and Shear Stress Path at Selected Fracture Subcontact for 1×10^{-4} Annual Probability of Exceedance Hazard (Simulation 16)

Table 6-18. Summary of Joint Slip/Separation and Bridge Damage for 1×10^{-4} Ground Motions for Selected Cases

Parameter	Case 40	Case 23	Case 45	Case 31
Total Joint Area (m^2)	4251	3026	4737	3400
Total Bridge Area (m^2)	885	550	1054	720
Percentage of Joint Slip/Separation	26.68%	17.68%	26.73%	14.35%
Percentage of Bridge Damaged	0.00%	0.19%	0.00%	0.02%

Table 6-19. Summary of 3DEC Rockfall Prediction for 1×10-4 Annual Probability of Exceedance Hazard

Parameter	Value
Simulations Completed	32
Total Number of Rockfall	428
Total Volume of Rockfall (m^3)	39.4
Total Length of Drift Simulated (m)	800
Number of Blocks per km	535
Volume of Rockfall per km (m^3)	49.3

Table 6-20. Statistical Summary of the Rockfall Impact Parameters, 1×10^{-4} Annual Probability of Exceedance Hazard

	Block Mass (tonnes)	Relative Impact Velocity (m/sec)	Impact Angle (degree)	Impact Momentum (kg·m/sec)	Impact Energy (Joules)
Mean	0.22	2.43	169.15	601	1022
Median	0.10	2.25	141.29	213	232
Standard Deviation	0.33	1.38	108.31	1092	2224
Skewness	3.47	0.54	0.36	4	5
Range	2.69	7.17	357.12	9273	20358
Minimum	0.02	0.03	2.70	1	0
Maximum	2.72	7.20	359.82	9274	20358
Sum	95.00	NA	NA	257069	437350

NA = Not Applicable

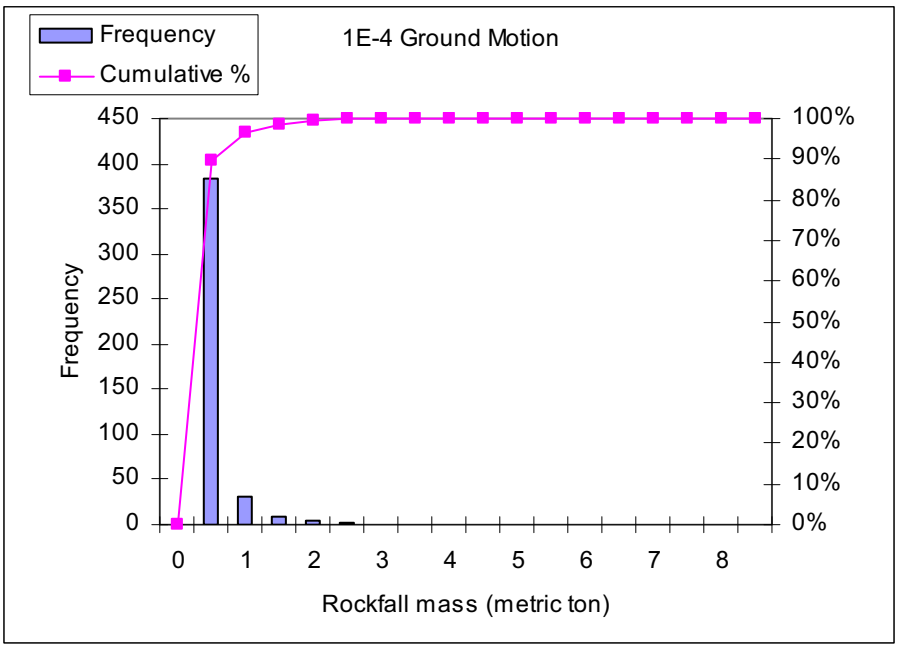

Figure 6-70. Histogram for Block Mass (1×10^{-4} Annual Probability of Exceedance Hazard)

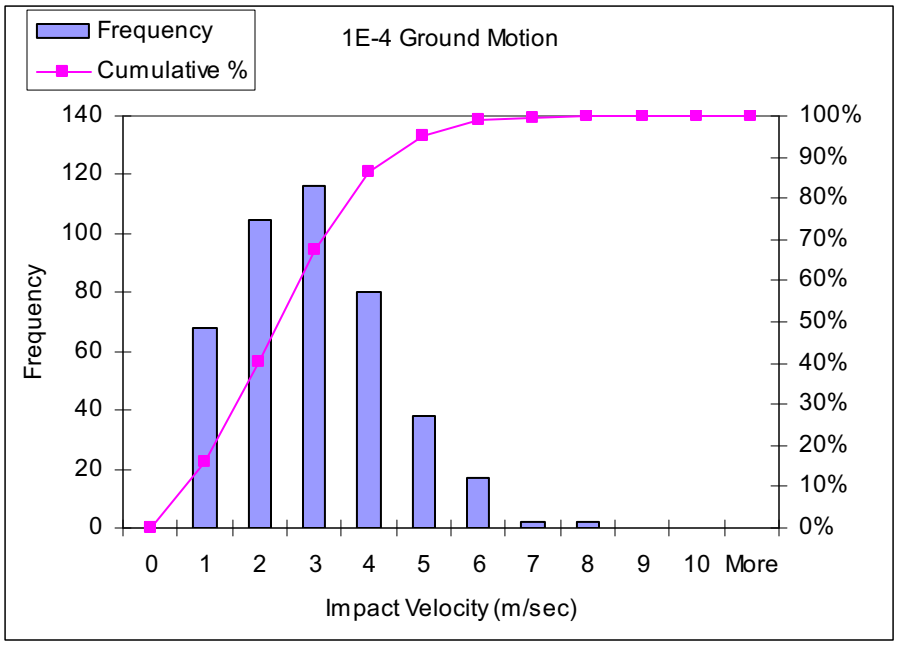

Figure 6-71. Histogram for Impact Velocity (1×10^{-4} Annual Probability of Exceedance Hazard)

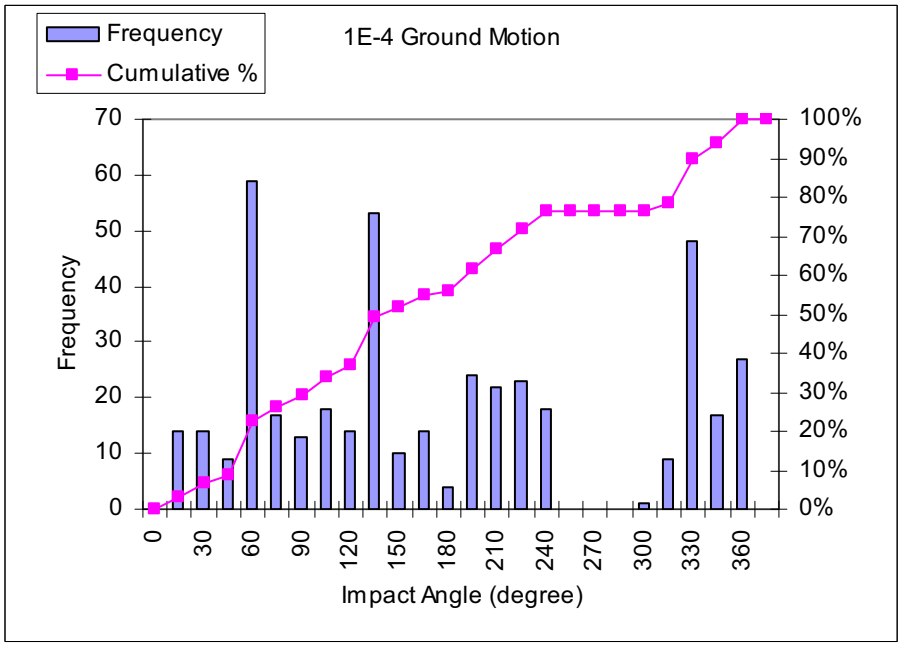

Figure 6-72. Histogram for Impact Angle (1×10^{-4} Annual Probability of Exceedance Hazard)

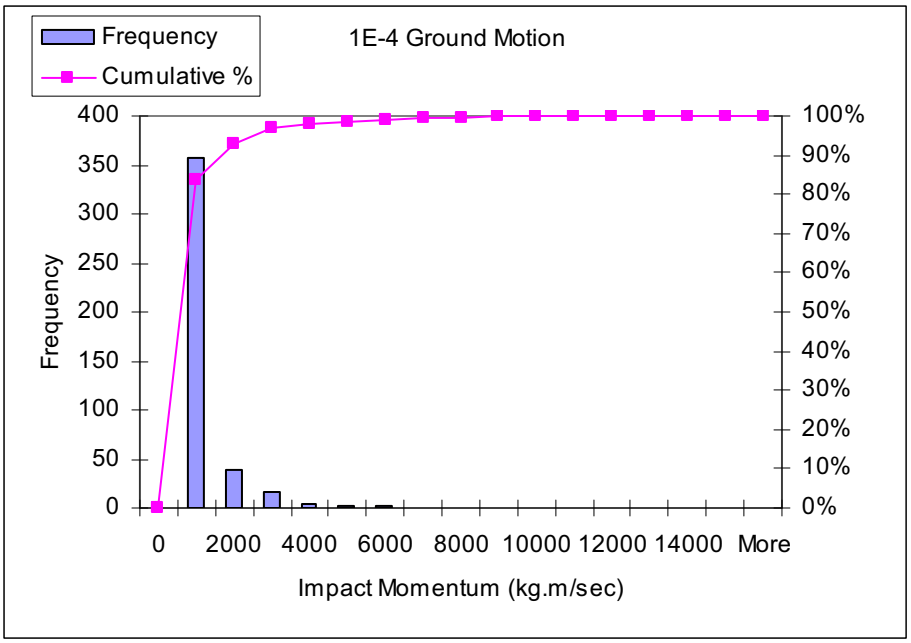

Figure 6-73. Histogram for Impact Momentum (1×10^{-4} Annual Probability of Exceedance Hazard)

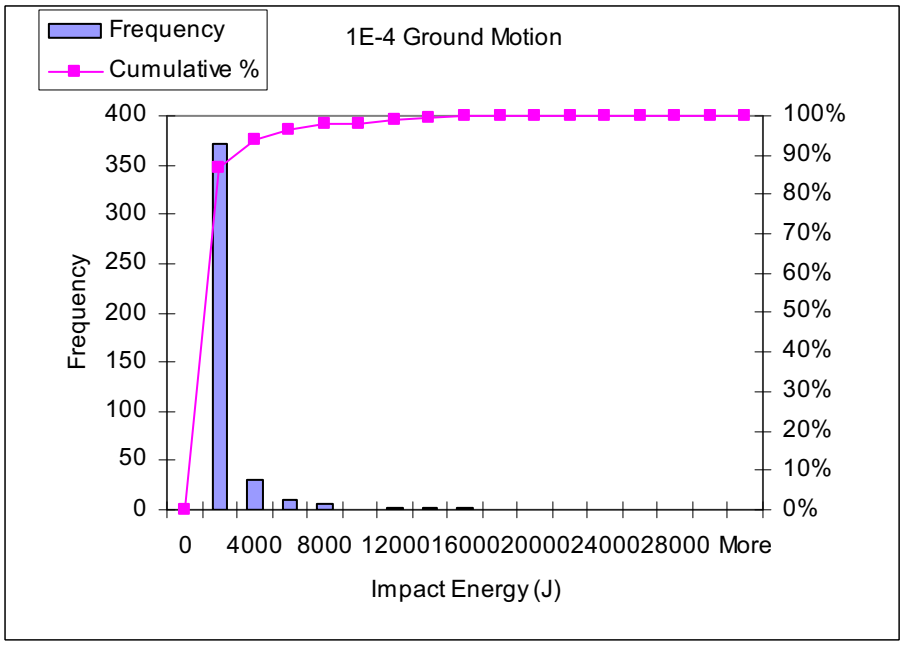

Figure 6-74. Histogram for Impact Energy (1×10^{-4} Annual Probability of Exceedance Hazard)

6.3.1.3 Thermal Consideration in Nonlithophysal Units

The extensive analysis of drift stability in nonlithophysal units discussed in Section 6.3.1.2 has been conducted considering an in situ stress state perturbed by the excavation of the emplacement drifts only. The effects of the thermally generated stresses in the rock mass surrounding the repository were not taken into account. This section provides the results for the analyses including thermal consideration.

3DEC was not used for the thermal-mechanical analysis of the drift in the nonlithophysal units because it has a simplistic model of heat conduction based on analytic solutions. The analytic solutions deal with complicated boundaries in an approximate way. Instead, the analysis for the nonlithophysal units was done as a three-step process. Variation of temperatures throughout the rock mass due to heating was calculated using NUFT (Section 6.2), which generated temperature fields for a number of times after waste emplacement. This implies that the mechanical models that use those temperature fields will be subjected to discrete temperature and, consequently, stress changes when moving from one temperature state to another. In reality, those changes are continuous. Because the mechanical models of drift stability are non-linear, their results are path-dependent. To ensure that the model results are not affected by discrete stress changes, the temperature increment was limited to around 5°C. It was difficult to perform thermal stress calculations in the 3DEC model because it is limited to a certain region around the drift. Also, the model axes are oblique relative to the drift axis, making it very difficult to extend the model to the plane of symmetry between the drifts, which is necessary for stress calculation due to heating. Therefore, the stress changes due to the temperature changes, as calculated by NUFT and described in Section 6.2, were calculated using the continuum code FLAC. In the next step, elastic stress states are imported from FLAC into 3DEC in a sequential manner. For each elastic stress change due to temperature change, 3DEC is first run elastically to equilibrium (all joints were elastic). Subsequently, the finite strength was assigned to the joints, and the new equilibrium was determined.

Thermal-mechanical analysis was conducted for two sets of thermal rock mass properties (discussed in Section 6.2):

- Base case, using the mean values of thermal conductivity and specific heat
- Thermal sensitivity case, using the values for thermal conductivity and specific heat one standard deviation smaller than the mean.

The values for the sensitivity case thermal properties are provided in Section 6.2.

The fracture patterns included for thermal-mechanical analysis were selected based on the rockfall results from seismic analyses of 1×10^{-5} annual probability of exceedance. Three fracture patterns, corresponding to the cases with most rockfall (Case 38 with Fracture Pattern 29), the median rockfall (Case 45 with Fracture Pattern 39), and the least rockfall (Case 63 with Fracture Pattern 96), were selected. The results for these fracture patterns with other levels of ground motion also indicate the selected patterns are adequate to represent the range of rockfall.

Rockfall induced by thermal loading are found to be minor. Tables 6-21 and 6-22 present the rockfall predictions considering only thermal loading for the thermal base case and sensitivity case respectively. The results are presented for the beginning of heating (1 year), at the peak of temperature (80 years), and at the end of the regulatory period (10,000 years). The block size for rockfall induced by thermal effect is small with a mean size less than 0.2 metric ton. The impact of thermal properties on rockfall is insignificant considering the close amount of rockfall predicted for the base case and sensitivity case. The stress paths (shear stress versus normal stress) on the fractures around the drift (in the wall and the roof) for Case 63 with Fracture Pattern 96 considering the base case thermal properties, are shown in Figures 6-75 and 6-76. Stress paths at similar locations for other cases considered in the thermal-mechanical analyses have also been generated and reviewed. For most of the points (particularly in the wall), the stress paths move away from the slip surface, indicating increasing block stability. The analysis is carried out considering the blocks to be elastic. To demonstrate that heating will not induce stress levels inside the blocks sufficient to cause damage, stress paths from the linearly elastic model (for nonlithophysal rock stiffness) are shown in Figures 6-77 and 6-78 relative to the Mohr-Coulomb yield surface (using an unconfined compressive strength of 70 MPa and a 40° friction angle). The unconfined compressive strength of 70 MPa is the recommended rock mass strength value presented in Figure E-22. The friction angle of 40° is a conservative estimate based on the range of rock mass friction angle reported in Subsurface Geotechnical Report (BSC 2003 DIRS [166660], Table 8-41). In both the wall and the roof, thermally induced stress variations are well within the elastic region. The approach of linear block behavior during thermal loading is justified. Stress paths for Case 63 considering the thermal properties one standard deviation smaller than the mean, are presented in Figures 6-79 and 6-80. The paths are similar to the base case results presented in Figures 6-75 and 6-76 with normal and shear stresses slightly magnified. The effect of seismic shaking, in addition to thermal loading, is discussed in Section 6.3.1.4.

Table 6-21. Rockfall in Nonlithophysal Rock Due to Heating, Base Case of Thermal Properties

Case	1 yr		80 yr		10,000 yr	
	Number of Rockfall	Rockfall Volume (m^3)	Number of Rockfall	Rockfall Volume (m^3)	Number of Rockfall	Rockfall Volume (m^3)
38	15	0.50	28	0.88	28	0.88
45	0	0.00	20	0.79	25	0.80
63	1	0.09	1	0.09	3	0.13

Table 6-22. Rockfall in Nonlithophysal Rock Due to Heating, Sensitivity Case of Thermal Properties

Case	1 yr		80 yr		10,000 yr	
	Number of Rockfall	Rockfall Volume (m^3)	Number of Rockfall	Rockfall Volume (m^3)	Number of Rockfall	Rockfall Volume (m^3)
38	11	0.40	34	2.49	35	2.50
45	0	0.00	18	0.60	20	0.62
63	2	0.10	2	0.10	3	0.13

6.3.1.4 Combined Seismic and Thermal Effects in Nonlithophysal Units

The effect of the thermal stresses on seismic drift stability depends on how the stress state, throughout the rock mass and on the pre-existing fractures, changes in the stress space relative to the failure surface. If the stress state (particularly in the vicinity of the drifts) predominantly moves away from the failure surface due to stress changes caused by heating, the rock mass becomes more stable and resistant to ground shaking. However, if the stress state predominantly moves toward, or reaches, the yield surface (i.e., rock mass yields during the heating), there will be more rockfall caused by ground motion. It is difficult to determine a single index or condition that characterizes this effect in an integrated way for the entire rock mass.

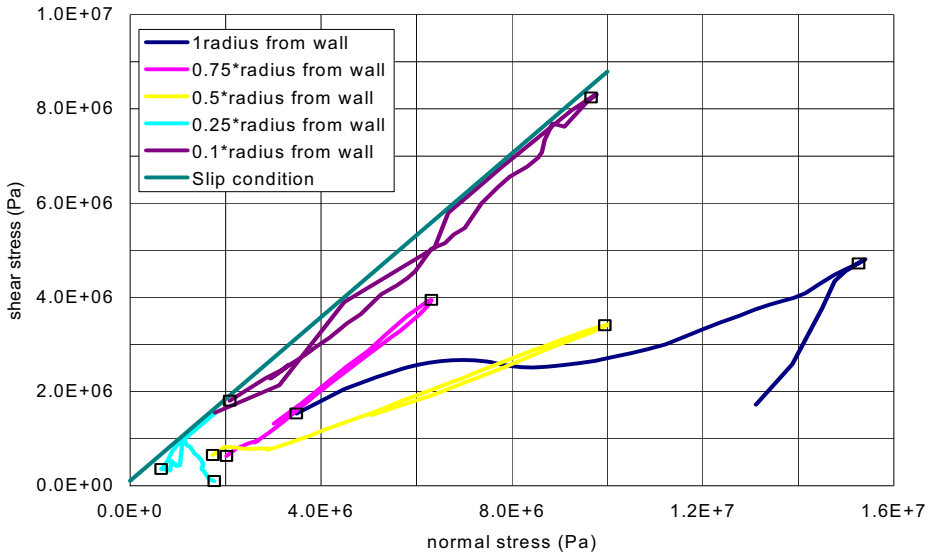

Figure 6-75. Stress Paths at Selected Fractures in the Drift Wall: Case 63 with Fracture Pattern 96

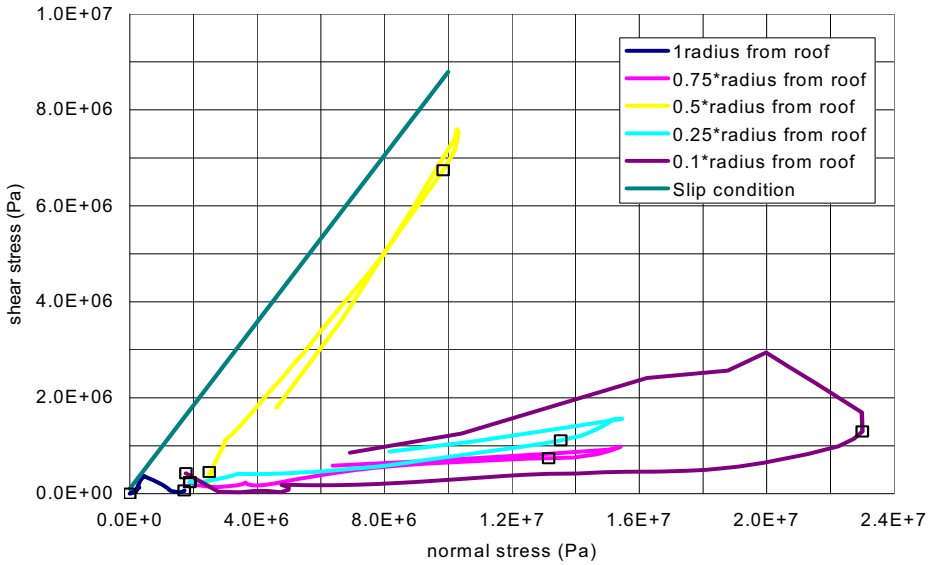

Figure 6-76. Stress Paths at Selected Fractures in the Drift Roof: Case 63 with Fracture Pattern 96

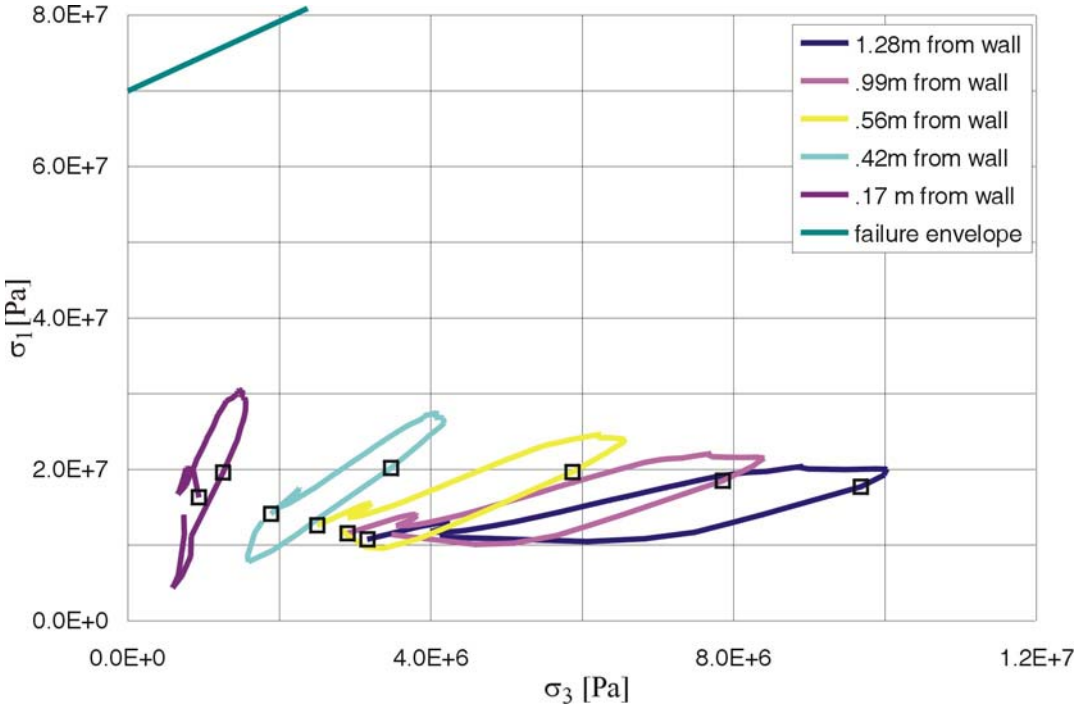

Figure 6-77. Stress Paths in the Drift Wall: Elastic Model

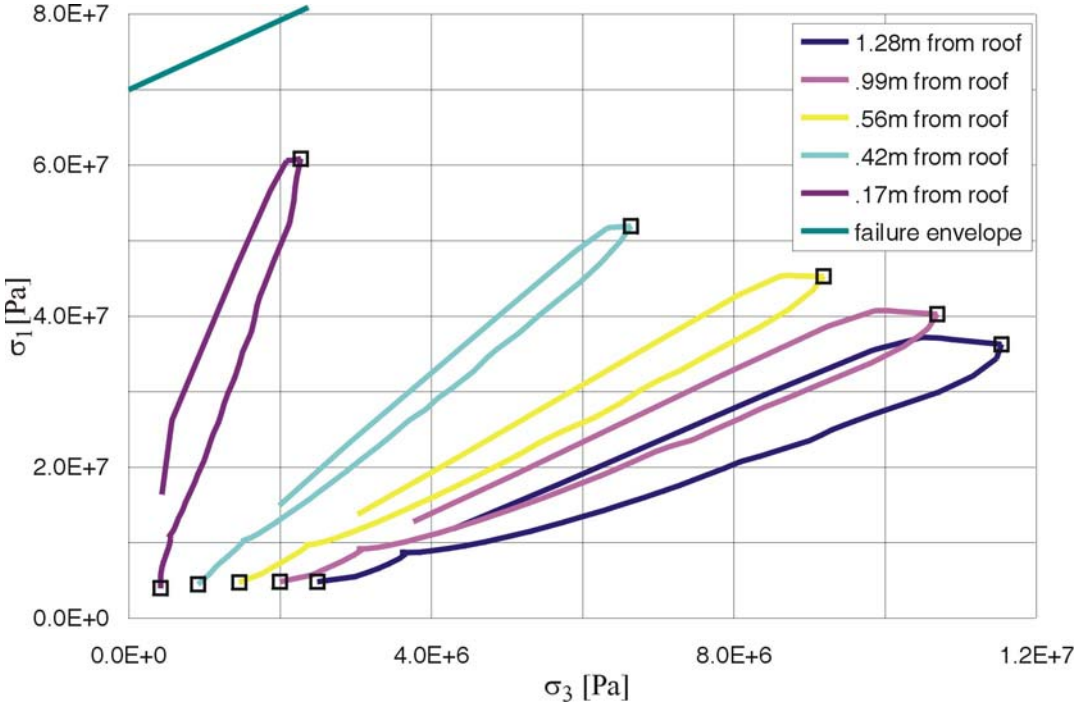

Figure 6-78. Stress Paths in the Drift Roof: Elastic Model

Temperatures around the emplacement drift will increase for a certain period of time after emplacement of the waste; however, as a result of decay of the released heat, the temperatures will also decrease. Consequently, the stress state around the repository during the regulatory period will be transient. A simplified approach was adopted in which rockfall caused by ground shaking was estimated for the "most critical" stress state during the regulatory period. Stress paths at a number of locations on the joints surrounding the drift were recorded during the temperature changes. The critical state (or time after waste emplacement) was determined by qualitative inspection of those stress paths. The model in the most critical state during the regulatory period was then subjected to a ground motion corresponding to 1×10^{-5} probability of annual occurrence.

The effect of seismic shaking combined with thermal-mechanical effects was considered for the three cases presented in Section 6.3.1.3. Stress paths at five points on fractures in the wall and the roof of the drift (shown in Figures 6-75 and 6-76) move away, in general, from the yield. The critical state seems to be the in situ stress state (marked with a square at the beginning of each curve) for which extensive seismic stability analysis had been conducted. Another state of interest was the other extreme point on the stress path curves (also marked with a square), which, for Case 63 represented in Figures 6-75 and 6-76, corresponds to 80 years after waste emplacement. Comparison of rockfall with seismic shaking at the in situ stress state and at 80 years after waste emplacement is provided in Table 6-23. It is apparent that heating significantly reduces the amount of rockfall.

Comparison of rockfall with seismic shaking at the in situ stress state and at 80 years after waste emplacement for the thermal sensitivity case is provided in Table 6-24. These results are consistent with the base case prediction presented in Table 6-23.

The results of rockfall thermal-mechanical and seismic analyses indicate that the condition with seismic shaking at in situ state (the cases considered in Section 6.3.1.2) is conservative since a higher number of unstable blocks and a larger amount of rockfall are predicted for the in situ state. Temperatures throughout the regulatory period will be higher than in situ temperatures.

Table 6-23. Rockfall in Nonlithophysal Rock Due to 10^{-5} Ground Motion Combined with Thermal-Mechanical Effects, Base Case of Thermal Properties

Case	Ground Motion	Time of Earthquake at 0 yr		Time of Earthquake at 80 yr	
		Number of Rockfall	Rockfall Volume (m^3)	Number of Rockfall	Rockfall Volume (m^3)
38	3	173	42.03	56	13.59
45	10	14	2.49	5	1.07
63	11	0	0.00	2	5.93

Table 6-24. Rockfall in Nonlithophysal Rock Due to 10^{-5} Ground Motion Combined with Thermal-Mechanical Effects, Sensitivity Case of Thermal Properties

Case	Ground Motion	Time of Earthquake at 0 yr		Time of Earthquake at 80 yr	
		Number of Rockfall	Rockfall Volume (m^3)	Number of Rockfall	Rockfall Volume (m^3)
38	3	173	42.03	43	11.41
45	10	14	2.49	6	1.63
63	11	0	0.00	3	7.93

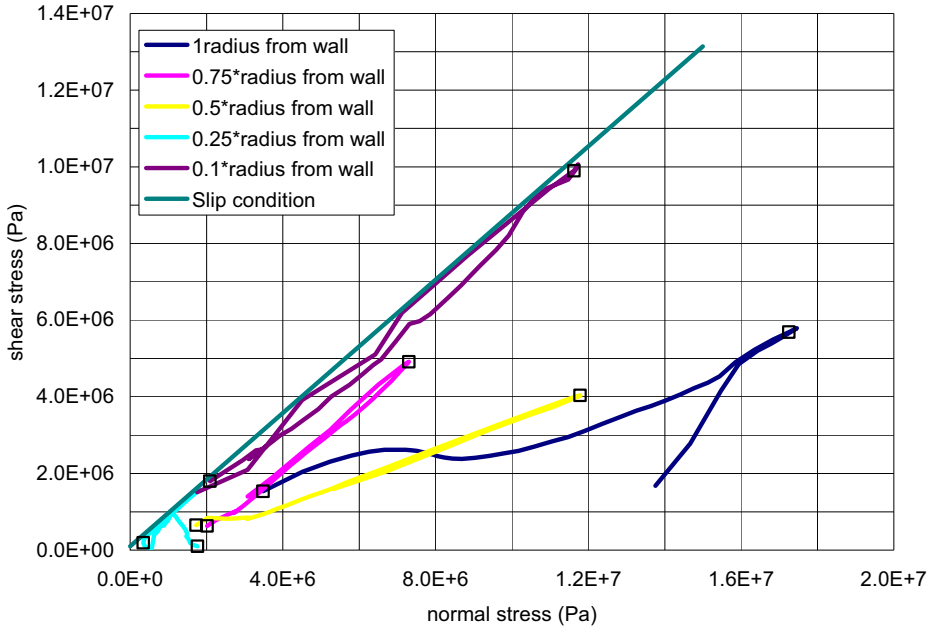

Figure 6-79. Stress Paths at Selected Fractures in the Drift Wall: Case 63 with Fracture Pattern 96, Thermal Sensitivity Case

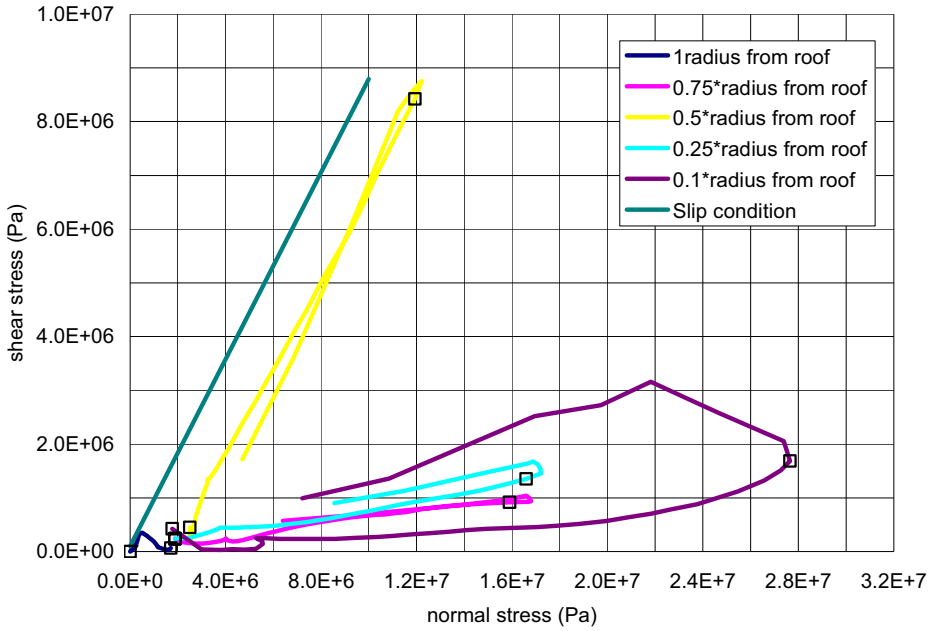

Figure 6-80. Stress Paths at Selected Fractures in the Drift Roof: Case 63 with Fracture Pattern 96, Thermal Sensitivity Case

6.3.1.5 Rock Joint Degradation in Nonlithophysal Units

Degradation Due to Time-Dependent Alteration of Rock Matrix or Joint Filling Materials from Postclosure Thermal and Moisture Conditions–The rock mass surrounding the excavations may undergo over-stressing from thermal heating and/or time-dependent damage associated with static fatigue resulting from stress corrosion mechanisms. Another likely long-term effect includes the increasing amounts of moisture/air induced weathering along the joints close to the tunnels. This damaged and/or weathered material may result in block fallout in the nonlithophysal units.

The time-to-failure for intact nonlithophysal rock blocks shows significantly less time dependency than for the lithophysal rock described in Appendix S (see Figure S-17). Therefore, insignificant time-related fracture growth is expected in the intact rock blocks. However, the potential exists for time-dependent yield of roughness (asperities) on fracture surfaces subjected to long-term shear stress. Time-related degradation of tunnels due to wetting and drying cycles is an important factor for drift stability in some rock types. These rock types are typically those in which highly-altered rock, or rock with significant swelling clay along fracture planes occurs. In the case of the host repository horizon at Yucca Mountain, these issues are not particularly important. Clay is not a common mineral in the crystallized rocks of the repository host horizon, nor are clay minerals a volumetrically significant fracture-coating material. Data to support this observation are described below.

A number of detailed geological studies have been conducted at the Yucca Mountain site to define the basic mineralogy of the rocks, and the petrologic and geochemical processes that

occurred during the formation of the Topopah Spring Tuff, and have continued from that time. These studies have included a detailed description of the mineralogy of the repository host horizon from samples and observations developed from surface-based core holes through the repository block, as well as from the ESF and ECRB Cross-Drift. From the standpoint of mechanical degradation of the rock mass, these studies show:

- The Topopah Spring Tuff is largely composed of fine-grained feldspars and silicate-based rocks that formed during the cooling of the rock mass shortly after deposition. Clay-forming minerals were typically not formed during the petrogenesis of the repository host horizon.

- Clays typically do not form significant fracture-fill materials in the crystallized rocks of the Topopah Spring Tuff.

- There are limitations on the environmental conditions needed to form clays and indicate the minimum likelihood that clays might form along fractures in the near field of a repository. Therefore, mineral alteration during the postclosure is considered negligible.

The following discussion summarizes the data obtained from a number of studies that support the above points.

1. **Mineralization in the Repository Host Horizon–**The Topopah Spring Tuff is a compositionally zoned pyroclastic flow deposit. High-silica rhyolite forms approximately the lower two-thirds of the section and trachyte (or quartz latite) in the upper one-third of the section. The crystallized rocks that formed during the cooling of the deposit consist primarily of very fine-grained intergrowths of feldspar and silica polymorphs of quartz and cristobalite. These minerals typically crystallized from volcanic glass at temperatures of approximately 800° C. X-ray diffraction analyses of 444 core samples from 13 boreholes that penetrate 3.5 km of the crystallized Topopah Springs Tuff indicate that there are different ratios of feldspar and silica polymorphs in the crystal-rich rocks (DTNs LADB831321AN98.002 [DIRS 109003], LADV831321AQ97.001 [DIRS 107142], LADV831321AQ99.001 [DIRS 109044], LA000000000086.002 [DIRS 107144]). In the crystal-rich member, 93 samples have mean percentages of feldspar (69.1percent), quartz (2.4 percent), cristobalite (13.3 percent), and tridymite (11.2 per cent), and in the crystal-poor member, 351 samples have mean percentages of feldspar (55.7 per cent), quartz (15.8 per cent), cristobalite (19.3 percent), and tridymite (5.1 percent). The total of the percentages cited for these two members do not sum to 100 percent because there are minor amounts of other minerals in many of these rocks. Smectite values vary from trace amounts to 15 percent with a mean value of 3.1 percent. These compositions of rocks form the walls of fractures where the minerals are very fine-grained and form various textures; however, the minerals are relatively uniformly distributed at scales of millimeters to centimeters. These data indicate that concentrations of smectite minerals along fractures do not occur as a result of crystallization during cooling.

2. **Clay Infillings Are Rarely Observed Along Fractures in the ESF and ECRB Cross-Drift–**Detailed line survey data collected in the ECRB Cross-Drift indicate that

of the 1,816 fractures in the 2.66-km long tunnel, only 10 (or 0.4per cent) of the discontinuities such as fractures, shears, and faults have some amount of clay (DTNs GS990408314224.001 [DIRS 108396], GS990408314224.002 [DIRS 105625]). These 10 discontinuities are filled (or partially filled) with clay and "broken or crushed rock or sand". Detailed studies of the clast textures, structures, and architectures of the "broken or crushed rock or sand" fill materials have not been completed, but general observations indicate many of these features do not show evidence of mechanical degradation and shear. Buesch and Lung (2003 [DIRS 170297]) describe volcaniclastic tuffaceous sandstone and claystone as fracture-fill material in the crystallized rocks of the Tiva Canyon and Topopah Spring Tuff. They proposed that volcanic glass particles settled by gravity along open fractures from the superjacent nonwelded bedded tuffs, and the clay formed in place (possibly millions of years later) by water seeping along the fractures and reacting with the glass. This mechanism is entirely consistent with occurrences of clays in the ECRB Cross-Drift detailed line survey data. Detailed line survey data from the crystallized Topopah Spring Tuff in the ESF Main Drift indicate that only 4 per cent of the fractures recorded have clay as filling material.

The *Integrated Issue Resolution Status Report* of NRC (NRC 2002 [DIRS 159538], Section 2.1.7.3.3.2, pp. 2.1.7-19 and 2.1.7-20) specifically discussed the work by Carlos et al. (1995 [DIRS 101326]) in regard to fracture fillings. Carlos et al. (1995 DIRS 101326]) described the qualitative amount of materials in the fractures only, but typically they did not describe the amount or thickness of the mineral coatings. For example, if a mineral such as clay (smectite) is listed as "major abundance", then this means that greater than 20 percent of the minerals in the fractures, but the mineral coating might be less than 1-mm thick. Only for mordenite in the crystallized Topopah Spring Tuff did Carlos et al. (1995 DIRS 101326]) describe about 1 percent of the fractures with this mineral and the amount increased with depth to more than 20 percent (and more than 50 percent in some boreholes). The relevant point for this discussion is that selective fractures were sampled and the intention was not to quantify the relative proportion of fractures with specific minerals, nor to quantify the thickness or continuity of the mineral coatings. However, there is one detailed study of mineral coatings on fracture walls in core with descriptions of the percentages of the amount of mineral coatings and thickness of the coatings (DTN: LA9912SL831151.001 [DIRS 146447]). Borehole ESF-HD-TEMP-2 is a 60 m (200-ft) long, horizontal borehole in the Heated Drift Test, and the rocks are in the middle nonlithophysal (Tptpmn) zone of the Topopah Spring Tuff. Only fractures in two 1.3 m (4.3-ft) long segments of core were described [7.6 to 8.9 m (25.0 to 29.3 ft) and 18.9 to 20.3 m (62.15 to 66.45 ft)]. Clay forms localized deposits on the fracture surfaces that typically are less than 5 percent of the fracture surface area with thickness typically about 0.1 mm and a few deposits as much as 0.5-mm thick. These descriptions demonstrate that clay does not form continuous coatings on fracture walls and that the coats are very thin.

3. **Alteration of Repository Host Rocks is Not Expected in the Repository Environment**–Conditions such as temperature, chemistry of water, and amount of water needed for the alteration of feldspars in the crystallized host rock to form clay

and other sheet silicate minerals (sericite) are not considered to have been present within the Topopah Spring Tuff since its formation. Sericite is a general term for very fine-grained sheet silicates (illites) that form with other alteration products in hydrothermal systems at temperatures near or above 400°C, typically in acidic aqueous solutions (Jackson 1997 [DIRS 109119]). As pointed out by the predicted temperature conditions expected in the repository environment (e.g., Figure 6-25), these conditions are not anticipated in the near-field environment of the repository. Even in samples from the Drift Scale Test boreholes, the clays on fractures appeared to have been there prior to the test and were not affected by the experimental conditions.

In summary, these petrologic and empirical relations indicate that clays typically do not form significant fracture-fill materials in the crystallized rocks of the Topopah Spring Tuff. They also indicate that the expected repository environmental conditions are not conducive to formation of clays during the postclosure period. Therefore, the impact of geochemical alteration within the postclosure environment is expected to have a negligible impact on drift degradation processes.

3DEC Analysis for Time-Dependent Joint Degradation–Drift stability due to the effect of time-dependent rock joint strength degradation is assessed based on a conservative estimate of the reduction of joint cohesion and friction angle. The reduced joint strength parameters are estimated to be represented by the residual state (after joint shear) with joint cohesion reduced to 0 and the joint friction angle reduced to 30°. The reduced friction angle is a typical value for a smooth joint reported by Goodman (1980 [DIRS 101966], p. 158) and is consistent with the observation of the cooling joints from direct shear test results (Table E-5). Dilation angle is also conservatively presumed to be zero considering the asperities on fracture surfaces had been sheared off, resulting in greater rockfall. The degradated joint strength and dilatational properties were applied in 1×10^{-5} seismic motion Cases 38, 45, and 63. These three cases cover the range of rockfall condition from the most rockfall to the least rockfall. The predicted number of rockfall and the total rockfall volume are presented in Table 6-25 with a comparison to the results of the base case. Approximately 30 to 40 percent rockfall increase is observed for the high rockfall case (Case 38), while the results were very similar for the median rockfall case (Case 45). The maximum block sizes are the same for the base case and the degraded joint case. As for the least rockfall case, limited rockfall is also observed even with degraded joints. In all, the degraded joint state results in higher rockfall prediction, but the amount of rockfall stays within the same order of magnitude as the base case.

Table 6-25. Predicted Rockfall for Degraded Joints with Comparison to the Base Case Results

Case	Degradated State (cohesion = 0, friction angle = 30°, dilation angle = 0°)			Base Case (cohesion = 0.1 MPa, friction angle = 41°, dilation angle = 0°)		
	Number of Blocks	Maximum Block (m^3)	Rockfall Volume (m^3)	Number of Blocks	Maximum Block (m^3)	Rockfall Volume (m^3)
38	233	3.53	59.23	173	3.53	42.03
45	16	0.84	2.21	14	0.84	2.49
63	7	0.13	0.39	0	0	0.00

6.3.1.6 Sensitivity Study of the Parameters

There are four major variable sets included in the three-dimensional discontinuum analysis: ground motion, joint geometrical properties, joint and intact mechanical properties, and thermal stress history. For the ground motion parameters, four levels of annual probability of exceedance (1×10^{-4}, 1×10^{-5}, 1×10^{-6}, and 1×10^{-7}) are included, and 15 sets of ground motions were used for each hazard level in the postclosure consideration. The description of the ground motions used is provided in Section 6.3.1 and Appendix X. Results for the sensitivity study on the probability level, peak ground velocities, energy contents, and orientation of horizontal motions in the 3DEC model to the rockfall prediction are presented in Section 6.3.1.6.1.

The variability of joint geometrical properties is incorporated into the application of FracMan to generate a 100-m cube fracture network. A total of 50 drift locations were selected from the 100-m cube fractured rock mass for the 3DEC analyses. Results from the analyses of 50 drift locations (or fracture patterns) cover the variability of joint geometrical properties as verified in Appendix K.

The results presented in previous sections are based on the base case material properties presented in Table 6-3. The impact of the variability of joint properties to rockfall prediction is described in Section 6.3.1.6.2. Variation of the rock bridge strength is considered in Section 6.3.1.6.3. A linear elastic material is used as the intact block material for the base case. The likelihood of breaking and spalling of the intact rock subject to vibratory ground motions is discussed in Section 6.3.1.6.4. Other sensitivity and uncertainty studies include model dimension and block deletion after impacting the drip shield. These are addressed in Sections 6.3.1.6.5 and 6.3.1.6.6, respectively.

Sensitivity analyses were conducted using the representative cases with 1×10^{-5} annual probability of exceedance ground motions except for the consideration of block deletion in Section 6.3.1.6.6. Similar to the thermal-mechanical analyses, three cases corresponding to the case with most rockfall (Case 38 with Fracture Pattern 29 and Ground Motion 3), the case with the median rockfall (Case 45 with Fracture Pattern 39 and Ground Motion 10), and the case with least rockfall (Case 63 with Fracture Pattern 96 and Ground Motion 11), were selected.

6.3.1.6.1 Ground Motion Parameters

The ground motion time histories were truncated at 5 percent and 95 percent energy content to shorten the time required to conduct the dynamic analyses. The analyses show that the majority of the rockfall occurs coincident with the arrival of the strong motion, which is typically within the first 15 seconds of shaking. The truncating of the ground motion appears to have minor impact on the amount of rockfall.

Four levels of annual probability of exceedance (1×10^{-4}, 1×10^{-5}, 1×10^{-6}, and 1×10^{-7}) plus 15 sets of ground motions for each postclosure level were included in the drift degradation study to ensure a reasonable distribution of spectral shapes and time history durations. Results for the sensitivity study on the probability level, peak ground velocities, energy contents, and orientation of horizontal motions in the 3DEC model to the rockfall prediction are presented in this section.

Probability Levels–The predicted rockfall results for each level of ground motions are presented in the subsections of Section 6.3.1.2. The results are summarized and compared in this section to observe the trend of rockfall versus ground motions with various annual probability of exceedance. Figure 6-81 shows the comparison of histograms of block mass for the ground motions considered. The rockfall number increases as the frequency of occurrence of ground motion gets lower. Figure 6-82 presents the cumulative percentage of block size distribution with block mass in a logarithmic scale. Essentially, the results show that the motions result in the same general negative exponential distribution of block sizes. As expected, a higher portion of large blocks is predicted for lower frequency ground motions.

A comparison of the rockfall statistics is provided in Tables 6-26 and 6-27. The number and volume of blocks per km increase substantially in going from the preclosure motion to postclosure motions. The predicted rockfall volume per km for 1×10^{-7} ground motions is approximately 12 times of that for 1×10^{-4} ground motions. The predicted mean, median, and maximum block size also show a large increase from the preclosure motion to postclosure motions. However, the differences of the block size statistics in between the postclosure motions are relatively minor, especially for the results of 1×10^{-6} and 1×10^{-7} ground motions.

Table 6-26. Comparison of Rockfall Statistics for Preclosure and Postclosure Events

Statistic	Ground Motion			
	10^{-4}	10^{-5}	10^{-6}	10^{-7}
Runs Completed	32	50	50	44
Total Number of Rockfall	428	1764	2797	3387
Total Volume of Rockfall (m^3)	39.4	255.4	497.7	705.2
Total Length of Drift Simulated (m)	800	1250	1250	1100
Number of Blocks per km	535	1414	2238	3079
Volume of Rockfall per km (m^3/km)	49.3	204.3	398.2	641.1

Table 6-27. Statistic Summary of the Block Size (metric ton) for Preclosure and Postclosure Events

Statistic	Ground Motion			
	10^{-4}	10^{-5}	10^{-6}	10^{-7}
Mean	0.22	0.35	0.43	0.50
Median	0.10	0.12	0.13	0.15
Standard Deviation	0.33	0.93	1.30	1.43
Skewness	3.47	10.03	11.61	8.81
Range	2.69	19.04	28.19	28.26
Minimum	0.02	0.02	0.02	0.02
Maximum	2.72	19.07	28.22	28.29
Sum	95.00	615.97	1200.43	1699.57

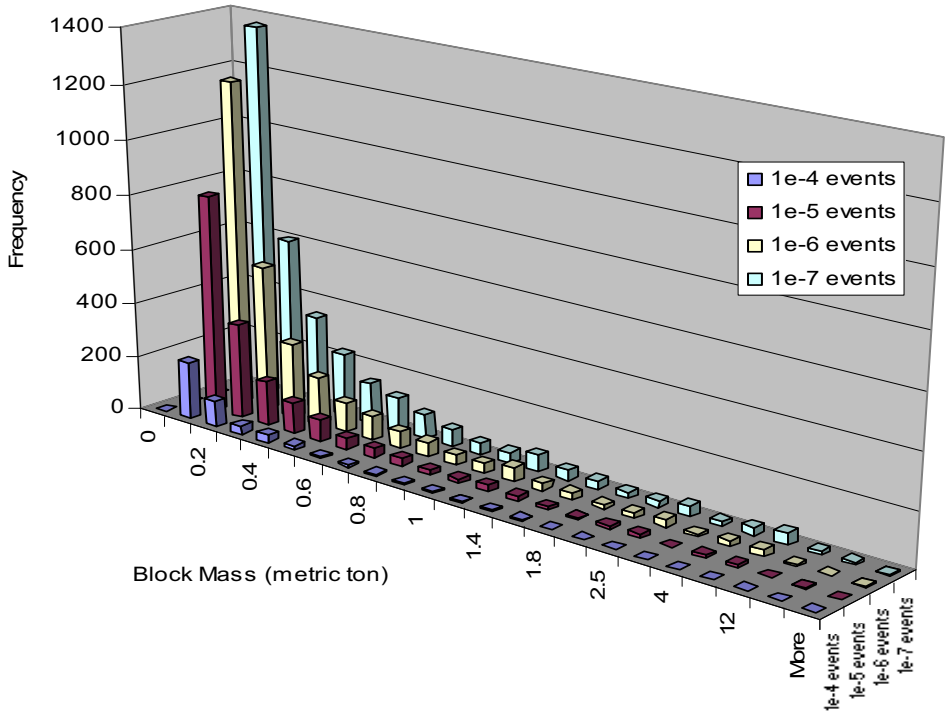

Figure 6-81. Comparison of Histograms of Block Mass from Preclosure and Postclosure Ground Motions

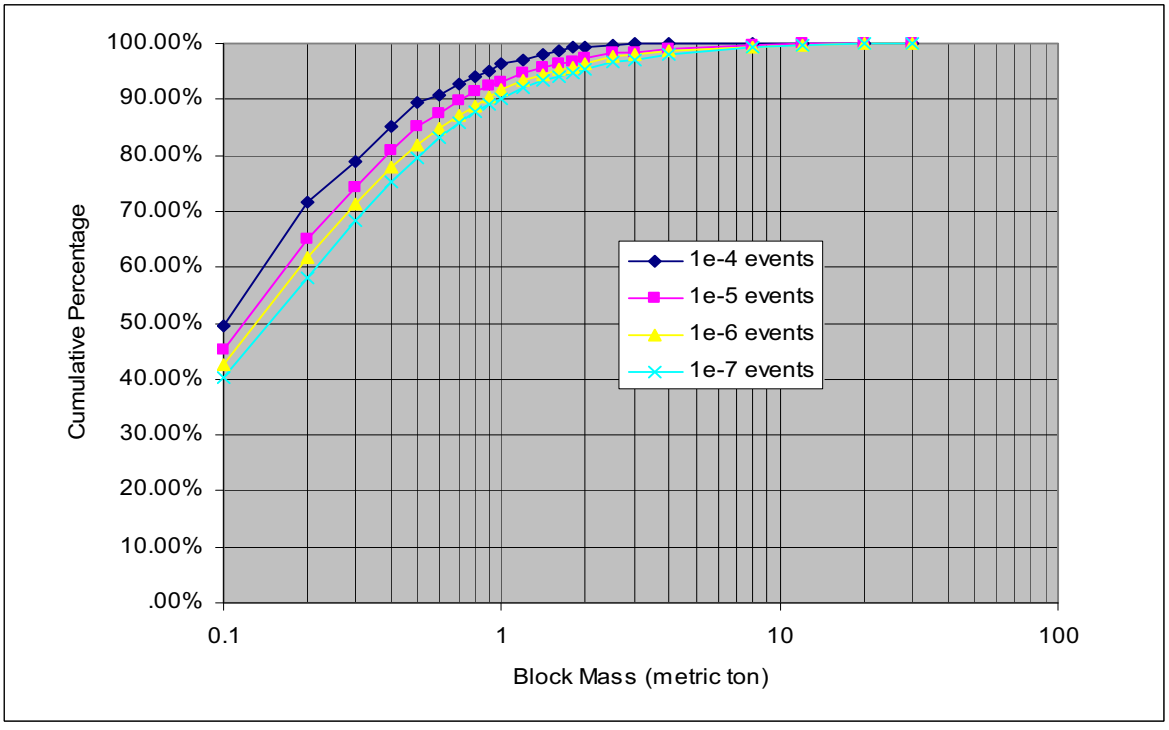

Figure 6-82. Comparison of Block Size Distribution from Preclosure and Postclosure Ground Motions

Peak Ground Velocities and Energy Contents–Correlation of the rockfall volume per 3DEC simulation with the peak ground velocity and energy content in terms of Arias Intensity is presented in Figures 6-83 and 6-84. The three levels of postclosure ground motions are included. At any given level of PGV, the variability in rockfall based on the variability in fracture pattern and ground motion frequency characteristics results in a fairly wide distribution in response. Although no strong relationship is observed between rockfall volume and PGV, a roughly linear relationship exists between the upper bound to rockfall volume and PGV on this semi-log plot. It appears that the predominant mechanism for variability in rockfall at a given level of PGV is the fracture pattern.

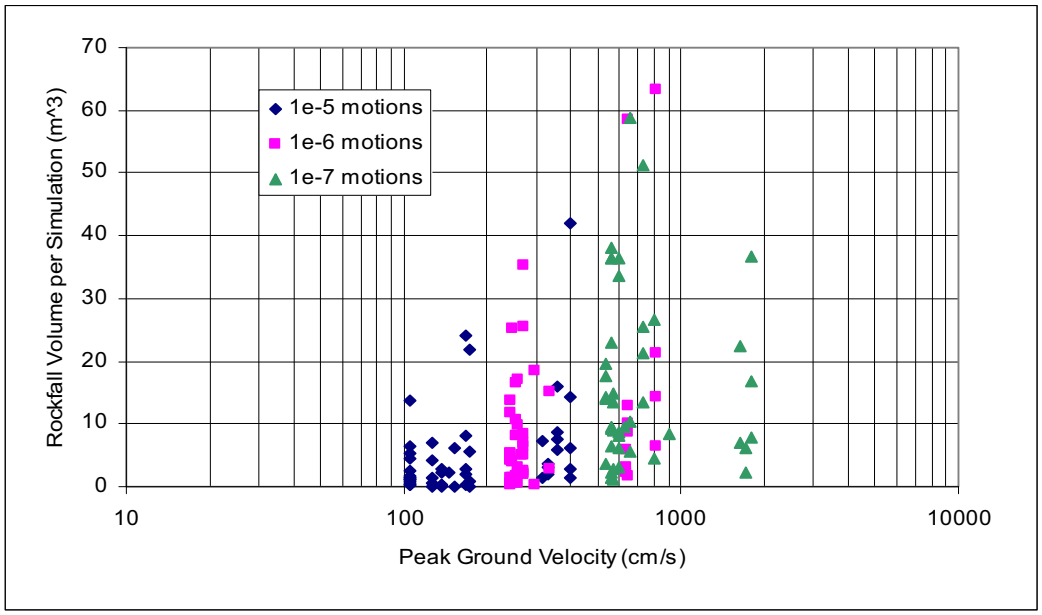

Figure 6-83. Rockfall Volume vs. Peak Ground Velocity

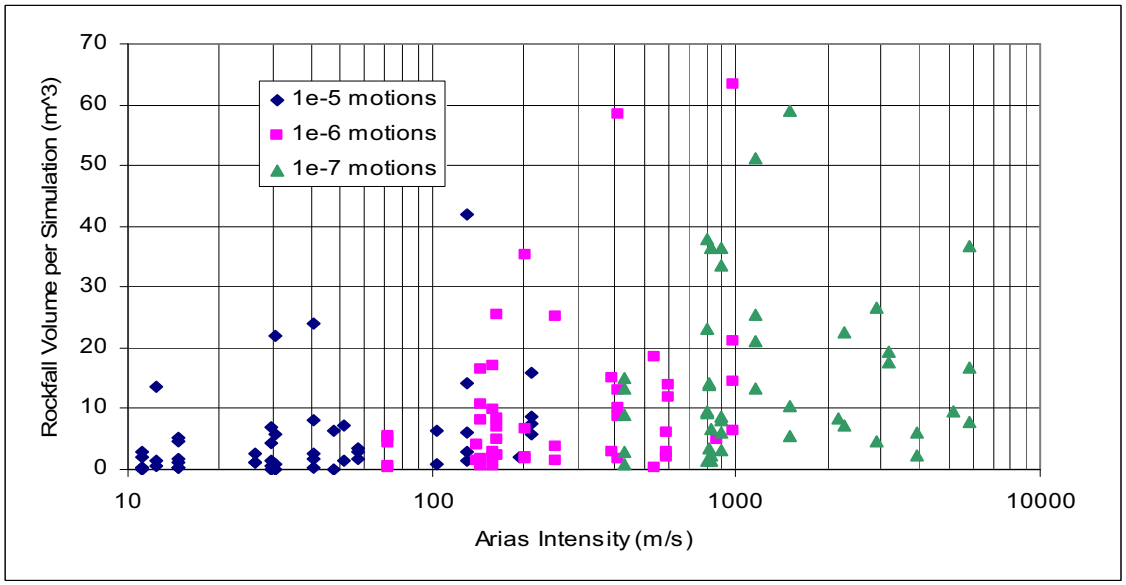

Figure 6-84. Rockfall Volume vs. Arias Intensity

Orientation of Horizontal Motions–The orientation of horizontal motions is conveniently specified as H1 parallel to the x-axis and H2 parallel to the z-axis (the North direction) in the 3DEC model (3DEC coordinate system is shown in Figure L-1). An alternative approach with H1 parallel to the z-axis (North) and H2 parallel to the x-axis was used to check the sensitivity of the orientation. Table 6-28 presents the comparison of the predicted rockfall with the two approaches. In general the difference is minor because the amplitudes of the peak motions are similar for the two horizontal components of the ground motion.

Table 6-28. Rockfall in Nonlithophysal Rock Due to 10^{-5} Ground Motion Combined with Thermal-Mechanical Effects, Base Case of Thermal Properties

Case	Ground Motion	Original Approach (H2 in North)		Alternative Approach (H1 in North)	
		Number of Rockfall	Rockfall Volume (m^3)	Number of Rockfall	Rockfall Volume (m^3)
38	3	173	42.03	170	39.04
45	10	14	2.49	18	2.92
63	11	0	0.00	0	0.00

6.3.1.6.2 Joint Mechanical Properties

Joint mechanical properties in 3DEC modeling consist of cohesion, friction angle, dilation angle, normal stiffness, and shear stiffness. The base case joint mechanical properties, listed in Table 6-3, were based on the rotary shear tests of the cored specimen as derived in Appendix E. With limited joint test results available and the fact that the use of rotary shear devices in rock mechanics is limited, some of the parameters in the base case, such as cohesion and dilation angle, were scaled down from the testing results for conservatism, to allow for potential over-prediction of rockfall.

The direct shear test results (Table E-5) are used to provide the range of variation in the sensitivity study. A range of joint mechanical properties, as shown in Table 6-29, was selected for the sensitivity study. Three categories were included to cover the possible range of variation. Category 1 represents the weakest fractures observed, whereas Category 3 represents the strongest fractures. The values of friction angle were established based on the residual friction angle of 30° (see Section 6.3.1.5) and three tiers of dilation angles. The dilation angles were selected based on the empirical estimate of peak dilation angle for the Yucca Mountain joint set (Duan 2003 [DIRS 163586], p.41). The ranges of the peak friction and dilation angle are selected to be consistent with the reported direct shear test results presented in Appendix E (Table E-5). A conservative estimate of cohesion of 0.1 MPa remained the same as the base case.

The joint stiffness values were taken from both the rotary shear test and direct shear test results. The mean and standard deviation of the shear stiffness values for the cooling joint from the direct shear tests (Table E-5) were used to estimate the values presented in Table 6-29. Shear stiffness for Category 2 joint is set to be equivalent to the mean value, whereas the shear stiffness values for Category 1 and 3 joints is estimated to be the mean value minus one standard deviation and the mean value plus one standard deviation respectively. Because the normal stiffness is not reported from the direct shear tests, the mean and standard deviation of the normal stiffness value

from rotary shear tests (Table E-4) were used to estimate the values used for the three categories. The same approach is adopted for normal stiffness as for shear stiffness with the mean value assigned for Category 2 joints and the standard deviation as the range of variation.

The results for the sensitivity of joint properties to the rockfall prediction are presented in Table 6-30. Results for the three categories are quite similar irrespective of the variation of the mechanical properties used for each category. In general, the results are also similar to those for the base case. The exception is Case 38 with approximately 50 percent more rockfall for the sensitivity cases compared to the base case. It was observed that the blocks jammed at the roof preventing additional rockfall, was due to the large amount of rockfall that occurred in a short time for this case. Jamming appears to occur at earlier time for the base case than other sensitivity cases, this contributes to less rockfall for the base case. Comparison of the size distribution of the base case and sensitivity cases for Case 38 are shown in Figure 6-85. The distributions are similar, with the distributions for the base case and joint Categories 2 and 3 nearly identical. The results show that the mechanical properties variation for rockfall is a secondary effect compared to the variation of fracture pattern.

Table 6-29. Three Categories of Joint Properties Used in the Sensitivity Study

Joint Category	Joint Cohesion (Pa)	Joint Dilation Angle	Peak Friction Angle	Joint Normal Stiffness (Pa/m)	Joint Shear Stiffness (Pa/m)
1	1.0E+5	1.4	31.4	7.20E+10	5.30E+09
2	1.0E+5	4.4	34.4	9.40E+10	1.10E+10
3	1.0E+5	11	41	1.16E+11	1.67E+10

Table 6-30. Sensitivity of Joint Properties for Rockfall Prediction

	Base Case		Joint Category 1		Joint Category 2		Joint Category 3	
Case	Number of Rockfall	Rockfall Volume (m^3)	Number of Rockfall	Rockfall Volume (m^3)	Number of Rockfall	Rockfall Volume (m^3)	Number of Rockfall	Rockfall Volume (m^3)
38	173	42.03	237	78.95	257	66.48	251	65.45
45	14	2.49	16	2.21	12	2.07	16	2.37
63	0	0	3	0.12	6	0.35	3	0.19

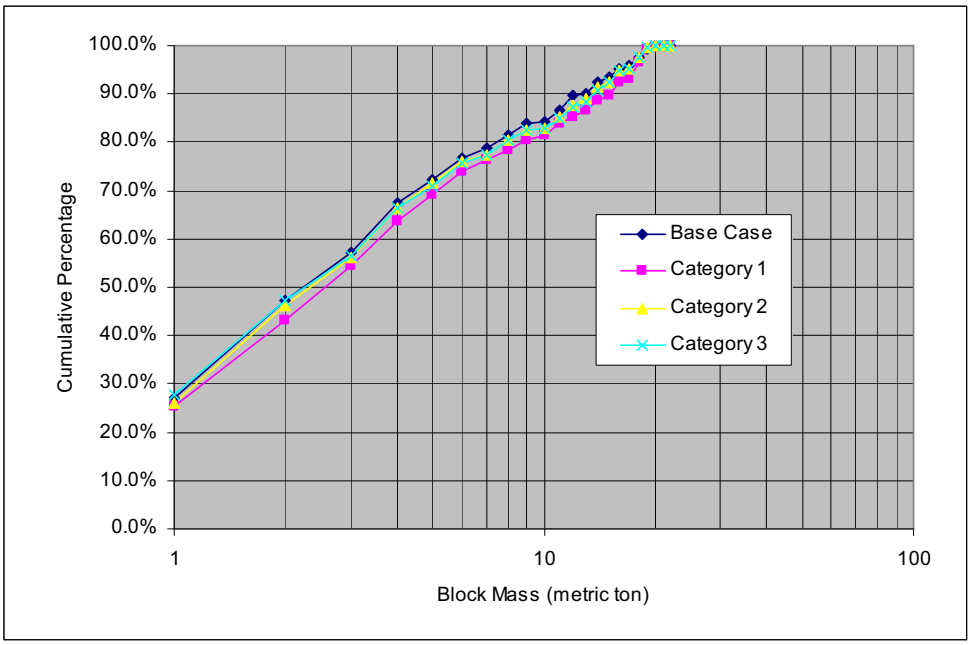

Figure 6-85. Comparison of Block Size Distribution for Variation of Joint Mechanical Properties (Case 38)

6.3.1.6.3 Rock Bridge Strength Parameters

Rock bridges were generated as the extension of finite trace length fractures to form the distinct blocks in the 3DEC model (see Figure H-1 in Appendix H). The strength parameters of the rock bridges used for the base case (listed in Table 6-3) are the best estimate of the intact rock strength. Rock bridge damage appears to have a strong relationship with peak ground velocity. In general, less than 1 percent of the bridge area is damaged when subjected to 1×10^{-5} ground motions, with about 5 percent bridge damage for 1×10^{-6} ground motions, reaching to 20 percent bridge damage for 1×10^{-7} ground motions. However, for certain large ground motions (such as ground motion #3), much higher damage percentage is expected. Figure 6-86 shows the correlation between the damage percentage and the peak ground velocity. As shown in the figure, the coefficient of determination (R^2) is estimated to be around 0.95, indicating a strong relationship. Note that over 60 percent of the bridge area could be damaged with the extremely conservative 16 m/sec peak ground velocity seismic shaking.

A range of bridge strength parameters, in terms of cohesion, friction angle, and tensile strength, as shown in Table 6-31, was selected for the sensitivity study. Three categories were included to cover the possible range of variation. The base case joint strength parameters are used for Category 1 to represent the extreme case where the bridges are sheared off to become fractures. The extreme case could be interpreted as a simulation where the jointed rock mass has been previously subjected to a ground motion greater than 16 m/sec. The mean values of the intact strength parameters listed in Table E-7 (tensile strength for TSw2) and Figure E-2 (cohesion and friction angle) are used for Category 2. The mean plus one standard deviation values are assigned as the strength parameters for Category 3 representing the upper bound for the rock bridge strength.

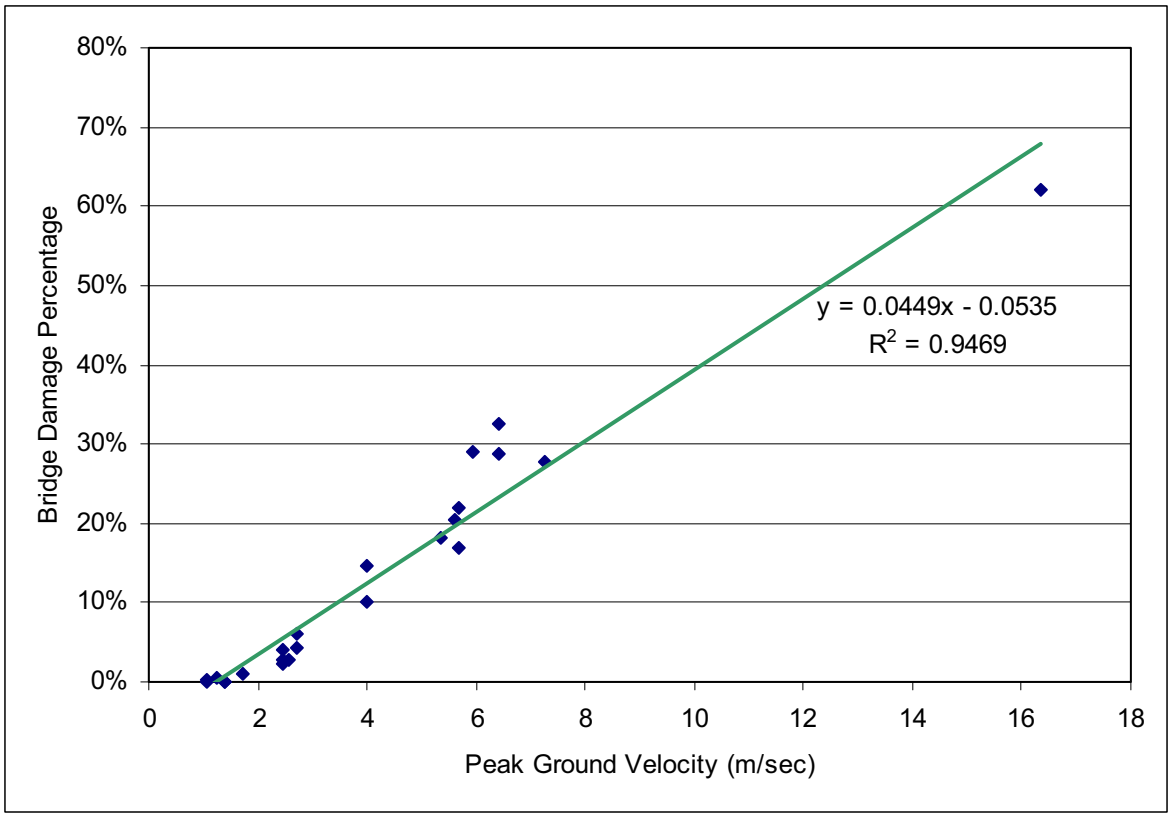

Figure 6-86. Correlation of Rock Bridge Damage Percentage and Peak Ground Velocity

Table 6-31. Three Categories of Rock Bridge Strength Parameters Used in the Sensitivity Study

Rock Bridge Category	Cohesion (Pa)	Friction Angle	Tensile Strength (Pa)
1	1.00E+5	41	0
2	3.60E+7	50	8.90E+6
3	4.00E+7	56	1.22E+7

The results for the sensitivity of rock bridge strength parameters to the rockfall prediction when subjected to 1×10^{-5} ground motions are presented in Table 6-32. Increase of rockfall is predicted for Category 1, representing the extreme case with the bridges sheared off. Significant increase is observed for the median rockfall case (Case 45) and minor increase is detected for the most (Case 38) and least (Case 63) rockfall cases. Results for Categories 2 and 3 are similar to the base case. The results show that within the range of variation for the intact strength parameters (Categories 2 and 3), rock bridge strength parameters have an insignificant impact on rockfall prediction. However, if the rock bridges are sheared off as represented by Category 1, a significant increase of rockfall is likely.

Since the damage percentage varies with different levels of ground motions, additional analyses for the median rock fall case (Case 45) subjected to 1×10^{-6} and 1×10^{-7} ground motions were also

conducted. Table 6-33 presents the results with lower probability ground motions. In general, the trend for rockfall is similar to the results for 1×10^{-5} ground motions.

Table 6-32. Sensitivity of Rock Bridge Strength Parameters for Rockfall Prediction

Case	Base Case		Rock Bridge Category 1		Rock Bridge Category 2		Rock Bridge Category 3	
	Number of Rockfall	Rockfall Volume (m^3)	Number of Rockfall	Rockfall Volume (m^3)	Number of Rockfall	Rockfall Volume (m^3)	Number of Rockfall	Rockfall Volume (m^3)
38	173	42.03	221	61.08	184	45.97	201	56.99
45	14	2.49	47	8.92	14	2.49	13	2.34
63	0	0	6	0.27	1	0.09	0	0

Table 6-33. Sensitivity of Rock Bridge Strength Parameters for Case 45 with 1×10^{-6} and 1×10^{-7} Ground Motions

Ground Motion Level	Base Case		Rock Bridge Category 1		Rock Bridge Category 2		Rock Bridge Category 3	
	Number of Rockfall	Rockfall Volume (m^3)	Number of Rockfall	Rockfall Volume (m^3)	Number of Rockfall	Rockfall Volume (m^3)	Number of Rockfall	Rockfall Volume (m^3)
1×10^{-6}	29	4.19	97	19.75	34	5.52	23	3.29
1×10^{-7}	86	14.27	219	47.64	94	15.49	97	16.01

6.3.1.6.4 Intact Block Failure Response Under Low-Probability Ground Motions

6.3.1.6.4.1 Introduction

At the lower probability levels, the ground motions show extreme peak ground velocities levels, ranging from 2.44 m/sec at the 1×10^{-6} to 5.35 m/sec at the 1×10^{-7} annual exceedance probabilities. The previous calculations and estimates of dislodged block masses and volumes assumed that the rock blocks were, in general, elastic. The only block failure that was allowed was breakage of solid rock "bridges" that occur along the extension of fracture planes, between the end of the fracture and its possible termination against adjacent fractures. Thus, in the current model, it is possible for a block to split into several smaller blocks if the seismic stresses are sufficient to fail the rock bridge in shear or in tension. The following discussion provides a simplified analysis of a more general failure mechanism of intact blocks in shear or in tension. The average principal stresses in blocks surrounding the emplacement drift are examined for the 1×10^{-6} and 1×10^{-7} cases to determine if widespread block failure is possible at these hazard levels. If so, then either the amount of rockfall or the size of dislodged rock masses derived from the previous calculations could be in error. Initially, a discussion is given on analyses aimed at providing a physical bound to peak ground velocities experienced at the Yucca Mountain site. Although no bounds on the PGV of time histories have been used in the damage assessments made from analyses presented in this document, an estimate of the maximum PGV is useful here to determine whether the modeling approach needs to include intact block failure mechanisms. An analysis of the peak stress conditions in blocks surrounding the emplacement drift is then conducted to determine the extent of potential shear or tensile failure mechanisms.

6.3.1.6.4.2 Bounding of the Peak Ground Velocity

The ground motion hazard determined in the Probabilistic Seismic Hazard Assessment expert elicitation is unbounded. Because the ground motion experts characterized aleatory variability in ground motion using unbounded lognormal distributions, as the Probabilistic Seismic Hazard Assessment calculations are extended to lower and lower annual probabilities of exceedence, the mean ground motions increase without bound, eventually reaching levels that are not credible. These levels of ground motion are not credible in that they eventually result in seismic strains that would cause the rock mass (in absence of any excavation) to fail through formation of fractures, an effect that is not observed at Yucca Mountain. As stated in 10 CFR 63.102(J) [DIRS 156605] with respect to events that are to be included in the TSPA, "the event class for seismicity includes the range of credible earthquakes for the Yucca Mountain site." Therefore, to ensure the ground motions considered in the *Seismic Consequence Abstraction* (BSC 2004 [DIRS 169183]) and TSPA are credible, an analysis was conducted to determine a bound to PGV at the repository level. This analysis, presented in *Peak Ground Velocities for Seismic Events at Yucca Mountain, Nevada* (BSC 2004 [DIRS 170137], estimates an upper bound to the ground motions at the Yucca Mountain site based on the shear strain increments (relative to the in situ stress state) required to damage (fracture) the Tptpll[5]. The analysis presented argues that, since seismic induced fracturing is not observed in subsurface exposures of the Tptpll, ground motions equal to or greater than that which would produce shear strains equal to the fracturing limit have not occurred since the Topopah Spring unit was erupted and cooled, some 12.8 million years ago. The shear strain limits are defined from the large core lithophysal rock compression testing and from numerical extrapolation using the PFC and UDEC programs similar to that described in Appendix E, Section E4. Even though bounding peak ground velocities have been estimated, they have not been used explicitly in the calculations of seismic damage presented in this document. In other words, damage has been assessed for time histories with PGVs in excess of the bounding values defined in *Peak Ground Velocities for Seismic Events at Yucca Mountain, Nevada* (BSC 2004 [DIRS 170137]). Instead, the damage to EBS components is bounded within the *Seismic Consequence Abstraction* (BSC 2004 [DIRS 169183], Section 6.4.4); i.e., damage associated with PGVs in excess of 5 m/sec is bounded at the 5 m/sec level.

The details of the derivation of the bounding PGVs based on shear strain limits of the Tptpll can be found in the PGV study (BSC 2004 [DIRS 170137]). The result of the analyses presented there are two potential bounding distributions of horizontal PGV at the repository level – one based on the assumption of a uniform distribution and one based on a triangular distribution (Figure 6-87). The lower and upper limits for the distributions are assessed at 150 and 500 cm/s, respectively, based on the range of shear-strain increments at yield derived from the combined laboratory testing and numerical simulations and the corresponding horizontal PGV values that produce these shear strain increments. To translate the shear-strain threshold probability distribution into a distribution for horizontal PGV at the waste emplacement level, the results of the ground-motion site-response modeling were used. The average horizontal PGV values

[5] Tensile strains may also be induced by the vertically propagating wave associated with the seismic event. A number of the ground motion time histories at the 1×10^{-5}, 1×10^{-6} and 1×10^{-7} annual exceedance probabilities are characterized by a vertical component that is larger than the horizontal component. The tensile strain limit of the rock is less than the shear strain limit, which is used to derive the bounded horizontal PGV. Therefore, using shear strain limit will result in larger bounded ground motions than use of both shear and tensile strain limits. The bounded PGVs based on a shear strain limit alone are thus conservative in nature.

associated with the average shear-strain values from the site-response results are used to transpose the shear-strain threshold probability distribution. The average horizontal PGV values calculated, assuming PGV values are normally distributed, yield higher PGVs than those calculated for a lognormal distribution. The resulting distribution for horizontal PGV departs slightly from a triangular shape because the relation between shear-strain threshold and horizontal PGV is not linear. This distribution ranges from a minimum value of 151 cm/s to a maximum value of 451 cm/s and has a mode of 236 cm/s. The uniform distribution of bounding PGVs is used in the *Seismic Consequence Abstraction* (BSC 2004 [DIRS 169183]) to bound mechanical damage to EBS components since it produces a more conservative approach with an upper bound of 5 m/sec to the horizontal PGV at the repository level.

In summary, the PGV at the repository level has been shown, based on physical strain limitations of the lithophysal rock mass, to be, at most, 5 m/sec. Depending of the distribution assumed, the maximum could also be as low as approximately 4.5 m/sec with a mode of 2.36 m/sec.

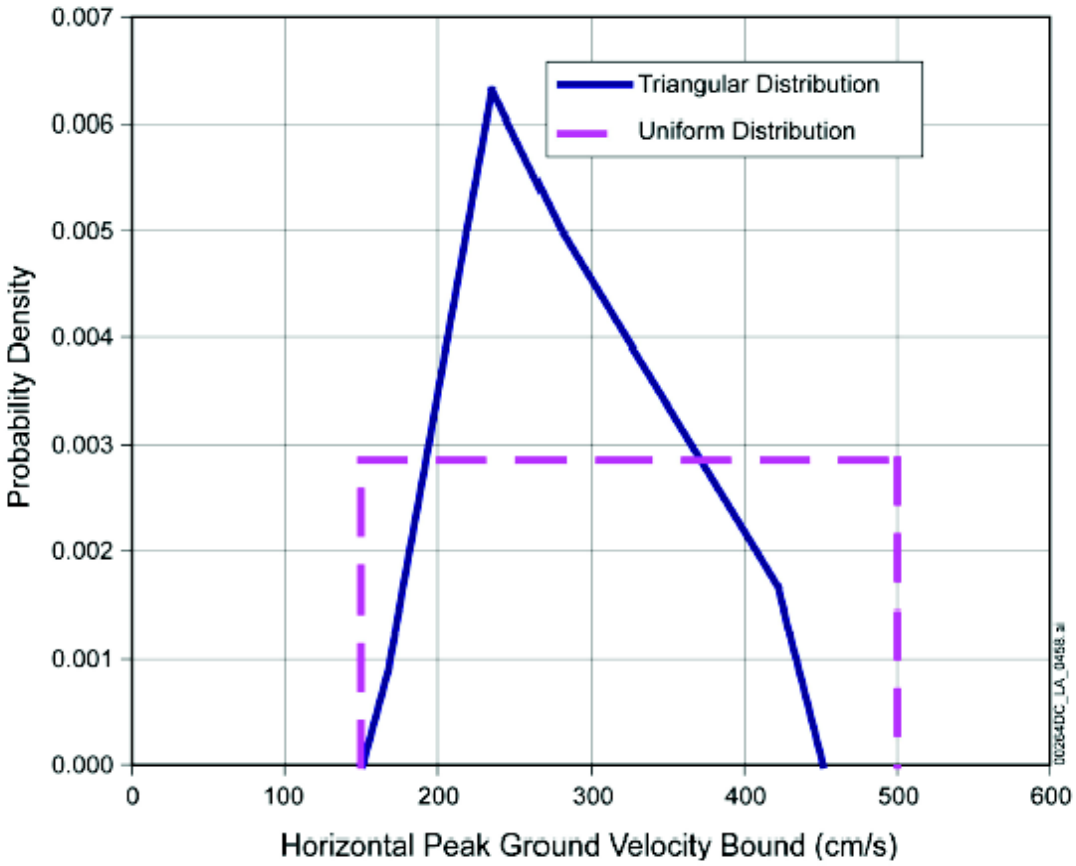

Source: BSC 2004 [DIRS 170137].

Figure 6-87. Probability Density Functions for the Bound to Horizontal Peak Ground Velocity at the Waste Emplacement Level

6.3.1.6.4.3 Analysis of Intact Block Failure Mechanism

Tensile stresses in the rock mass are induced by both the shear (horizontal component) and during the reversal of the compression (vertical component). The tensile strength of the rock mass is a consequence of the tensile strength of the solid rock bridges that occur between discontinuous fracture traces. Therefore, as the rock mass is loaded in a transient tensile fashion by the combined effect of the shear and compression waves, the intact blocks could be split into a number of smaller blocks through tensile (or shear) failure of the rock bridges. These smaller blocks can then become unstable under the successive shaking of the ground motion, with subsequent collapse into the drift.

To examine the potential for intact block breakage, the analyses conducted to examine the impact of rock bridge failure are reviewed here. The base case 1×10^{-6} and 1×10^{-7} nonlithophysal 3DEC model, described in Section 6.3.1 are based on fracture geometries (i.e., the orientation, radius and spacing distribution) obtained from a synthetic fracture representation developed from field mapping. A general result of this fracture representation is a distinct block system that is formed by solid rock bridges and finite trace fractures as shown in Appendix H (Figure H-1). In the base case analyses, the strength of the solid rock bridges, which is represented as bonded "patches" along fracture planes, is governed by the shear and tensile strength of the solid Tptpmn, as given in Table 6-3 (cohesion of 47.2 MPa, friction angle of 42^o and tensile strength of 11.56 MPa). During a simulation, the stress conditions acting on these solid rock bridges are monitored, and failure in shear or tension can occur. If failure occurs, the cohesive and tensile strength of the bridge is reduced to zero, and the bonded "patch" is fractured. Thus, the block within which the bridge is located can be fractured into multiple blocks. As described in Section 6.3.1.6.3, less than 1 percent of the rock bridges are damaged during the 1×10^{-5} ground motions, about 5 percent during the 1×10^{-6} ground motions, and about 20 percent for the 1×10^{-7} ground motions. Figure 6-86 presented the rock bridge damage percentage estimated from the 3DEC modeling as a function of the PGV of the ground motion. As seen in this figure, the damage to rock bridges is approximately 20 percent or less (for PGVs less than 5 m/s) in terms of total rockfall, with the results presented in Tables 6-9, 6-12 and 6-15 for the 1×10^{-5}, 1×10^{-6}, and 1×10^{-7} cases, respectively.

A sensitivity study of rock bridge strength, presented in Section 6.3.1.6.3 provides a conservative assessment of the case in which the tensile strength of the rock bridges is assumed to be zero. This case effectively represents the condition in which the tensile strength of the rock mass is conservatively assumed to be zero as no rock bridges exist. These analyses indicate that the rockfall volume (for the median rockfall case 45) increases between 3 to 5 times for the 1×10^{-6} and the 1×10^{-7} cases (summarized in Table 6-33). The ground motion time histories for the median rockfall condition (Case 45) for the 1×10^{-6} and the 1×10^{-7} annual exceedance probabilities are shown in Figure 6-88. The rockfall for Case 45, for the base case rock bridge strength and the case in which the rock bridge tensile strength is set to zero are shown in Figures 6-89 to 6-90 for the 1×10^{-6} and the 1×10^{-7} ground motions. As seen in these figures, the rockfall increases significantly with the assumption of zero rock bridge tensile strength, but total collapse is not evident.

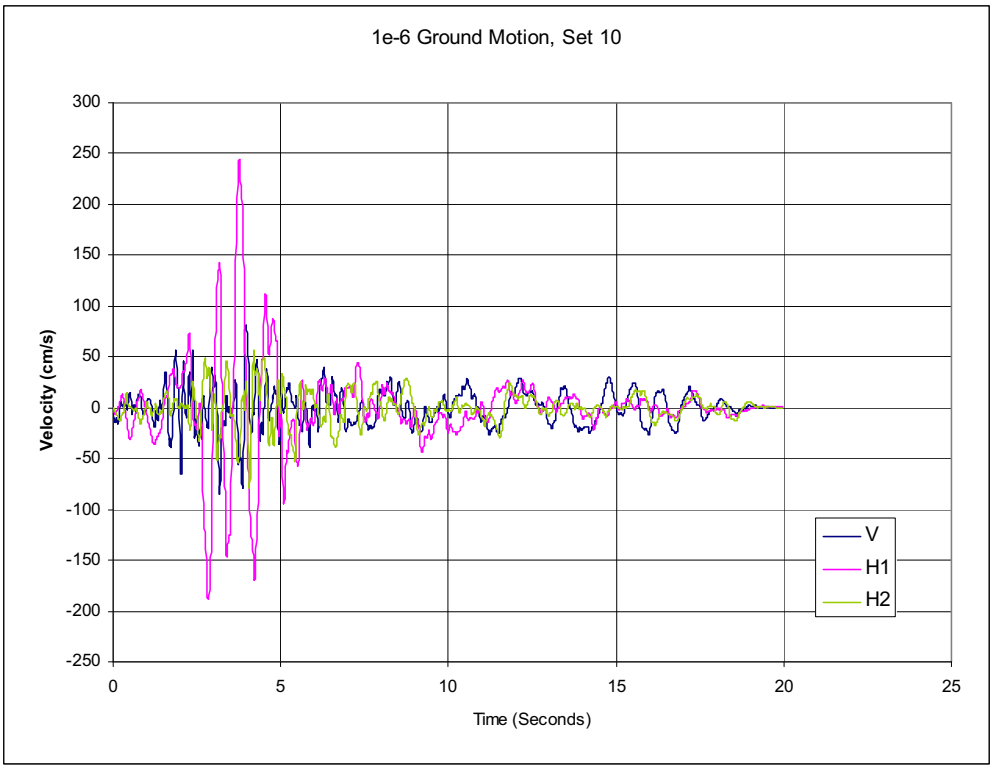

a)

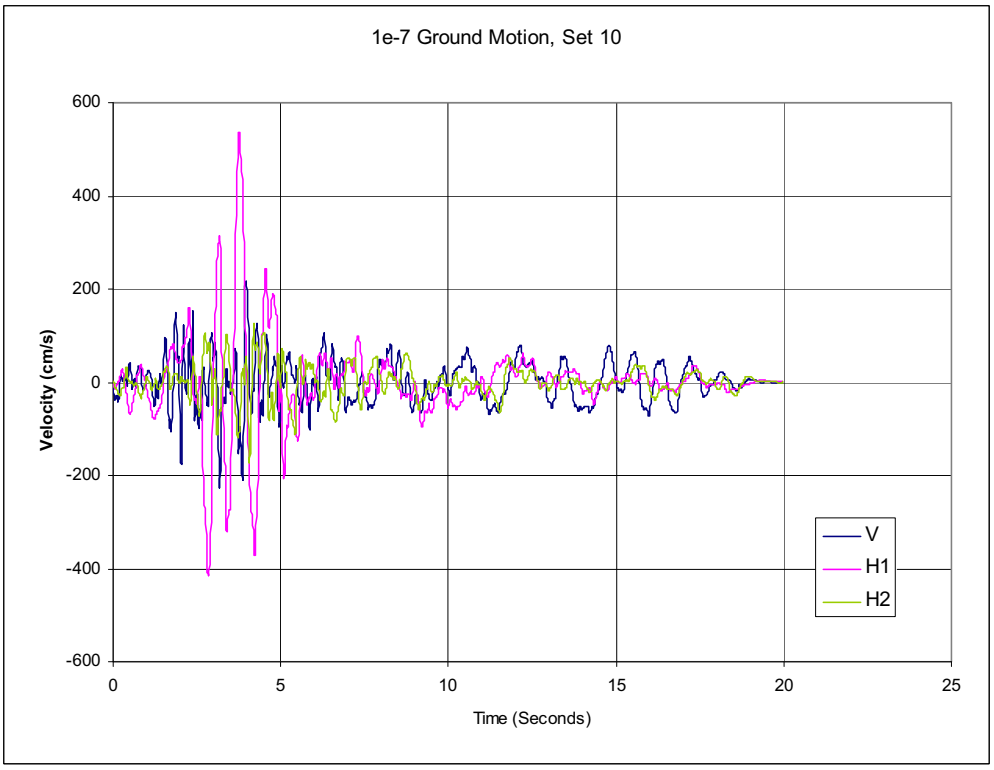

b)

Figure 6-88. $1x10^{-6}$ (a) and the $1x10^{-7}$ (b) Ground Motion Time Histories in Terms of Peak Ground Velocity for Median Rockfall Condition, Case 45

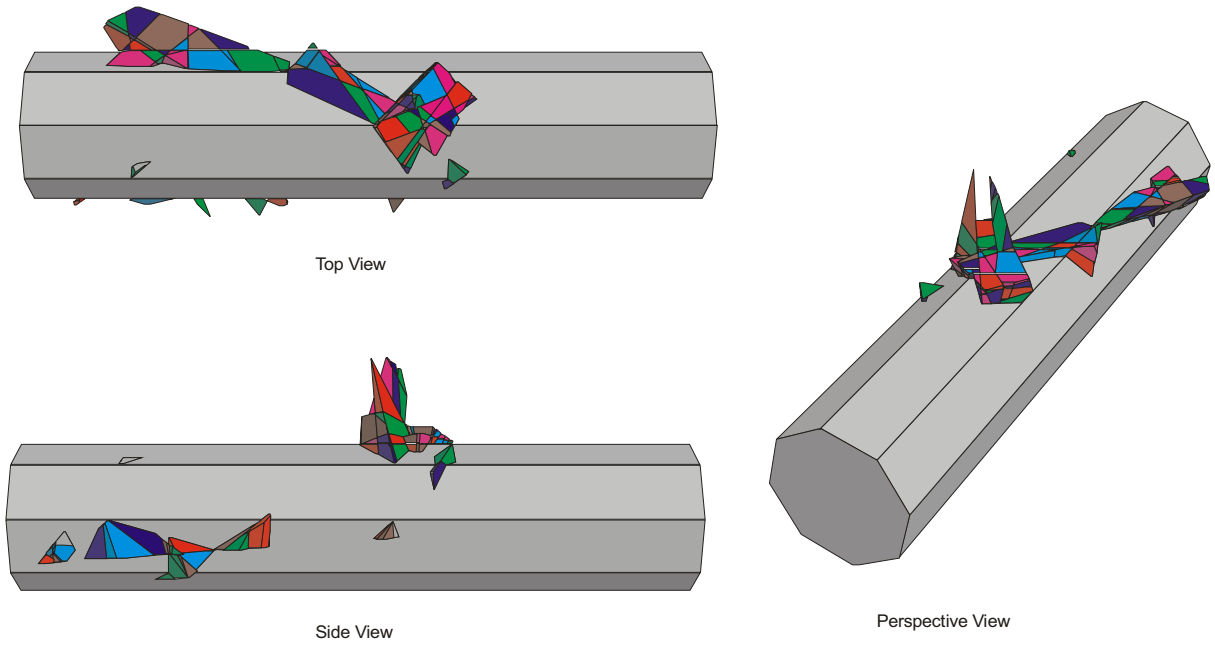

a)

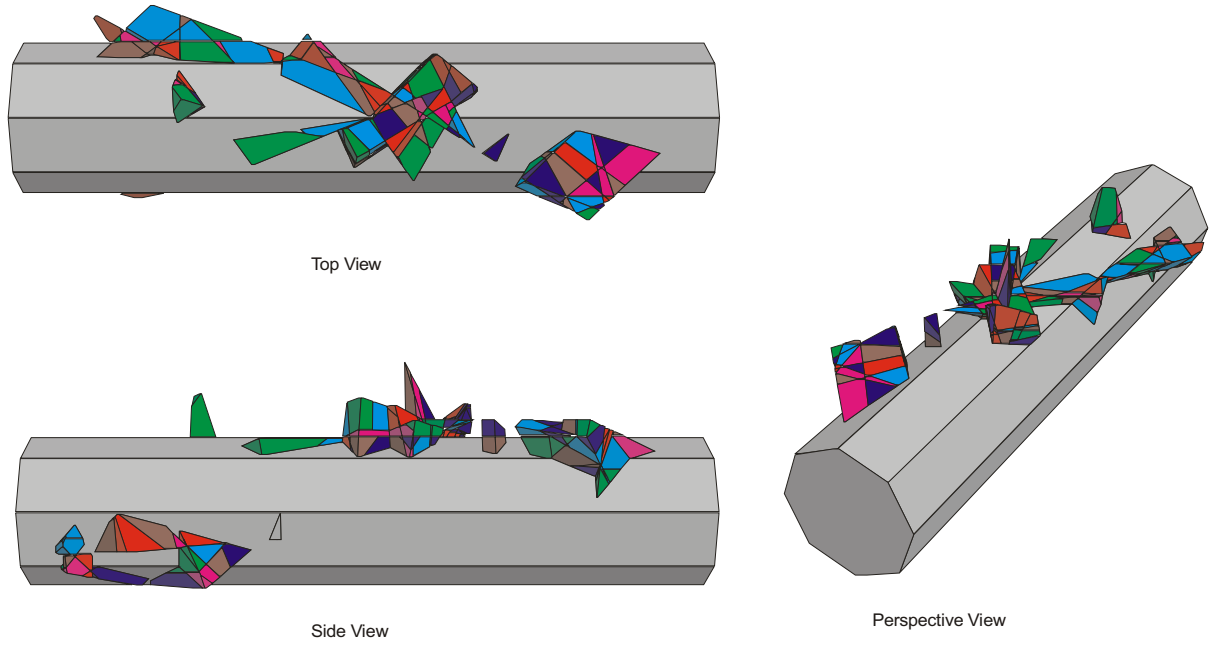

b)

NOTE: Base case rock bridge strength properties given by cohesion of 47.2 MPa, friction angle of 42° and tensile strength of 11.56 MPa. Low rock bridge strength properties given by by cohesion of 0.1 MPa, friction angle of 41° and tensile strength of 0.

Figure 6-89. Three-dimensional Visualization of Rockfall for the Median Rockfall Condition (Case 45), and Base Case (a) and Low (b) Rock Bridge Strength Properties, $1x10^{-6}$ Ground Motion

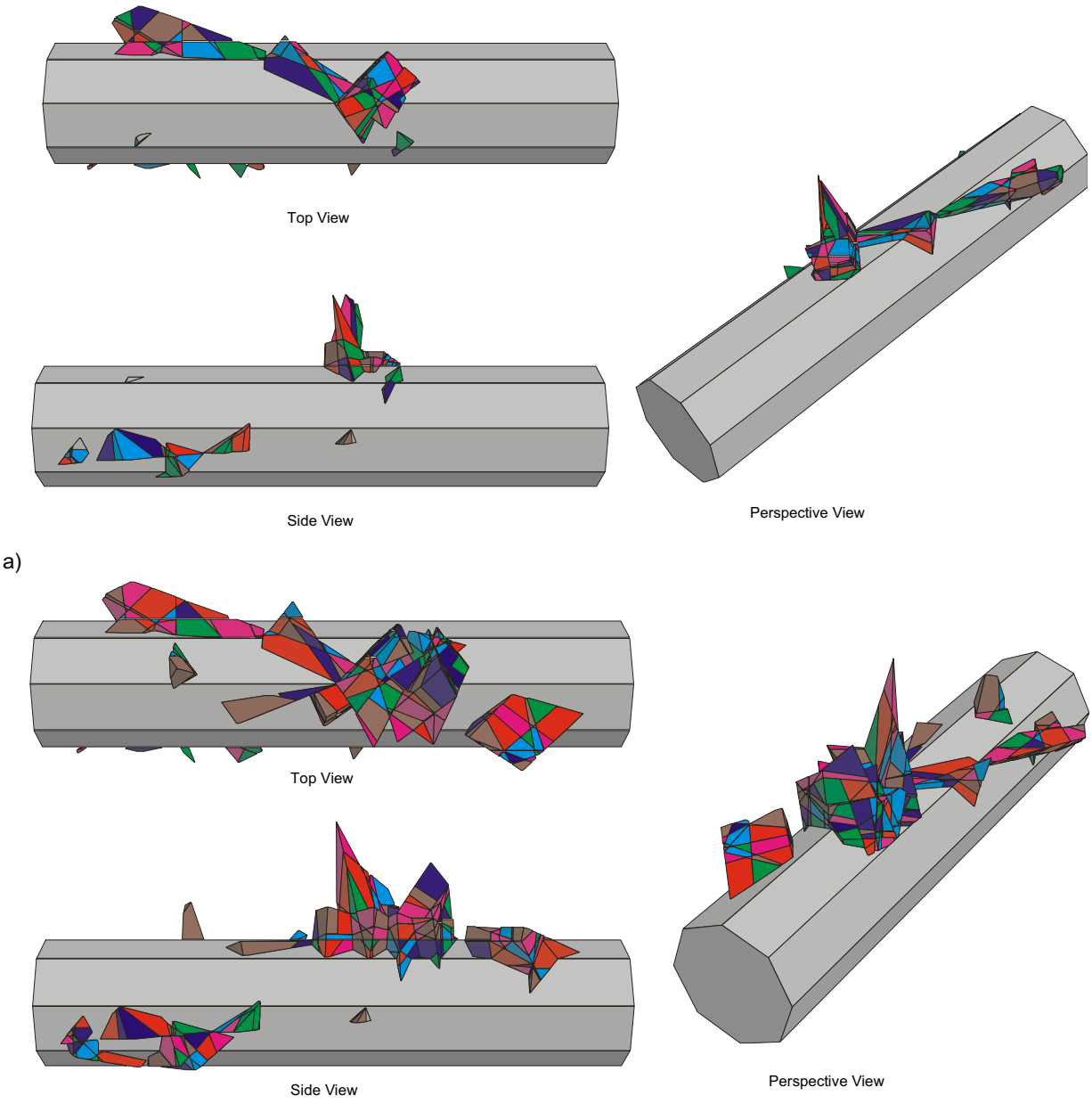

NOTE: Base case rock bridge strength properties given by cohesion of 47.2 MPa, friction angle of 42° and tensile strength of 11.56 MPa. Low rock bridge strength properties given by cohesion of 0.1 MPa, friction angle of 41° and tensile strength of 0.

Figure 6-90. Three-dimensional Visualization of Rockfall for the Median Rockfall Condition (Case 45), and Base Case (a) and Low (b) Rock Bridge Strength Properties, $1x10^{-7}$ Ground Motion

In summary, the rock mass tensile strength is a function of the strength of the solid rock bridges occurring along pre-existing fractures, as well as the geometry of the fractures themselves. The impact of fracture of the solid rock blocks as a potential mechanism in the nonlithophysal rocks was examined via a sensitivity study of the shear and tensile strength of the solid rock bridges. This sensitivity study showed that the damage to rock bridges is an approximate linear function

of the PGV of the ground motion (Figure 6-86), with a maximum damage for base case rock bridge properties of about 20 percent. The impact of assumption of a conservative rock mass tensile strength was examined by assuming the rock bridges had zero tensile strength. Significantly more rockfall occurs for this case, but total drift collapse in the nonlithophysal rock is still not indicated for any of the ground motions examined.

6.3.1.6.5 Model Dimension

As described in Section 6.3.1.1, the 3DEC base case model is slightly larger than a 25-m cube (the actual size is 25 m x 27.5 m x 25 m) with the tunnel oriented at 75 degrees azimuth. The region with detail fractures imported from FracMan is one diameter at the side of the tunnel (dimension s) and two diameters on top of the tunnel for the base case (dimension t). Additional analyses with various modeling dimensions were conducted to investigate the sensitivity of model dimension to rockfall prediction. Table 6-34 lists the additional three model dimensions used for the sensitivity runs. The length along the X-axis (15 degrees clockwise from the drift axis) remains constant at 25 m for all cases (3DEC coordinate system is shown in Figure L-1).

Table 6-34. Various Model Dimension for Sensitivity Study

Model Size	Model Dimension (m)	s (m)	t (m)
Small	25×25×25	2.75	5.5
base case	25×27.5×25	5.5	11
large 1	25×33.75×30	8	16.5
large 2	25×38.75×37.5	11	22

s = horizontal distance away from the side wall; t = vertical distance away from the roof

Cases 38, 45, and 63 with 1×10^{-5} ground motions were selected for the sensitivity study to cover the range of rockfall prediction. Figure 6-91 shows the cross-sectional views of Case 45 (the median rockfall case) for the four various dimensions. The predicted rockfall for the four model dimensions are presented in Table 6-35. In general, the four models predict a similar amount of rockfall. The exception is the small model for Case 38 that predicts approximately 40 percent less rockfall than the base case. In all, the base case appears to be adequate to provide a reasonable estimate for rockfall.

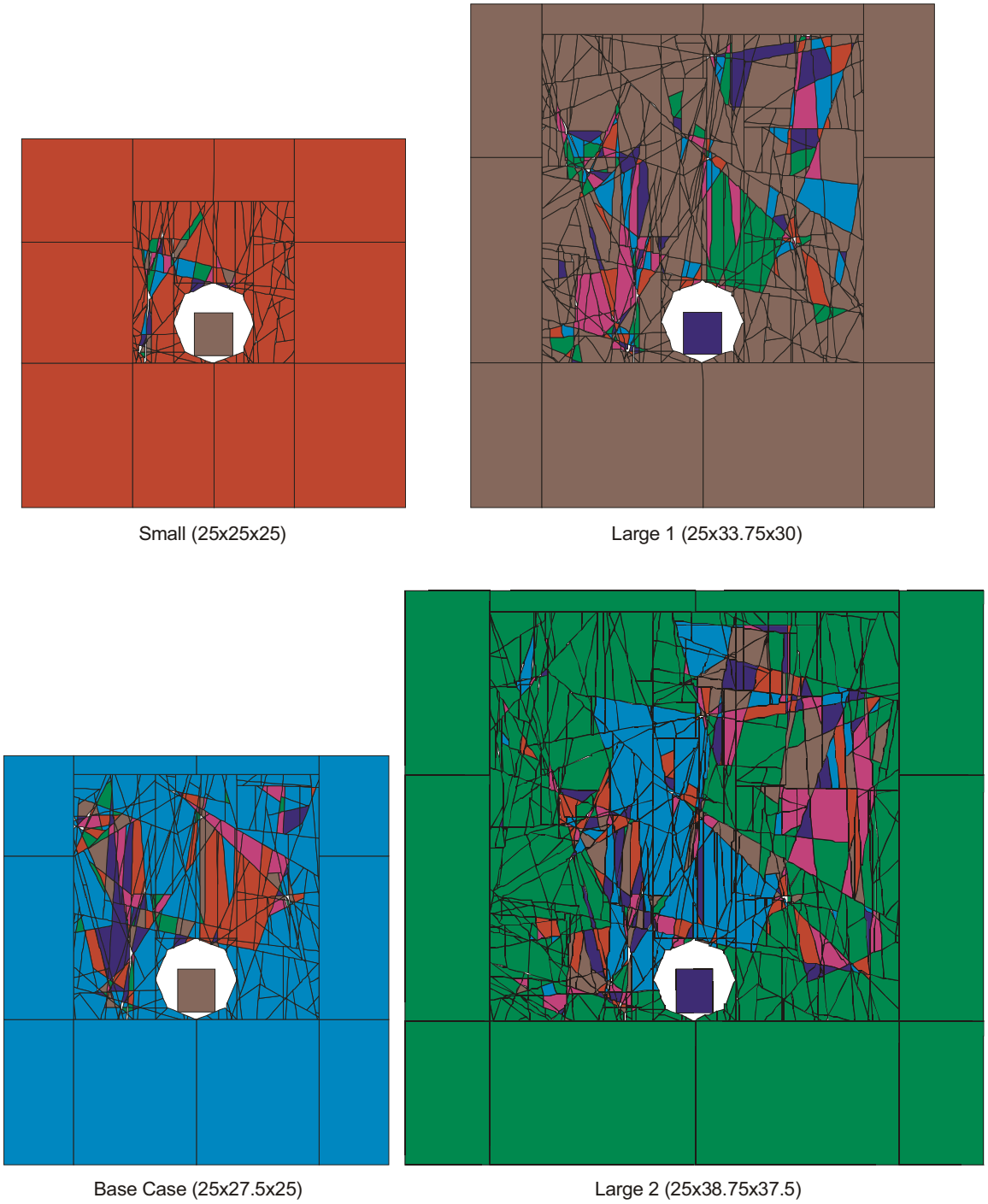

Figure 6-91. Cross Section of the Four Model Dimensions Selected for Sensitivity Study, Case 45

Table 6-35. Predicted Rockfall for Various Model Dimensions

Model Size	Model Dimension	Case 38		Case 45		Case 63	
		Number of Blocks	Rockfall Volume (m^3)	Number of Blocks	Rockfall Volume (m^3)	Number of Blocks	Rockfall Volume (m^3)
small	25×25×25	157	27.33	13	2.29	0	0
base case	25×27.5×25	173	42.03	14	2.49	0	0
large 1	25×33.75×30	179	54.61	15	2.51	6	0.68
large 2	25×38.75×37.5	154	34.29	14	2.38	3	0.41

6.3.1.6.6 Block Deletion

As described in Section 6.3.1.1, a drip shield block anchored at the invert is included in the model to record the information of the locations and relative velocities for the rockfall impact. An algorithm was developed to delete the fallen block after the impact. The deletion is to facilitate the recording of all *possible* rockfall on the drip shield. If the blocks are not deleted for the heavy rockfall cases, the drip shield will be covered with fallen rocks so that some of the rockfall at the later part of seismic shaking will not directly impact the drip shield. The two cases with the most rockfall subjected to 1×10^{-7} ground motions (Case 64 [Fracture Pattern 49 and Ground Motion 14] and Case 40 [Fracture Pattern 99 and Ground Motion 6]) are selected to assess the impact of no deletion to rockfall prediction.

Figures 6-92 and 6-93 show the two selected cases in which the block deletion algorithm is not included. As expected, with the fallen blocks piled on the drip shield, the blocks on top do not directly impact the drip shield. Table 6-36 compares the results for rockfall prediction with and without the block deletion algorithm. Rockfall volume for the cases without block deletion is approximately half of the amount for the cases with block deletion. The effect of blocks not directly impacting the drip shield will be the dead load added onto the drip shield. The accumulation of dead load on top of the drip shield for the fallen rock is addressed in Section 6.4.2.5.

Table 6-36. Predicted Rockfall With and Without Block Deletion After Impact

Case	With Block Deletion		Without Block Deletion	
	Number of Blocks	Rockfall Volume (m^3)	Number of Blocks	Rockfall Volume (m^3)
64	269	58.93	186	28.69
40	120	51.29	69	20.49

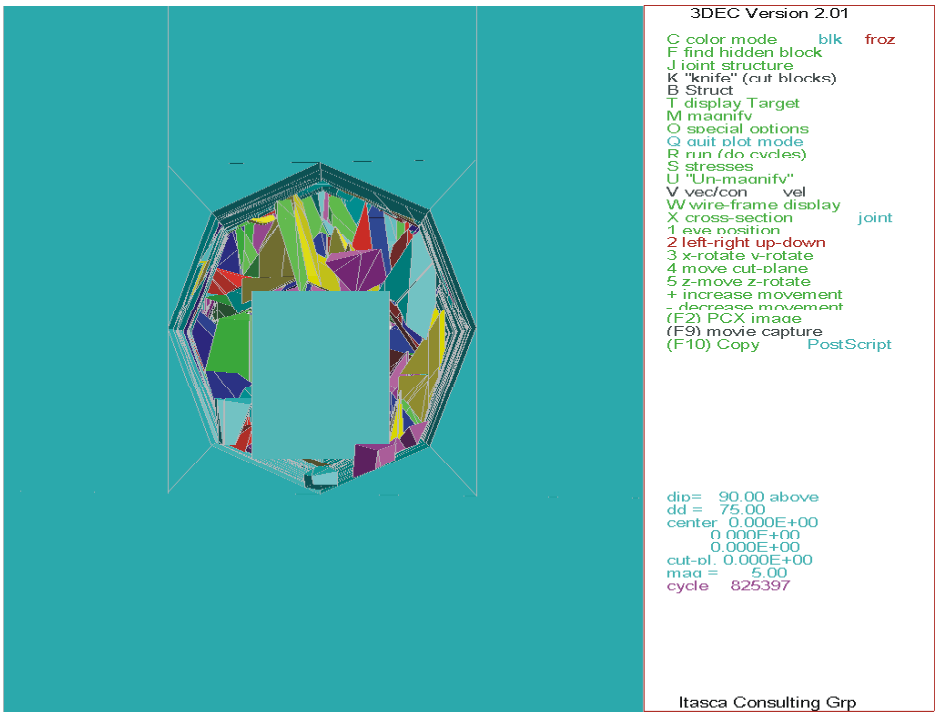

Figure 6-92. Blocks Accumulated Above the Drip Shield Without Implementing Block Deletion Algorithm, Case 64, Fracture Pattern 49, 1×10^{-7} Ground Motion Set #14

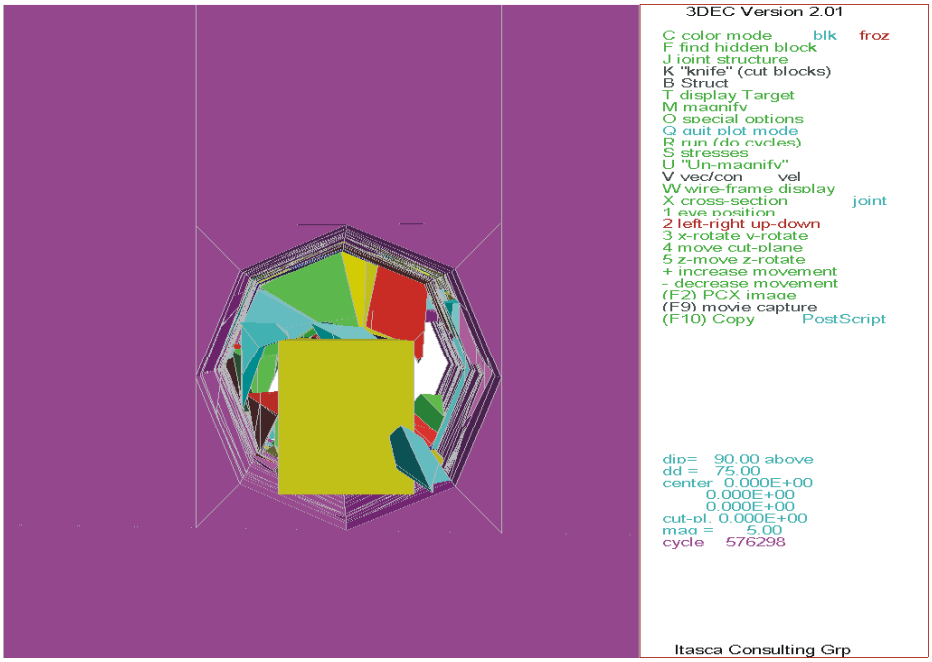

Figure 6-93. Blocks Accumulated Above the Drip Shield Without Implementing Block Deletion Algorithm, Case 40, Fracture Pattern 99, 1×10^{-7} Ground Motion Set #6

6.3.2 Consideration of Intensely Fractured Zone

6.3.2.1 Introduction

An intensely fractured zone is observed at ESF main loop Stations 42+00 to 51+50 with an approximate 1000-m length. A description of this fracture zone is provided in *Geology of the Main Drift - Station 28+00 to 55+00, Exploratory Studies Facility, Yucca Mountain Project, Yucca Mountain, Nevada* (Albin et al. 1997 [DIRS 101367], p. 58):

> The fracture zone between Sta. 42+00 and 51+50 is a zone of intense Set 1 fracturing. This zone appears to be strata bound within the Tptpmn. The zone does not crop out on the surface. Down-hole video from drill hole SD-12, located 39.4 m west of tunnel Sta. 46+49, shows a similar zone of intensely fractured rock only within the Tptpmn. The Main Drift in the area of the fracture zone is parallel to the Ghost Dance Fault and is approximately 100 m west of and in the hanging wall of the fault. It is not known whether the fracture zone is continuous across the Ghost Dance fault as only limited information exists east of the Main Drift.

According to Albin et al. (1997 [DIRS 101367]), the two likely hypotheses for the origin of this zone are tectonic and/or cooling of the ash-flow sheet. Figures 6-94 and 6-95 show the intensely fractured rock mass with a predominant joint set of 134/83 (strike/dip). Set 2 and Set 3 fractures are sparse compared to Set 1 fractures. The mean and median joint spacing for the predominant Set 1 fractures were calculated to be 0.24 m and 0.12 m, respectively.

Figure 6-94. Photo Showing the Intensely Fractured Zone in ESF Main Drift

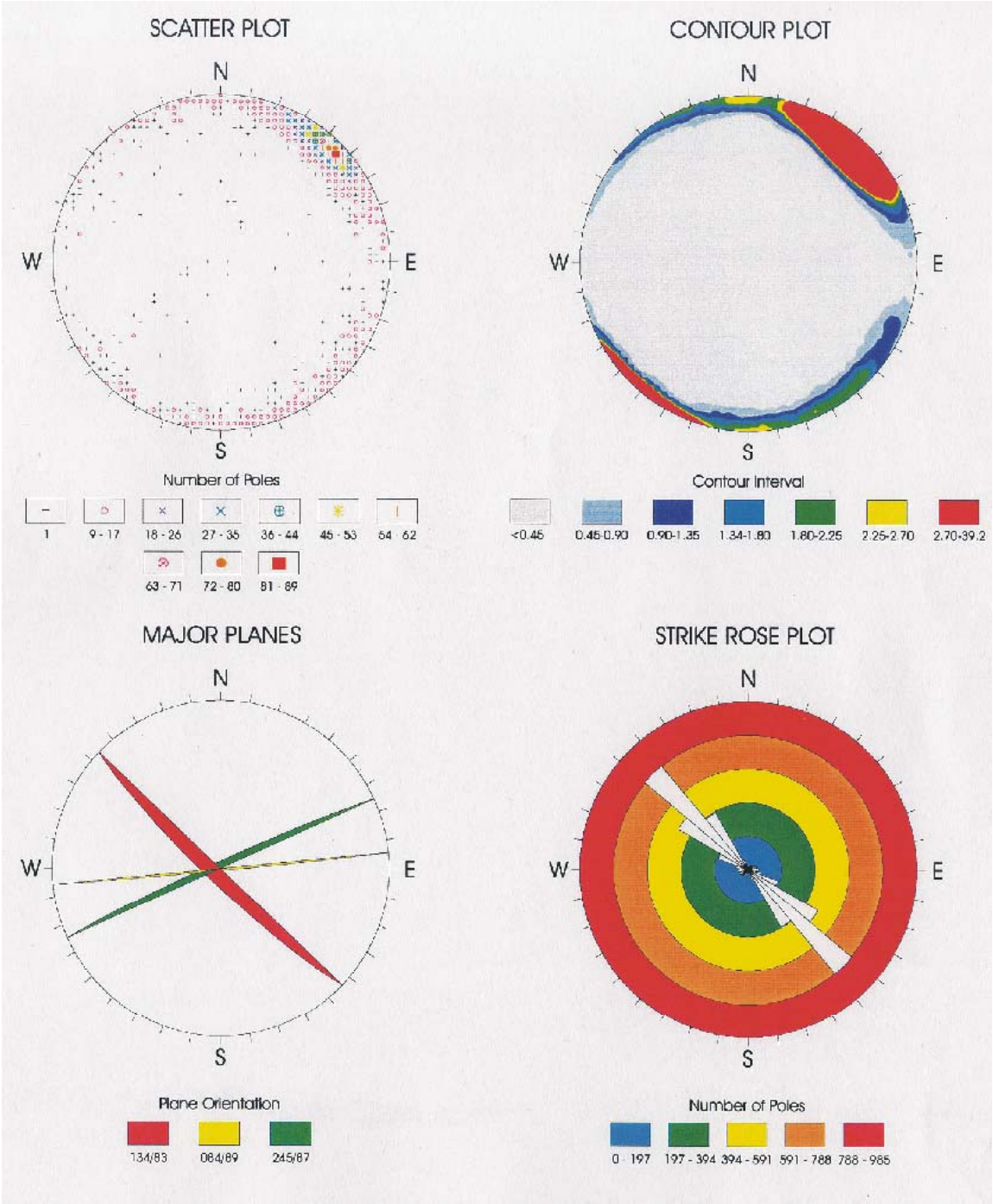

Source: CRWMS M&O 1998 [DIRS 102679], p. II-66.

Figure 6-95. Fracture Analysis for the Intensely Fractured Zone

6.3.2.2 Numerical Modeling

A 3DEC analysis, which is used for rockfall modeling of the nonlithophysal jointed rock mass, is not suitable for such highly fractured rock. A three-dimensional continuum analysis with ubiquitous joint model (FLAC3D analysis) was adopted to account for the highly fractured and anisotropic nature of the rock mass in this zone. The ubiquitous joint model is ideal for conditions with one predominant fracture set in the rock mass.

Figure 6-96 shows a 25-m cube FLAC3D model constructed for the analysis. To simplify the model, the tunnel axis was oriented parallel to the y-axis and the input fracture orientation was adjusted based on the coordinate system shown in Figure 6-96. The intact rock deformation properties and joint strength properties used in the model are identical to the 3DEC base case model presented in Table 6-3. A typical modeling sequence was simulated with initial consolidation and tunnel excavation. The lateral and bottom boundaries were fixed at the direction normal to the boundary surface, whereas the in situ static pressure was applied to the top boundary for the consolidation and excavation stages. Both the preclosure seismic motion (5×10^{-4} seismic ground motion) and the postclosure seismic motion (1×10^{-6} seismic ground motion Set 1 (DTN MO0301TMHIS106.001, see Appendix X)) were applied to the model with free-field boundary condition imposed. These analyses do not include thermal loading.

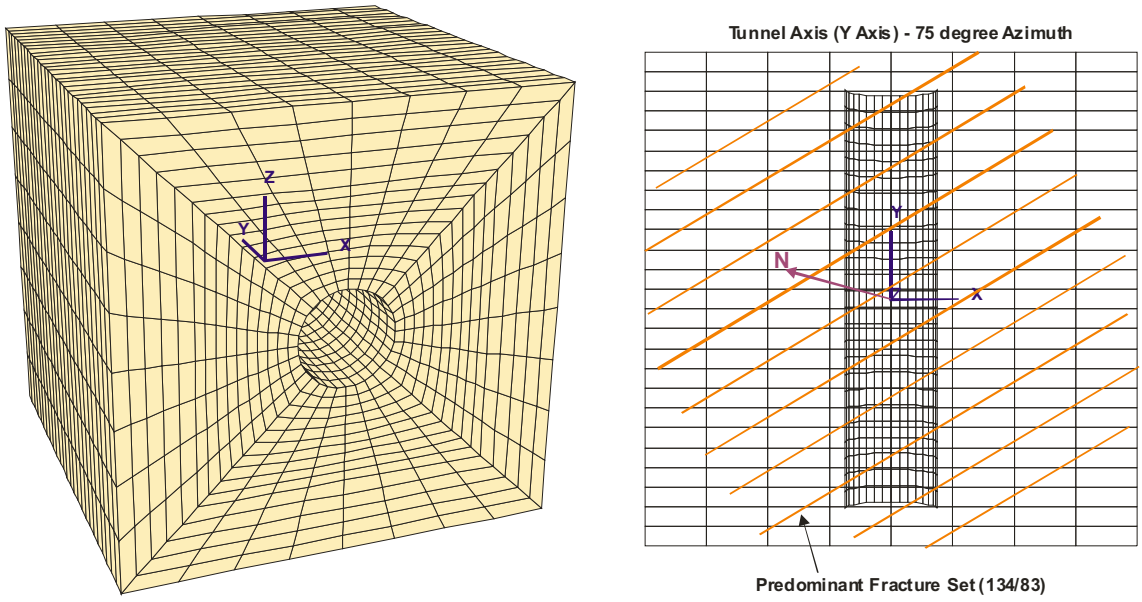

Figure 6-96. FLAC3D Model Mesh and Fracture Orientation

Figures 6-97 to 6-99 show the yield state, in-plane shear stress contours, and principal stress tensor for the 5×10^{-4} preclosure seismic analysis after approximately 29 seconds of ground motion. The same set of figures for the postclosure seismic analysis is presented in Figures 6-100 to 6-102. Yielding is confined within an element around the opening for the 5×10^{-4} preclosure analysis as shown in Figure 6-97. The drift appears to be stable for the entire duration of seismic shaking in this case. However, extensive yielding is observed in the model region for both the 1×10^{-4} preclosure and postclosure seismic analyses. The extensile stresses imposed by the large amplitude of seismic motion exceed the in situ compressive stress on the ubiquitous joint planes, tensile and shear failure is observed at these planes. The stress path of shear and normal stresses at the roof projected onto the predominant joint plane are presented in Figures 6-103 and 6-104 for the preclosure (5×10^{-4} seismic ground motion) and postclosure (1×10^{-6} seismic ground motion set 1) analyses, respectively. Perturbation of stresses is minor in the preclosure case, whereas large stress variation is observed in the postclosure case. The stress states at the predominant joint plane reach the Mohr-Coulomb failure envelope under the postclosure seismic motion as shown in Figure 6-104.

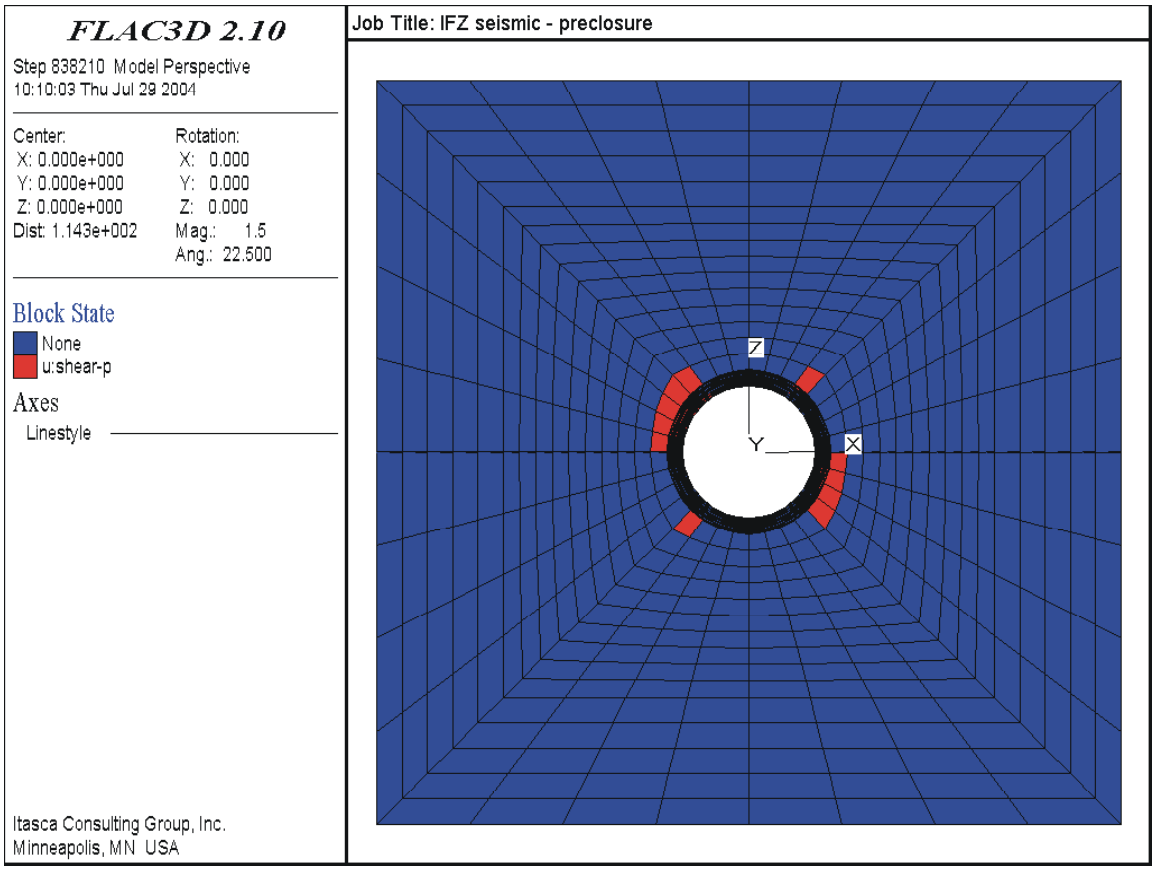

Figure 6-97. Yield State Prediction - 5×10^{-4} Preclosure Ground Motion at 29 Seconds

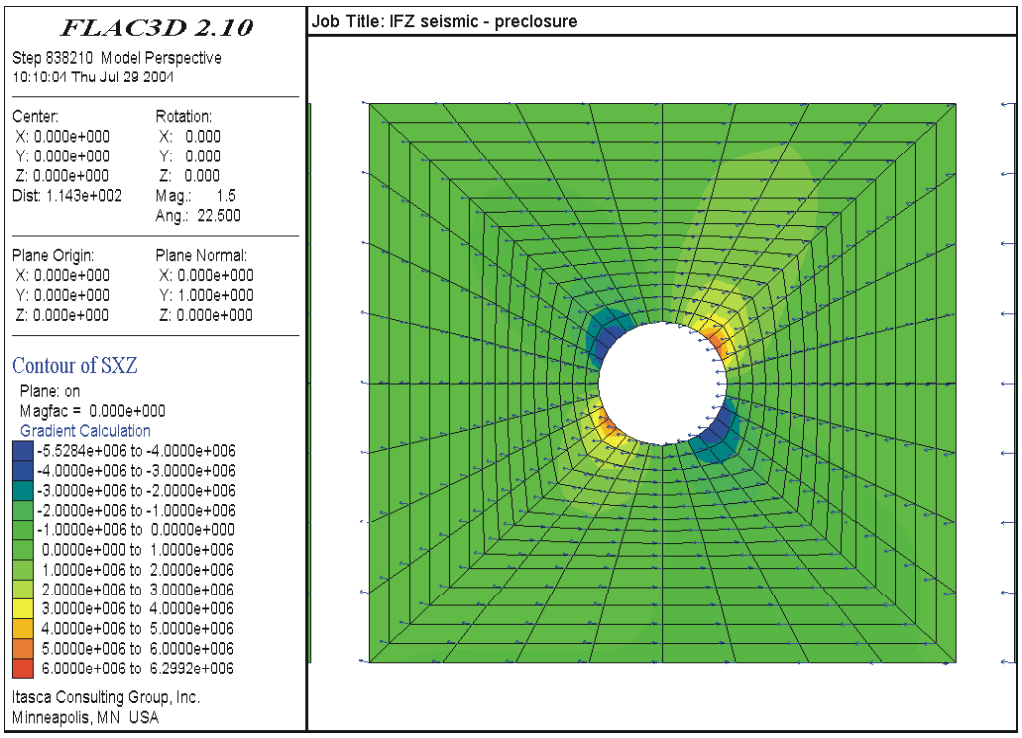

Figure 6-98. In-Plane Shear Stress Contours - 5×10^{-4} Preclosure Ground Motion at 29 Seconds

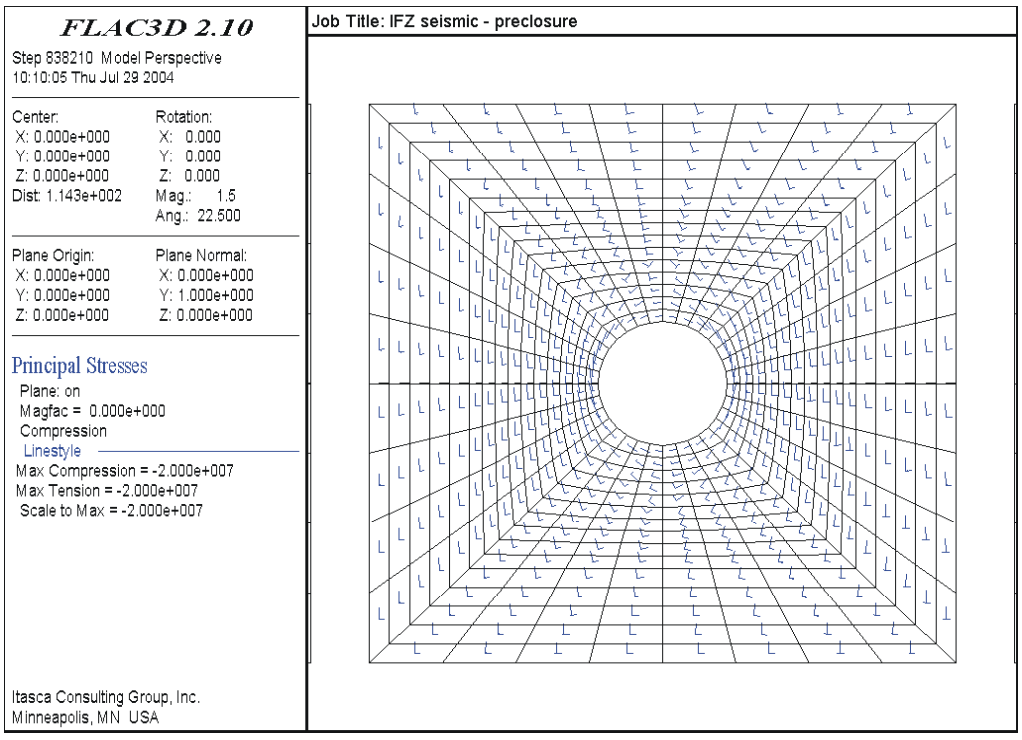

Figure 6-99. Principal Stress Tensor - 5×10^{-4} Preclosure Ground Motion at 29 Seconds

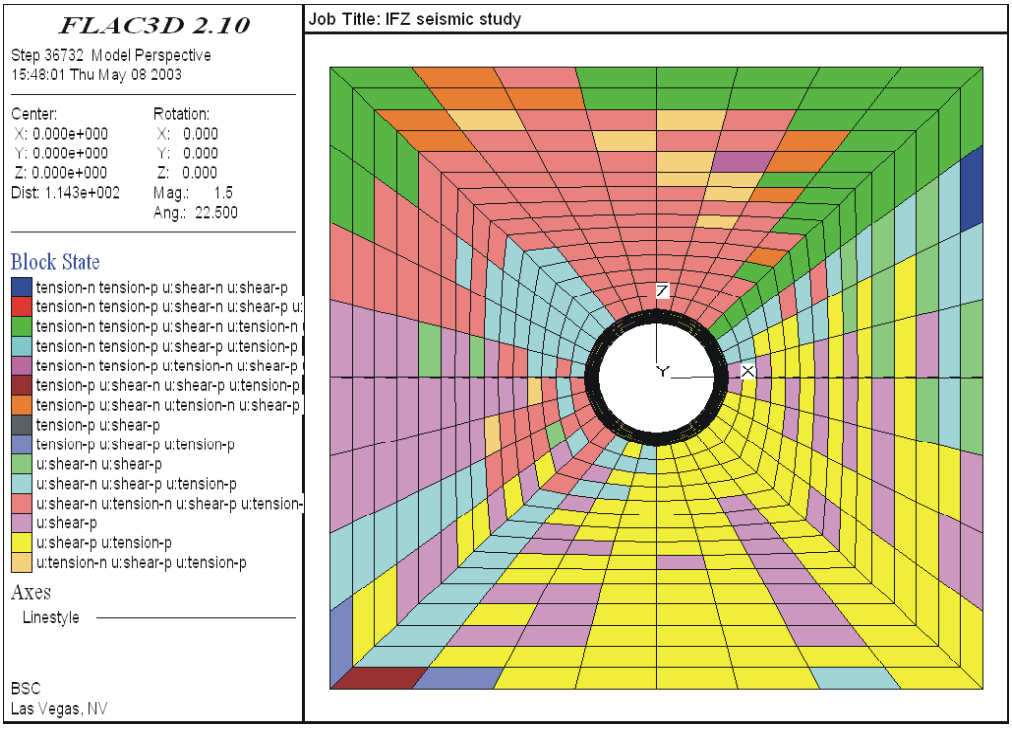

Figure 6-100. Yield State Prediction - Postclosure Ground Motion at Two Seconds

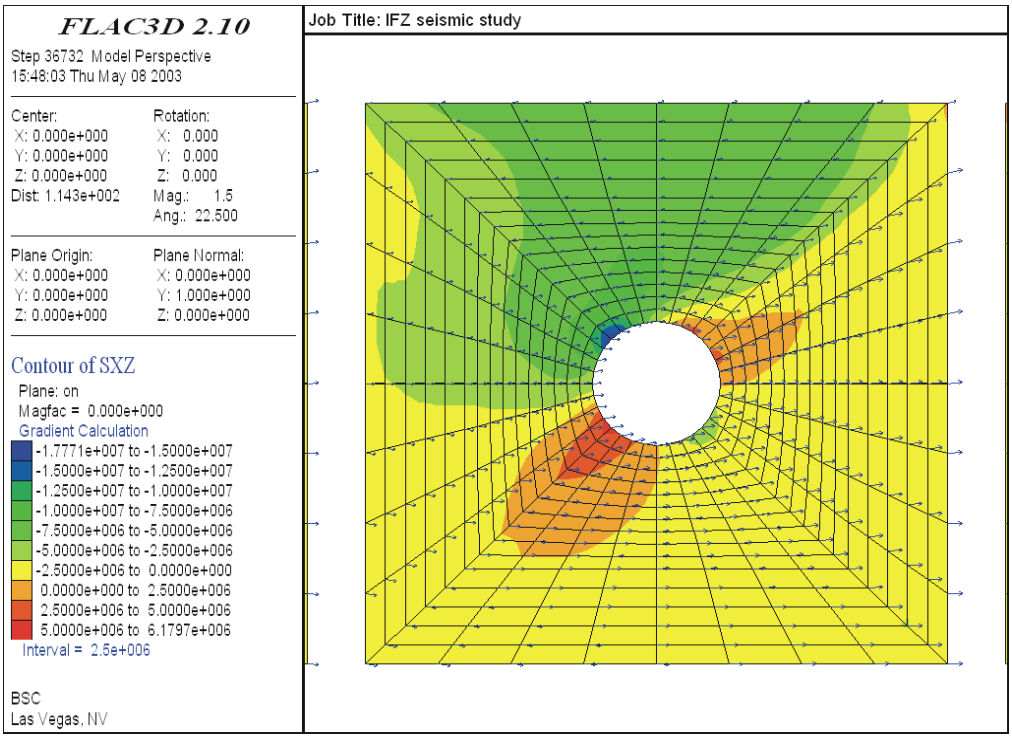

Figure 6-101. In-Plane Shear Stress Contours - Postclosure Ground Motion at Two Seconds

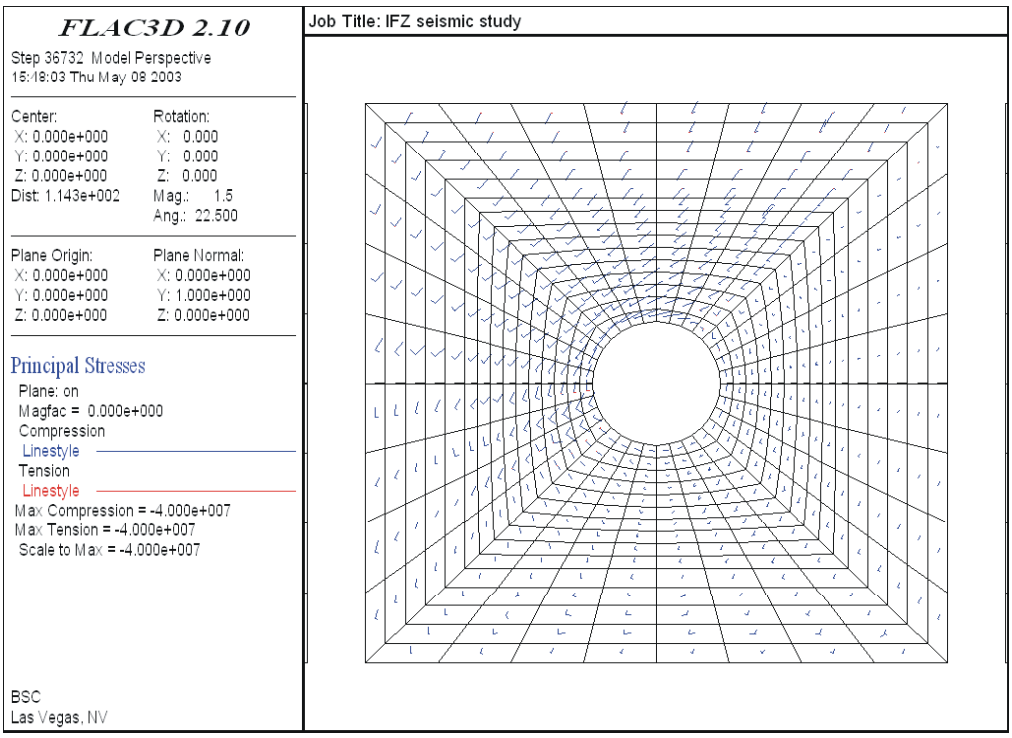

Figure 6-102. Principal Stress Tensor - Postclosure Ground Motion at Two Seconds

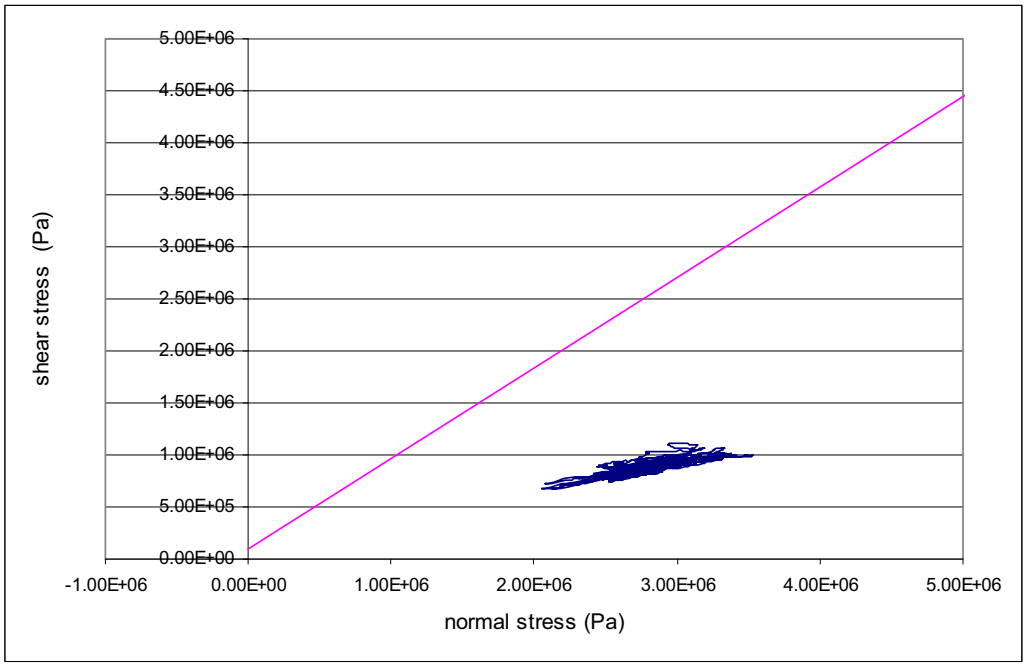

Figure 6-103. Stress Path at Roof Under Preclosure Seismic Motion

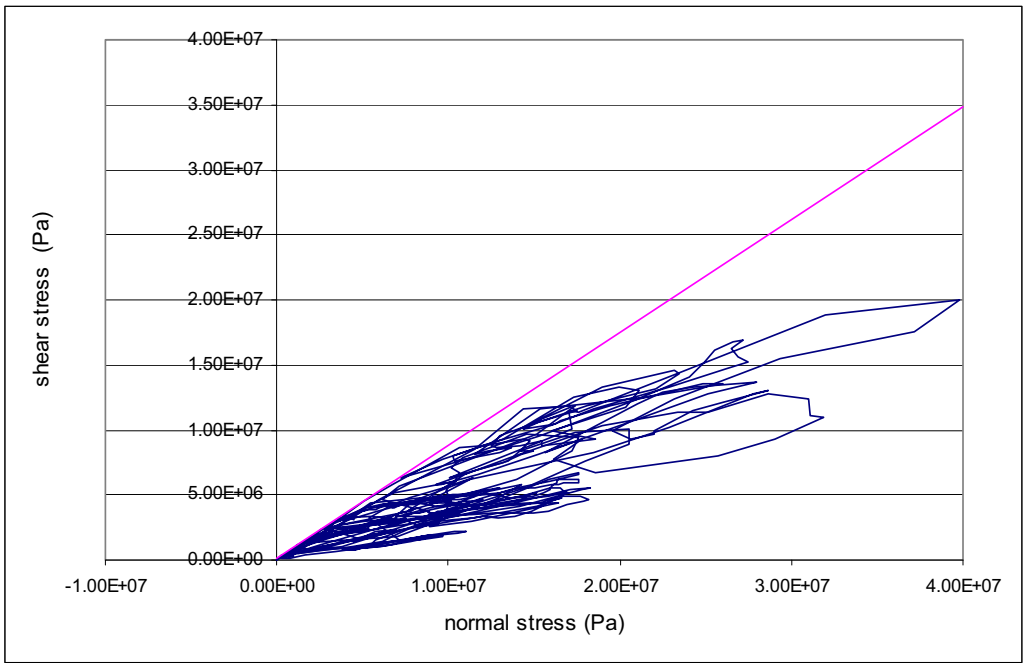

Figure 6-104. Stress Path at Roof Under Postclosure Seismic Motion

The ubiquitous joint model used in the analysis considers through-going joints in the model region. However, rock bridges do exist and will provide additional strength to resist the extensile and shear strains induced by the seismic motions. The prediction of yielding in the model region for the postclosure ground motion is therefore conservative. Based on the FLAC3D analysis results presented in this section, and the spalling type of failure predicted in Section 6.3.1.6, extensive failure around the drift opening is likely.

6.3.3 Impact of Small-Scale Fractures on Rockfall in Nonlithophysal Units

Small-scale fractures were mapped in six 6-m panels (DTN: GS040108314224.001 [DIRS 169591]) as described in Section 6.1.4.1. Two of the six panels are located in the Tptpmn unit (Stations 11+15 and 13+00). The small-scale fracture data in these two panels are used in this study to determine their impact to block formation. The ranges of fracture traces mapped in these two panels are tabulated in Table 6-37 and presented in Figure 6-105. As shown in Figure 6-105, the fracture trace length distributions are the typical negative exponential nature with the concentration in the range of 10 cm to 20 cm. The fractures with trace lengths longer than 1 m account for less than 20 percent of the fractures mapped in these two panels.

Due to the extraordinary computational effort, it is not practical to incorporate the small trace length fractures into a distinct block code, such as 3DEC used in the seismic and thermal analysis presented in Section 6.3.1. The probabilistic key-block code DRKBA, with an efficient key-block simulation algorithm, is therefore selected to assess the impact of small-scale fractures to rockfall. The assessment is based on a static condition with comparison of the results of two cases: including the small-scale fractures and excluding the small-scale fractures.

Table 6-37. Range of Fracture Traces in Panels 11+15 and 13+00

Trace Length Bin(m)	Frequency	Cumulative %
0	0	.00%
0.1	87	22.25%
0.2	112	50.90%
0.3	53	64.45%
0.4	31	72.38%
0.5	12	75.45%
0.6	9	77.75%
0.7	5	79.03%
0.8	3	79.80%
0.9	7	81.59%
1	8	83.63%
1.1	10	86.19%
1.2	2	86.70%
1.3	6	88.24%
1.4	0	88.24%
1.5	4	89.26%
2	12	92.33%
2.5	9	94.63%
3	7	96.42%
More	14	100.00%

NOTE: See *small scale filtering.xls* file in Appendix A.

Because the fractures with trace lengths greater than 1 m have already been accounted for in the existing joint data for DRKBA analysis, the fractures included in the 6-m panels were first filtered out. Additionally, fractures with trace lengths less than 15 cm are filtered out to reduce the computational effort for key-block analysis. This criterion is reasonable because the block volume formed by small traces less than 15 cm would be too small to be considered relevant to the damage of waste package or drip shield. The orientation of the remaining small-scale fractures is presented in the fracture pole plot as shown in Figure 6-106.

6.3.3.1 DRKBA Comparative Analysis

For the comparative analysis, the primary excavation is a horizontal 3-m diameter drift trending 75 degrees. The region around the excavation has been modeled with a grid consisting of 2,744,000 nodes. The nodes are spaced 15 cm (0.5 ft) apart, with each node representing 0.0035 cubic meters (0.125 cubic foot) of the rock mass. The smaller size tunnel is used because of the excessive computer memory required for the mesh compatible to 5.5-m diameter drift. Because of the comparative nature of the analysis, and the focus of small-scale fractures in this analysis, the smaller size tunnel is justified.

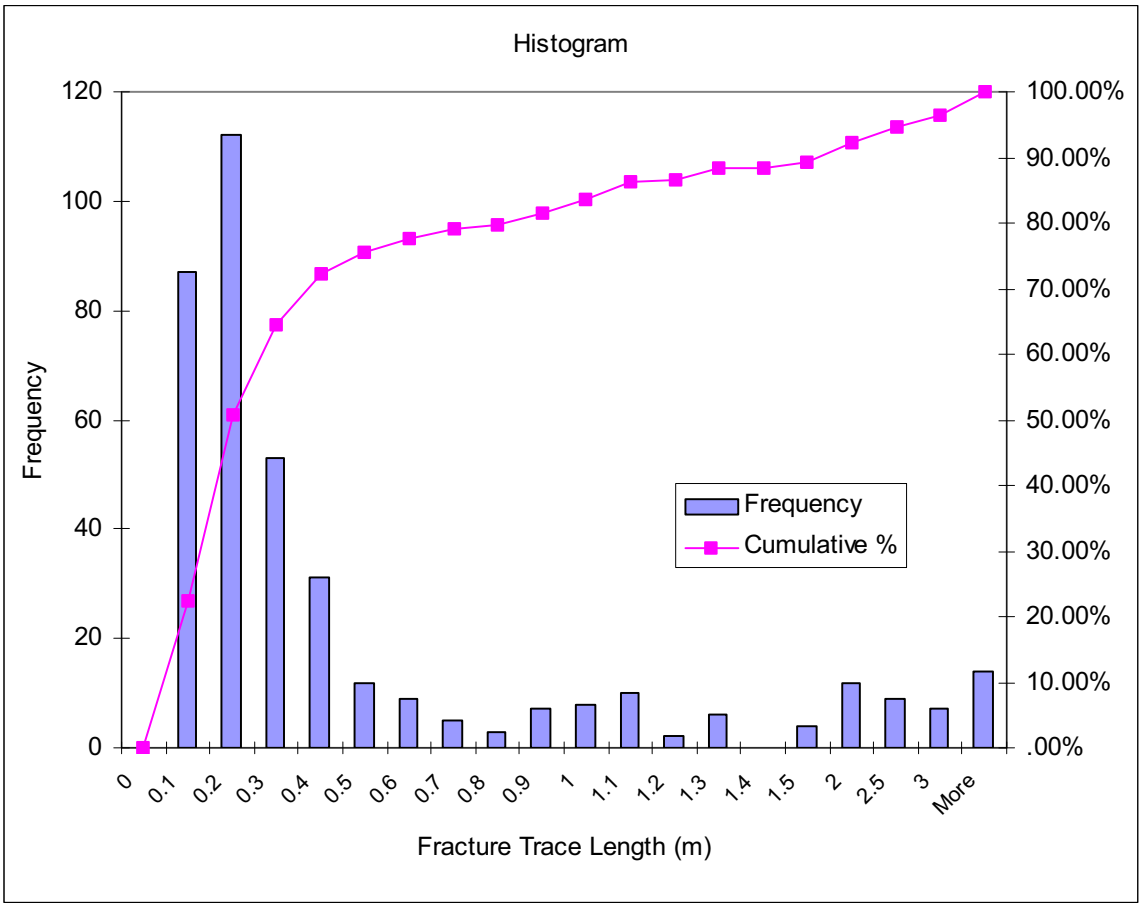

NOTE: See *small scale filtering.xls* file in Appendix A.

Figure 6-105. Histogram Fracture Traces in Panels 11+15 and 11+30

For each Monte Carlo simulation, an 18.3-m long (60-ft) tunnel has been modeled in three-dimensional space. Eighteen plane equations were used to describe the circumference of the circular tunnel. In addition, two plane equations were used to describe each end of the tunnel. Random joint patterns are generated with joint centers positioned in three-dimensional space, considering each joint set in sequence for each Monte Carlo simulation. The forming of key blocks is therefore different in each Monte Carlo simulation. Four hundred Monte Carlo simulations were used in this analysis.

In addition to the four joint sets identified based on the mapped fractures data with trace length greater than 1m (Section 6.1), a random set representing the small-scale fractures is included in the DRKBA analysis for the case considering the small-scale fractures. The required input parameters for each individual joint set and its derivation are provided in Appendix D. Cohesion and friction angle of the joints are simulated with the bivariate normal distribution. Mean and standard deviation for the cohesion and friction angle are provided in Appendix E. Cohesion values were conservatively reduced, providing increased rockfall (Appendix D, Section D2).

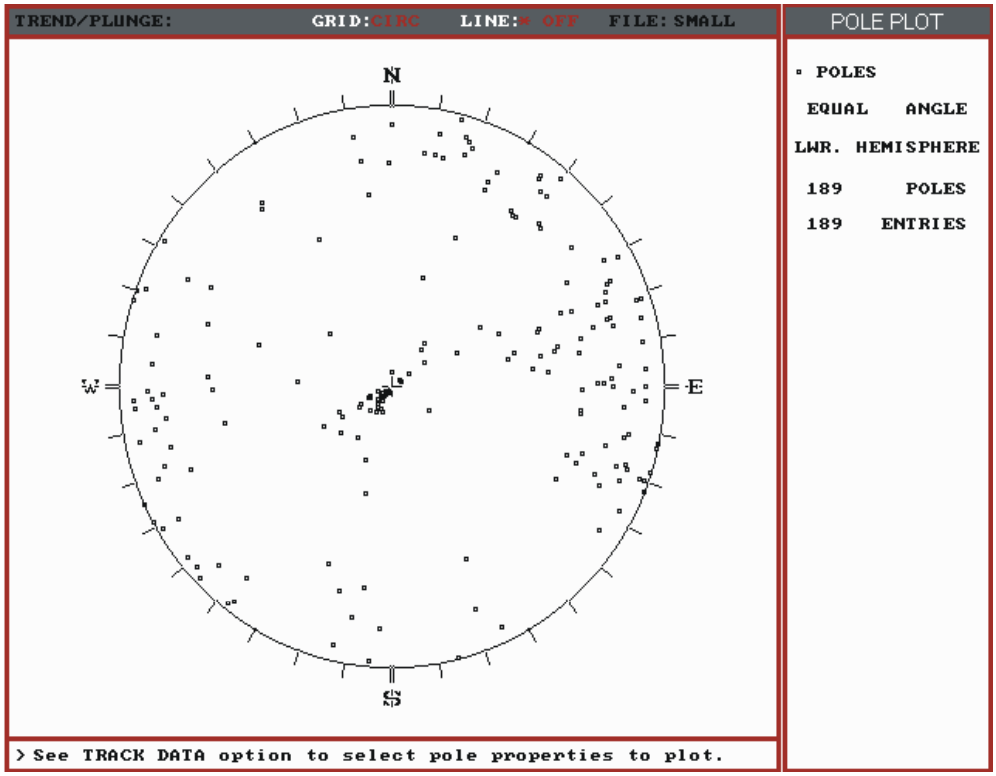

Figure 6-106. Pole Plots for the Filtered Small-Scale Fractures

6.3.3.2 Comparison of Analysis Results

Figure 6-107 presents the key-block analysis results in the format of cumulative frequency of occurrence for both cases. The cumulative frequencies of occurrence corresponding to 50-, 75-, 90-, 95-, and 98-percentile block volume for each unit are listed in Table 6-38. The maximum block sizes predicted from the analyses are also presented in this table. In general, the block size predicted considering the small-scale fractures is smaller than the case without including the small-scale fractures as shown in Table 6-38. The maximum block predicted is 7.4 cubic meters for the case without small-scale fractures compared with 3.25 cubic meters for the case including the small-scale fractures. The results also show that by considering the small-scale fractures, more blocks would form. Three hundred and forty-seven blocks were generated in the case with inclusion of the small-scale fractures, compared to 325 blocks predicted in the case without the small-scale fractures. The results are summarized in Table 6-39. Approximately 10 percent more blocks are predicted when considering the small-scale fractures. It is therefore concluded that small-scale fractures have a minor impact on key-block development in the nonlithophysal units.

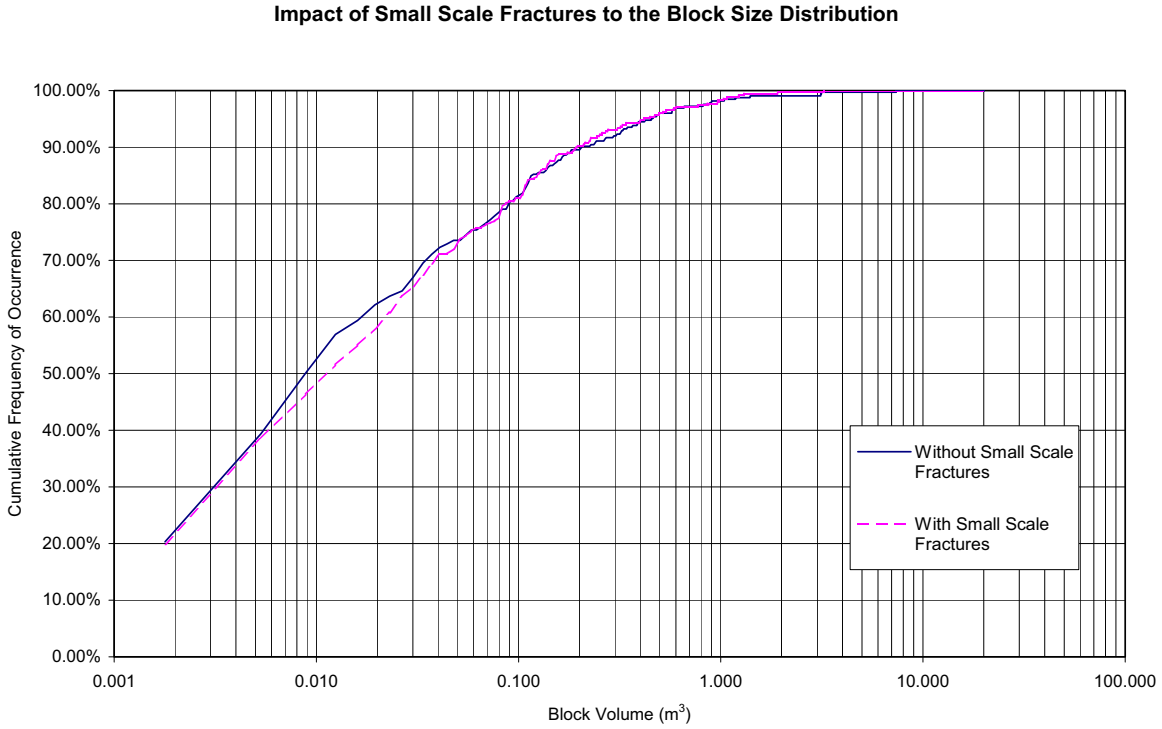

Figure 6-107. Block Size Distribution Predicted from DRKBA Analyses

Table 6-38. Block Volume (in cubic meter) Corresponding to Various Levels of Predicted Cumulative Frequency of Occurrence

Cumulative Frequency of Occurrence	Without Small-Scale Fractures	With Small-Scale Fractures
50%	0.01	0.01
75%	0.05	0.05
90%	0.20	0.19
95%	0.45	0.42
98%	0.90	0.97
100%	7.36	3.25

NOTE: Calculation of block volumes documented in Appendix D (Section D11).

Table 6-39. Summary of Results for DRKBA Comparative Analysis

	Without Small-Scale Fractures	With Small-Scale Fractures
Total Number of Blocks	325	347
Number of Blocks per km	44	47
Total Volume of Blocks (m^3)	38.0	32.0
Volume of Blocks per km (m^3/km)	5.2	4.4

NOTE: Calculation of block information is documented in Appendix D, Section D11; and Appendix A (small scale fracture *results.xls*).

6.3.4 Drift Profile and Block Geometry Prediction in Nonlithophysal Units

The distinct block approach applied in this analysis has provided an assessment of existing fracture data to determine probable occurrences of rock blocks that would fall onto the drip shield in the absence of ground support. The 3DEC approach considers progressive block failure, such that when an initial rock block fails and is removed, an additional failure surface may open up allowing other blocks to fall. Progressive block failure continues until the crown becomes geometrically and mechanically stable, and no additional blocks can fall. The final progressive failure surface provides the basis for the drift profile predictions presented in this section.

The deteriorated drift profiles from selected simulations are shown in Figures 6-108 to 6-114. These profiles were the outcome of the 3DEC analysis with the rock mass and opening subject to in situ and seismic loadings. In general, the drifts are more stable under the thermal loading as shown in Sections 6.3.1.3 and 6.3.1.4; the drift profiles for the cases considering thermal loading are not included.

The selected drift profiles include the profiles with the greatest and median rockfall cases for the 1×10^{-5}, 1×10^{-6}, and 1×10^{-7} hazard levels (Figures 6-108 and 6-111). In addition, the greatest rockfall profile for the preclosure consideration (1×10^{-4} hazard level) is shown in Figure 6-114. The median case profile is selected as the 50 percentile among the simulations predicting rockfall for the given hazard level. The median case profile ranking was based on the total rockfall volume within the simulation. Due to the limited amount of rockfall predicted for the 1×10^{-4} seismic hazard, only the greatest rockfall profile is presented. The total rockfall volume and the number of blocks predicted for each simulation presented are listed in Table 6-40. The profile for each simulation includes the side view and perspective view of the drift with predicted fallen blocks. Also included are selected cross sections at the locations indicated in the side view figure. Failure of intact rock bridges may occur for the postclosure level of ground motions as described in Section 6.3.1.6. Additional break up of rock around the opening is likely when subject to postclosure level of ground motions.

The drift profile for the intensely fractured zone cannot be directly obtained from the FLAC3D ubiquitous joint model (described in Section 6.3.2) because the model is a continuum. Considering the small yield zone shown in Figure 6-97 for the preclosure ground shaking, minor spalling is expected along the sidewall for the preclosure period. However, severe spalling is likely for the seismic shaking due to postclosure ground motions with an extensive yield zone shown in Figure 6-100. It is estimated that the likely profile for the intensely fractured zone with the postclosure consideration will be similar to Figure 6-90.

There are many different sizes and shapes of rock blocks predicted to impact the drip shield. Because block geometry information is mainly used for drip shield impact calculations, the geometry of large blocks is provided in this section. A total of 7 blocks simulated were selected, each with a volume greater than 6 metric tons. The block geometric information for each individual block is presented in Appendix I (Figures I-1 to I-7).

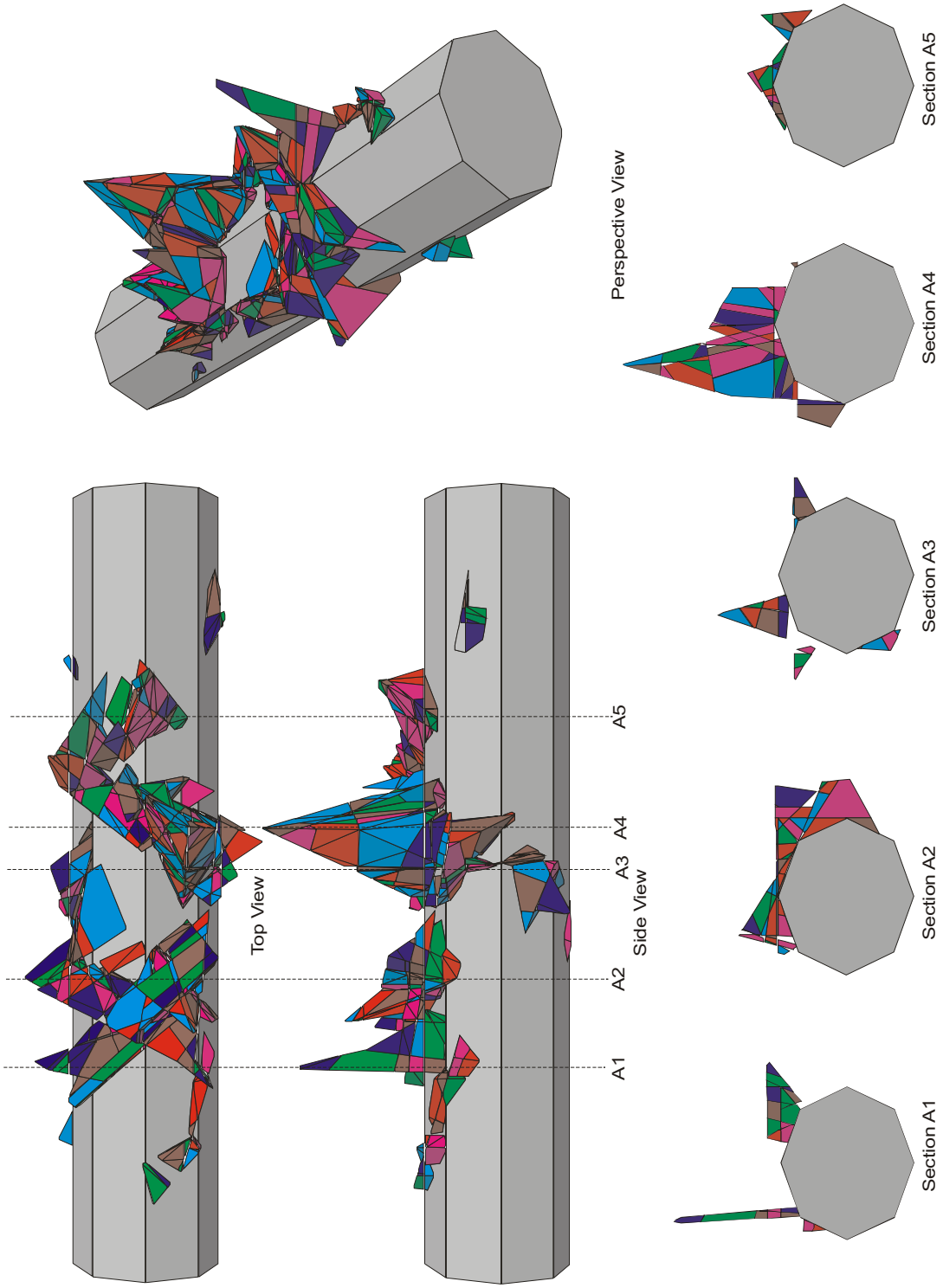

Figure 6-108. Drift Profile for 1×10^{-7} Hazard Level, Case with Greatest Amount of Rockfall

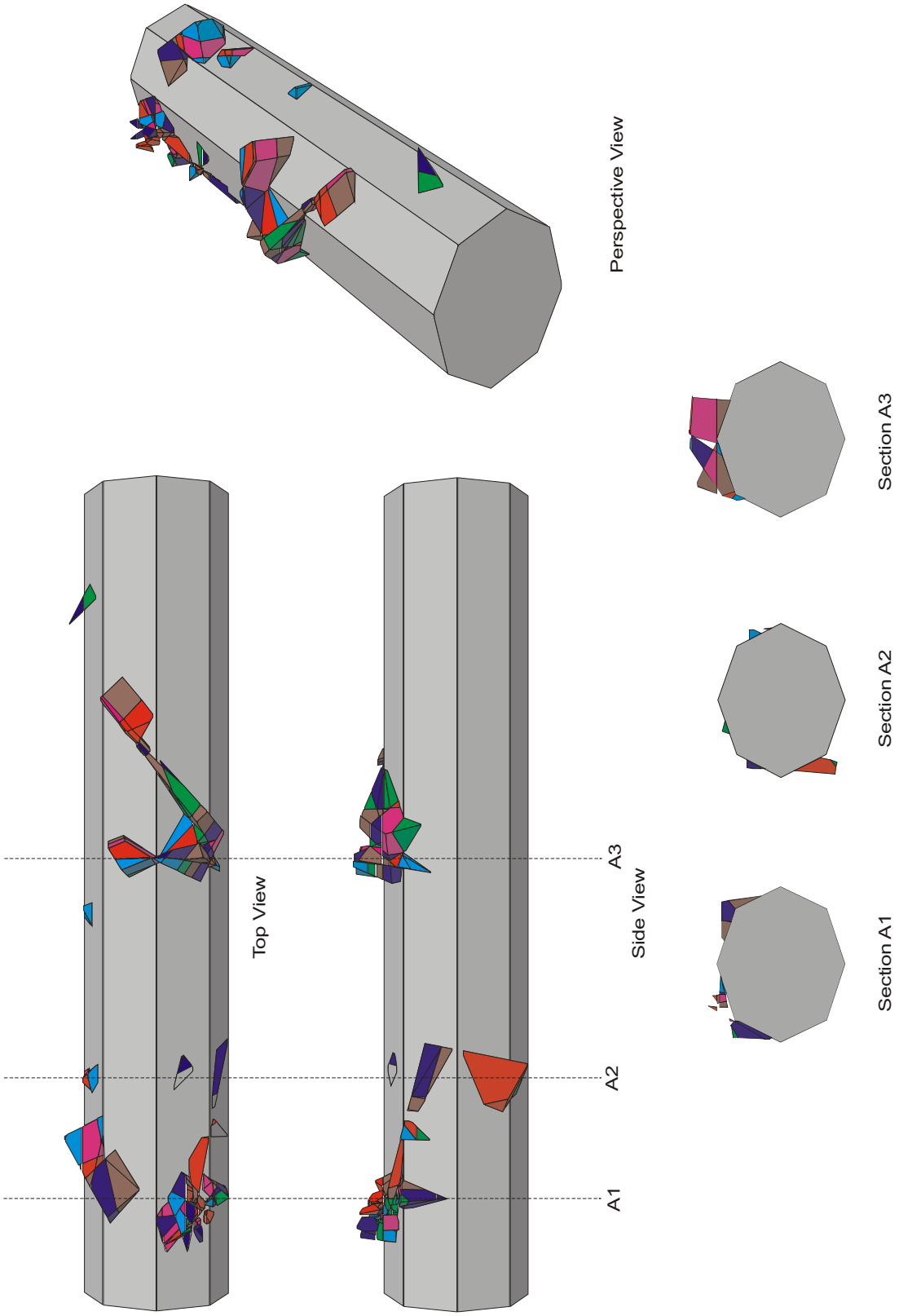

Figure 6-109. Drift Profile for 1×10^{-7} Hazard Level, Median Rockfall Case

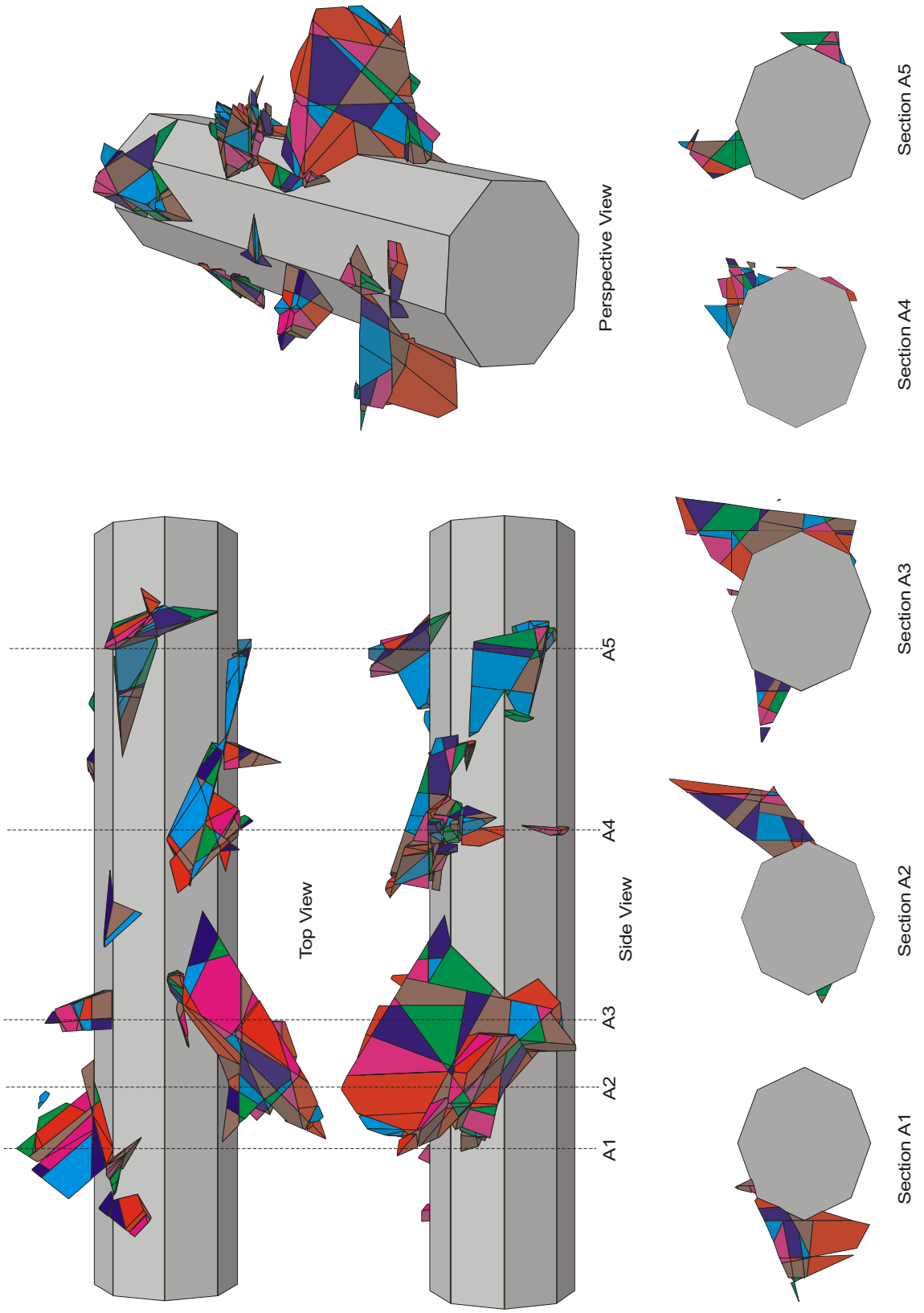

Figure 6-110. Drift Profile for 1×10^{-6} Hazard Level, Case with Greatest Amount of Rockfall

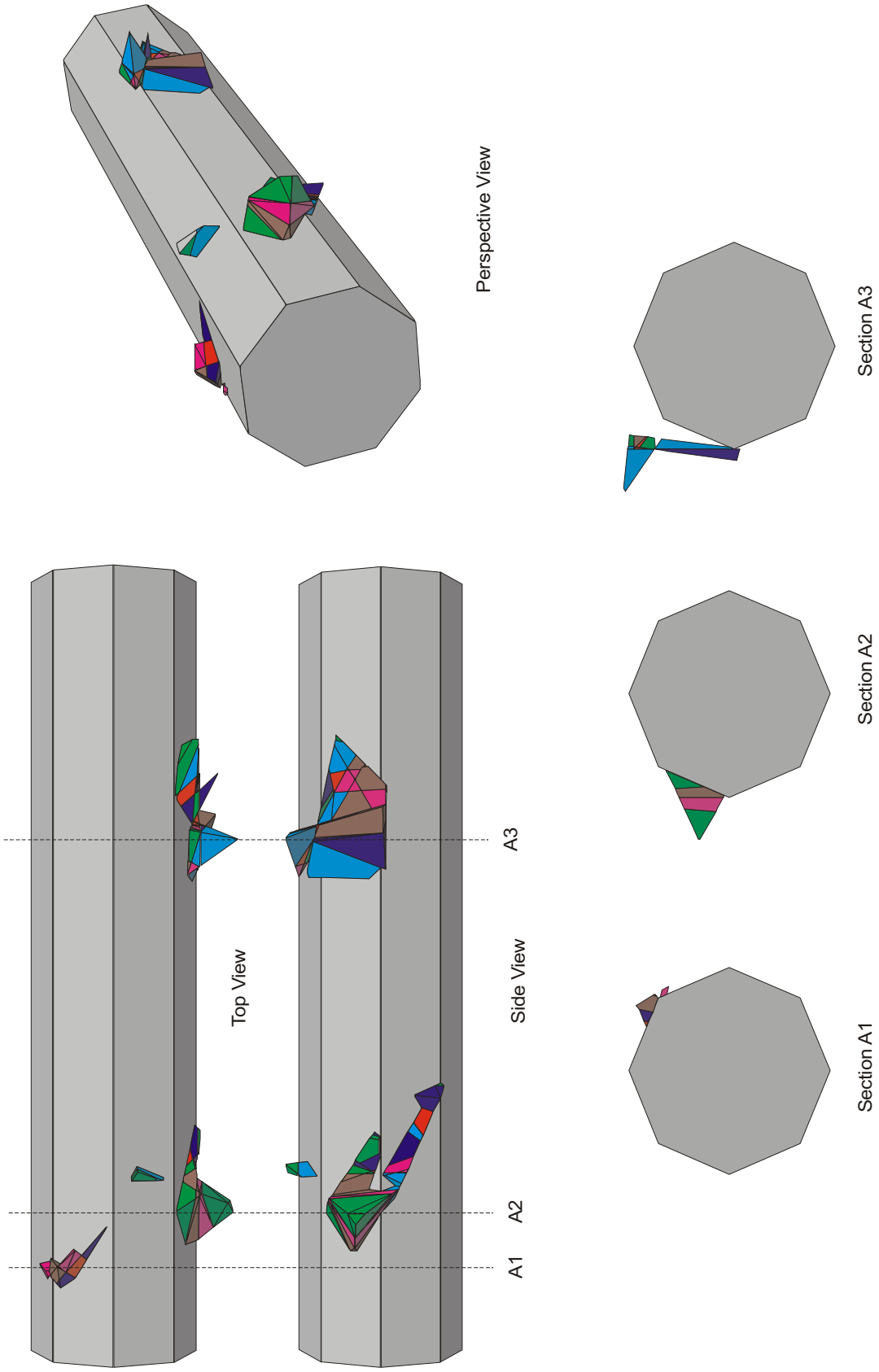

Figure 6-111. Drift Profile for 1×10^{-6} Hazard Level, Median Rockfall Case

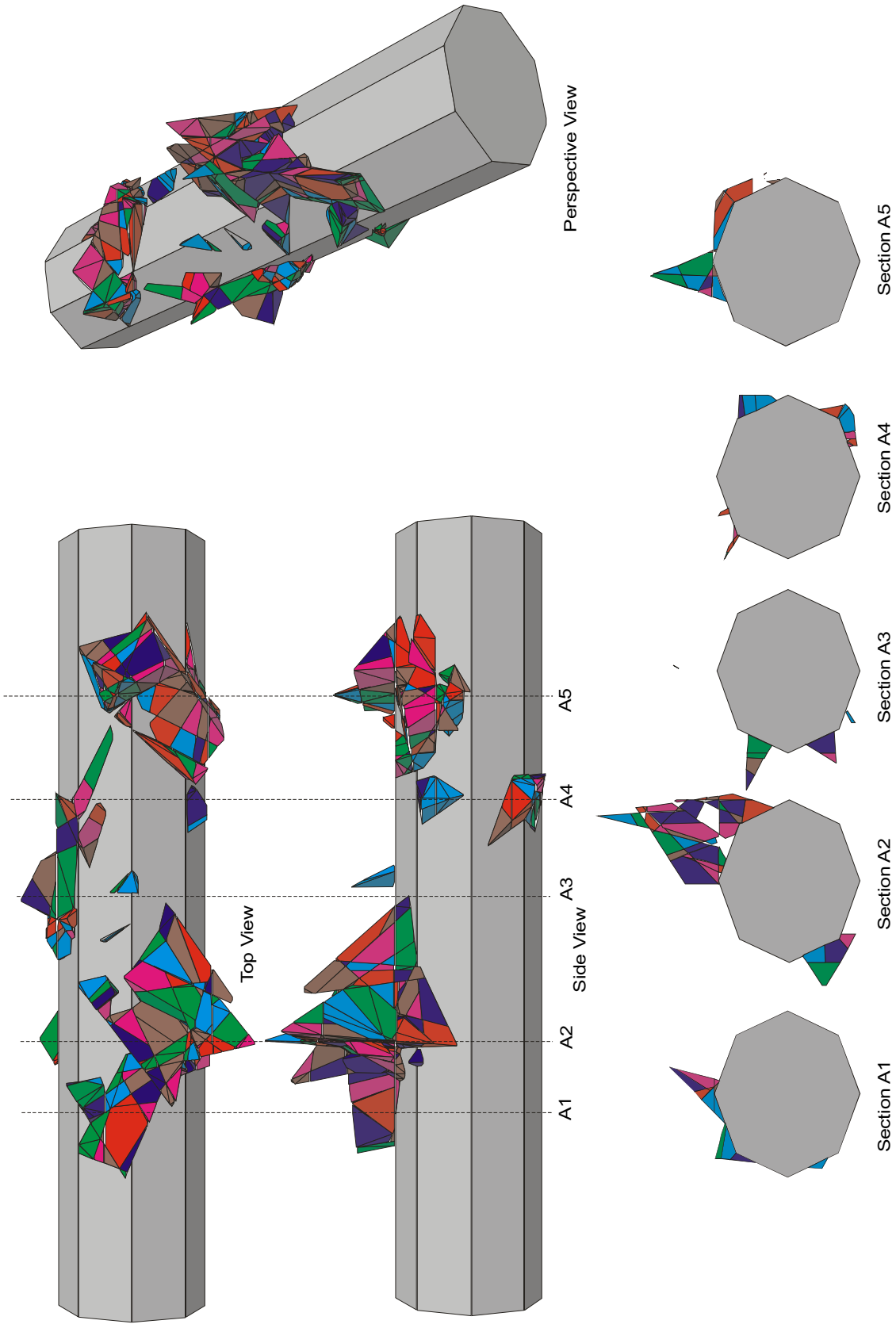

Figure 6-112. Drift Profile for 1×10^{-5} Hazard Level, Case with Greatest Amount of Rockfall

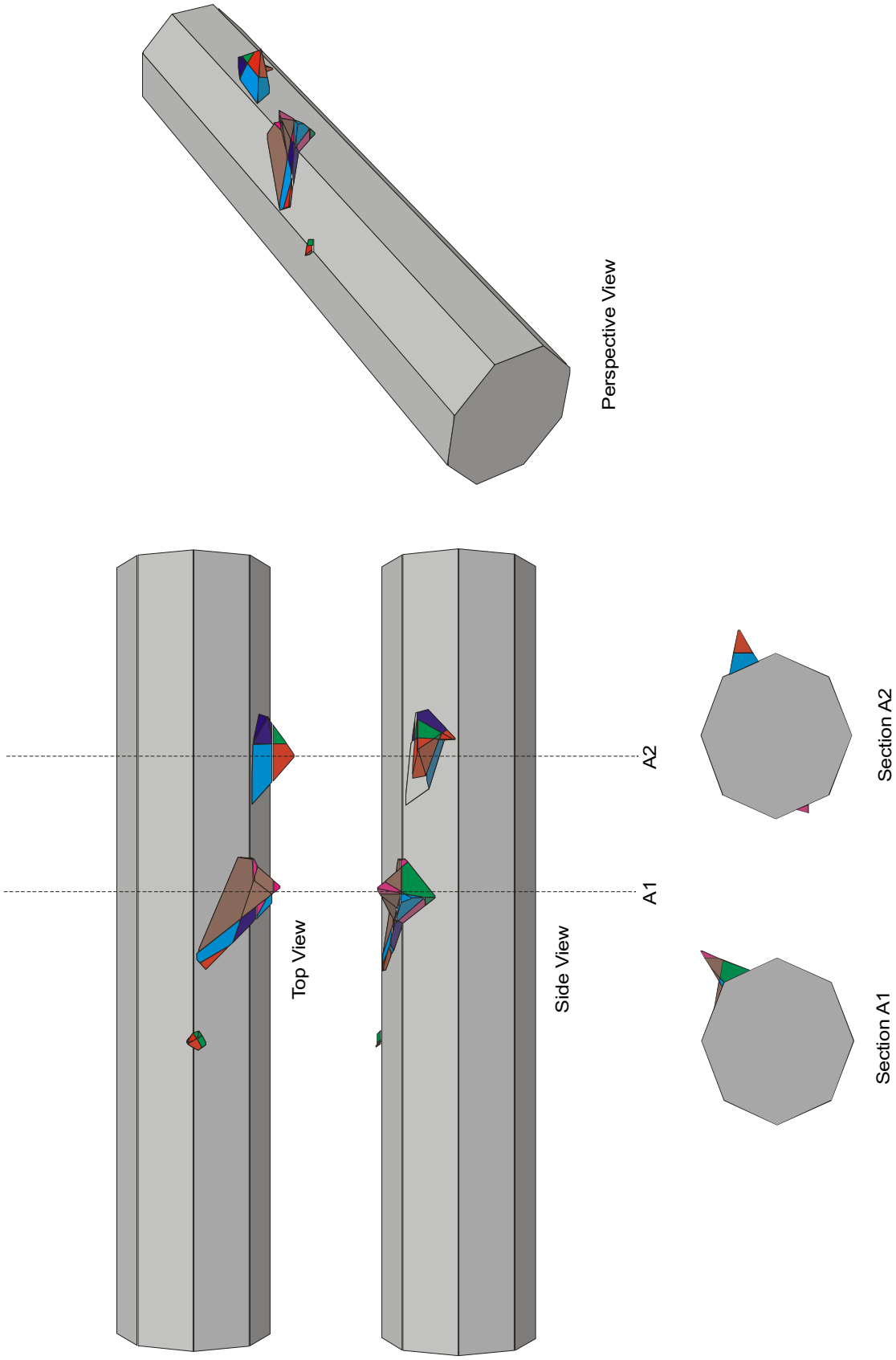

Figure 6-113. Drift Profile for 1×10^{-5} Hazard Level, Median Rockfall Case

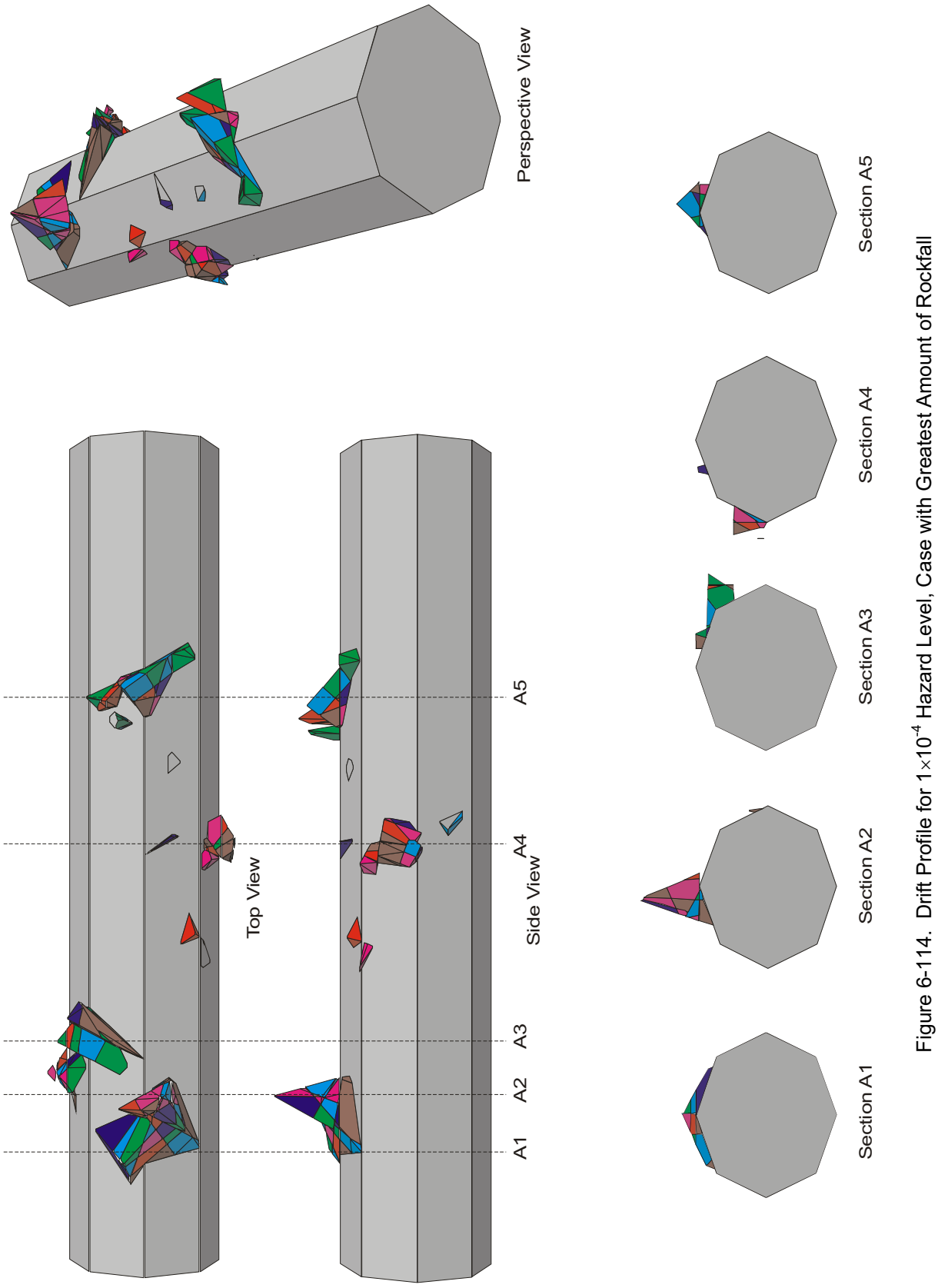

Figure 6-114. Drift Profile for 1×10^{-4} Hazard Level, Case with Greatest Amount of Rockfall

Table 6-40. Predicted Number of Rockfall and Volume for the Presented Drift Profile

Simulation	Number of Blocks	Total Volume (m^3)
1×10^{-7} hazard, worst case profile	269	58.93
1×10^{-7} hazard, median case profile	77	10.43
1×10^{-6} hazard, worst case profile	167	63.33
1×10^{-6} hazard, median case profile	36	5.19
1×10^{-4} hazard, worst case profile	62	7.17

6.4 ROCKFALL IN THE LITHOPHYSAL UNITS

6.4.1 Problem Approach

6.4.1.1 Estimate of Block Size

Analysis of rockfall in the lithophysal units presents a significantly different problem than that given in the previous section with regard to nonlithophysal rocks. In general, the nonlithophysal rocks are composed of strong, intact blocks of welded tuff that are separated by fracture planes. The fracture surfaces provide the primary weaknesses in the system and control the failure mode and resulting rock block dimensions. For this reason, it is necessary that the fracture planes be explicitly represented within the model to allow estimation of block dimensions, masses, and velocities.

Lithophysal units, particularly the Tptpll, are characterized by lithophysal voids interconnected by intense fracturing. Fracture sets are not as clearly defined as in the Tptpmn. Average fracture spacing is less than 1 m and, at certain locations, this spacing is much smaller, on the order of 0.1 to 0.3 m (as discussed in Section 6.1.4.1). In addition to fracturing on different scales, the lithophysal rock mass is characterized by the presence of almost uniformly distributed holes (lithophysae) of varying size (from less than 1-cm to greater than 1-m in diameter). The lithophysae account for up to about 30 percent of the rock mass volume (see Section 6.1.4.2 for a detailed discussion on lithophysae). It is assumed in the following analyses that, when stressed beyond its strength limits, the lithophysal rock mass will break into relatively small block sizes controlled by the spacing of natural fractures (Section 5.2.2). Therefore, as opposed to the 3DEC modeling of the Tptpmn, the modeling of the lithophysal rock does not attempt to calculate the block sizes resulting from yield but considers them to be on the order of 0.1 to 0.3 m (or smaller) in dimension. The models developed here are discontinuum models in which the rock mass is discretize into random block sizes with dimensions on the order of 0.1 to 0.2 m.

6.4.1.2 Approach to Modeling of Lithophysal Rock–Homogeneity and Bounding Rock Mass Properties Estimates

Lithophysal Porosity and Consideration of a Homogeneous Rock Mass–The size of the internal lithophysae structure and fracture spacing is much smaller than the drift size (i.e., 5.5-m diameter). There is no preferred direction in the fracture or lithophysae orientation that would justify introduction of anisotropy into drift scale modeling. As discussed in Appendices E, O, and T, lithophysal porosity varies in a bedded or stratiform fashion with layering orientation

coincident with the dip of the Tptpll. For example, the areas of highest lithophysal porosity (i.e., greater than about 20 percent) lie in a thin band in the upper portion of the Tptpll unit, just below the contact with the Tptpmn. Here, the largest lithophysae are also found. The lowest levels of lithophysal porosity are found near the bottom of the Tptpll where it grades into the nonlithophysal Tptpln. Figure 6-115 is a histogram that shows the variability in lithophysal porosity for the entire Tptpll as obtained from angular traverse measurements in the ECRB Cross-Drift.

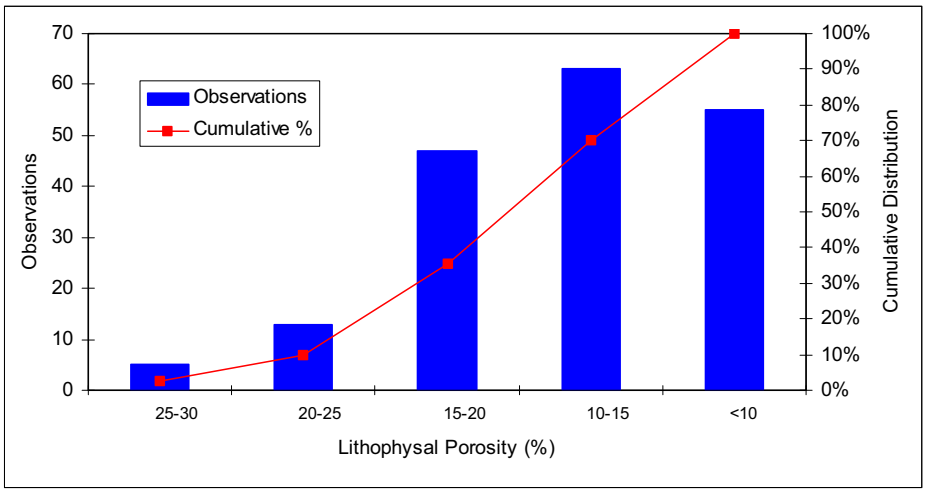

NOTE: Lithophysal porosity data are from ECRB Cross-Drift station 14+44 to 23+26 (Appendix O, Section O6.6; see Microsoft Excel file, *Drift Deg AMR AF T-A-P Fit.xls*, worksheet "Volume Percent - Stats", which can be accessed through the Technical Data Management System using DTN: MO0408MWDDDMIO.002).

Figure 6-115. Histogram of the Percentage of Lithophysal Porosity as Determined from Field Measurements in the ECRB Cross-Drift Taken on 5-m Intervals

This figure shows that about 10 percent of the Tptpll is composed of a rock mass with lithophysal porosity levels greater than 20 percent. These levels tend to be concentrated near the top of the unit. Approximately 25 percent of the Tptpll has lithophysal porosity between 15 and 20 percent, approximately 35 percent with lithophysal porosity between 10 and 15 percent, and approximately 30 percent with lithophysal porosities less than 10 percent.

As discussed in Appendix E, the lithophysal rock mass strength and Young's modulus are dependent on the percentage of lithophysal porosity. The initial base case approach taken to modeling of this rock mass, is to subdivide the rock mass strength and modulus into a series of "categories" based on lithophysal porosity percentage. The rock mass strength and modulus are determined from large-diameter core testing of lithophysal rocks as well as numerical extrapolations using the Particle Flow Code program (PFC). The process of estimation of rock mass properties is given in detail in Appendix E.

Parameter studies are then conducted to examine the mechanical response of emplacement drifts to in situ, thermal, and seismic stressing considering homogeneous rock mass properties (i.e., constant lithophysal porosity) for a given drift cross section. Since the modeling is conducted for the complete range of properties represented by the "categories," the full range of response is examined. To examine the conservatism inherent in this approach (i.e., the use of parametric

studies based on the consideration of a homogeneous rock mass and a range of rock mass properties) additional analyses are conducted in which the spatial variability of the rock mass lithophysal porosity is taken into account. Appendix T describes a model of the spatial variability of lithophysal porosity within the Tptpll, based on field mapping studies. This three-dimensional geometric model of the Tptpll lithophysal porosity is sampled to create two-dimensional cross section representations that can be used for investigation of spatial variability on both rock mass properties and drift stability. As discussed in Appendix E, these representations are used for investigation of the impact of spatial variability of porosity on the ultimate strength and modulus of the rock mass. The discussion in Appendix E compares the laboratory test data to these spatial variability examinations. It is confirmed that the lowest ranges of strength categories based on lithophysal porosities greater than 20 percent, do yield conservative estimates of rock mass strength. Full drift scale modeling presented in Section 6.4.2.2, again using two dimensional cross sections taken from the geometrical spatial variability representations, is used for comparison of conservatism to the base case models that consider homogeneous rock property ranges.

Base Case Rock Mass Properties–As discussed above, the assessment of rock mass properties for lithophysal rock is documented in Appendix E (Section E4.1). Large diameter room-dry and saturated laboratory testing is supplemented by numerical model extrapolations to examine the impact of in situ lithophysal porosities, shapes, sizes, and distributions on the rock mass mechanical properties. This information is used to define a set of base case mechanical properties and estimates of ranges of these properties for parameter analysis. Five base case categories were developed to represent the range of rock mass properties as summarized in Table 6-41. The validity of this approach to represent the lithophysal rock mass is discussed in Section 7.3. Categories 1 through 5 represent variability of rock mass quality throughout the repository emplacement level. These categories can be related approximately to levels of lithophysal porosity in the Tptpll (see Table 6-41).

Table 6-41. Categories of the Lithophysal Rock Mass Selected for Analysis

Category	Base Case Properties				Bounding Unconfined Compressive Strength		Estimated Lithophysal Porosity
	Unconfined Compressive Strength (MPa)	Young's Modulus, E (GPa)	Bulk Modulus, K (GPa)	Shear Modulus, G (GPa)	Lower Bound (MPa)	Upper Bound (MPa)	
1	10	1.9	1.07	0.80	10	11	35
2	15	6.4	3.54	2.65	10	23	28
3	20	10.8	6.01	4.51	10	32	21
4	25	15.3	8.48	6.36	13	40	13
5	30	19.7	10.95	8.21	16	47	7

NOTE: The calculation of rock strength properties is documented in Appendix E (Section E4.1).

6.4.2 UDEC Discontinuum Analysis of the Lithophysal Rock Mass

6.4.2.1 Model Development

The objective of the analysis presented in this section is to predict the amount of rockfall in the emplacement drifts due to:

- Drift excavation
- Stresses induced by the heat released from the waste packages
- Seismic ground motions with varying probabilities of occurrence
- Time-dependent strength degradation.

The standard approach in geotechnical engineering for solving problems of stability of underground excavations is through the use of models based on continuum mechanics. Such an approach is quite effective if the main interest is estimating stress redistribution around an opening or solving for tunnel wall displacements. However, difficulties are encountered if a continuum model is used for prediction of instability. Continuum approaches use constitutive models to describe the mechanical behavior of a material. A linearly elastic-perfectly plastic Mohr-Coulomb constitutive model is often used to represent mechanical behavior of a rock mass (i.e., see Hoek 2000 [DIRS 160705]). The material strength of a perfectly plastic Mohr-Coulomb model does not decrease as a function of plastic (i.e., post-yield) deformation. This, combined with the use of a continuum-based modeling approach,[6] means that the model of a drift may show indications of material yielding (i.e., plastic deformation) in different portions of the model, but will never actually predict rockfall. It was decided, based on these considerations, to use UDEC, a two-dimensional discontinuum program (Section 3.1) for drift stability analysis in lithophysal rock. In the UDEC lithophysal rockfall model, the rock mass is represented as an assembly of polygonal elastic blocks. As described in Section 7.6 of this report, the objective of the UDEC lithophysal rock mass model is to provide a model in which the rock mass has the proper deformability and strength characteristics of the rock mass, and will respond elastically for stresses up to its peak strength. However, after the peak strength is reached, the model must be capable of representing the failure process, including fracturing and dislodging of blocks under quasi-static and dynamic loading. This can be accomplished by subdivision of the rock mass into many blocks of approximately the same size as those that may ultimately be formed during yielding, due to the inherent ubiquitous fracturing within the Tptpll. These fractures can be bonded by the strength and stiffness values that allow correct representation of the rock mass strength and modulus given by the strength categories in Table 6-41. Prior to yielding, the fractures in the rock mass are essentially "invisible" or "incipient" and the rock mass will behave in an elastic, isotropic fashion during loading and unloading. However, once the shear or tension strength of the incipient fractures is reached, the rock mass can realistically fail through propagation of fractures and form unstable rock blocks that are free to dislodge and fall into the excavation as the forces dictate. An important aspect of

[6] A continuum model is one in which the elements used to discretize the rock mass are intimately connected at their nodal points. These elements can represent yielding in an indirect way via the use of non-linear constitutive models that relate stress to strain, but cannot fracture apart or separate as may occur in reality. Thus, partial or total collapse of a tunnel and the specific volume or mass of rockfall occurring during a simulation cannot be estimated with reliability.

this approach is that the fracture properties must be calibrated to reproduce the desired overall rock mass strength and modulus for each of the rock strength categories in Table 6-41.

The entire rock mass domain is discretized into blocks using a technique referred to as Voronoi tessellations[7] (Itasca Consulting Group 2002 [DIRS 160331]), to achieve randomly-shaped blocks of roughly uniform size. The initially-bonded fractures between blocks represent the approximate spacing and ubiquitous and random nature of the existing fracturing within the Tptpll (see Section 5.2.2), and are considered to be linearly elastic-brittle. The elastic behavior of fractures (and thus the rock mass deformability) is controlled by their normal and shear stiffnesses (fracture stiffness is constant). The initially-bonded fractures can sustain a finite tensile stress as prescribed by their tensile strength. The Coulomb slip condition governs the onset of shear failure as a function of fracture cohesion and friction angle. If a bonded fracture fails, either in tension or shear, its tensile strength, friction coefficient, and cohesion are reset to residual values. This model allows for the formation of broken fractures between blocks, and possible subsequent separation and instability (under action of gravity) of portions of rock mass around a drift. No ground support was considered in the analyses as it was considered to be non-functional in the postclosure period. The cases of thermal and seismic loading considered in this section were also analyzed using a continuum, linearly elastic approximation. The analyses were done using the finite difference code FLAC (Section 3.1) to provide both a check against the UDEC lithophysal rockfall model, and to provide an elastic-based reference for gaining insight into interpretation of the results from the complex UDEC lithophysal rockfall model.

Additional details for the justification and calibration of the lithophysal rockfall model are provided in Section 7.6. The calibration process of the UDEC block model requires calibration of the mechanical properties of the initially-bonded fractures so they reproduce the desired rock mass properties of the lithophysal rock. As stated previously, the rock mass properties are subdivided into five rock strength and modulus categories that span the range of expected lithophysal rock mass porosity. It is therefore necessary that the bonded fractures of the lithophysal rock mass be calibrated to each of these five rock mass categories. In addition, two average block sizes are examined for representation of the Tptpll fractures–0.2 m and 0.3 m. Because the rock mass properties are a function of the fracture spacing, it is necessary to calibrate the bonded fracture properties for each of these representations. The calibrated properties of the bonded fractures are listed in Tables 6-42 and 6-43 for UDEC lithophysal rockfall models with average block sizes of 0.2 m and 0.3 m, respectively. Note that, if not indicated otherwise, the analysis was done using a block size of 0.3 m.

The geometry of the UDEC lithophysal rockfall model is shown in Figure 6-116. As indicated, only the region around the drift where inelastic deformation is expected is discretized into Voronoi blocks. The rest of the model is composed of a few large, elastic blocks that act to transmit forces from the boundaries to the inner portions of the model. Verification of the proper extent of the thermo-mechanical boundary conditions of the model can be found in Appendix U. The overall stiffness of the discretized portion of the model (i.e., stiffness of blocks and joints together) is the same as the stiffness of the large elastic blocks, which represent far-field behavior. This provides mechanical compatibility of the inner and outer portions of the model.

[7] The Voronoi tessellation is simply a block discretization method available within the UDEC program that allows a rock mass to be subdivided into a number of randomly-shaped blocks that have a specified average dimension.

Table 6-42. Calibrated Properties of the Bonded Fractures and Intact Blocks in the Model with 0.2 m Block Size

Category	Friction Angle (deg)	Residual Friction Angle (deg)	Cohesion (MPa)	Tension (MPa)	Normal Stiffness (GPa/m)	Shear Stiffness (GPa/m)	Block Bulk Modulus (GPa)	Block Shear Modulus (GPa)
1	35	15	3.91	1.56	13.40	6.69	13.00	9.75
2	35	15	5.86	2.34	45.10	22.50	43.60	32.80
3	35	15	7.82	3.12	76.20	38.00	73.60	55.40
4	35	15	9.77	3.90	108.00	53.90	104.00	78.50
5	35	15	11.70	4.68	139.00	69.40	134.00	101.00

NOTE: Residual cohesion and tensile strength are zero. See Section 7.6 for calibration methodology.

Table 6-43. Calibrated Properties of the Bonded Fractures and Intact Blocks in the Model with 0.3 m Block Size

Category	Friction Angle (deg)	Residual Friction Angle (deg)	Cohesion (MPa)	Tension (MPa)	Normal Stiffness (GPa/m)	Shear Stiffness (GPa/m)	Block Bulk Modulus (GPa)	Block Shear Modulus (GPa)
1	35	15	3.83	1.53	9.34	4.67	9.03	6.80
2	35	15	5.85	2.34	31.48	15.72	30.44	22.88
3	35	15	7.94	3.18	53.08	26.57	51.37	38.60
4	35	15	10.09	4.03	74.90	37.60	72.80	54.70
5	35	15	12.30	4.92	97.00	48.40	93.60	70.50

NOTE: Residual cohesion and tensile strength are zero. See Section 7.6 for calibration methodology.

6.4.2.2 Seismic Consideration in Lithophysal Units

Ground Motions–Drift stability was analyzed for different conditions of ground motion:

- Ground motion with 5×10^{-4} probability of annual occurrence (preclosure earthquake, DTN: MO0407TMHIS104.003 [DIRS 170599])
- Ground motion with 1×10^{-4} probability of annual occurrence (preclosure earthquake, DTN: MO0306SDSAVDTH.000 [DIRS 164033])
- Ground motion with 1×10^{-5} probability of annual occurrence (postclosure earthquake, DTN: MO0402AVDTM105.001 [DIRS 168890])
- Ground motion with 1×10^{-6} probability of annual occurrence (postclosure earthquake, DTN: MO0301TMHIS106.001 [DIRS 161868]).

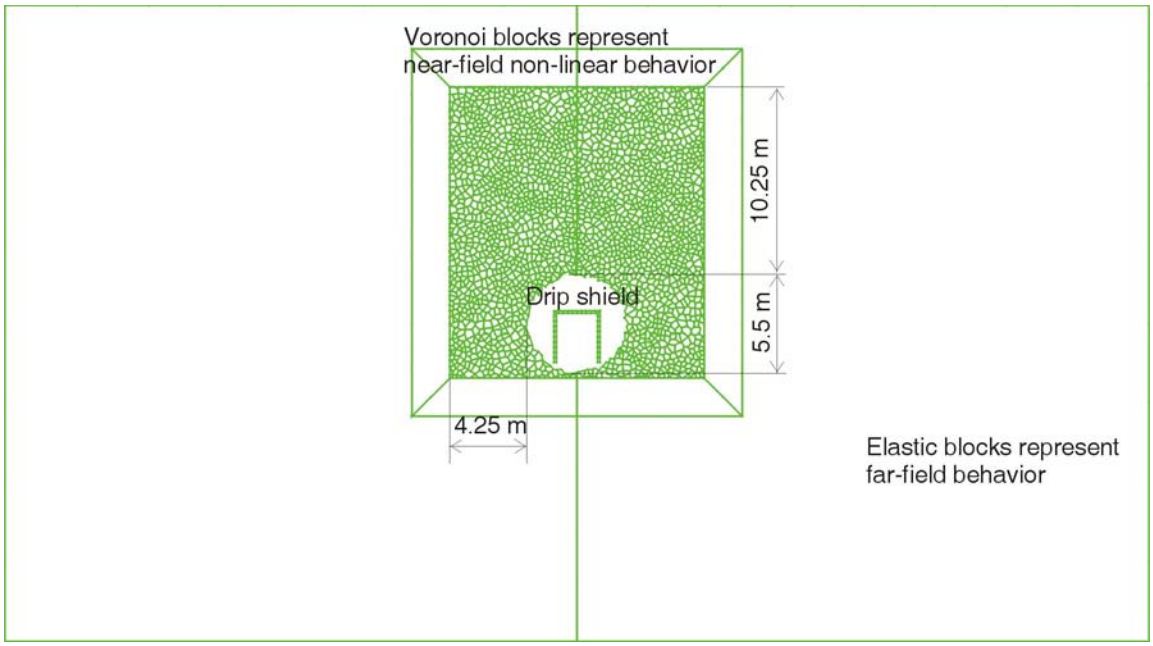

NOTE: Simplified drip shield geometry is based on BSC 2004 [DIRS 169220].

Figure 6-116. Geometry and Initial Conditions of the UDEC Lithophysal Rockfall Model

The ground motions are discussed in detail in Section 6.3.1.2.1. Fifteen ground motions (two horizontal and one vertical component of motion) were considered in the analysis for 1×10^{-5} and 1×10^{-6} probabilities of annual occurrence. Only one ground motion was considered for each preclosure level (i.e., 5×10^{-4} and 1×10^{-4} probabilities of annual occurrence). Because there is just one ground motion case for each preclosure level, the 5×10^{-4} and 1×10^{-4} probabilities of annual occurrence ground motions were analyzed for the five rock mass categories.

For the 1×10^{-5} ground motion, three rock strength categories that span the range of lithophysal porosities were chosen (Categories 1, 3, and 5). For each of these categories, the 15 ground motion sets were analyzed. Because the 1×10^{-5} analyses show a large range in damage level depending on the rock strength and ground motion set, more extensive examination was made. Analyses were conducted for each of the three categories *lower bound* values (Table 6-41) in addition to the base case values. Analyses using a model with simulated spatial variability in lithophysal porosity (and thus spatial variability in mechanical properties) were also conducted as a check against the base case models that consider constant properties.

Instead of simulating all possible combinations of the 15 cases of ground motion for 1×10^{-6} probability with five rock mass categories, only 15 realizations shown in Table 6-44 were simulated (note that 15 ground motions are numbered 1 through 14 in sequence, and 16). Based on Latin Hypercube sampling (see *Sampling of Stochastic Input Parameters for Rockfall Calculations and for Structural Response Calculations Under Vibratory Ground Motion* (BSC 2004 [DIRS 169999]) and DTN: MO0301SPASIP27.004 [DIRS 161869]), realizations from Table 6-44 are selected as representative of the possible realizations. Combinations in Table 6-44 include rock mass Categories 1 through 5, as representative of the variability of lithophysal rock mass quality on the repository level. It was planned to conduct simulations of

drift stability for ground motions with 1×10^{-7} probability of annual occurrence. However, the results of analyses for 1×10^{-6} probability of annual occurrence (complete collapse of the emplacement drifts) determined such an analysis unnecessary.

Table 6-44. Simulated Combinations of 10^{-6} Ground Motions and Rock Mass Categories

Realization Number	Ground Motion Time History Number	Rock Mass Category Number
1	4	3
2	8	5
3	16	4
4	12	1
5	2	3
6	8	1
7	14	2
8	4	4
9	10	2
10	6	3
11	9	1
12	1	1
13	1	3
14	7	4
15	11	4

Source: DTN: MO0301SPASIP27.004 [DIRS 161869].

NOTE: Realization numbers 1 through 15 are from the sampling in the lithophysal zone provided by the source DTN.

Model Initial and Boundary Conditions–An in situ (before excavation) stress state, defined by 7 MPa vertical and 3.5 MPa horizontal stresses, is used throughout the simulations, which is consistent with the 3DEC modeling in Section 6.3. The vertical stress represents the stress state at a depth of 300 m, and the lateral stress represents the horizontal component projected in the plane perpendicular to the emplacement drifts, whose azimuth is oriented at 72 degrees east of north. The equilibrium state of the model after excavation of a drift represents the initial condition for the dynamic analysis. This equilibrium state is achieved by performing a quasi-static simulation (because the mathematical formulation of UDEC is fully dynamic in nature) in which the in situ stresses are applied to the model that is allowed to equilibrate. The geometry and the boundary and initial conditions used in the initial quasi-static simulation preceding the dynamic simulation are illustrated in Figure 6-117.

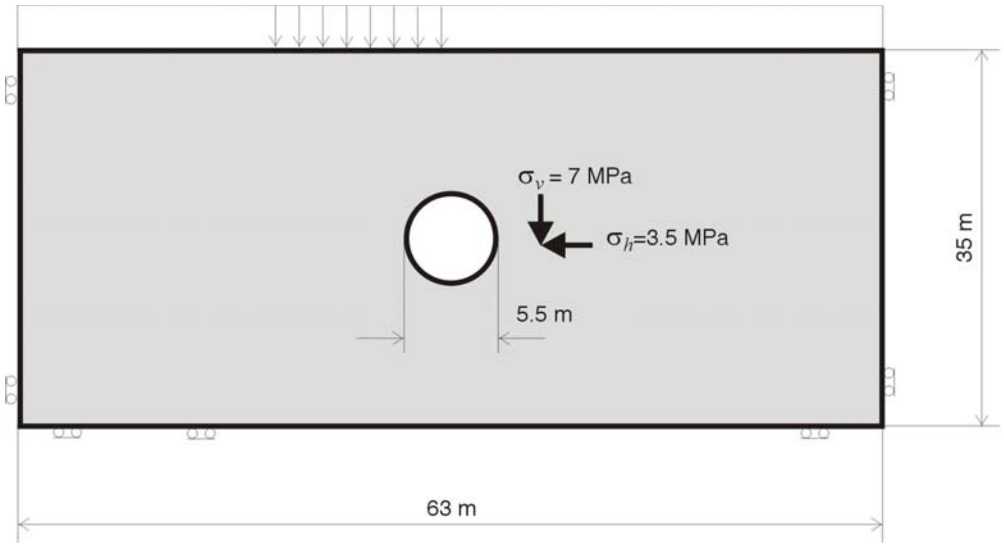

Figure 6-117. Dynamic Model, Initial and Boundary Conditions: Initial Quasi-Static Simulation

The boundary conditions as used in the dynamic analysis are illustrated in Figure 6-118. Quiet boundaries (indicated in Figure 6-118 as viscous boundaries) were used on the outside boundaries of the models. These boundaries prevent reflection of outgoing seismic waves back into the model. Quiet boundaries were combined with free-field boundaries on the vertical outside boundaries. The free-field boundaries perform a one-dimensional simulation of vertically-propagating plane waves representing motion of a truncated, semi-infinite medium, thereby preventing distortion of vertically-propagating plane waves along the quiet boundaries. Dynamic loading was applied at the bottom of the model to provide vertically propagating shear and compression waves. Although the dynamic loading was specified as velocity time-histories, it was applied at the bottom model boundary as a time-varying stress boundary condition. This is possible because there is a direct correspondence between velocity and induced stress for plane waves in elastodynamics, and, therefore, time-varying velocity or stress boundary conditions are equivalent. The relationships used are given as follows (Itasca Consulting Group 2002 [DIRS 160331], Manuals/3DEC/Optional Features/Section 2: Dynamic Analysis, Section 2.6):

$$\begin{aligned} \sigma_y &= 2\rho C_p v_v \\ \sigma_{xy} &= 2\rho C_s v_h \end{aligned} \qquad \text{(Eq. 6-7)}$$

where ρ is rock density; C_p and C_s are P and S wave velocities, respectively; and v_v and v_h are vertical and horizontal velocity components. The factor 2 in Equation 6-7 is due to correction for the quiet boundaries. Figure 6-119 shows specified component 1 of the horizontal velocity history for ground motion 4 of 1×10^{-6} probability. Velocity histories at the bottom and the top of the model (shown in Figure 6-119), recorded during the simulation, confirm that the applied stress boundary condition results in ground motion velocity time histories that are the same as the specified velocity boundary condition. Comparison of the velocities at the top and bottom of the model (identical histories slightly offset in time) confirms that the free-field boundaries operate correctly in elimination of boundary effects.

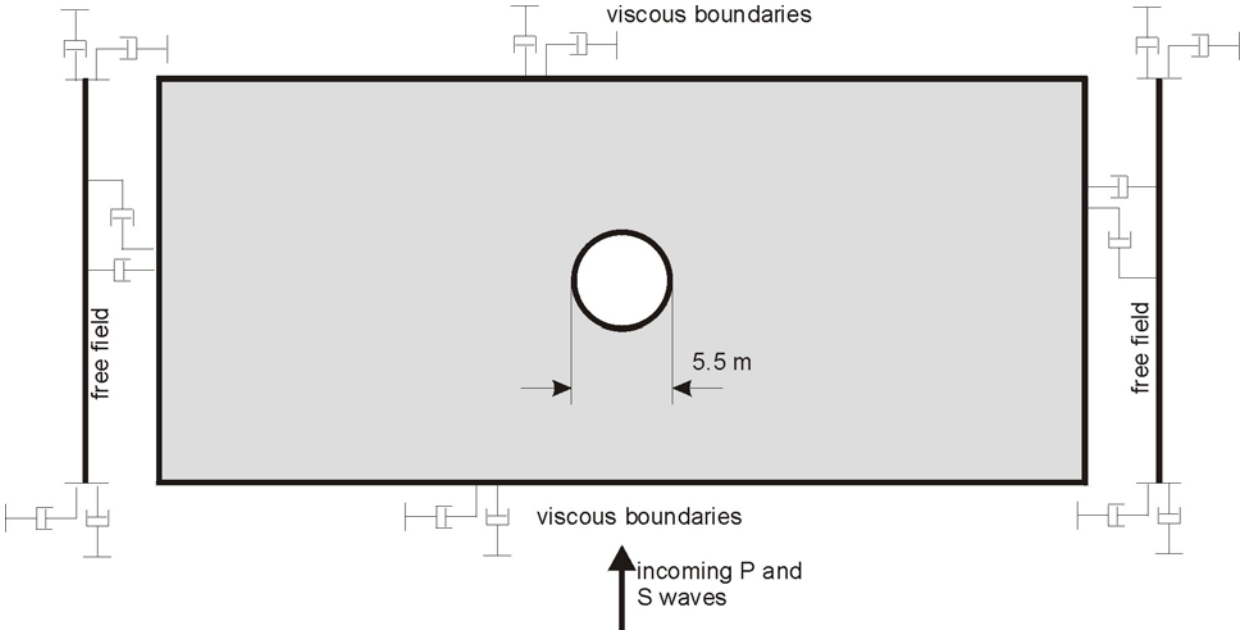

Figure 6-118. Model Boundary Conditions for Dynamic Simulation

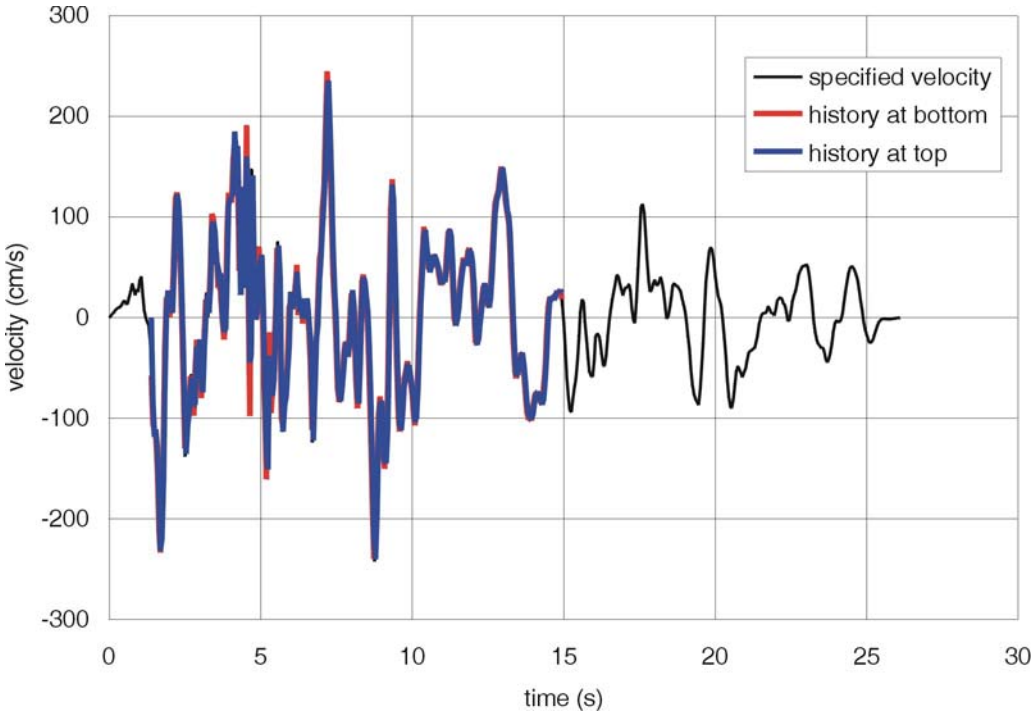

Source: DTN: MO0301TMHIS106.001 [DIRS 161868] provides the specified horizontal velocity.

NOTE: The horizontal velocities recorded at the top and at the bottom of the model coincide with the specified velocity.

Figure 6-119. Horizontal Velocity, Component 1 for Ground Motion 4 of 1×10^{-6} Probability

6.4.2.2.1 Analysis of Drift Response to Preclosure Ground Motion

The analyses indicate that preclosure ground motion levels (i.e., with probabilities of annual occurrence of 5×10^{-4} and 1×10^{-4}) will not induce any rockfall for rock mass strength Categories 2 through 5. A relatively small amount of rockfall from the drift walls (shown in Figure 6-120) is expected for unsupported excavations in Category 1, which represents less than 5 percent of the Tptpll (see Figure 6-115 and Appendix E). The elastic stress paths from the 1×10^{-4} preclosure ground motion simulation for the Category 1 rock mass (shown in Figures 6-121 and 6-122 in the wall and roof, respectively), and the Category 5 rock mass (shown in Figures 6-123 and 6-124 in the wall and roof, respectively), indicate that this level of ground motion causes small oscillations of the stress state relative to the initial equilibrium. With the exception of the monitoring location at the drift wall for the Category 1 rock mass, the stress states are within the elastic region throughout the duration of the 1×10^{-4} preclosure ground motion. The observed rockfall is a consequence of regions that are above the yield limit after excavation of the drift (i.e., the wall in the Category 1 rock mass) being shaken down in the absence of ground support.

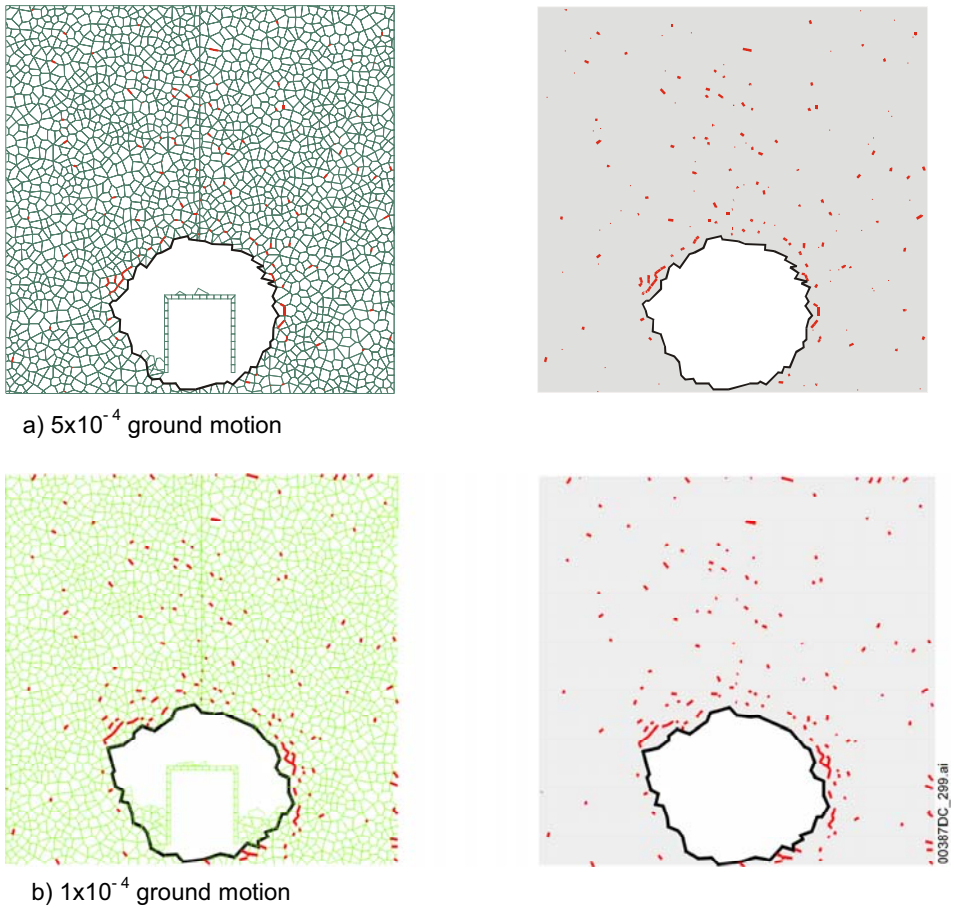

NOTE: Rock mass Categories 2 to 5 show no damage. Red lines indicate block bonds that have failed in shear or tension.

Figure 6-120. Geometry of the Model after Simulation for Preclosure Ground Motions: Rock Mass Category 1

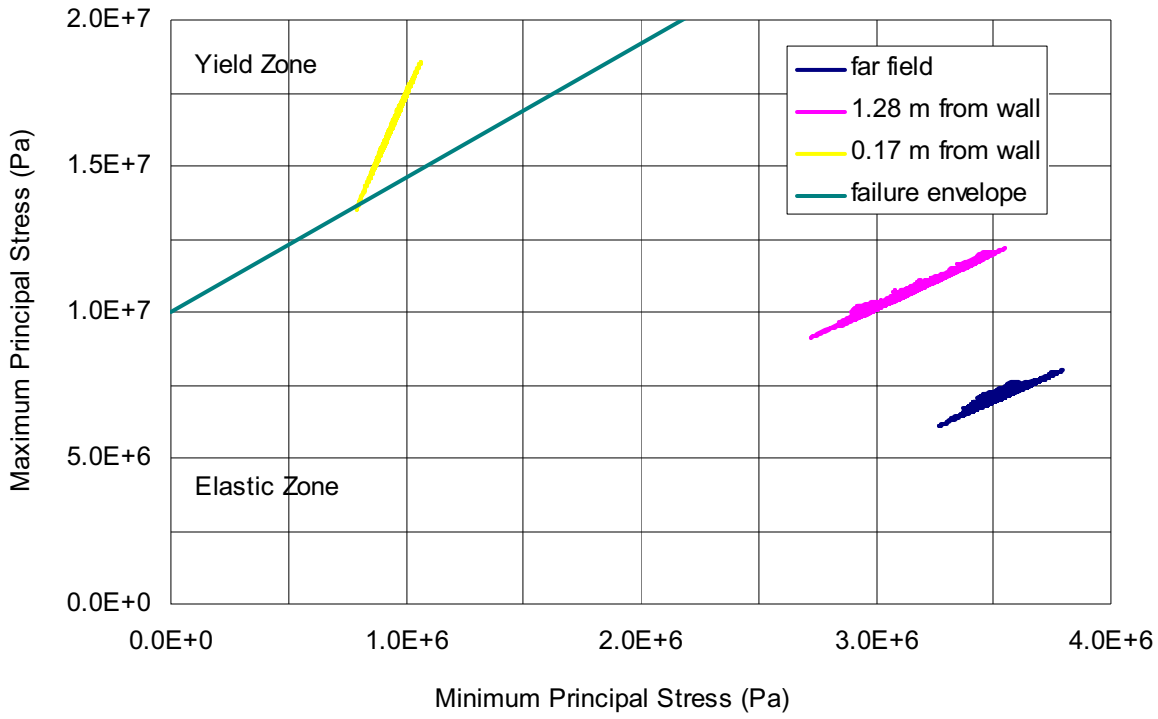

Figure 6-121. Elastic Stress Paths in the Drift Wall Due to 1×10^{-4} Preclosure Ground Motion: Category 1

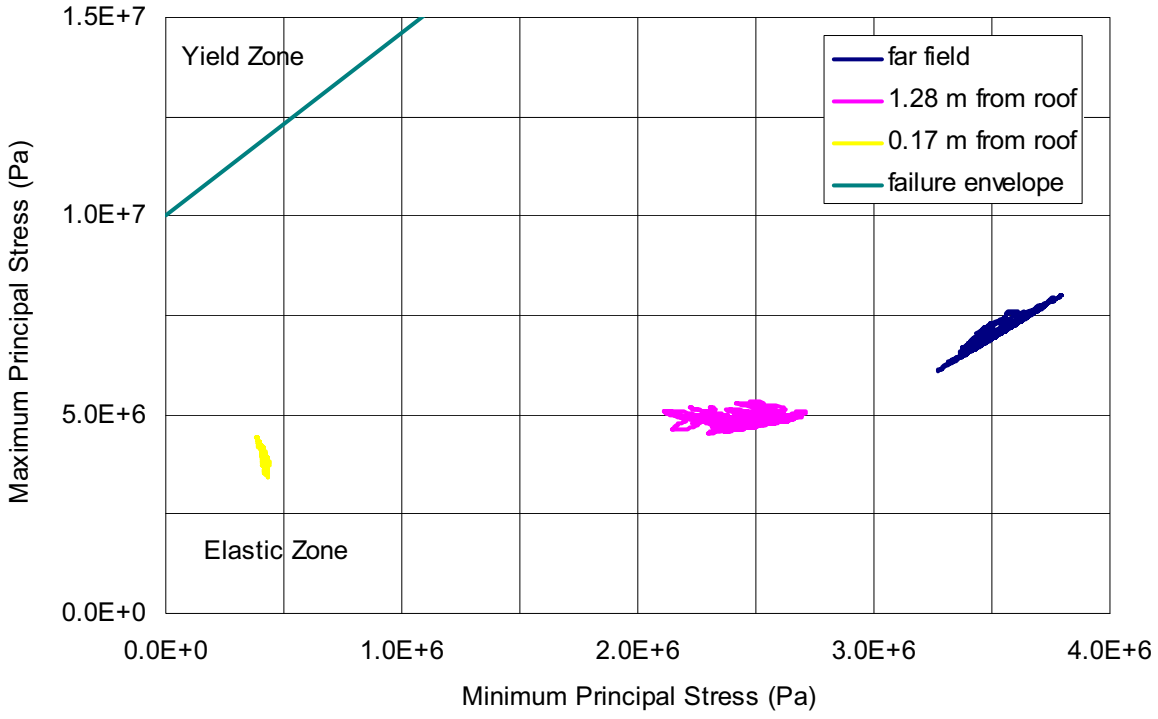

Figure 6-122. Elastic Stress Paths in the Drift Roof Due to 1×10^{-4} Preclosure Ground Motion: Category 1

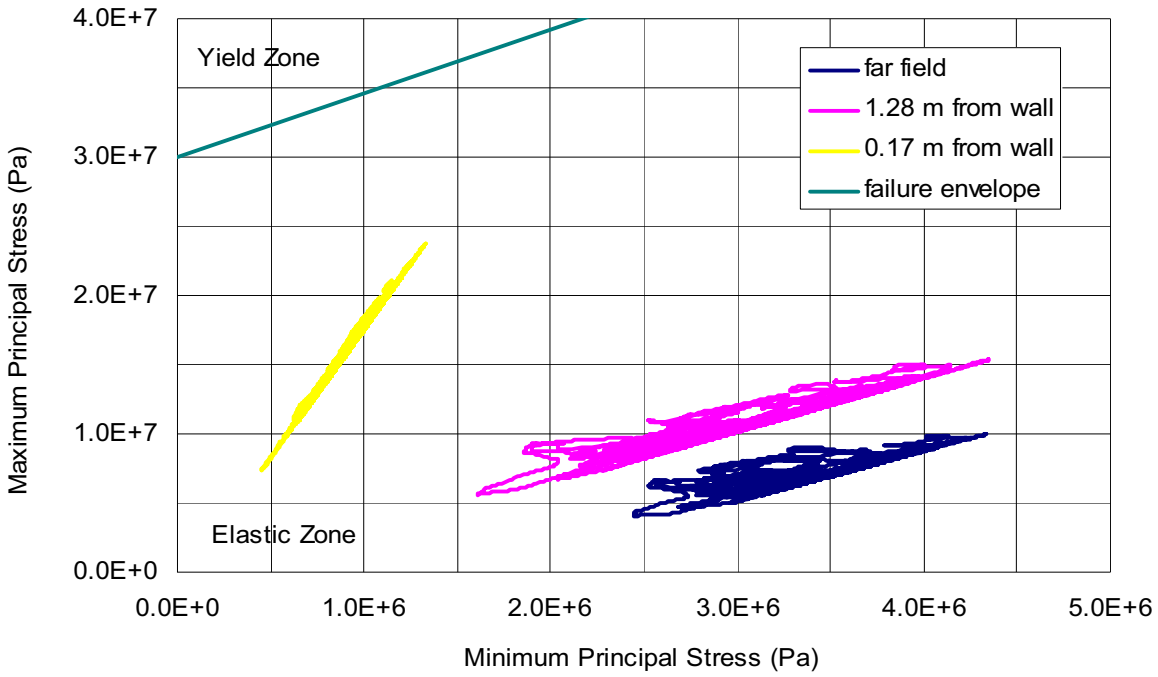

Figure 6-123. Elastic Stress Paths in the Drift Wall Due to 1×10^{-4} Preclosure Ground Motion: Category 5

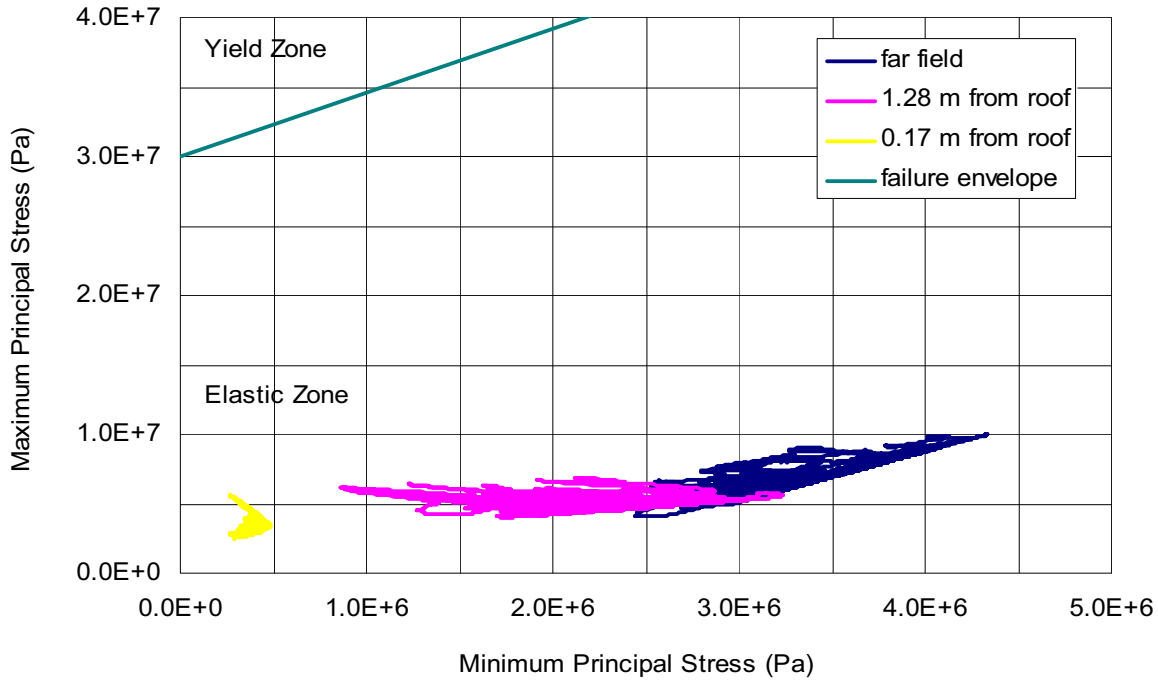

Figure 6-124. Elastic Stress Paths in the Drift Roof Due to 1×10^{-4} Preclosure Ground Motion: Category 5

6.4.2.2.2 Analysis of Drift Response to Postclosure Ground Motions

6.4.2.2.2.1 Analysis of 1×10^{-5} Ground Motions

The 1×10^{-5} annual exceedance frequency is described by 15 sets of three ground motions–one vertical and two horizontal. These ground motions were developed by scaling horizontal component 1 to a repository level target peak ground velocity (PGV), and scaling other components to maintain inter-component variability. For a detailed discussion of the development of the ground motion time histories see *Development of Earthquake Ground Motion Input for Preclosure Seismic Design and Postclosure Performance Assessment of a Geologic Repository at Yucca Mountain, NV* (BSC 2004 [DIRS 170027]). Table 6-45 summarizes the peak ground velocities for each of the motions.

Table 6-45. Summary of 10^{-5} Ground Motion Characteristics

Ground Motion	Horizontal Component 1 PGV (cm/sec)	Horizontal Component 2 PGV (cm/sec)	Vertical Component PGV (cm/sec)
Set 1	104.58	83.31	70.88
Set 2	104.58	125.02	145.25
Set 3	104.58	262.05	398.11
Set 4	104.59	100.41	152.27
Set 5	104.58	166.71	106.52
Set 6	104.54	45.61	173.88
Set 7	104.51	89.33	333.16
Set 8	104.56	152.20	98.16
Set 9	104.59	357.76	281.76
Set 10	104.60	31.81	50.16
Set 11	104.60	126.04	120.31
Set 12	104.54	70.34	100.60
Set 13	104.58	103.75	318.01
Set 14	104.62	40.87	92.78
Set 15	104.56	67.43	137.53

Source: DTN: MO0402AVDTM105.001 [DIRS 168890].

The vertical (V) and horizontal component 1 (H1) are applied at the base of the cross-sectional UDEC lithophysal rockfall model for consistency with three-dimensional waste package vibratory motion models in which the H1 component acts in the drift cross-sectional plane and H2 acts along the axis of the tunnel (BSC 2004 [DIRS 167083]). As seen in Table 6-45, approximately 25 percent (4 of 15) of the ground motion sets have a largest associated PGV in excess of 300 cm/sec, approximately 60 percent (9 of 15) with largest associated PGV of 100 to approximately 150 cm/sec, and approximately 15 percent (2 of 15) with largest associated PGV between 150 and 175 cm/sec. In a significant number of the ground motion sets, the vertical component has the largest associated PGV.

Parametric Analyses–All 15 motion sets were applied to base case rock mass strength Categories 1, 3, and 5 to cover the range of rock qualities. As discussed previously, Category 1 (and Category 2) is viewed as a condition of localized, high porosity (possibly

large lithophysae) and represents less than 10 percent of the Tptpll. Category 3 (and Category 4) is viewed as a typical condition encountered in the Tptpll, representing approximately 60 percent of the Tptpll, and Category 5 viewed as the higher rock mass quality areas in the Tptpll, representing approximately 30 percent of the Tptpll. The sequencing of modeling initially involved application of in situ stresses to the rock mass and the unsupported emplacement drift, and allowed the system to equilibrate with any associated rockfall. Each ground motion is applied to the base of the model in the form of the time-varying vertical and horizontal motions, which are allowed to run through to the cutoff time of 95 percent of total energy.

Results–The level of damage induced by the ground motion is quantified here by the area (volume) of the rock that is detached from the surrounding rock mass and falls into the tunnel. Because the model is two dimensional, it essentially represents a 1-m thick slice of material parallel to the axis of the drift. The damage is thus given in terms of volume/m of emplacement drift, or m^3/m. This could be converted to metric tons by multiplying by the density, which, for the lithophysal rock, is approximately 2 $tons/m^3$ (the matrix density is approximately 2.5 $tons/m^3$).

Figures 6-125 to 6-127 show representative examples of the mechanism and level of damage induced for rock strength Categories 1, 3, and 5 for ground motions 12 (104 cm/sec PGV), 4 (152 cm/sec PGV), and 7 (333 cm/sec PGV). These ground motions cover the approximate range of PGVs for the 15 motions. The damage levels are further plotted for each rock mass strength category as a function of PGV in Figure 6-128. The analyses show that the damage appears to be primarily related to the magnitude of PGV, but is highly variable, particularly at large PGV, presumably due to the variability in the time histories and their impact on the energy (or power) contained in the waveform. An approximate linear upper bound to the damage can be seen in this plot in a fashion similar to that shown in Figure 6-83 for rockfall as a function of PGV in nonlithophysal rock. The variability in the response is a function of the properties of the ground motion time histories, not the rock properties, since constant modulus and strength are considered for a given category.

To investigate further the correlation to energy content of the ground motion, the vertical time history for each ground motion was run through a Fast Fourier Transform. The Fast Fourier Transform performs an integration of the square of the velocity over the duration of the time history, thus producing a power spectral density for velocity. This term is proportional to the integrated kinetic energy [kinetic energy = $\frac{1}{2}(mv^2)$] of the time history. The damage as a function of the velocity power spectral density for the vertical ground motion for each of the 45 analyses is plotted in Figure 6-129. This plot shows that the damage is linearly related to the energy associated with the velocity time history. Therefore, although PGV appears to be reasonably associated with the damage level and provides a means of bounding the response, the energy in the time history is a better indicator of the potential damage.

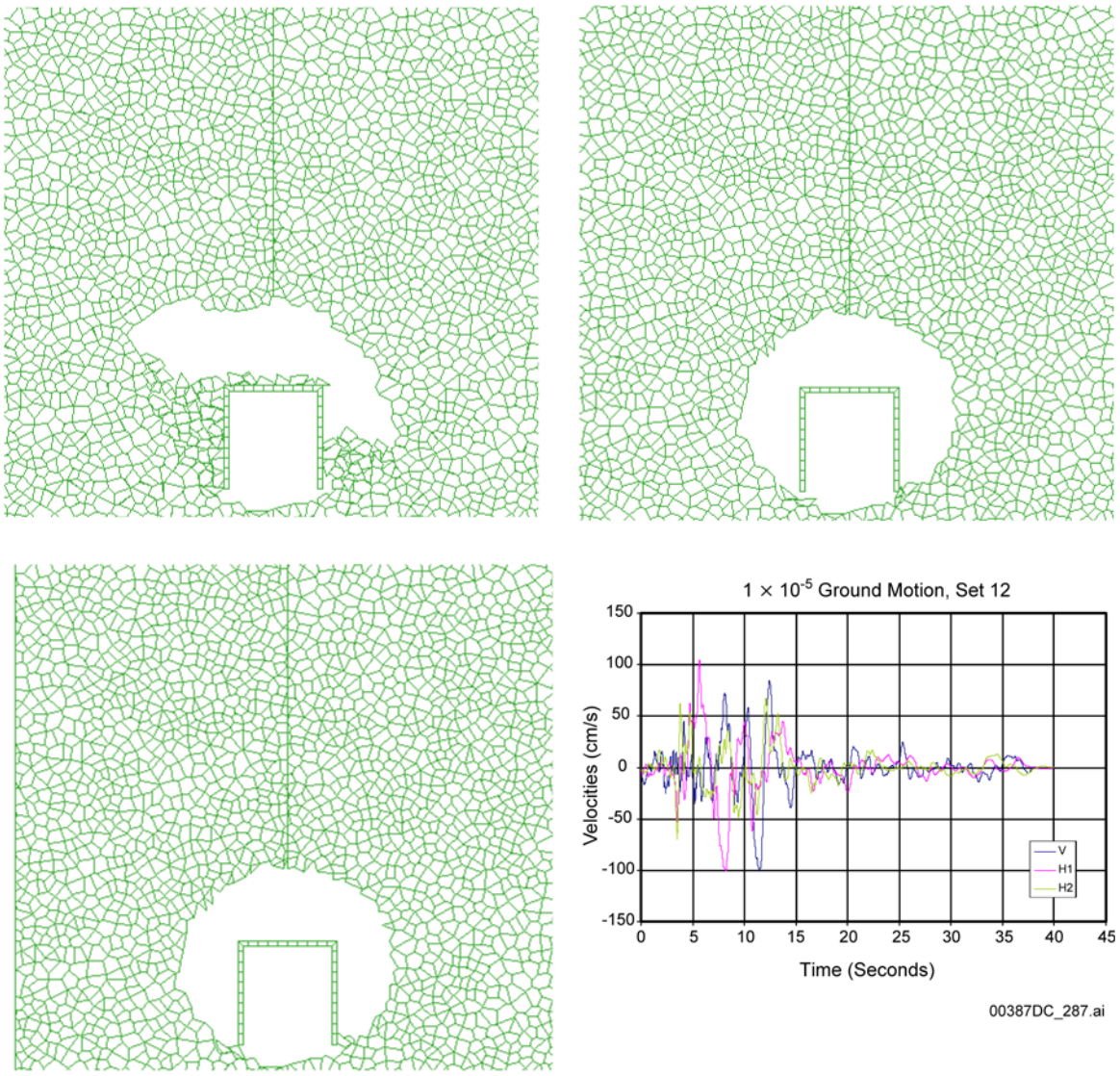

NOTE: (upper left) Rock Strength Category 1 (5.6 m^2/m drift length), (upper right) Category 3 (0.02 m^2/m), (lower left) Category 5 (0.1 m^2/m), and (lower right) Ground Motion History 12, PGV=104 cm/sec.

Figure 6-125. Example of Comparison of Damage Levels for Lower End of PGV (104 cm/sec) for 1×10^{-5} Annual Exceedance Level

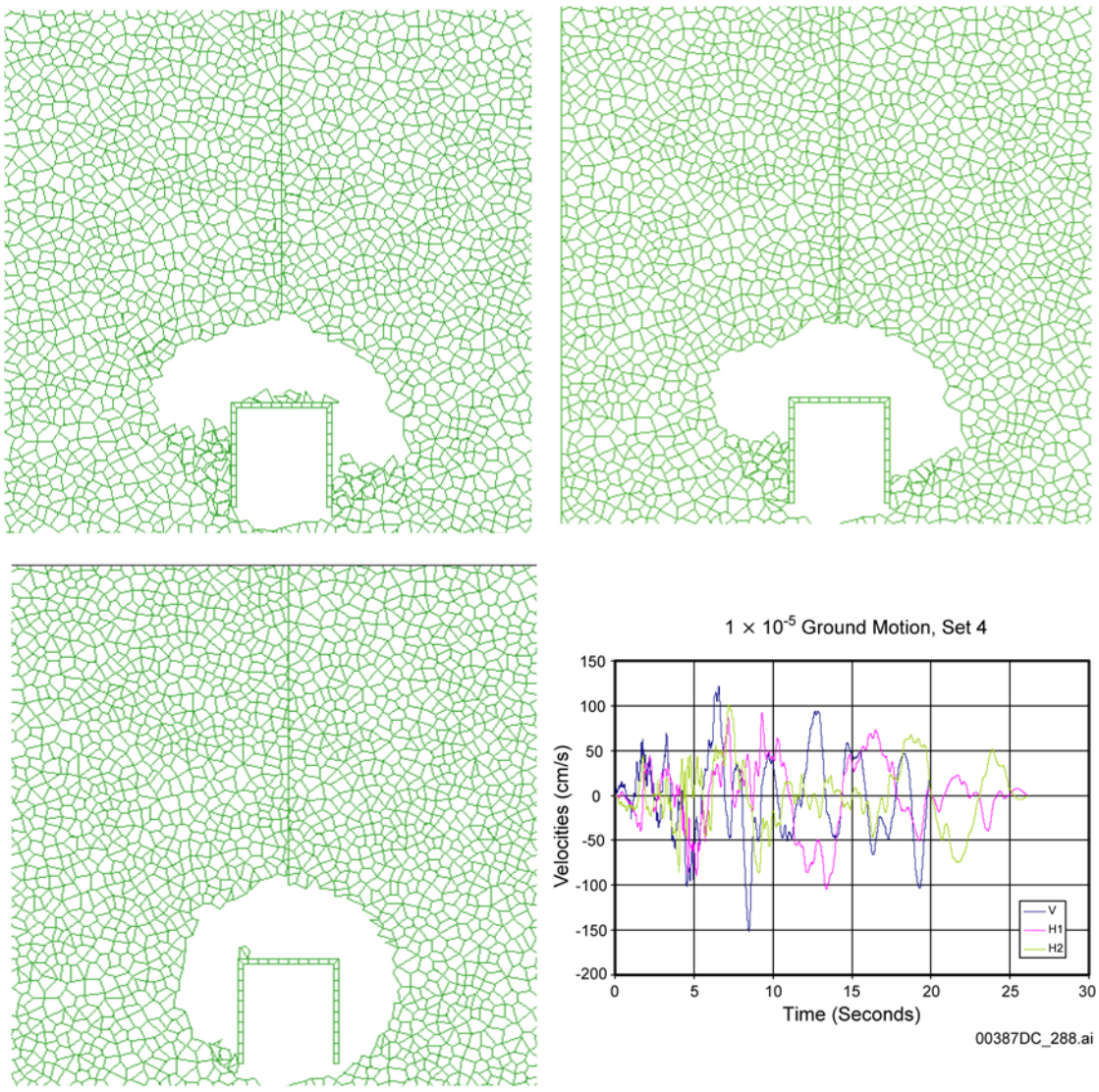

NOTE: (upper left) Rock Strength Category 1 (3.3 m^2/m drift length), (upper right) Category 3 (2.2 m^2/m), (lower left) Category 5 (0.3 m^2/m), and (lower right) Ground Motion History 4, PGV=152 cm/sec.

Figure 6-126. Example of Comparison of Damage Levels for PGV of 152 cm/sec for 1×10^{-5} Annual Exceedance Level

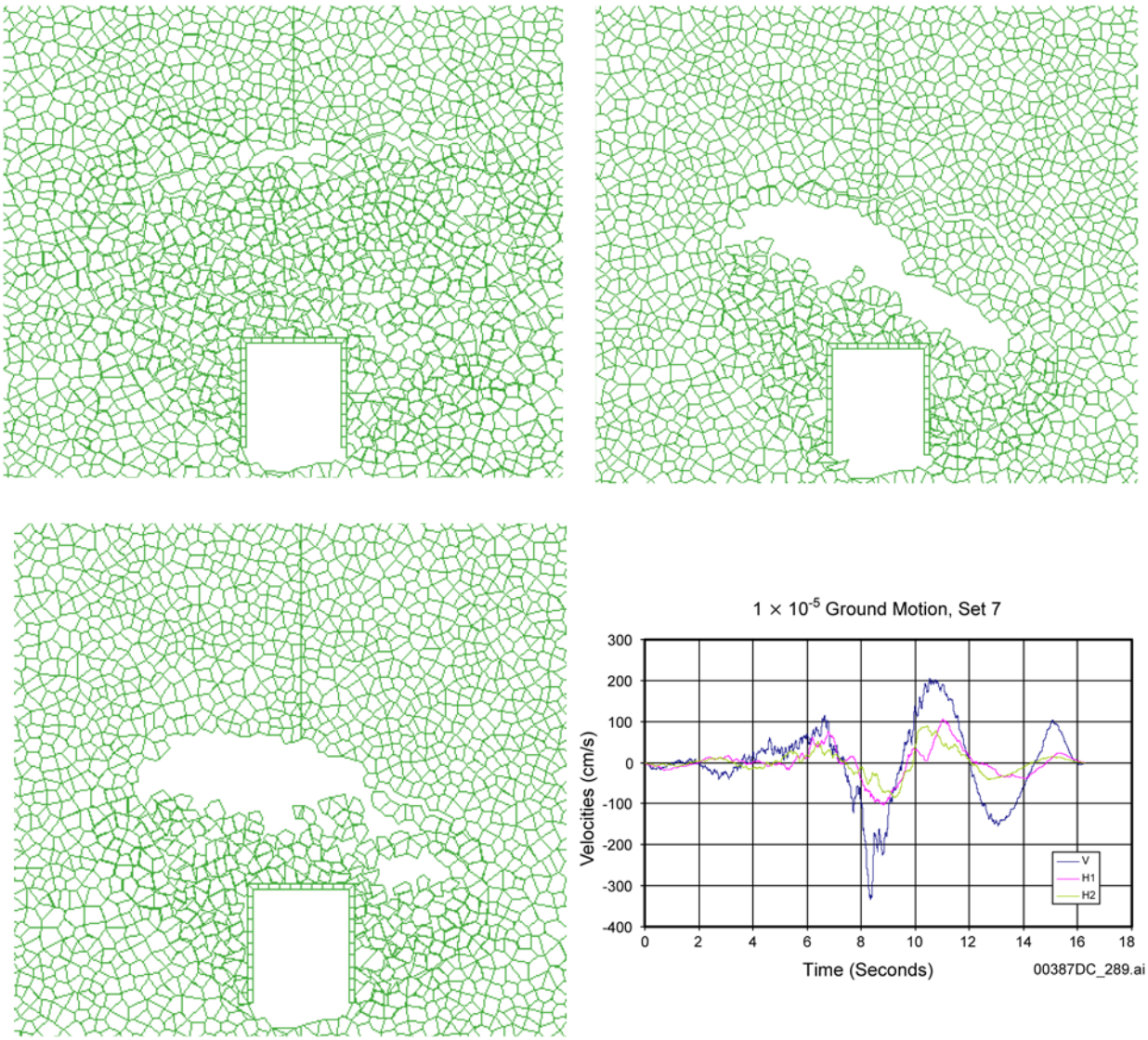

NOTE: (upper left) Rock Strength Category 1 (40.6 m^2/m drift length), (upper right) Category 5 (19.7 m^2/m), (lower left) Category 3 (15.4 m^2/m), and (lower right) Ground Motion History 7, PGV=333 cm/sec.

Figure 6-127. Example of Comparison of Damage Levels for Upper End of PGV (333 cm/sec) for 1×10^{-5} m/sec

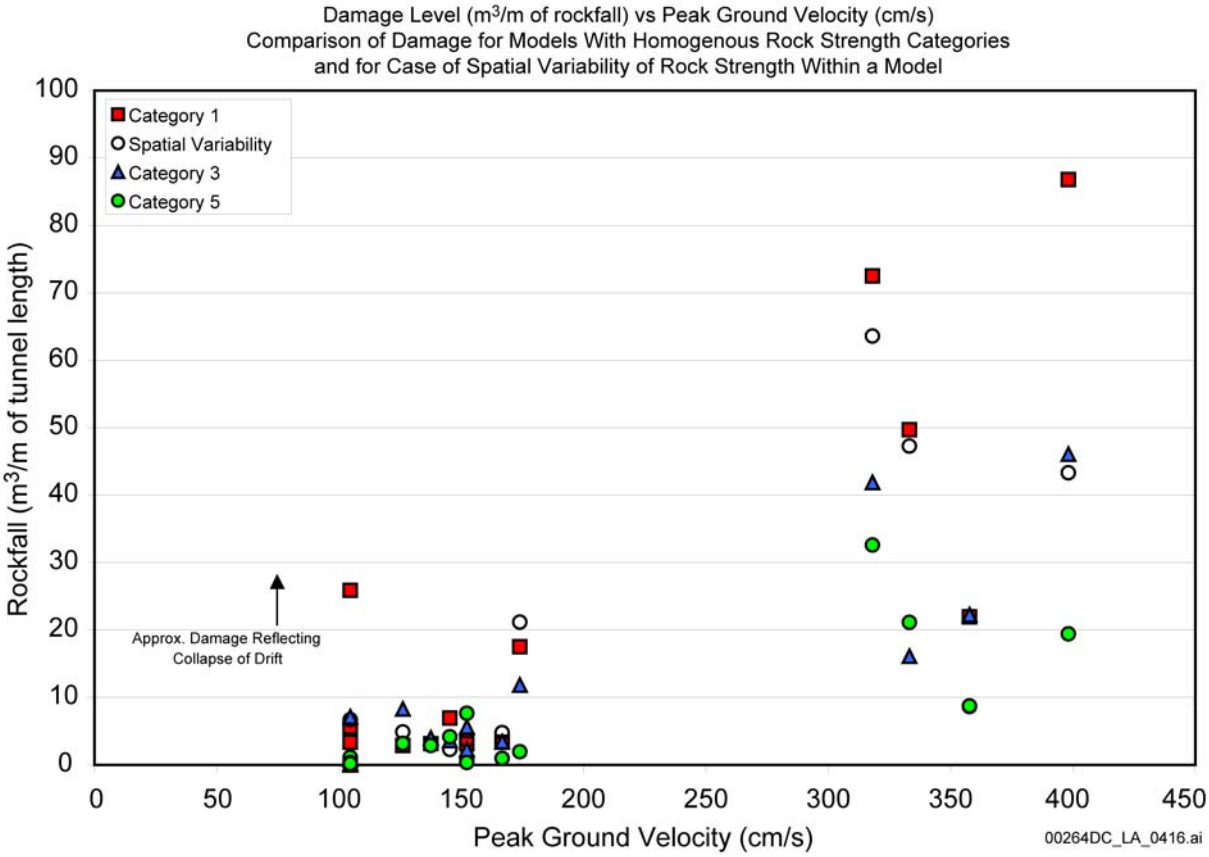

NOTE: Damage levels for the 15 ground motions are given. Results for spatially variable lithophysal porosity are also given for comparison.

Figure 6-128. Estimate 1×10^{-5} Damage Level, Expressed as m^2/m of Emplacement Drift Length for Rock Strength Categories 1, 3, and 5 for the 15 Ground Motion Time Histories

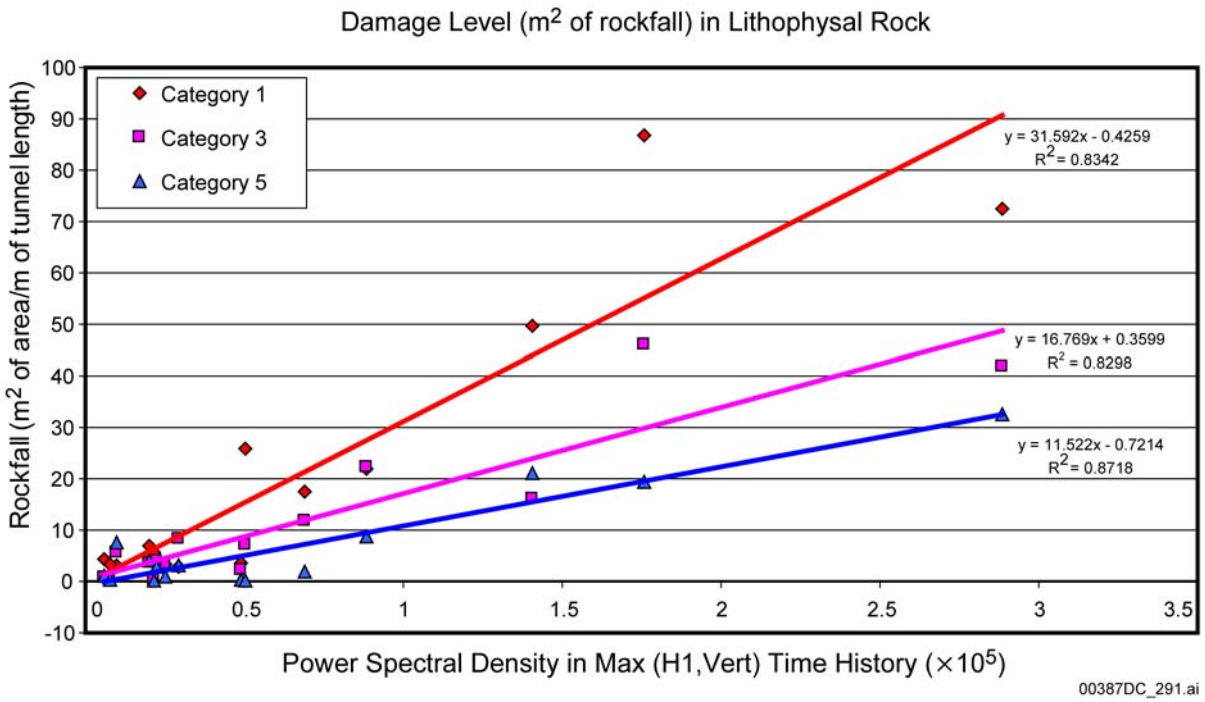

NOTE: The power spectral density is obtained by integrating the square of the velocity time history, producing a value proportional to the kinetic energy.

Figure 6-129. Rockfall Damage as a Function of the Energy Associated With the Vertical Velocity Time History

Discussion–The drift damage mechanism consists primarily of shear failure at the springlines of the tunnel coinciding with passage of the compressive stress increase associated with PGV peaks in the time history. The in situ stress field has major vertical and secondary horizontal stress components. The vertical compression or horizontal shear wave essentially results in a free field dynamic stress increase as shown in Equation 6-7 (note that the correction factor of 2 in Equation 6-7 is for boundary conditions only, and therefore is not required). These dynamic components are superimposed on the existing in situ stress field to cause additional stressing or relaxation of the rock mass surrounding the drift. The end-result of this superposition is that the stress tensor rotates about the general vertical axis as the ground velocities oscillate over the duration of the strong ground motion. If the addition of dynamic plus in situ stress is large enough, shear failure occurs primarily at the springlines, resulting in development of an elliptic shape of the opening as the rock mass yields and rockfall occurs and falls along the sides of the drip shield. The extent of shear failure and rockfall around the circumference of the tunnel, up and down from the springline, is due to both the general ratio of rock mass strength to stress, but also to the ratio of the vertical to horizontal PGV. The greater the horizontal component, the greater the rotation of the stress tensor, which results in greater inclination of the major principal stress. Generally, this shear failure mechanism occurs with the arrival of the PGV peaks. Compressive stresses also appear responsible for some cases in which roof slabbing is observed where the rock mass strength and stiffness are larger (i.e., Category 5). A second failure mechanism observed includes tensile failure of the rock mass resulting from the reversal of the ground motion and inducement of dynamic tensile straining in the rock mass.

In general, it appears that the rock mass failure and the rockfall occur simultaneously with the arrival of velocity peaks in the time histories. In a similar fashion, the peak ground velocity has been recognized by many authors as the primary contributing factor to dynamic rock mass failure in mine tunnels, slopes, and dams (e.g., MRD 1995 [DIRS 169719], Volume 2, Section 6.2.3; Newmark 1965 [DIRS 169515]). In the present case, the shear or tensile failure mechanism results in a predicted creation of blocks resulting from fracture of the rock mass along the ubiquitous fracture network of the material. The blocks that contact the drip shield are relatively small in size, and governed by the inherent fracture network and lithophysae spacing. The UDEC lithophysal rockfall model studies have primarily used a 0.3-m average fracture spacing in developing the block structure, although simulations with 0.2-m spacing have also been conducted. In each case, the transient dynamic stress changes, in addition to pre-existing in situ stresses, result in breakage of the bonds between the blocks in the rockfall zone around the tunnel. In other words, the stressing does not create large blocks that impact the drip shield, but small component blocks defined by the inherent fracturing of the Tptpll.

Although the damage levels appear to correlate somewhat better to the energy content of the time history, correlation to PGV provides a simpler method for interpretation of the results. Correlation to PGV is also consistent with that used in waste package and drip shield vibratory motion damage abstractions (*Seismic Consequence Abstraction*, BSC 2004 [DIRS 169183]). An approximate relationship of damage level to PGV in terms of both m^3/m of drift length and physical interpretation can be roughly approximated as follows:

- Peak ground velocities below about 1 m/sec result in relatively minor damage to unsupported drifts.

- Peak ground velocities below about 1.5 m/sec result in an approximate damage level below 5 m^3/m. This damage level is characterized by a range from minor spalling to damage characterized by rock particles filling the invert along the sides of the drip shield (see Figure 6-125).

- Peak ground velocities from approximately 1.5 to 2 m/sec result in damage levels from 5 to 15 m^3/m. This damage level is characterized by rock particles covering the sides of the drip shield to, approximately, the height of the drip shield, and may cover the top of the drip shield (see Figure 6-126).

- Peak ground velocities in excess of about 2 m/sec result in damage levels above 15 m^3/m. This damage level is characterized by complete collapse of the tunnel (see Figure 6-127).

Dynamic Drip Shield Loading From 1×10^{-5} Ground Motions–Collapse of a tunnel in lithophysal rock results in loading applied to the drip shield. The rock loads fall under three primary categories:

- Dynamic loading from the rock particles striking the drip shield

- Quasi-static loading of the drip shield due to the dead weight of the fallen rock at rest on the drip shield

- Dynamic loading of the drip shield due to rockfall induced by drift collapse.

In this section, the dynamic loading of the drip shield due to rockfall induced by drift collapse from the 1×10^{-5} ground motion, is examined. The quasi-static load on the drip shield once the seismic shaking stops and the system comes to force equilibrium, is discussed in Section 6.4.2.5. In these analyses, the drip shield is considered deformable, with the geometry consistent with *Seismic Consequence Abstraction* (BSC 2004 [DIRS 169183]; and see Figure 6-130). The drip shield is idealized as a two-dimensional model of the actual geometry and deformability of the drip shield using the standard UDEC element structure. The drip shield is subdivided into 30 total segments of equal length. The elements are considered to be elastic, and, thus, no potential yield response is modeled. The purpose of these analyses is to provide estimates of both dynamic and quasi-static structural loading to the detailed dynamic analysis of drip shield structural response using the LS-DYNA three-dimensional finite element model (*Drip Shield Structural Response to Rock Fall*, BSC 2004 [DIRS 168993]). Because the UDEC lithophysal rockfall model is two-dimensional and does not attempt to model the detailed structure of the drip shield, the stiffness of the elements must be adjusted to provide an equivalent overall deformability to the actual three-dimensional structure. The stiffness of the UDEC elements has been calibrated against the three-dimensional LS-DYNA model to reproduce the deformability of the actual drip shield design (see Appendix Y). The dynamic loading from detached rock particles during the seismic shaking (includes the effect of relative velocity of between the drip shield and the falling rock) is examined here.

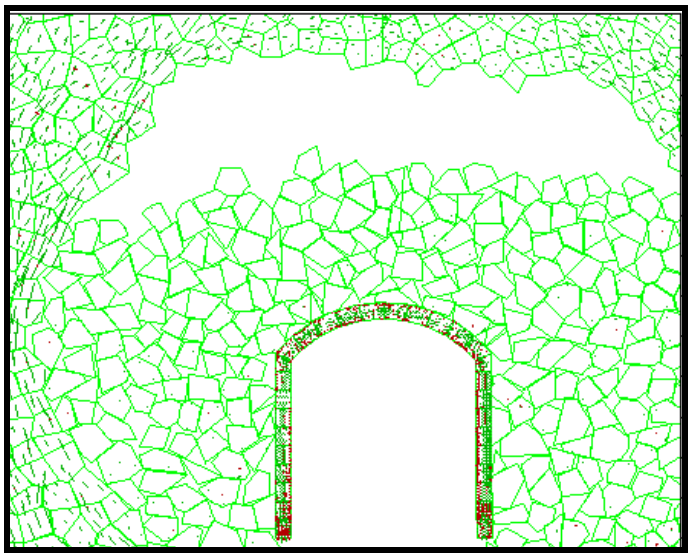

NOTE: Case with drift collapse for Rock Mass Category 1 and Ground Motion Set 9 with PGV of 2.82 m/sec.

Figure 6-130. Representation of the Drip Shield as a Deformable Structure With Actual Geometries and Footings That are Either Free to Slide or to Slide and Separate From the Invert

An example of the dynamic impact loading from side and top impacts to the deformable drip shield resulting from the 1×10^{-5} ground motion (PGV=3.33 m/sec case) are given in Figure 6-131.[8] In this figure, the average pressure across an element (in Pa) is given as a function of time (in seconds). In general, the transient stress at any given element is approximately one order of magnitude greater than the eventual dead weight load of bulked rock for the case of a completely-collapsed tunnel at equilibrium (see Section 6.4.2.5). However, due to the relatively small size of the rock particles developed in the lithophysal rock (in comparison to the much larger blocks in the nonlithophysal material), the nonlithophysal dynamic impact loading to the drip shield provides a more conservative, bounding case. Therefore, the nonlithophysal rockfall case provides the primary input for dynamic impact loading for the damage analysis and design of the drip shield. Dead weight quasi-static loading of the drip shield as described in Section 6.4.2.5 is felt to be a more important loading mechanism in the lithophysal rock mass.

6.4.2.2.2.2 Analysis of 1×10^{-6} Ground Motions

Drift Failure Response - Ground motions with a probability of an annual occurrence of 1×10^{-6} cause complete collapse of the emplacement drifts irrespective of the rock mass category and ground motion case. The model geometries after simulations of realization numbers 1 through 6 from Table 6-44 are shown in Figure 6-132. Elastic stress paths (for ground motion case 1) shown in Figures 6-133 and 6-134, for the Category 1 rock mass, and Figures 6-135 and 6-136, for the Category 5 rock mass, demonstrate different mechanisms of drift collapse depending on the rock mass quality. In poor quality rock masses (e.g., Category 1), far-field stress (unaffected by the drift) is mostly elastic during the history of the ground shaking. However, stress amplifications and concentrations around the drift cause intense yielding in tension and shear, which eventually causes the drift to collapse. In the case of better rock mass quality (e.g., Category 5), the rock mass fails in tension even for far-field conditions (away from the drift), and tensile fractures propagate throughout the rock mass. The drift creates an open space into which the loose blocks collapse.

Dynamic Drip Shield Loading From 1×10^{-6} Ground Motions–Collapse of a tunnel in lithophysal rock results in loading applied to the drip shield. The dynamic loading of the drip shield due to rockfall induced by drift collapse from the 1×10^{-6} ground motion is examined and presented in Appendix P (Figures P-29 to P-31). The quasi-static load on the drip shield once the seismic shaking stops and the system comes to force equilibrium, is discussed in Section 6.4.2.5.

[8] The dynamic loading of the drip shield by small rock blocks from the Tptpll determined from 1×10^{-5} ground motions is considered to be reasonable for the ground motions that cause complete collapse since the rock blocks fall from the same height under gravity.

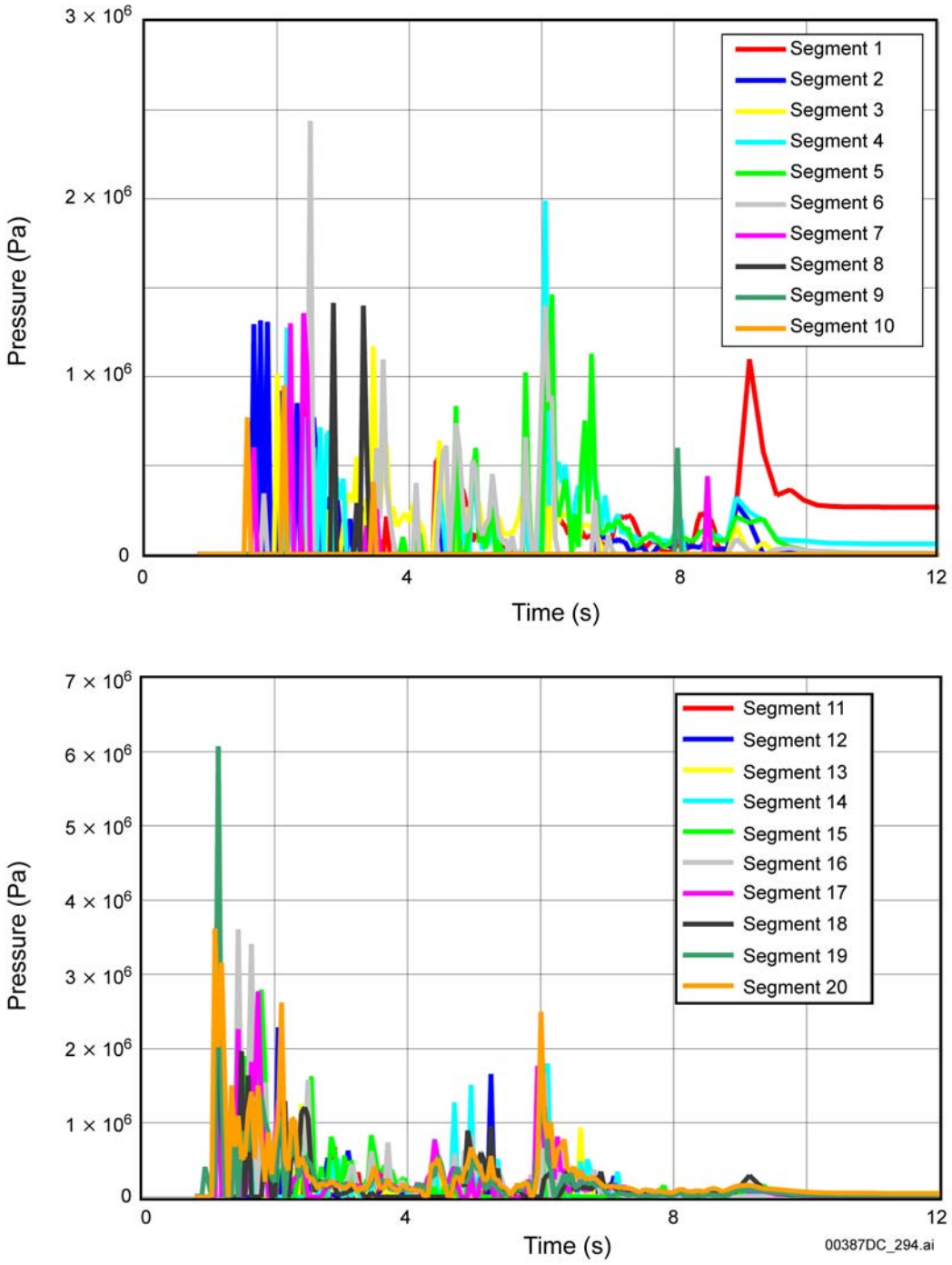

NOTE: Segments 1–10 are found along the wall, starting at the footing.

Figure 6-131. Example of Dynamic Impact Loading with 1×10^{-5} Ground Motions to the Right Wall (top) and Roof (bottom) of Deformable Drip Shield With Arched Roof

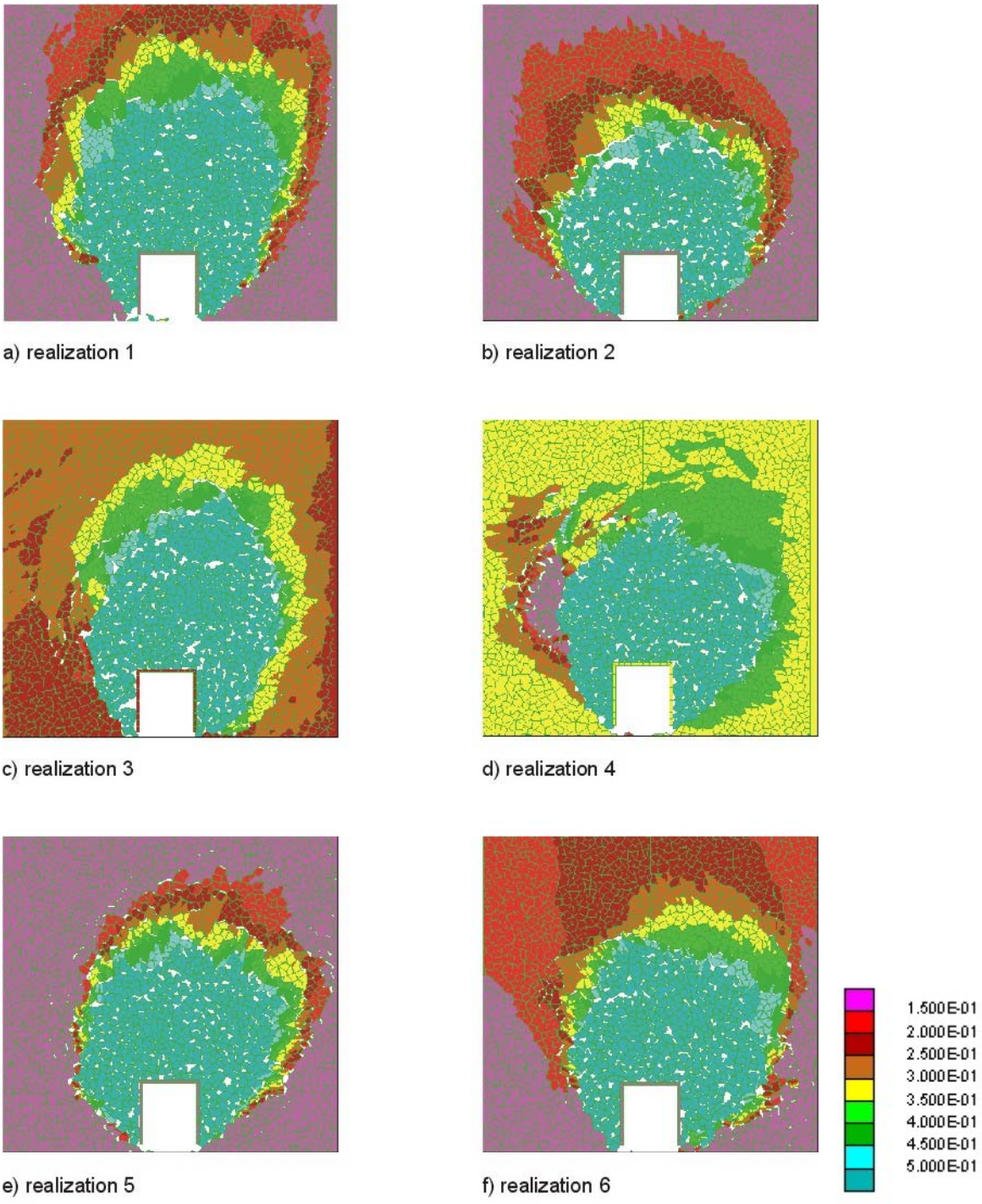

NOTE: Blocks are colored by magnitude of displacement (m).

Figure 6-132. Geometry of the Model After Simulations for Postclosure Ground Motions (Probability 1×10^{-6}): Realizations 1 Through 6 from Table 6-44

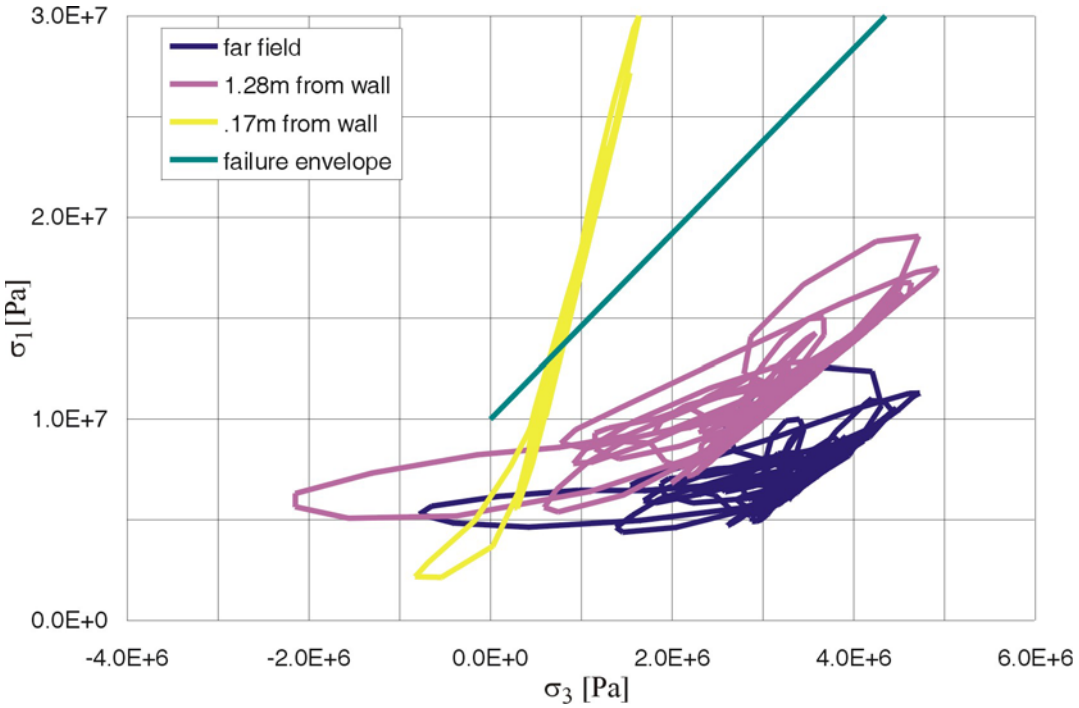

Figure 6-133. Elastic Stress Paths in the Drift Wall Due to Postclosure Ground Motion No. 1: Category 1

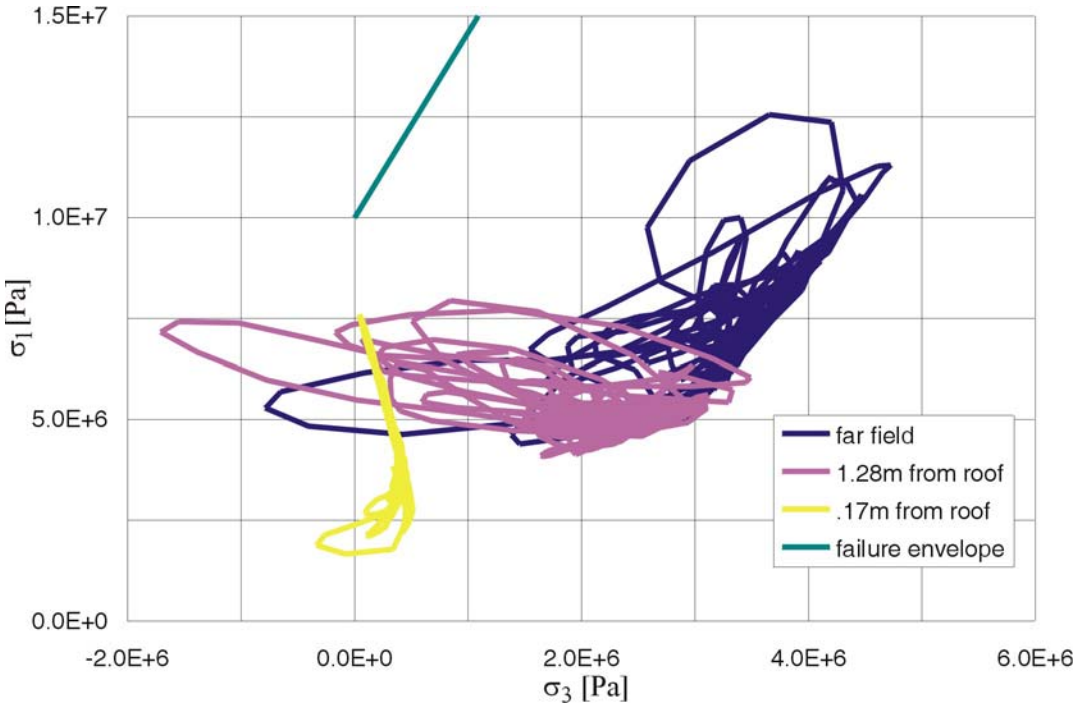

Figure 6-134. Elastic Stress Paths in the Drift Roof Due to Postclosure Ground Motion No. 1: Category 1

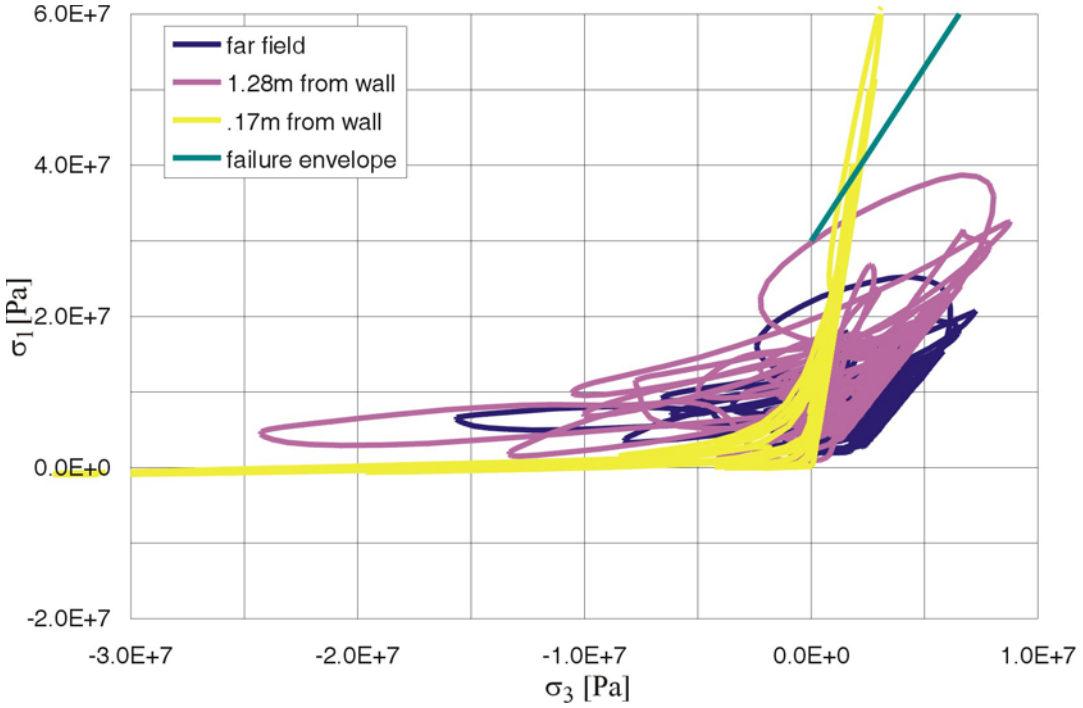

Figure 6-135. Elastic Stress Paths in the Drift Wall Due to Postclosure Ground Motion No. 1: Category 5

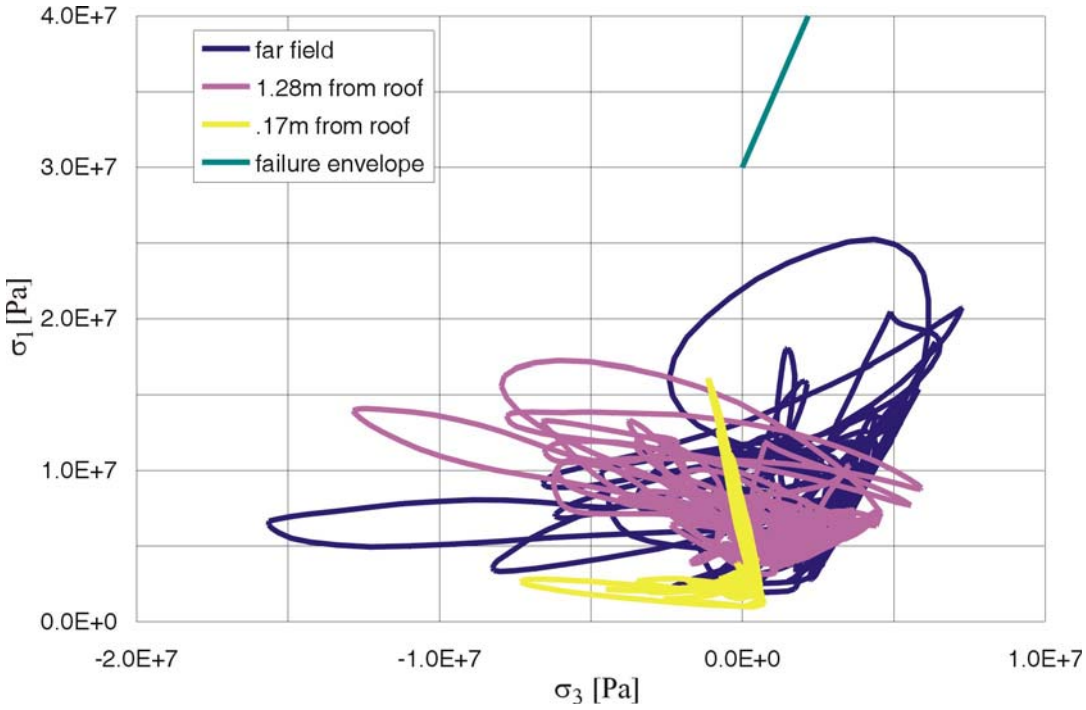

Figure 6-136. Elastic Stress Paths in the Drift Roof Due to Postclosure Ground Motion No. 1: Category 5

6.4.2.2.3 Sensitivity of Mechanical Properties to Rockfall Prediction

The base case and bounding case rock mechanical properties are presented in Table 6-41. Uncertainties for the range of rock properties are considered in the previous sections with 5 categories of rock mass properties which cover the strength range of 10 to 30 MPa. Consideration was also given to the likely scatterness of the strength within the same category (the lower and upper bounds column in Table 6-41). This section presents the results for the analyses based on lower bound strength properties. The upper bound with higher strength will yield more stable drift conditions compared with the base case and hence is not considered in the sensitivity study. The region of analyses is simplified as homogeneous material for the base case and lower bound case. Sensitivity of spatial variation within the model region is also considered.

6.4.2.2.3.1 Consideration of Lower Bound Strength

Based on the assessment of rock mass properties documented in Appendix E (Section E4.1), the lower bound strength ranges from 10 MPa to 16 MPa for the 5 categories compared with the range of 10 MPa to 30 MPa for the base case. In fact, 10 MPa lower bound strength was assigned to categories 1 to 3 (Table 6-41). Categories 3 and 5 were selected for the seismic analysis sensitivity consideration. Since rockfall results presented in the previous sections indicate that minor spalling or no damage is predicted for the preclosure ground motion and drift collapse predicted for the 1×10^{-6} ground motions, the sensitivity case only considers 1×10^{-5} ground motions. The 15 ground motions were applied to categories 3 and 5 rock. Collapse of the drift is observed for most of the cases even with category 5 rock. Figure 6-137 shows the results for category 5 rock subject to ground motion set 12 (PGV = 104 cm/sec), set 4 (PGV = 152 cm/sec), and set 7 (PGV = 333 cm/sec), the same selection as presented in Figures 6-125 to 6-127. The results represent a very conservative for the nominal case with the consideration in that the surrounding rock is homogeneous and entirely biased to the low-strength end of the distribution within its category. Since the lower bound is estimated based on the saturated samples as shown in Figure E-18, the results indicate that the saturated drift environment is likely to collapse when subject to 1×10^{-5} ground motions. But for nominal case with relatively dry condition, spatial variation of rock around the drift is most realistic and should be considered. This is described in the following subsection.

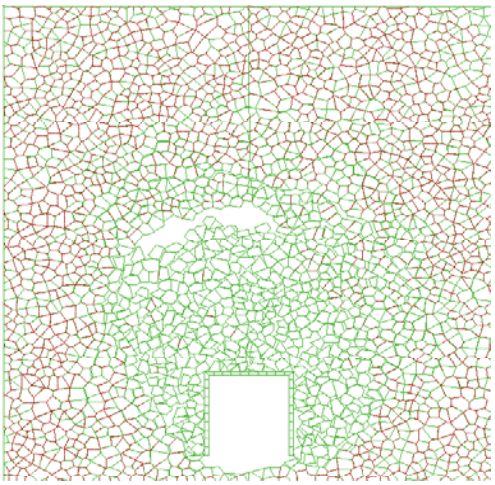

a) ground motion set 12, peak ground motion = 104 cm/sec

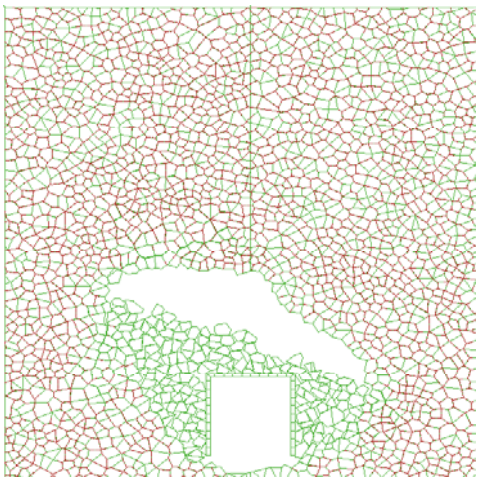

b) ground motion set 4, peak ground motion = 152 cm/sec

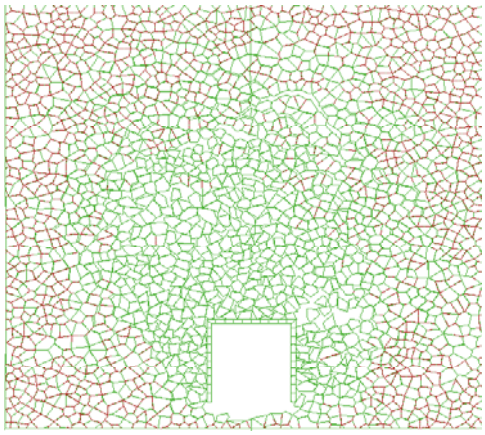

c) ground motion set 7, peak ground motion = 333 cm/sec

Figure 6-137. Drift Damage for Category 5 Lower Bound Strength Subject to 1×10^{-5} Ground Motions

6.4.2.2.3.2 Impact of Spatial Variability on Drift Stability

In the previous analyses, the rock mass properties were considered homogeneous for a given drift cross-section. Here, the impact of considering actual spatial variability of lithophysal porosity on damage from 1×10^{-5} ground motions is examined. A representative section of the Tptpll was extracted from the upper portion of the lithophysal porosity model as described in Appendix T. This model contains a wide range of lithophysal porosity averaging approximately 15 percent, but ranging from greater than 20 percent to less than 10 percent. The resulting UDEC lithophysal rockfall model showing spatially variable porosity is given in Figure 6-138.

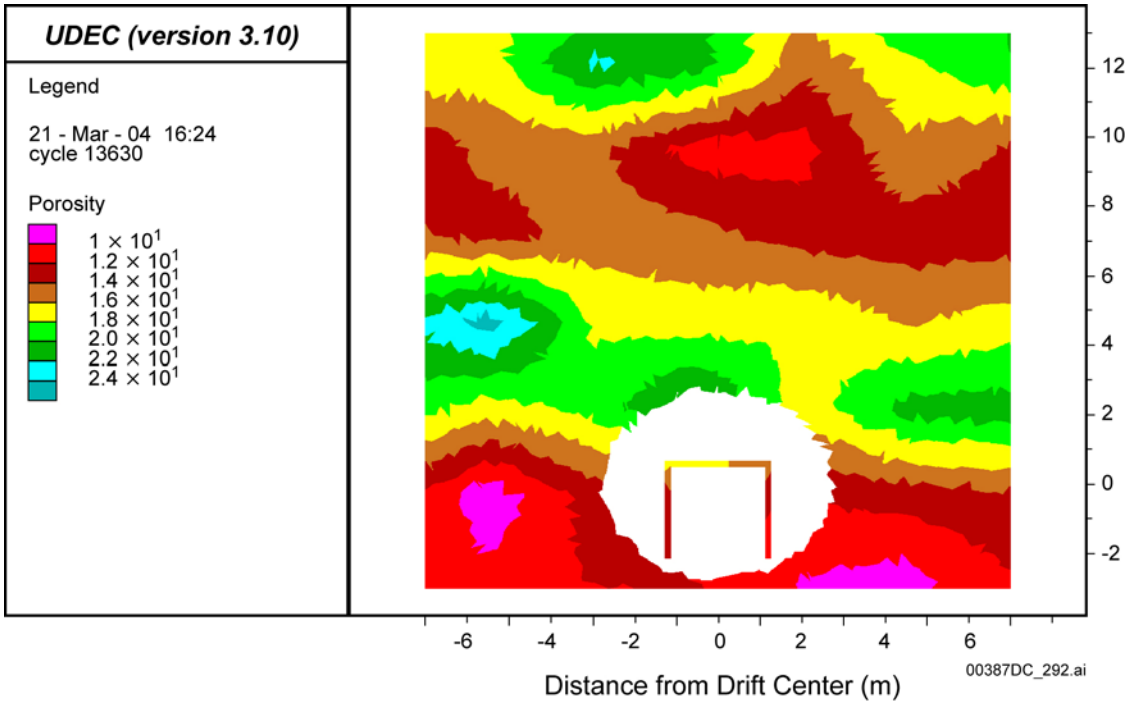

NOTE: Lithophysal porosity variability derived from Appendix T, Figure T-5.

Figure 6-138. Contours of Lithophysal Porosity Contoured on the UDEC Spatial Variability Model

Rock mass strength properties for Categories 1 to 5 were assigned to regions within the model based on the lithophysal porosity levels (Table E-10), achieving spatial variability in strength and moduli. This model was subjected to the 15 1×10^{-5} ground motions, and damage levels were determined. The results of the dynamic simulations, in terms of damage versus PGV, are shown in Figure 6-128. The damage levels are approximately within the range of that predicted for Category 3 rock mass, as expected, because the mean lithophysal porosity of the model falls within the range of the Category 3 levels. This analysis indicates that the use of homogenous rock properties that span the range of strength categories does span the range of expected response, including conservative damage for the low strength categories.

6.4.2.2.4 Estimation of Drift Profile for Feeds to the Abstraction of Drift Seepage

The analyses presented here have provided an estimate of the extent of drift degradation due seismic shaking as a function of annual probability of exceedance. A summary of the resulting drift profiles extracted from the UDEC lithophysal rockfall modeling is provided in output DTN: MO0306MWDDPPDR.000 [DIRS 164736] for the worst case for preclosure and postclosure damage from seismic loading. The drift profile exhibiting the greatest breakout resulting from preclosure ground motion is shown in Figure 6-120. The drift profile exhibiting the greatest breakout resulting from 1×10^{-6} postclosure ground motion is shown in Figure 6-132, which shows complete collapse of the drift opening. The 1×10^{-7} postclosure ground motion also results in complete drift collapse.

Among other factors, the seepage flux depends on both the size and geometry of the drift and the capillary strength of the fractured rock surrounding the drift opening (BSC 2004 [DIRS 169131], Section 6.4.2.4). In partially or fully collapsed drifts, the larger size and potentially different crown shape after collapse will reduce the potential for flow diversion compared to the initial drift geometry; furthermore, the larger footprint of the collapsed drift leads to an increase in the total amount of percolation flux arriving at the drifts, which, in turn, can affect the total amount of seepage. In addition, the capillary-barrier behavior at the drift wall can be affected by the rubble rock particles filling the opening, as the capillary strength inside the opening will be different from the zero capillarity condition in the initially-open drift. Thus, the geometry of the degraded drift and the capillary strength of the rubble material inside the drift are of importance in the abstraction of drift seepage.

Appendix R includes the drift profiles for strength Category 1 rock with consideration of seismic loading, thermal loading (discussed in Section 6.4.2.3), and strength degradation (discussed in Sections 6.4.2.4 and 6.4.2.5). Thirty scenarios are provided. Appendix R also provides information for degraded rock mass characteristics around the opening that may be of potential importance from a seepage or capillary strength standpoint. The information consists of the stress tensor for UDEC zones, aperture change along the joints, and averaged volumetric strain.

6.4.2.3 Thermal Consideration in Lithophysal Units

6.4.2.3.1 Thermal Loading

Geometry and boundary conditions used in the model for predictions of thermally induced rockfall are shown in Figure 6-139. A detailed discussion of the boundary conditions for the thermal-mechanical model is provided in Appendix W. The model does not perform complete thermal-mechanical simulations. Instead, temperature fields calculated with the code NUFT, for 1.45 kW/m and 50 years of forced ventilation, are imported into UDEC (thermal calculation described in Section 6.2, see Appendix U for methodology for importing temperatures). Two cases of ventilation efficiency were considered: 90 and 70 percent. Stresses are calculated for each new temperature state based on the temperature increment (from the previous temperature state) and the coefficient of thermal expansion. For the considered cases, the same coefficient of thermal expansion as a function of temperature, was used. To have gradual evolution of stresses during the simulated time, 45 temperature fields (corresponding to different

times after waste emplacements) were imported from NUFT to UDEC. For each new temperature field, a simulation was conducted in two steps:

- The model was run to equilibrium elastically (i.e., the unbroken bonds were made infinitely strong)
- After the model had reached equilibrium, the actual strength was assigned to the unbroken bonds and the model was run again to the equilibrium.

The reason for the two-step approach was to reduce the impact of non-gradual stress changes due to incremental changes of the temperature state. The entire analysis was conducted considering that rock mass strength does not degrade with time. Any observed damage and rockfall are consequences of the thermally induced stresses only. The three cases of thermal calculation (described in Section 6.2) were considered for the drift stability analysis in lithophysal rock mass:

- Base case (average thermal properties and 90 percent ventilation efficiency)
- Case 2, sensitivity calculation for thermal properties (thermal properties one standard deviation smaller than the average properties)
- Case 3, sensitivity calculation for the heat removal ratio (average thermal properties and 70 percent ventilation efficiency).

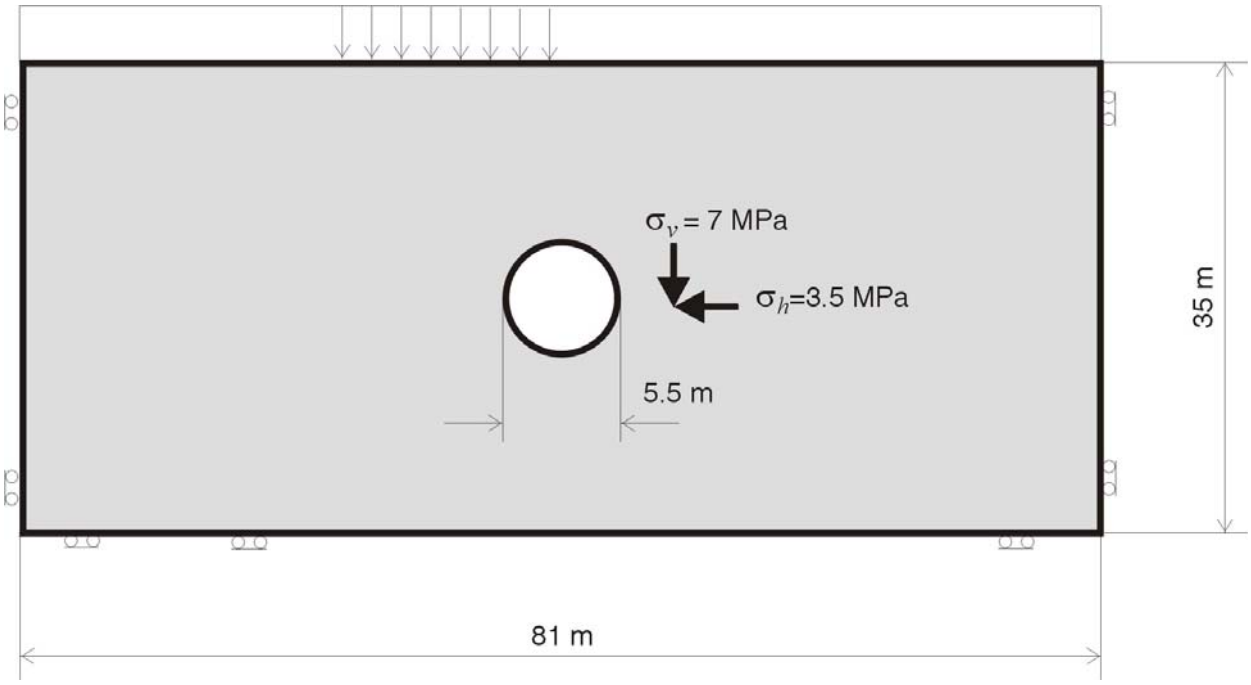

Figure 6-139. Thermal-Mechanical Model Initial and Boundary Conditions

The simulation was conducted for the five mechanical properties categories of the rock mass. It is observed that the amount of thermally induced rockfall is generally small. The temperature and stress fields for rock mass Category 1 with the base case thermal properties and 90 percent ventilation efficiency are shown in Figure 6-140. The figure shows the model state after 80 and 10,000 years of heating for the consideration of no time-dependent change in rock strength. There is no significant rockfall or damage induced by heating. Conditions are similar for other rock mass categories. Elastic stress paths during 10,000 years of temperature variation are shown in Figures 6-141 and 6-142, for rock mass Category 1 in the wall and roof, respectively; and in Figures 6-143 and 6-144, for rock mass Category 5 in the wall and roof, respectively. The elastic stress paths confirm the results of the UDEC lithophysal rockfall model. The drift wall in the Category 1 rock mass is in the yielding state after drift excavation. Heating does not increase damage significantly (Figure 6-141). The stress state in the drift roof in Category 1 (shown in Figure 6-142) moves closer to the yield surface during heating, but it remains elastic. The thermal stress increase in the drift roof in the Category 5 rock mass (Young's modulus of 19.7 MPa) moves the stress state barely above the yield surface (Figure 6-144) during the relatively short period when the temperature reaches the maximum, around 80 years after waste emplacement. This is consistent with observation of minor rockfall from the drift roof in rock mass Category 5.

The rockfall simulations using temperatures from Cases 2 and 3 of the thermal calculation do not show any increase in rockfall compared to the base case.

6.4.2.3.2 Combined Seismic and Thermal Effect in Lithophysal Units

Stability of the emplacement drifts located in the lithophysal rock units was investigated for both thermal and seismic loading conditions independently for both seismic and thermal loading conditions in Sections 6.4.2.2 and 6.4.2.3.1, respectively. The initial condition for the seismic analysis discussed in Section 6.4.2.2 was in situ stress state perturbed by excavation of the drifts only. An additional analysis, presented in this section, was done to assess the effect of changing thermal stress in the rock mass around the repository after waste emplacement as an initial condition for seismic ground shaking. Using a similar approach as for the nonlithophysal rock (Section 6.3.1.4), stress paths during the regulatory period of 10,000 years were recorded at a number of locations around the drift. Temperatures from the thermal calculations for the base case and the sensitivity calculation for the heat removal ratio (case 3 in Section 6.2) were considered. The critical state was qualitatively determined from those paths, based on locations of stress states along that path relative to the yield surface. The critical state was used as an initial condition for the seismic analysis. Because the ground motion with 1×10^{-6} probability of annual occurrence results in complete drift collapse, it was not of particular interest to investigate the effect of that level of ground motion combined with thermally induced initial stresses. Instead, ground motions with 1×10^{-4} and 1×10^{-5} probability of annual occurrence were considered. Since the predicted temperatures are similar for the base case and the sensitivity case 2 at preclosure period, the sensitivity case 2 is not considered for the evaluation of the combined seismic and thermal effect. Rock mass categories 1 and 5 were considered in this analysis.

Stress paths (transient change in principal stresses) at 14 different locations around the drifts in rock mass category 5 during the regulatory period of 10,000 years are shown in Figures 6-141,

6-142, and 6-143. A yield condition corresponding to 30 MPa uniaxial compressive strength, and a friction angle of 40º is also indicated in the figures. The stress state at a point close to the drift springline (shown in Figure 6-141), is above the yield surface, indicating yielding. Because those stresses are at the points inside the elastic blocks (inelastic behavior of this model is due to inelastic deformation of joints only), it is possible that they lie outside the yielding surface. The initial stress state and the state after 80 years of heating, selected as critical on the stress path, are marked on the plots with the squares.

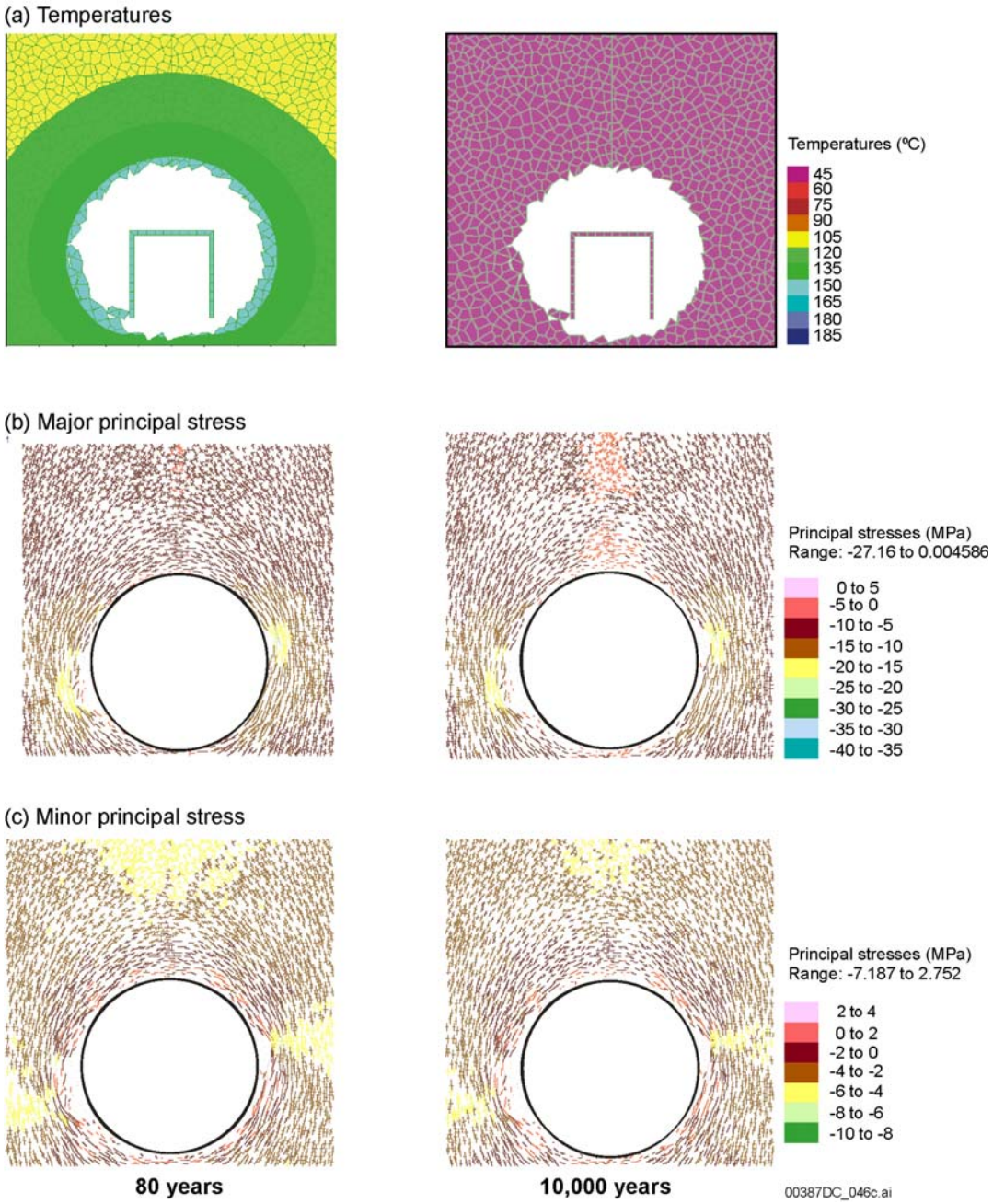

Figure 6-140. Thermally Induced Rockfall and Stresses After 80 and 10,000 years of Heating in Rock Mass Category 1

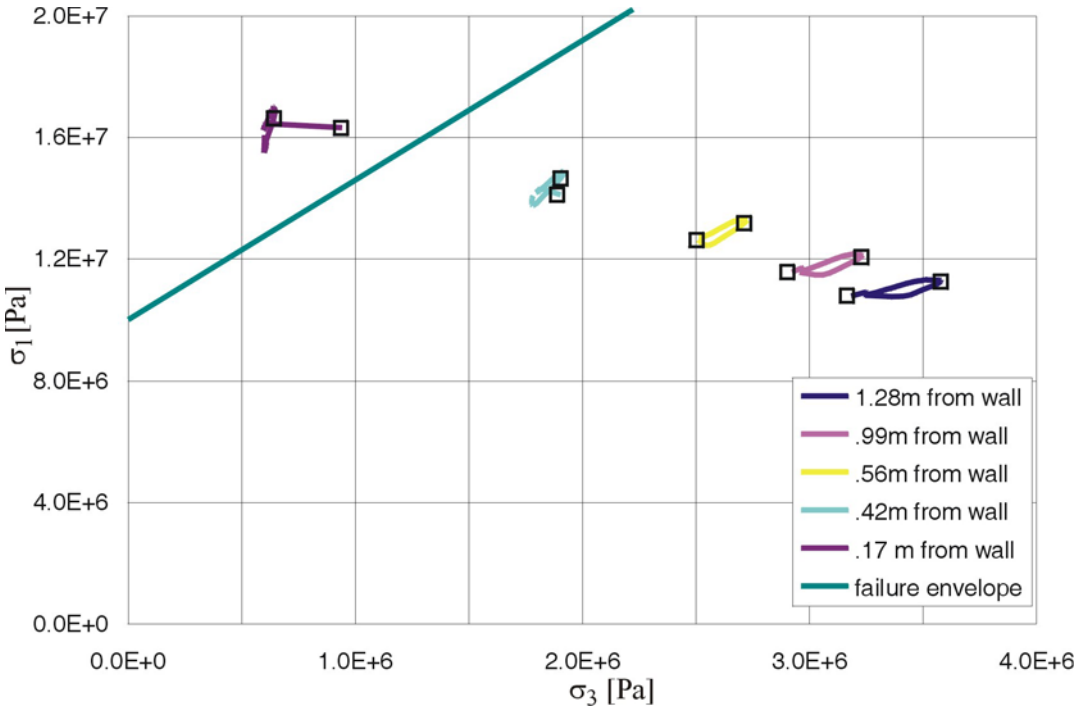

Figure 6-141. Elastic Stress Paths in the Drift Wall Due to Temperature History: Category 1

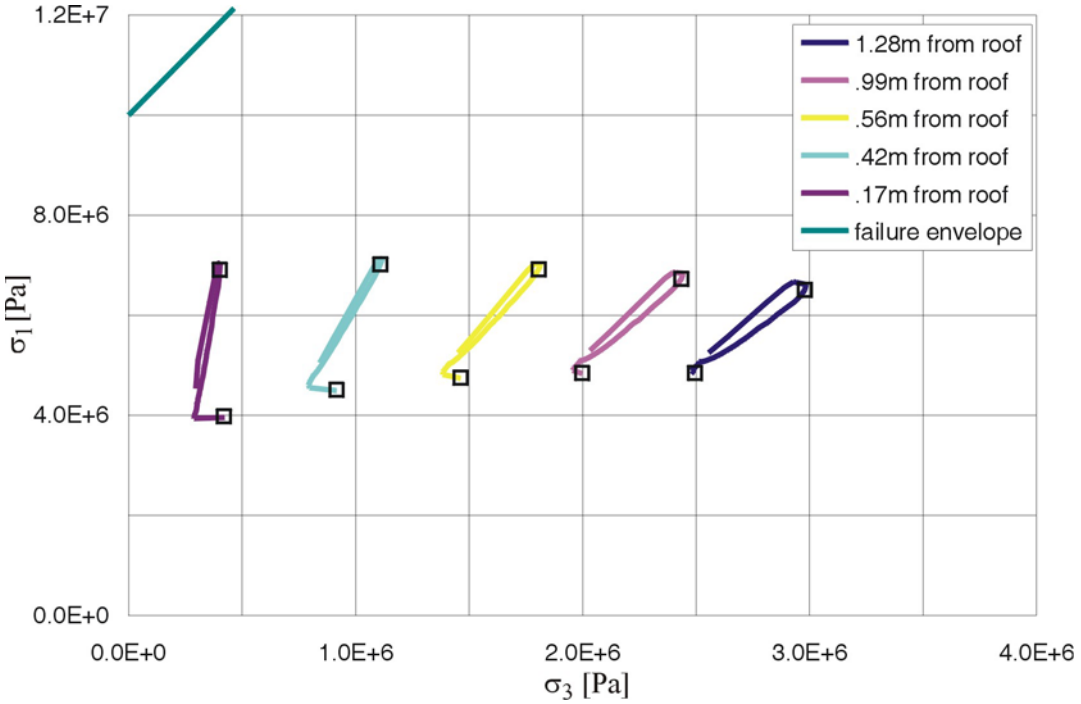

Figure 6-142. Elastic Stress Paths in the Drift Roof Due to Temperature History: Category 1

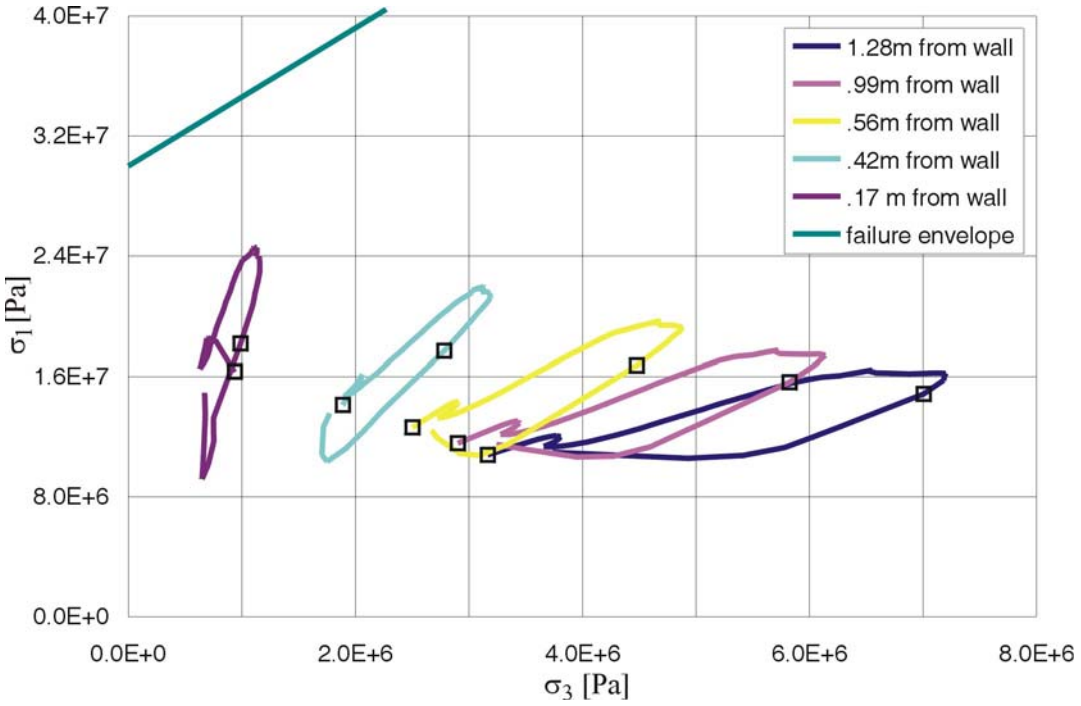

Figure 6-143. Elastic Stress Paths in the Drift Wall Due to Temperature History: Category 5

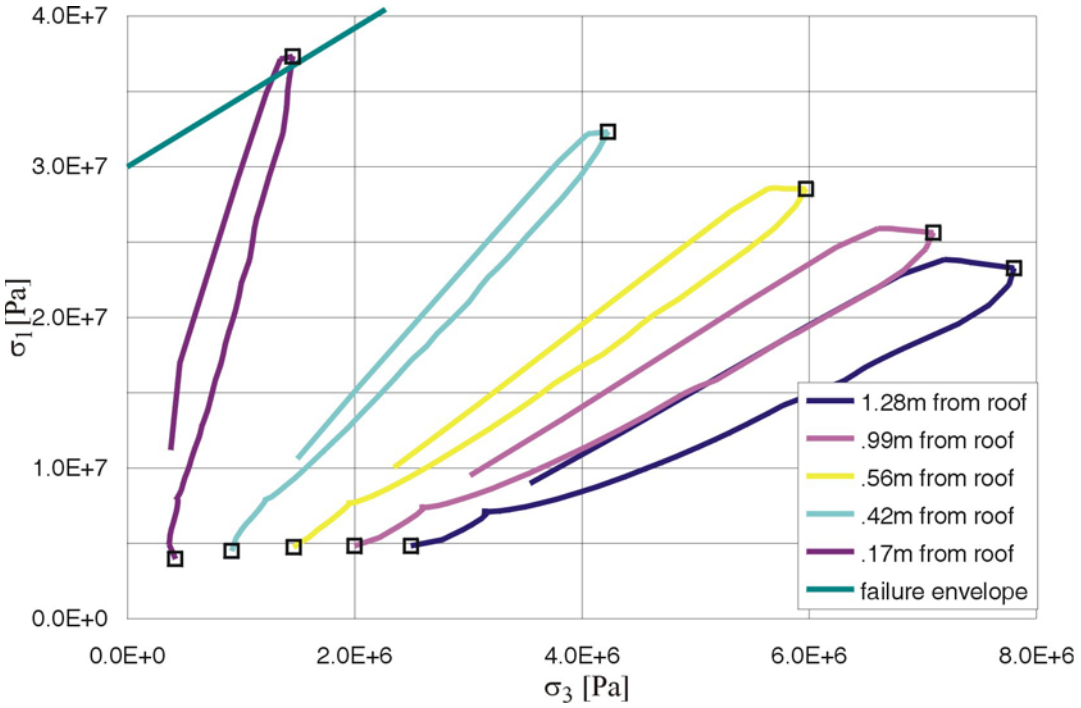

Figure 6-144. Elastic Stress Paths in the Drift Roof Due to Temperature History: Category 5

Seismic analysis after 80 years of heating for rock mass category 1 resulted in an increased rockfall compared to rockfall from the seismic shaking of the rock mass at an in situ stress state (see Figure 6-145 for results with 1×10^{-4} ground motion). Very little rockfall is induced in rock mass category 5 in the case of 70 percent ventilation efficiency. For the cases with 80 years heating and 1×10^{-5} ground motions shaking, 3 sets of ground motions were considered: (a) set 10 with peak ground velocity = 104.6 cm/sec, (b) set 6 with peak ground velocity = 173.88 cm/sec, and (c) set 13 with peak ground velocity = 318.01 cm/sec. The results are presented in Figures 6-146 to 6-148. Rockfall with set 10 ground motion are similar to the results for preclosure ground motions. However, more extensive rockfall is observed for ground motion sets 6 and 13. The results show increase of rockfall for category 5 rock mass when comparing with seismic only scenario with large ground motions as shown in Figure 6-127.

The result of an increase in rockfall for lithophysal rock mass category 1 with thermal loading is in an apparent contradiction with the results of the same analysis for the nonlithophysal units. Thermal stresses in the case of nonlithophysal rock resulted in reduced rockfall. However, the mechanism of rockfall is completely different for these two cases. In the case of the nonlithophysal rock mass, rockfall is due to sliding of blocks along the pre-existing joints, and an increase in the initial stress increases confinement on the joints, thereby increasing their resistance to sliding. In the case of the lithophysal rock mass, ground motion with 1×10^{-4} probability of annual occurrence causes rockfall by shaking down already damaged rock mass around the drift. Therefore, the heating induces additional damage (compared to damage caused by drift excavation), which does not necessarily result in a rockfall under static loading conditions, but is shaken down by the 1×10^{-4} ground motion.

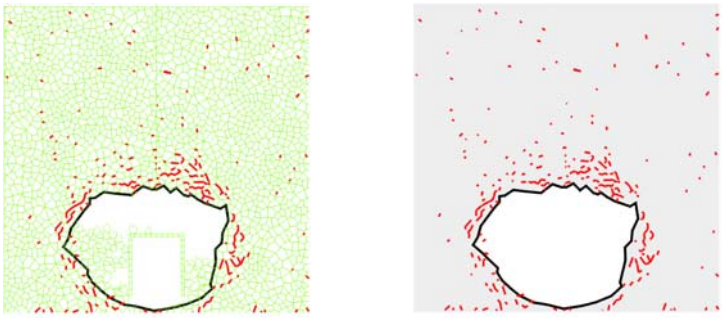

a) category 1

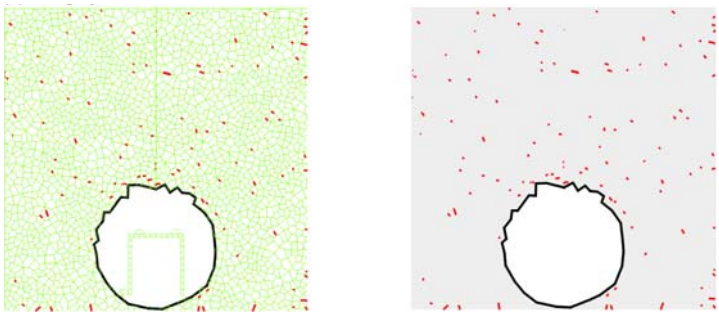

b) category 5

Figure 6-145. Rockfall and Fractures Induced Around a Drift by 1×10^{-4} Preclosure Ground Motion After the Peak Thermal Condition Occurring at 80 Years of Heating (30 Years after Closure) in Rock Mass Categories 1 and 5

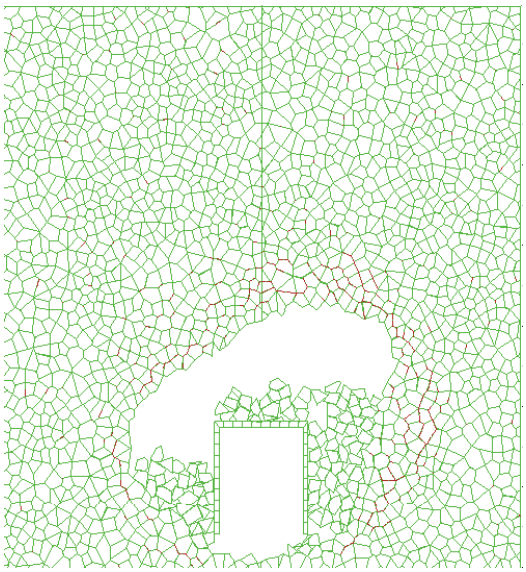

a) Category 1

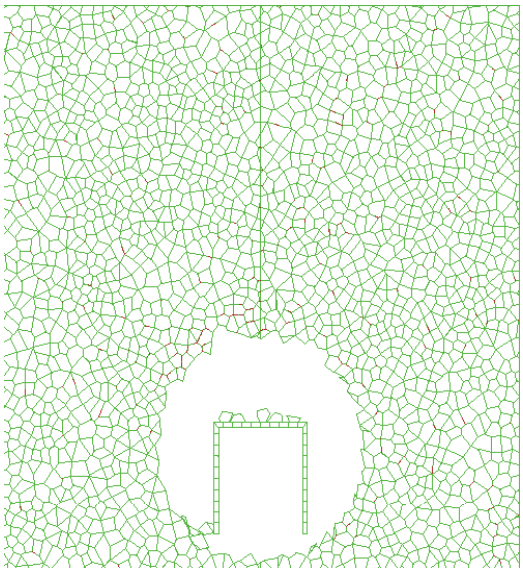

b) Category 5

Figure 6-146. Rockfall and Fractures Induced Around a Drift by 1×10^{-5} Earthquake Set 10 (peak ground velocity = 104.6 cm/sec) After 80 Years of Heating in Rock Mass Categories 1 and 5

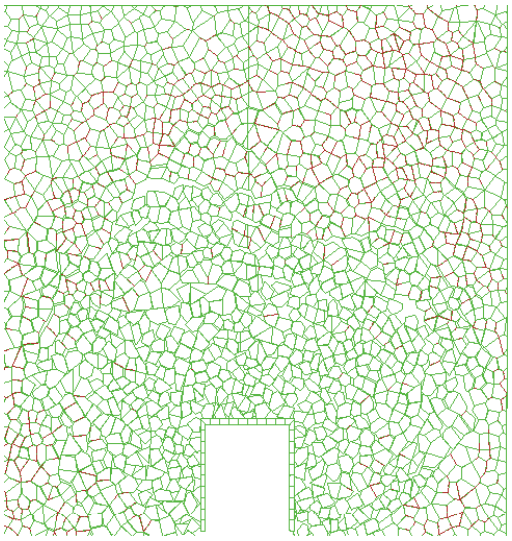

a) Category 1

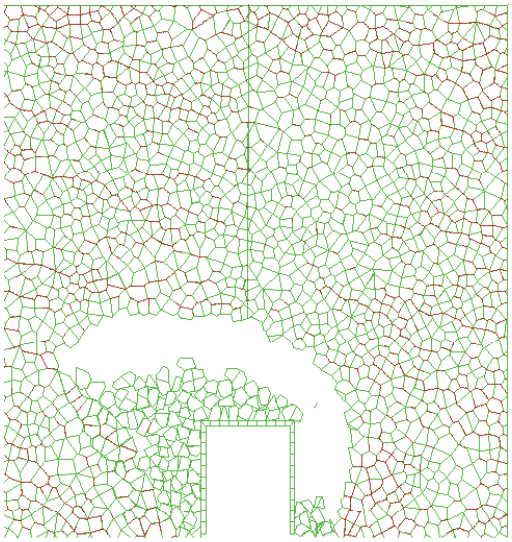

b) Category 5

Figure 6-147. Rockfall and Fractures Induced Around a Drift by 1×10^{-5} Earthquake Set 6 (peak ground velocity = 173.88 cm/sec) After 80 Years of Heating in Rock Mass Categories 1 and 5

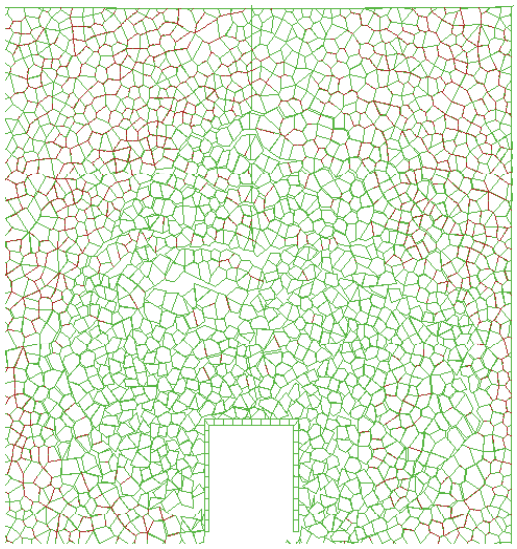

a) Category 1

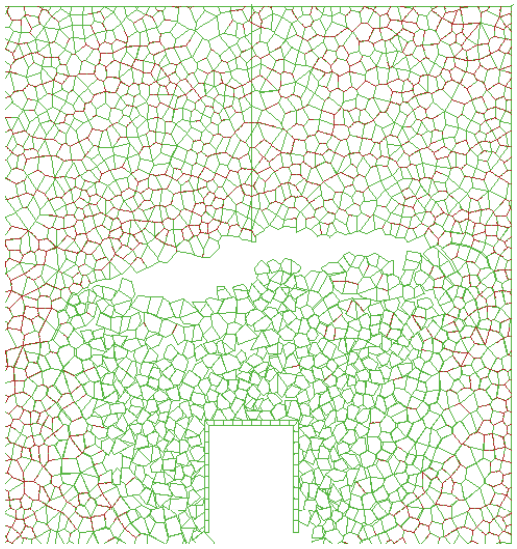

b) Category 5

Figure 6-148. Rockfall and Fractures Induced Around a Drift by 1×10^{-5} Earthquake Set 13 (peak ground velocity = 318.01 cm/sec) After 80 Years of Heating in Rock Mass Categories 1 and 5

6.4.2.4 Time-Dependent Consideration in Lithophysal Units

Underground and surface excavations, which are designed to be stable after excavation, degrade with time, and some eventually collapse completely. The degradation of excavations in hard rocks has not been studied extensively, because most underground excavations have service lives of 100 years or less and are maintained as required. However, there are many examples of stable, unsupported excavations associated with mining, and civil construction or

naturally-occurring caves in numerous rock types that are stable, or have suffered only minor instability for hundreds or even thousands of years. Thus, there is no certainty that collapse of unsupported excavations, particularly those subjected to low stress, relatively dry conditions, is inevitable.

The primary reason for eventual yield and collapse is that a hard rock mass, exposed to humidity and temperature of the open atmosphere, may undergo strength decay with time when it is loaded to stress levels higher than about 50 to 60 percent of its short-term strength. The rate of strength decay depends on, among other parameters, rock type (particularly the mineralogy and grain structure), stress state, relative humidity, and temperature. Stress corrosion is considered the primary mechanism causing strength degradation of hard rocks (Potyondy and Cundall 2001 [DIRS 156895], Section 3).

The emplacement drifts at Yucca Mountain will be stable under existing conditions (in situ stresses and rock mass strength) with ground support as demonstrated by the ESF and ECRB Cross-Drift observations. However, it is expected that the ground support will completely lose its integrity during the 10,000-year regulatory period, and drift degradation, to some extent, will occur due to strength decay of the rock mass. Drift degradation is an important issue for repository design and performance because drifts must remain stable during the preclosure operational period and, eventually, rubble resulting from degradation could impact in-drift environmental conditions, seepage, and the integrity and performance of the drip shields. Estimation of the rate of drift degradation for the duration of the 10,000-year regulatory period is, therefore, required.

6.4.2.4.1 Empirical Observations of Degradation and Collapse of Excavations

6.4.2.4.1.1 Unsupported Excavation Spans and Stand-Up Time

There is currently no accepted methodology for estimating the time-dependent degradation behavior of tunnels in hard rocks. However, a number of empirical correlations have been developed for providing a means of estimating maximum stable spans of unsupported excavations and the length of time that an unsupported excavation may remain open and still provide a safe working environment (termed stand-up time) (Bieniawski 1989 [DIRS 101715]). Because these correlations are often used in estimating the time of instability of excavations, this appendix discusses their applicability to the postclosure stability of emplacement drifts at Yucca Mountain.

Emplacement drifts for the repository are 5.5 m in diameter, are separated from one another by a center-to-center distance of 81 m, and are located at a nominal depth of 300 m below ground surface. The large ratio of drift diameter to spacing and diameter to depth means that each emplacement drift is mechanically isolated from one another and from the effects of the ground surface. Eventually there is thermal interaction between tunnels, but the local mechanical effects related to isolated tunnels is of greatest importance to short-term and long-term stability. Comparison of the maximum unsupported span from mining practice to the span of the proposed emplacement drifts is a reasonable means of estimating collapse potential.

As the span of an excavation is made larger, there eventually becomes a point when instability and unsafe working conditions result. Empirical correlations (e.g., Hoek and Brown 1982 [DIRS 120981], p. 287) of the maximum safe unsupported span and the time that this span may remain unsupported have been developed to assist tunneling engineers in planning excavations that are safe for tunnel construction workers. These correlations, which are typically based on some measure of rock mass quality, are inherently conservative in nature due to their purpose: to ensure personnel safety. The correlations are not based on case histories of actual collapse. For example, stand-up time is typically projected to be on the order of hours or days, even for good quality rock masses and may be only on the order of years (e.g., Hoek and Brown 1982 [DIRS 120981], Figure 6). Examples of the existing tunnels at the Yucca Mountain site and Hoover Dam indicate that stand-up time is a worker-safety-related indicator and is not relevant to predictions of degradation or collapse time. These remarks indicate that construction-related span and stand-up time correlations have only limited application to postclosure predictions of drift degradation at the Yucca Mountain site.

Stand-up time curves provide an estimate for potential of rockfall as a function of span, rock-mass quality, and time after excavation. The stress state around an excavation (e.g., depth of the excavation) is not a parameter that affects the stand-up time estimate. The stress state in the rock mass around the excavation, scaled to the short-term strength of the rock mass, is one of the most important factors controlling stability of the rock mass and evolution of stability as a function of time. Stand-up time curves were developed based on empirical evidence of instability of excavations in particular stress conditions (e.g., deep South African mines), and their application to completely different conditions is not relevant.

6.4.2.4.1.2 Evidence of Maximum Unsupported Span from Mining Case Examples

The mining industry, on the other hand, routinely drives unsupported excavations to large spans with the express purpose of inducing collapse for caving of ore bodies. Therefore, empirical evidence of maximum unsupported spans from mining case examples is more relevant to the estimation of the actual spans of excavations that induce degradation and ultimate collapse. The span of an excavation required to induce caving and collapse has been the topic of extensive study in the mining industry because certain types of mining methods (e.g., block and panel caving) are predicated to induce caving when a rock mass is undercut. Brown (2003 [DIRS 169527]) provides a summary of worldwide caving operations and the spans of excavations necessary to induce collapse as a function of the rock mass quality (i.e., strength). Figure 6-149 provides a summary of worldwide experience in excavation span and collapse potential for cave mining. The plot provides a correlation between rock mass quality rating (in terms of rock mass rating) and the hydraulic radius (plan view area/perimeter) of excavations that produce: (1) stable spans, (2) transitional excavations in which instability may begin but caving is not yet occurring, and (3) caving. As the rock mass quality rating decreases, the spans at which collapse occurs also decrease. To apply these data to emplacement tunnels at Yucca Mountain, an estimate of the rock mass quality is required. The case of lithophysal rock is presented here because it is the weakest of the host horizon units. As described in *Subsurface Geotechnical Parameters Report* (BSC 2003 [DIRS 166660], Section 9.2.5), the estimated rock mass quality rating in terms of Geologic Strength Index or Rock Mass Rating (GSI or RMR) for the lithophysal rocks at Yucca Mountain is in the range of approximately 50 to 60. For this range of RMR, the hydraulic radius of a flat-roofed excavation required for caving is in the range

of approximately 25 to 35 m (Figure 6-149). A transitional zone between stable excavations and caving for the lithophysal rock RMR range occurs for hydraulic radii of 15 to 20 m. For the proposed 5.5-m diameter emplacement drifts, the hydraulic radius is simply equal to the radius (2.75 m). Therefore, field practice indicates that the stable to transitional caving–stable state is characterized by a hydraulic radius for lithophysal tuff in the range of 15 to 20 m. The boundary between transitional stable/caving to a caving state is characterized by a hydraulic radius in the range of approximately 25 to 35 m. Note that the typical mining undercut has a flat roof, which promotes instability, while the shape of the emplacement drifts is circular, which promotes stability. The emplacement drift hydraulic radius is, therefore, approximately 5 to 7 times below what would be considered to be a transitional state between stable and caving conditions. Based on field experience in caving, the hydraulic radius of the emplacement drifts is well below the level of the hydraulic radius estimated to be in a transitional state of collapse and even further below the level for assurance of complete collapse. Therefore, it is not surprising that the existing ESF and ECRB Cross-Drift (7.62- and 5-m diameter, respectively) are stable and show no evidence of degradation nearly a decade after excavation, even though the ground support is minimal.

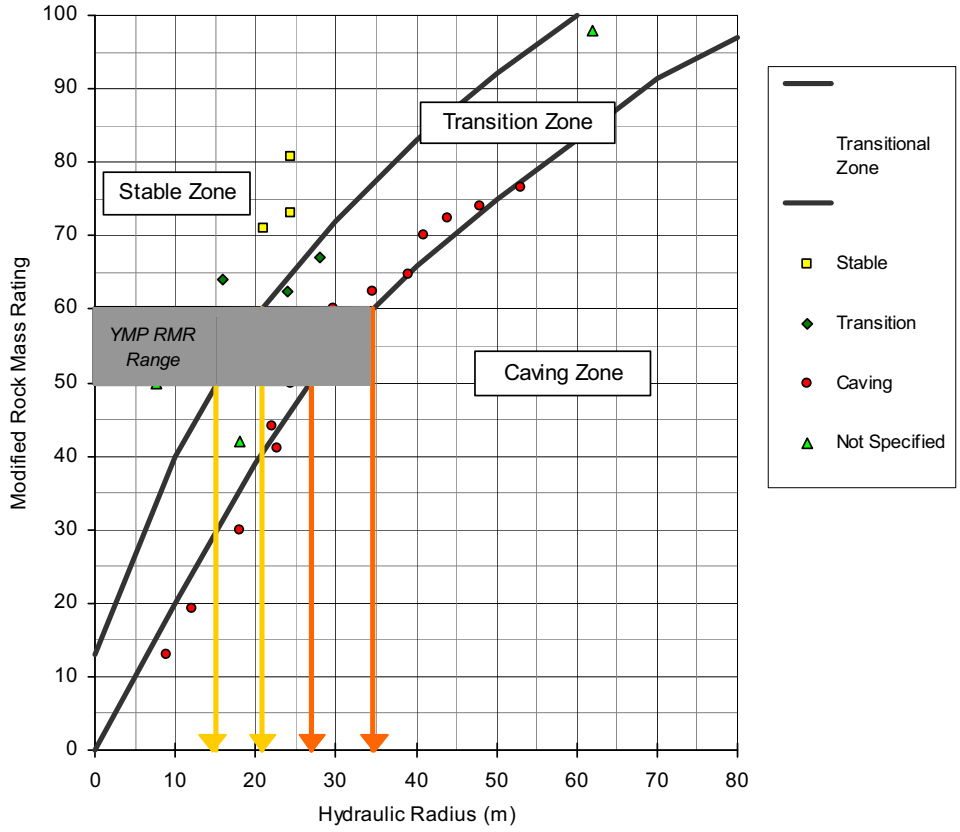

Source: Brown 2003 [DIRS 169527], Figure 3.1.

NOTE: Caving potential is expressed in terms of the modified rock mass rating and hydraulic radius. Modified rock mass rating is equivalent to rock mass rating in case of Yucca Mountain excavations. Stable and caving regions are separated by a transition zone.

Figure 6-149. Excavation Dimensions Required for Caving Gained from Field Experience in Block and Panel Caving Mines

6.4.2.4.1.3 Observations of Yucca Mountain Tunnels and Excavations at Hoover Dam

Unsupported or lightly supported tunnels (although perhaps not considered safe from a personnel standpoint) can stand in a stable condition for long time periods, particularly in good quality rock masses. For example, the ESF (7.62 m diameter) and ECRB Cross-Drift (5 m diameter) tunnels at the Yucca Mountain site were constructed in 1995 to 1997 and in 1998, respectively. Although the ESF main loop is located largely in the Tptpmn, the ECRB Cross-Drift cuts through and exposes all of the repository host horizon units. The tunnels are, in general, lightly supported with friction rock bolts and light wire mesh in the tunnel roof, with occasional friction bolts in the tunnel walls. There is no evidence of significant deterioration or degradation of the rock mass, and no significant episodes of rockfall have occurred.

An external review panel convened to examine Yucca Mountain drift stability (Brekke et al. 1999 [DIRS 119404]) found that excavations of the North Ramp through the upper lithophysal zone and the ECRB Cross-Drift through the lower lithophysal zone show that both zones have properties that are favorable for stability with minimum ground support. The panel also found that rock conditions in the lower lithophysal zone in the ECRB Cross-Drift were similar to those observed in the upper lithophysal zone in the North Ramp; that continuous joints were not apparent, and there was almost no overbreak or loosening of the slabs or blocks; and that zones with more frequent short fractures were present and could be described as fracture zones, but even in these areas, overbreak and block loosening were largely absent. Tunnel deformation measurements have been regularly monitored since excavation, showing stable conditions. The conclusion is that the tunnels in both the lithophysal and nonlithophysal rock masses are in a stable and self-supporting mode with no obvious deterioration in 5 to 8 years. Additionally, the Drift Scale Test involved heating a representative repository-scale tunnel in the nonlithophysal rock mass, first, to postclosure temperature distributions, followed by a thermal overdrive experiment to test rock strength limits. The experiment, now well into its cool-down phase, showed stable and predictable conditions at expected repository peak temperature conditions. Overdrive to approximately 200°C drift-wall temperatures showed predictable, minor spalling of a small portion of the center of the crown of the drift (Section 7.6.5.3). Cool-down has showed no observable loosening or instability of the tunnel. This experiment confirmed modeling estimates of stable drift conditions for expected repository temperature and combined in situ and thermal stress conditions.

The Hoover Dam, with abutments excavated in Tertiary pyroclastic flows, was completed by the Bureau of Reclamation in 1936. Along with the construction of the dam itself are a series of tunnels and adits (Figure 6-150) that were excavated to accommodate the various penstocks, valves, access ways, spillways, and river bypasses. With the exception of the visitor center elevator shaft (completed in the 1990s), the excavations were completed with simple drill and blast methods ("simple" meaning here that no smooth-wall blasting techniques were used). Some of the larger openings, generally those more than 6 m (20 ft) high, were excavated using heading-and-bench methods to develop the full size of the openings. Many of the tunnels and adits were excavated to greater than 12 m (40 ft) in diameter. While some of the penstock and spillway tunnels were lined with concrete, many of the adits and access ways remain unlined.

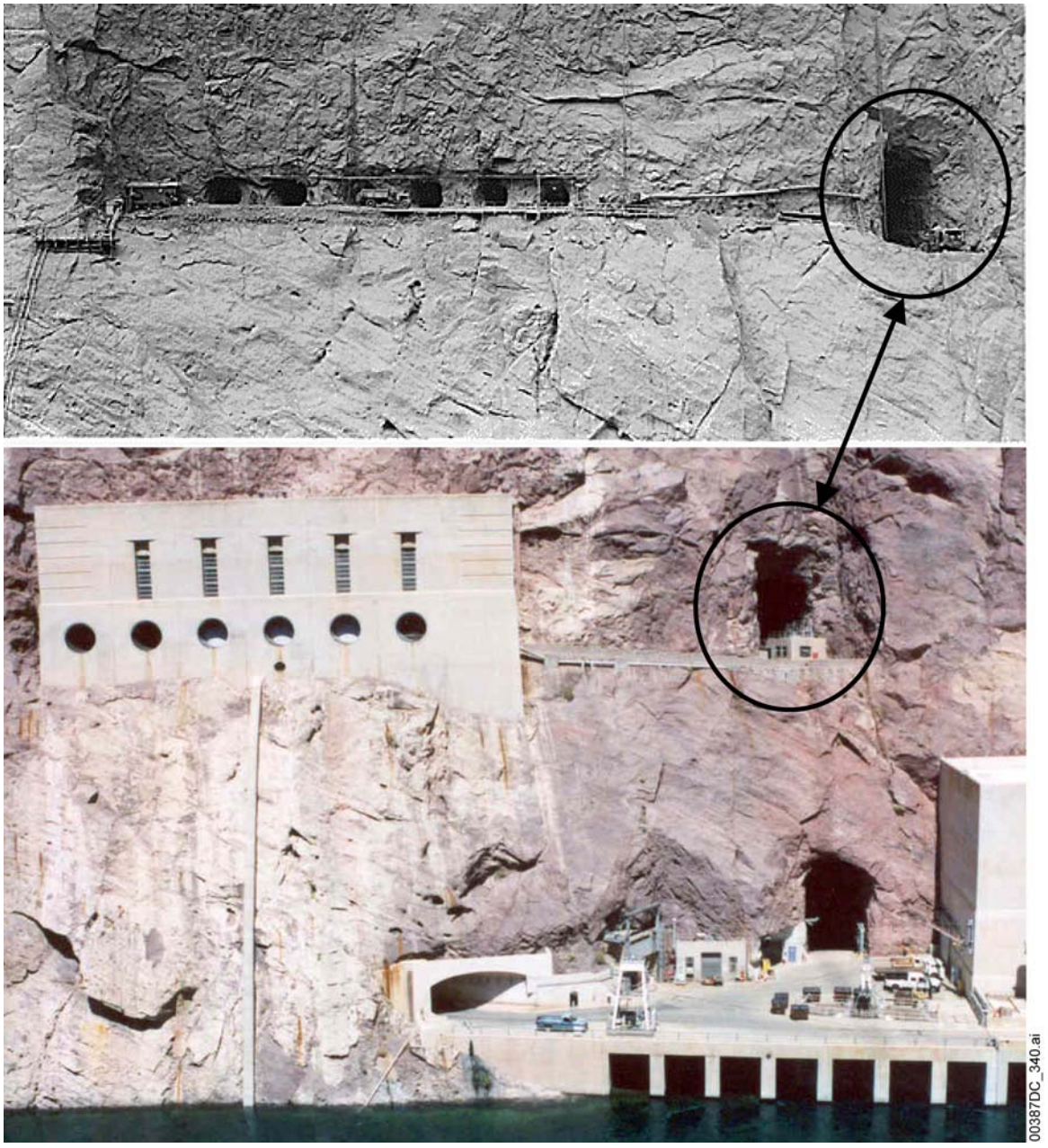

NOTE: Construction adit, shown at right, is approximately 40 ft high.

Figure 6-150. Excavation for Nevada Canyon Wall Outlet Works (Top) Showing Construction Adit in 1933 and (Bottom) in 2004

The rock at the site is the tuff of Hoover Dam, a fairly localized unit composed of andesitic to dacitic pyroclastic flows and breccias. At the dam, the volcanics are slightly to densely welded, and slightly weathered to unweathered. At the penstock adits, the rock is moderately hard to hard and contains abundant lithic fragments and occasional corroded pumice fragments. The rock is slightly to moderately fractured, with most fractures devoid of fracture filling. Many of the discontinuities exposed in the adits are frequently shears and small faults displaying distinct slickensides. Where the adits extend below the phreatic surface, occasional calcium carbonate precipitate is present adjacent to active or old seeps.

The adits were excavated downstream of the power plant to allow insertion of large, steel penstock sections into tunnels that paralleled the canyon walls. The adits are in still in use, housing the sewage treatment system and other support utilities necessary to the function of the dam. The adits are approximately 40 ft (12 m) high by 35 ft (10.7 m) wide (Figure 6-151) becoming slightly taller with depth. After the drill and blast excavation, the adits were left unlined and unsupported, and continue to be unsupported to the present time. Rock fall in the adits has been limited to very occasional centimeter-size fragments, even without ground support.

Additionally, there are numerous access ways throughout the lower canyon walls in and around the Hoover Dam power plant. These smaller tunnels, 6 to 15 ft (1.8 to 4.6 m) in diameter, allow access by personnel and tourists to various areas of the power plant and penstocks. Few of these tunnels are supported either by rock bolts or mesh. No steel supports are visible in the Hoover excavations. As with the adits, rock in the access ways and tunnels has been limited to rare centimeter-size fragments that are removed by the janitorial staff.

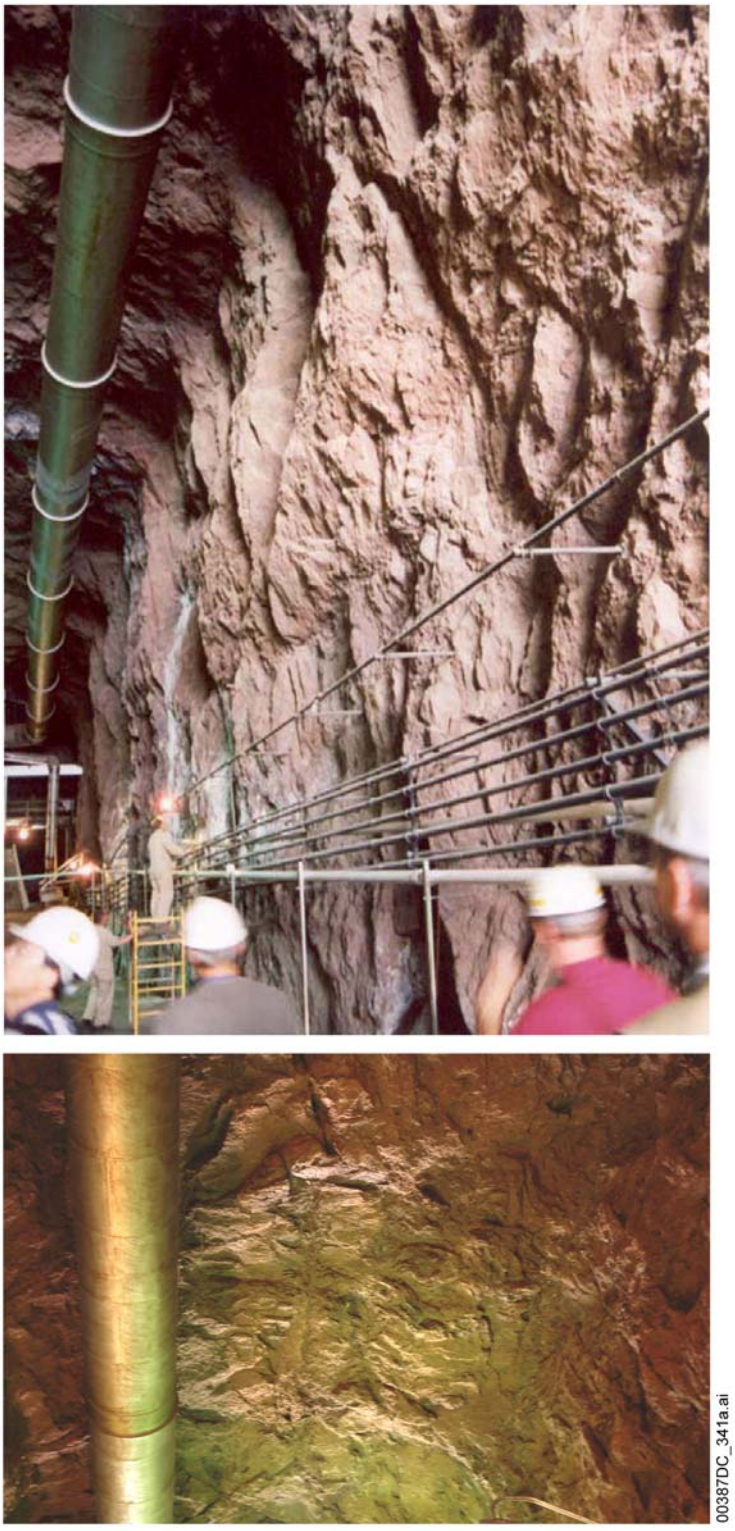

NOTE: Irregular tunnel walls resulting from drill-and-blast excavations (top) and close-up view of the tunnel crown showing evidence of drill half-barrels (bottom).

Figure 6-151. 2004 Photographs of Unsupported Construction Adit at Hoover Dam, Excavated in 1931

6.4.2.4.2 Mechanics-Based Approach to Analysis of Time-Dependent Degradation of Repository Excavations

6.4.2.4.2.1 Background on Time Dependent Characteristics of Brittle Rocks

One of the most striking characteristics of brittle rocks is that at temperatures well below the melting point, a rock subjected to a constant load exhibits a continuous increase in strain with time. This time-dependent deformation is termed creep. Studies on creep indicate that the observed strain depends upon the applied stress, the temperature, the partial pressure of water, and the confining pressure (e.g., Martin 1972 [DIRS 169721]). Moreover, the same mechanism responsible for the strain of brittle rocks in constant strain-rate tests is also operative in creep. That is, cracking, both along grain boundaries and through individual grains, produces the observed strain (e.g., Brace et al. 1966 [DIRS 101990]). Above approximately one half to two-thirds of the compressive strength, the dominant mode of deformation for brittle rocks is the opening and growth of cracks parallel to the major principal stress direction or axial orientation in unconfined compression. It is typically considered that the strain rate of hard rocks in creep is related to the time-dependent growth of these cracks.

Verification of the relationship between time-dependent crack growth and creep strain rate in brittle rock is performed through laboratory testing. Experimental results indicate that stable time-dependent crack growth at a constant compressive load or at a constant stress intensity factor occurs in quartz and glass in the presence of water vapor. Moreover, the rate of crack growth depends on the applied stress, the temperature, and the partial pressure of water in the atmosphere surrounding the crack. The relative weakening of quartz or silicate glass, reflected by an increase in the rate of crack growth with an increase in any of the three variables, is consistent with the general theory of stress corrosion in silicates proposed by Charles (1959 [DIRS 170308]). He postulated that the velocity of a slowly propagating crack with a high tensile stress at the crack tip is proportional to the rate of the hydration reaction at the crack tip. The following equation (Martin 1972 [DIRS 169721]) quantifies the general relationship for environment-sensitive crack growth.

$$\nu = \nu_0 \beta P^n \exp\left(\frac{\Delta F - V^* \sigma}{RT} + \frac{\gamma V_m}{\rho RT}\right) \qquad \text{(Eq. 6-8)}$$

where ν is the rate of crack growth, ν_0 is the initial flaw size, P is the partial pressure of water, ΔF is the activation energy for the process, T is temperature, R is the universal gas constant, V^* is the activation volume, σ is stress, γ is the surface energy of the solid, V_m is the molar volume of the solid, ρ is the radius of curvature of the crack tip, and β and n are constants.

If the partial pressure of water, the temperature, and the applied stress are constant, a constant crack propagation velocity will be observed. When any one of the thermodynamic variables is increased, the crack velocity increases. This expression has been verified with experimental studies (Wiederhorn 1968 [DIRS 170309]; Martin 1972 [DIRS 169721]; Scholz 1972 [DIRS 169724]).

The validation of Equation 6-8 is extremely important. First, it establishes a rate-dependent process for the propagation of cracks in quartz and silicate glass. If the same behavior is

observed in rocks then it implies that time can be scaled from very short times to extremely long times in the absence of other competing mechanisms. Specifically, if moisture-assisted stable crack growth is the primary mechanism of creep in brittle rocks, measurements made at laboratory scales of up to 10^6 seconds can be extrapolated to much longer scales on the order of 10^{11} to 10^{14} seconds. Presently there are no other independent data that suggest other competing mechanisms for time dependent deformation in brittle rocks at temperatures below 300°C. Based on these results and verifications by other experimenters, there is confidence that Equation 6-8 accurately represents the behavior of the rate of crack growth at the crack tip for brittle silicate materials at temperatures below 300°C.

Next, the behavior of brittle rocks can be examined during creep and compared to the observations of stable, time-dependent crack growth gained from tests on quartz and glass. A creep test is conducted by rapid application of uniaxial or triaxial load to a rock sample to a given differential stress, followed by holding the load constant while monitoring the longitudinal and lateral strains. Typically, creep is reported in terms of three distinct phases: (1) primary or transient creep, (2) secondary or steady-state creep, and (3) tertiary or accelerating creep (Figure 6-152).

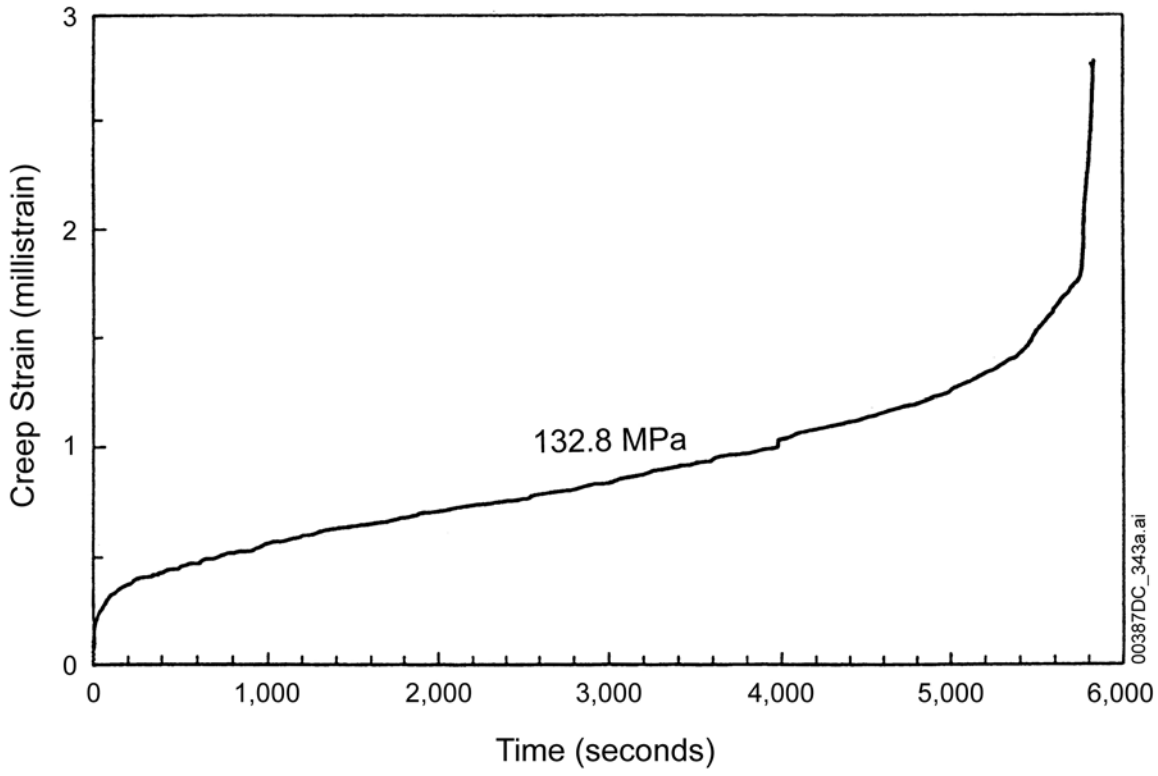

Source: Martin et al. 1997 [DIRS 165960], Figure 4.

NOTE: Specimen failed at tertiary creep phase.

Figure 6-152. Example of Creep Strain Plotted as a Function of Time for a Static Fatigue Test Conducted on a Sample of Topopah Spring Tuff at a Constant Differential Stress of 132.8 MPa, a Confining Pressure of 5.0 MPa, a Pore Pressure of 1 MPa, and a Temperature of 150°C.

Transient creep has been reported for a variety of rock types over a wide range of temperatures and pressures. The strain in this region decelerates rapidly and is often reported as proportional to the logarithm of time. Moreover, both the lateral and the longitudinal strains exhibit this logarithmic time dependence.

At low stresses, transient creep may account for the observed strain. However, at high stresses, secondary creep is often observed. Generally, in secondary creep, often called steady-state creep, the strain is proportional to time. The total strain caused by both primary and secondary creep is often represented by an equation of the form

$$\varepsilon = A + B \log t + Ct \qquad \text{(Eq. 6-9)}$$

where ε is strain, t is time, and A, B, and C are constants.

If secondary creep is allowed to continue, eventually the strain rate increases (tertiary creep) and the rock fails. The three stages of creep have been observed in granite, quartzite, and tuff (Martin 1972 [DIRS 169721]; Martin et al. 1997 [DIRS 165960]). A typical creep curve for a specimen of welded tuff from the middle nonlithophysal unit of the Topopah Spring (Tptpmn) is shown in Figure 6-152. The three stages of creep are clearly evident.

Stable crack growth in quartz reported by Martin (1972 [DIRS 169721]) and Martin and Durham (1975 [DIRS 170301]), illustrated specific characteristics that are related to creep deformation. In these studies, the specimens were loaded to a fixed compressive stress and the growth of a crack parallel to the applied load was observed. Each specimen was tested in a controlled environment and the change in crack length was noted as a function of time. A typical data set obtained on a single specimen of quartz tested at a temperature of 241°C and a partial pressure of water of 4.5×10^{-2} kPa is shown in Figure 6-153. The test specimen geometry is shown in the upper left portion of the graph. At a stress of 66 MPa, the change in crack length with time is very similar to that observed in the creep of brittle crystalline rocks. The crack exhibits an initial period of rapidly decelerating growth followed by a quasi-linear or secondary segment. After 6.3×10^4 seconds, the stress was increased to 74 MPa. Immediately, the rate of crack growth increased. The same characteristics observed at the lower stress were exhibited for the 74 MPa segment. There was a strong transient followed by a secondary or quasi-linear crack growth segment. At approximately 8×10^4 seconds, the stress was increased to 83 MPa. The rate of crack growth increased dramatically; and the experiment was terminated when the crack length reached 3.7 mm. These data are consistent with Equation 6-8; that is, the rate of crack growth increased with increasing stress and nearly vanishes at low stresses. Additional experiments showed that increasing either the partial pressure of water surrounding the crack or the temperature also results in an increase in the rate of crack growth.

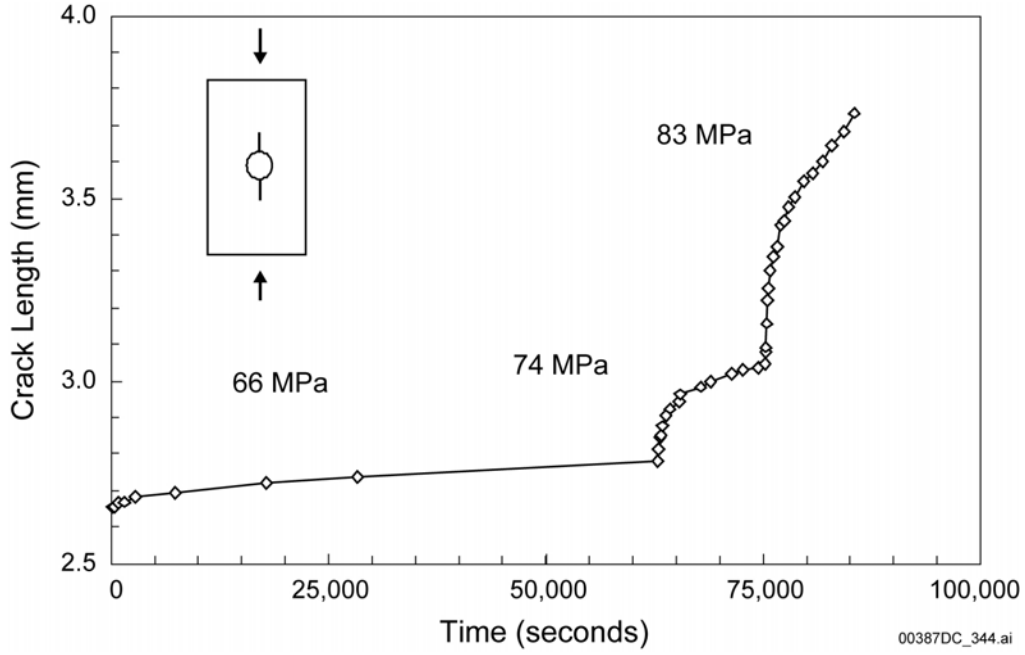

Source: Martin 1972 [DIRS 169721].

NOTE: The experiment was conducted at 241°C and a partial pressure of water of 4.05×10^{-2} kPa.

Figure 6-153. Crack Length as a Function of Time for an Axial Crack Growth Experiment in Single Crystal Quartz

The above discussion points out that creep experiments with complex, silicate rocks display the same basic time-dependent response as demonstrated by crack-growth studies in single crystals of quartz and glass. From a practical standpoint, it is advantageous to define the ultimate time-to-failure in terms of the stress, temperature and partial pressure of water, rather than in terms of crack growth. Time-to-failure is typically defined using the creep test to determine the static fatigue of a material. Static fatigue refers to the failure time of a rock or single crystal at constant stress, temperature, confining pressure, and partial pressure of water without regard to the strain history. Scholz (1972 [DIRS 169724]) conducted a series of static fatigue tests in compression on single crystal quartz. He observed that the mean time to failure, $\langle t \rangle$, depended on the partial pressure of water (P), stress (σ), activation energy (ΔF), and temperature (T) according to:

$$\langle t \rangle = t_0 P^{-a} \exp\left(\frac{\Delta F}{RT} - K'^{\sigma}\right) \qquad \text{(Eq. 6-10)}$$

where a and K' are constants.

The foregoing discussion demonstrates that:

- The strength of brittle silicate rocks such as tuff is not a single-valued function of any parameter, but is a complex continuum that depends on the state of stress, the saturation (pore pressure), the temperature, and the time (including strain rate).

- Studies of the basic growth of single fractures and the creep strain resulting from microcrack growth in complex silicate rocks demonstrate that the same basic stress corrosion mechanism is responsible for time-dependent crack growth and the ultimate time-to-failure of the material.

- The stress corrosion mechanism gives rise to a logarithmic relationship of time-to-failure as a function of the state of stress, the temperature, and the pore pressure.

- As a result of the basic understanding of the static fatigue mechanism in brittle rocks, it is possible to extrapolate long-term failure response from relatively short-term static fatigue experiments in the laboratory.

Since the effects of time-dependent fracture development on weakening of tuff and its impact on drift degradation may be important in the postclosure repository environment, creep experiments on tuff samples have been conducted to determine its static fatigue response under appropriate environmental conditions.

6.4.2.4.2.2 Static Fatigue Testing to Define Time-Dependent Behavior of Welded Tuff

The typical way to define the time-dependent strength of rock is to establish the time required for failure of heated, saturated rock samples that are subjected to an applied constant axial stress. Creep test experiments are conducted to determine the static fatigue strength of the rock associated with tertiary creep rupture. These tests, typically conducted in uniaxial or triaxial compression, involve rapidly increasing the applied axial stress to a given percentage of the estimated compressive strength of the same size rock samples. The stress is then held constant until the sample spontaneously fails due to time-dependent rupture. A plot of the logarithm of the time-to-failure versus the ratio of the applied stress to the unconfined compressive strength is developed. The plot is typically linear, reflecting the basic mechanisms of stress corrosion as described above. Rock samples subjected to stress levels that are small in comparison to the compressive strength (i.e., below about 50 to 60 percent) result in excessively long times to failure and cannot be tested practically in the lab due to the long test duration. However, these loading conditions are not of interest for drift stability in the postclosure time frame of hundreds to thousands of years. The loading conditions of interest to time-dependent degradation at Yucca Mountain are those in which the applied stresses from in situ and thermal loading in the drift wall periphery are a high percentage of the rock strength (e.g., greater than approximately 60 to 70 percent). Here, the time to failure may result in significant degradation in hundreds to thousands of years. In this case, relatively short-term laboratory experiments (on the order of days to weeks) can supply time constants capable of describing the stress corrosion process.

A series of triaxial static fatigue experiments were conducted on heated and saturated nonlithophysal cores from the Tptpmn in 1997 (Martin et al. 1997 [DIRS 169721]) and in 2004 (DTN: SN0406L0212303.002 [DIRS 170289]). Triaxial experiments on 50.8 mm diameter cores with a confining pressure of 5 MPa and pore water pressure of 4.5 MPa were conducted so that pore water of the saturated samples would remain in a liquid state as the temperatures were increased over boiling (125°C and 150°C). The resulting effective stress (the confining pressure minus the pore water pressure) was approximately 0.5 MPa, or essentially a state of uniaxial compression. This procedure was used to ensure a conservative state in which saturated samples were maintained at postclosure rock temperatures. Figure 6-154 shows a typical specimen ready for testing.

The results of the testing on nonlithophysal cores of Tptpmn, as well as those from similar testing of Lac du Bonnet granite performed for the Canadian high-level radioactive waste program (Schmidtke and Lajtai 1985 [DIRS 164774]; Lau et al. 2000 [DIRS 164769]) are given in Figure 6-155. Granite results are included as a means of comparing the effects of rock type and for demonstrating the similarity in the general nature of the time-to-failure data for different rock types. Scatter in the data is due to sample inhomogeneity, as well as the fact that the driving stress ratio (the horizontal axis) uses an estimated value for the unconfined compressive strength (adjusted for sample porosity) for normalizing the applied stress level.

Since there is significant variability in the unconfined compressive strength of each sample, there will be a scatter in the resulting plot of time-to-failure versus driving stress ratio. As seen in Figure 6-155, the welded tuff has a significantly slower time static fatigue failure than granite, as evidenced by the steeper slope of the linear fit to the data. This slower time-to-failure is presumably a result of the relatively homogeneous, fine-grained, high silica content nature of the tuff, as opposed to the heterogeneous nature of the grain structure of granite.

Figure 6-154. Triaxial Static Fatigue Experimental Setup and Posttest Sample for Heated, Saturated, 50.8 mm Diameter Samples of Tptpmn

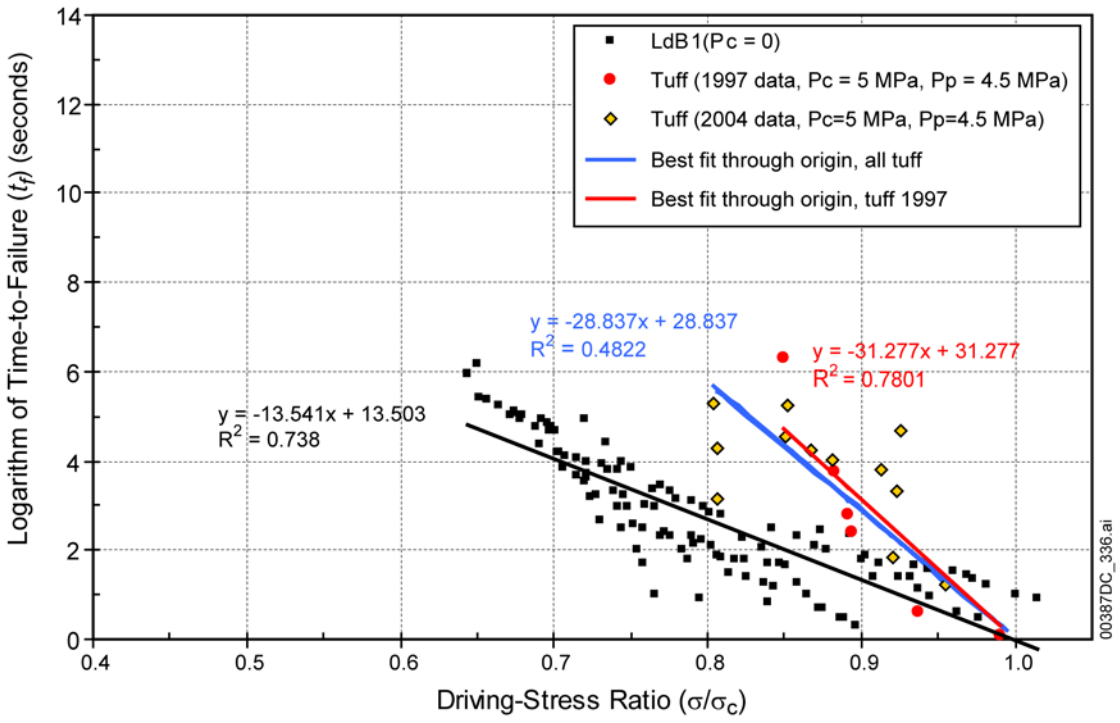

Source: Schmidtke and Lajtai 1985 [DIRS 164774] (Lac du Bonnet data); Martin et al. 1997 [DIRS 165960] (tuff 1997 data); DTN: SN0406L0212303.002 [DIRS 170289] (tuff 2004 data).

NOTE: Tests of Lac du Bonnet granite were conducted at 25°C. The driving stress ratio is defined as the ratio of applied constant test stress to the estimated unconfined compressive strength. 1997 tuff tests were conducted at 150°C, 2004 tuff tests were conducted at 125°C. LdB = Lac du Bonnet. Linear fits to 1997 Lac du Bonnet only and 1997 and 2004 tuff tests are shown. Samples that did not fail are also shown but not used in developing linear fits to data.

Figure 6-155. Static-Fatigue Data for Unconfined and Triaxial Compression of Heated, Saturated Welded Tuff and Lac du Bonnet Granite

Linear fits to the unconfined compression data of Lac du Bonnet granite and to the tuff 1997 data only and to the welded tuff data (including both 1997 and 2004 data) are given. The fits to both sets of welded tuff data are given because the analysis of drift degradation presented in the following section was conducted based on fits to only the 1997 data. After these analyses were completed, the additional 2004 data were collected. The linear fits to the data sets show the general consistency of the overall slope of the fits, although there is considerably more scatter in the 2004 test results. Due to data uncertainty, a lower bound for the slope of the time-to-failure curve based on the Lac du Bonnet data, was also used in numerical modeling estimates. The static fatigue testing was performed on saturated tuff cores at elevated temperature, ensuring that the impact of water on time-dependent yielding was accounted for in the estimation of time-dependent effects on drift stability.

6.4.2.4.2.3 Development of a Mechanical Model for Simulating Time-Dependency in Nonlithophysal and Lithophysal Rock

After an estimate of the relationship of stress level to time-to-failure for nonlithophysal tuff has been defined through testing, it is necessary to establish the impact of lithophysal porosity on the time dependence and to generalize the results into a time-dependent strength model that can be used to estimate drift stability. The methodology for development of a mechanical model for representing time-dependent degradation effects in welded tuff is described below.

The particle flow code PFC2D (BSC 2002 [DIRS 161950]) and PFC3D (BSC 2002 [DIRS 160612]) discontinuum numerical modeling tools were used for understanding the impact of lithophysal porosity on time-to-failure as a function of applied stress. A modification to the basic particle flow code program was developed for simulation of time-dependent, stress corrosion cracking of rock. This model, termed the particle flow code stress corrosion model, was used for simulating time-dependent tunnel fracturing of Lac du Bonnet granite for the Canadian waste disposal research program. In this model, time-dependent intergranular bond fracture strength was developed based on the general concept of a stress corrosion mechanism. The long-term behavior is controlled by three particle flow code stress corrosion model parameters, β_1, β_2, and σ_a. The terms β_1 and β_2 (rate constants) and σ_a (microactivation stress) do not affect short-term material properties. These material parameters are derived from calibration against the time-to-failure data supplied by static fatigue testing (e.g., Figure 6-155). The particle flow code stress corrosion model has been extensively documented and calibrated against static fatigue testing of Lac du Bonnet granite and validated against time-dependent tunnel breakout observed at the Underground Research Laboratory in Manitoba, Canada (Potyondy and Cundall 2001 [DIRS 156895]). Details of the stress corrosion model in particle flow code and its calibration are presented in Appendix S.

Prior to representing time dependency, it was necessary to demonstrate that the particle flow code model can reproduce the basic, non-time-dependent mechanical behavior of nonlithophysal and lithophysal tuff. The calibration of the model against laboratory compression data from small cores of nonlithophysal tuff and from large cores of lithophysal tuff from the Tptpul and Tptpll was described in Section 7.5. The same basic particle flow code model, incorporating a time-dependent particle bonding strength, was then calibrated to reproduce the time-to-failure dependent response of nonlithophysal tuff determined from the static fatigue testing. The calibration of the model is carried out by conducting simulated creep tests on nonlithophysal samples in exactly the same way they are performed in the laboratory. Figure 6-156 presents a typical simulated creep test in which axial load is applied to the particle flow code sample and held constant at 80 percent of its unconfined compressive strength. Tensile fractures (cracks) develop spontaneously in the model as a function of time based on the time-dependent bond strength of the constituent grains. The plot shows the development of a network of tensile stress corrosion cracks that accumulate and propagate within the sample until a macroscopic shear failure mechanism develops with resulting brittle rupture during the tertiary creep stage. The simulated creep test shows the three stages of creep: transient, secondary and tertiary, and reproduces the typical response of creep experiments in tuff (e.g., Figure 6-152).

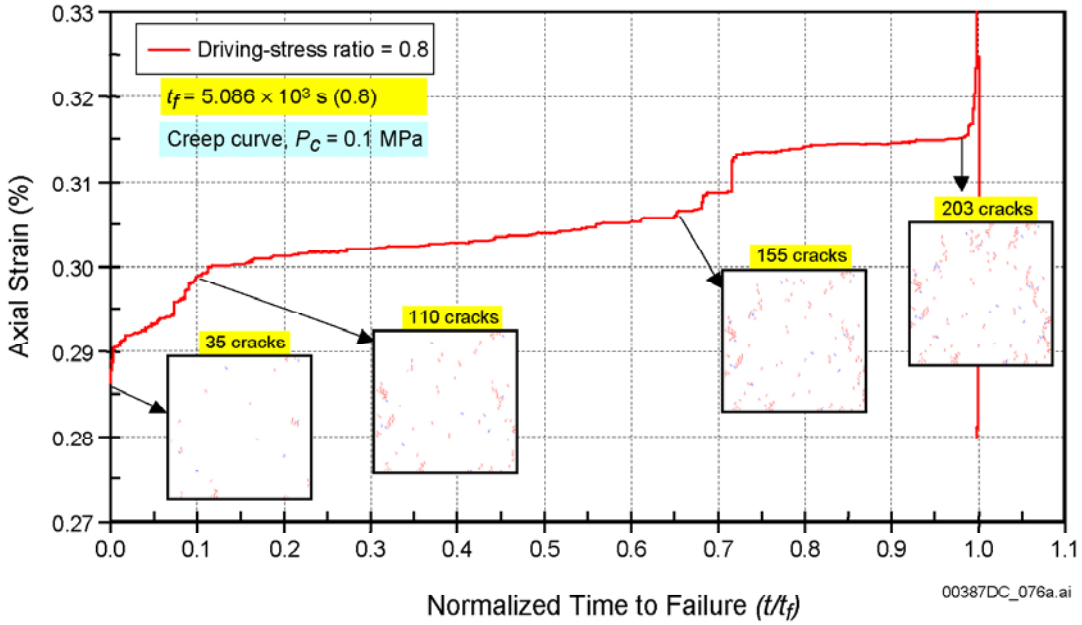

NOTE: Numerical simulation of creep test run by holding applied axial stress constant at 0.8 times the unconfined compressive strength. The damage, in terms of new crack growth, is displayed at various times along the creep curve. Brittle failure of the sample occurs when sufficient time-dependent crack growth results in failure mechanism.

Figure 6-156. Example of Simulated Creep Curve and Brittle Rupture Calibration for Nonlithophysal Tuff, (in This Case, Providing a Lower-Bound Estimate by Using Lac du Bonnet Granite Time-to-Failure Curve) Static-Fatigue Test at Driving-Stress Ratio (Ratio of Applied Stress to Unconfined Compression Strength) of 0.8

A large number of particle flow code simulations of static fatigue tests of nonlithophysal rock was run at a wide range of driving stress ratios, and two particle flow code stress corrosion parameters were calibrated, so that the model was able to reproduce the basic time-to-failure fits shown in Figure 6-155 for tuff and granite. The third stress corrosion parameter, the activation stress, was conservatively considered to be 0. The consequence of this consideration is that the long-term strength of the particle flow code synthetic material is 0. It is well known that real rocks have long-term (true) strength that is on the order of 50 percent of the short-term strength. In other words, if the load is less than long-term strength, the rock will never fail, irrespective of duration of the load. The model was then used to investigate the impact of lithophysal porosity on the rate of time dependence. It is considered that time-dependent behavior of the matrix is the same for both lithophysal and nonlithophysal rocks. A series of simulated creep experiments for lithophysal porosities of 11 percent and 20 percent were conducted, resulting in the generation of a set of time-to-failure versus driving stress ratio plots for various levels of lithophysal porosity (Figure 6-157).

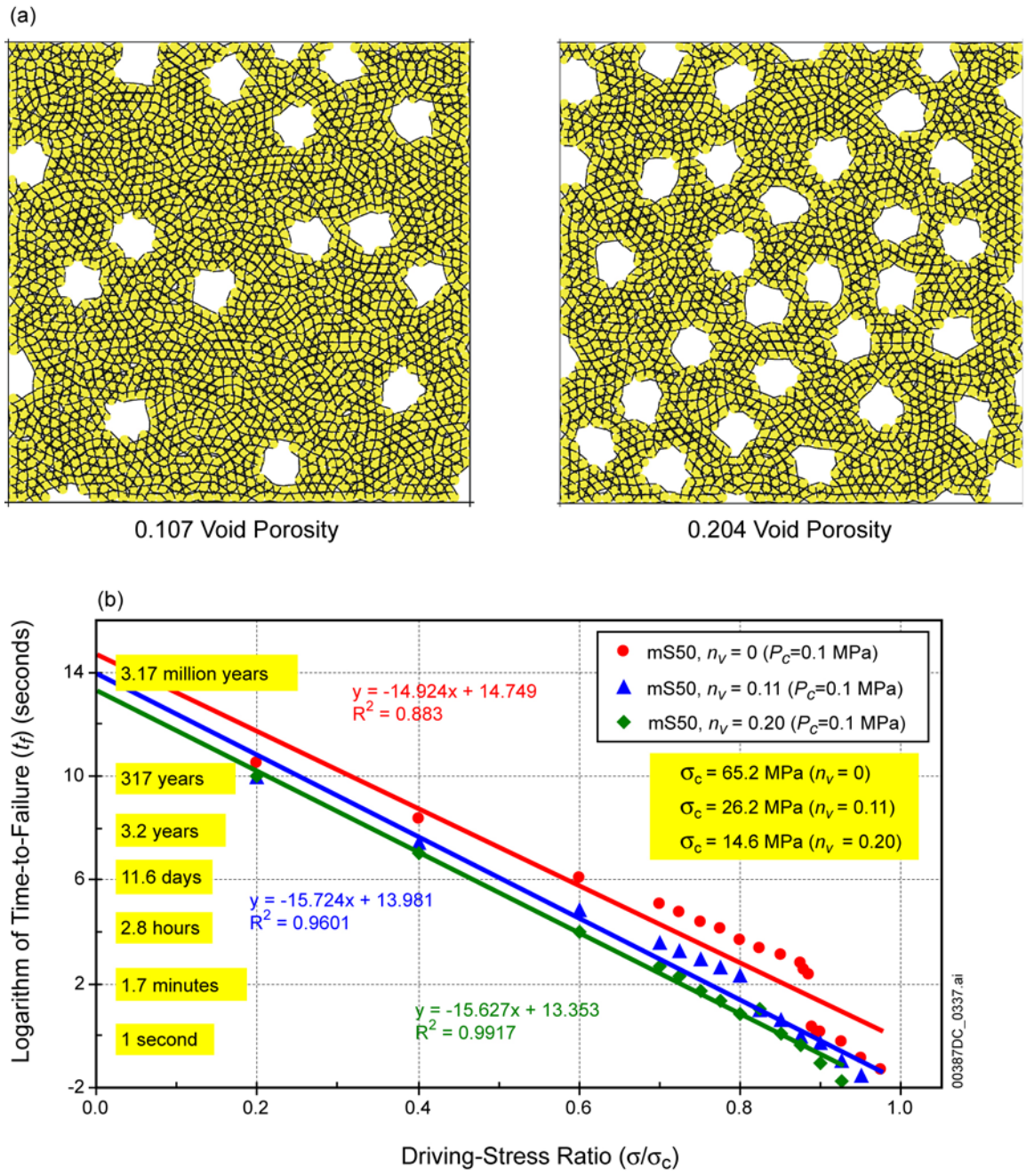

NOTE: The time dependency has approximately the same slope for the void porosities for the straight-line fit. Lithophysae are simulated as circles with a diameter of 90 mm. mS50 is the designation for the material properties of the matrix derived from nonlithophysal calibrations.

Figure 6-157. Example Particle Flow Code Specimens with Void Porosities of 0.107 and 0.204 (a) and Effect of Void Porosity on Time-to-Failure Response for Lithophysal Tuff Material, in This Case, Providing a Lower Bound Estimate by Using Lac du Bonnet Granite Time-to-Failure Curve (0% to 20% Void Porosity, n_v) (b)

6.4.2.4.2.4 Drift-Scale Model for Simulation of Time-Degradation of Emplacement Drifts

The particle flow code model for time dependency of lithophysal rock, shown in Figure 6-157, is computationally very large and is difficult to apply on the scale of a complete emplacement drift. To overcome these computational limitations, a drift-scale model using the UDEC discontinuum program was developed for investigation of non-time-dependent drift degradation analyses in lithophysal rocks as presented in the previous sections. The same model is used for time-dependent drift-scale analyses with the exception that the strength properties of the model are adjusted as a function of time. The relationships for time-to-failure as a function of lithophysal porosity developed from the laboratory testing and particle flow code extrapolations are used to define time-dependent strength properties for the drift-scale UDEC model. The approach to definition of time-dependent effects on strength in UDEC is simplistic in that it relates rock mass damage resulting from stress corrosion cracking directly to a loss of cohesion and tensile strength of the rock mass. The degree of strength loss was determined by (1) conducting a series of particle flow code numerical creep tests at different values of driving stress ratio and (2) interrupting the particle flow code creep test simulations at various times during a simulated test and conducting numerical compression and tensile strength tests on the damaged sample. For example, Figure 6-156 shows four "snapshots" of the crack-damaged state of a simulated rock sample at various times along the creep curve. The strength properties of these damaged states were determined, and the resulting cohesion and tensile strength defined as a function of time for a given driving stress ratio. The strength loss was generalized into a damage coefficient that varies from 0 to 1 (0 indicates no strength loss, while 1 is complete strength loss). The cohesion and tensile strength of the rock is multiplied by this coefficient to derive the strength properties of the rock mass as a function of time. Essentially, this approach relates the reduction in strength properties (shear and tensile strength) to the increase in fracture density or damage to the rock mass. Figure 6-158a shows the form of the damage coefficient as a function of time for various driving stress ratios as derived from the particle flow code stress corrosion model for a nonlithophysal simulation. As seen in this plot, damage occurs in a brittle fashion with abrupt failure near the peak strength. The amount of damage accumulated prior to the abrupt failure (as shown by the damage coefficient) is less than 10 percent for high driving stress ratios (e.g., >0.6), whereas damage accumulation is significantly larger for low driving stress ratios (e.g., <0.6). A simplified representation of the damage coefficient evolution in terms of time is shown in Figure 6-158b.

The UDEC drift-scale model is composed of many small elastic blocks that are bonded across incipient, ubiquitous fractures with shear and tensile strength components. While the non-time-dependent UDEC drift-scale model considers constant strength properties for the incipient fractures, the time-dependent damage model is transient in nature and assigns cohesion and tensile strength based on the damage coefficient as a function of time after excavation (i.e., Figure 6-158b).

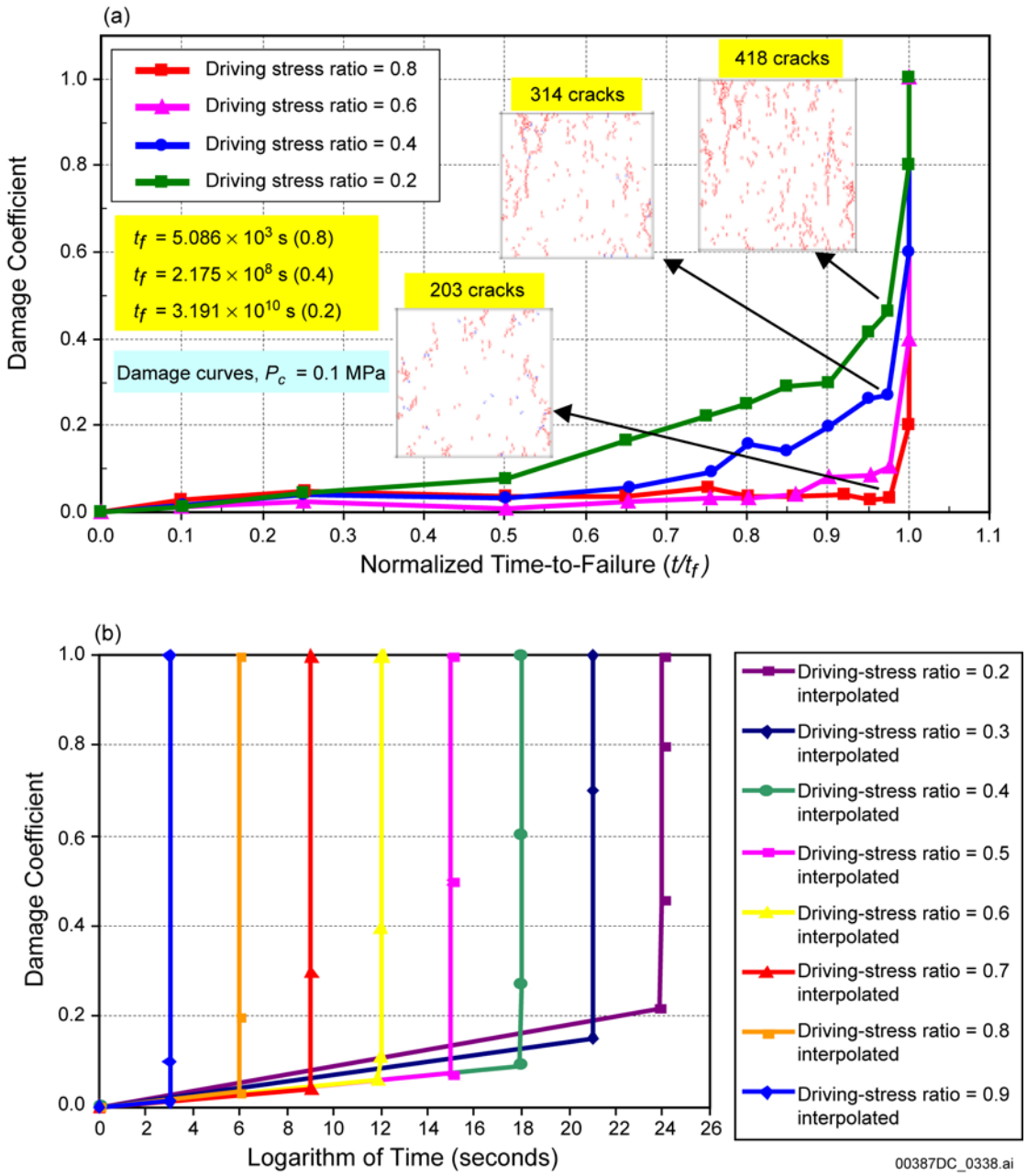

NOTE: Each curve has a vertical asymptote at a time-to-failure for a given driving-stress ratio, which is provided by the best fit to tuff (1997 data) given in Figure S-27 (Appendix S). Plot (a) was developed by using the Lac du Bonnet granite time-to-failure curve.

Figure 6-158. Time Evolution of Damage Due to Strength Degradation Coefficient for Nonlithophysal Tuff Material During Static-Fatigue Tests at Driving-Stress Ratios Ranging from 0.2 to 0.8 (a) and Idealized Damage Coefficient as a Function of Time for a Range of Applied Stress Conditions (b)

6.4.2.4.2.5 Time-Dependent Drift Degradation Analyses for In Situ Stress Only

A series of parametric drift degradation simulations were conducted for the range of potential lithophysal rock mass strength categories in the Tptpll. Time-dependent drift degradation analyses for the postclosure time frame were conducted for each of these strength categories. When performing a time-dependent drift degradation analysis, the cohesion and tensile strength at each incipient fracture location is adjusted as a function of time, with yield considered to occur in a brittle fashion when the time-to-failure is reached (Figure 6-158). Thus, as the drift is excavated and as transient thermal stresses develop, time-dependent yield and fracture can occur around the excavation, resulting in redistribution of stress and possible propagation of drift breakout, collapse, and rockfall.

The model was run by first excavating the emplacement drift under in situ stresses only, followed by application of the transient rock mass temperature conditions. The time-dependent fracture state and drift stability was examined at 1, 5, 10, 100, 1,000, and 10,000 years during the heating and cooling phases of the postclosure period. Additional analyses were conducted to examine the effect of seismic loading with the application of the 10^{-4} annual exceedance level ground motion time histories (approx. 0.5 m/s peak ground velocity). This ground motion was applied to the time-degraded model at the time of peak thermal stress (approximately 30 years after closure), at 1,000 years, and at 10,000 years. The 10^{-4} event was chosen to determine if the added seismic stress and shaking would be sufficient to dislodge time-degraded, fractured, and loosened rock that may still be in place on tunnel walls.

The resulting time-dependent drift degradation estimates for mechanical property categories 1, 2, 3, and 5 for loading by in situ stresses only for 1 to 10,000 years are presented in Figures S-37 to S-40 in Appendix S. The results for the lowest rock qualities (categories 1 and 2) show significant deterioration of the drifts would be expected soon after excavation as a result of in situ stress loading only. Observations in the ECRB Cross-Drift and the ESF, which have been excavated for 6 or more years, show no progressive raveling or overbreak (e.g., Brekke et al. 1999 [DIRS 119404], p. 2-5). This observation holds even in those areas of high lithophysal porosity found near the top of the Tptpll. Categories 3 and 5 show little time-dependent effect from in situ stressing only. These results point out that the best estimate of tuff time dependence, coupled with the considerations of brittle rock failure and constant, homogeneous properties within a given model cross section produces conservative damage estimates. Category 3 is considered to represent an average condition of lithophysal porosity for the Tptpll and shows little overbreak with time. Analyses presented in Section 6.4.2.2.3 examine the impact of spatially variable rock properties within a given model section based on the mapped variability of lithophysal porosity in the ECRB Cross-Drift. The spatially variable model has a range of rock categories distributed throughout the cross section, and results of analyses show time-dependent drift degradation response similar to that shown for category 3 mechanical properties. An important conclusion from these initial in-situ-stress-only analyses is that best estimate time-dependent fracture growth within the tuff matrix is not expected to lead to collapse modes and significant drift degradation.

6.4.2.4.2.6 Time-Dependent Drift Degradation Analyses for Combined Thermal and Time-Dependent Effects

Throughout the regulatory period of 10,000 years, the emplacement drifts and surrounding rock mass will be subject to a heating cycle. Time-dependent strength degradation will happen concurrently with transient, thermally induced stress changes. Increased stresses around the excavation will accelerate the process of strength degradation. The results of numerical simulation of drift degradation as a result of these two processes are shown in Figures S-42 to S-44 in Appendix S. Time-dependent strength degradation is assessed using the tuff best-fit static-fatigue line. As expected, most rockfall occurs in category 2 rock mass, as shown in Figure S-42. Initially, most of the rockfall comes from the walls, which are loaded almost to a yielding state for this rock mass category under in situ stress conditions only. Strength degradation combined with a temperature increase, which at early times increases the hoop stress in the walls (not only in the roof), results in some rockfall from the wall at 5 and 10 years after emplacement of the waste. The large increase in the temperature and, consequently, in the stresses after the forced ventilation stops causes additional rockfall (at 80 years). At this stage, stress increase is predominantly in the roof. Therefore, some rockfall comes from the roof. It is counterintuitive that more rockfall is predicted in category 5 (Figure S-44) than in category 3 (Figure S-43). However, a large stiffness of category 5 lithophysal rock mass causes a large (larger than in category 3) increase in the hoop stress and yielding in the roof, even considering the short-term yield strength of the rock mass.

It should be noted that static-fatigue curves are temperature dependent. This dependence is not explicitly included in the analysis. However, the tuff data are obtained from tests conducted at 150°C, which is larger than the maximum temperature of the rock mass anticipated throughout the repository for postclosure. Consequently, the results obtained in this analysis, although for isothermal static-fatigue curves, are conservative.

6.4.2.4.2.7 Time-Dependent Drift Degradation Analyses for Combined Seismic, Thermal and Time-Dependent Effects

The 10^{-4} ground motion was applied to category 2 and 5 rock mechanical property cases at two time periods: (1) at the time peak thermal stress state (nominally at 80 years after emplacement, or 30 years after cessation of 50 years of forced ventilation) and (2) at 10,000 years at the completion of the postclosure heating and cooling cycle. Figures 6-159 and 6-162 show the resulting predicted degraded drift states for these cases. Essentially, the application of the 10^{-4} ground motion (peak ground velocity of approximately 0.5 m/s) dislodges any fractured and loosened rock created by the thermal stress and time dependency. As seen in these figures, the impact of time dependency of strength properties is to widen the diameter of the emplacement drifts in the lower quality (category 2) rock due to progressive shear failure at the sidewalls. In the highest quality (category 5) rock, additional progressive yield of the roof is evident. Roof yield in higher quality rock is due to the higher modulus of the rock mass and, thus, higher roof-parallel thermally induced stresses during the heating cycle. This is similar to the roof crown spalling effect observed in the Drift Scale Test.

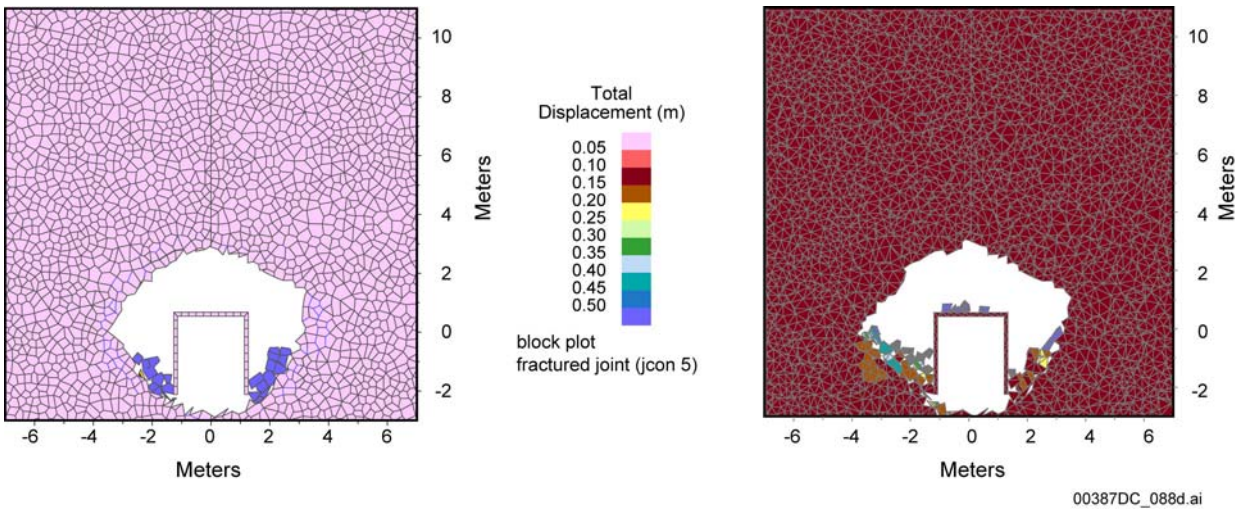

(a) before earthquake (b) after earthquake

NOTE: Displacement magnitudes are in meters.

Figure 6-159. Effect of 10^{-4} Ground Motion After 80 Years of Heating in Category 2: Blocks Colored by Contours of Displacement Magnitude

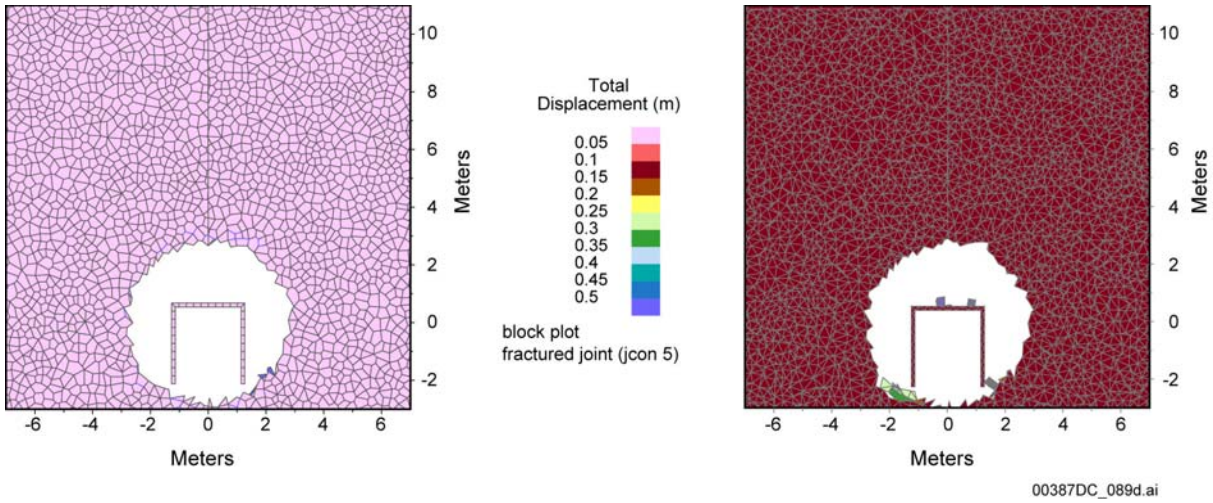

(a) before earthquake (b) after earthquake

Figure 6-160. Effect of 10^{-4} Ground Motion After 80 Years of Heating in Category 5: Blocks Colored by Contours of Displacement Magnitude

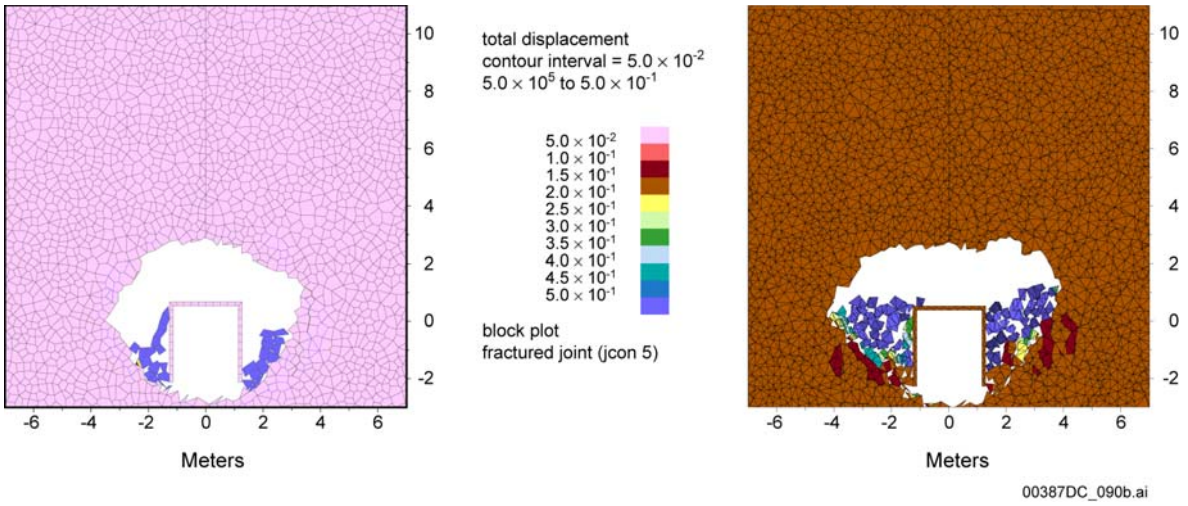

(a) before earthquake

(b) after earthquake

Figure 6-161. Effect of 10^{-4} Ground Motion After 10,000 Years of Heating in Category 2: Blocks Colored by Contours of Displacement Magnitude

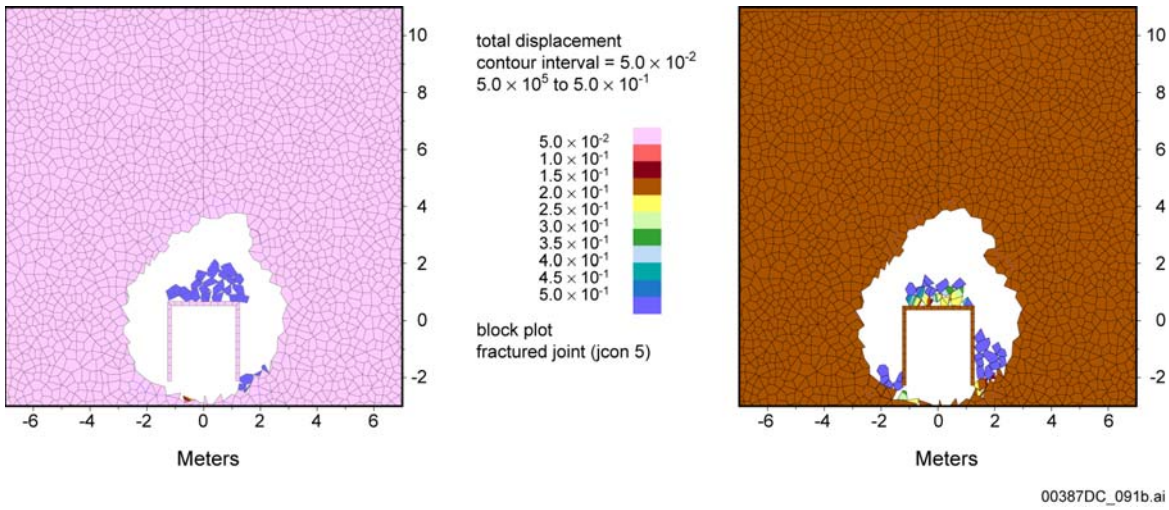

(a) before earthquake

(b) after earthquake

Figure 6-162. Effect of 10^{-4} Ground Motion After 10,000 Years of Heating in Category 5: Blocks Colored by Contours of Displacement Magnitude

6.4.2.4.3 Summary of Time-Dependent Consideration

6.4.2.4.3.1 Summary of Empirical Observations

The safety-related empirical correlations for maximum unsupported span and stand-up time of excavations developed for the tunneling industry are not relevant for prediction of long-term response of repository excavations. The span of the emplacement drifts is significantly less than that required to initiate collapse, as indicated by practice in the mining industry. The excavations will be developed using nonblasting methods (i.e., using a tunnel boring machine) and with a circular shape that minimizes overbreak and promotes stability. Observations of existing tunnels in the repository host horizon at the Yucca Mountain site as well as in similar rock at Hoover Dam show stable conditions with minimal or no ground support.

6.4.2.4.3.2 Effect of Drift Collapse on the In-Drift Environment

Estimates of the coupled thermal-hydrologic behavior of the rock mass in the near vicinity of the drifts is examined in *Multiscale Thermohydrologic Model* (BSC 2004 [DIRS 169565]). Numerical parameter analyses of the impact of waste heating on fluid pressures on fractures and infiltration into the emplacement drifts were conducted using the multiscale thermal-hydrologic model. For the range of hydrologic properties of the four host-rock units, the fracture permeability is sufficiently large and fractures are sufficiently well connected to allow gravity-driven drainage of water to occur in an unrestricted fashion. Thus, percolation flux, not fracture permeability, is the rate-limiting quantity governing the magnitude of gravity-driven liquid-phase flow to the boiling–dryout zone. Additionally, the analyses show that potential pressure buildup along fractures due to vapor pressure from boiling of water is also negligible due to the free-draining nature of the fractured rock mass. From a mechanical stability standpoint, this means that fluid pressure on fractures during the drying and rewetting phases of the postclosure period has a negligible effect on drift stability. These predictions are borne out by the Drift Scale Test in which no mechanical drift instabilities occurred for thermal conditions representative of repository postclosure conditions.

A parameter study was conducted to examine the impact of drift collapse on in-drift thermal-hydrologic parameters (BSC 2004 [DIRS 169565]). The multiscale thermal-hydrologic model was used to examine the effect of a rubble-filled drift on waste package and invert temperature and relative humidity at the waste package and invert. The drift was considered to collapse (instantaneously) to twice the initial diameter (i.e., 11 m collapsed diameter) and is filled with rubble with a bulking factor of 0.231. The thermal conductivity of the rubble (K_{th}) is defined as the intact rock thermal conductivity of the Tptpll multiplied by the factor (1/(1 + bulking factor)). Two thermal conductivity values (a high case calculated as defined above for a bulking factor of 0.231, and a low case, which is taken to be one-half the high case value) of the dry and wet rubble thermal conductivity were used in the analyses, as shown in Table 6-46.

Table 6-46. Thermal Conductivity of Rubble

Property	Intact Host-Rock Property Value	Host-Rock Rubble Property Value	Basis for Rubble Property Value
Bulk dry thermal conductivity	1.28 W/m·K	1 W/m·K (High-K_{th} case)[a] 0.5 W/m·K (Low-K_{th} case)	Intact Value × 1/(1 + BF) (High-K_{th} rubble value)/2
Bulk wet thermal conductivity	1.89 W/m·K	1.515 W/m·K (High-K_{th} case)[b] 0.7575 W/m·K (Low-K_{th} case)	Intact Value × 1/(1 + BF) (High-K_{th} rubble value)/2

Source: BSC 2004 [DIRS 169565], Table 6.2-3.

[a] This value is rounded down slightly.

[b] Value is close to, but slightly less than, the value obtained from the Intact Value x 1/(1 + BF), in order to be consistent with the slight reduction made to the dry K_{th} value, which was rounded down.

Figure 6-163 shows the in-drift thermal-hydrologic parameters as functions of time from repository closure for the case of the hottest waste package, which is the 21-PWR Absorber Plate waste package. These plots show three cases: (1) an open, noncollapsed drift, (2) a collapsed, rubble-filled drift with high K_{th} for the rubble, and (3) a collapsed, rubble-filled drift with low K_{th}. The temperature (or any of the other environmental parameters plotted) will follow the intact drift curve until the time of collapse. At that point, the temperature (or other parameters) will translate vertically to one of the other curves, depending on the thermal conductivity of the rubble.

Examination of the waste package temperature curve (Figure 6-163a) shows that significant impact to peak waste package temperature results only if drift collapse occurs within the first 100 to 200 years after closure. After that time, the waste package temperature will always be below the peak temperature for the intact drift case, which occurs within about 20 to 30 years after closure. The total time at which the waste package surface remains above boiling for the hottest waste package case is approximately 1,000 years for the intact drift, 1,500 years for the high K_{th} case, and 2,000 years for the low K_{th} case. The relative humidity at the waste package decreases significantly for collapsed cases.

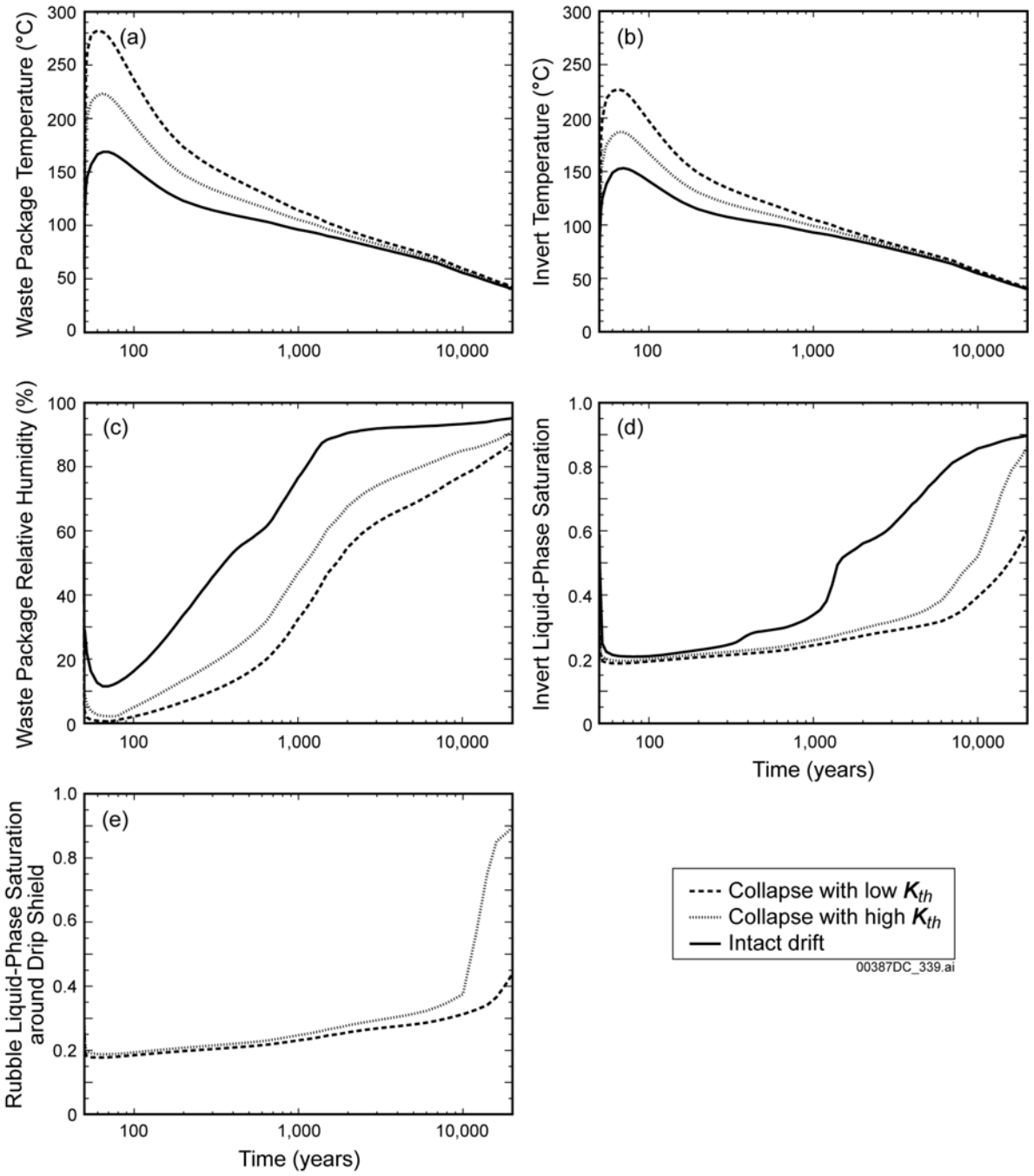

Source: BSC 2004 [DIRS 169565], Figure 6.3-56.

NOTE: The cases are: (1) intact-drift (nominal) case, (2) low-probability-seismic collapsed drift with high-K_{th} host-rock rubble, and (3) low-probability-seismic collapsed drift with low-K_{th} rubble. The plotted variables are (a) waste package temperature, (b) invert temperature, (c) waste package relative humidity, (d) invert liquid-phase saturation, and (e) matrix liquid-phase saturation of the rubble surrounding the drip shield.

Figure 6-163. Thermal-Hydrologic Variables for the "Hottest" Waste Package (21-PWR Absorber Plate Waste Package) at the P2WR5C10 Location in the Tptpll (tsw35) Unit for the Mean Infiltration Flux Case

6.4.2.5 Quasi-Static Drip Shield Loading from Rockfall

6.4.2.5.1 Introduction

Two types of drip shield loading cases are examined:

- Dynamic impact loading due to rockfall resulting from the seismic event or simple gravity fall
- Quasi-static loading of the drip shield once rockfall has come to rest and the weight of the rock lies on the crown and sides of the drip shield.

Loading in the dynamic case is discussed in Section 6.4.2.2 for the case of lithophysal rock, and in Section 6.3.1.2 for nonlithophysal rock. Since the rock block size estimated in the nonlithophysal rock is substantially larger than that projected for the lithophysal units, it is considered that the estimates of impact energy from those calculations will provide an upper bound to the dynamic loading in lithophysal rocks. In lithophysal rocks, a potentially more important drip shield loading mechanism is from quasi-static load developed from the accumulated weight of rubble on the drip shield. Although the discussion here centers on the lithophysal units, the rock blocks resulting from failure in nonlithophysal rocks are expected to result in similar ultimate dead weight loading.

As the lithophysal rock mass fails, pre-existing and new fractures will break, forming block sizes of relatively small volume (estimated to be on the order of cm on a side). The falling rock blocks will come to rest on the invert of the tunnel and the drip shield. Because the fallen blocks do not perfectly fit together as they did in the in situ rock mass, there will be an overall increase in volume (termed "bulking"). Eventually, if the failure process continues, the tunnel will completely fill with bulked rock and will choke off further failure because the backpressure provided by the rubble will stabilize further yield.

To determine the ultimate load on the drip shield, it is necessary to estimate the amount of bulking that will take place, and the shape of the resulting failed excavation profile. These two factors define the height and density of the rock load that lies on the drip shield. The vertical weight of the accumulated rubble will rest on the drip shield roof, with load transferred to the invert via its vertical supports. Lateral loading, developed from the vertical weight of the rubble, as well as from passive loading in response to drip shield deformation, will also act on the sidewalls of the drip shield structure. The most conservative consideration of loading is that rock rubble acts as a fluid with the density of the bulked rock, and that the overlying height simply rests downward on the drip shield. The rubble is, in fact, a coarse, frictional and dilatant material that has shear strength, and is able to carry load itself. Therefore, realistic estimates of load need to account for the interaction of the rubble and the deformability of the drip shield itself. As the drip shield deforms during loading, an equilibrium state will be reached in which the rubble itself and the drip shield will share in load bearing. The load carried by the rubble and transmitted to the solid rock invert of the tunnel is termed "arching." Measurements of strain in cut-and-cover tunnels with thin-conduit arched liners have verified the significant effect of arching and the conservatism inherent in assumptions of full-column height, dead weight loading (e.g., Lefebvre et. al. 1976 [DIRS 168919]; Byrne et. al. 1990 [DIRS 168921]).

In the following discussion the bulking of rock is discussed and a review of analytical and numerical methods for estimating the drip shield loading are described and compared. The preferred methodology for estimating the drip shield load is to use the same UDEC discontinuum numerical modeling method used previously to simulate the process of rock mass failure, rubble bulking, and interaction of the rubble and the deformable drip shield. In this fashion, the process is modeled naturally and assumptions regarding ultimate failed height and shape of the excavation are unnecessary, as they are when using analytical approaches. The purpose of this section is to provide estimates of the rock rubble loading to the drip shield. Calculations of the structural response of the drip shield to this loading is addressed in *Structural Stability of a Drip Shield Under Quasi-Static Pressure*.

6.4.2.5.2 Bulking of the Rubble

When the rock mass above underground openings collapses, it increases volume (i.e., it bulks). During the collapse, either sudden or gradual, rock mass disintegrates in a number of pieces (blocks), which fall separately rotating along the way. When blocks equilibrate after caving, they do not fit together, resulting in increased porosity and overall volume. Rock mass of volume V in the in situ conditions has volume V_B after caving, where:

$$V_B = (1 + B)V \qquad \text{(Eq. 6-11)}$$

where B is the bulking factor.

Amount of bulking (i.e., the bulking factor, B) depends on, among other things, the lithology, pre-existing internal structure (jointing, bedding), and the mechanism of collapse. For example, density of crushed limestone is in the range between 1360 kg/m^3 and 1440 kg/m^3, while density of the crushed dolomite is in the range between 1280 kg/m^3 and 1600 kg/m^3 (Fruchtbaum 1988 [DIRS 161774], Section 14). Considering that the specific gravity of limestones and dolomites is approximately 2.6 (Bauer et al. 1991 [DIRS 161775], Tables 10 and 11), and using an in situ porosity of 20 percent (Goodman 1980 [DIRS 101966], Section 2.3), the in situ density of limestones and dolomites is approximately 2200 kg/m^3. Consequently, bulking of these rocks from in situ state to a crushed state is between 37.5 and 72 percent. Duncan et al. (1980 [DIRS 161776], Table 5) reported that porosity of the rock fill for dams is between 23 and 36 percent. The rock fill used for dams is crushed to satisfy certain size requirements and is compacted during construction, which leads to reduction of its porosity. It appears from this discussion that bulking factor for the caved rock can be conservatively selected to be in the range between 0.2 and 0.4.

Caving of the underground excavations is a self-limiting process in many situations. At a certain stage of caving, due to bulking, the volume of the caved rock completely fills the volume of the original excavation and the volume occupied by the collapsed rock before onset of collapse. When the cave is completely filled, the broken rock provides the backpressure, which prevents further collapse of the rock mass.

6.4.2.5.3 Estimation of Collapse Dimensions and Drift Profile

Analytical Models of Collapse Height–Analytical methods consider that the cave above the emplacement drift grows until it becomes filled with the broken rock. The extent of the caved rock is calculated as a function of the bulking factor, *B*, considering that the cave stabilizes only when it is completely filled with the broken rock. In addition to the bulking factor, the shape of the cave must also be considered. In these analyses, neither the in situ stress conditions, nor the rock mass mechanical properties enter into the solution—the results are governed simply by the modeling considerations and kinematic solutions. Two extreme conditions illustrated in Figures 6-164 and 6-165 and were considered.

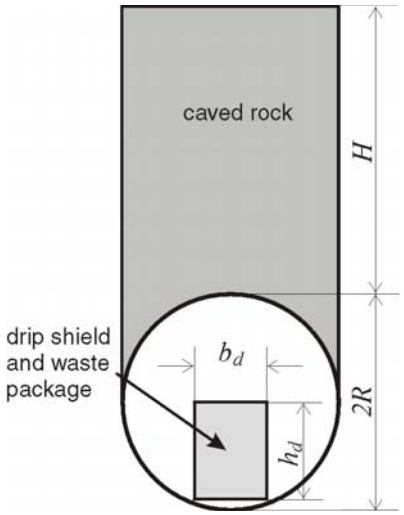

Figure 6-164. "Piping" Type of Caving Mechanism

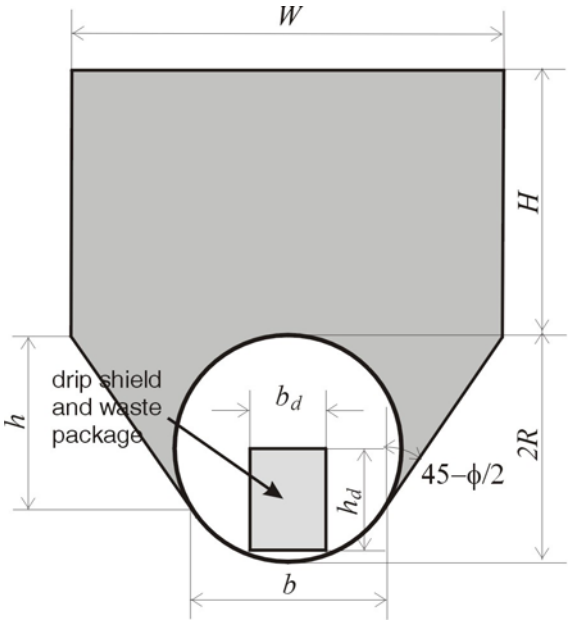

Figure 6-165. Terzaghi Type of Caving Mechanism

The "piping" mode of roof collapse (shown in Figure 6-164) is typical for conditions when the rock mass is bedded and there is a relatively large ratio of the span of the excavation to its depth. This type of roof collapse is typical for coal mines (with bedded sediments as overburden) using the longwall mining method, and almost always occurs suddenly. Roof piping collapse is highly unlikely as a potential mode of drift collapse at the Yucca Mountain site for the following reasons:

- None of the rock mass units are layered
- Drifts are deep below the ground surface (i.e., the depth is >> the diameter of the tunnels)
- Drift collapse due to strength decay will evolve gradually over a long period of time, rather than form as a sudden mechanism.

The piping mechanism is considered here as an unlikely and conservative extreme condition and is a mechanism that results in the largest vertical extent of the cave, *H*.

The other extreme condition of the rock mass collapse around the underground opening (shown in Figure 6-165) corresponds to the limit equilibrium conditions around a shallow tunnel, which Terzaghi (1943 [DIRS 162180]) used as a basis for calculation of the load on tunnel supports. Slip lines, related to plastic yield in the rock, extend from the drift walls at an angle of 45 degrees–$\phi/2$ from the vertical direction, where ϕ is the friction angle.

The cave height, *H*, is calculated for both of these cases as a function of the bulking factor, *B*. The vertical pressure of the collapsed rock exerted on the drip shield is calculated considering that the rock filling the cave acts on the drip shield as a dead weight. Expressions for the height of the cave are shown in Equations 6-12 and 6-13 for the piping and Terzaghi failure mechanisms, respectively, which have been derived based on the consideration of the geometries shown in Figures 6-164 and 6-165:

$$\frac{H}{2R} = \frac{1}{2}\left[\frac{\pi}{2B} - \frac{b_d h_d}{2BR^2} - \left(1 - \frac{\pi}{4}\right)\right] \qquad \text{(Eq. 6-12)}$$

$$\frac{H}{2R} = \frac{\frac{\pi}{B} - \frac{b_d h_d}{BR^2} - \frac{b+W}{2R^2}h + \frac{V_s}{R^2}}{\frac{2W}{R}} \qquad \text{(Eq. 6-13)}$$

where

$$\frac{b}{R} = 2\cos\left(\frac{\pi}{4} - \frac{\phi}{2}\right)$$

$$\frac{h}{R} = 1 + \sin\left(\frac{\pi}{4} - \frac{\phi}{2}\right) \qquad \text{(Eq. 6-14)}$$

$$\frac{W}{R} = 2\left\{\cos\left(\frac{\pi}{4}-\frac{\phi}{2}\right)+\left[1+\sin\left(\frac{\pi}{4}-\frac{\phi}{2}\right)\right]\tan\left(\frac{\pi}{4}-\frac{\phi}{2}\right)\right\}$$

$$\frac{V_s}{R^2} = \frac{3\pi}{4}-\frac{\phi}{2}+2\cos\left(\frac{\pi}{4}-\frac{\phi}{2}\right)\sin\left(\frac{\pi}{4}-\frac{\phi}{2}\right)$$

The predictions of the ultimate cave height are shown in Figure 6-166 for the range of bulking factors between 0.2 and 0.4. As expected, the cave height is larger in the case of the piping mechanism than in the case of the Terzaghi failure mechanism. The cave height varies (for the two cases considered and for the bulking factor in the range between 0.2 and 0.4) between approximately 1 and 2.5 drift diameters.

The vertical pressure of the broken rock on the drip shield is calculated from the following equation, also derived based on the consideration of the geometries shown in Figures 6-164 and 6-165:

$$p = \left(H + R - t\right)\frac{\rho g}{1+B} \qquad \text{(Eq. 6-15)}$$

where t is the height of the upper surface of the drip shield above the drift centerline. Calculated vertical pressure on the drip shield as a function of the bulking factor is shown in Figure 6-167.

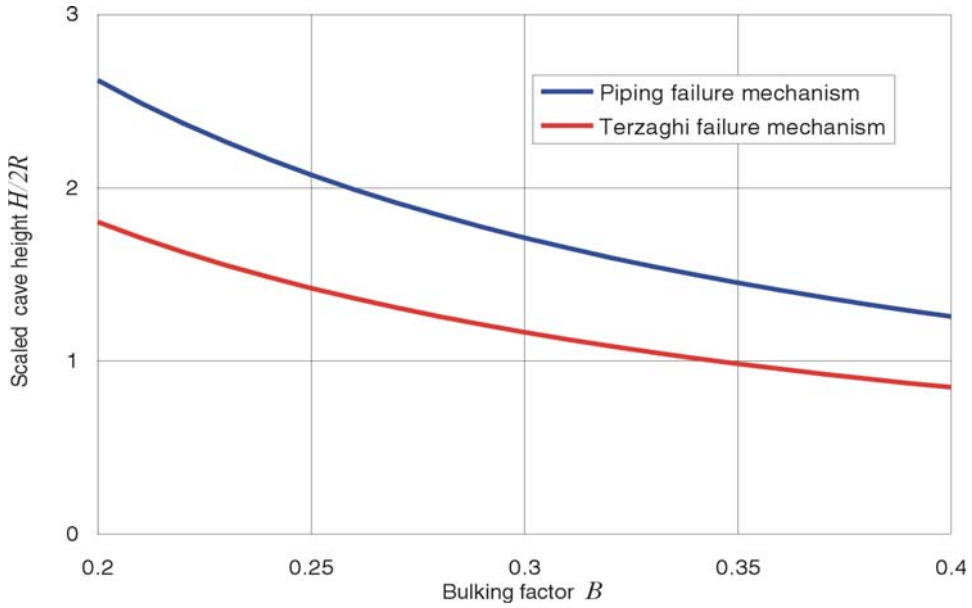

Figure 6-166. Cave Height as a Function of Bulking Factor: Analytical Solution

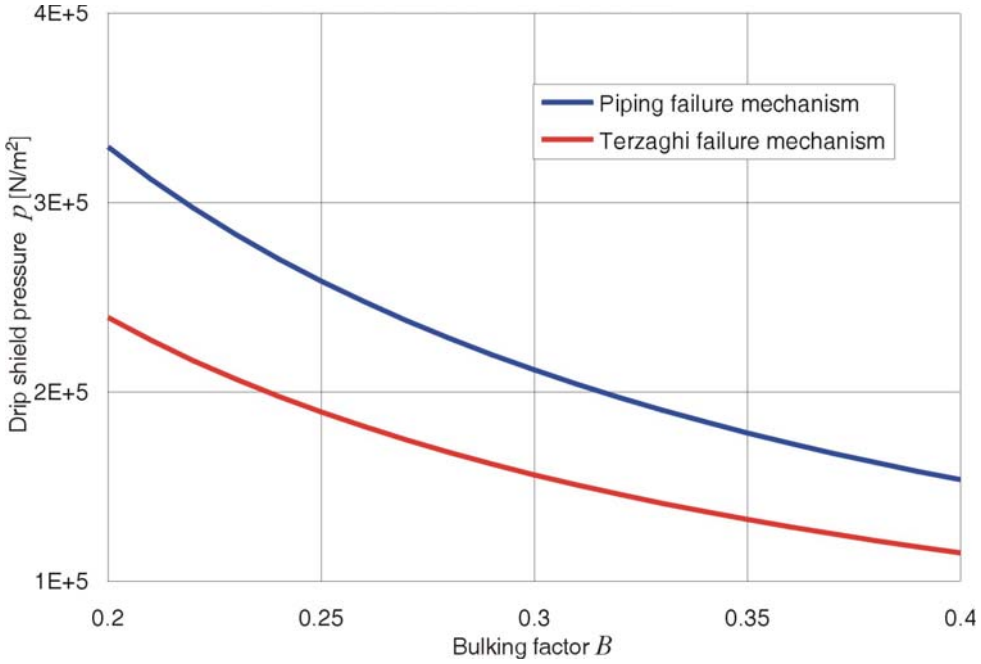

Figure 6-167. Vertical Load on the Drip Shield as a Function of Bulking Factor: Analytical Solutions

Numerical Continuum Approach–The analytical methods described previously in this section require an estimation of both the bulking factor and the ultimate shape of the collapsed zone that forms. A continuum-based numerical assessment of caving provides the next level of sophistication of analysis beyond analytical methods in that they take into account the rock mass strength properties and stress state while automatically estimating the ultimate cave shape. The bulking factor and friction angle of the caved rock must still be considered in this analysis, although the potential effect of stress arching within the broken rock is accounted for in determination of the ultimate load of the broken rock resting on the drip shield. A simplistic methodology was used in implementing caving into the numerical model. A model of the drift in a Mohr-Coulomb rock mass was developed using the FLAC continuum numerical code. "Roller" boundary conditions were used on the vertical and the bottom model boundaries. A stress boundary condition was applied on the top model boundary. The model uses symmetry conditions along the vertical plane through the drift center. The model width was set equal to 10 drift radii. The total model height is either 16 or 25 drift radii, depending on vertical extent of the zone of the caved rock mass. The model bottom boundary is 4.8 radii below the drift center.

The estimated strength of the lithophysal rock mass was used initially for solution of the equilibrium state under in situ stress conditions (strength properties are from Table E-10, Category 1, with a friction angle of 40 degrees). After initial equilibrium, the cohesion and tensile strength of the rock mass were reduced gradually, in steps, to induce collapse and formation of the caved zone. In this case, the bulking factor is estimated, but the model is allowed to achieve the cave shape and dimension dictated by the rock mass properties and stress conditions. At each stage of strength reduction, the model was run until either equilibrium was achieved, or there was clear indication that equilibrium could not be achieved (i.e., the rock mass around the drift was collapsing as evidenced by continued deformation).

The onset of collapse was detected by monitoring the deformations of the excavation (an example is shown in Figure 6-168). When collapse is detected, the model simulation is interrupted, and the cave height calculated based on the estimated bulking factor and the volume of the rock mass within the destabilized region. The accumulation of rubble is represented by filling the previously empty drift and the caved region with elements with the estimated properties of caved rock. The properties of the caved rock were selected to have no cohesion or tensile strength, and its density accounting for the bulking factor. The simulation is then continued, allowing excavation collapse to progress. Equilibrium will eventually be achieved when the caved rock elements provide a back-pressure to the excavation surface sufficient to prevent further yielding. The ultimate vertical pressures induced by the caved rock can be extracted from the model at the drip shield location. As was the case with the analytical solutions, the numerical model can be used to examine loads from two limiting mechanisms:

- A piping mechanism (shown in Figure 6-169, where the caved region is assigned zero cohesion), in which the cave width was limited to the drift width
- A Terzaghi mechanism (shown in Figure 6-170), in which cave width coincides with the width of the destabilized region of the rock mass.

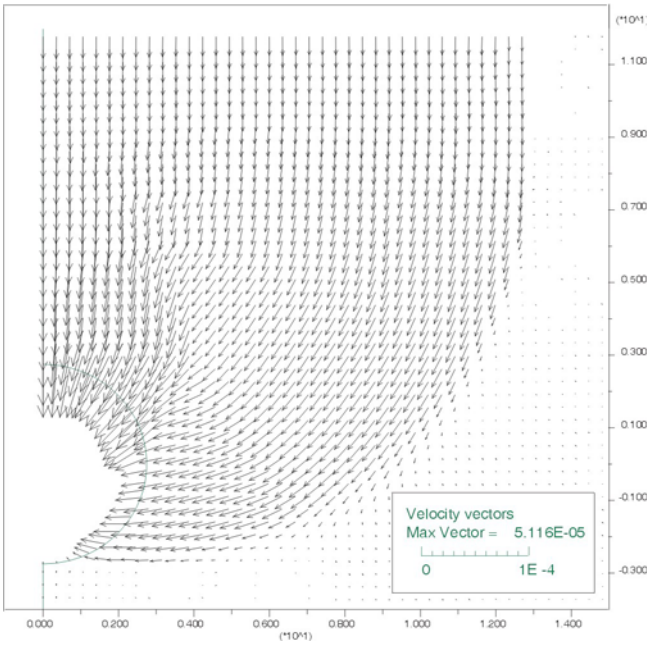

Figure 6-168. Failure Mechanism of a Deep Tunnel in Cohesionless, Mohr-Coulomb Material as Predicted by the FLAC Continuum Model

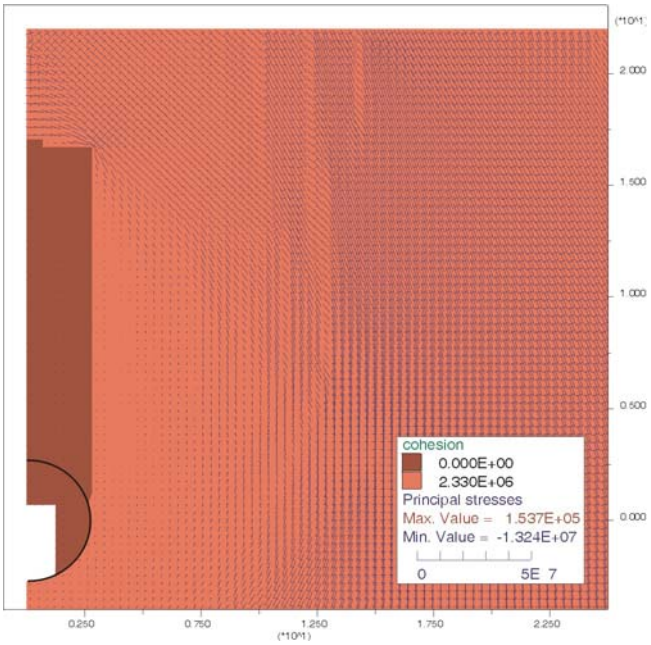

Figure 6-169. Piping Failure Mechanism Represented in the in the FLAC Continuum Model: Bulking Factor B = 0.2

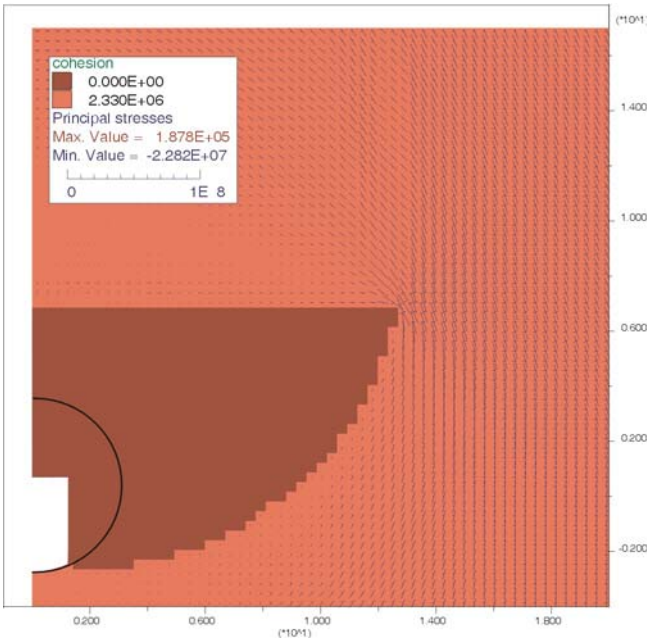

Figure 6-170. Terzaghi Failure Mechanism Represented in the FLAC Continuum Model: Bulking Factor B = 0.1

Subsequently, the drift and the caved region were filled with zones (caved rock selected to have no cohesion or tensile strength, and density accounting for the bulking), and the model was run to the equilibrium to determine the load on the drip shield.

Clearly, the failure mechanism shown in Figure 6-168 is not a realistic mechanism of the drift collapse at Yucca Mountain. This mechanism is more typical for the shallow tunnels in a soil-like media where shearing is the predominant mechanism of inelastic deformation. For emplacement drifts, collapse of the rock mass from the roof will occur much before the deep-seated shear failure in the walls can be mobilized.

Results of the continuum analysis of rock pressure on the drip shield as a function of the bulking factor and different failure mechanism types are summarized in Table 6-47.

Table 6-47. Summary of Pressures on the Drip Shield Calculated from the Continuum Model

Case	Property Category	Failure Type	Bulking	Pressure (kN/m^2)	
				Top of Drip Shield	Side of Drip Shield
1	1	Terzaghi	0.1	269.2	47.1
2	1	pipe	0.1	403.3	39.6
3	1	Terzaghi	0.2	203.6	27.3
4	1	pipe	0.2	295.6	28.3
5	1	Terzaghi	0.4	117.9	20.1
6	1	pipe	0.4	161.6	17.8

Source: DTN: MO0408MWDDDMIO.002, file FLAC drip shield pressures.xls.

Numerical Discontinuum Approach–The analytical and continuum modeling representations of the collapse zone and drip shield loading discussed previously are considered to be overly conservative in the predictions of the resulting cavity size and transfer of the load through the caved rock. Consequently, predicted loads on the drip shield are quite large. The conservatism arises due to the considerations inherent in these methods. To attempt to achieve more realistic rubble loading of the drip shield, the problem was solved using the UDEC two-dimensional discontinuum numerical code. As in Section 6.4.1, the rock mass was represented as an assembly of polygonal blocks of random shape, but with a defined average dimension. The size and the shape of the blocks were the same as used in the previous stability analyses, and were chosen to be approximately the size expected to form during yielding of the Tptpll–within the range of approximately 0.2 to 0.3 m. The blocks are much smaller than the diameter of the drift, and therefore do not affect the collapse mode of the drift or its ultimate shape. The same rock mass material model as used in Section 6.4.1, which was calibrated to strength categories 1 to 5 of the rock mass (associated micro properties are shown in Tables 6-42 and 6-43), is used in these analyses of drift collapse.

The simulations are initiated at the in situ stress equilibrium state for a given rock mass strength value. Since the goal of these studies is to understand the maximum ultimate shape of the cavity and associated rubble load, the tunnel is forced to collapse in the numerical model. To force collapse of the tunnel, shear (cohesion) and tensile strength of the rock mass were subsequently reduced in a series of five increments, each equal to 20 percent of the initial strength. For each step of strength reduction, the model was run to equilibrium, allowing development of shear or tensile fractures in the rock mass and subsequent loosening, detachment, and gravity-fall of

blocks. At the end of the simulation, when cohesion and tensile strength were completely reduced to zero, the model provides an estimate of the maximum extent of the collapsed rock mass, the maximum pressures on the drip shield, and the ultimate shape of the collapse drift. An example of the evolution of rockfall and the cave size for as a function of strength degradation is shown in Figure 6-171. The model shows that in this case (lithophysal rock mass Category 1 and rectangular, rigid, drip shield) the emplacement drift begins significant degradation after about 50 percent reduction in the cohesive strength of the rock mass.[1] The drift is completely filled with caved rock after 80 percent degradation of the cohesive rock strength for the poorest rock quality case shown here (Figure 6-171). In the analyses shown here, complete collapse of the drifts was forced. The amount of strength degradation required to produce collapse (e.g., 80 percent) depends on the initial strength level. For example, in the case of rock mass Category 5 (not shown), which has an unconfined compressive strength of 30 MPa (or three times more than the uniaxial compressive strength for Category 1), there will be some rockfall from the walls, but the drifts will generally remain open even after 80 percent strength degradation.

This modeling approach differs from the analytical and continuum-based methods in that the bulking of the caved rock is not a model parameter but is a result of the modeling. The bulking in reality depends on the size and the shape of the falling blocks, which are predetermined by the size and the shape of the randomly shaped blocks in the model. An average block dimension of 0.2 m was selected for two reasons:

- This dimension is consistent with the spacing of fractures in the Tptpll, and represents a reasonable estimate of the expected block dimensions on failure

- The use of 0.2 m blocks results in bulking factors of approximately 16 to 17 percent which is on the low end of observed field bulking factors in rock and is therefore considered to yield a conservative result of both cave height and drip shield load.

Six realizations of different random block geometries with average dimension of 0.2 m were run to achieve complete collapse. In each case, a deformable drip shield was considered in which the contacts of the footings to the invert were free to slide (frictional) or to separate from the invert as the forces dictate (for details of the drip shield formulation and verification, see Appendix Y). The drip shield is considered to be elastic with stiffness calibrated to be equivalent to the deformability of the three-dimensional frame structure as derived from the LS-DYNA finite element model[2] (Appendix V). The drip shield is represented by 30 elements starting at element number 1 at the right hand footing, and numbered counterclockwise to the left side footing. Figure 6-172 shows an example of the final collapsed shape of the tunnel and the rubble lying on

[1] This agrees, in general, with the predictions of little time-dependent collapse in the previous section. The static fatigue data does not indicate that a reduction in strength of the rock mass of 50 percent occurs in the regulatory period.

[2] The purpose of the two-dimensional UDEC analyses is to determine rubble loading to the drip shield, but not to perform a structural analysis of the drip shield itself. The loads are fed to a detailed three-dimensional structural analysis of the drip shield described in a separate calculation. However, it is important to account for the deformability of the drip shield in determination of the interaction of the rubble and the structure and the subsequent loads that develop. Therefore, the two-dimensional UDEC model of the drip shield was calibrated to provide the proper equivalent stiffness and deformability through comparison to a series of simple loading problems from LS-DYNA as described in Appendix Y.

the drip shield. Figure 6-173 provides contours of displacement of the rock mass and rubble to illustrate the ultimate collapse height of the tunnel. As seen, the height of collapse is approximately 6 m or slightly more than 1 diameter above the roof of the drip shield. The bulking factor of the rubble is approximately 19 percent in this case (see Appendix V for discussion of calculation of bulking factors from model results). The resultant pressure on each element at quasi-static equilibrium for each element for the six realizations, along with the average for the realizations, is given in Figure 6-174. As seen in this plot the average loads on the right- and left-hand sides are approximately the same, while the average pressure on the top of the drip shield is about 50 percent higher.

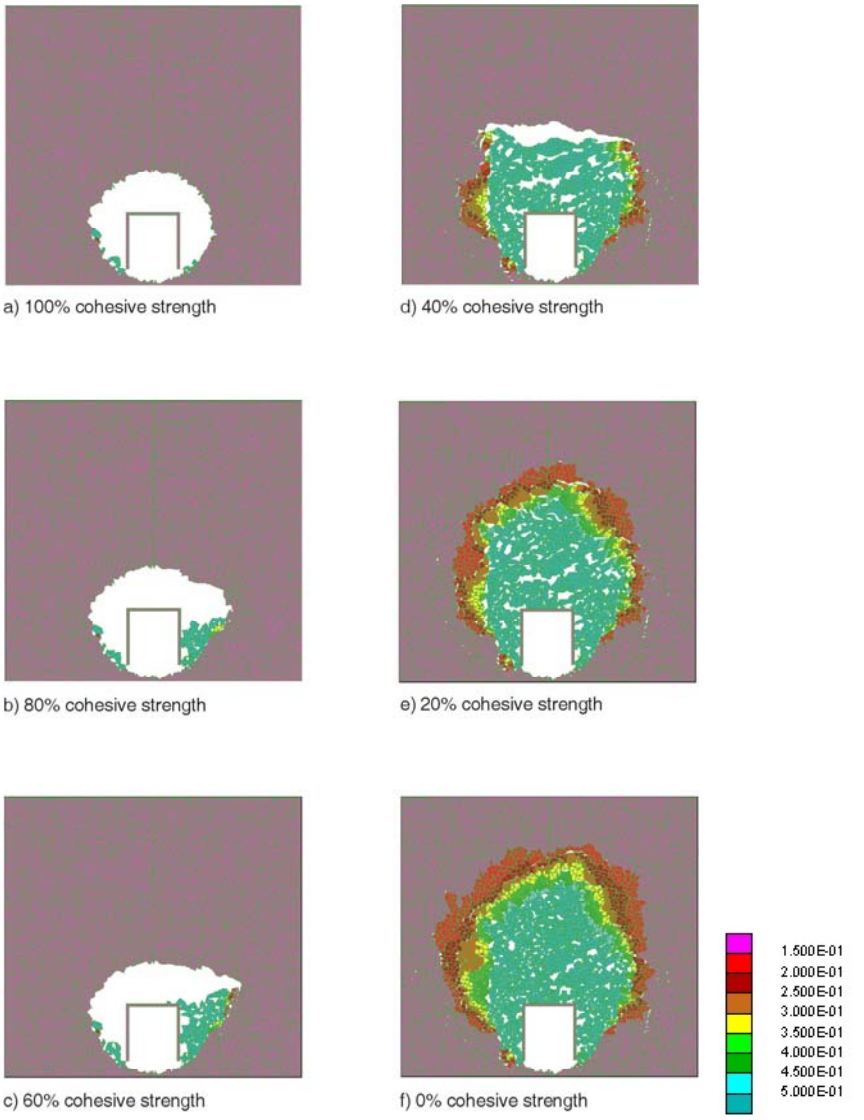

NOTE: Displacement contours are given to assist in visualizing the collapsed area vs. the surrounding undisturbed rock mass. Displacement scale is in meters. Other strength categories will require larger percent strength reduction to produce similar profiles, although the ultimate caved profile will be similar.

Figure 6-171. Evolution of the Cave as a Function of the Cohesive Strength, Category 1 Rock Mass Strength

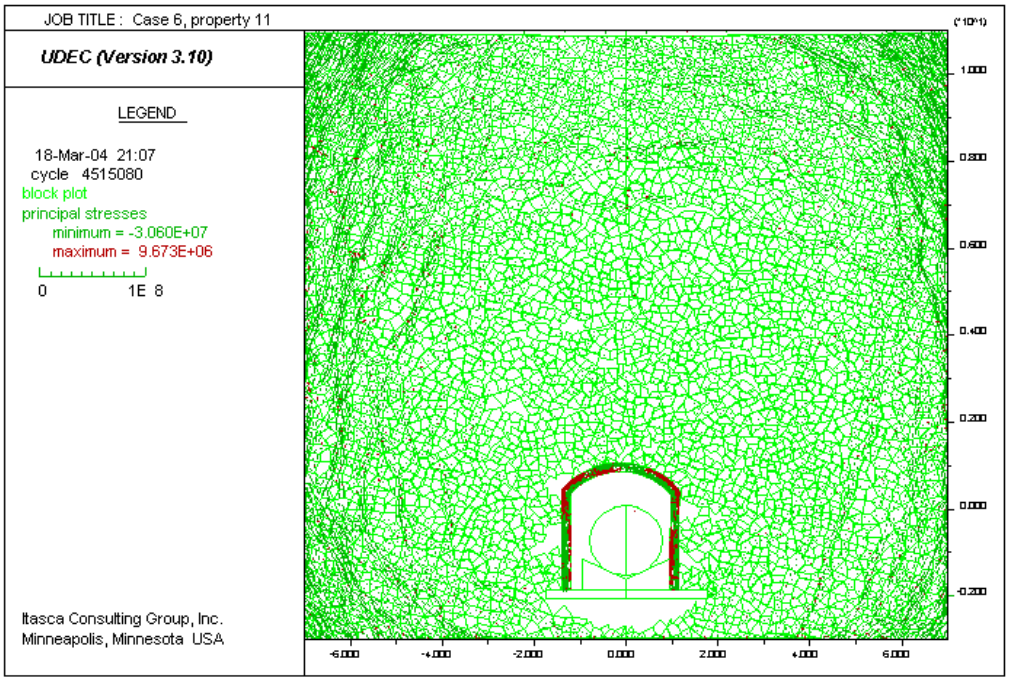

Figure 6-172. Realization 1 for Quasi-static Drift Degradation, Rock Mass Category 1, 0.2 m Block Size: Equilibrium State for Deformable Drip Shield

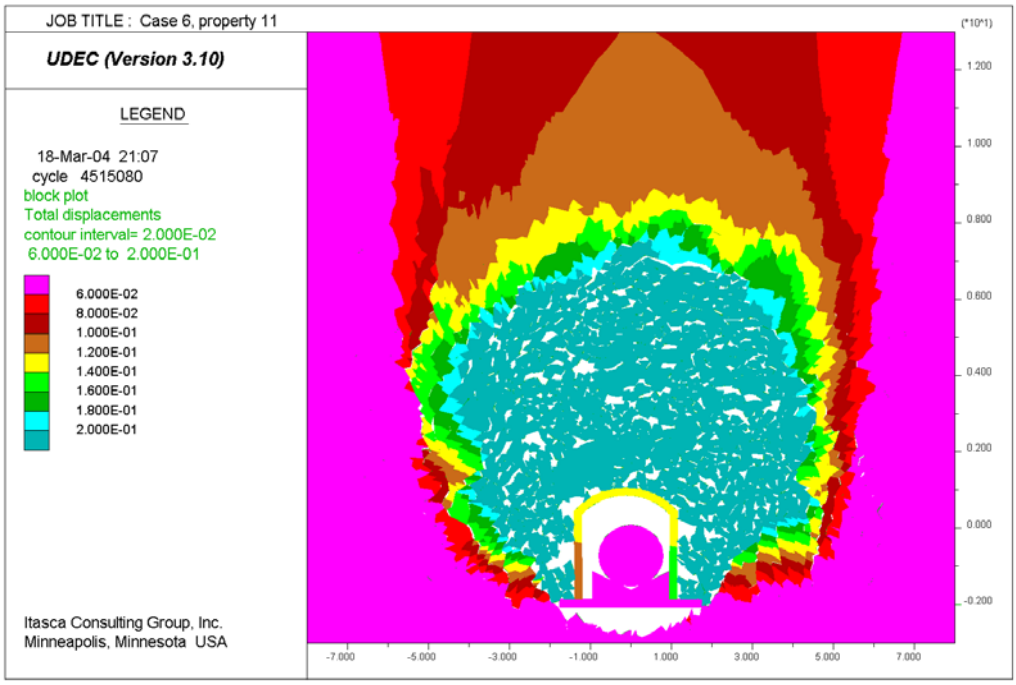

Figure 6-173. Quasi-static Drift Degradation, Rock Mass Category 1, 0.2 m Block Size: Contours of Displacement (m) Magnitude for Deformable Drip Shield Showing Approximate Collapse Height of 7 m (about 6 m above top of drip shield crown)

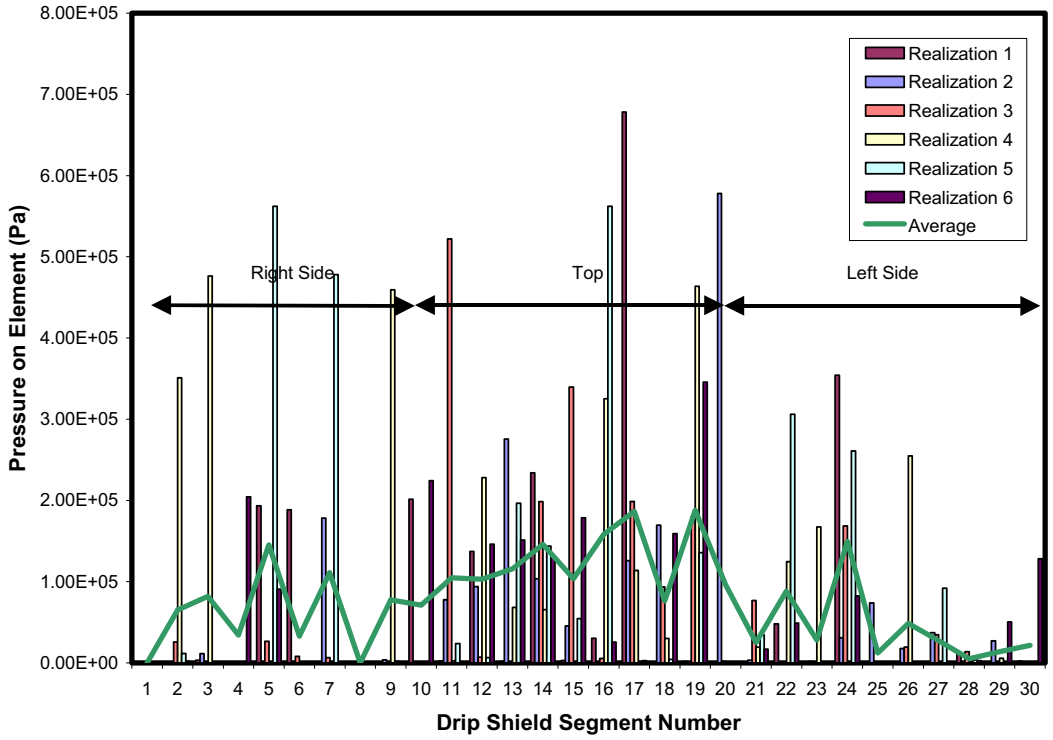

NOTE: Average pressure on each segment is shown for the six realizations plus average for the six realizations combined. Segment numbering starts at 1 at right side footing and continues counterclockwise to the left footing. Those elements on the right, top, and left sides of the drip shield are shown in the figure. This data provided in output DTN: MO0407MWDDSLCR.000 (file *final drip shield quasi-static pressures.xls*).

Figure 6-174. Quasi-static Pressure on Drip Shield Segments for Six Realizations for Random, 0.2m Block Geometries

The effect of point-loads on the drip shield by rock blocks can be seen in Figure 6-174. Occasional, isolated point loads (as well as locations where the segment is not in contact with rock blocks) occur that may be several times larger than neighboring segments. The average pressure on the crown of the drip shield is approximately 0.15 MPa, with a peak pressure on the crown at about 0.7 MPa. The pressure distributions given in Figure 6-174 are used as direct feeds to a sensitivity analysis of quasi-static structural analysis of the drip shield as described in *Structural Stability of a Drip Shield Under Quasi-Static Pressure*. These analyses are considered to be base case conditions for drip shield load.

An examination of the ultimate load-bearing capacity of the drip shield is provided in *Structural Stability of a Drip Shield Under Quasi-Static Pressure*. That analysis requires that increased levels of load be applied to the drip shield until a failure mechanism develops. The UDEC model was used to define increasing rubble pressures applied to the drip shield as input to this analysis. Larger gravitational rubble pressures were simulated in the model by increasing the density of the rock particles that comprise the rubble, and allowing the model to come to equilibrium while the increased rubble pressures on the drip shield are monitored. This method allows simulation of the effect of increased vertical pressure on the drip shield (due to larger heights of the caved zone) while also estimating the associated effect of increased vertical

pressure on the lateral loads. The result of these calculations, considering rock rubble density increases of 1.5, 2, 2.5, 3 and 4 times is shown in Figure 6-175. This plot shows the pressure distribution around the drip shield, as averaged from six realizations at each level of density, along with the base case given in Figure 6-174. The increase in average vertical pressure across the top of the drip shield can be roughly related to an equivalent height of failed rock.

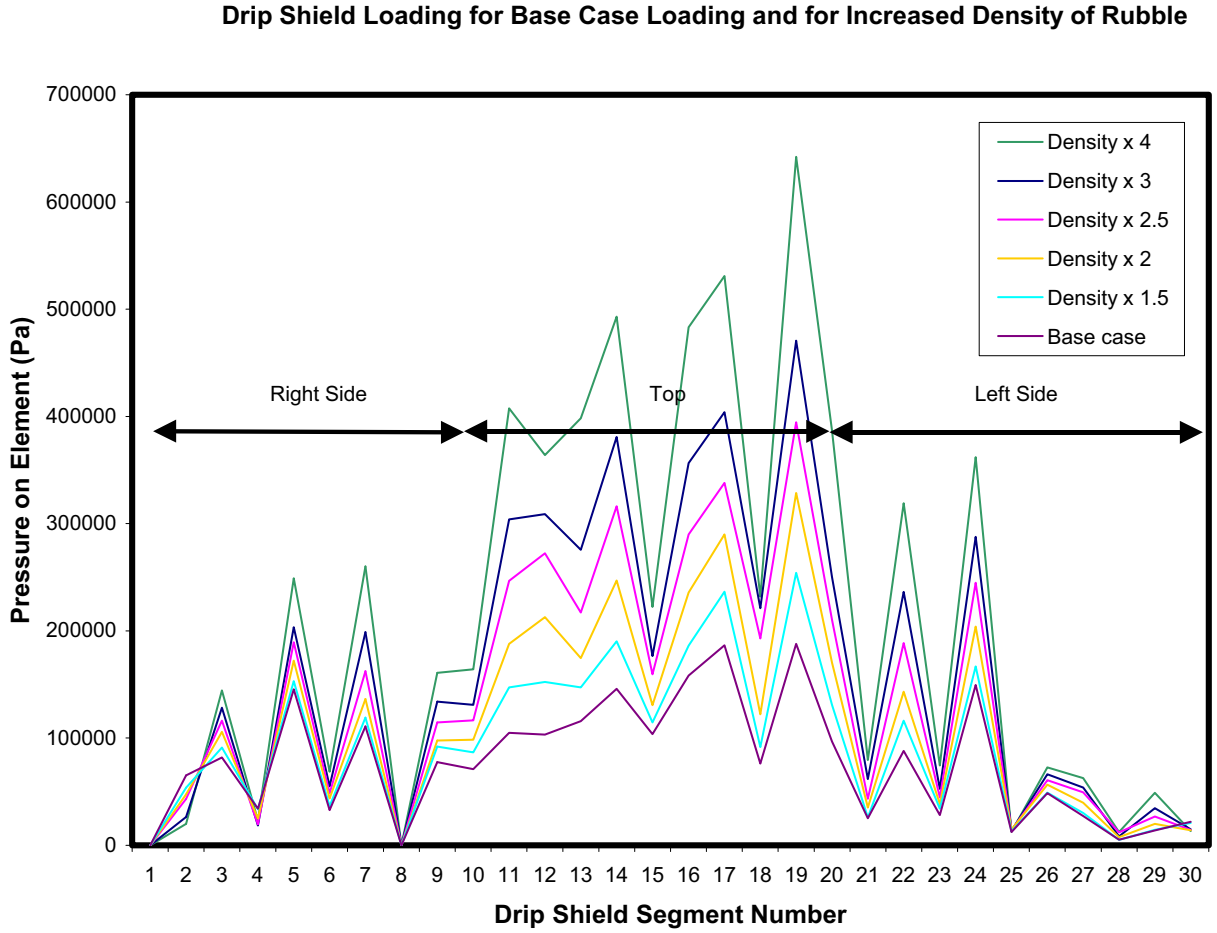

NOTE: Each curve represents the averaging of 6 realizations of rubble distribution. This data provided in output DTN: MO0407MWDDSLCR.000 (file *drip shield quasi-static pressures fs 4.xls*).

Figure 6-175. Drip Shield Pressures for Base Case and for Consideration of Increase in the Density of the Rubble

Effect of Seismic Ground Shaking on Bulking Factor and Stress Arching in Rubble from Previously-Collapsed Drift–Vibratory shaking may cause settlement (irreversible deformation) of granular materials due to packing of grains. This phenomenon is the primary reason for liquefaction of water saturated granular media during seismic shaking. Seismic events occurring after potential collapse of the emplacement drifts may cause additional compaction of the caved rock inside the drift and, consequently, could reduce the positive arching effect within the rubble and increase the load of the caved rock mass on the drip shield. To investigate this effect, the state of the model of the emplacement drift degradation after total collapse of the drift (with rigid, rectangular drip shield) is subjected to shaking by the ground motion with 1×10^{-4}

probability of annual recurrence (10,000 year ground motion).[3] A rigid drip shield was considered in this simulation as it will conservatively overestimate stress transfer to the drip shield when additional compaction of the fill occurs.

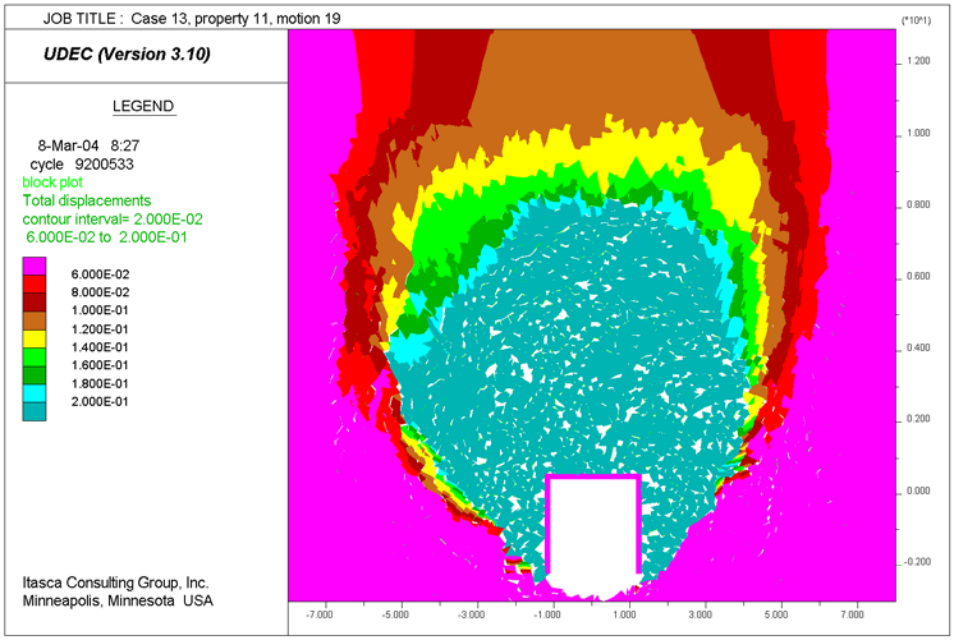

Figure 6-176. Contours of Displacement Magnitudes (M) for Previously Collapsed Drift After Subsequent Shaking by Ground Motions With 1×10^{-4} Probability Of Annual Recurrence

The state of the model and the load of the caved rock mass on the drip shield before and after ground shaking are compared. The contours of displacement magnitudes (relative to the displacement of the model base, which is not zero at the end of the simulation) after the shaking of the model are shown in Figure 6-176. It can be concluded, comparing Figures 6-171f and 6-176, that the size and the shape of the region of the caved rock do not change significantly after dynamic load. Such a result is expected since the 10,000-year ground motion does not cause significant damage of an open drift, and the rubble provides a stabilizing support to the interior of the cave. Therefore, little additional rock mass damage takes place when the drift is already filled with broken rock. The plot of the stress tensor field in the caved blocks around the drip shield before and after ground shaking shows the stress arching formed within the caved rock and the effect of shaking on the stress transmission in the rubble (Figure 6-177). The model indicates that this level of ground shaking does affect arching to some extent.

Observations from the plot of stress arching in the caved rock mass are confirmed in Figure 6-178 and Table 6-48. There is significant increase in the load on the right side of the drip shield as rock blocks come into point contact with the drip shield. In this case, since the drip shield is rigid and footings rigidly attached to the invert, no sliding occurs to more equally distribute loads on opposing sides of the drip shield. However, the increase in the load on the top of the drip shield is relatively small–less than 10 percent. There is practically no change in the bulking factor, because shaking does not create any additional collapse.

[3] Only one ground motion was supplied for the 1×10^{-4} annual recurrence level.

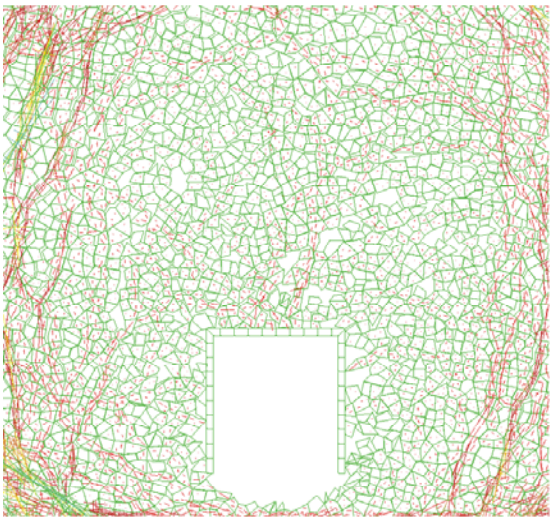

a) before shaking

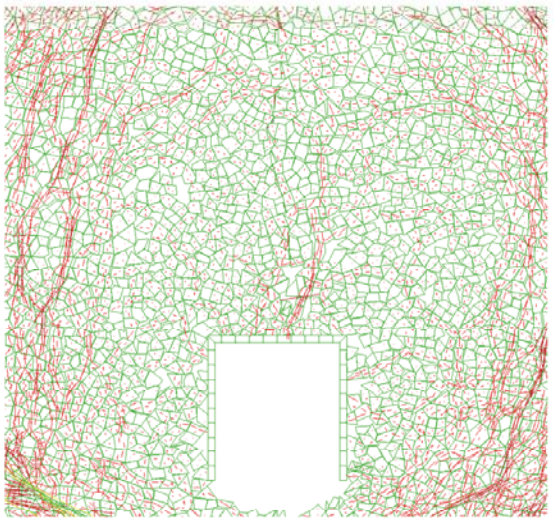

b) after shaking

NOTE: Stress arching is shown by the stress tensor field colored by the magnitudes of the major principal stress. Somewhat greater stress transfer to the drip shield is shown after shaking.

Figure 6-177. Stress Arching (stress tensor field colored by the magnitudes of the major principal stress) Before and After Shaking, Showing Somewhat Greater Stress Transfer to the Drip Shield

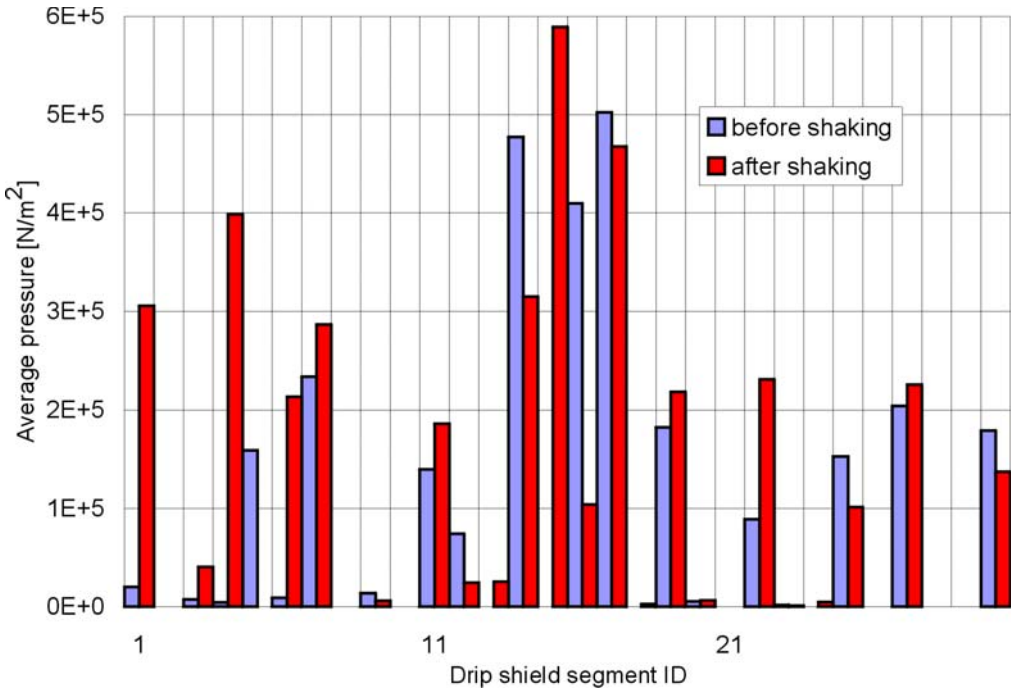

NOTE: Outside outline of the drip shield is divided into 30 segments (10 per height and 10 per width), which are numbered from 1 to 30 starting from lower right end in the counter-clockwise direction.

Figure 6-178. Pressures on the Rigid, Rectangular Drip Shield After Shaking by the Seismic Event With 1×10^{-4} Probability of Annual Recurrence

Table 6-48. Effect of Seismic Shaking on Load of Caved Rock on the Rigid, Rectangular Drip Shield

Loading Condition	Pressure (kN/m^2)			Bulking Factor
	Left Side	Top	Right Side	
before shaking	62.6	179.2	44.8	0.19
after shaking	70.2	193.9	125.1	0.21

Summary of Quasi-static Loading of the Drip Shield–The predictions of the average vertical pressure of the caved rock on the drip shield by the three modeling approaches are summarized in Figure 6-179. As expected, the analytical models yield the largest loads due to the conservative considerations of dead weight on the drip shield and no stress arching in the rubble. The continuum numerical model accounts more accurately for transfer of load by friction from the caved rock to the surrounding stable rock mass. Consequently, predicted loads for small bulking factors and large cavity size are much smaller than analytical predictions. When the bulking factor is large, the height of the cave becomes small. Stress arching cannot be realized within the small column of the caved rock and, consequently, prediction between analytical and continuum models are identical. The most accurate approach, using the discontinuum model, does not use an imposed condition about the shape of the caved region or the bulking factor of the rubble. It also correctly accounts for load transfer through the caved rock. The predictions of the pressures on the drip shield using this approach are smaller than the predictions of the analytical and continuum models for the values of the bulking factor. The non-uniform and averaged quasi-static drip shield pressure distribution, illustrated in Figure 6-174, as well as the

increased pressures for estimation of the ultimate load bearing capacity of the drip shield are used as a direct feed to the structural analysis of the drip shield as provided in *Structural Stability of a Drip Shield Under Quasi-Static Pressure*. Further compaction of the rubble during subsequent seismic events may result in re-adjustment of point loads to the lining, but does not appear to result in reduction in bulking factor of the rubble material.

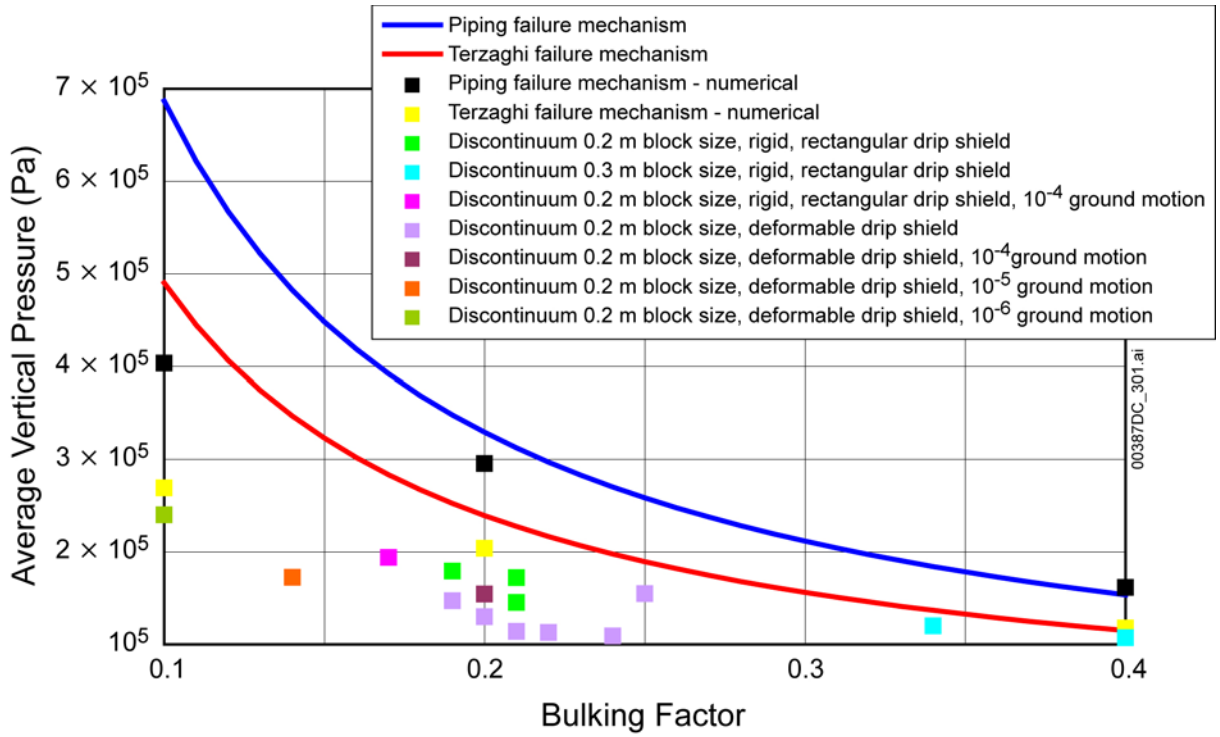

NOTE: Two different sizes of the randomly shaped blocks used in the discontinuum analyses were used to produce a range of bulking factors.

Figure 6-179. Summary of Vertical Load on the Drip Shield as a Function of Bulking Factor

6.4.3 Investigation of Potential Key Blocks in Lithophysal Units

The stability analyses of the lithophysal rock mass presented thus far consider that the ubiquitous fracture fabric in this unit will control failure mode, resulting in raveling of small rock particles. However, a set of widely spaced, longer trace length cooling fractures exists that are not truncated by the small-scale fractures. It is possible that, in addition to the raveling mode of failure, that larger rock blocks (key blocks) are formed by these longer fractures. This section describes the probability of key-block existence, or the possibility that wedge-type failure may occur in the lithophysal units. The general approach used for analyses of wedge-type failure in the nonlithophysal units, as described in Section 6.3.1, is also applied in this study. The three-dimensional discontinuum code 3DEC is used for the mechanical analysis of the jointed rock mass simulated by FracMan. Since small-scale fractures have minor effect on wedge formation as confirmed in Section 6.3.3, only the fractures with trace lengths greater than or equal to 1 m long are included here.

In a similar manner as that used for examination of the nonlithophysal base case, a total of 50 fracture modeling regions were selected from the 100-m cube simulated FracMan fractured rock mass for the Tptpll unit (Appendix B). Because the coordinates of the 50 fracture modeling regions selected for the nonlithophysal units were randomly generated, they were also used in the lithophysal units. For conservatism and efficiency, fracture strength parameters (cohesion and friction angle) were reduced to small values to evaluate the probability of key-block existence. With strength parameter values assigned as 0, the predicted rockfall is equivalent to the blocks that are kinematically admissible to fall regardless of the frictional resistance of fracture surfaces.

The summary of the analyses is presented in Table 6-49. Twenty-one distinct rock blocks are formed by the longer fractures in the 50 simulations. Notice that the distinct blocks are all of the blocks that exist in the rock mass regardless of whether the blocks are kinematically or mechanically suitable to fall. A typical cross section of the analysis with prediction of the distinct block is provided in Figure 6-180. Only two blocks were predicted to fall into the drift with block volume of 0.16 m^3 and 0.08 m^3. With only two blocks predicted for 1.25 km of drift simulated while using extremely conservative (i.e., low) fracture strength properties, the probability of key-block occurrence in lithophysal units is very low and not considered further. This analysis confirms that raveling of small blocks is expected to be the dominant potential failure mode of drifts in lithophysal rocks.

Table 6-49. Summary of 3DEC Rockfall Prediction for Lithophysal Units

Parameter	Value
Simulations Completed	50
Number of Simulations Predicting No Rockfall	48
Number of Simulations Predicting No Distinct Block	37
Total Number of Rockfall	2
Total Volume of Rockfall (m^3)	0.24
Total Length of Drift Simulated (m)	1250
Number of Blocks per km	1.6
Volume of Rockfall per km (m^3/km)	0.19

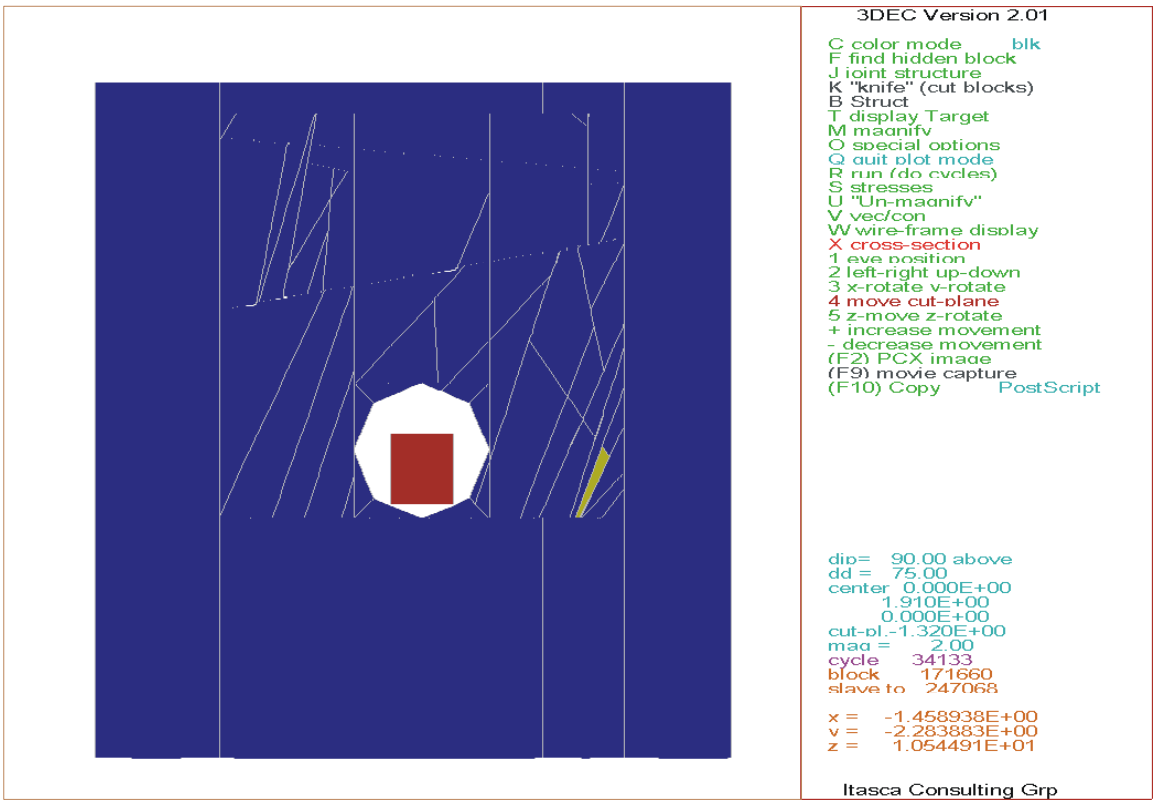

NOTE: The fracture traces shown in this cross section do not necessarily form a coherent block in three-dimensions. The only distinct block formed in this cross section is shown in yellow, and is obviously not "removable".

Figure 6-180. Cross Section of a Typical Simulated Lithophysal Rock Mass in 3DEC

6.5 UNCERTAINTIES AND LIMITATIONS

The task of predicting and characterizing drift degradation anticipated within repository emplacement drifts throughout the 10,000-year period of compliance for postclosure performance has several inherent uncertainties and limitations. These uncertainties are associated with both the modeling methods and the model inputs. To provide a meaningful assessment of drift degradation, the uncertainties must be identified and adequately represented within the model. The uncertainties associated with modeling methods are addressed with model validation (Section 7). Additionally, a discussion of alternative conceptual models has been provided (Section 6.7), which provides justification for use of the modeling methods employed in this document, thereby demonstrating that the drift degradation models presented in this report are adequate to account for the uncertainties and limitations.

This section provides a discussion of uncertainties associated with model inputs. The discussion below has been rank-ordered according to importance in control of drift degradation under in situ, thermal, and seismic loading. That is, the parameters and their associated uncertainty that have the most significant impact on model results are discussed first. In general, those uncertainties associated with drift degradation in lithophysal rocks are considered to be most significant due to the relatively larger amount of emplacement area located in them. The rock

mass properties for lithophysal rock and fracture geometry in nonlithophysal rock have the greatest impact on drift degradation. The seismic ground motions, particularly those at low annual probability levels, have a large impact on stability of both nonlithophysal and lithophysal rock masses.

Rock Mass Mechanical Properties Data–Rock mass mechanical properties data for nonlithophysal rock are calculated using rock mass classification data collected from field mapping within the ESF and intact rock properties data collected from laboratory testing. The uncertainties associated with the intact rock properties data are described above. The uncertainties associated with the rock mass classification data are epistemic, and are assessed to be low because an abundance of data has been collected based on established, industry-accepted methods. There is a moderate degree of epistemic uncertainty associated with the calculation approach for assessing rock mass properties, since they are based on empirical methods and have an inherent characteristic of imprecision. This uncertainty has been accounted for by using two separate empirical calculation methods and demonstrating that the results are similar. The rock mass properties data are primarily used in the thermal-mechanical calculation to determine stresses within the model as described in Section 6.2, and are a relatively insensitive parameter to the stress calculations.

Rock mass mechanical properties data for lithophysal rock are based on large-diameter uniaxial compression test data and in situ slot test data (Appendix E, Section E4.1). The epistemic uncertainty associated with this rock mass data for lithophysal rock is assessed to be high. To account for this uncertainty in the rockfall model for lithophysal rock, five categories of rock properties were included in the model to assess the impact of the ranges in rock mass properties data. Additionally, the PFC numerical model was calibrated to reproduce the large-core laboratory mechanical properties data and its dependency on lithophysal porosity as well as the observed failure mechanisms. The model was then used to build confidence in the understanding of the bounding ranges of lithophysal rock mass properties through numerical extrapolations to examine the effect of lithophysal cavity porosity, size, shape and distribution variability as defined by field mapping. This work is described in detail in Appendix E, Section E4.1. The impact of use of the range of rock properties on drift degradation and rockfall was explored through use of sensitivity studies in Section 6.4.

Seismic Ground Motion Data–The seismic time histories used to evaluate rockfall reflect a number of variabilities, including epistemic uncertainty and randomness (aleatoric uncertainty). Epistemic uncertainties (due to incomplete knowledge) in the characterization of seismic sources and median ground motion attenuation, along with randomness in seismic ground motion, were explicitly incorporated into the probabilistic seismic hazard analysis. The mean results of that analysis form the basis for the site-specific ground motions used in this report. At annual probabilities of exceedance lower than about 1×10^{-6}, the mean hazard exceeds the 85th percentile of the hazard uncertainty distribution.

Development of site-specific ground motions incorporates additional epistemic uncertainty in the velocity and dynamic properties of site materials. Observed randomness of site materials is also addressed. Finally, randomness in the spectral content and duration of time histories that produce the same peak ground motion is accommodated in the drift degradation analyses through the use of 15 sets of time histories for each of the two postclosure hazard levels considered. The

earthquake magnitudes and epicentral distances of the recorded strong motion data that form an input to these time histories, reflect the range of magnitudes and distances contributing most strongly to seismic hazard at the site for the given annual probabilities of ground motion exceedance.

While the seismic ground motion inputs developed in this manner fully account for the underlying uncertainties and randomness, the result is that for annual exceedance probabilities of about 1×10^{-6} and lower, some realizations of ground motion are larger than the largest ground motions observed and may not be physically realizable. Nonetheless, these ground motions are consistent with and demonstrate fully the current state of uncertainty and randomness in deriving ground motion inputs for very low annual probabilities of exceedance. Lacking a technical basis to limit such ground motions to smaller values, these inputs are used in the analyses supporting TSPA-license application (LA) [4].

Static Fatigue and Long-Term Strength Data–The long-term strength predictions (Section 6.4.2.4 and Appendix S) are based on very limited static-fatigue test data, which provide time-dependent strength behavior of the lithophysal rock. A static-fatigue (creep) test involves applying a constant compressive stress to a specimen, and recording the time to failure (Potyondy 2003 [DIRS 165550], Section 1.4). One of the main limitations of the predictions of time-dependent behavior of excavations in a rock mass for a period of 10 years or longer after excavation, is that existing static-fatigue testing (for any rock) is typically performed for no more than a few months. Predictions for longer time frames are based on extrapolation of existing testing data, and involve a significant level of uncertainty. The static-fatigue curve is usually considered to be a straight line in a logarithm plot of time-to-failure versus driving-stress ratio, which is fitted to experimental data. However, it appears from available data for Lac du Bonnet granite (see Appendix S, Figure S-27) that the fitted static-fatigue curve underestimates time-to-failure compared to experimental data in the range of driving-stress ratios between 0.65 and 0.70 (which corresponds to the longest measured times-to-failure). It seems that a curved line (instead of straight line) would be a better fit for long times-to-failure. Consequently, predictions obtained using the straight line are conservative, because the straight line appears to under-predict time-to-failure for low values of the driving stress.

Failure times and the *evolution* of the damage of the rock are provided by standard creep (i.e., strain versus time) plots derived from the laboratory static-fatigue test. The PFC stress corrosion model was calibrated to reproduce the time-evolution of damage response as determined from these laboratory tests. The sensitivity of the PFC stress corrosion predictions to damage rate has been investigated to determine how damage rates affect the final result of the model (i.e., the rockfall induced by time-dependent strength degradation). Damage curves were generated for tuff best fit static-fatigue (see Appendix S, Figure S-29), where the damage rates for the driving stress levels are considered to be the same, equal to the maximum rate predicted by the PFC

[4] An analysis to provide an estimate of the bounding peak ground velocity for the Yucca Mountain site has been developed (BSC 2004, [DIRS 170137]). This estimate is based on examination of the maximum shear strain that the lithophysal rock can withstand, and relating this to the peak ground velocity that will produce this strain. Since no seismic-related shear damage can be observed in the field in the lithophysal rocks, it is argued that no seismic event has occurred with peak ground velocity exceeding this failure limit in the approximately 12.8 million years since the Topopah Spring tuff has been deposited and cooled. However, non-bounded ground motion time histories were used in the analyses presented in this document.

stress corrosion model. The rockfall predictions due to time-dependent strength reduction using a range of damage curves have been compared, and it is clear that the considered variation of damage rates has no practical effect on predicted rockfall (see Appendix S, Figure S-31). The time-to-failure is the main factor controlling evolution of the rockfall due to time-dependent strength reduction. Consequently, UDEC predictions are not very sensitive to the damage rate input from the PFC stress corrosion model.

Further investigation of uncertainty in the time-dependent UDEC modeling of drift degradation was performed by using the time-dependent strength degradation obtained from extensive Lac du Bonnet granite as a lower bound to the time-dependent strength loss of Topopah Spring tuff. Although the extent of drift degradation is greater when using these lower bound considerations, the overall conclusions regarding extent of collapse and timing of collapse are not significantly different (Appendix S).

Fracture Geometry Data for Nonlithophysal Rock–The natural variability of fractures within a rock mass represents epistemic uncertainty (i.e., uncertainty due to incomplete knowledge) in the design of structures in rock. The large amount of fracture data collected at the YMP provides a very good representation of the range of fracture geometry anticipated at the emplacement drift horizon. The range of fracture geometry variability from tunnel mapping has been captured in the rockfall model for nonlithophysal rock through multiple simulations of the rock mass. Section 6.1.6 describes the generation of representative rock volumes using FracMan with the consideration of the natural variability of fracture geometry. The representativeness of the FracMan-generated rock volume is verified in Section 6.1.6 through comparison of the FracMan synthetic fracture network to the statistical variability of the fractures as measured by field mapping. Section 6.3.1.2.2 documents the random selection of the fracture-modeling region in the rockfall analyses to cover the uncertainties associated with fracture orientation, intensity and length. The fracture geometry is concluded to be the dominant factor for wedge-type rockfall in nonlithophysal rock. The uncertainty associated with joint geometry data in the rockfall models is assessed to be low.

Intact Rock Physical and Mechanical Properties Data–A sufficient amount of intact rock physical and mechanical properties data has been collected for the nonlithophysal rock units. The epistemic uncertainty associated with this intact data for nonlithophysal rock is assessed to be low. Conversely, the amount of intact rock physical and mechanical properties data for the lithophysal units is limited. The epistemic uncertainty associated with this intact data for lithophysal rock is assessed to be high. To account for this uncertainty in the rockfall model for lithophysal rock, five categories of rock properties were included in the model to assess the impact of the ranges in intact properties data. The difference of rockfall prediction for the range of properties considered is provided in Section 6.4.

Fracture Mechanical Properties Data–The amount of fracture mechanical properties data for both the nonlithophysal and lithophysal rock units is limited; therefore, the uncertainty associated with this data is epistemic, and is relatively high. To account for this uncertainty in the rockfall models, sensitivity analyses for the possible range of fracture strength parameters, dilation angle, and fracture stiffness were conducted and the results are presented in Section 6.3.1.6. Fracture mechanical properties are judged to have a secondary effect on rockfall compared with fracture geometry data.

Rock Thermal Properties Data–A sufficient amount of rock thermal properties data has been collected for the nonlithophysal rock units. The epistemic uncertainty associated with this thermal properties data for nonlithophysal rock is assessed to be low. Conversely, the amount of rock thermal properties data for the lithophysal units is limited. Therefore, the epistemic uncertainty associated with this thermal properties data for lithophysal rock is assessed to be high. Uncertainty assessments are provided in the data source documentation identified in Table 4-1 and in Appendix E (Section E5). Sensitivity calculations for thermal properties were conducted with one standard deviation less values used for thermal conductivity and specific heat as described in Section 6.2, Section 6.3.1.3, and Section 6.4.2.3. The sensitivity case results in approximately 23°C higher peak temperature comparing with the base case but with minor impact to the rockfall prediction.

Repository Layout Information–The repository layout data are based on design information, which is currently in the preliminary design stage. This design information is subject to change before being finalized. The model results documented in this report are applicable for the emplacement drift diameter and emplacement drift alignment provided by repository design and performance assessment information exchange drawings (BSC 2004 [DIRS 164519]; BSC 2004 [DIRS 168489]) and Section 5.1.4 and 8.7 of *Underground Layout Configuration* (BSC 2003 [DIRS 165572]). The rockfall models are sensitive to both emplacement drift diameter and alignment. While no changes are expected to the emplacement drift diameter and alignment, and any change to this design information would require reevaluation.

6.6 DRIFT DEGRADATION FEPS

The development of a comprehensive list of features, events, and processes (FEPs) potentially relevant to postclosure of the repository is an ongoing, iterative process based on site-specific information, design, and regulations. The approach for developing an initial list of FEPs was documented by *The Development of Information Catalogued in REV00 of the YMP FEP Database* (Freeze et al. 2001 [DIRS 154365]). To support TSPA-LA, the FEP list was re-evaluated and is provided by DTN: MO0407SEPFEPLA.000 [DIRS 170760]. Table 6-50 provides a list of FEPs addressed in this model document that have been included in TSPA-LA (based on MO0407SEPFEPLA.000 [DIRS 170760]), and provides specific references to sections within this document. Additionally, Table 6-51 provides a list of FEPs addressed in this model document that have been excluded in TSPA-LA (based on MO0407SEPFEPLA.000 [DIRS 170760]).

Table 6-50. Included FEPs Addressed by This Model Report

FEP No.	FEP Name	Section Where the FEP is Discussed
1.2.03.02.0A	Seismic ground motion damages EBS components	This report provides rockfall models that are based on site characterization data, including joint geometry and rock strength data, coupled with anticipated thermal stresses and seismic ground motion. Based on the analyses presented in this report (Section 6.3 and 6.4), postclosure ground motion levels are sufficient to produce collapse of drifts in the lithophysal rock units (which represent approximately 85 percent of the emplacement drifts). Minor to moderate degradation or collapse of drift is anticipated in the nonlithophysal rock units throughout the regulatory period for postclosure performance.
1.2.03.02.0B	Seismic-induced rockfall damages EBS components	This report provides rockfall models that are based on site characterization data. Probabilistic descriptions of rock size and rockfall frequency are provided for use in engineering design analyses (Sections 6.3 and 6.4). The block size distributions presented in this report are similar to the block size distributions developed using the approach in the previous version of this document (Section 7.7.5). However, the frequency of blocks has increased with the larger ground motions used in this report compared to the previous approach (Section 7.7.5).
1.2.03.02.0C	Seismic induced drift collapse damages EBS components	This report provides rockfall models that are based on site characterization data, including joint geometry and rock strength data, coupled with anticipated thermal stresses and seismic ground motion. Based on the analyses presented in this report (Section 6.3 and 6.4), minor degradation or collapse of drift is anticipated for the static (i.e., no seismic) case and during the preclosure period. The mechanical degradation or collapse of drift predicted for the static case and during the preclosure period is similar to the results from the previous approach using DRKBA (Section 7.7.5). Based on the analyses presented in this report (Section 6.3 and 6.4), postclosure ground motion levels are sufficient to produce collapse of drifts in the lithophysal rock units (which represent approximately 85 percent of the emplacement drifts). Minor to moderate degradation or collapse of drift is anticipated in the nonlithophysal rock units throughout the regulatory period for postclosure performance.
1.2.03.02.0D	Seismic induced drift collapse alters in-drift thermo-hydrology	This report provides rockfall models that are based on site characterization data, including joint geometry and rock strength data, coupled with anticipated thermal stresses and seismic ground motion. Based on the analyses presented in this report (Section 6.3 and 6.4), minor degradation or collapse of drift is anticipated for the static (i.e., no seismic) case and during the preclosure period. The mechanical degradation or collapse of drift predicted for the static case and during the preclosure period is similar to the results from the previous approach using DRKBA (Section 7.7.5). Based on the analyses presented in this report (Section 6.3 and 6.4), postclosure ground motion levels are sufficient to produce collapse of drifts in the lithophysal rock units (which represent approximately 85 percent of the emplacement drifts). Minor to moderate degradation or collapse of drift is anticipated in the nonlithophysal rock units throughout the regulatory period for postclosure performance.

NOTE: The screening decision to determine the include/exclude status of the FEP is documented in MO0407SEPFEPLA.000 [DIRS 170760].

Table 6-51. Excluded FEPs Addressed by This Model Report

FEP No.	FEP Name	Section Where the FEP is Discussed
1.1.02.00.0B	Mechanical effects of excavation/ construction in EBS	This report provides rockfall models that are based on observation of rock characteristics representing the as-built (post-excavation) condition, so that potential excavation effects, if any, are considered. For example, the field mapping data of geologic features presented in Section 6.1.4 were collected post-excavation in the ESF, and therefore include excavation effects. Similarly, the calculation of rock mass properties in Appendix E (Section E4) inherently includes these excavation effects. Therefore, the effects of excavation on rock mass response are reflected in the results presented in this report.
2.1.06.02.0A	Mechanical effects of rock reinforcement materials in EBS	In this model report, no credit is taken for ground support in rockfall models (Section 6.0). Therefore, the consideration of the mechanical effects of rock reinforcement is implicit in the modeling approaches discussed in Sections 6.3 and 6.4. The rockfall models presented in this report (Sections 6.3 and 6.4) provide a bounding scenario in the analysis of the effects of rock reinforcement on drift degradation.
2.1.07.01.0A	Rockfall	This report provides rockfall models that are based on site characterization data. Probabilistic descriptions of rock size and rockfall frequency are provided for use in engineering design analyses (Sections 6.3 and 6.4). The block size distributions and frequency of blocks presented in this report for static (i.e., no seismic) and preclosure ground motion are similar to the block size data developed using the approach in the previous version of this document (Section 7.7.5).
2.1.07.02.0A	Drift collapse	This report provides rockfall models that are based on site characterization data. Based on the analyses presented in this report (Section 6.3 and 6.4), minor degradation or collapse of drift is anticipated for the static (i.e., no seismic) case and during the preclosure period. The mechanical degradation or collapse of drift predicted for the static case and during the preclosure period is similar to the results from the previous approach using DRKBA (Section 7.7.5).
2.1.11.07.0A	Thermal expansion/ stress of in-drift EBS components	This report provides rockfall models that include the potential impact of thermally induced stress changes in the rock mass (Section 6.2). The effects of thermally induced stress changes on drift degradation are documented in Sections 6.3.1.3 (nonlithophysal rock) and 6.4.2.3 (lithophysal rock).

NOTE: The screening decision to determine the include/exclude status of the FEP is documented in MO0407SEPFEPLA.000 [DIRS 170760].

6.7 DOCUMENTATION OF ALTERNATIVE CONCEPTUAL MODELS

Alternative conceptual models are based on assumptions and simplifications that are different from those employed in the base case models (i.e., the rockfall model for nonlithophysal rock (Section 6.3) and the rockfall model for lithophysal rock (Section 6.4)). An important reason for considering alternative conceptual models is to help build confidence that changes in modeling assumptions or simplifications will not change conclusions regarding subsystem and total system performance. Conceptual model uncertainty results from sparse observational data and a lack of available information to corroborate or refute plausible alternative interpretations of the subsystem and the processes occurring within the subsystem.

The alternative conceptual models considered in this analysis of drift degradation are summarized in Table 6-52.

Table 6-52. Alternative Conceptual Models Considered

Alternative Conceptual Model	Key Assumptions	Screening Assessment and Basis
Continuum model of lithophysal rock	Lithophysae and fractures are smeared into the elements in the equivalent continuum representation of the rock mass. Rock damage is expressed as element yielding following the selected failure criterion.	The continuum model, such as FLAC or FLAC3D, is capable of modeling the material yielding behavior with elasto-plastic constitutive model. Yielding occurs when the stress state within the element reach the strength criterion specified by the constitutive law, the yielding of elements in the continuum, however, is not equivalent to rockfall. To estimate the extent of rockfall based on the depth of yielding is not realistic. Therefore, this alternative conceptual model is excluded from further evaluation.
Continuum model of nonlithophysal rock	Fractures are smeared into the elements in the equivalent continuum representation of the rock mass. Element contains the weak plane information for potential shear slipping.	The compliant joint model (Chen 1987 [DIRS 101800]) is capable of analyzing jointed media behavior with fractures smeared into the elements. The model includes a continuum approximation based on average discontinuous displacements across joint planes within a representative elementary volume. The model also includes a material constitutive description based on linear elastic matrix material behavior and nonlinear normal and shear joint behavior between joint planes. The continuum model provides global rock mass response with predominant weak plane orientation, but cannot predict wedge-type failure. Therefore, this alternative conceptual model is excluded from further evaluation.
Hudson and Priest (1979 DIRS 104915]) model of nonlithophysal rock for estimating block size distribution	All joint planes are assumed to be perfectly planar, persistent, and extend throughout the rock volume of interest. The distribution of joint spacing values along a line is assumed to be of negative exponential form.	The approach to determine block size distribution using the Hudson and Priest approach has been documented by *Preliminary Block Size Calculation* (CRWMS M&O 1998 [DIRS 102723], Section 5.3). This approach provides a generalized statistical representation of the joint geometry. In particular, the assumption of continuous joints is not consistent with the discontinuous joints observed in the ESF. Since joint geometry is a primary factor in the assessment of block development, the generalized approach by Hudson and Priest does not provide the level of detail required to accurately model drift degradation. Therefore, this alternative conceptual model is excluded from further evaluation.

6.8 RESOLUTION OF KEY TECHNICAL ISSUES

The NRC is conducting an ongoing review of the information provided by the YMP to allow early identification and resolution of potential licensing issues. The NRC has identified several key technical issues (KTIs) and associated sub-issues, along with acceptance criteria for resolution of the issue. The drift degradation analysis provides information that is directly related to the KTI on Repository Design and Thermal-Mechanical Effects (NRC 2002 [DIRS 159538]). To provide a clear understanding of the technical issues, a NRC/DOE Technical Exchange and Management Meeting on Repository Design and Thermal-Mechanical Effects was held in February of 2001. As a result of this meeting, a number of agreements between the NRC and DOE were formally adopted (Reamer and Williams 2001 [DIRS 154348]), outlining the plan for resolution of the technical issues. The agreement items addressed in this report are presented verbatim as follows:

- RDTME 3.04–Provide in the Design Parameter Analysis Report (or some other document) site-specific properties of the host rock, as a minimum those included in the NRC handout, together with the spatial and temporal variations and uncertainties in such properties, as an update to the information contained in the March 1997 Yucca Mountain Site Geotechnical Report. The DOE will: (1) evaluate the adequacy of the currently available measured and derived data to support the potential repository licensing case and identify areas where available data may warrant additional field measurements or testing to reduce uncertainty. DOE will provide a design parameters analysis report (or other document) that will include the results of these evaluations, expected to be available to NRC in FY 2002; and (2) acquire data and/or perform additional analyses as necessary to respond to the needs identified in 1 above. The DOE will provide these results prior to any potential license application.

- RDTME 3.05–Provide the Rock Mass Classification Analysis (or some other document) including the technical basis for accounting for the effects of lithophysae. The DOE will provide a rock mass classification analysis (or other document), including the technical basis for accounting for the effects of lithophysae, expected to be available to NRC in FY 2002.

- RDTME 3.07– The DOE should account for the effect of sustained loading on intact rock strength or provide justification for not accounting for it. The DOE will assess the effects of sustained loading on intact rock strength. The DOE will provide the results of this assessment in a design parameters analysis report (or other document), expected to be available to NRC in FY 2002.

- RDTME 3.10–Provide technical basis for the assessment that two-dimensional modeling for emplacement drifts is considered to be adequate, considering the fact that neither the in-situ stress field nor the principle fracture orientation are parallel or perpendicular to emplacement drift orientation. The DOE will provide the technical bases for the modeling methods used in ground control analysis in a revision to the Ground Control for Emplacement Drifts for site recommendation, ANL-EBS-GE-000002 (or other document) supporting any potential license application. This is expected to be available to NRC in FY 2003.

- RDTME 3.15–Provide field data and analysis of rock bridges between rock joints that are treated as cohesion in DRKBA modeling together with a technical basis for how a reduction in cohesion adequately accounts for thermal effects. The DOE will provide clarification of the approach and technical basis for how reduction in cohesion adequately accounts for thermal effects, including any additional applicable supporting data and analyses. Additionally, the adequacy of the cohesion reduction approach will be verified according to the approach described in Subissue 3, Agreement 22 [RDTME 3.19], of the Repository Design and Thermal-Mechanical Effects Technical Exchange. This will be documented in a revision to the Drift Degradation Analysis, ANL-EBS-MD-000027, expected to be available to NRC in FY 2003.

- RDTME 3.16–Provide a technical basis for the DOE position that the method used to model joint planes as circular discs does not under-represent the smaller trace-length fractures. The DOE will analyze the available small trace-length fracture data from the Exploratory Studies Facility and Enhanced Characterization of the Repository Block, including their effect on block development. This will be documented in a revision to the Drift Degradation Analysis, ANL-EBS-MD-000027, expected to be available to NRC in FY 2003.

- RDTME 3.17–Provide the technical basis for effective maximum rock size including consideration of the effect of variation of the joint dip angle. The DOE will provide the technical basis for effective maximum rock size including consideration of the effect of variation of the joint dip angle. This will be documented in revisions to the Drift Degradation Analysis, ANL-EBS-MD-000027, and the Rockfall on Drip Shield, CAL-EBS-ME-000001, expected to be available to NRC in FY 2003.

- RDTME 3.19–The acceptability of the process models that determine whether rockfall can be screened out from performance assessment abstractions needs to be substantiated by the DOE by doing the following: (1) provide revised DRKBA analyses using appropriate range of strength properties for rock joints from the Design Analysis Parameters Report, accounting for their long-term degradation; (2) provide an analysis of block sizes based on the full distribution of joint trace length data from the Fracture Geometry Analysis Report for the Stratigraphic Units of the Repository Host Horizon, including small joints trace lengths; (3) verify the results of the revised DRKBA analyses using: (a) appropriate boundary conditions for thermal and seismic loading; (b) critical fracture patterns from the DRKBA Monte Carlo simulations (at least two patterns for each rock unit); (c) thermal and mechanical properties for rock blocks and joints from the Design Analysis Parameters Report; (d) long-term degradation of rock block and joint strength parameters; and (e) site-specific ground motion time histories appropriate for post-closure period; provide a detailed documentation of the analyses results; and (4) in view of the uncertainties related to the rockfall analyses and the importance of the outcome of the analyses to the performance of the repository, evaluate the impacts of rockfall in performance assessment calculations. DOE believes that the Drift Degradation Analysis is consistent with current understanding of the Yucca Mountain site and the level of detail of the design to date. As understanding of the site and the design evolve, DOE will: (1) provide revised DRKBA analyses using appropriate range of strength properties for rock joints from a design parameters analysis

report (or other document), accounting for their long-term degradation; (2) provide an analysis of block sizes based on the full distribution of joint trace length data from the Fracture Geometry Analysis for the Stratigraphic Units of the Repository Host Horizon, ANL-EBS-GE-000006, supplemented by available small joint trace length data; (3) verify the results of the revised DRKBA analyses using: (a) appropriate boundary conditions for thermal and seismic loading; (b) critical fracture patterns from the DRKBA Monte Carlo simulations (at least two patterns for each rock unit); (c) thermal and mechanical properties for rock blocks and joints from a design parameters analysis report (or other document); (d) long-term degradation of joint strength parameters; and (e) site-specific ground motion time histories appropriate for post-closure period. This will be documented in a revision to the Drift Degradation Analysis, ANL-EBS-MD-000027, expected to be available to NRC in FY 2003. Based on the results of the analyses above and subsequent drip shield calculation revisions, DOE will reconsider the screening decision for inclusion or exclusion of rockfall in performance assessment analysis. Any changes to screening decisions will be documented in analyses prior to any potential license application

The contribution toward fulfillment of these agreement items provided by this model report is identified in Table 6-53.

Table 6-53. Repository Design and Thermal-Mechanical Effects KTI Agreement Items Addressed in This Model Report

Agreement Item	Approach and Section Reference	Status of Agreement
RDTME 3.04	Geotechnical data to support the drift degradation analyses documented in this report are identified in Section 4, Section 7, and Appendix E. Discussions of data adequacy are provided throughout Sections 6, 7, and 8. Newly acquired data from lithophysal rocks have been used to develop the lithophysal rockfall model, including data from laboratory compression testing on large-diameter cores. Note that the primary document addressing this agreement item is *Subsurface Geotechnical Parameters Report* (BSC 2003 [DIRS 166660]).	The data and information provided in this model report contributes to the closure of this agreement.
RDTME 3.05	The technical basis for accounting for the effects of lithophysae is presented in Section 6.4. The validity of this approach is discussed in Sections 7.3 and 7.4. Note that the primary document addressing this agreement item is *Subsurface Geotechnical Parameters Report* (BSC 2003 [DIRS 166660]).	The data and information provided in this model report contributes to the closure of this agreement.
RDTME 3.07	The technical basis for accounting for the effects of time-dependent degradation is presented in Sections 6.3.1.5, 6.4.2.4, and Appendix S.	The data and information provided in this model report are intended to fully address the requirements of this agreement.
RDTME 3.10	The assessment of an appropriate approach to model the rock mass is a function of the specific repository host rock type: lithophysal or nonlithophysal rock (Section 7.1). For nonlithophysal rock, jointing controls the mechanical response, which is generally anisotropic in nature. Therefore, two-dimensional modeling of nonlithophysal rock is not realistic for rockfall modeling, and a three-dimensional modeling approach must be used. Conversely, lithophysal rock is characterized by the presence of more-or-less uniformly distributed voids (lithophysae) of varying size. Additionally, in the Tptpll, short trace length interlithophysae fracturing exists. Under these conditions, the representation of lithophysal rock as a homogeneous, isotropic rock mass is appropriate. Therefore, in models of drift stability, the use of a two-dimensional model in the plane perpendicular to the axis is adequate.	The data and information provided in this model report are intended to fully address the requirements of this agreement.
RDTME 3.15	Additional clarification of the approach and technical basis for how reduction in cohesion adequately accounts for thermal effects in the DRKBA analyses is provided in Appendix D. However, the DRKBA analyses now provide a confirmatory role in the assessment of drift degradation. The drift degradation analyses are primarily conducted using UDEC and 3DEC, in which thermal loads have been explicitly modeled (Sections 6.3 and 6.4). The adequacy of the methods to account for thermal effects on drift degradation is validated in Section 7.8.	The data and information provided in this model report are intended to fully address the requirements of this agreement.
RDTME 3.16	The available small trace-length fracture data have been analyzed and included in this report, documenting their effect on block development (Section 6.3.3).	The data and information provided in this model report are intended to fully address the requirements of this agreement.

Table 6-53. Repository Design and Thermal-Mechanical Effects KTI Agreement Items Addressed in This Model Report (Continued)

Agreement Item	Approach and Section Reference	Status of Agreement
RDTME 3.17	The approach for determining the effective maximum rock size has been revised in this model report. The approach of varying the joint geometry input to UNWEDGE is no longer applied. The maximum rock size and shape is taken directly from the 3DEC output, which includes the variation in joint strike, dip, spacing, and persistence. The variation of joint geometry parameters is based on field mapping data from the ESF, which has been input into the rockfall model (Sections 6.1.6 and 6.3).	The data and information provided in this model report are intended to fully address the requirements of this agreement.
RDTME 3.19	(1) In this revision of this model report, the DRKBA analyses provide a confirmatory role in the assessment of drift degradation. The primary analysis for degradation of nonlithophysal rock is provided using 3DEC (Section 6.3), while lithophysal rock is analyzed using UDEC (Section 6.4). An appropriate range of joint strength properties has been applied as documented in Section 6.3.1.6. Long-term degradation has been accounted for as documented in Section 6.3.1.5. (2) An analysis of block sizes based on the full distribution of joint trace length data has been included in this report (Sections 6.1.4 and 6.1.6), including the available small joint trace length data (Section 6.3.3). (3) As indicated above, the DRKBA results now provide a confirmatory role in the assessment of drift degradation. 3DEC has replaced DRKBA as the primary code for analyzing structural block development in the nonlithophysal rock units. The 3DEC and DRKBA results are in good agreement (Section 7.7.5). (a) Appropriate boundary conditions for thermal and seismic loading have been included in 3DEC as documented in Section 6.3.1.1. (b) A total of 50 fracture patterns have been analyzed, which were drawn from the same fracture population used in the DRKBA analyses (Section 6.3.1.1). (c) Thermal and mechanical properties for rock blocks and joints are available in the Technical Data Management System as documented in Section 4.1. (d) Long-term degradation of joint strength has been included as documented in Section 6.3.1.5. (e) Site-specific ground motion time histories appropriate for postclosure period have been modeled as documented in Sections 6.3.1.2 and 6.4.2.2.	The data and information provided in this model report are intended to fully address the requirements of this agreement.

INTENTIONALLY LEFT BLANK

7. VALIDATION

7.1 INTRODUCTION

This section contains a discussion of the activities that were conducted to validate the mechanical material models and their implementation within qualified discontinuum numerical programs for mechanical representation of the repository host rocks. It is noted that the term "model" here refers first to the development and validation of the mechanical material models or representations for the two specific repository host rock types: lithophysal and nonlithophysal rocks. Secondly, validation refers to the examination of the implementation of these material models in a general numerical modeling scheme. In the case of the lithophysal rock, it is necessary to first discuss the existing laboratory database as a precursor to discussion of the implementation of this data in a numerical scheme. Validation of this implementation is addressed through comparison examples of the models to field and laboratory data.

Corroborating/supporting data, models, and information that are used to complete the model validation activities include the following:

- Confidence Building During Model Development to Establish Scientific Basis and Accuracy for Intended Use (Section 7.2.1)
  - Cundall and Strack 1979 [DIRS 162194]
  - Itasca Consulting Group 2002 [DIRS 160331]
  - Konietzky 2003 [DIRS 162198]

- Confidence Building During Development of a Mechanical Material Model for Lithophysal Rocks and Selection of Input Parameters (Sections 7.3 and 7.4)
  - Hoek 2000 [DIRS 160705]
  - Itasca Consulting Group 2002 [DIRS 160331]
  - Potyondy and Cundall 2001 [DIRS 156895]
  - Price et al. 1985 [DIRS 106602]

- Confidence Building During PFC Model Development (Section 7.5.1)
  - Itasca Consulting Group 2002 [DIRS 160331]
  - Price 1986 [DIRS 106589]
  - Price et al. 1985 [DIRS 106602]

- Post-Development Validation for the PFC Model (Section 7.5.2)
  - Potyondy 2003 [DIRS 165550]
  - Potyondy and Cundall 2001 [DIRS 156895]

- Confidence Building During Development of the Lithophysal Rockfall Model (Sections 7.6.1 and 7.6.4)
  - Itasca Consulting Group 2002 [DIRS 160331]

- Post-Development Validation for Lithophysal Rock (Section 7.6.5)
  - Hoek 2000 [DIRS 160705]
  - MO0001SEPDSTPC.000 [DIRS 153836]
  - MO0002ABBLSLDS.000 [DIRS 147304]
  - MO0007SEPDSTPC.001 [DIRS 153707]
  - MO0107SEPDSTPC.003 [DIRS 158321]
  - MO0202SEPDSTTV.001 [DIRS 158320]
  - MO9807DSTSET01.000 [DIRS 113644]
  - MO9906DSTSET03.000 [DIRS 113673]
  - Price 1986 [DIRS 106589]
  - Price et al. 1985 [DIRS 106602]
  - Senseny 1993 [DIRS 162017]
  - Williams 2001 [DIRS 159516]

- Post-Development Validation for Nonlithophysal Rock (Section 7.7)
  - Itasca Consulting Group 2002 [DIRS 160331]
  - GS030283114222.001 [DIRS 161913]
  - Senseny and Pucik 1999 [DIRS 168479]

The scope of the validation and the order of presentation are as follows:

- **Lithophysal rocks**

  - Mechanical Material Behavior–A discussion of the mechanical behavior of the lithophysal rocks is presented as the basis for development of the mechanical material model. The properties of this rock are controlled by the degree of lithophysal porosity as well as the interlithophysal fracturing. The lithophysae vary in size, shape, and in porosity vertically within the flow, but are distributed relatively uniformly locally within each unit. Since the diameter of the lithophysae are generally much less than the tunnel diameter, and, further, because they are uniformly distributed, a two-dimensional, isotropic equivalent mechanical material model can be used to describe their response to gravitational, thermal, and seismic loading. The mechanical material properties of the upper (Tptpul) and lower (Tptpll) lithophysal units of the Topopah Spring formation have been determined from laboratory compression testing on large (11.5-in and 10.5-in diameter) cores, and from in situ flatjack (slot) compression testing in the ESF main loop and ECRB Cross-Drift.

  - Particle Flow Model of Rock Mass Behavior–The purpose of the PFC program is primarily as a simulation tool for developing a detailed understanding of the effects of lithophysal porosity on rock mass behavior. The program is used to supplement limited field testing by providing a means for examining the effects of lithophysae variability on rock mass properties (i.e., as a supplement to laboratory and field testing). A mechanical material model for representing the elasticity and yield of these rocks is developed from the basic laboratory data using a "micromechanical" numerical model (i.e., PFC). The PFC model predictions are compared to laboratory measured rock properties as a means of validation. The drift degradation analyses

include time-dependent rock mass behavior modeled using the PFC model that incorporates a stress corrosion cracking representation. The PFC stress corrosion modeling approach provides a representation of subcritical crack growth in rocks that embraces both the microscopic processes of reactions and thermal activation at crack tips and the more mesoscopic processes of microcrack-microstructure-macrocrack interaction.

– Lithophysal Rockfall Mechanical Model Component Validation–Although the PFC program could theoretically be used to model tunnel-scale stability issues, the simulation times are too long for existing computer resources. Therefore, it is necessary to develop a simpler, engineering-based approach to represent the potential yielding and fracturing behavior of lithophysal rock. This is done by creating an equivalent lithophysal mechanical model, which is implemented in the UDEC discontinuum program. The equivalent model is first calibrated such that it reproduces the basic laboratory mechanical response (as well as the PFC model response). Post-development model validation is accomplished via comparison to laboratory data, field observation of ECRB Cross-Drift tunnel mechanical response, and field thermal testing and brittle yield observed in the Drift Scale Thermal Test in the ESF. A continuum approach using different constitutive models is included to validate the UDEC Voronoi block model of lithophysal rock. Additionally, a comparison of the mathematical model implemented in the UDEC program to a number of other dynamic jointed rock models for modeling of blast-related, lined tunnel stability conducted for the Defense Nuclear Agency is also given as a confidence-building exercise. These blasting simulations provide a difficult challenge for the models. The UDEC code itself is commercial software that is widely used internationally for design and research in rock engineering. The program has been extensively validated against analytic solutions and design problems that are documented in the User's Manual (Itasca Consulting Group 2002 [DIRS 160331]). This validation provides a comparison of UDEC to several discontinuum and continuum-based programs for solution of tunnels subjected to dynamic loading.

- **Nonlithophysal rocks**

  – Nonlithophysal Rockfall Model Validation–The 3DEC discontinuum program is used to model the mechanical response of the fracture-rock block system in three dimensions. Fracture mechanical property data, in the form of shear strength and stiffness properties, are derived from rotary and direct shear test measurements as well as empirical correlations derived from underground mapping. Validation of the ability of the nonlithophysal rockfall model implemented in the 3DEC program to represent this direct shear response for fractures as derived from laboratory direct shear testing of large cores is presented. Validation of the dynamic stability of a jointed rock mass through comparison of 3DEC to instrumented field tests is also provided. Specific, well-documented field examples of tunnels subjected to earthquake loading that would be suitable as validation examples were not identified. Therefore, the validation of the mathematical model for nonlithophysal rock implemented in the 3DEC program is performed through corroboration with an alternative numerical model (i.e., the key-block software, DRKBA) to validate the

model results on block size distribution and rockfall frequency, and through use of an external technical review to validate the overall modeling approach. The 3DEC code itself is commercial software that has been used in international rock engineering practice for nearly 20 years.

7.2 MODEL VALIDATION LEVEL AND CRITERIA FOR VALIDATION BASED ON INTENDED USE

The drift degradation analysis provides input to the *Seismic Consequence Abstraction* which, in turn, supplies input to the Seismic Scenario Class in the TSPA. The input to the *Seismic Consequence Abstraction* falls into two general areas:

1. Rockfall – Damage to emplacement drifts as a function of peak ground velocity. The damage takes the form dynamic impact of rock blocks to the drip shield, and static load of the accumulated rubble on the drip shield following partial or complete collapse of the drift.

2. Drift Profile Change – Breakout and enlargement of the emplacement drifts as a function of peak ground velocity for lithophysal and nonlithophysal units.

Rockfall masses, velocities and drip shield impact locations, output from the drift degradation analyses, are used for structural stability and damage estimates of the drip shield. The *Seismic Consequence Abstraction* conservatively assumes that complete collapse of drifts in the lithophysal rocks occurs coincident with the 1×10^{-4} (approximate PGV of 0.5 m/sec) event. Static load from accumulated rubble was determined for the assumption of complete collapse of the emplacement drifts. The load distributions at 30 elements around the drip shield from six different complete collapse simulations (using the UDEC program) are used as input to structural analysis of the drip shield.

The drift profile changes estimated from collapse of the drifts are used in the *Abstraction of Drift Seepage* to estimate changes in seepage flux to emplacement drifts in the event of a seismic event. Again, since complete collapse is assumed for the 1×10^{-4} level, then drift profile changes to two times the original diameter.

Based on the intended use described above, the *Technical Work Plan for: Regulatory Integration Modeling of Drift Degradation, Waste Package and Drip Shield Vibratory Motion and Seismic Consequences* (BSC 2004 [DIRS 171520], Section 2.2.1) requires Level III Validation.

7.2.1 Confidence Building During Model Development to Establish Scientific Basis and Accuracy for Intended Use

Section 2.2.1.4 of the *Technical Work Plan for: Regulatory Integration Modeling of Drift Degradation, Waste Package and Drip Shield Vibratory Motion and Seismic Consequences* (BSC 2004 [DIRS 171520], Section 2.2.2) specifies criteria for *confidence building during model development*. Additionally, the development of the model should be documented in accordance with the requirements of Section 5.3.2(b) of AP-SIII.10Q. The development of the drift degradation models for lithophysal and nonlithophysal rock types have been conducted according to these criteria, as follows:

1. *Selection of input parameters and/or input data, and a discussion of how the selection process builds confidence in the model. [AP-SIII.10 Q 5.3.2(b) (1) and AP-2.27Q Attachment 3 Level I (a)]*

   The types and quality of the data selected as input builds confidence in the model. The geotechnical parameters and information that are inputs to the drift degradation analyses are site specific and have been collected by either field mapping or laboratory testing. The site specific geotechnical information includes:

   a. Fracture geometry
   b. Fracture mechanical properties
   c. Intact rock physical and mechanical properties
   d. Rock mass mechanical properties
   e. Seismic ground motion
   f. Rock thermal properties
   g. Repository layout information.

   Section 4.1 provides a discussion of the inputs and Table 4-1 identifies the data and design parameters used. A detailed discussion of the mineralogy, texture, fracturing, and porosity are given in Section 6.1.4 and in Appendix O. Further justification for the bases of selection of input parameters for the mechanical model for lithophysal rocks is covered in Section 7.3.2. Discussions of parameter ranges and uncertainties are covered in Section 6.5. Model assumptions have been described in Section 5. Thus, this requirement can be considered satisfied.

2. *Description of calibration activities, and/or initial boundary condition runs, and/or run convergences, simulation conditions set up to span the range of intended use and avoid inconsistent outputs, and a discussion of how the activity or activities build confidence in the model. Inclusion of a discussion of impacts of any non-convergence runs. [(AP-SIII.10Q 5.3.2(b)(2) and AP-2.27Q Attachment 3 Level I (e)]*

   A general discussion of the overall model domain, rock mass characteristics, and generation of representative rock volumes are described in Section 6.1. Additional discussions are provided in section 7.4, 7.5, 7.6, and 7.7. The set-up of the thermal-mechanical simulations is described in Section 6.2 and Appendix C. The set-up of the three-dimensional simulations of drift degradation in the nonlithophysal units is described in Section 6.3 and Appendix C. The set-up of the simulations for drift degradation in the lithophysal units is discussed in Section 6.4. Calibration activities for the models are described in Sections 7.5.1 and 7.6.4. The input and output files for the simulations (all simulations completed and therefore converged) are listed in Appendix A. The simulation conditions accounted for the rock types encountered at the repository horizon (lithophysal and nonlithophysal units), account for the effects of thermal-mechanical coupling, and addressed the seismic loading using site-specific ground motions for the preclosure and postclosure periods. Therefore, the drift degradation analyses have addressed the conditions that span the range of its intended use. This requirement can be considered satisfied.

3. *Discussion of the impacts of uncertainties to the model results including how the model results represent the range of possible outcomes consistent with important uncertainties. [(AP-SIII.10 Q 5.3.2(b)(3) and AP-2.27Q Attachment 3 Level 1 (d) and (f)].*

   Treatment of uncertainty is discussed in Section 6.5. Uncertainties associated with model inputs are listed in the order of their impact on model results as follows:

   a. Rock mass mechanical properties data
   b. Seismic ground motion data
   c. Static fatigue and long-term strength data
   d. Fracture geometry data
   e. Intact rock physical and mechanical properties data
   f. Fracture mechanical properties data
   g. Rock thermal properties data

   Sensitivity studies that represent the range of possible outcomes of these parameters can be found in Sections 6.3.1 and Sections 6.4.2. An evaluation of alternative conceptual models can be found in Section 6.7. These criteria can be considered satisfied.

4. *Formulation of defensible assumptions and simplifications. [AP-2.27Q Attachment 3 Level I (b)].*

   Discussions of assumptions are provided in Section 5. Simplifications required for the set-up of the three-dimensional analyses of the nonlithophysal units are discussed in Section 6.3.1. Discussions of the simplifications necessary for the two-dimensional analyses of lithophysal units are provided in Sections 6.4.1 and 7.6.2.

5. *Consistency with physical principles, such as conservation of mass, energy, and momentum. [AP-2.27Q Attachment 3 Level I (c)]*

   Consistency with physical principles, such as conservation of mass, energy, and momentum is maintained through the selection and use of the appropriate geotechnical codes identified in Section 3. The numerical models discussed are commercially available software codes that have been extensively and rigorously tested. The programs have extensive User's Manuals that provide detailed derivation of the implementation of the governing equations, the mathematical description of the constitutive models, and verification of the accuracy and limitations of the programs through comparison of results to analytical solutions and example problems. These derivations and verification of ability to satisfy equilibrium and energy conservation are provided in the software User's Manual (Itasca Consulting Group 2002 [DIRS 160331]). Additional discussion can also be found in Section 7.6.7.2 regarding the use of UDEC and accounting for thermally induced expansion and stresses.

   The UDEC and 3DEC programs have been commercially marketed for approximately 20 years, and are used extensively in the civil construction, mining, waste disposal, and geotechnical industries. The UDEC program, originally developed under contract to the U.S. Army Corps of Engineers' Waterways Experiment Station in the mid-1970s, was initially used as a publicly available research tool in geomechanics. The predecessor of

UDEC, the Rigid Block Model, was developed in the early 1970's (Itasca Consulting Group 2002 [DIRS 160331]). Both UDEC and 3DEC have been used for design studies and analysis of field experiments on nuclear waste repository projects in the United States, Canada, Sweden, United Kingdom, France, and Finland. The PFC program has been available commercially for approximately eight years, although its initial development as a program for research in soil and granular materials mechanics dates to the late 1970's (Cundall and Strack 1979 [DIRS 162194]). Currently, PFC is being used extensively as a research and design tool in geomechanics, powder compaction, structural geology and tectonics, oil production, etc. A recent symposium dedicated to use of PFC (Konietzky 2003 [DIRS 162198]) provides a description of the extent of application of this approach.

7.2.2 Confidence Building After Model Development to Support the Scientific Basis of the Model

Post-development model validation is to be performed using two or more methods as described in Section 5.3.2c of AP-SIII.10Q, *Models*, consistent with Level III model validation expectations. Validation of drift degradation models is accomplished by the following methods:

- Corroboration with laboratory measurements or relevant observations not previously used to develop or calibrate the model
- Corroboration with results of alternative mathematical models developed independently
- Corroboration with data published in refereed journals or literature
- Technical review by reviewers independent of the development, checking, and interdisciplinary review of the model documentation.

The model validation activities discussed in this report follow the Level III validation requirements given in AP-SIII.10Q, at a minimum, while exceeding these requirements in some instances. No further activities are needed to complete this model validation for its intended use.

7.2.3 Validation Criteria

The prediction of rockfall requires that the models be able to represent:

- The geologic structure that creates rock blocks surrounding the tunnels needs to be developed from field geologic mapping and represented in a realistic fashion in the numerical rockfall model.
- The rock mass transient stresses induced by heating or ground motions
- The interaction of the stresses and geologic structure, including, in the lithophysal rock, the potential for intact rock mass failure, fracturing, and formation of rock blocks that can detach themselves from the surrounding rock mass.

With these points in mind, the criteria for a Level III validation of the drift degradation models, which address both adequacy of the scientific basis and accuracy of the model, are as follows:

For mechanical models of nonlithophysal rock:

- The geometry and variability of geologic structure need to be represented in the rockfall (3DEC) model in a qualitatively reasonable fashion. The "synthetic" fracture geometries and their variability developed by FracMan and used as input to 3DEC needs to be quantitatively calibrated against field-measured geometry data from detailed line surveys and full periphery geologic maps. This calibration, presented in Section 6.1.6 ensures that the resulting block geometries will reflect in situ block structure.

- The mechanical constitutive model of the fractures in 3DEC needs to be validated against the laboratory direct shear testing data.

- The ability of the numerical model to accurately represent seismic boundary conditions and wave transmission through the rock mass needs to be verified.

- The overall ability of the model to adequately represent the dynamic stressing effects of the ground motion on tunnel stability needs to be validated.

For mechanical models of lithophysal rock:

- The material model and analyses must account for the variability of rock mass properties resulting from variability of porosity in the lithophysal rock.

- The material model and its numerical implementation must provide the ability to represent, in a realistic fashion, the yielding response of lithophysal rock in laboratory specimens and around tunnels, and the associated fracturing into blocks that can detach themselves from the surrounding rock.

- The model must account for dynamic boundary conditions properly, and the subsequent interaction of dynamic stresses with rock mass yielding.

7.3 DEVELOPMENT OF A MECHANICAL MATERIAL MODEL FOR LITHOPHYSAL ROCKS AND SELECTION OF INPUT PARAMETERS

7.3.1 Introduction

Prior to presentation of validation exercises for the lithophysal rockfall model, a description of the development of the model is given. This is done so that the basic considerations inherent in the model development that impact validation methods can be understood.

7.3.2 Description of the Lithophysal Rocks

The Tptpul and Tptpll comprise roughly 85 percent of the repository emplacement area. A detailed description of the mineralogy, texture, fracturing, and porosity are given in Section 6.1.4 and in Appendix O. A review of the aspects of the geology important to the mechanical behavior

is provided in this section. From a mechanical standpoint, the lithophysal rocks are composed of two distinct components: the matrix groundmass (including fracturing) and the porosity. The matrix groundmass is mineralogically, similar to the matrix of the nonlithophysal rocks. The primary difference in the groundmass of the Tptpll and Tptpul is in the type and extent of fractures. The Tptpll is intensely fractured with short-length, rough, and interlocking inter-lithophysal fractures which have a predominant vertical orientation with spacing on the order of centimeters. Figure 7-1a is a photograph of a 12-in. diameter core sample removed from the Tptpll showing the intensely fractured nature of this unit, creating intact block sizes a centimeters on a side. The rough and interlocking nature of the fractures is an important feature in that the periphery of excavations are stable under in situ conditions without failure along fracture boundaries. This is contrasted by Figure 7-1b showing the wall of an alcove in the Tptpul, off the ECRB Cross-Drift, showing the typical unfractured matrix groundmass in this unit.

The rock mass porosity in the lithophysal units has been shown to be the primary physical factor that governs elastic and strength properties (Price et al. 1985 [DIRS 106602]). The porosity is found in three basic components: the matrix grain to grain porosity, which averages around 10 percent in the Topopah Spring sub-units (Price et al. 1985 [DIRS 106602]); the lithophysal void porosity; and the porosity of alteration, which includes lithophysal rims and spots. Figure 7-2 shows the variation in lithophysal cavity percentage within the Tptpll in the ECRB Cross-Drift as determined by direct tape and angular measurement (Appendix O). This plot shows that the lithophysal cavity porosity varies from approximately 10 to 30 percent with variability on a scale of 5 to 10 m.

The lithophysal cavities vary in size and shape, with characteristics that are somewhat different in the Tptpul and Tptpll.

The lithophysae in the Tptpul:

- Tend to be smaller (roughly 1 to 10 cm in diameter)
- Are more uniform in size and distribution within the unit
- Vary in infilling and rim thicknesses
- Have a volume percentage that varies consistently with stratigraphic position
- Are stratigraphically predictable.

In contrast, the lithophysae in the Tptpll:

- Tend to be highly variable in size, from roughly 1 cm to 1.8 m in size
- Have shapes that are highly variable from smooth and spherical to irregular and sharp boundaries
- Have infilling and rim thickness that vary widely with vertical and horizontal spacing
- Have volume percentages that vary consistently with stratigraphic position
- Are stratigraphically predictable.

a)

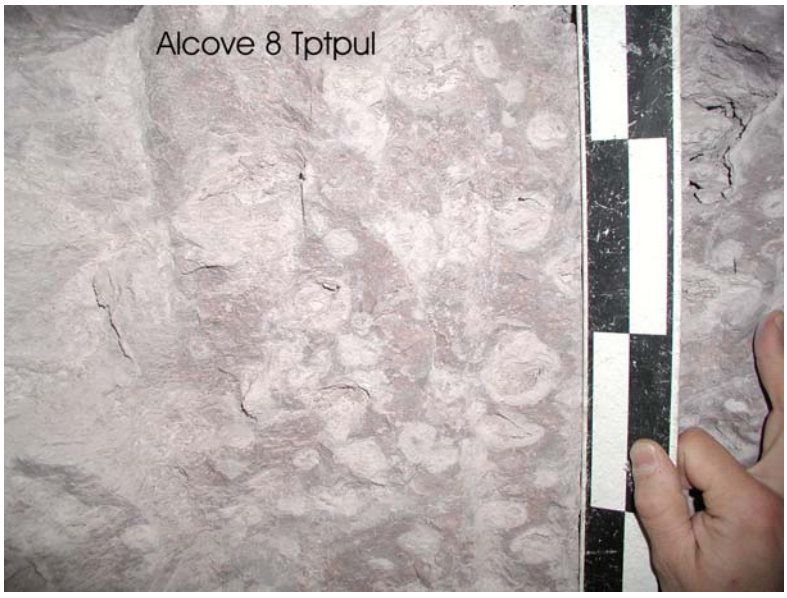

b)

NOTE: The core (top photo) was drilled with water and the porous rims and fractures (many of which have rims) retain water and appear dark, whereas the matrix-groundmass, which has minimal porosity, dries in a relatively short amount of time.

Figure 7-1. (a) Matrix Fracturing in the Tptpll in 12-in-Diameter Core and (b) Lack of Fracturing in Matrix of Tptpul as Seen in the Wall of Alcove 8 off the ECRB Cross-Drift

In general, the lithophysae diameter is much less than the diameter of the emplacement drifts (5.5 m). As shown in Figure 7-2, the variability of the porosity along the ECRB Cross-Drift is on the order of 5 m (additional data analysis is provided in Appendix O). In representing the mechanical response of the lithophysal rocks, it is judged to be adequate to use a two dimensional, cross-sectional modeling approach in which the rock mass is considered to be of constant porosity, homogeneous and isotropic within that section.

7.3.3 Model Requirements for Drift Degradation Prediction

To represent drift degradation mechanisms and rockfall, the mechanical model and the numerical method in which it is embedded must have the following capabilities:

- The model must provide a general capability of modeling in situ stress and thermal and seismic loading of the rock mass.
- The model must represent the effects of porosity and matrix pre-existing fracturing on the elastic and strength properties of the material.

The model must allow internal fracturing and detachment of the rock mass (i.e., rockfall) to occur in response to gravity, thermal effects, and seismic shaking.

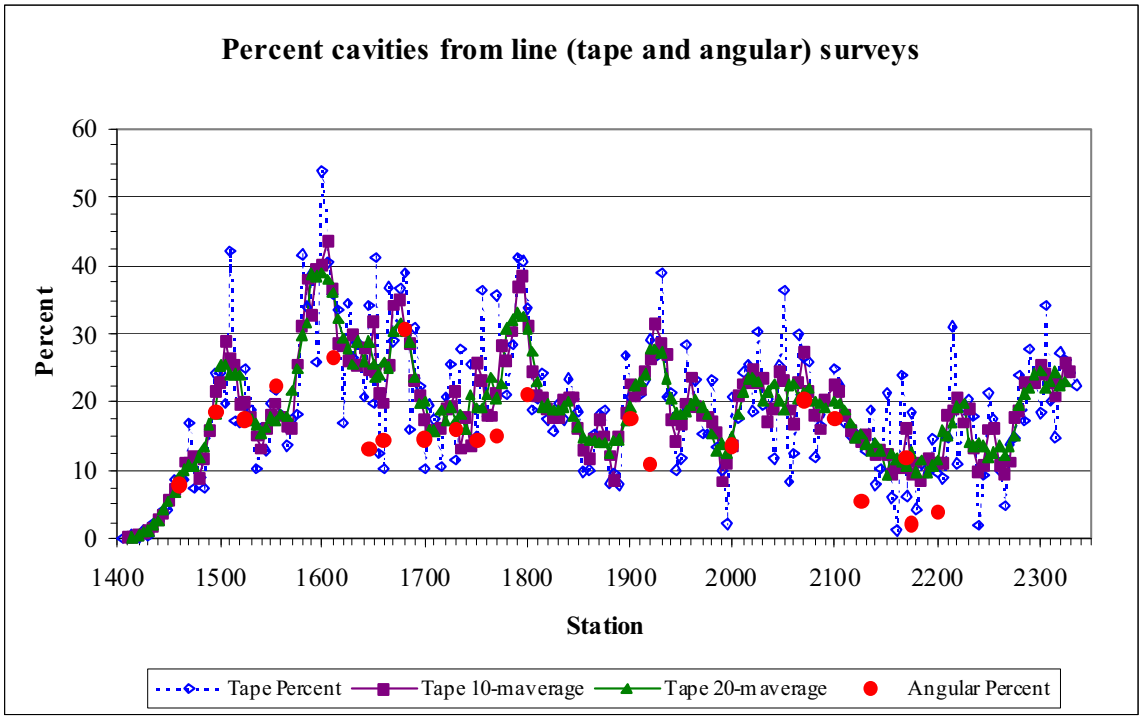

Source: Tape percent and Angular percent from DTN: GS021008314224.002 [DIRS 161910]; Tape 10-m average and Tape 20-m average from DTN: MO0408MWDDDMIO.002, file *Drift Deg AMR AC T-Trav.xls*.

Figure 7-2. Variation in Lithophysal Cavities in the Tptpll in the ECRB Cross-Drift from Top (Left) to Bottom of the Sub-Unit as Estimated by Tape and Angular Measurement Collected at 5-m Intervals

The above model requirements imply the necessity of use of a discontinuum approach to representation of the rock mass, as described in Sections 6.3.1 and 6.4.2.

7.3.4 Laboratory and Field Database for Constitutive Model Development

The development of the laboratory and field database of material properties for lithophysal rocks is presented in detail in Appendix E, Section E.4. This section describes large core laboratory testing program that has been used to define the relationship of compressive strength and Young's modulus to lithophysal porosity content. The use of the PFC model (described later) to extrapolate the impact of lithophysae size, shape and distribution on the mechanical properties is also presented, and the proposed bounding ranges determined. The rock mass mechanical properties ranges are subdivided into five equally divided categories for subsequent sensitivity studies as described in Section 6.4. These properties provide the basis for the model development described in Section 7.4.

7.4 STRATEGY FOR DEVELOPMENT OF A MECHANICAL MATERIAL MODEL FOR LITHOPHYSAL ROCKS (CONFIDENCE BUILDING DURING MODEL DEVELOPMENT)

7.4.1 Continuum-Based Approach to Representing Rock Masses

The objective of the drift degradation analyses presented in this report is to predict the amount and particle size distribution of rockfall in the repository drifts due to stresses induced by the heat released by the emplaced waste, due to seismically related ground motions, and due to time-dependent strength loss of the rock mass. A standard approach for solving excavation stability problems in geotechnical engineering is the use of numerical models based on continuum mechanics (Figure 7-3). This alternative conceptual model is discussed in Section 6.7. Such an approach is quite effective if the rock mass, in response to stressing, eventually arrives at a state of mechanical stability and where the primary purpose of the modeling is the computation of stress redistribution around an opening or determination of the final displacement profiles. However, difficulties are encountered if a continuum model is used for prediction of a mechanical system (i.e., a tunnel) that does not arrive at stable condition. Continuum models use constitutive relations to describe the mechanical behavior of a material. In rock, the mechanical effects of fractures and other features are "lumped" into the constitutive model, often using empirically based methods that take into account the spacing and continuity of the fractures, the roughness and alteration of the fracture surfaces, and the laboratory-determined properties of the intact rock blocks (e.g., Hoek 2000 [DIRS 160705]).

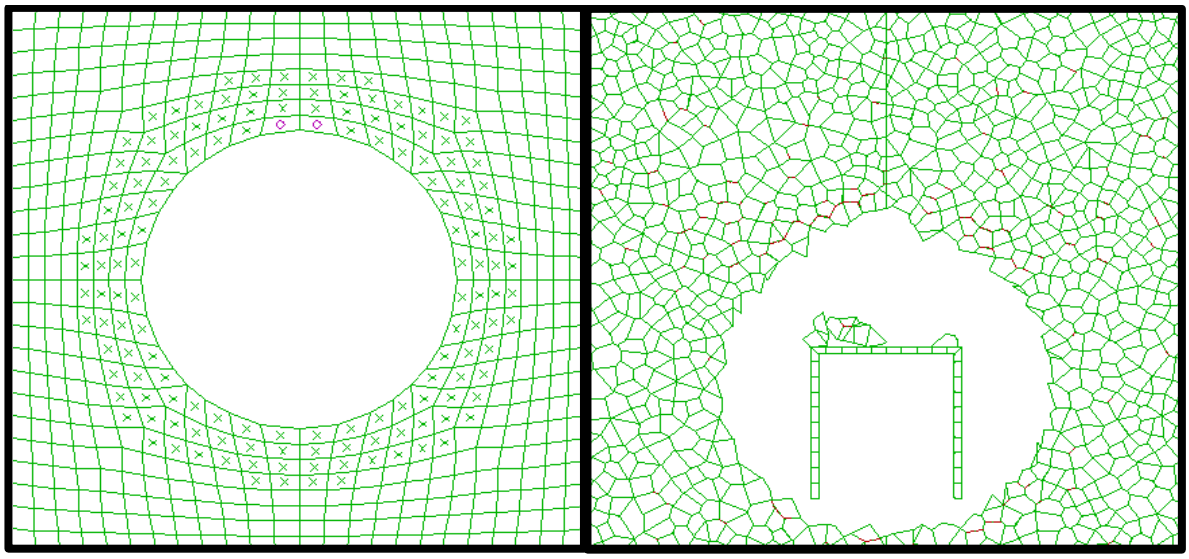

NOTE: The continuum approach models yield of the rock through use of a material model that enforces plasticity relations (note marked elements). Rock breakage and separation is not possible in this approach. The discontinuum approach also represents the rock mass using similar material models, but provides the capability for the rock mass to fracture and break apart on potential fracture surfaces.

Figure 7-3. Schematic Illustration of Continuum (Left) and Discontinuum (Right) Approaches to Modeling Drift Stability

A linearly elastic–perfectly plastic material model with Mohr-Coulomb yield criteria is a constitutive model often used to represent mechanical behavior of a rock mass. Because the material strength of a perfectly plastic, Mohr-Coulomb model does not decrease as a function of plastic deformation, this model will show indications of material yielding (i.e., plastic deformation) in different portions of the model, but will never actually predict the instability or rockfall. To be able to predict rockfall, it is necessary to use some kind of strain-softening constitutive model, in which strength degrades as a function of deformation after the peak-strength of material has been reached. However, the strain-softening model, within the framework of continuum mechanics, is the subject of much research and debate, and not applicable with any degree of certainty to estimates of physical fracture and rockfall as required here. For this reason, continuum modeling methods are not used to represent rockfall.

7.4.2 Discontinuum Approach to Representing Rock Masses

The estimation of rockfall requires that the modeling technique and mechanical material model be capable of representing physical fracture of the rock mass and separation of the intact rock mass into blocks of material. In particular, an estimate of the size distribution of particles is desired. This requires the use of a discontinuum numerical method (i.e., a method in which slip and separation of contacting rock blocks can be estimated [Figure 7-3]). The following strategy is based on use of discontinuum methods for development of a material model for lithophysal rocks.

7.4.3 Strategy for Discontinuum Material Model Development

Typically, development of a mechanical material model for a rock mass is based on extensive laboratory testing of rock core, determination of strength and moduli reduction factors via in situ mapping of rock quality, followed by validation against field measurement. Such an approach to development of a material model for the lithophysal rocks presents a number of challenges. As discussed in the previous section, it is problematic to conduct an extensive mechanical properties testing program on lithophysal rocks due to the need to obtain and test large cores or to create large in situ samples from sawing or drilling. Additionally, direct determination of the true triaxial stress behavior of samples is difficult since pressure vessels to provide confinement to large core samples are not available. It is also not possible to conduct testing on a wide range of lithophysae shapes and size distributions. Finally, geotechnical classification systems are not particularly applicable to the lithophysal rocks due to a lack of contemporary experience in construction and testing in this type of rock mass.

As described previously, the database available for model development includes: 1) uniaxial and triaxial compression and direct pull tensile testing of nonlithophysal rock; and, 2) uniaxial compression testing of large scale cores and in situ blocks of lithophysal tuff. To overcome these sampling and testing limitations, an alternative strategy is used here, as illustrated in Figure 7-4. In this section, an approach is described in which a physics-based "micromechanical," discontinuum numerical modeling program—the PFC program (Itasca Consulting Group 2002 [DIRS 160331]; Potyondy and Cundall 2001 [DIRS 156895])—is used as a numerical "laboratory" to simulate and test the basic deformation and failure response mechanisms of lithophysal tuff. The PFC program was chosen due to its ability to simulate the physics of deformation and fracture of a bonded granular matrix that contains void space of varying shape, size and porosity. The program is first validated against the existing laboratory compression data. Specifically, it is demonstrated that a detailed understanding of the basic physical mechanisms of the rock mass behavior can be obtained without resorting to empiricism or complex constitutive modeling. The model is then used to extend the laboratory data by conducting numerical experiments on simulated samples of lithophysal tuffs at various physical conditions of porosity, lithophysae shape and distribution, as well as various levels of confinement and applied stress. From this modeling, it is possible to understand the size-scaling and variability issues introduced by lithophysae shape and distribution, and their impact on rock mass properties and failure criteria.

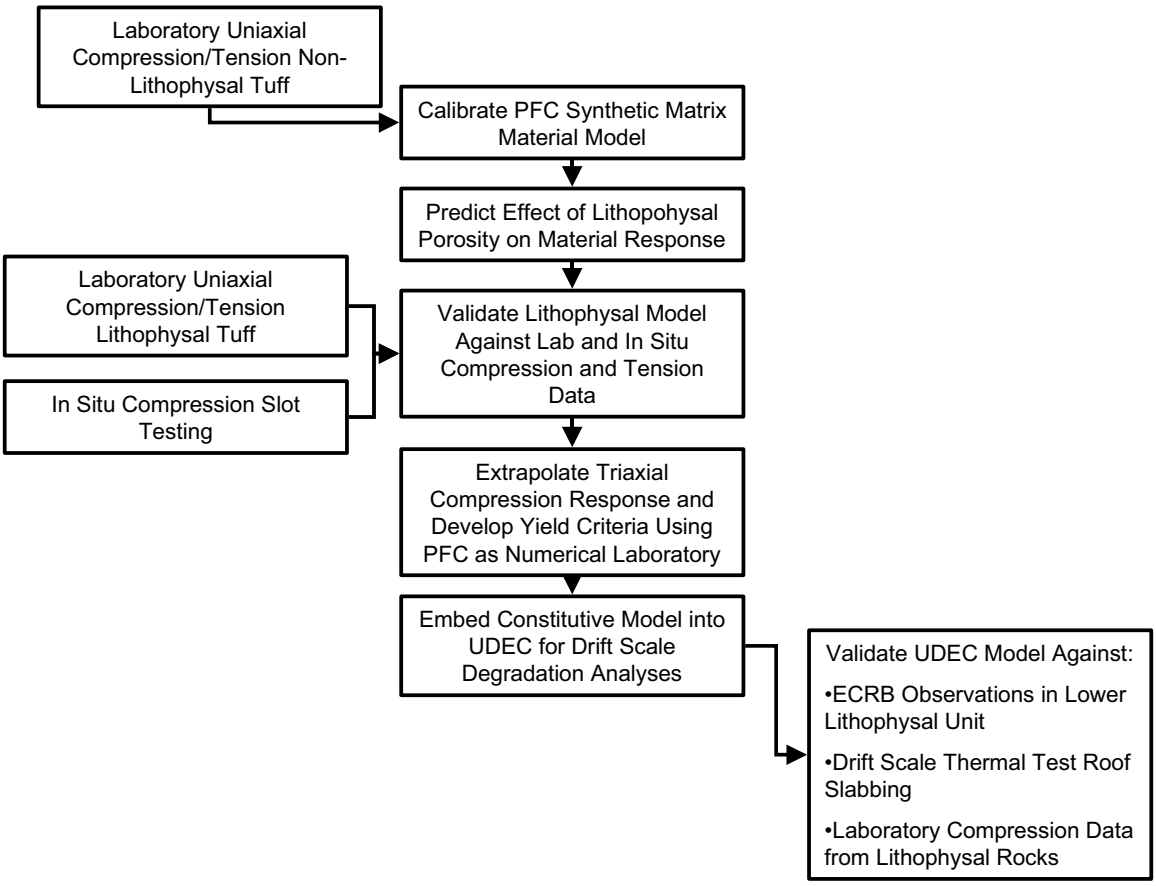

Figure 7-4. General Approach to Validation of Mechanical Material Model for Lithophysal Rocks

Although possible, it is impractical to use the PFC program as a general modeling tool to investigate drift degradation due to the extensive computing demands that result from large-scale problems. Instead, the material model developed from the testing and PFC extrapolation is embedded in the UDEC discontinuum program, which has been used efficiently to examine tunnel-scale seismic, heating and time-degradation issues (see Section 6.4.2).

7.5 VALIDATION OF THE PFC–A MICROMECHANICAL MODEL REPRESENTATION OF THE MECHANICAL BEHAVIOR OF LITHOPHYSAL ROCK

7.5.1 The PFC Model (Confidence Building During Model Development)

The Particle Flow Code has been qualified for use as indicated in Section 3. The PFC approach (Figure 7-5) represents rock as a number of small, rigid, spherical grains that are bonded together at their contacts with a shear and tensile strength, as well as a grain to grain friction angle after the "contact bond" has been broken. If cementing exists between grains, it can be represented with a "parallel bond" that provides a rotational resistance as well. Details on the mechanics of the PFC program are provided in *Itasca Software–Cutting Edge Tools for Computational Mechanics* (Itasca Consulting Group 2002 [DIRS 160331]). The deformability of the contacts between particles is represented by a normal and shear stiffness at the contact point. Porosity is

developed naturally in the model by control of the shape and size of void space between chains of bonded grains. The contact properties and porosity distribution are referred to as "microstructural" properties. Thus, the input conditions necessary for the model are very simple, only contact strength and stiffness. However, as shown below, extremely rich constitutive behavior may develop *naturally* based on porosity and the few straightforward input properties and their variability throughout the rock.

When load is applied to the grain assembly, forces are transmitted across contacts. If the shear or tensile strength of the contact is reached, failure will occur, and the adjacent particles are free to slide past one another, or to separate. In either case, a fracture is formed and the forces must reorient in some fashion, thus redistributing loads. Realistic failure mechanisms may then develop which can be compared to those observed in the laboratory. Calibration of the model against laboratory testing is necessary via sensitivity studies in which the contact strength and stiffness values are varied and the macroscopic stress-strain response is compared to that monitored.

A discussion of the PFC calibration and extrapolations is provided in this section, including a summary of the approach and results. The PFC program in both two- and three-dimensions was "calibrated" first against laboratory strength tests of nonlithophysal rocks. Since it is considered that the matrix or groundmass material of the Tptpul, Tptpmn, and Tptpll is essentially the same, both mineralogically and mechanically, it is necessary to first make certain the PFC model can represent the mechanical response of the material without lithophysal voids. Once the matrix material response is identified, then representation of the mechanical behavior of the lithophysal material is possible with the simple addition of void space (assuming the consideration of similar matrix is correct).

The tuff can be divided into lithophysal and nonlithophysal types. These two rock types differ significantly in their microstructural and mechanical properties. In the lithophysal tuff, the vast majority of the porosity is concentrated in lithophysae and surrounding vapor-phase altered material, whereas in the nonlithophysal tuffs porosity is more evenly distributed throughout the material. The nonlithophysal tuffs have effective porosities that range from approximately 0.1 to 0.4 (Price et al. 1985 [DIRS 106602], Figure 15). The high-porosity nonlithophysal tuffs have large effective porosities because of the voids between grains, whereas similar effective porosities in lithophysal tuffs arise from the presence of lithophysae and vapor-phase altered material (Price et al. 1985 [DIRS 106602], pp. 25-28). The matrix fabric of the lithophysal tuff is microscopically identical to that of moderately to densely welded nonlithophysal tuff. Price et. al. (1985 [DIRS 106602]) divide the lithophysal tuff into the following three components: a fine-grained matrix (*M*), large lithophysae (*L*), and vapor-phase altered material (*A*) surrounding the lithophysae. Based on the approach described by Price et al. (1985 [DIRS 106602]) for determining bulk properties of lithophysal tuff, the porosity of component-i is denoted by

$$\phi_i = \frac{(V_v)_i}{V_i}, \qquad i = \{M, A, L\} \qquad \text{(Eq. 7-1)}$$

and the volume fraction of component-i by

$$P_i = \frac{V_i}{V,} \qquad i = \{M, A, L\} \qquad \text{(Eq. 7-2)}$$

where $(V_v)_i$ is the void volume of component-i, V_i is the solid volume of component-i and V is the total volume. The total porosity can be expressed as

$$\phi = \frac{(V_v)_M + (V_v)_A + (V_v)_L}{V} = \phi_M P_M + \phi_A P_A + \phi_L P_L \qquad \text{(Eq. 7-3)}$$

The PFC material models lithophysal tuff as a base material with discrete voids. The base material represents both the matrix (*M*) and the vapor-phase altered material (*A*) in a smeared fashion, and the discrete voids represent the lithophysae (*L*). The void porosity, n_v, defined by Equation 7-1, of the PFC model corresponds with the volume fraction, P_i, of the lithophysal tuff. The relative distributions of these components for the lithophysal tuff and the PFC model are shown in Figure 7-6. Note that the PFC base material has an inherent porosity (approximately 0.17 and 0.36, for PFC2D and PFC3D, respectively) that does not correspond with that of the tuff; the tuff microstructure at this small-scale is not reproduced by the PFC material. Only the void porosity of the PFC material can be compared with the lithophysal volume fraction. Also note that P_A as a function of P_L is not known, but P_A must approach zero as P_L approaches zero. The microproperties of the PFC material are kept constant for the values of $n_v = P_i$, and thus, the PFC materials with low void porosity are overestimating the weakening effect of the vapor-phase altered material. One approach to incorporate this effect in the PFC models would be to modify the PFC microproperties as a function of n_v such that they match the laboratory data for the lithophysal tuff in the non-zero range of n_v and match the nonlithophysal tuff when $n_v = 0$. This approach has not been adopted here.

The void-filled PFC material can be calibrated by matching the variation of modulus and strength with volume fraction of lithophysal tuff. The laboratory data used for calibration is that shown in Appendix E (Table E-9). The nonlithophysal tuff exhibits a size effect such that larger specimens are weaker with unconfined compressive strength values ranging from approximately 190 to 90 MPa as specimen diameter ranges from 25 to 230 mm (Price 1986 [DIRS 106589]). The form of a size effect for lithophysal tuff has not been identified, but is considered to be similar to that of the nonlithophysal tuff. The effect of specimen size is not investigated for the PFC models; instead, the PFC models are either 1:1 or 2:1 aspect ratio specimens of one-meter diameter, and microproperties are chosen to match the laboratory data.

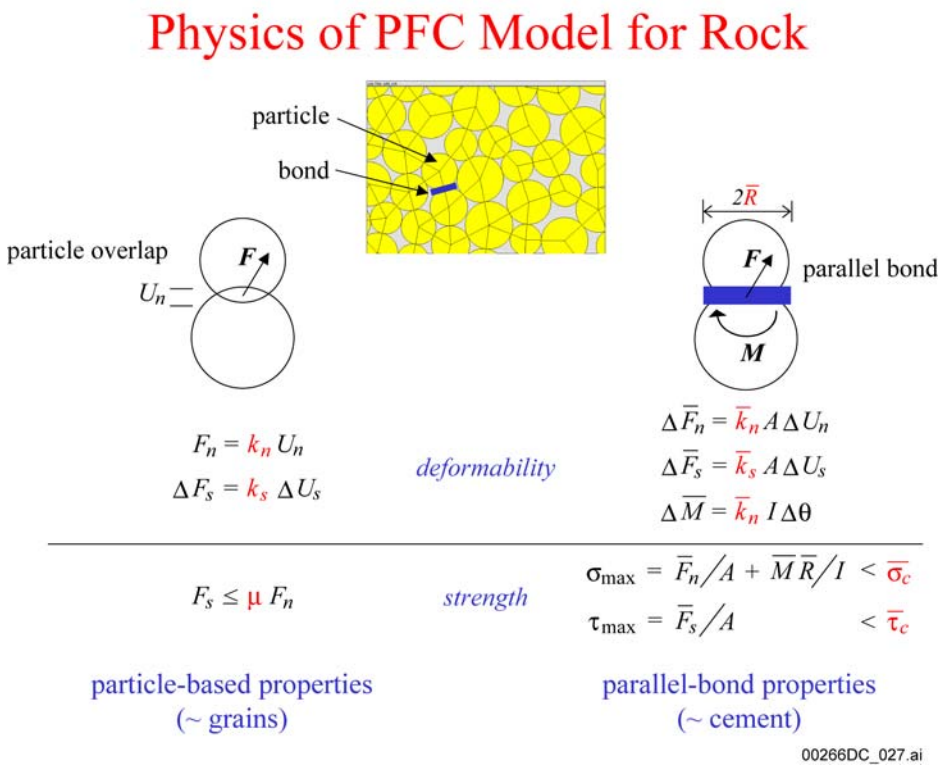

NOTE: Mechanical response in the PFC program is governed by the strength and deformability relationships of the bonds between rigid particles. Two bond types are provided: a simple contact bond (left), and a parallel bond (right), which simulates cement between particles that resists moments as well as shear and normal loads.

F_n = normal contact force
k_n = normal stiffness
U_n = relative normal displacement
ΔF_s = shear contact force increment
k_s = shear stiffness
ΔU_s = relative shear displacement increment
$\Delta \overline{F}_n$ = axial-directed force increment for bond
$\overline{k}_n$ = bond normal stiffness
A = area of bond cross-section
ΔU_n = relative normal displacement increment
$\Delta \overline{F}_s$ = shear-directed force increment for bond
$\overline{k}_s$ = bond shear stiffness
ΔU_s = relative shear displacement increment
$\Delta \overline{M}$ = bending moment increment for bond
I = moment of inertia of the bond cross-section
$\Delta\theta$ = increment of rotational angle
F_s = shear contact force
μ = contact friction coefficient
σ_{max} = maximum tensile stress acting on the bond periphery
τ_{max} = maximum shear stress acting on the bond periphery
$\overline{R}$ = particle radius
$\overline{F}_n$ = axial-directed force for bond
$\overline{F}_s$ = shear-directed force for bond

Figure 7-5. The Basic Mechanics of the PFC Program

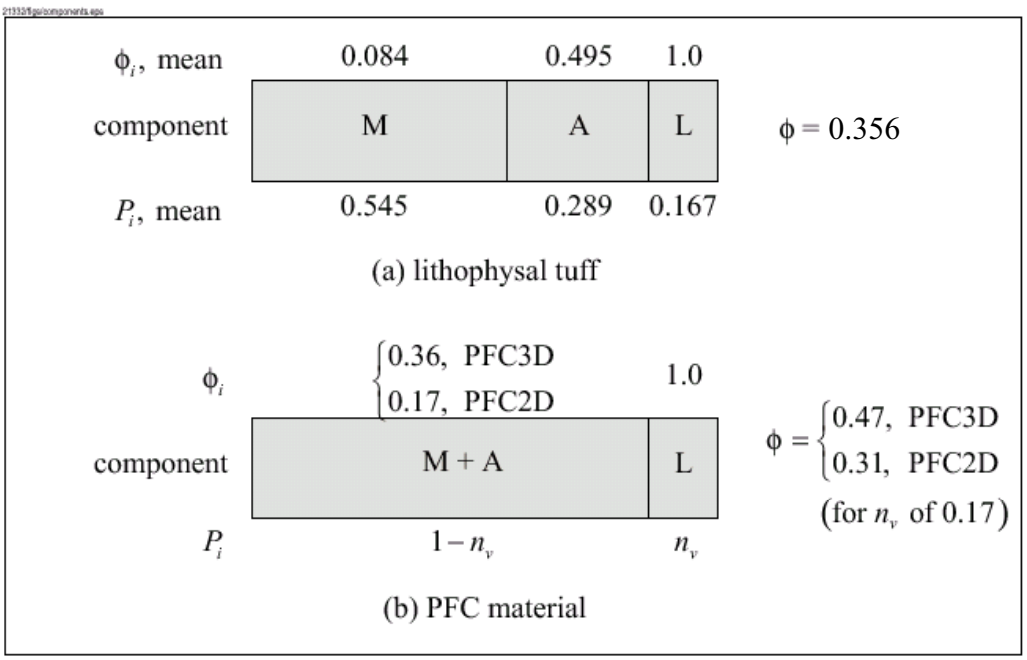

Figure 7-6. Relative Distributions of the Three Components of Lithophysal Tuff for (a) Real Material (Price et al. 1985 [DIRS 106602]) and (b) PFC Materials

7.5.2 Validation Exercises for the PFC Model

The PFC model of lithophysal rock is used to extrapolate both quasi-static and time-dependent compression data from existing laboratory test data to examine the impacts of variable size, shape and distribution of lithophysae. This extrapolated information is used to assist in defining the bounding ranges of in situ properties of lithophysal rocks. These ranges are, in turn, used as input to drift-scale calculations of emplacement drift stability resulting from in situ, thermal and seismic loading as well as time-dependent strength loss. Since the PFC model provides input to drift degradation studies, it is considered to require a Level III validation, which requires at least two post-development validation exercises. The following section provides three post-development exercises. The first example tests the ability of the PFC model to provide a reasonable reproduction of the mechanical response of lithophysal rock as determined from large core laboratory testing. The second validation example tests the ability of the PFC model to reproduce the basic creep response of the nonlithophysal matrix material through comparison of the model output to the primary, secondary and tertiary creep response as observed from laboratory creep experiments. The third validation exercise presented is an external technical review of the PFC model for representation of the time-dependent response of Topopah Spring tuff.

7.5.2.1 PFC Post-development Validation Exercise 1 – Simulation of the Stress-Strain Behavior of Nonlithophysal and Lithophysal Rock in Compression and Tension

The PFC2D and 3D models were first calibrated against laboratory strength and modulus data from large diameter core testing at an approximate mean lithophysal porosity of 15 percent using an idealized model that represented lithophysae as circular voids that are uniformly distributed through the samples. The purpose of the calibration is to set an approximate value for the particle bond strength and stiffness. This calibration was followed by validation through prediction and comparison of the model to the entire large-core compression testing from cores obtained from the Tptpll and Tptpll in the ECRB Cross-Drift and from the Busted Butte site (see Section E.4). Additionally, the mode of failure of rock samples in compression must be similar to that observed in the laboratory.

A sensitivity analysis of the PFC model is then conducted using model samples developed from field "panel" maps created in the Tptpll in the ECRB Cross-Drift. These panel maps (see Appendix O) are used to create PFC samples by "stenciling" the irregular shapes and distributions from 18 panel maps to create realistic lithophysae geometries for the PFC test samples. These samples are then used to conduct simulated uniaxial compression tests to examine the impact of realistic lithophysae geometries on variability in mechanical properties.

Figures 7-7 and 7-8 show PFC2D and PFC3D models of several lithophysal rock "samples" at increasing void ratios that are used to conduct numerical laboratory experiments. Particles are removed to create circular or spherical voids with random location.

Examples of the predicted stress-strain behavior and post-test fracturing response of simulated uniaxial compression simulations for nonlithophysal and lithophysal samples with circular voids and void porosities of 0, 10 and 20 percent are shown in Figures 7-9 to 7-11. The models show numerous physical features that correspond well to those observed in laboratory response. The nonlithophysal samples fail through formation of conjugate shear fractures composed of coalescing tensile bond breakages. The response is highly elastic to the point of brittle failure (i.e., there is little observable hysteresis on load-unload cycles directly up to the yield limit). This behavior is a function of the uniform grain structure and welding of the matrix material. The addition of lithophysal voids results in significant decreases in both the strength and modulus. The failure mechanism in this case is a function of tensile splitting between adjacent lithophysal voids due to induced tensile stresses in the thin webbing between voids. The PFC model shows that the failure strength is simply governed by the ratio of void span to webbing thickness. With voids randomly distributed, the thinnest of webbing will fail first, shunting load to other solid webs, resulting in progressive failure of the weakest "link." The resulting stress-strain behavior becomes less brittle in nature due to this progressive failure mode.

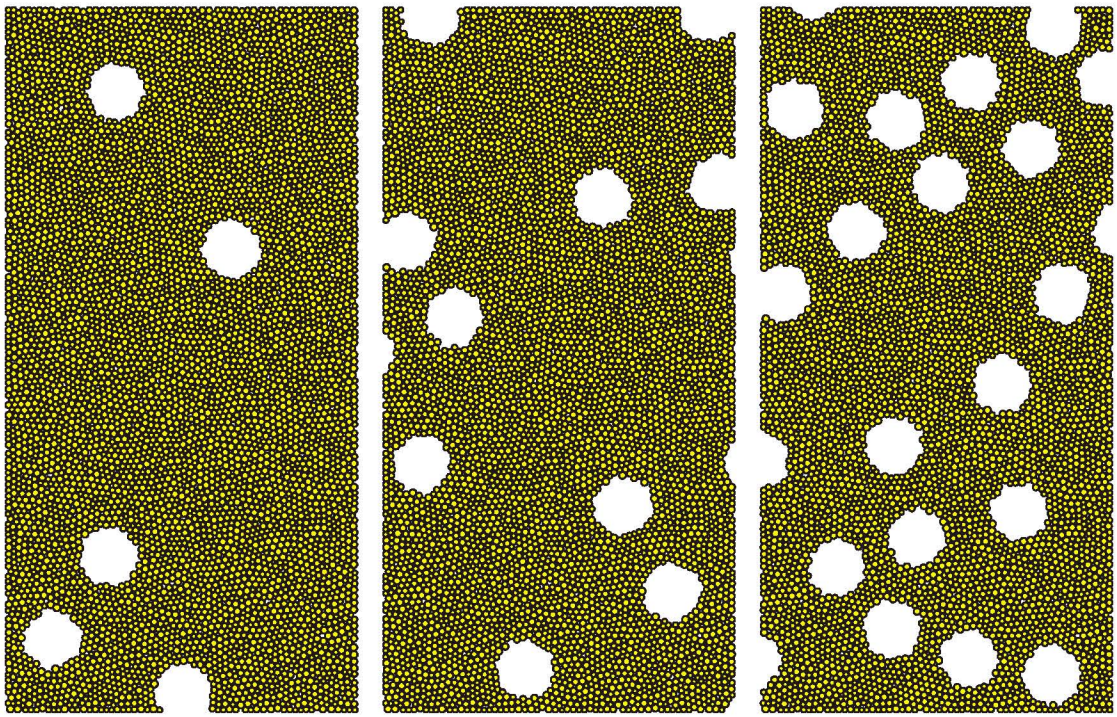

NOTE: Circular Voids; Radius = 83 mm; nv = 0.05, 0.10, and 0.20.

Figure 7-7. PFC2D Unconfined Compressive Strength Test Specimens

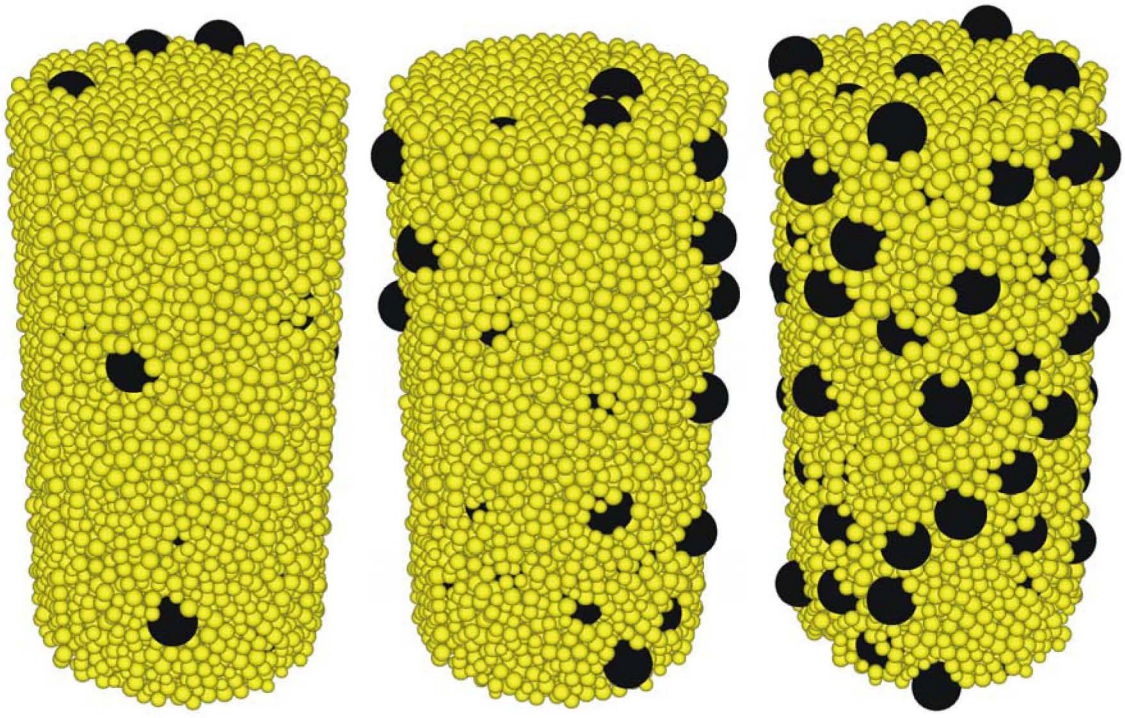

NOTE: Spherical voids; Radius = 83 mm; n_v = 0.05, 0.10, and 0.20.

Figure 7-8. PFC3D Unconfined Compressive Strength Test Specimens

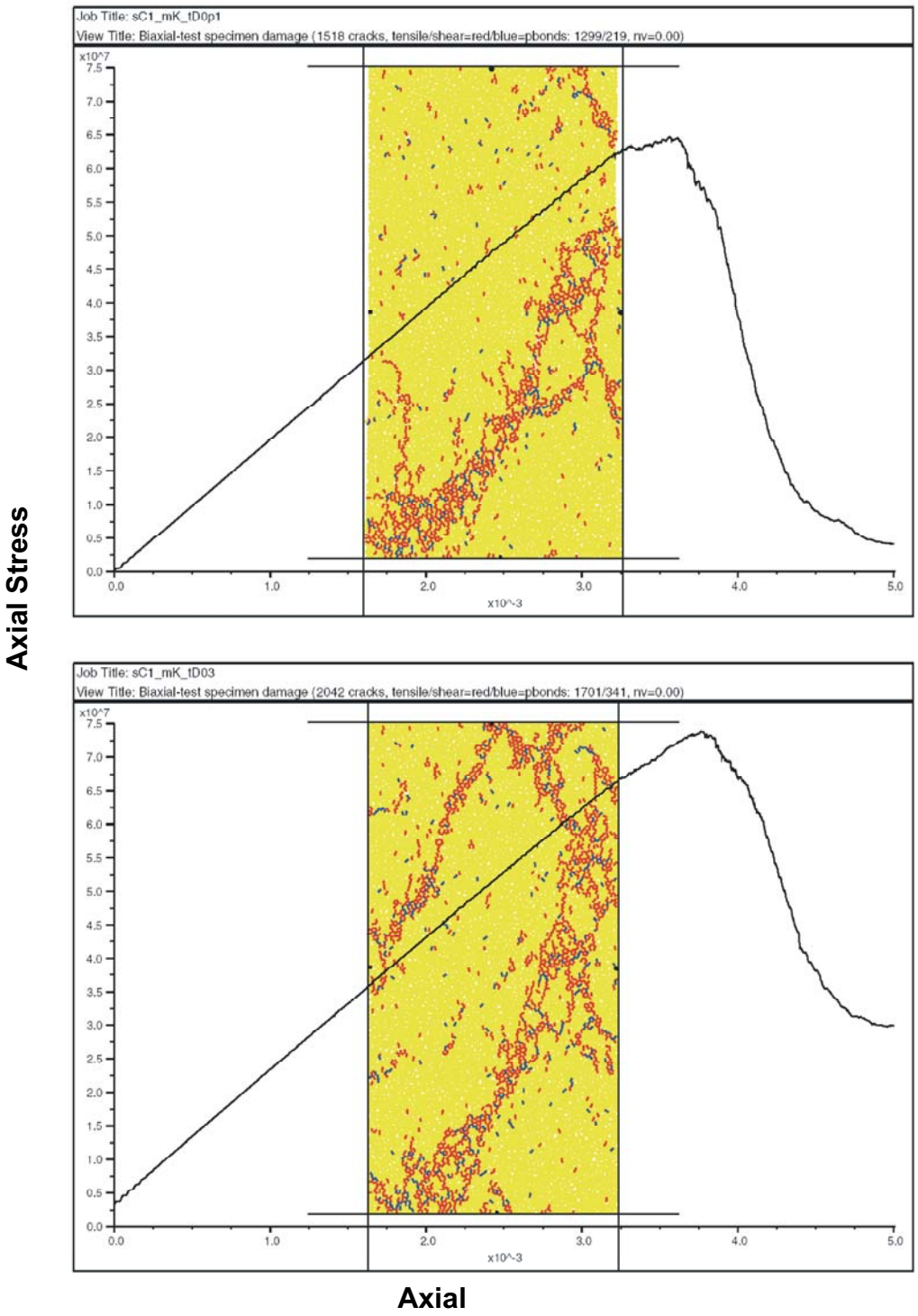

NOTE: Final sample damage state is plotted with bond failures in tension (red) and shear (blue). Samples fail with typical conjugate shear fractures. Two confining pressures are shown: 0.1 MPa (top) and 3 MPa (bottom). The primary impact of confinement is slightly increased peak and residual strength.

Figure 7-9. PFC2D Simulation of Confined Compression of 2:1 L:D (Length:Diameter) Samples of Nonlithophysal Material (nv = 0) Composed of Several Thousand Bonded Particles

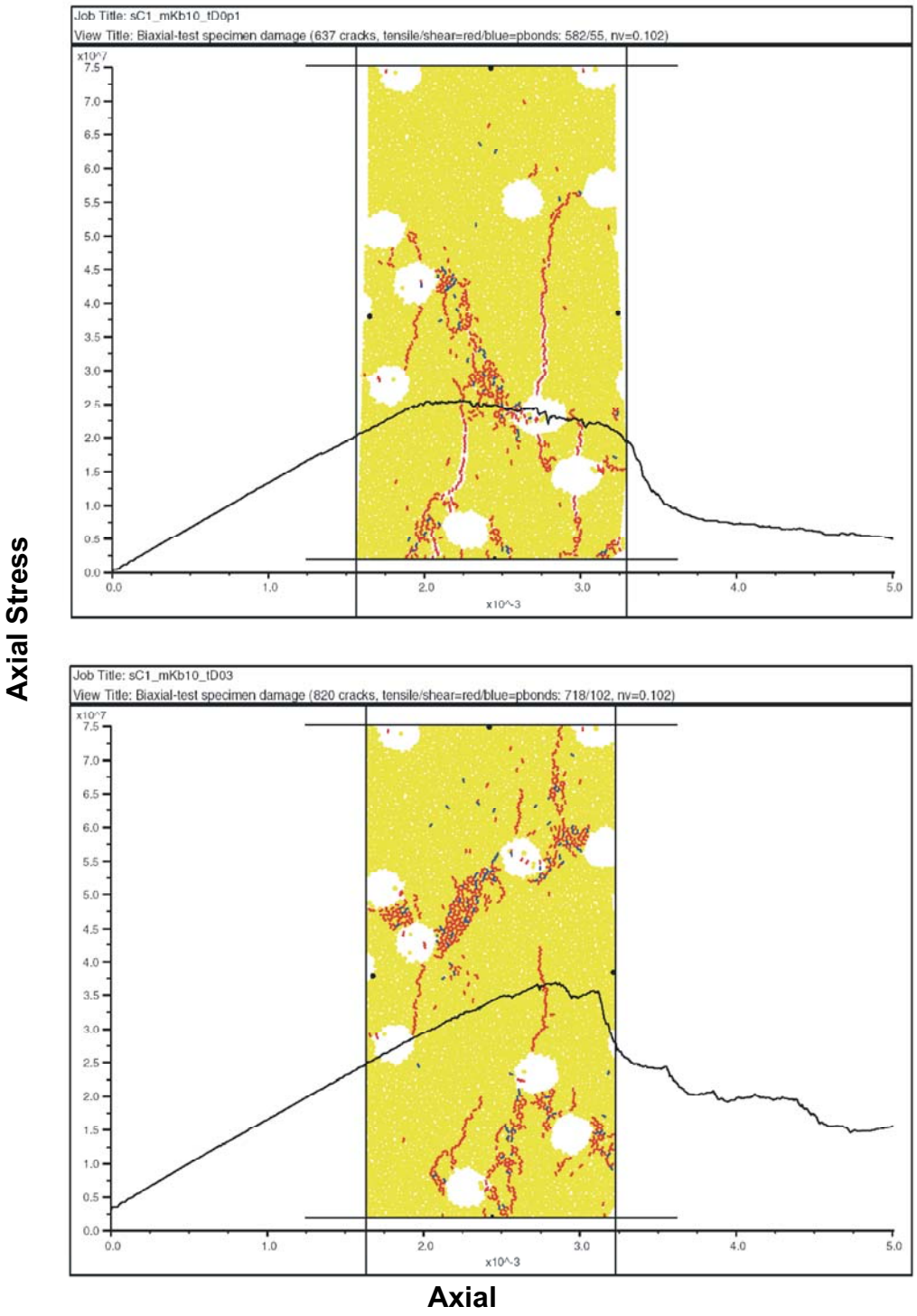

NOTE: Final sample damage state is plotted with bond failures in tension (red) and shear (blue). Two confining pressures are shown: 0.1 MPa (top) and 3 MPa (bottom). Samples fail in an axial splitting mode which is most pronounced in the low confinement model at left. Note that confinement increases peak strength with increased residual strength.

Figure 7-10. PFC2D Simulation of Confined Compression of 2:1 L:D (Length:Diameter) Samples of Lithophysal Material (n_v = 0.10) Composed of Several Thousand Bonded Particles

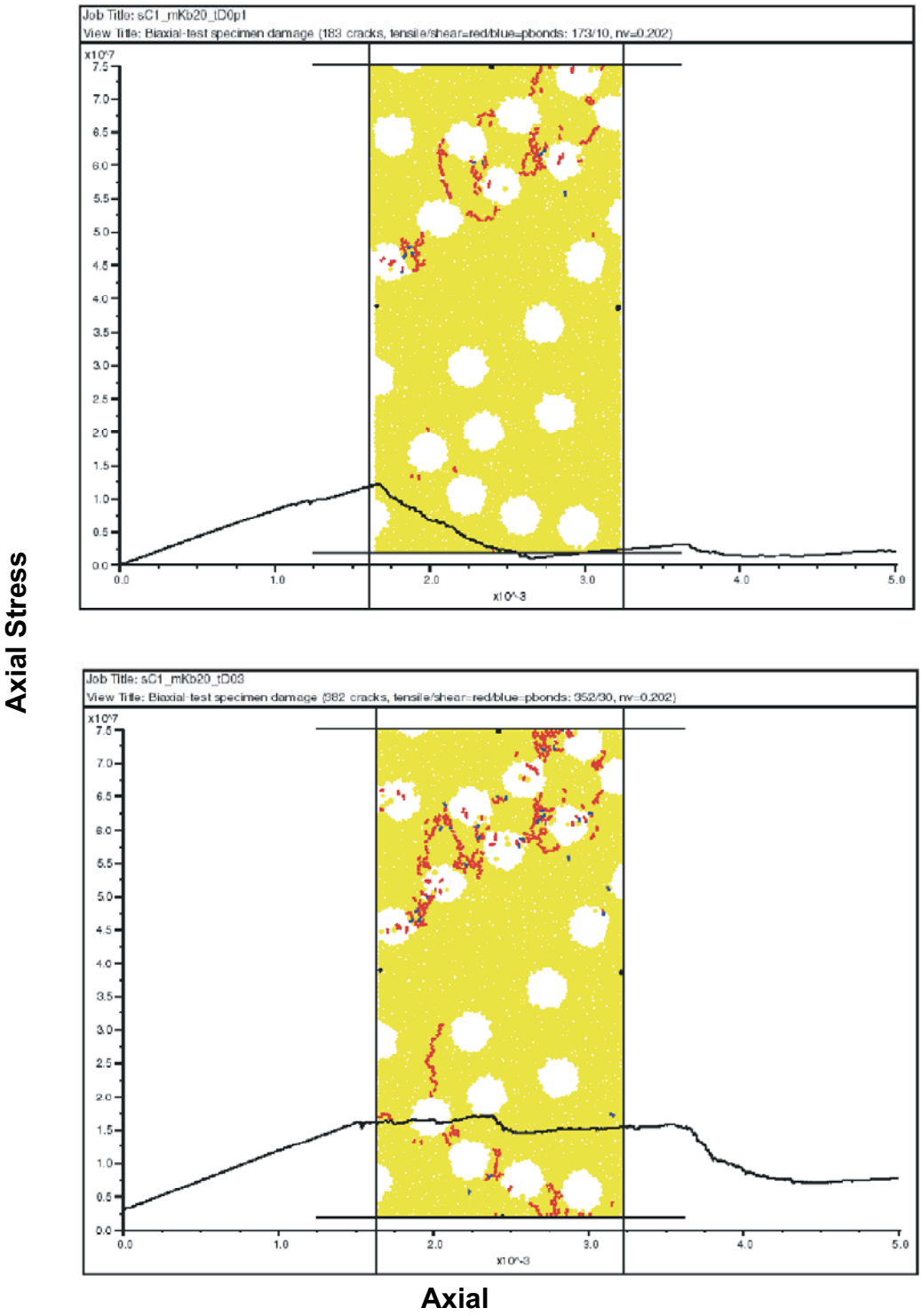

NOTE: Final sample damage state is plotted with bond failures in tension (red) and shear (blue). Two confining pressures are shown: 0.1 MPa (top) and 3 MPa (bottom). Samples fail due to tensile splitting between adjacent voids in the low confinement model at left. Note that confinement results in a slight increase in peak strength with increased residual strength at high values of void porosity.

Figure 7-11. PFC2D Simulation of Confined Compression of 2:1 L:D (Length:Diameter) Samples of Lithophysal Material (n_v = 0.20) Composed of Several Thousand Bonded Particles

The impact of lithophysae on direct tension strength follows the same general mechanism: the voids result in less area of solid rock for any given cross-section . For a constant applied force, the stress in the remaining solid will be higher, thus reducing the overall averaged tensile strength of the sample. Particles are removed to create circular or spherical voids with random location subject to the constraint that no two voids are closer than one-half of the void radius (17.1 mm mean void diameter and 41.5 mm minimum bridge length).

The properties of the lithophysal tuff samples (i.e., Young's modulus and unconfined compressive strength) from the ESF main loop and ECRB Cross-Drift (Appendix E, Table E-9) are plotted along with those of the circular-void PFC model in Figures 7-12 and 7-13, as a function of lithophysal porosity. Figure 7-14 presents the same laboratory and numerical test results in the form of unconfined compressive strength versus Young's modulus. Both PFC models provide reasonable correspondence to the large core laboratory data. The PFC models show the same general decrease in both strength and modulus with lithophysal porosity. The PFC models are performed for circular, constant diameter lithophysal voids. As described in Appendix E, Section E4.1.4.1, the scatter in the laboratory data is a result of the variability in size, shape and distribution of the lithophysal voids. The PFC model was used to simulate compression testing of in situ variability of lithophysal voids on actual field-mapped sections of the Tptpll in the ECRB Cross-Drift. Figure 7-15 shows PFC test samples stenciled from field panel maps, and the corresponding stress-strain curves obtained from test simulations. The impact of actual lithophysal shape, size and distribution on the variability of uniaxial compression strength and modulus results in the same general trend of strength and modulus decrease with lithophysal porosity, but introduces a considerable scatter in the range of results. This scatter is primarily due to the distribution of the voids within a test sample, and, in particular, the non-uniformity of the voids. The distribution of thickness of the solid rock "bridge" between voids weakens the samples as the bridge size decreases. Figure 7-16 shows a comparison of the laboratory test data against the PFC modeling of test samples from field panel maps. It is seen here that, when the variability of the actual lithophysae structure and distribution are taken into account, the scatter in PFC model results fall within the range of the large core laboratory test results. Bounding ranges, as described in Section E.4, can then be assigned for the complete range of expected lithophysal mechanical response.

This validation exercise shows that:

- The PFC model can reproduce the general failure mechanism observed in the laboratory – i.e., tensile splitting between adjacent lithophysae
- The PFC model can reproduce the general trend of strength and modulus as functions of the lithophysal porosity as seen in the test data
- The PFC model successfully provides an explanation for the observed scatter in the strength and modulus as functions of the lithophysal porosity. The model shows that the variability is a result of the shape and distribution of the lithophysae within a sample volume.

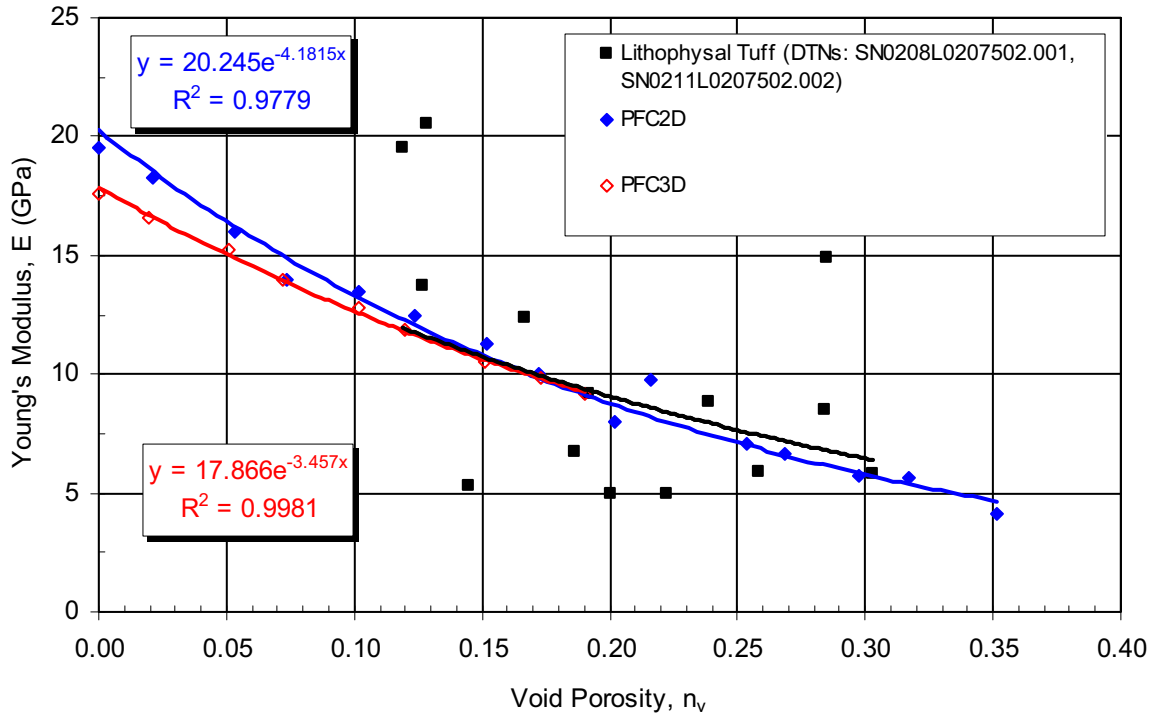

Figure 7-12. Young's Modulus Versus Void Porosity for Lithophysal Tuff and PFC Materials

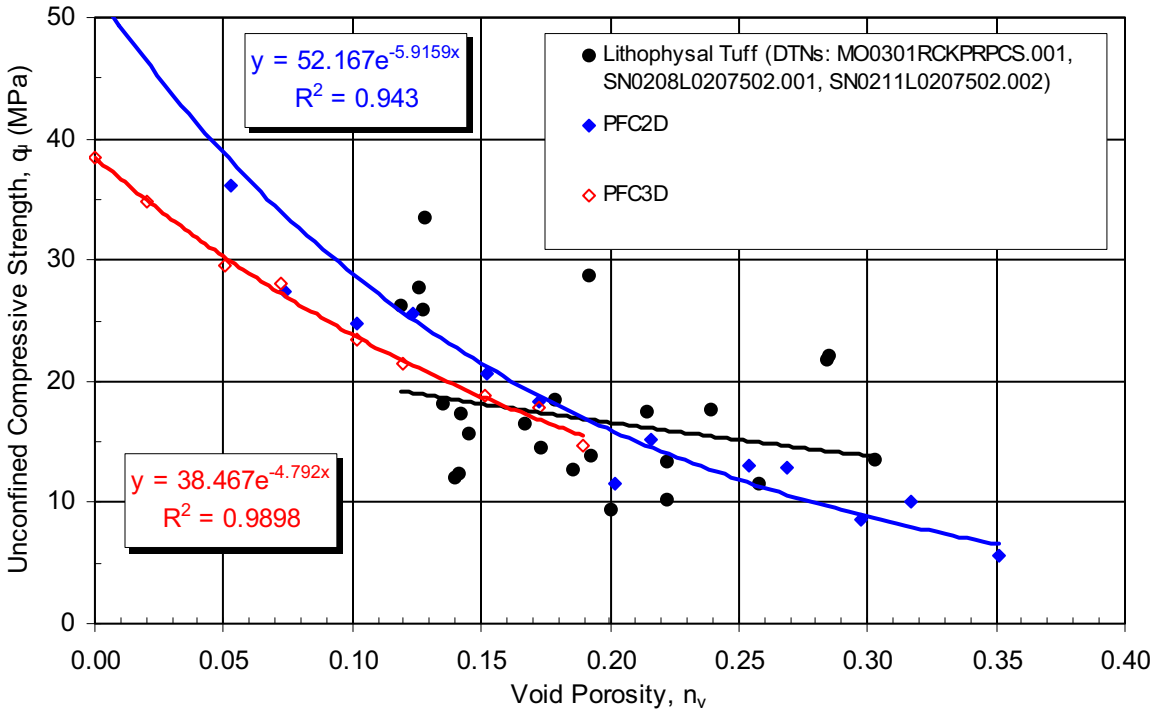

Figure 7-13. Unconfined Compressive Strength Versus Void Porosity for Lithophysal Tuff and PFC Materials

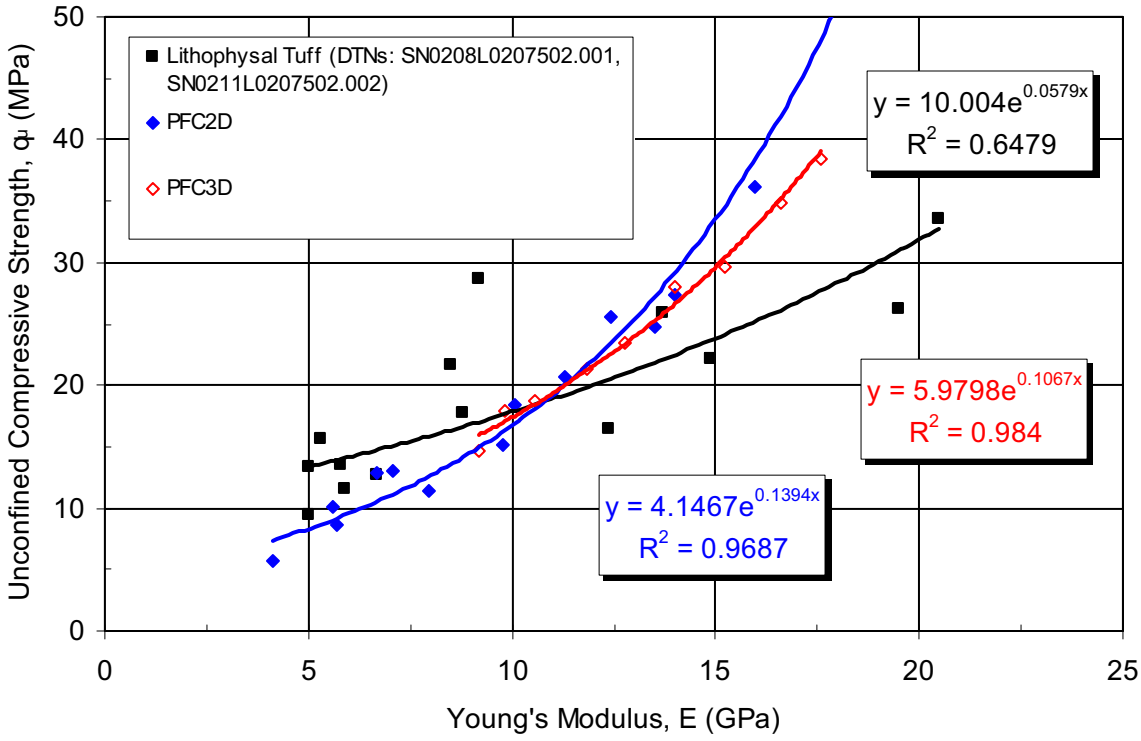

Figure 7-14. Unconfined Compressive Strength Versus Young's Modulus for Lithophysal Tuff and PFC Materials

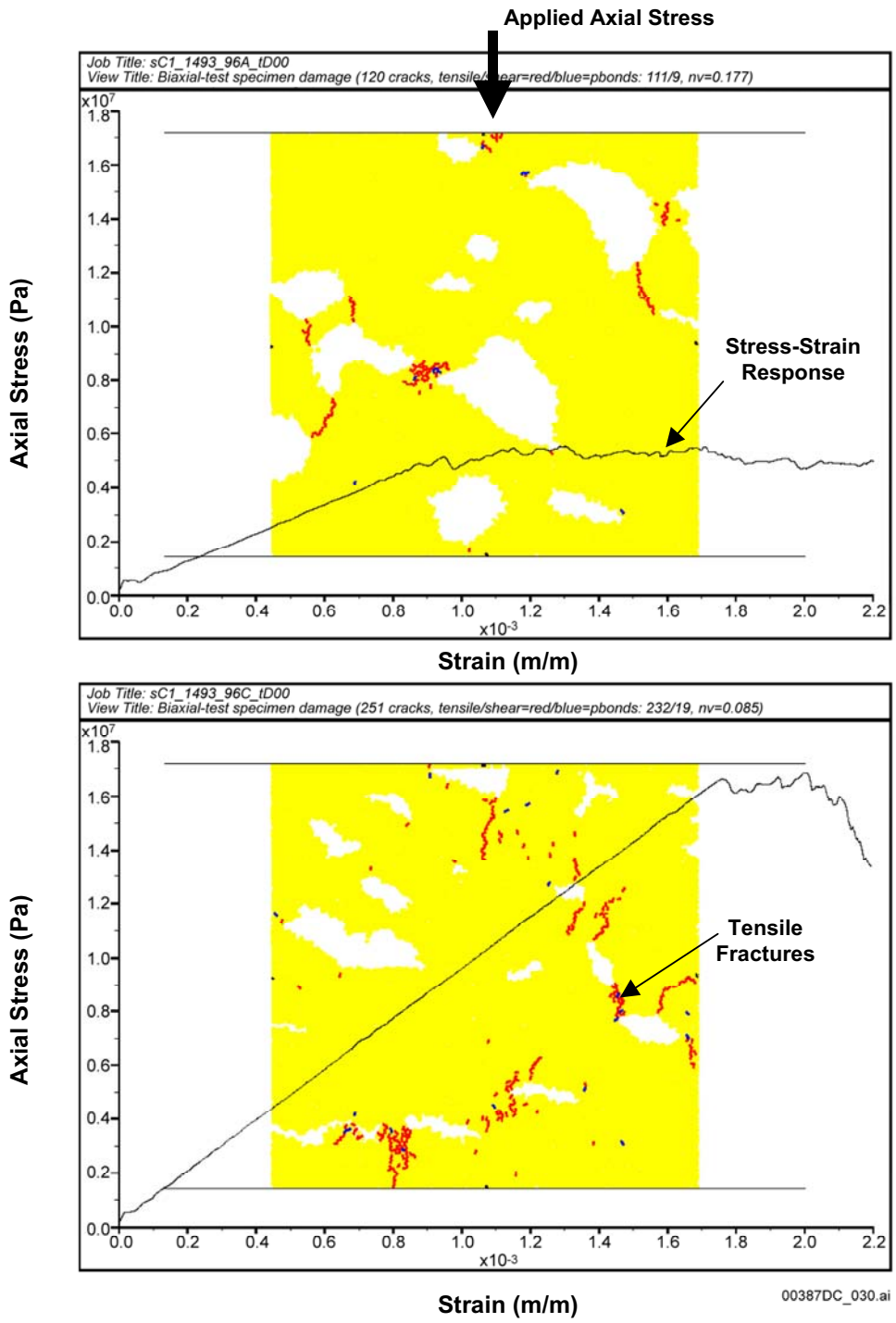

NOTE: Specimen is composed of several thousand bonded particles. Red lines are tensile fractures that have propagated between lithophysae to ultimately form a failure mechanism. Superimposed stress-strain curve illustrates impact of lithophysae distribution on strength, modulus and post-peak failure mechanism. Vertical axis is axial stress in Pa; horizontal axis is strain in m/m.

Figure 7-15. Examples of Particle Flow Code Compression Tests Using Simulated Rock Specimens Developed by "Stenciling" Field Panel Maps in the Enhanced Characterization of the Repository Block

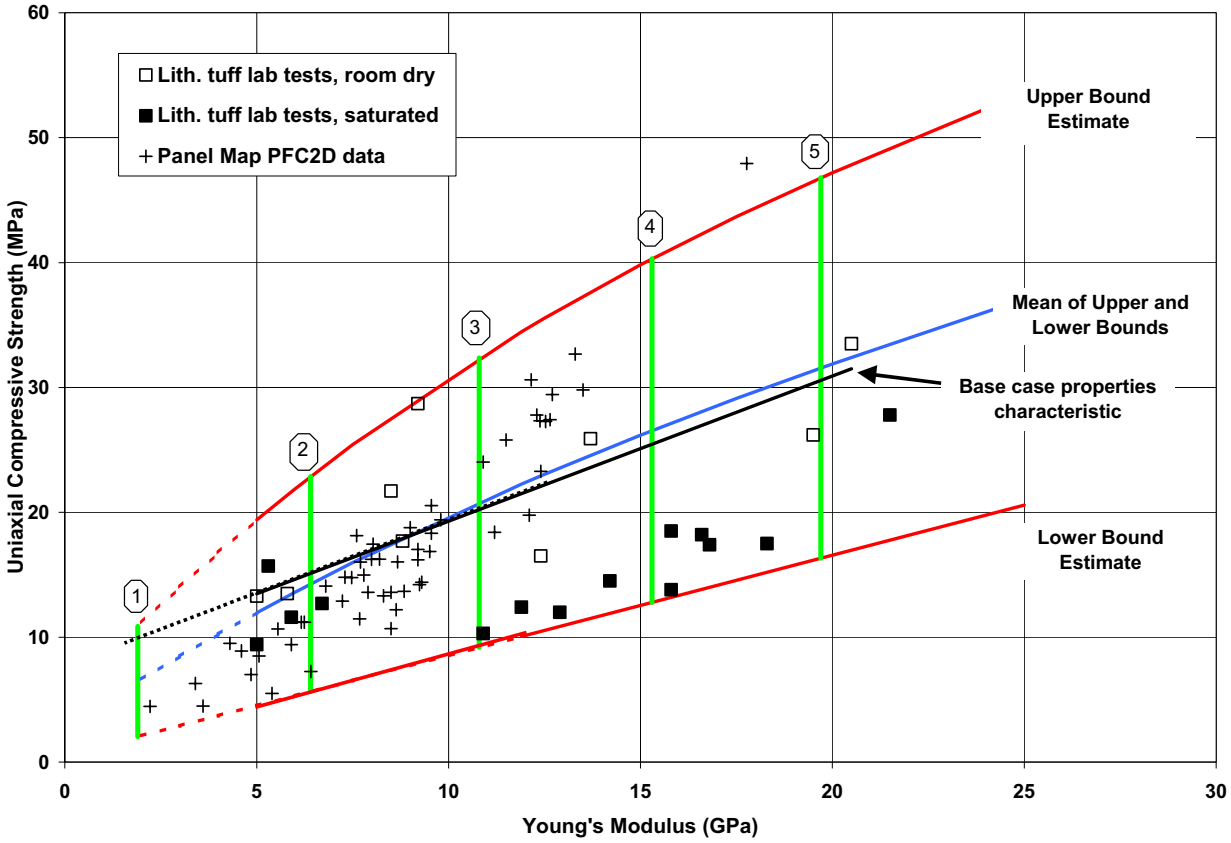

NOTE: Approximate upper and lower bounds are shown.

Figure 7-16. Unconfined Compressive Strength Versus Young's Modulus Showing Large Core Data and Results from PFC Panel Map Lithophysae Shape Study

7.5.2.2 PFC Post-Development Validation Exercise 2 – Comparison of PFC Stress Corrosion Model Ability to Reproduce Typical Primary, Secondary and Tertiary Creep Response of the Tptpmn

The drift degradation analyses include time-dependent rock mass behavior modeled using the PFC model that incorporates a stress corrosion cracking representation. The PFC stress corrosion modeling approach provides a representation of subcritical crack growth in rocks that embraces both the microscopic processes of reactions and thermal activation at crack tips and the more mesoscopic processes of microcrack-microstructure-macrocrack interaction. The PFC stress corrosion model is described in detail by Potyondy (2003 [DIRS 165550]) and reviewed in Appendix S. The PFC stress corrosion model is calibrated by adjusting the particle bond strength and radius as a function of time to provide a match to the time-to-failure curve produced by performing a series of laboratory static fatigue tests (Appendix S, Figure S-27). The PFC stress corrosion model bypasses the need to idealize the rock in the classical Linear Elastic Fracture Mechanics sense, yet can itself reproduce the Linear Elastic Fracture Mechanics behavior. That is, to model static-fatigue behavior, there is no need to begin with a Linear Elastic Fracture Mechanics material, which is an elastic body with classical sharp cracks. Such discrete cracks form naturally in the PFC material as the result of bond breakages. The PFC

material is comprised of complex grain-scale discontinuities, which induce the micro-tensions that drive the stress-corrosion process, and these discontinuities are not necessarily the same as the discontinuities in an elastic body with classical sharp cracks. This suggests that the PFC stress corrosion model may be more appropriate for use in modeling the physical behavior mechanisms of rock than a more idealized Linear Elastic Fracture Mechanics material.

Much of the development of the PFC stress corrosion model was funded by Atomic Energy of Canada Limited and Ontario Power Generation during the years 1995-2001 as part of a joint thermal-mechanical stability study (Potyondy and Cundall 2001 [DIRS 156895]). One aim of this model development was to improve the fundamental understanding of short- and long-term rock-mass behavior around underground openings at ambient and elevated temperatures. The study was conducted in tunnels constructed in the Lac du Bonnet granites (Manitoba, Canada) as part of the joint Atomic Energy of Canada Limited and Ontario Power Generation Underground Research Laboratory project.

The result of this work was the development and verification of the Bonded-Particle Model for Rock — a mechanistically based numerical model used for predicting excavation-induced rock-mass damage and long-term strength (by incorporating a damage process based on a stress-corrosion mechanism) in Lac du Bonnet granite (Potyondy and Cundall 2001 [DIRS 156895]).

A validation of the PFC stress corrosion model is to compare the general nature of time-dependency of the strain of rock samples when subjected to constant axial load. This test is typically termed a "creep" test, and involves rapid application of axial load to a rock sample to a specific load level that is typically greater than 80 or 90 percent of the considered strength of the material. This load is held constant while axial and lateral strain in the sample is monitored as a function of time. The sample will typically undergo three stages of creep that can easily be discerned from the strain versus time curve. These are the initial primary or transient creep stage that exhibits rapidly-decelerating strain, followed by the secondary or steady-state creep stage in which strain occurs at a constant rate for extended time periods. The steady state creep stage is characterized by slow growth of microcracks either along or through grain boundaries. Finally, as the sample reaches its static fatigue limit, brittle materials will enter another stage of rapid strain rate increase leading to brittle failure. During this stage of deformation, the microcracks form major through-going fractures, which results in formation of a macroscopic failure mechanism. An example of a typical creep test for the Tptpmn is given in Section 6.4.2.4 (see Figure 6-152). Each creep stage can clearly be seen from this curve.

The PFC stress corrosion model adjusts the particle bond strength properties and radius to represent the basic time-dependent weakening effects resulting from stress corrosion. The bonding properties are calibrated to reproduce the slope of the time-to-failure plots derived from static fatigue experiments. However, the model should also reproduce the general time-dependent creep response of the Tptpmn, and should be able to show equivalent transient, steady-state and tertiary creep phases. Figure 7-17 shows a typical PFC-generated creep curve from a simulated constant load (at 80 percent of the uniaxial compressive strength) creep experiment. The time-to-failure (i.e., the point of tertiary creep rupture at t/t_f) is set via calibration to static fatigue experiments, thus establishing a match of the specific time of creep rupture. Tensile fractures (cracks) develop spontaneously in the model as a function of time

based on the time-dependent bond strength of the constituent grains. The plot shows the development of a network of tensile stress corrosion cracks that accumulate and propagate within the sample until a macroscopic shear failure mechanism develops with resulting brittle rupture during the tertiary creep stage. The simulated creep test shows the three stages of creep: transient, secondary and tertiary, and reproduces the typical response of creep experiments in tuff (e.g., Figure 6-152).

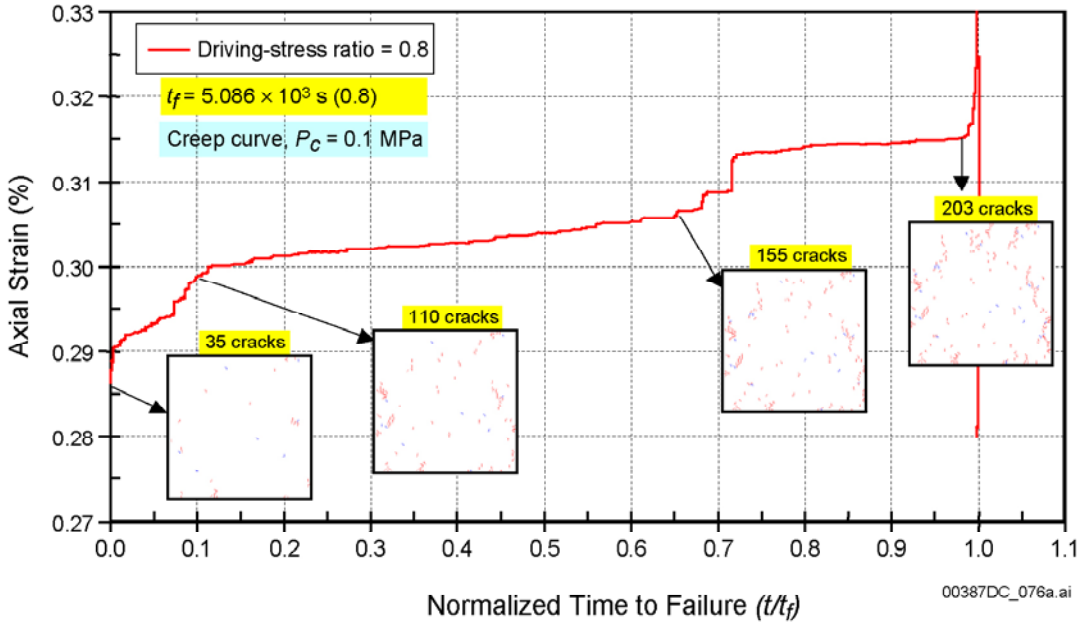

Source: Appendix S, Figure S-13.

NOTE: Numerical simulation of creep test run by holding applied axial stress constant at 0.8 times the unconfined compressive strength. The damage, in terms of new crack growth, is displayed at various times along the creep curve. Brittle failure of the sample occurs when sufficient time-dependent crack growth results in failure mechanism.

Figure 7-17. Simulated Creep Curve and Brittle Rupture Calibration for Nonlithophysal Tuff, Static-Fatigue Test at Driving-Stress Ratio (Ratio of Applied Stress to Unconfined Compression Strength) of 0.8

In conclusion, the PFC stress corrosion model is shown to spontaneously reproduce the observed primary, secondary and tertiary stages of creep observed in laboratory. The approximate evolution of each stage and the proportionate length of each stage is reasonably similar to that observed in the laboratory.

7.5.2.3 PFC Post-Development Validation Exercise 3 – Model Validation by Technical Review

Two outside expert technical reviews were conducted as a means of validation, as discussed in procedure AP-SIII.10Q, *Models*. The first independent technical review is provided by Dr. Jaak Daemen, Professor of Mining Engineering and Department Chair at the University of Nevada, Reno. Dr. Daemen received his Ph.D. in Geological Engineering from the University of Minnesota where his research involved development of the analytical and numerical solutions for

ground support – rock mass interaction. His current research involves time-dependent testing of joints and intact tuff from the Yucca Mountain nuclear waste disposal site.

The second independent technical review is provided by Mr. Ronald Price and Dr. Randolph Martin. Mr. Price is a Senior Member of Technical Staff at Sandia National Laboratories in Albuquerque, New Mexico. He has a M.S. in Geology from the Center for Tectonophysics at Texas A&M University. Since his arrival at Sandia in 1980, Mr. Price has planned, carried out and published results from laboratory studies on many different rock types and for many applications, with special emphasis on Yucca Mountain tuffs, for over 22 years. Dr. Martin is the President of and Principal Scientist at New England Research, Inc. in White River Junction, Vermont. He has a Ph.D. from MIT and has a wide range of experience managing and performing both field and laboratory rock mechanics projects, specifically including time-dependent crack growth and creep of rocks. Dr. Martin's seminal work in the area of static fatigue, coupled with Mr. Price's depth of knowledge of tuff rheological properties, makes them particularly valuable in the review of this material.

The technical review reports are provided in Appendix S (Section S5). In general, the technical reviews find the PFC stress corrosion approach to be adequate for the simulation of long-term drift degradation. The model approach, data selection and ranges were found to be adequate. The model boundary conditions and methodology for application of the static-fatigue test data were also felt to be proper. The reviewers noted that limited test data to build confidence in the model is the model's primary limitation. Since the technical reviews have been completed, additional time-dependent testing data has been provided and is included in the analysis of time-dependent drift degradation (Section 6.4.2.4.2).

7.5.2.4 Conclusion from Particle Flow Code (PFC) Model Validation - Comparison to Criteria

Consistent with the stated level of confidence required for the model, the above PFC studies have shown the following:

- The PFC model is able to reproduce the basic failure mechanisms observed in the laboratory for nonlithophysal and lithophysal rocks (lithophysal rock validation criteria, Section 7.2.3).

- The model provides information that allows understanding of the detailed mechanism of failure in lithophysal rocks and accounts for the strength and moduli reduction mechanism with increasing lithophysal void percentage. The presence of voids in a sample under compression creates stress concentrations around the voids, promoting tensile splitting phenomena between voids. The result is a weakening effect that increases as a function of increasing void volume, and decreasing web thickness between voids (lithophysal rock validation criteria, Section 7.2.3).

- The strength and modulus reduction with void porosity predicted by the model compares reasonably well with that observed in the laboratory. Thus, the PFC model is able to capture the impact of lithophysal porosity variability on strength and deformability properties (lithophysal rock validation criteria, Section 7.2.3).

- The PFC model is able to spontaneously reproduce the basic time-dependency behavior of the tuff as determined from creep testing. The model is able to reasonably reproduce the primary, secondary and tertiary phases of creep, and provides an understanding of the underlying mechanism of stress corrosion-based microcrack propagation.

7.6 DEVELOPMENT AND VALIDATION OF A DRIFT-SCALE MODELING METHOD FOR LITHOPHYSAL ROCK USING THE UDEC PROGRAM

As was noted in Section 7.1, the PFC program is computationally intensive and, therefore, not particularly practical for use as a modeling tool for drift-scale analyses as required. The method used here is to calibrate a similar modeling approach based on the UDEC (Section 3.1) discontinuum program to the laboratory data and then validate this approach against:

- Observations of failure mechanism in the laboratory
- Field observations of tunnel response in the ECRB Cross-Drift
- Thermally induced fracture development in the Drift Scale Test within the Tptpmn unit
- Literature data from related field experiments in which blast-induced yield of a jointed rock mass and large deformations of a scaled, lined tunnel are induced.
- Comparison of the output predictions of rock mass stress and yield around emplacement drifts using the UDEC discontinuum model of lithophysal rock model to alternative continuum-based representations of the mechanical response of lithophysal rock.

Figure 7-4 provides a flow chart illustrating the calibration and validation strategy for UDEC. The following section describes the validation of the UDEC lithophysal rockfall model and exploration of its limitations.

7.6.1 Qualification of the UDEC Program (Confidence Building During Model Development)

The UDEC program has been qualified as documented in Section 3. The software documentation contained in the UDEC user's manuals (Itasca Consulting Group 2002 [DIRS 160331]) provides details of the analytical development of the program and the mechanical basis for the material constitutive models that it uses. Extensive documentation (Itasca Consulting Group 2002) is dedicated to verification of the ability of the model to solve analytical solutions that test the various aspects of the model (e.g., mechanical, thermal, porous media flow, dynamics).

7.6.2 Justification for a Two-Dimensional Isotropic Model of the Lithophysal Rock (Confidence Building During Model Development)

As was discussed in Section 7.3, the lithophysal units, particularly lower lithophysal zone (Tptpll), are characterized by the presence of more-or-less uniformly distributed voids (lithophysae) of varying size (from centimeter size to over 1 m in diameter). The lithophysae account for up to about 30 percent of the rock mass. Additionally, in the Tptpll, intense, short

trace length interlithophysae fracturing exists. Average joint spacing is on the order of cm to dm, creating block dimensions on the order of the fracture spacings, or cm to dm in dimension.

Under such conditions, representation of lithophysal rock units, in the models of drift stability, as a homogeneous, isotropic rock mass is appropriate. The size of the internal structure and spacing is much smaller than the drift size (i.e., 5.5-m diameter). There is no preferred direction in the orientation that would justify introduction of anisotropy. Heterogeneity was considered on the scale of the repository. The analysis was conducted using different properties of the rock mass to investigate the effect of varying quality of rock mass on drift stability. However, properties inside each model were considered homogeneous. Under such conditions, when there is no internal structure in the model, and properties are isotropic and homogeneous, the drift stability analysis was conducted using a two-dimensional model in the plane perpendicular to the drift axis. The model results of rockfall prediction (in a cross-section characterized by particular rock mass properties) are then used for estimating overall rockfall in the entire repository based on estimated distribution of different rock mass qualities throughout the repository.

7.6.3 Rock Mass Properties for Model Calibration

The rock mass properties for lithophysal rock mass were determined based on:

- Laboratory testing on 10.5-in diameter cores of Tptpll from Busted Butte
- Laboratory testing on 11.5-in diameter cores of Tptpll and Tptpul from ESF main loop and ECRB Cross-Drift
- PFC and UDEC extrapolations of mechanical response under triaxial stress conditions.

The division of rock mass properties into five categories based on the lithophysal porosity and size effect is described in Appendix E, Section E.4 and is shown graphically in Figure 7-16.

7.6.4 Model Calibration (Confidence Building During Model Development)

The two-dimensional distinct element code, UDEC (Section 3.1), is used here for drift stability analysis. The rock mass is represented as an assembly of polygonal, elastic blocks (Figure 7-18) that are bonded together across their boundaries to form a coherent solid. The goal is to provide a rock mass in which the overall mechanical behavior of the mass is consistent with the material model developed for the lithophysal rock, yet allow internal fracturing to form and blocks to loosen and detach as the evolving stress state dictates. In other words, the fractures are "invisible" to the model until yielding begins.

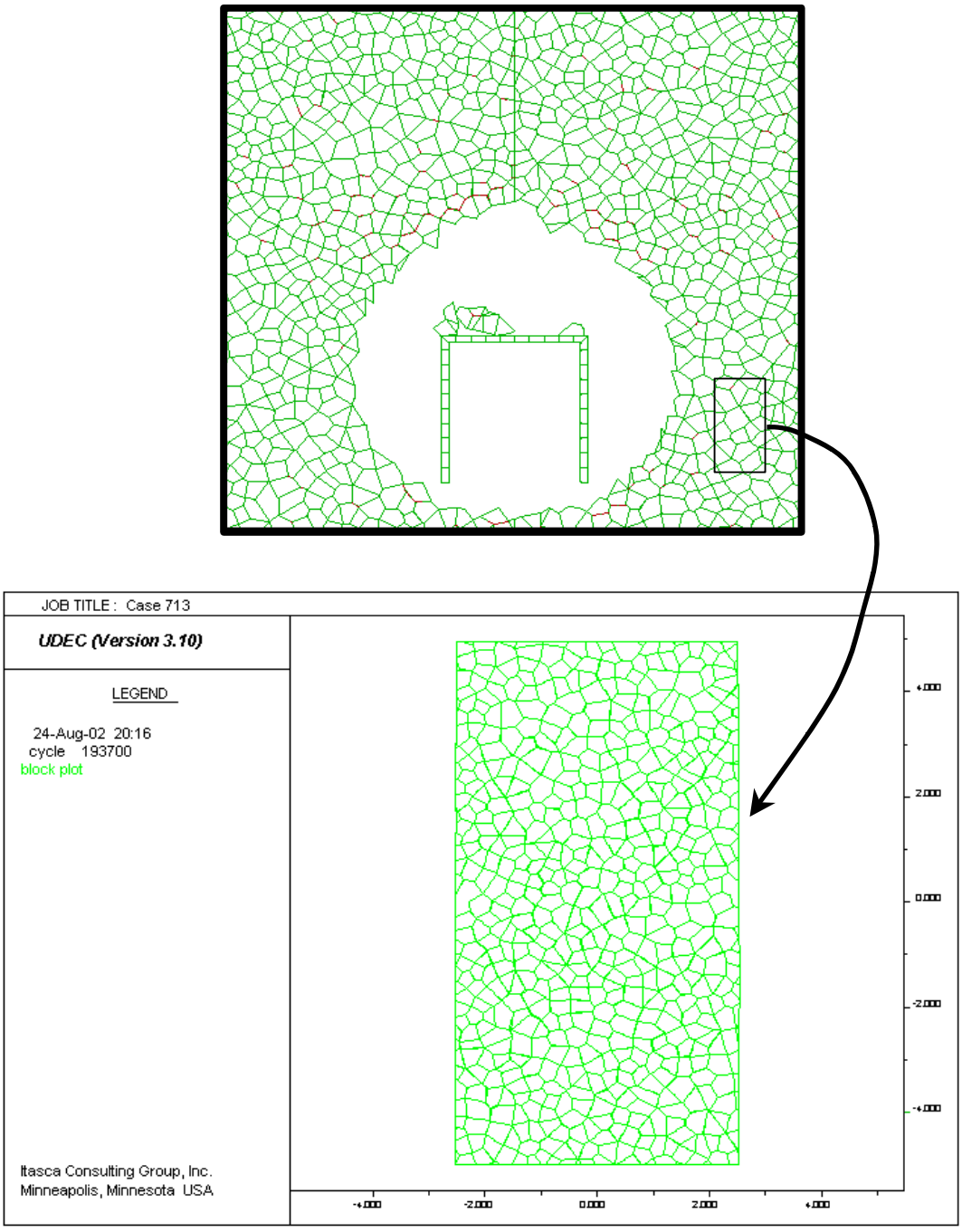

NOTE: Blocks are bonded at their contacts with a cohesion and tensile strength. When these break, the contacts become purely frictional. Specimen is "sampled" from equivalent rock mass representing the Tptpll.

Figure 7-18. UDEC Lithophysal Rock Specimen Composed of Many Irregular Blocks with Roughly Equi-Dimensional Side Lengths

Since the block boundaries can fail in tension and shear, they act as "potential or incipient fracture" locations should the stresses dictate that fracture is possible. It is important that the block assemblage contain blocks that are sufficiently small such that the model does not dictate where and how fractures can form and propagate. The entire tunnel domain is discretized into small blocks (using Voronoi tessellations, see Itasca Consulting Group 2002 [DIRS 160331]) that are roughly consistent with the maximum block size expected from core fracture spacings. The potential fractures between blocks are considered to behave mechanically according to a linearly elastic-perfectly plastic model. The elastic behavior of potential fractures is controlled by constant normal and shear stiffness, and are consistent with the Young's modulus of the intact rock blocks. The possible failure modes of the rock mass are controlled by the strength of the fractures. The fractures can sustain a finite tensile stress, whereas a Coulomb slip condition governs the onset of slip, as a function of joint cohesion and friction angle. If a potential fracture fails, either in tension or shear, tensile strength and cohesion are set to zero, whereas the friction angle is set to the residual value. This model allows for the formation of fractures between blocks, separation and instability (under action of gravity) of portions of the rock mass around a drift.

The blocks used in the UDEC lithophysal rockfall model do not represent the actual internal structure of the lithophysal rock mass. They are a tool in the numerical model used to simulate damage and fracturing of the rock mass (i.e., the potential fractures in this model do not correspond to actual features). Therefore, it is not possible to *directly* obtain the potential fracture properties in the UDEC lithophysal rockfall model to results of laboratory or field testing on samples of lithophysal rock. To assure that an assembly of Voronoi blocks behaves as a lithophysal rock mass, it has to be calibrated. Calibration is done by numerical simulation of tests (e.g., unconfined compressive strength tests), which are actually conducted in the laboratory or the field, and for which the test results are available. During the numerical experiment (calibration), the model parameters (i.e., potential fracture properties) are varied until macro-properties of the rock mass important for the drift stability analysis (e.g., Young's modulus and unconfined compressive strength) are matched with measurements from the actual tests. When the calibration is completed it is possible to say that the synthetic material (i.e., the assembly of Voronoi blocks) behaves (on the scale of a drift) equivalently to the lithophysal rock mass. Following calibration, the model can be used to conduct additional simulations under biaxial compression and tension to produce the yield criteria for the material. These yield criteria can be compared to typical empirically derived yield criteria for other rock types as a means of verification of the model.

The following parameters characterize the mechanical behavior of the UDEC Voronoi model:

- The block size scaled to the model size, or a number of blocks in the model.
- Elastic properties of blocks (E^m, ν^m).
- Properties of joints, both elastic (normal stiffness, k_n, and shear stiffness, k_s) and plastic (tensile strength, t^m, cohesion, c^m, and friction, ϕ^m). Note that plastic joint parameters are functions of shear and tensile plastic strains. In the simulations presented in this report, it is considered that cohesion and tensile strength soften to zero at the onset of yield.

The micro properties are illustrated in Figure 7-19. Because of the geometrical complexity of the model, a direct functional correlation between micro- and macro-properties (model response on a large scale) does not exist. Therefore, to match model macro-behavior, it is necessary to calibrate the model. During the calibration, which is done during simulation of simple uniaxial and biaxial experiments, the micro-properties are adjusted until the desired macro-behavior is matched. The calibration uses a trial-and-error approach, but some understanding of the model mechanics and previous experience can expedite convergence of the iterative process.

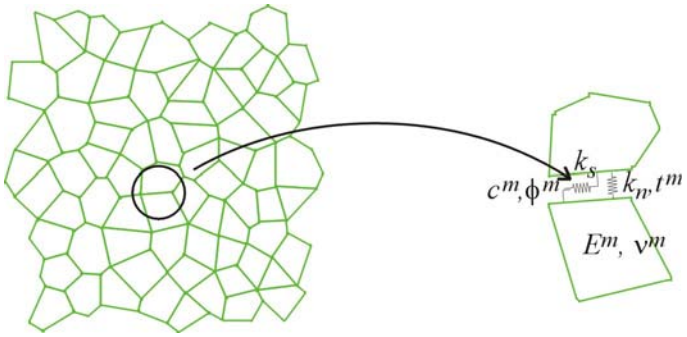

Figure 7-19. Micro Properties of the UDEC Voronoi Model

Elastic and strength properties can be decoupled during the iteration process (i.e., model deformability and strength can be calibrated separately). It is common to calibrate model elastic parameters first. Clearly, calibration of the elastic properties is a problem with a non-unique solution. The two elastic macro-properties (E and ν) are functions of block size and four micro properties (k_n, k_s, E^m, and ν^m). The block size is determined based on observed fracture spacing and the condition that the ratio between the drift radius and the block size is sufficiently large (>15). The Poisson's ratio of the blocks is selected to be equal to the macro Poisson's ratio, such that $\nu^m = \nu$. The additional requirement needed to match the macro Poisson's ratio is that the ratio between normal and shear joint stiffnesses is larger than 1. Simulations confirm that a Poisson's ratio of 0.2 is matched when $k_n / k_s \approx 2$. It is reasonable that the contribution of joints to model deformability is larger than the contribution of blocks, but it is desirable, from the perspective of convergence of the numerical model, that stiffnesses of blocks and joints are of the same order of magnitude. Therefore, based on guidance in the UDEC User's Manual (Itasca Consulting Group 2002 [DIRS 160331], Manuals/UDEC/User's Guide/Section 3: Problem Solving, Section 3.2.3), it was selected that

$$5 < \frac{K^m + \frac{4}{3} G^m}{b\, k_n} < 10 \qquad \text{(Eq. 7-4)}$$

where b is the average block size, and K^m and G^m are the bulk and shear moduli of the blocks, respectively. With these considerations, there is a single independent elastic micro-parameter (e.g., k_n). The proper macro deformability of the model is than matched by rescaling of the elastic micro-properties (k_n, k_s, K^m, and G^m).

Calibration of strength micro properties involves matching macro failure envelope and post-peak behavior by adjusting strength micro-properties. Note that model plastic deformation appears to be a function of the size and shape of blocks. The failure envelope, which, in general, is a surface in the principal stress space, reduces to a line if it is considered that the failure envelope is not a function of the intermediate principal stress. Test runs have proven that the micro friction angle, which is initially equal to 35° and softens in a brittle fashion to 15°, results in the desired post-peak behavior and strength increase as a function of confinement. In order to match the observed mode of failure of non-lithophysal tuff under unconfined loading conditions (i.e., axial splitting), the micro tensile strength is assigned to be less than 50 percent of the micro cohesion. After these relations are established, the proper peak strength is matched by rescaling micro cohesion and tensile strength.

Stress-strain curves obtained from numerical experiments with different conditions of confinement (unconfined, 1-MPa confinement, and 3-MPa confinement) and loading (tension and compression) are shown in Figure 7-20. The mode of failure is also illustrated for each case by a plot of displacement vectors at the final state of the model. The model matches unconfined compressive strength of 10 MPa and Young's modulus of 1.9 GPa for Category 1 (Table E-10). Laboratory testing data on the post-peak behavior of lithophysal rock is inconclusive. However, the model exhibits qualitatively reasonable post-peak behavior. The response for low confinement is brittle (see unconfined compressive strength curve in Figure 7-20). As confinement increases the response becomes more ductile, almost perfectly plastic for 3-MPa confinements (Figure 7-20). The mode of sample failure in the case of unconfined compressive strength is axial splitting, similarly to observations from laboratory experiments. The mode of failure for confined cases becomes more of the "shear band" type.

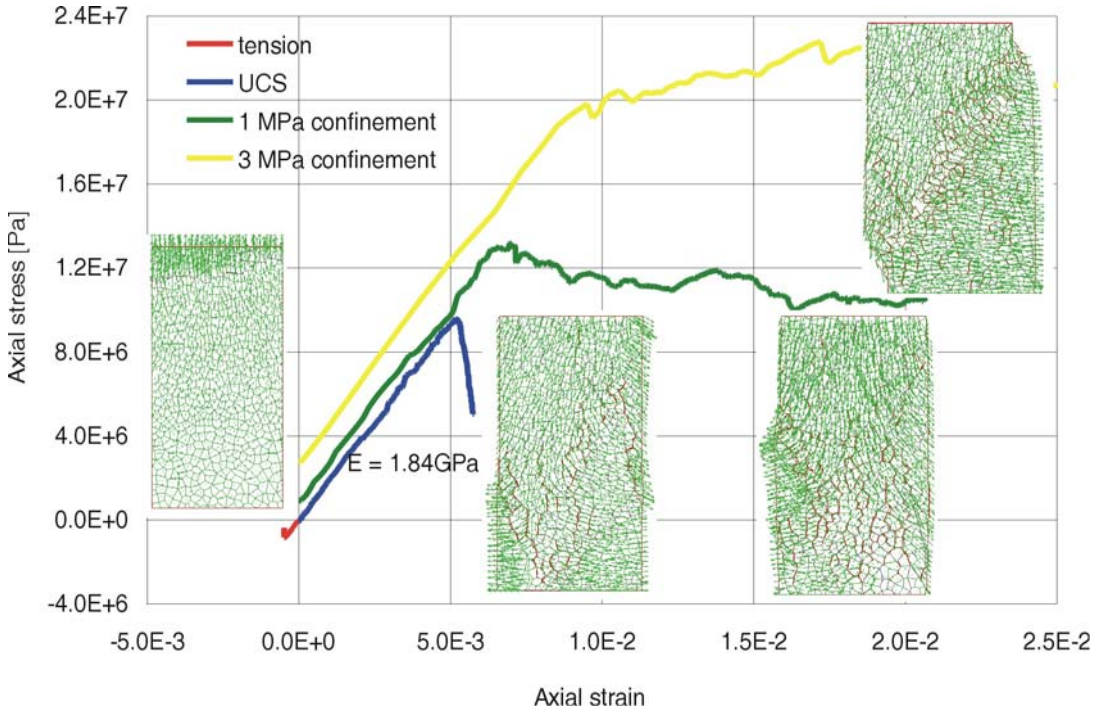

Figure 7-20. Numerical Experiment, Category 1: Stress-Strain Curves and Modes of Failure for Different Confinements and Loading Conditions

The failure envelope in the principal stress space, constructed based on numerical tests at different confinement levels, is shown in Figure 7-21. The failure envelope is curvilinear, as expected for a rock mass (similar to Hoek-Brown failure criterion). The initial friction angle (in the range of confining stress, σ_3, between 0 and 1 MPa) is 33°, but it decreases for larger confinement. The ratio between uniaxial compressive and tensile strengths is larger than 10.

The volumetric deformation of the model during the experiments is illustrated in Figure 7-22, which shows curves of volumetric strain versus axial strain. In general, these curves are bilinear. Initially, while the sample behaves elastically, its volume reduces due to the Poisson's effect. The initial slope of the curves is a function of the Poisson's ratio. Thus, the Poisson's ratio, ν, of the synthetic material can be calculated from the initial slope of the curve, s_e, according to the following formula derived from elasticity theory:

$$\nu = \frac{1 - s_e}{2 - s_e} \qquad \text{(Eq. 7-5)}$$

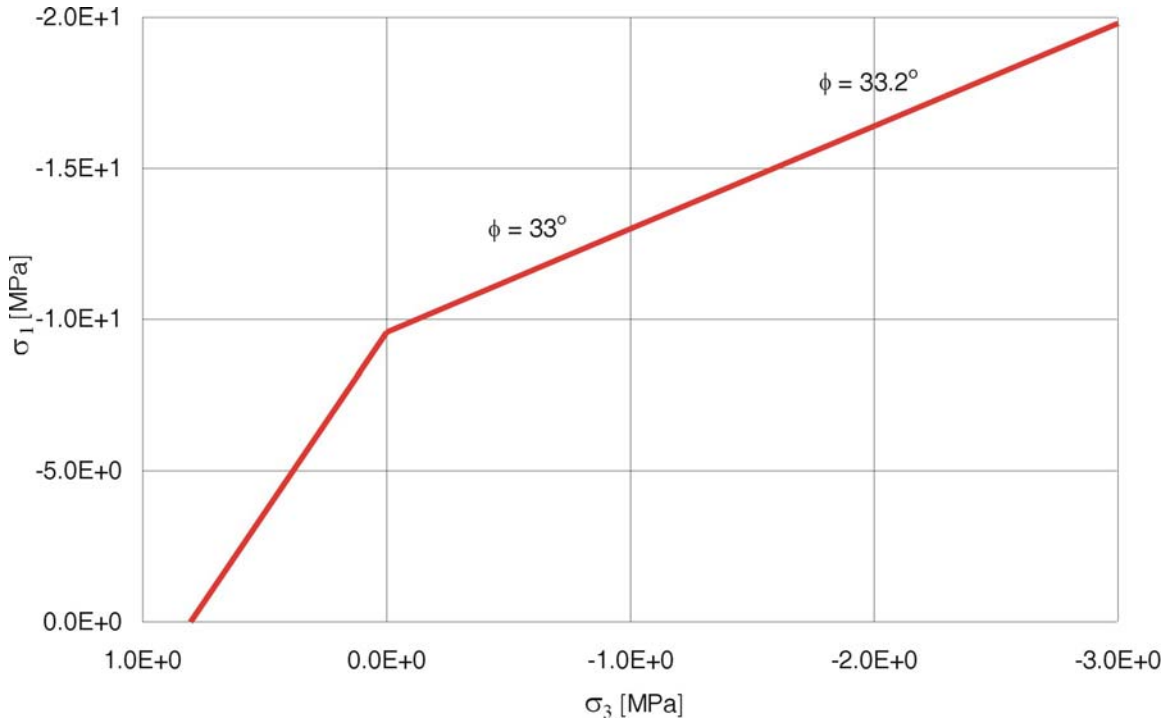

Figure 7-21. Numerical Experiment, Category 1: Failure Envelope

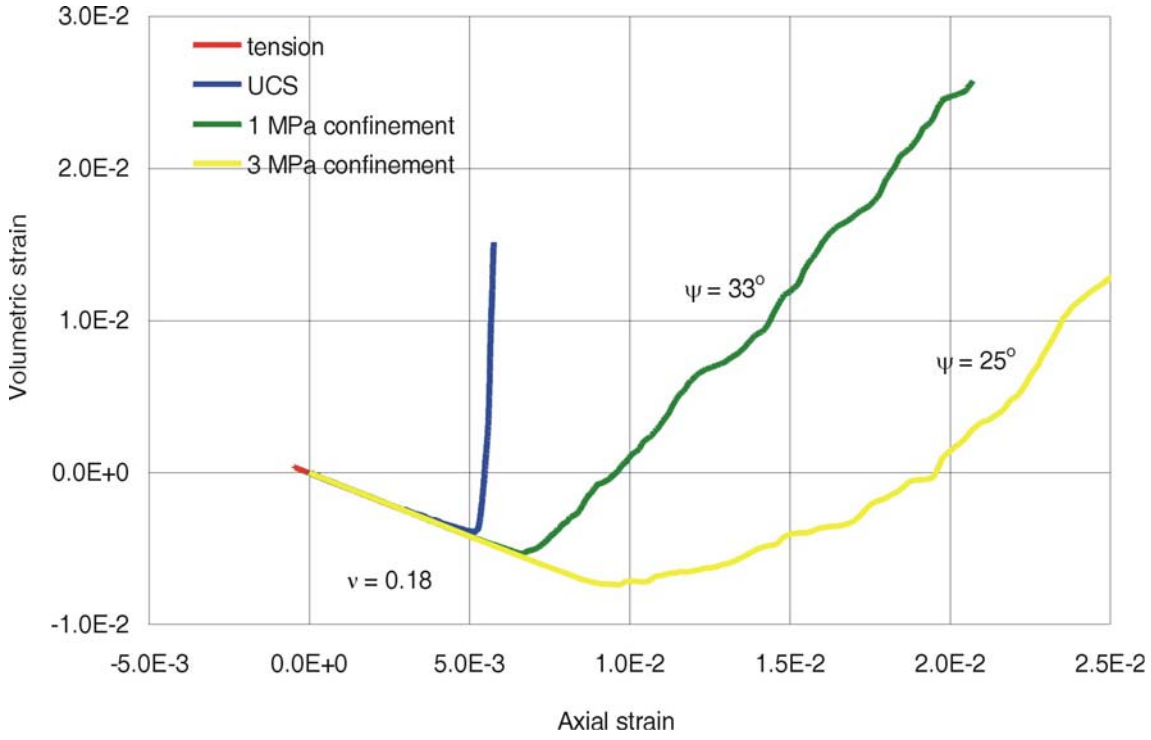

Figure 7-22. Numerical Experiment, Category 1: Volumetric Strain Versus Axial Strain for Different Confinements and Loading Conditions

As the material yields and starts plastic deformation, it usually dilates (increases volume). Consequently the curves in Figure 7-22 change the slope. Initially negative slopes, indicating contraction, become positive, indicating dilation. The slope of the curves during plastic deformation is a function of the dilation angle, which is the parameter used to characterize plastic volumetric deformation. The dilation angle, ψ, of the synthetic material can be calculated from the post-peak slope of the curve, s_p, according to the following formula, which was derived from Mohr-Coulomb plastic flow equations in *Itasca Software–Cutting Edge Tools for Computational Mechanics* (Itasca Consulting Group 2002 [DIRS 160331]):

$$\psi = \arcsin\left(\frac{s_p}{s_p + 2}\right) \qquad \text{(Eq. 7-6)}$$

The synthetic material clearly exhibits a very large dilation angle for unconfined compressive strength. Such behavior is expected because micro damage of the material during unconfined compressive strength testing is predominantly tensile fracturing, which results in extremely large dilation.

7.6.5 Post-Development Validation Strategy

Once calibrated, the UDEC lithophysal rockfall model and properties require validation against field observations and testing. The model is also validated against laboratory failure mechanisms and drift scale response by:

- Comparison of lithophysal sample failure mechanisms in the laboratory
- Comparison of the prediction of drift scale fracturing in the Tptpll at ECRB Cross-Drift depth to observations of tunnel sidewall fracturing in the ECRB Cross-Drift
- Comparison of roof spalling in the Drift Scale Heater Test in the Tptpmn during thermal overdrive experiments to UDEC lithophysal rockfall model predictions
- Comparison of several different numerical modeling techniques to UDEC for a field simulation of steel tube-reinforced tunnel to dynamic loading from a blast
- Additionally, the capabilities of the UDEC program for representing dynamic response of jointed or fractured media is demonstrated by code-to-code comparisons conducted through past dynamic tunnel stability analysis for the Defense Nuclear Agency.

7.6.5.1 UDEC Post-Development Validation Exercise 1 - Comparison of Predicted Failure Modes to Laboratory Observations (Corroboration with Relevant Observations)

The UDEC "potential fracture" model is formulated to allow fractures to form as the stresses dictate. An initial and simple validation is to compare the predictions of the model to observations and common knowledge from laboratory testing. In uniaxial compression, with 2:1 length-to-diameter specimens, the failure mode is typically in the form of axial splitting, or coalescence of axially oriented fractures observable on the surface of the sample. Figure 7-23 presents a typical UDEC plot of predicted fracturing (red tensile cracks) that forms axial to the sample axis. The block structure of the sample was previously shown in Figure 7-18, but is not shown in Figure 7-23 so that the formed cracks are clearly seen. The typical laboratory failure response is shown in the associated photograph of a large core sample from the Tptpul after testing. The axial fractures are clearly visible in this photo. The UDEC lithophysal rockfall model further is able to produce typical tensile fracture orientation from a simulated direct tension test (Figure 7-24). The model will seek out a unique fracture path composed of coalescing "potential fractures" to form a distinct separation plane.

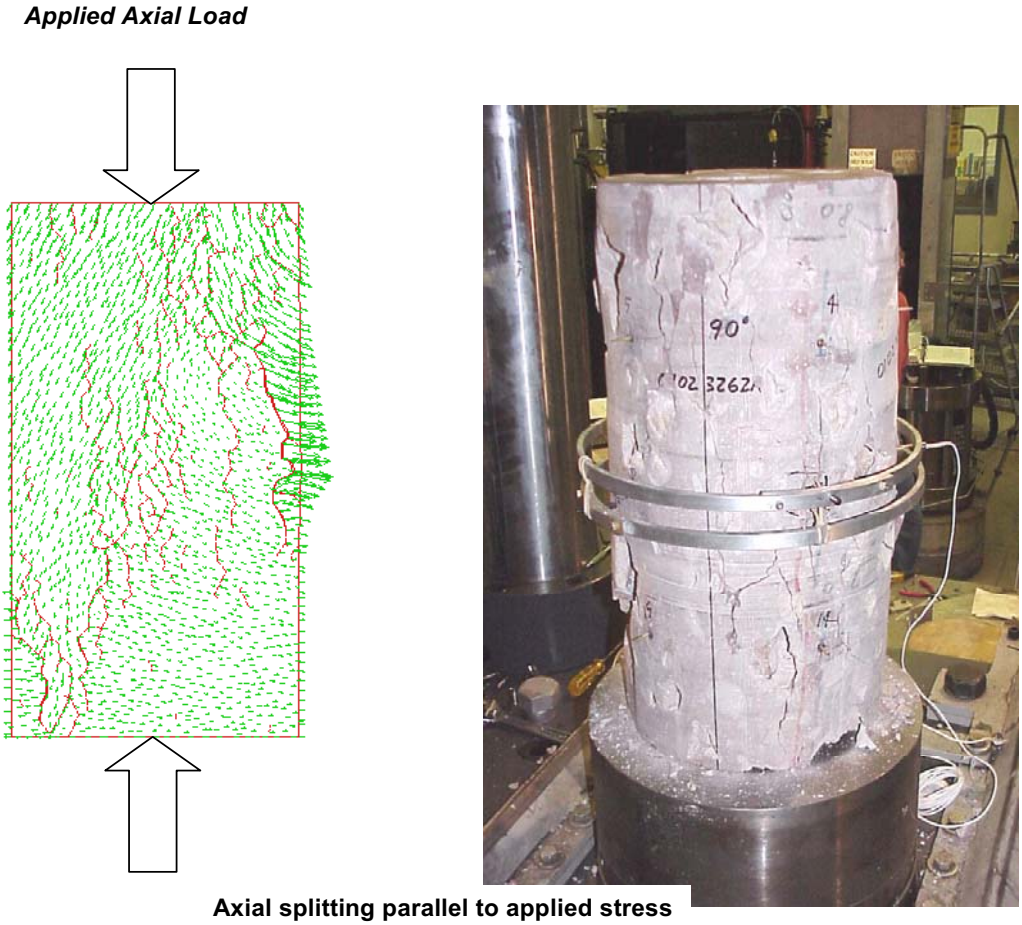

NOTE: The model predicts axial splitting when no confinement is applied as seen by the red tensile block boundary breakages (fractures) formed and by the velocity vectors that show the sidewall spalling. Core photo shows similar axial splitting phenomena.

Figure 7-23. UDEC Discontinuum Model of Failure of Lithophysal Tuff Specimen Under Uniaxial Compression

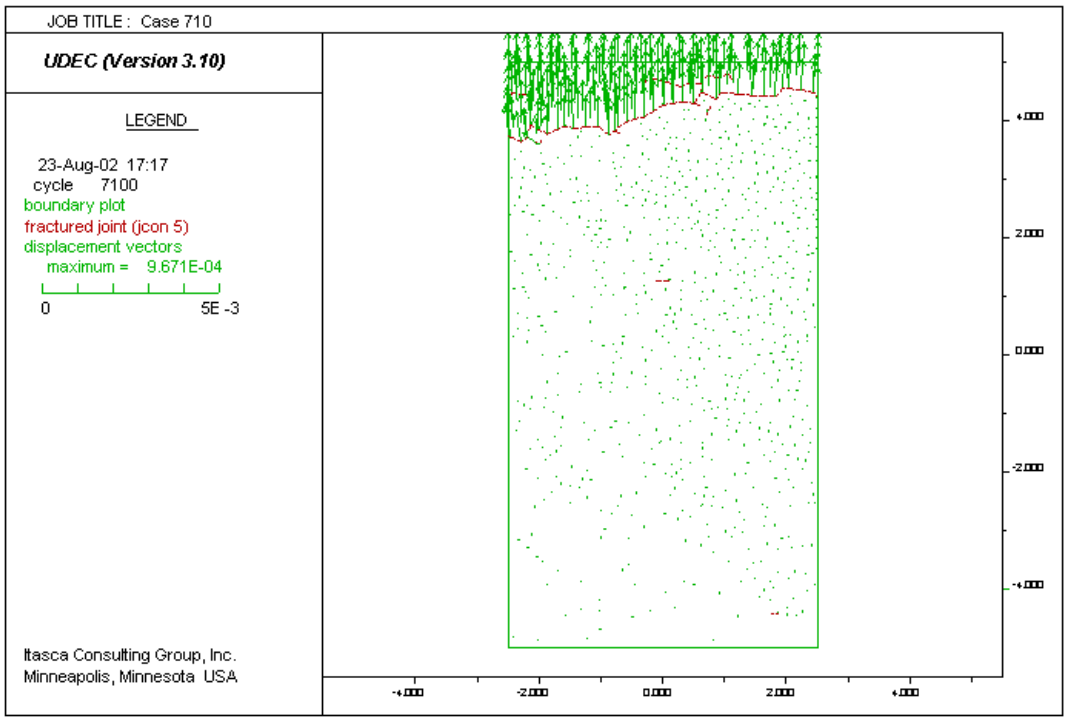

NOTE: A distinct tensile fracture formed from coalescence of individual breakages.

Figure 7-24. Predicted Failure Mode of UDEC Sample in Direct Tension Test

7.6.5.2 UDEC Post-Development Validation Exercise 2 - Comparison of Model Predictions to Observations in the ECRB Cross-Drift (Corroboration with Field Observations)

The proposed modeling approach was verified by comparison of predicted in situ stress-induced damage to the minor damage observed in sidewalls of ESF main loop and ECRB Cross-Drift in the lowest quality Tptpll. Additionally, no sidewall damage is observed in drifts in higher quality Tptpul at shallower depth. Tunnels in all rock units are stable after excavation, regardless of depth or rock quality. However, some damage, in the form of wall parallel fractures (opening of existing fracture fabric) at the springline (the point of highest shearing stress), can be observed in the sidewalls of the tunnels at greater depth in the Tptpll. Figure 7-25 shows formation/opening of wall-parallel fractures observed in 12-in. diameter boreholes drilled for geomechanical sampling in the sidewalls of the ESF main loop and ECRB Cross-Drift at the tunnel springline. The wall-parallel fractures are typical of stress-induced yield in tunnels. The boreholes drilled in the relatively low quality Tptpll at depths of 300 to 350 m show sidewall fracturing to depths of approximately 0.5 to 0.6 m. Holes drilled into relatively high quality Tptpul at depths of approximately 200 to 250 m show no fracturing.

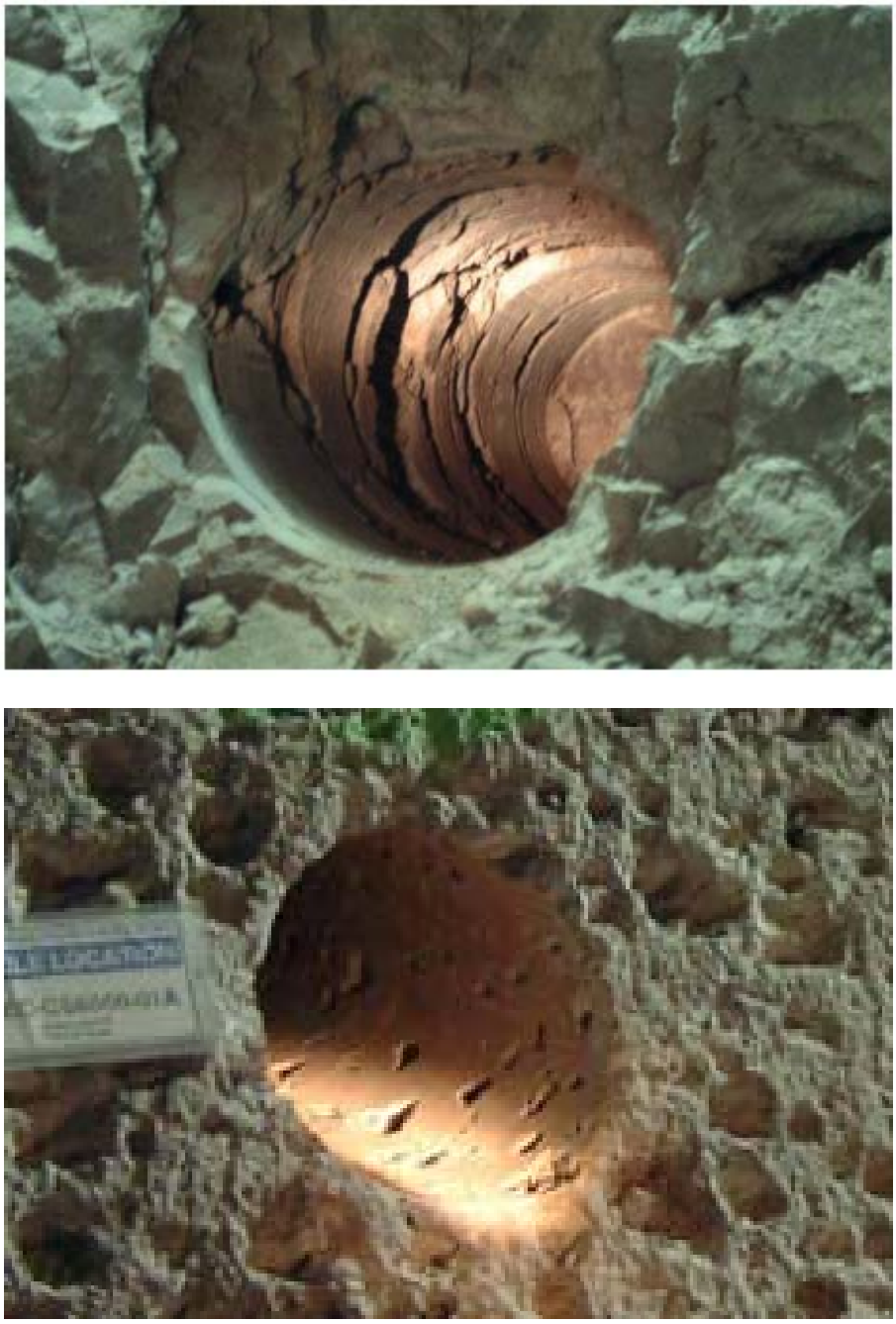

NOTE: Top photo shows sidewall fracturing/opening of preexisting wall-parallel fractures in a 12” diameter horizontal borehole drilled in the springline of the ESF in low quality Tptpll (approximately Category 1). Overburden depth is approximately 325 m. Depth of fracturing is approximately 1.5 to 2 ft (0.46 to 0.61m). The bottom photo shows a horizontal, 12-in diameter borehole drilled in the springline in good quality Tptpul (approximately Category 5) in ESF near site of slot test 2 showing no sidewall damage. The depth of overburden is approximately 250 m.

Figure 7-25. Observed Rock Mass Conditions at the Tunnel Springline in Lithophysal Rock in the ESF

The presence of these fractures and their depth into the drift wall, observed in large hole drilling, is a convenient feature from which an estimate of the rock mass strength properties and validation of the model can be made. A parametric study of drift stability and rock yield depth was conducted using the UDEC lithophysal model for the five strength categories (Appendix E, Section E.4) and imposed overburden depths of 250, 300, and 350 m, corresponding to the Tptpll and Tptpul. As seen in Figures 7-26 and 7-27, the model reproduces the approximate depth and orientation of drift wall-parallel fractures observed underground for strength Category 1. The failure of the rock is contained to the immediate springline due to the stress concentration resulting from the vertical maximum stress (vertical stress in MPa = 0.024 × depth (m), horizontal/vertical stress = 0.36 to 0.62 (SNF37100195002.001 [DIRS 131356])). The model results indicate that the rock adjacent to the drift wall yields in a state of uniaxial compression since the minimum stress at or near the drift wall is zero or small since the radial stress component is zero. The depth of fracturing is clearly visible in these models as the zone where stress relaxation has occurred. The models also show that, for the range of potential lithophysal rock properties, there is no drift wall yield at the depth of the Tptpul from strength Category 1.

In conclusion, this validation exercise shows that:

- The model is able to represent the observed wall fracturing at the Tptpll depth for a range of rock strengths that agree with laboratory measurements of uniaxial compressive strength (i.e., the observed yield is consistent with laboratory measured values).

- The model shows that reduction of depth to that of the Tptpul results in no yield of the drift wall, and thus no fracturing as observed.

7.6.5.3 UDEC Post-Development Validation Exercise 3 - Comparison of Model to Drift Scale Experiment in the Tptpmn (Corroboration with Field Experiments)

The Drift Scale Heater Test was conducted in the Tptpmn unit, primarily as a fluid migration experiment (Williams 2001 [DIRS 159516]). This test involved driving a 5-m × 5-m drift, 50-m in length completely within the Tptpmn. The drift was heated using simulated electrically heated canisters within the drift itself, as well as horizontally placed borehole heaters in the springline of the tunnel to additionally raise the ambient rock mass temperature (Figure 7-28). Heating was started in 1997 and lasted for four years until 2001. The experiment is currently in the cool-down phase. After three years of heating (from 1997 to 2000), the heater power was raised to provide a thermal overstressing condition. The rock temperature level was driven to approximately 200°C, or a maximum 180°C temperature rise. Spalling of rock was first observed in late 1999 as small chips of rock on the tunnel invert, however there was no observation of obvious larger rock fragments or bulking in the welded wire fabric. Therefore, it is unknown if these small particles are related to thermal stress effects. In April 2001, obvious loose rock was observed at several locations in the crown of the tunnel, contained behind the wire mesh (Figure 7-29). At least four zones of loosened rock were observed along the tunnel crown, using the rail mounted remote camera. It is not clear that these are all of the zones of spalling due to the difficulty in observation using this camera technique, however, it is clear that they are largely congregated along the tunnel crown. The rock plates held within the welded wire fabric from about 5 to 20 cm. This type of "slabbing" is typical of hard, brittle rock masses subjected to horizontal stresses in the crown that exceed their uniaxial compressive strength.

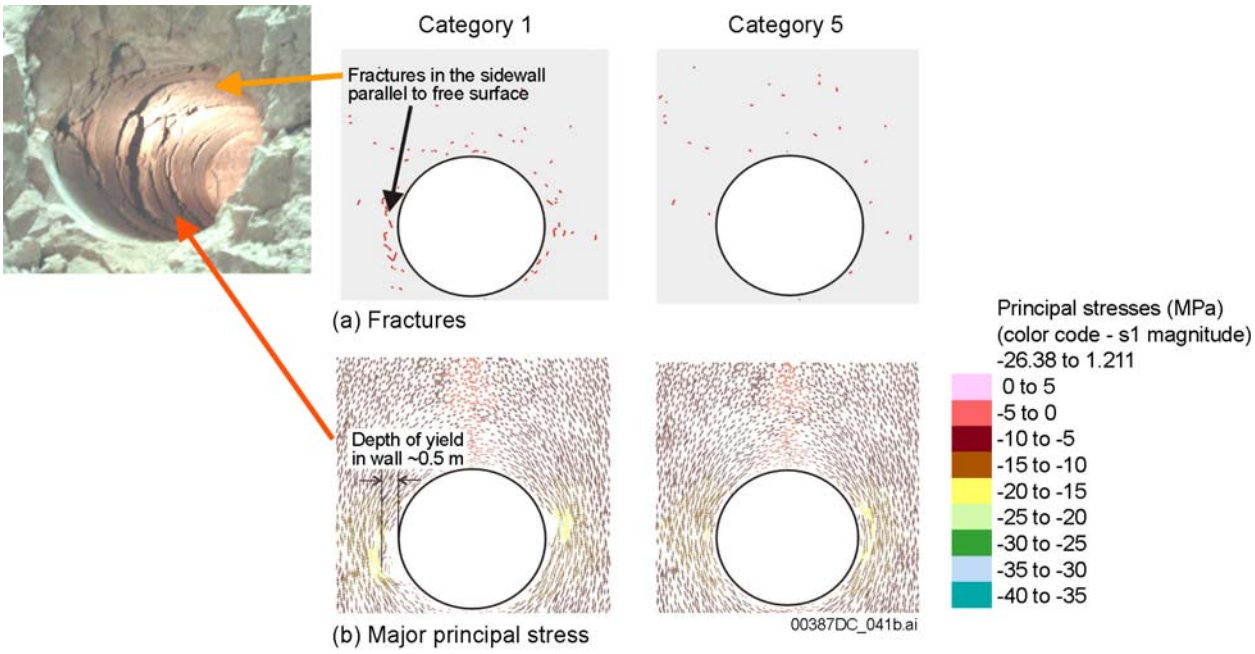

NOTE: Upper figure for Category 1 shows predicted fracturing to a depth of approximately 0.5 m in the sidewall of ECRB Cross-Drift. Lower picture shows stress vectors (in Pa) colored by the magnitude of the stress component. Depth of yield for Category 1 is limited to about 0.5 m in the immediate springline area. The model for Category 5 shows elastic rock mass response (i.e., no yield). Stress vectors in lower figure also shows elastic stress distributions with no readjustment due to yielding.

Figure 7-26. Estimate of Rock Mass Fracturing and Stress State Under In Situ Loading Only, Depth of 300 m, Tptpll, Strength Category 1 (Low-Strength Characteristics) and 5 (High-Strength Characteristics)

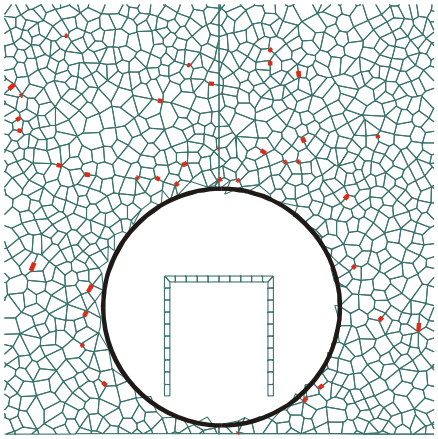

(a) Overburden at 250 m

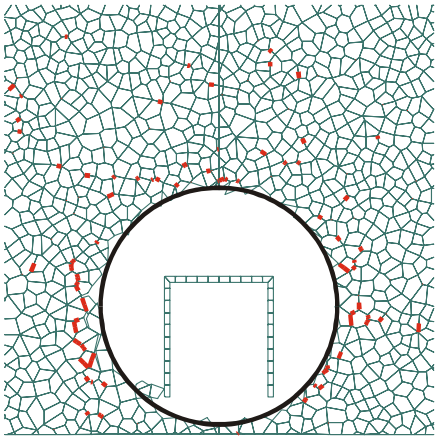

(b) Overburden at 300 m

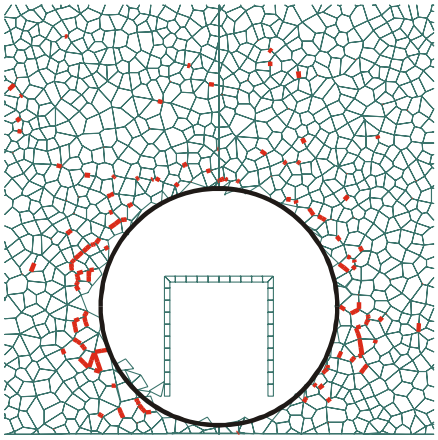

(c) Overburden at 350 m

Figure 7-27. Estimate of Stress-Induced Rock Mass Fracturing (seen as red block contacts) as a Function of Overburden Between 250 m and 350 m, Tptpll, Strength Category 1 (Low-Strength Characteristics)

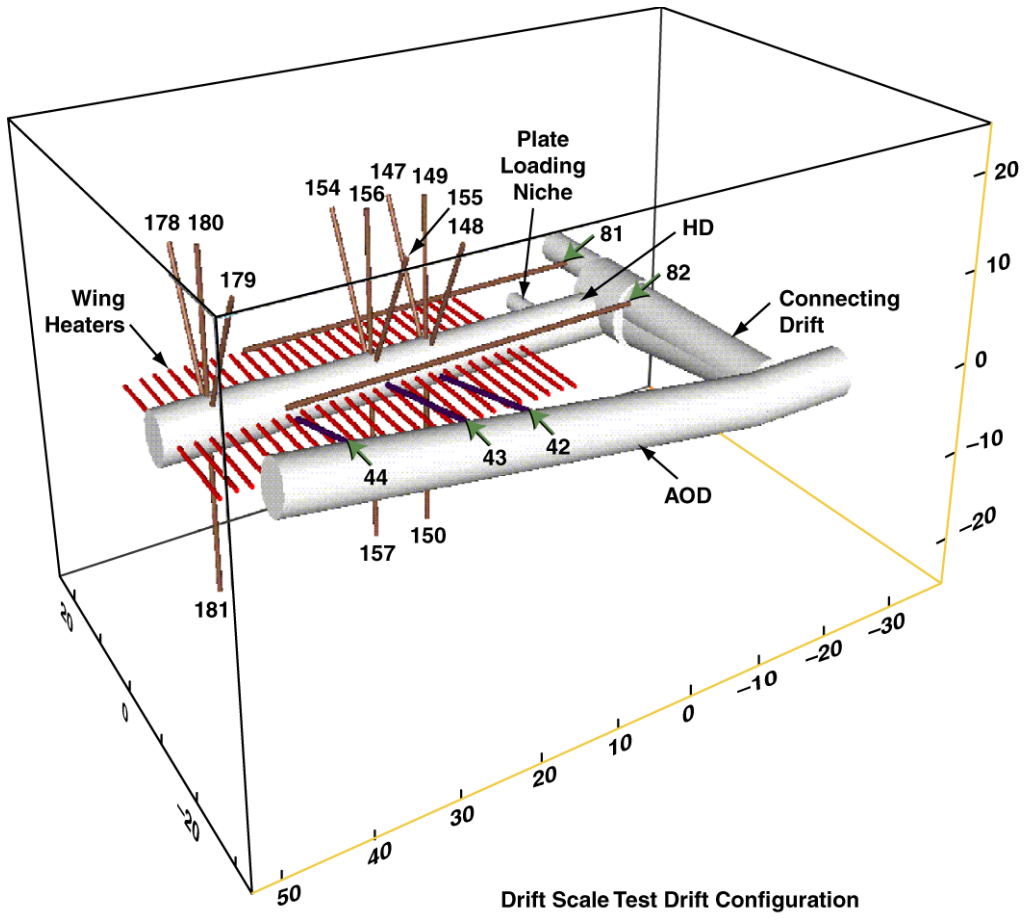

HD = Heated Drift; AOD = Access/Observation Drift

NOTE: Numbered boreholes contain rock mass monitoring instrumentation. Canister heaters are placed in the Heated Drift.

Figure 7-28. Perspective View of Heated Drift Scale Test Showing Wing Heaters

It is the goal of this validation exercise to demonstrate that the UDEC lithophysal rockfall model with random block subdivision is capable of reproducing thermal fracturing response at the proper approximate temperature and thermally induced stress levels as observed in the Drift Scale Heater Test. The first step in the validation is to calibrate the UDEC "potential" fracture properties against laboratory compression data. A compilation of the results of uniaxial compression strength test data for a range of sample sizes as described by Price (1986 [DIRS 106589]) is provided in Appendix E (Figure E-22). The sample sizes vary from 25 mm to approximately 230 mm, resulting in a curve that describes compressive strength as a function of sample size. Since the Drift Scale Heater Test represents in situ sample size, the UDEC lithophysal rockfall model is calibrated to the predicted field scale, represented by a sample size scale of approximately 1-m size, or 70 to 75 MPa, or about 50 percent of the strength of a standard 50-mm diameter sample (Figure E-22). This size-strength relationship compares quite favorably with suggestions for other rock types as used in common practice for rock engineering design purposes. Hoek (2000 [DIRS 160705]) suggests that the rock mass strength for a 1-m sample size approaches an approximate value of about 50 to 60 percent of the uniaxial compressive strength of 50-mm cores samples.

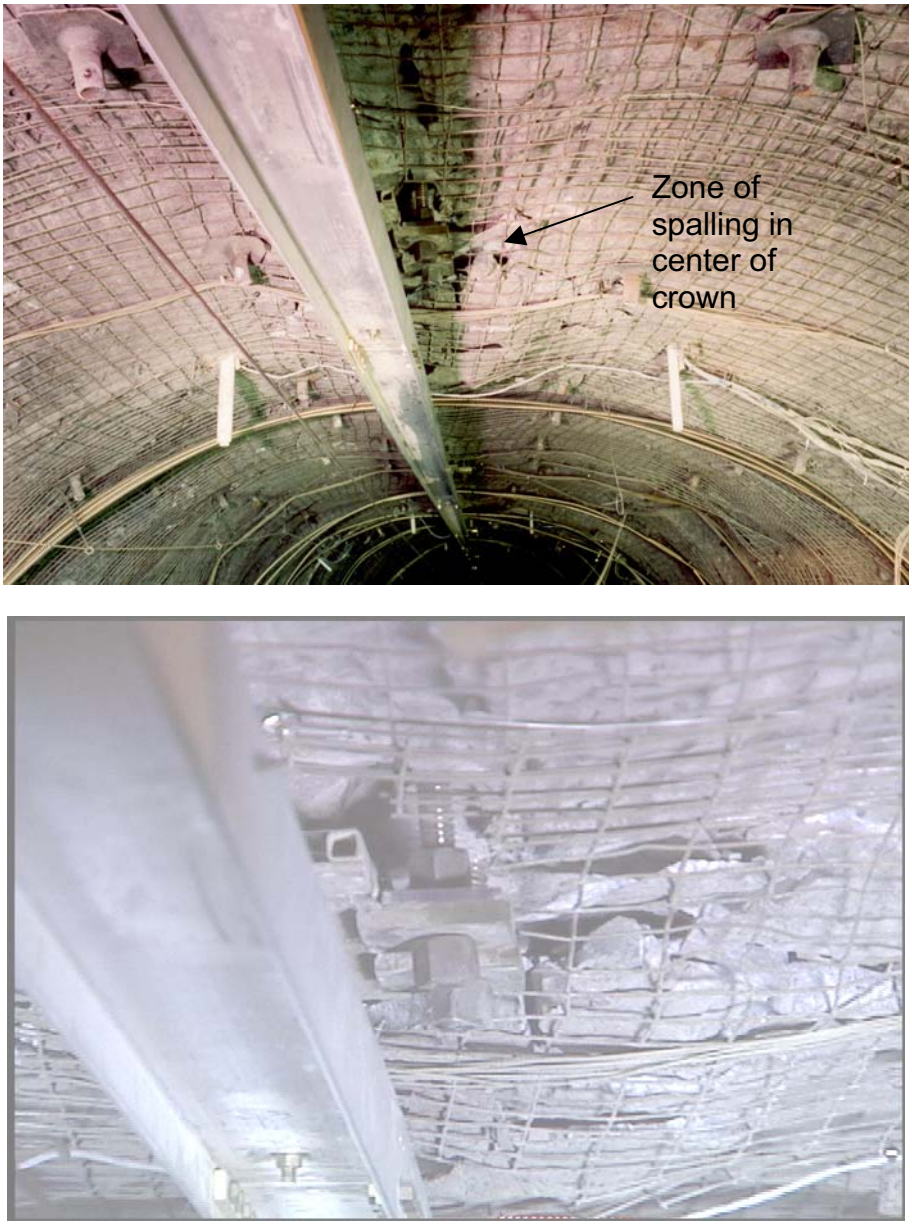

NOTE: Rock spalling is contained by 3-in × 3-in wire mesh and Swellex bolts. Top view shows general spalled region. Bottom view is a close up along the camera rail showing slabbing into small, flat pieces.

Figure 7-29. Minor Superficial Slabbing in the Center of the Roof Span Observed During Thermal Overstressing of the Heated Drift Scale Test

The UDEC lithophysal rockfall model was calibrated based on a sample uniaxial compressive strength of approximately 50 to 70 MPa, using an average Young's modulus of 30 GPa. The mean measured Young's modulus for Tptpmn data is 33.6 GPa ± 6.5 GPa from laboratory data (see Appendix E, Table E-6). Figure 7-30 shows the *representative* calibration of the UDEC equivalent Tptpmn material showing linear elastic behavior to peak strength, followed by a brittle post-peak failure mode. The term representative is used since the calibration is performed for a specific value of strength and modulus, whereas the data span a wide range of possible values. The rock mass surrounding the Drift Scale Heater Test drift was formed using randomly shaped, roughly spherical blocks using the Voronoi generation technique described in Section 6.4.2.1. The in situ stress state was selected to be 7 MPa vertical stress and 3.5 MPa lateral stress.

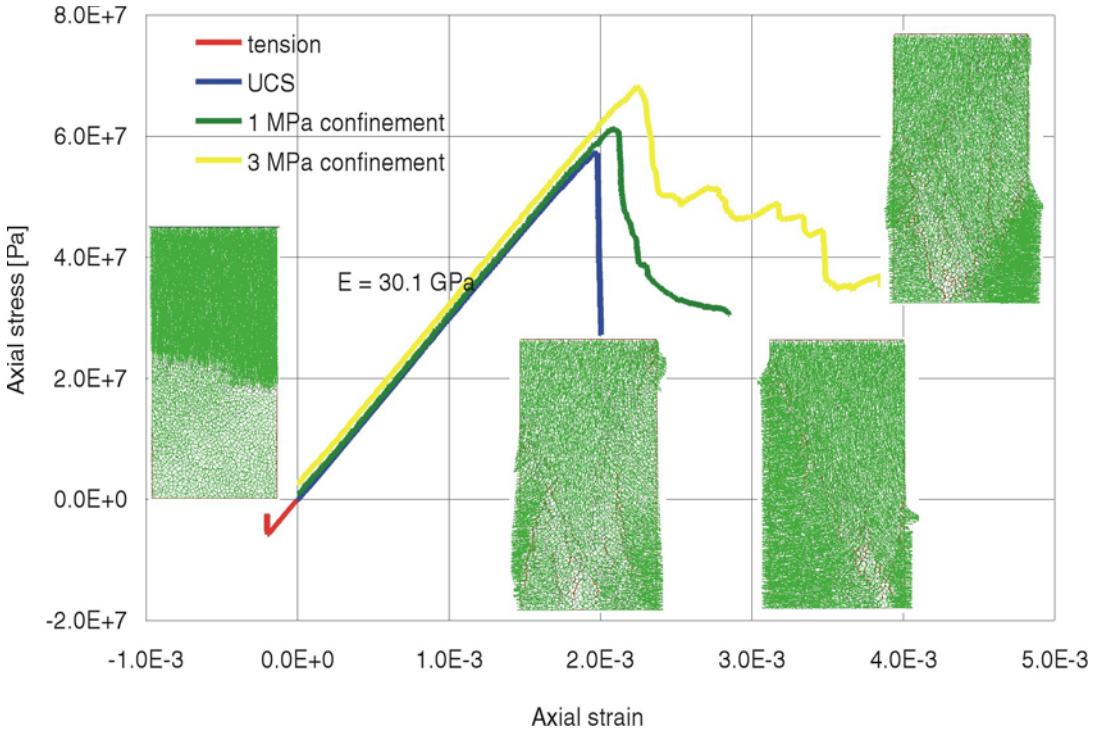

Figure 7-30. UDEC Sample Calibration to Size-Effect Strength Data for an Approximate 1-m Sample Size, Tptpmn

The model in situ stresses are applied and allowed to equilibrate prior to drift excavation. After excavation, the measured temperatures at thermocouple locations (DTNs: MO9807DSTSET01.000 [DIRS 113644]; MO9906DSTSET03.000 [DIRS 113673]; MO0001SEPDSTPC.000 [DIRS 153836]; MO0007SEPDSTPC.001 [DIRS 153707]; MO0107SEPDSTPC.003 [DIRS 158321]; MO0202SEPDSTTV.001 [DIRS 158320]; and MO0002ABBLSLDS.000 [DIRS 147304]) for a representative tunnel cross-section are used to linearly interpolate temperatures at UDEC lithophysal rockfall model gridpoints at successive one-year intervals. At each of these intervals, the model is allowed to equilibrate, developing thermally induced stresses that are added to the mining-induced stress conditions. The rock mass is free to fracture and deform under the influence of the stresses.

Figures 7-31 to 7-36 show the temperatures, major and minor principal stresses and predicted fracturing for the time period of 1997 to 2002. Initially, under mining-induced stresses only (1997), no fracturing of the rock mass has occurred. As early as 1998, the temperature rise in the rock mass exceeds 130°C around the drift periphery, and approximately 150°C along the wall heater holes. The vertically symmetric temperature field induces a significant tangential compression to the crown of the tunnel, which is approximately equal to the projected uniaxial compressive strength of the rock mass. A very small amount of non-coherent fracturing is predicted in the crown at this stage. At the year 2000, the rock mass temperature in the immediate crown reaches approximately 190°C, and slabbing occurs (as seen in the upper right hand portion of figure as red fractured contact planes between blocks). The roof-parallel slabbing (or spalling) occurs largely in the crown over a span of perhaps 2 meters, and rapidly equilibrates and dies out into the roof where the confinement is sufficient to suppress this response. A seen in these figures, a number of particles detach themselves and fall onto the invert. The spalling phenomenon appears to occur in much the same fashion as axial splitting of samples in uniaxial compression in the laboratory. The rock adjacent to the free surface is subjected to the tangential compression and radial tension which results in the fracturing parallel to the minimum principal stress.

The model response can be compared to field observations:

- With the selected strength parameters, the model shows no spalling behavior due to in situ mining-induced stresses only. No spalling is observed in the field.

- Small-scale fracture development can be observed early on in both the model and field. Small particles were observed on the drift floor as early as 1999 in the field while non-coherent fractures develop in the model in the crown as early as 1998.

- Large-scale spalling in the model is observed when the heater power is raised in the year 2000, thus creating a large change in thermally induced tangential compression and radial tension in the roof (Figure 7-34). A change in roof spalling and rock plates lying on the floor of the drift are observed in the Drift Scale Heater Test in early 2001. Depth of the spalling in the field is unknown at present as it is held in place by the rock support. However, the general location (restricted to the immediate crown) and lateral extent (a meter or two) of the simulated spalling (Figure 7-34) is consistent with field observation.

- The model spalling occurs when the rock stresses roughly equal the proposed uniaxial compressive strength of the rock mass, confirming the selection and calibration of the rock strength and its relationship to in situ modulus.

Obviously, the strength and moduli of the Tptpmn rock mass varies in situ. This validation exercise shows that, for rock mass properties within the ranges defined by Price et al. (1985 [DIRS 106602]), the model is able to produce thermally induced fracturing response similar in nature and extent to that observed at the proper temperature and thus thermally induced stress levels.

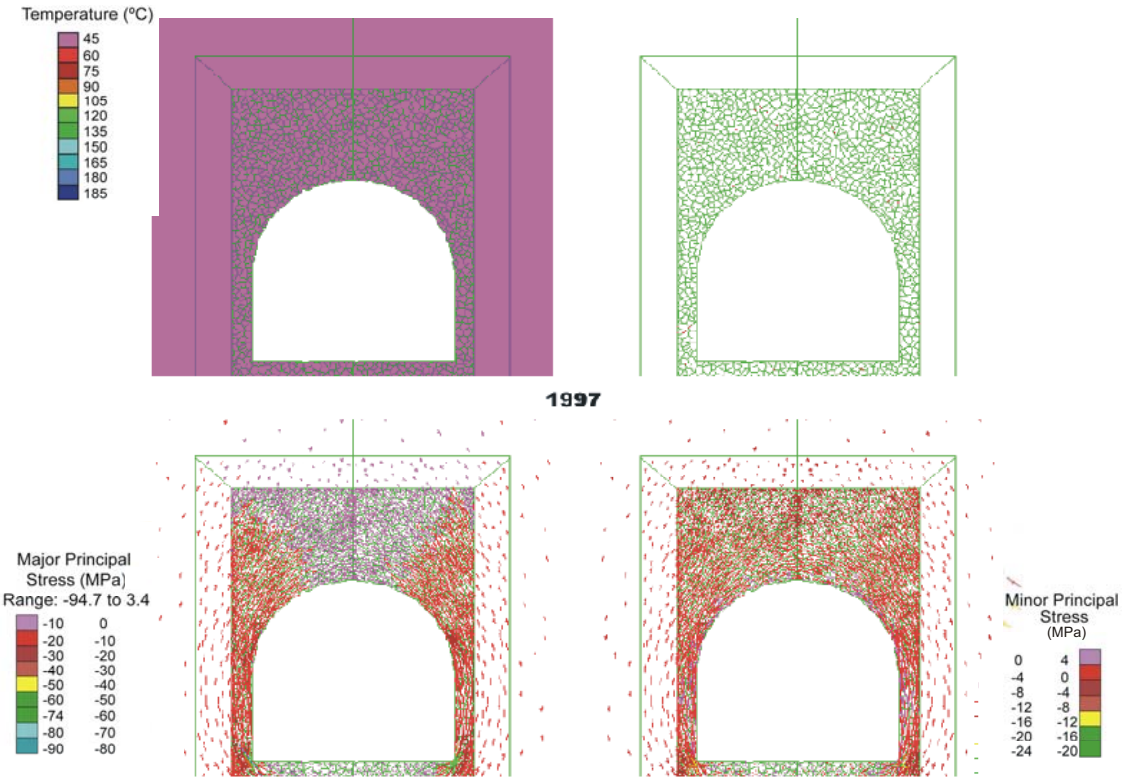

Source: DTNs: MO9807DSTSET01.000 [DIRS 113644]; MO9906DSTSET03.000 [DIRS 113673]; MO0001SEPDSTPC.000 [DIRS 153836]; MO0007SEPDSTPC.001 [DIRS 153707]; MO0107SEPDSTPC.003 [DIRS 158321]; MO0202SEPDSTTV.001 [DIRS 158320], MO0002ABBLSLDS.000 [DIRS 147304].

NOTE: Clockwise from upper left: temperatures, fractures, minimum principal stress, and maximum principal stress. Temperatures obtained from field thermal measurements; fracture and stress levels predicted from UDEC lithophysal rockfall model.

Figure 7-31. Results from Heated Drift Analysis with 1997 Temperature Conditions

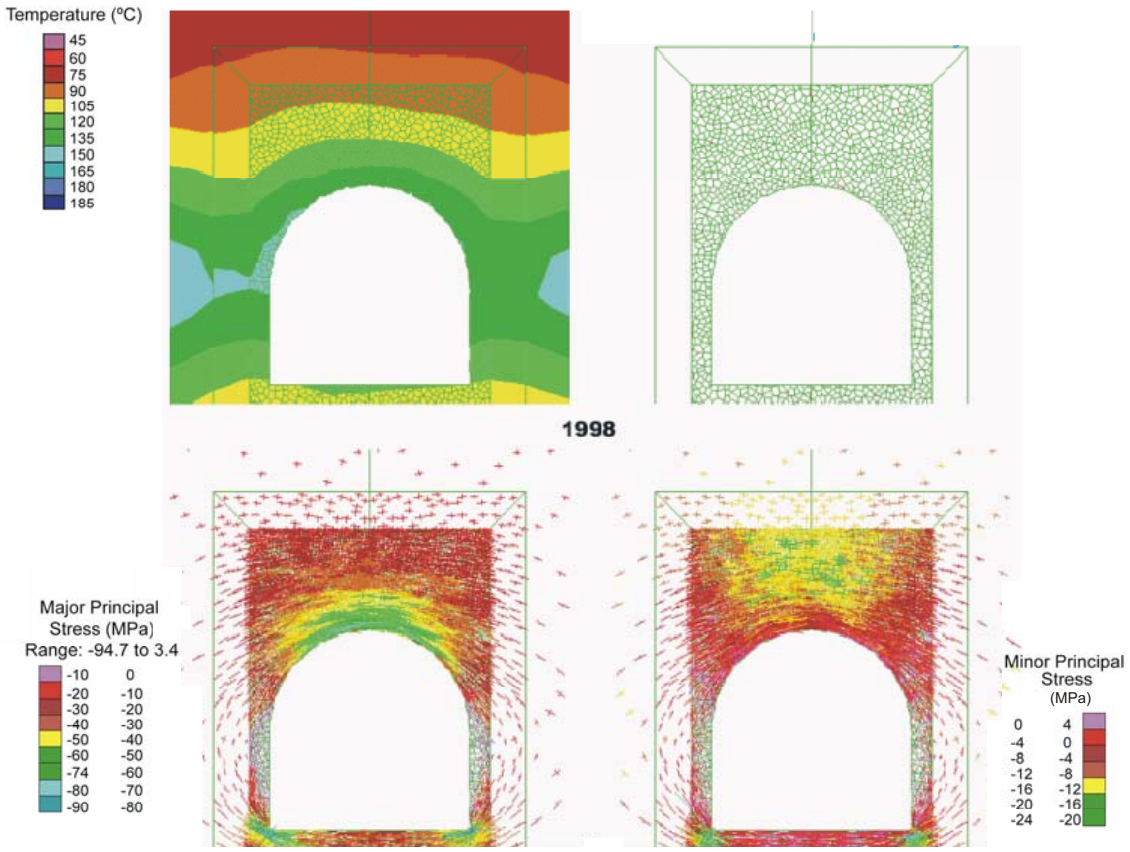

Source: DTNs: MO9807DSTSET01.000 [DIRS 113644]; MO9906DSTSET03.000 [DIRS 113673]; MO0001SEPDSTPC.000 [DIRS 153836]; MO0007SEPDSTPC.001 [DIRS 153707]; MO0107SEPDSTPC.003 [DIRS 158321]; MO0202SEPDSTTV.001 [DIRS 158320]; MO0002ABBLSLDS.000 [DIRS 147304].

NOTE: Clockwise from upper left: temperatures, fractures, minimum principal stress, and maximum principal stress. Temperatures obtained from field thermal measurements; fracture and stress levels predicted from UDEC lithophysal rockfall model. Conditions represent 1 year of heating in the Heated Drift.

Figure 7-32. Results from Heated Drift Analysis with 1998 Temperature Conditions

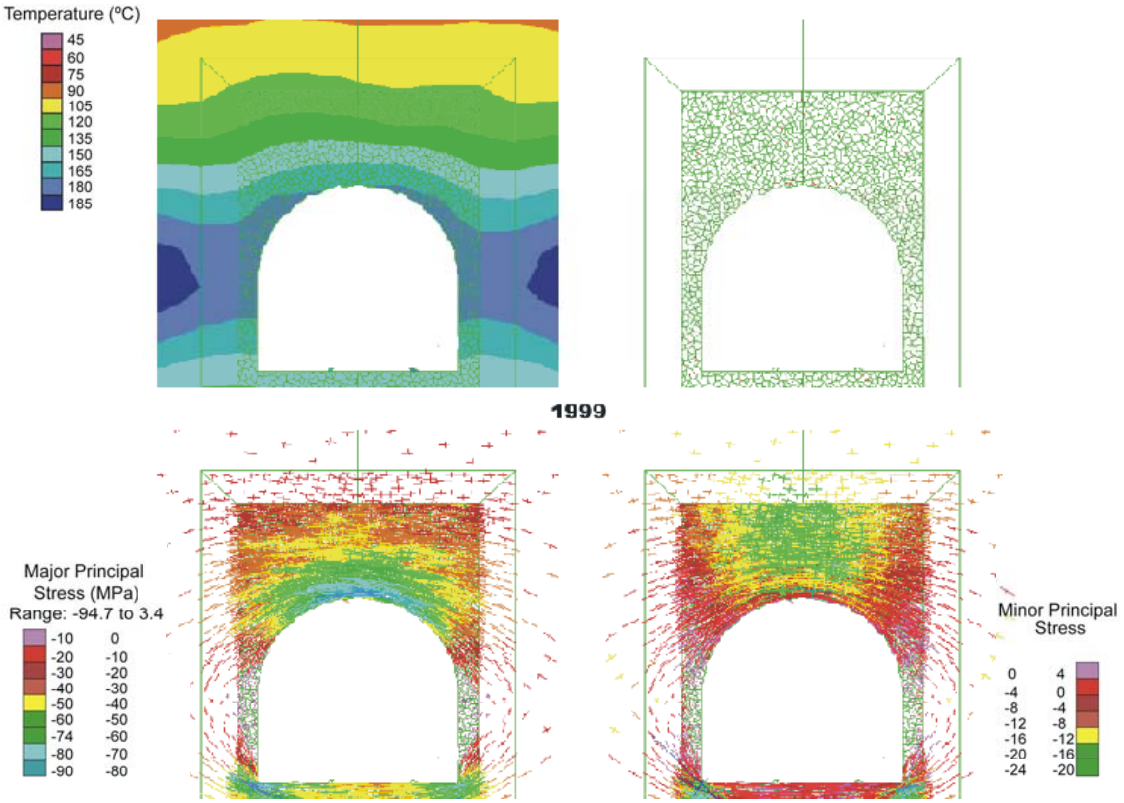

Source: DTNs: MO9807DSTSET01.000 [DIRS 113644]; MO9906DSTSET03.000 [DIRS 113673]; MO0001SEPDSTPC.000 [DIRS 153836]; MO0007SEPDSTPC.001 [DIRS 153707]; MO0107SEPDSTPC.003 [DIRS 158321]; MO0202SEPDSTTV.001 [DIRS 159320]; MO0002ABBLSLDS.000 [DIRS 147304].

NOTE: Clockwise from upper left: temperatures, fractures, minimum principal stress, and maximum principal stress. Temperatures obtained from field thermal measurements; fracture and stress levels predicted from UDEC lithophysal rockfall model. Conditions represent 2 years of heating in the Heated Drift.

Figure 7-33. Results from Heated Drift Analysis with 1999 Temperature Conditions

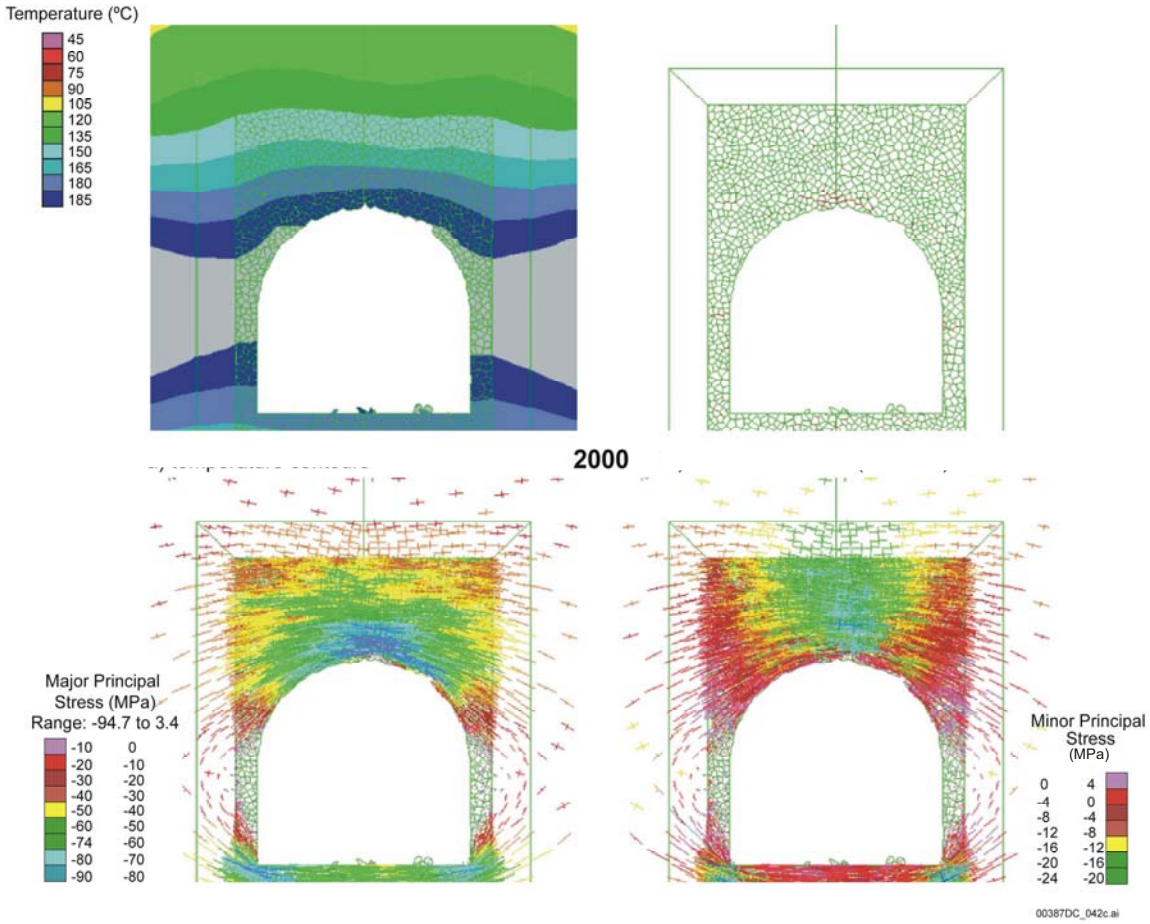

Source: DTNs: MO9807DSTSET01.000 [DIRS 113644]; MO9906DSTSET03.000 [DIRS 113673]; MO0001SEPDSTPC.000 [DIRS 153836]; MO0007SEPDSTPC.001 [DIRS 153707]; MO0107SEPDSTPC.003 [DIRS 158321]; MO0202SEPDSTTV.001 [DIRS 159320]; MO0002ABBLSLDS.000 [DIRS 147304].

NOTE: Clockwise from upper left: temperatures, fractures, minimum principal stress, and maximum principal stress. Temperatures obtained from field thermal measurements; fracture and stress levels predicted from UDEC lithophysal rockfall model. Conditions represent 3 years of heating in the Heated Drift.

Figure 7-34. Results from Heated Drift Analysis with 2000 Temperature Conditions

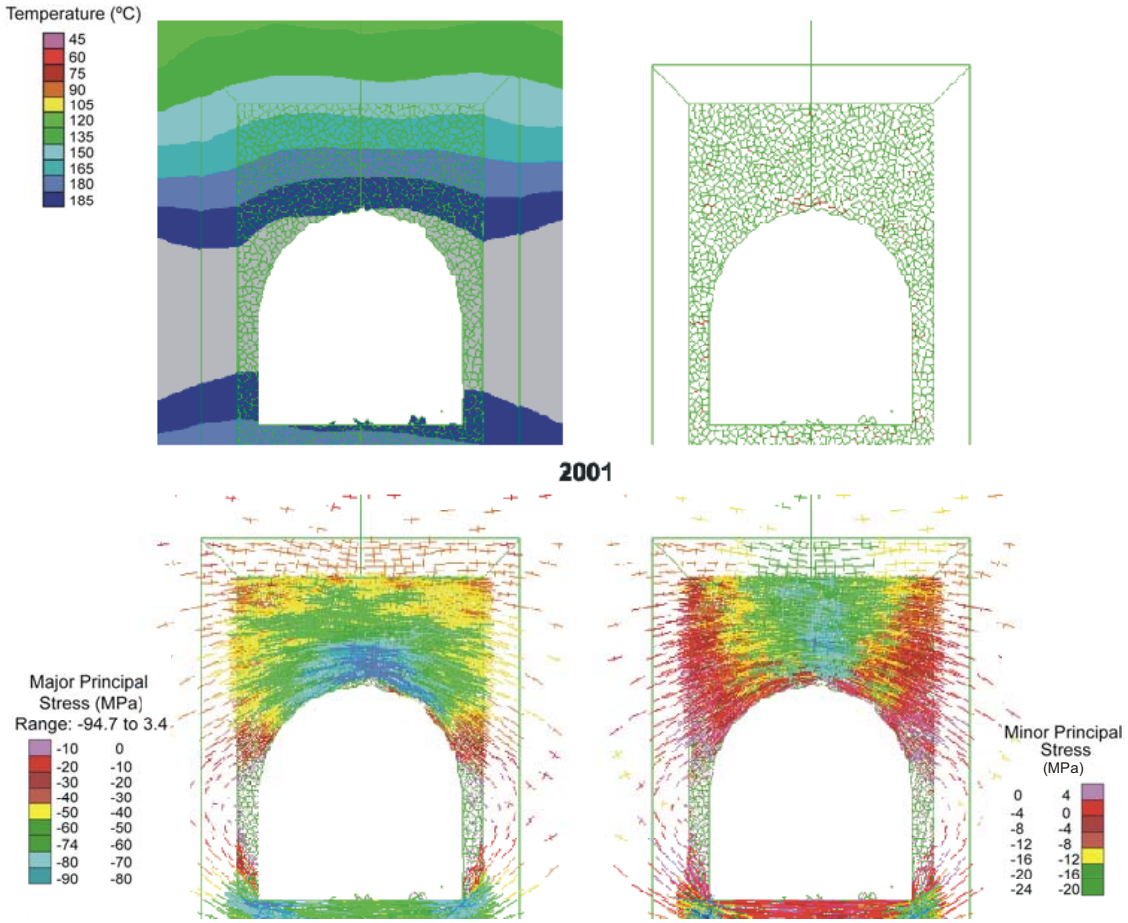

Source: DTNs: MO9807DSTSET01.000 [DIRS 113644]; MO9906DSTSET03.000 [DIRS 113673]; MO0001SEPDSTPC.000 [DIRS 153836]; MO0007SEPDSTPC.001 [DIRS 153707]; MO0107SEPDSTPC.003 [DIRS 158321]; MO0202SEPDSTTV.001 [DIRS 159320]; MO0002ABBLSLDS.000 [DIRS 147304].

NOTE: Clockwise from upper left: temperatures, fractures, minimum principal stress, and maximum principal stress. Temperatures obtained from field thermal measurements; fracture and stress levels predicted from UDEC lithophysal rockfall model. Conditions represent 4 years of heating in the Heated Drift.

Figure 7-35. Results from Heated Drift Analysis with 2001 Temperature Conditions

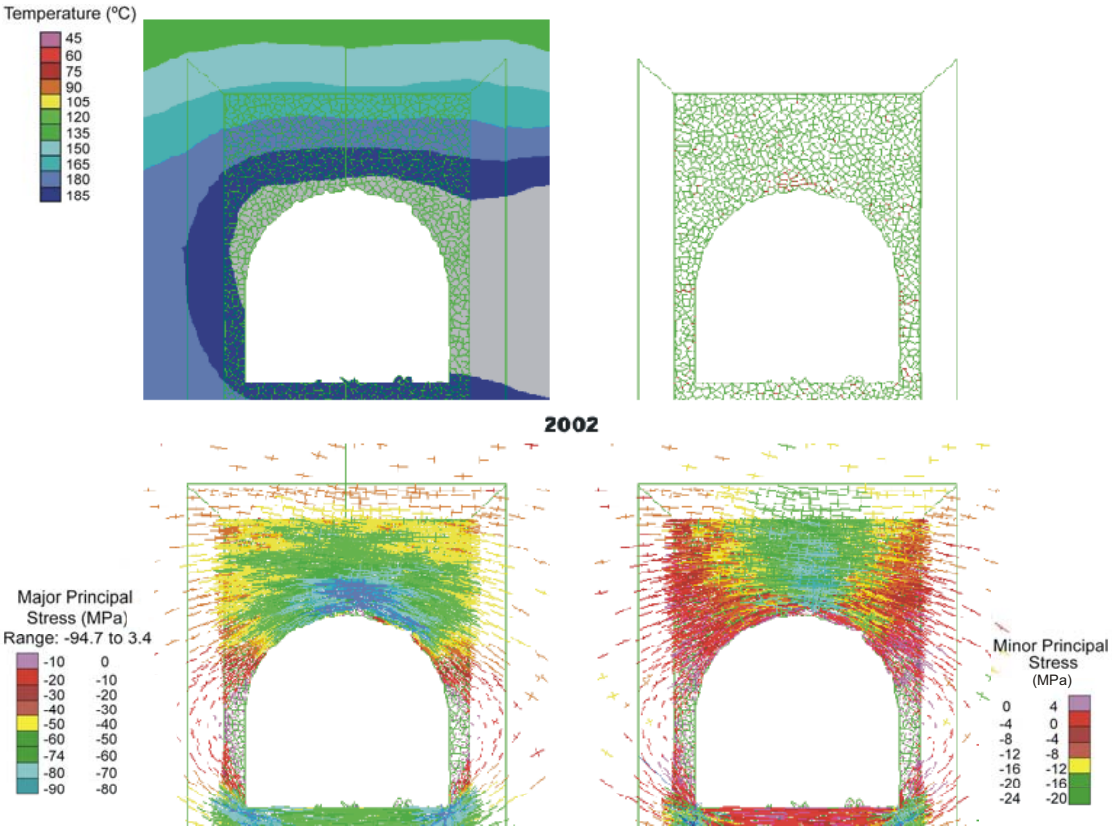

Source: DTNs: MO9807DSTSET01.000 [DIRS 113644]; MO9906DSTSET03.000 [DIRS 113673]; MO0001SEPDSTPC.000 [DIRS 153836]; MO0007SEPDSTPC.001 [DIRS 153707]; MO0107SEPDSTPC.003 [DIRS 158321]; MO0202SEPDSTTV.001 [DIRS 159320]; MO0002ABBLSLDS.000 [DIRS 147304].

NOTE: Clockwise from upper left: temperatures, fractures, minimum principal stress, and maximum principal stress. Temperatures obtained from field thermal measurements; fracture and stress levels predicted from UDEC lithophysal rockfall model. Conditions represent the cool-down period in the Heated Drift.

Figure 7-36. Results from Heated Drift Analysis with 2002 Temperature Conditions

7.6.5.4 UDEC Post-Development Validation Exercise 4 - Comparison of UDEC Voronoi Block Model with Continuum Constitutive Models (Corroboration of Results with Alternative Mathematical Models)

A UDEC model in which the rock mass is represented as an assembly of polygonal blocks is used to analyze the stability of the emplacement drifts located in the lithophysal rock. The main reason for using this approach, which is uncommon in engineering practice, was the requirement for the analysis to predict the rockfall. The Voronoi block model has an advantage over the continuum models in that fracturing of the rock mass, formation of loose blocks, and their rockfall can be simulated in a straightforward manner within the same model. However, the Voronoi block model must be calibrated in order to ensure that it behaves mechanically equivalent to the simulated rock mass. Another way of validating the UDEC Voronoi block model of lithophysal rock is to compare its results with those of the continuum approach using different constitutive models. The comparison is presented in this section.

Elastic Models of Drift Excavation–The Voronoi block model behaves as a linearly elastic model before fracturing occurs. Stress redistribution and deformation around the emplacement drift for the in situ stress state, in which the vertical stress is 7 MPa and the horizontal stress is 3.5 MPa, are analyzed using continuum, linearly elastic constitutive models in FLAC and the UDEC Voronoi block model. In order to ensure linearly elastic behavior of the UDEC Voronoi block model, the strength of the contact bonds between the blocks was considered to be infinitely large. The problem was solved using two different geometries of the Voronoi block model, with average block sizes of 0.2 m and 0.3 m. Comparison of stresses and displacements calculated using the different methods is presented in Figures 7-37 to 7-42. Stress profiles calculated in UDEC show more scatter because of the discontinuous nature of the model. However, the agreement, in general, is rather good. The systematic difference in the horizontal and vertical displacements shown in Figures 7-39 and 7-42 is due to the different outer boundary sizes of the UDEC and FLAC models. The smaller FLAC model results in larger vertical displacements, because a stress boundary condition was used on the top model boundary.

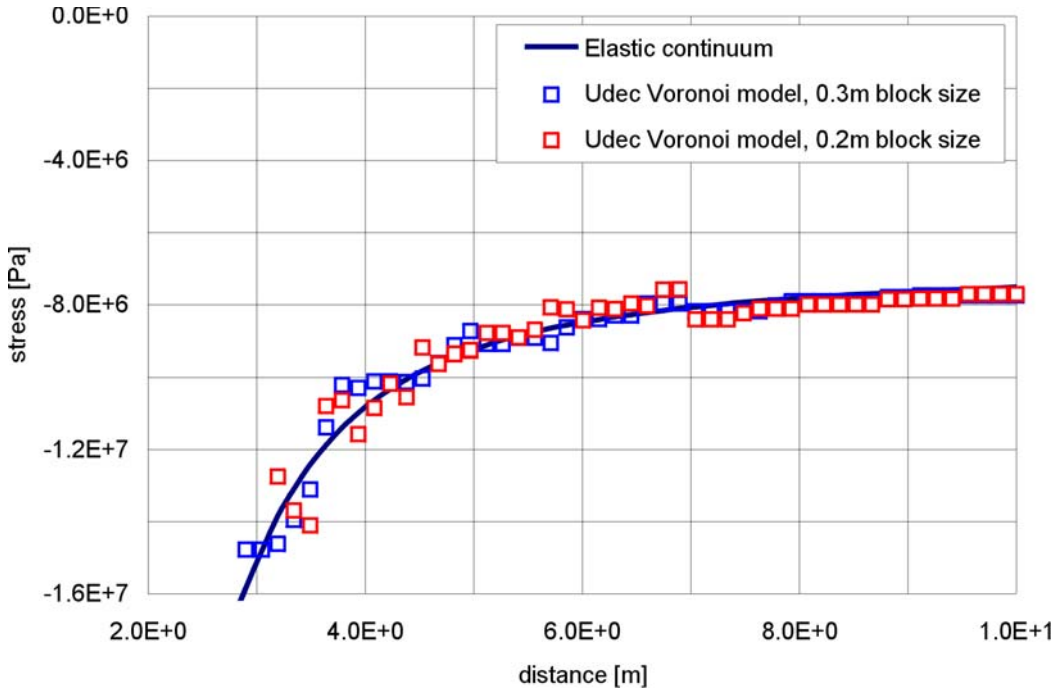

Figure 7-37. Elastic Models of Drift Excavation: Vertical Normal Stress Along the Horizontal Profile Through the Center of Tunnel (Distance is measured from the tunnel center)

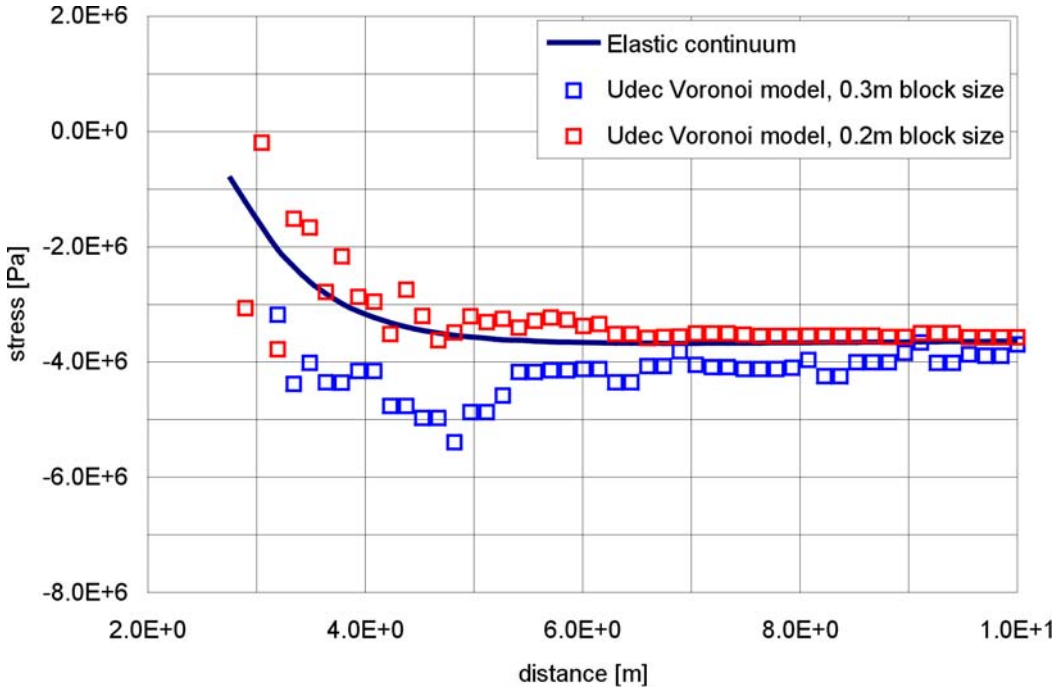

Figure 7-38. Elastic Models of Drift Excavation: Horizontal Normal Stress Along the Horizontal Profile Through the Center of Tunnel (Distance is measured from the tunnel center)

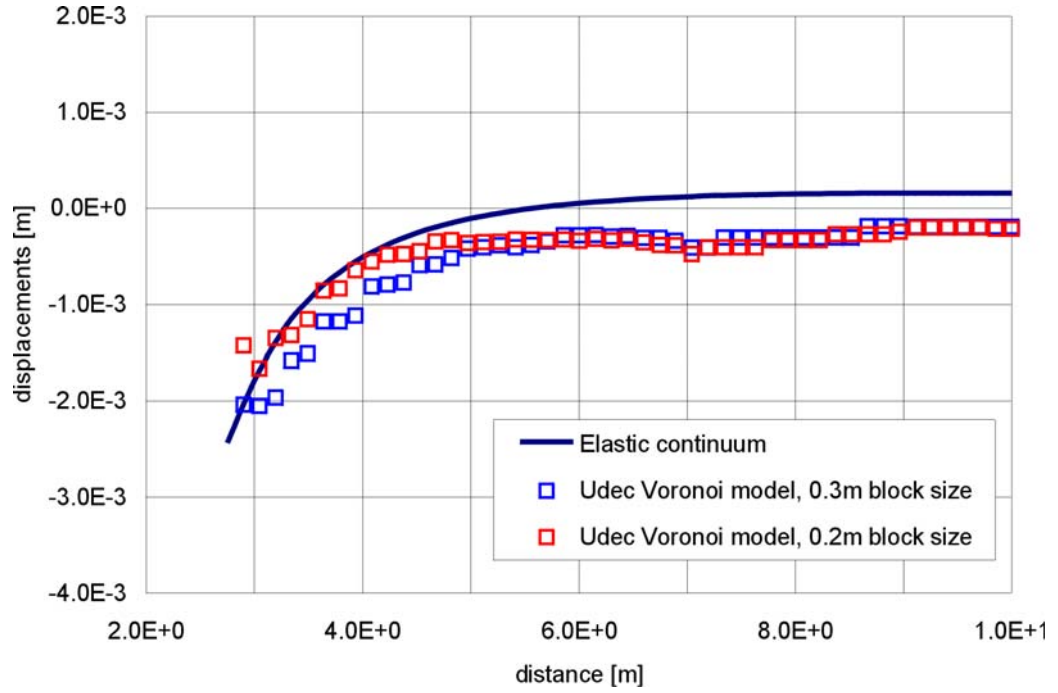

Figure 7-39. Elastic Models of Drift Excavation: Horizontal Displacement Along the Horizontal Profile Through the Center of Tunnel (Distance is measured from the tunnel center)

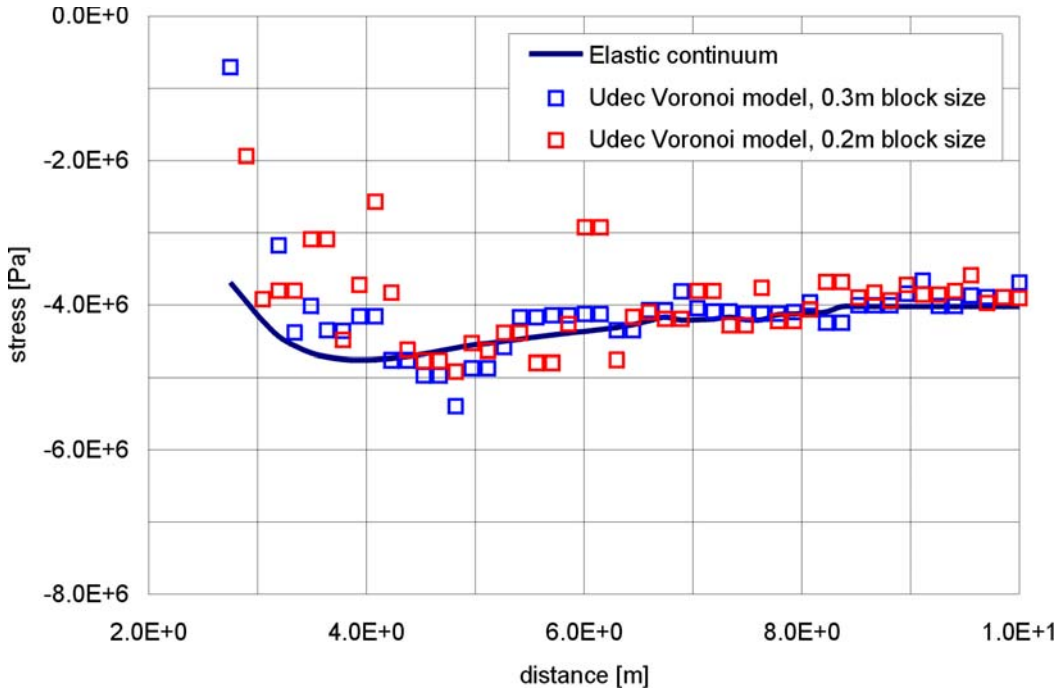

Figure 7-40. Elastic Models of Drift Excavation: Horizontal Normal Stress Along the Vertical Profile Through the Center of Tunnel (Distance is measured from the tunnel center)

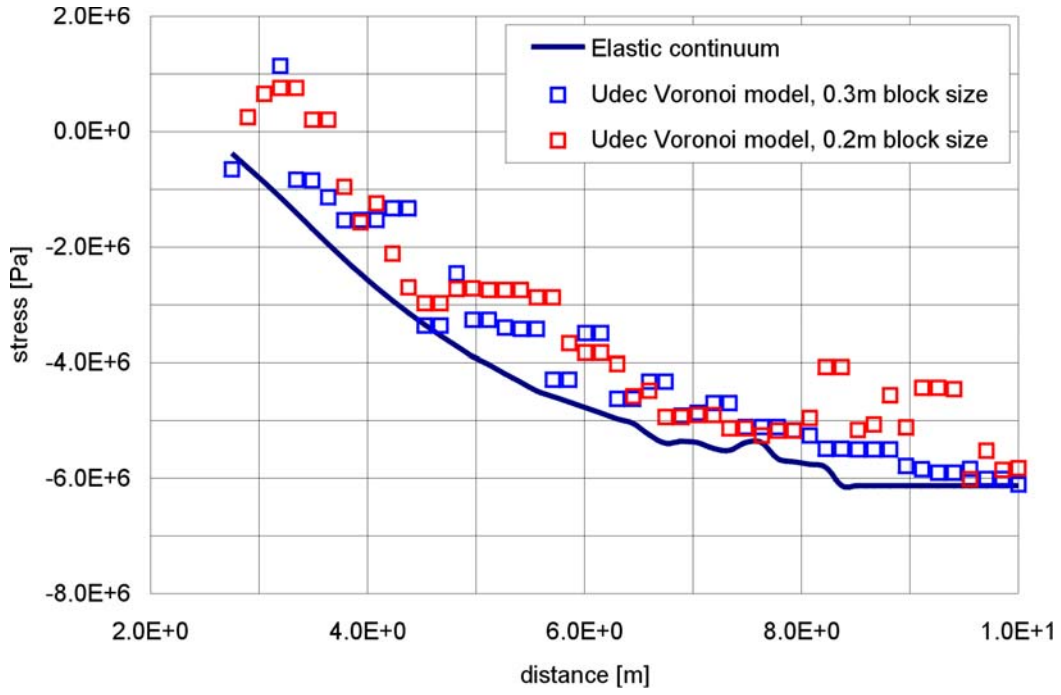

Figure 7-41. Elastic Models of Drift Excavation: Vertical Normal Stress Along the Vertical Profile Through the Center of Tunnel (Distance is measured from the tunnel center)

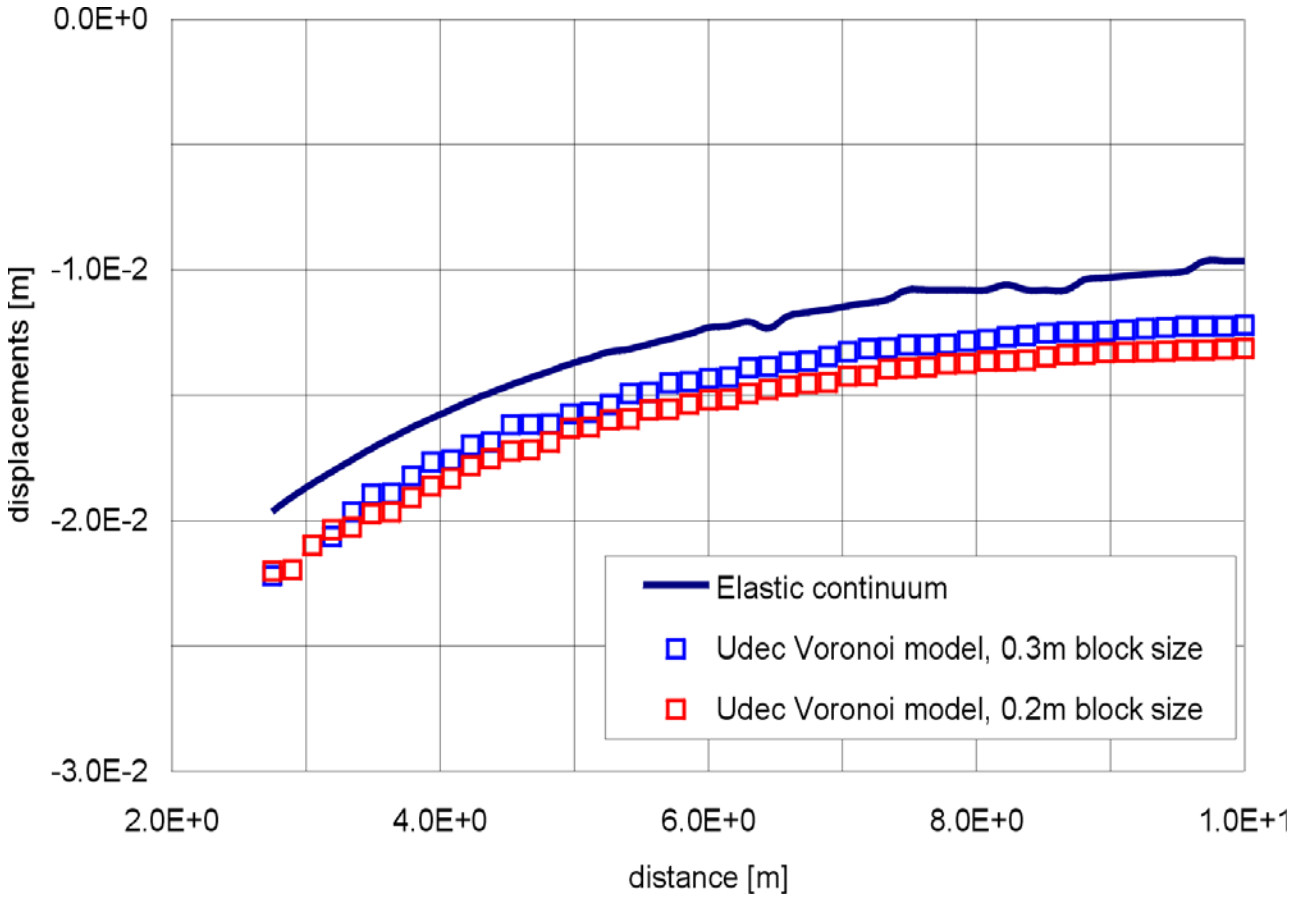

Figure 7-42. Elastic Models of Drift Excavation: Vertical Displacement Along the Vertical Profile Through the Center of Tunnel (Distance is measured from the tunnel center)

Inelastic Models of the Emplacement Drift–The results of damage, stress redistribution and deformation around the emplacement drift predicted using the UDEC Voronoi block model are compared with results obtained using the continuum approach and different considerations of constitutive behavior of the lithophysal rock mass. The micro properties of the joints and blocks in the UDEC model are calibrated to the stiffness and strength of lithophysal rock mass, Category 1, as determined from unconfined compression tests. The resulting constitutive behavior of the UDEC Voronoi block model is very complex, as illustrated by plots of failure envelope, stress-strain curves for different confinements and volumetric strain as a function of axial strain, shown in Figures 7-20 to 7-22. Unfortunately, the number and types of laboratory and in situ experiments was insufficient to describe the complete constitutive behavior of the lithophysal tuff with a high level of confidence, particularly in the post-peak strain range and for confined conditions. The mechanical behavior exhibited by the synthetic Voronoi block model seems to be quite reasonable and typical for hard, brittle rocks like the Topopah Spring. For unconfined conditions, the UDEC synthetic model softens in a rather brittle manner after reaching the peak stress. As confinement increases, the post-peak behavior becomes mode ductile; for 3-MPa confinement, it is almost perfectly plastic (i.e., there is no strength decrease for a considerable plastic strain). Because of the large uncertainty in the post-peak behavior of the rocks, simple continuum constitutive models are used commonly in engineering practice. The

following continuum constitutive models were selected for analyzing (using FLAC) stability of emplacement drifts under in situ stresses and thermal loads:

- Associated (dilation angle equal to friction angle), perfectly plastic Mohr-Coulomb model
- Associated Mohr-Coulomb with cohesion at yield softening in a brittle manner to 50 percent of its initial value
- Nonassociated (no dilation) Mohr-Coulomb with cohesion at yield softening in a brittle manner to 50 percent of its initial value
- Associated Mohr-Coulomb with complete loss of cohesion at yield in a brittle manner
- Cohesion softening – friction hardening model. In this model the cohesion softens to 25 percent of its initial value after 0.2 percent of plastic strain, while the friction angle increase from 0º to 40º after 0.5 percent of plastic strain.

The selected models certainly bound possible behavior of the lithophysal rock mass. The perfectly plastic Mohr-Coulomb model most likely will represent a lower bound of damage and deformation; perfectly brittle Mohr-Coulomb with complete loss of cohesion at yield is certainly a conservative case, an upper bound of damage and deformation around the emplacement drift.

Stability of the emplacement drift was analyzed for in situ and thermal stresses after 80 years of heating. Damage predicted around the emplacement drifts by different models at two states (after excavation and after 80 years of heating) is illustrated in Figure 7-43. Green and red crosses around the drift in the continuum models indicate locations in the model where plastic deformation took place. Green crosses indicate locations of plastic deformation that occurred sometimes in the past; red crosses indicate locations that currently are deforming plastically. Red lines in the plot from the UDEC model (at the bottom of Figure 7-43) represent the positions of microcracks—i.e., where the bonds between blocks are broken in tension or shear. Both the model with no residual cohesion and the cohesion softening – friction hardening model clearly overestimate the damage and deformation around the emplacement drifts. Conditions predicted by these two models do not exist anywhere inside the ESF or ECRB Cross-Drift. There is very good agreement between the damage predicted by the UDEC Voronoi model and two models with cohesion softening to 50 percent of its initial value. Also, predictions of these three models for Category 1 is consistent with fracturing observed in the boreholes drilled in the walls of the ECRB Cross-Drift in the poorest-quality estimated for the Tptpll. The UDEC model shows a number of fractures randomly scattered throughout the model. Those fractures are a consequence of the discontinuous nature of the model. As long as they are distributed and orientated randomly, they should be considered to be artifacts of the numerical method. The aligned and concentrated fractures in the drift wall represent stress-induced damage.

Stresses and displacements along the different profiles, as calculated by the different models, are shown in Figures 7-44 to 7-49 for the state after excavation of the emplacement drift and in Figures 7-50 to 7-55 for the state after 80 years of heating. Drift stability after excavation was analyzed with the UDEC Voronoi block model using 0.2-m and 0.3-m block sizes. Drift stability

after 80 years of heating was analyzed with the UDEC Voronoi block model using a 0.3-m block size only. In these cases, the UDEC Voronoi block predictions (for both stress and displacement predictions) fall inside the range of predictions by different continuum models.

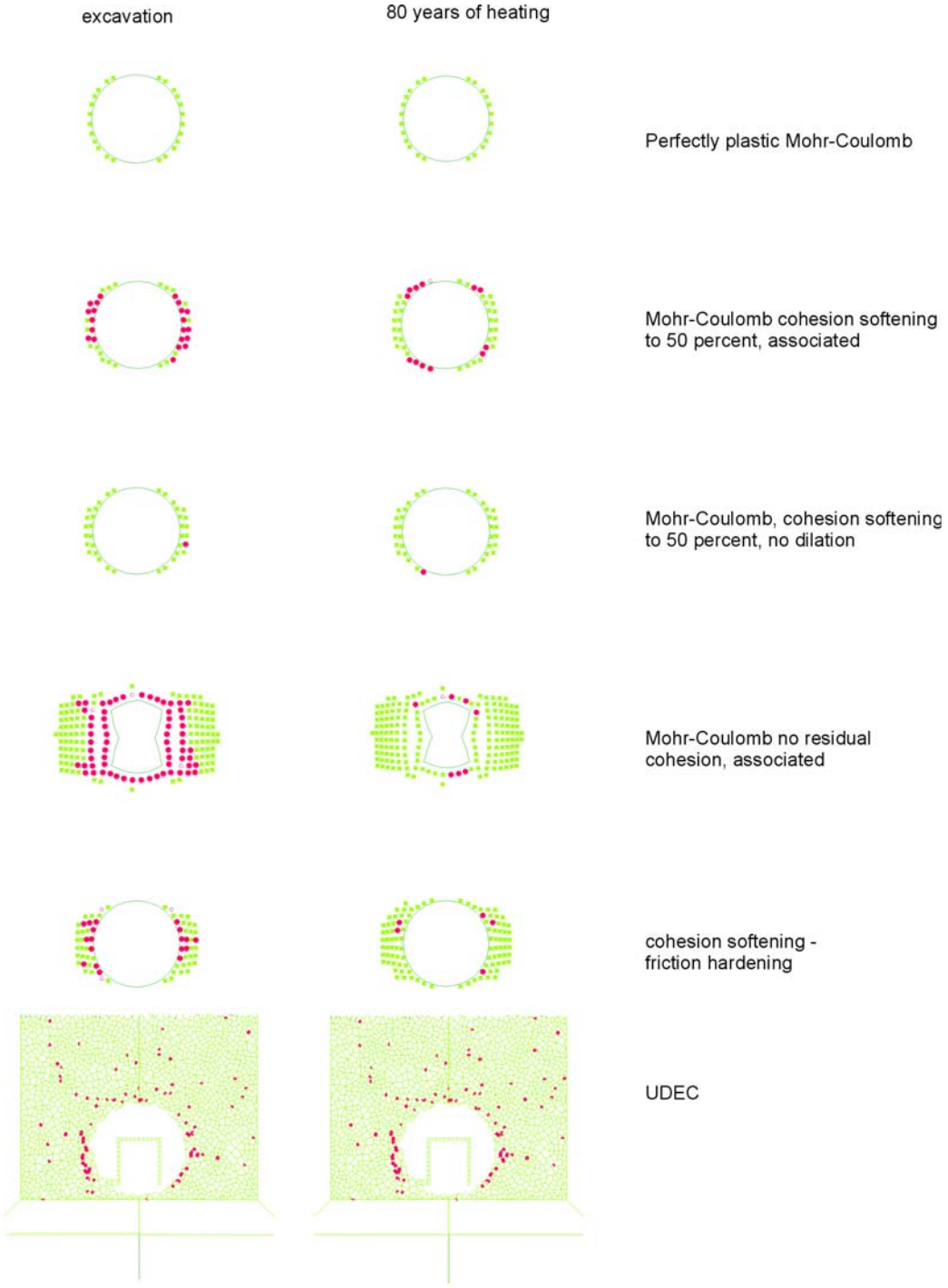

Figure 7-43. Damage Around the Emplacement Drifts Predicted Using Different Inelastic Models

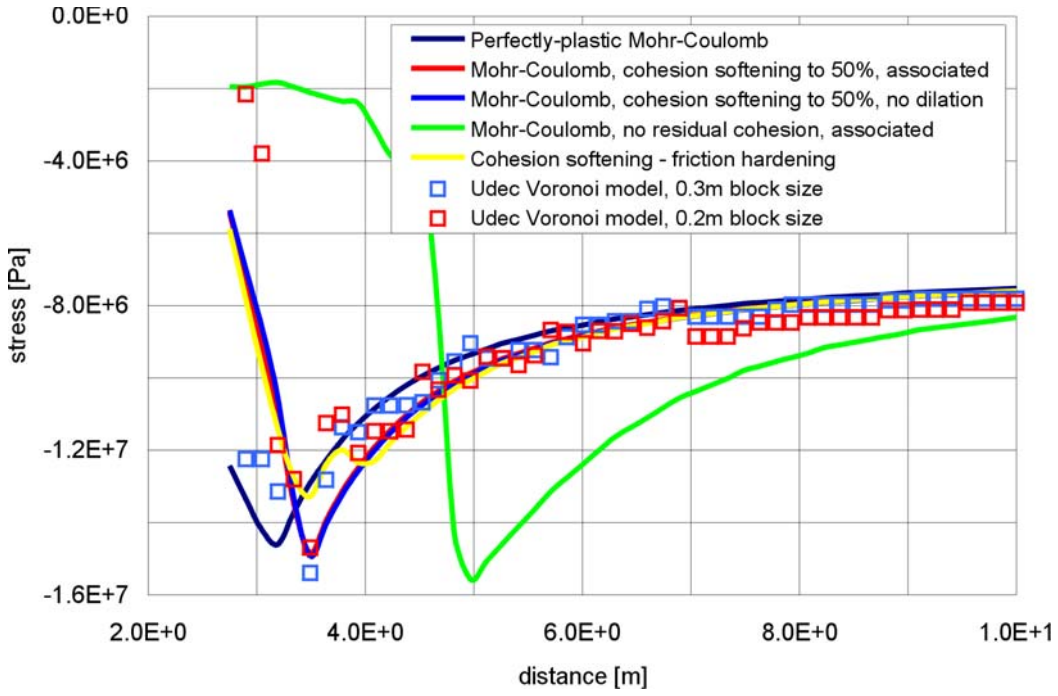

Figure 7-44. Inelastic Models of Drift Excavation: Vertical Normal Stress Along the Horizontal Profile Through the Center of Tunnel (Distance is measured from the tunnel center.)

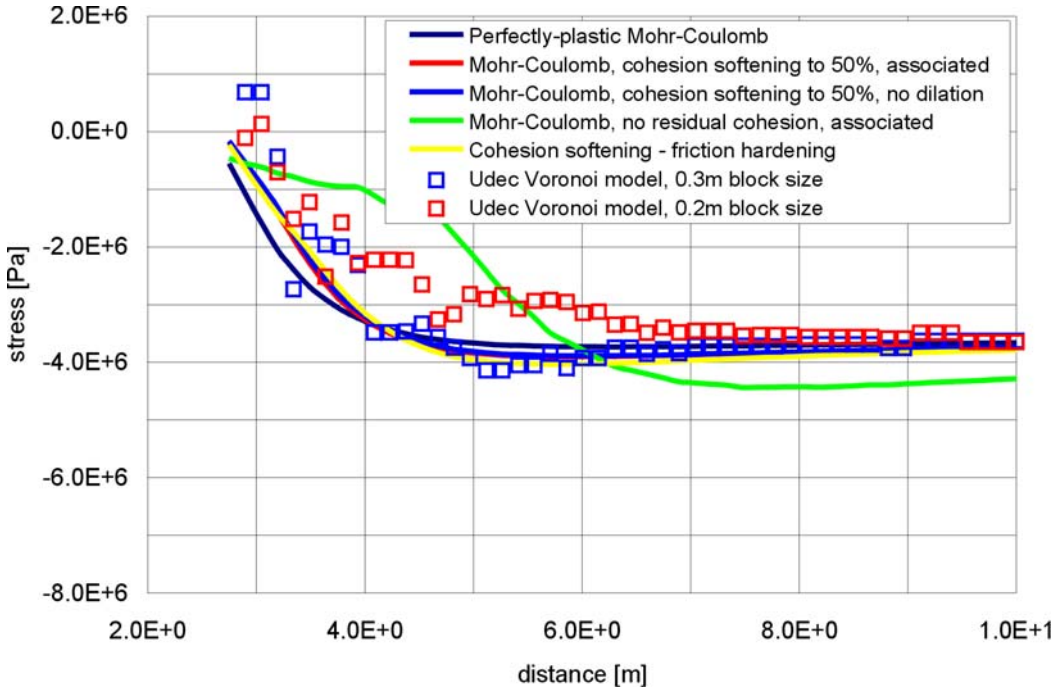

Figure 7-45. Inelastic Models of Drift Excavation: Horizontal Normal Stress Along the Horizontal Profile Through the Center of Tunnel (Distance is measured from the tunnel center)

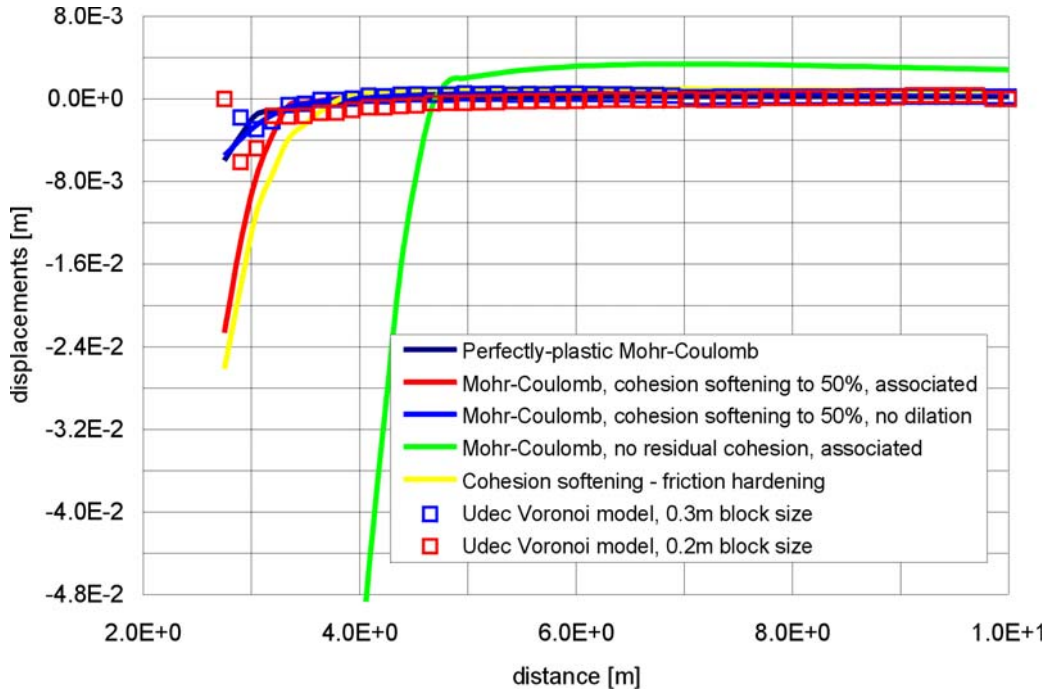

Figure 7-46. Inelastic Models of Drift Excavation: Horizontal Displacement Along the Horizontal Profile Through the Center of Tunnel (Distance is measured from the tunnel center)

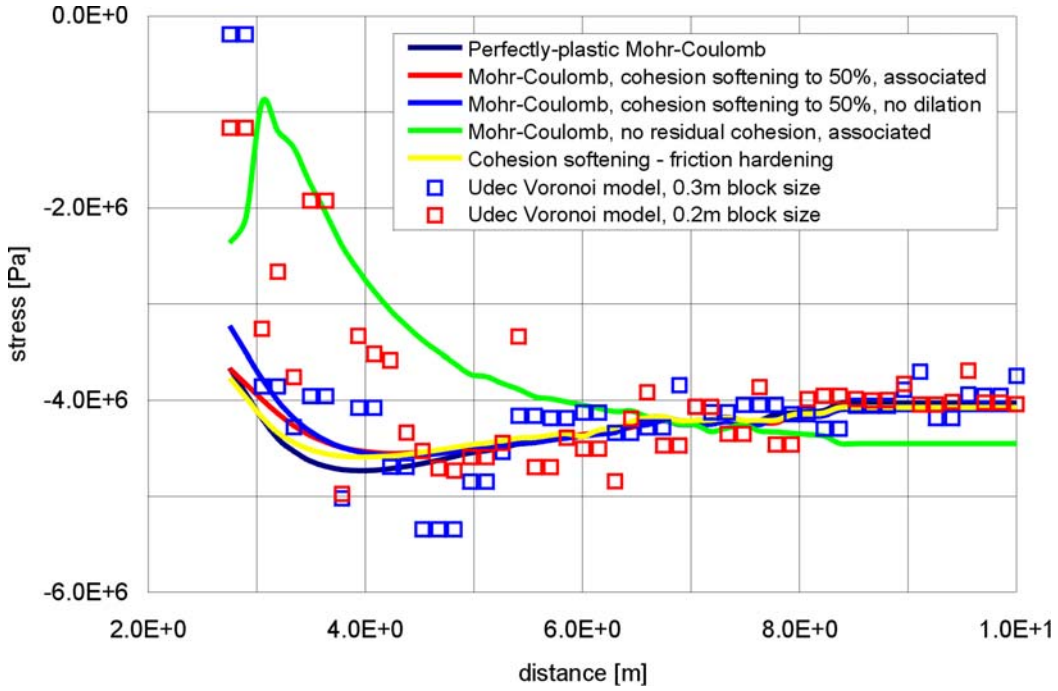

Figure 7-47. Inelastic Models of Drift Excavation: Horizontal Normal Stress Along the Vertical Profile Through the Center of Tunnel (Distance is measured from the tunnel center)

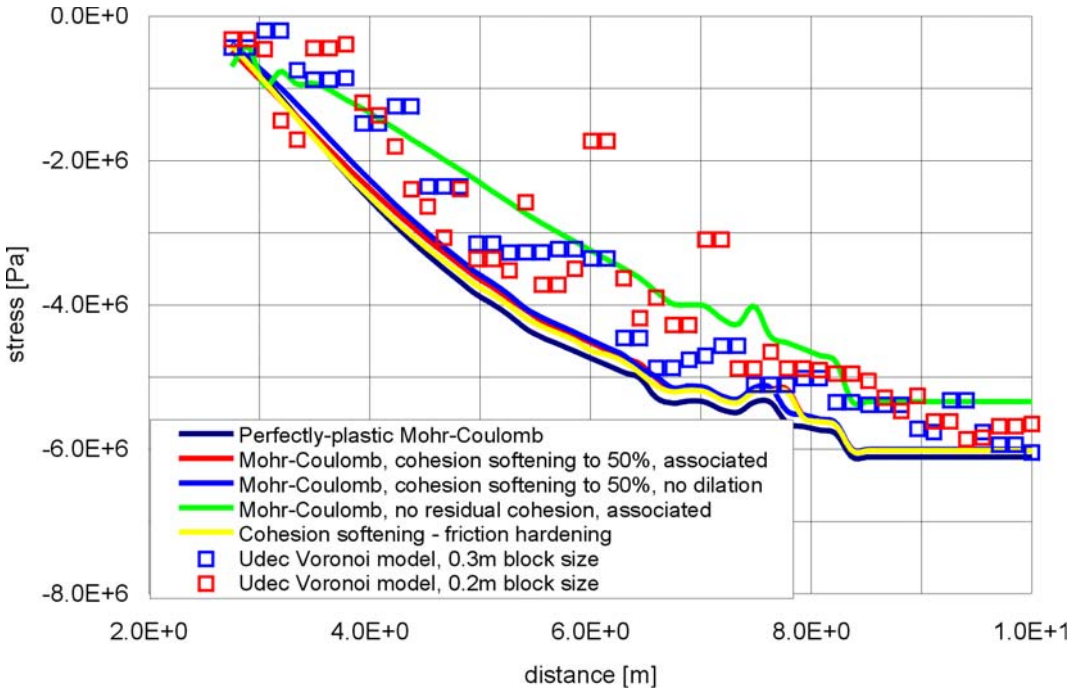

Figure 7-48. Inelastic Models of Drift Excavation: Vertical Normal Stress Along the Vertical Profile Through the Center of Tunnel (Distance is measured from the tunnel center)

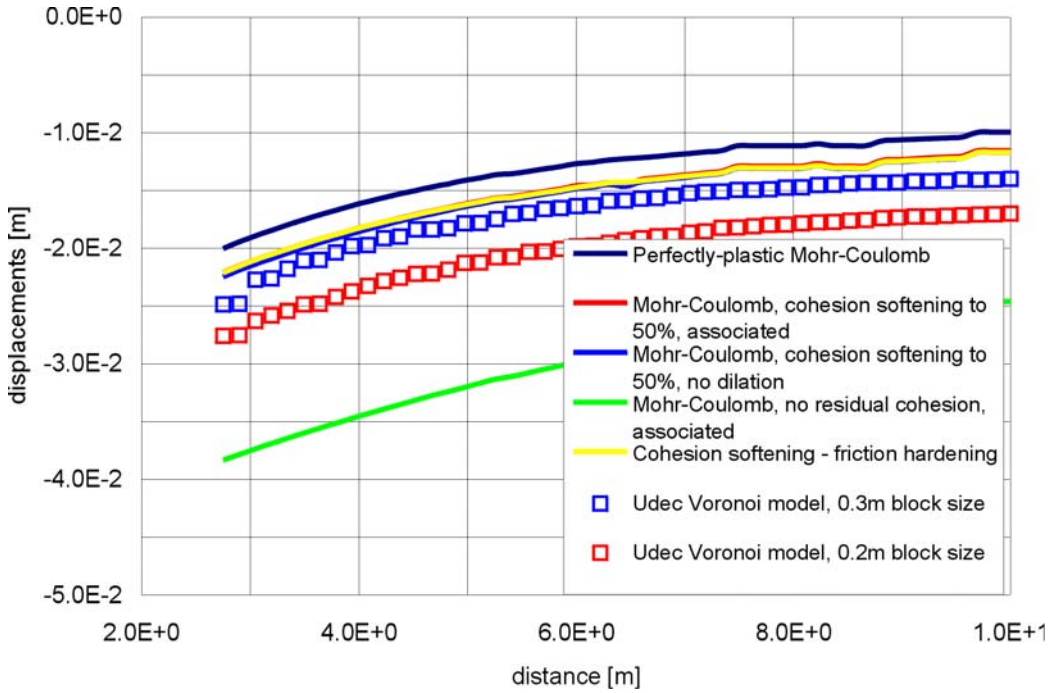

Figure 7-49. Inelastic Models of Drift Excavation: Vertical Displacement Along the Vertical Profile Through the Center of Tunnel (Distance is measured from the tunnel center)

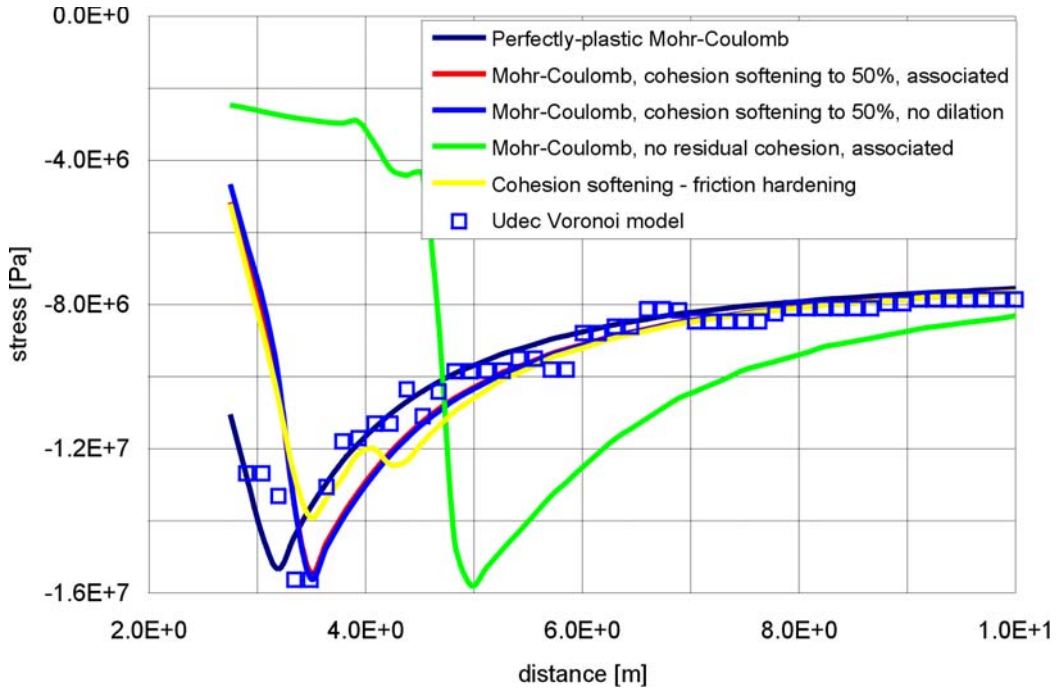

Figure 7-50. Inelastic Models After 80 Years of Heating: Vertical Normal Stress Along the Horizontal Profile Through the Center of Tunnel (Distance is measured from the tunnel center)

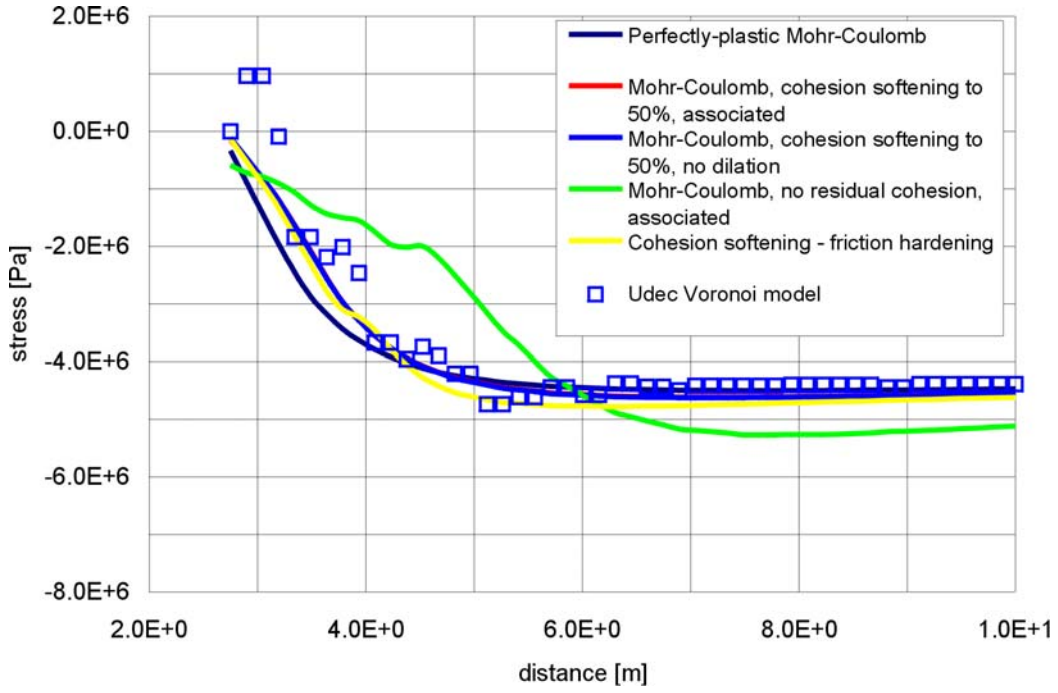

Figure 7-51. Inelastic Models After 80 Years of Heating: Horizontal Normal Stress Along the Horizontal Profile Through the Center of Tunnel (Distance is measured from the tunnel center)

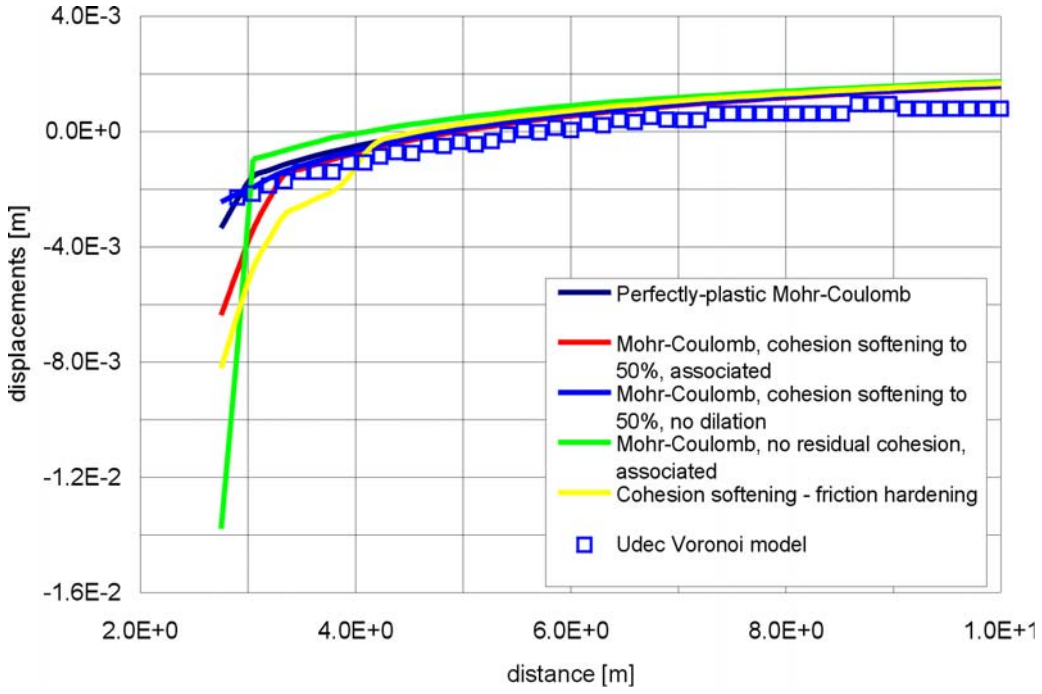

Figure 7-52. Inelastic Models After 80 Years of Heating: Horizontal Displacement Along the Horizontal Profile Through the Center of Tunnel (Distance is measured from the tunnel center)

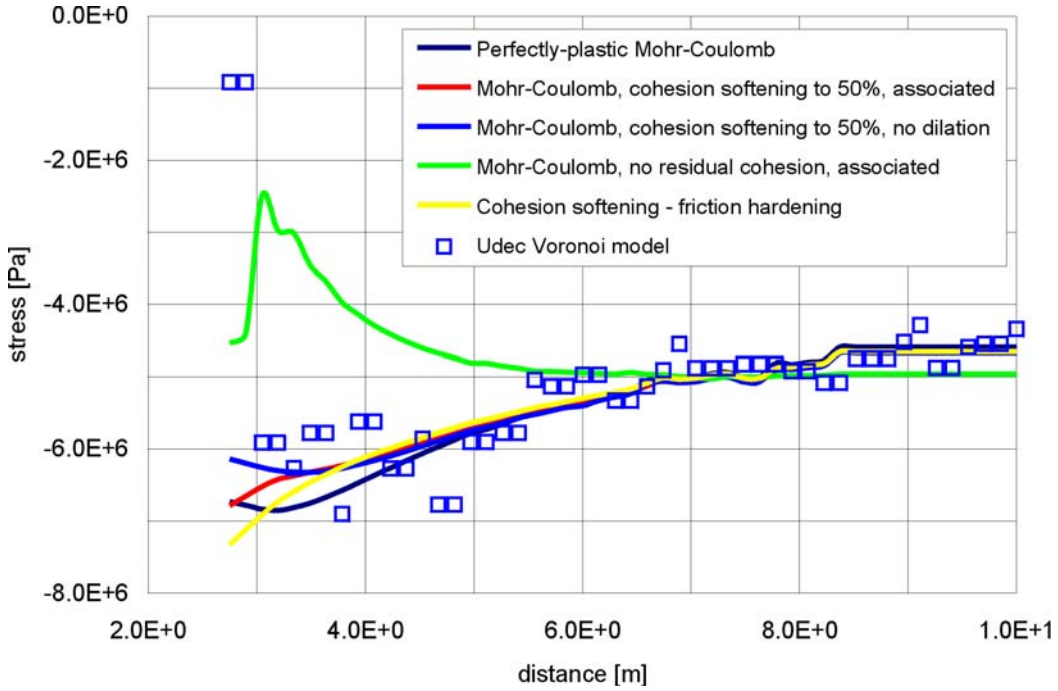

Figure 7-53. Inelastic Models After 80 Years of Heating: Horizontal Normal Stress Along the Vertical Profile Through the Center of Tunnel (Distance is measured from the tunnel center)

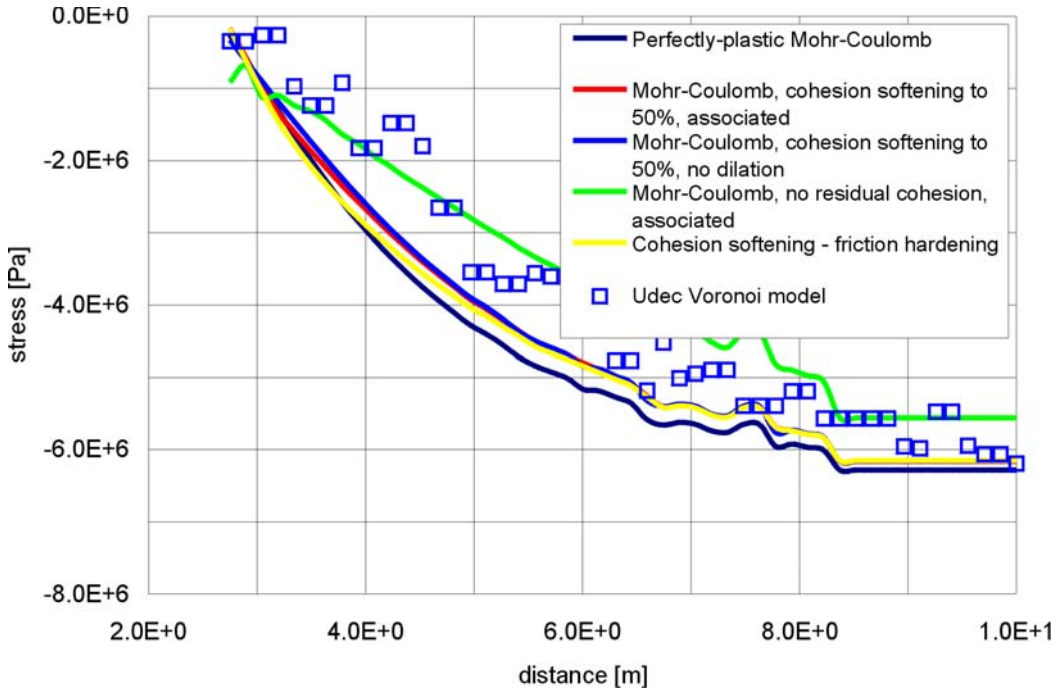

Figure 7-54. Inelastic Models After 80 Years of Heating: Vertical Normal Stress Along the Vertical Profile Through the Center of Tunnel (Distance is measured from the tunnel center)

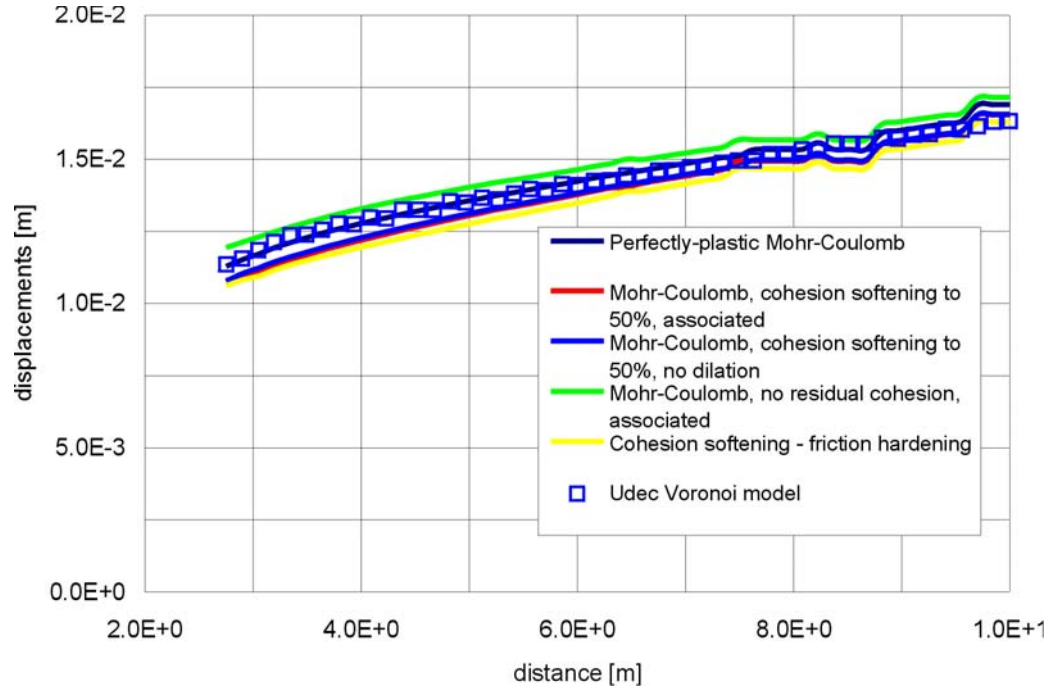

Figure 7-55. Inelastic Models After 80 Years of Heating: Vertical Displacement Along the Vertical Profile Through the Center of Tunnel (Distance is measured from the tunnel center)

Conclusion–Although stability analysis of underground excavations using the UDEC Voronoi block model is uncommon in engineering practice, it is used to predict rockfall in a lithophysal rock mass because of its clear advantages for this type of analysis (rockfall prediction) compared to standard, continuum-based approaches. However, it is demonstrated in this section that many results (i.e., extent of damage, stress and displacement profiles) of the UDEC Voronoi block model are very comparable to the results of continuum models which are commonly used for modeling of excavation stability in rock.

7.6.5.5 UDEC Post-Development Validation Exercise 5 – Comparison of the Mathematical Model Implemented in the UDEC Program to other Numerical Approaches in Solving Dynamic Tunnel Stability Problems in Fractured Rock (Corroboration with Information Published in the Literature)

The Defense Nuclear Agency conducted a comparison of a number of dynamic numerical modeling approaches for examination of their utility in simulating the effects of dynamic stress wave loading of fractured rock and tunnels in fractured rock (Senseny 1993 [DIRS 162017]). A series of five problems of increasing complexity were posed to five organizations using five distinct computer programs utilizing different assumptions and solution procedures. The input parameters and boundary and initial conditions were given, and the calculators were asked to provide their results to an independent reviewer for analysis and comparison. In other words, this test, termed a "benchmark calculation exercise" provided a blind comparison of various methods for modeling of a complex dynamic problem involving highly non-linear response.

The ultimate problem to be solved was that of a tunnel in explicitly jointed rock subjected to a spherically diverging wave initiated by a blast source (Figure 7-56). The intact rock is treated as a linearly elastic/perfectly plastic material, whereas the slip joint is treated as Coulomb frictional response. Thus, this problem has many aspects in common with the dynamic stability problems of importance for seismically induced rockfall. The principal difference with the present problem is that the dynamic source is different (a spherically diverging wave from a point source rather than shear and compression wave loading), although many of the same mechanical issues are faced in both types of problems.

To solve this overall problem, a series of smaller problems were first posed to test proper solution of fundamental components of the larger problem. These fundamental problems had analytical expressions that could be derived and used for comparison to the model output. The final two problems, which involve determination of the dynamic stressing and yielding of a circular, steel-lined tunnel in a jointed rock mass is complex and has no analytical solution. The problems are reviewed in Table 7-1.

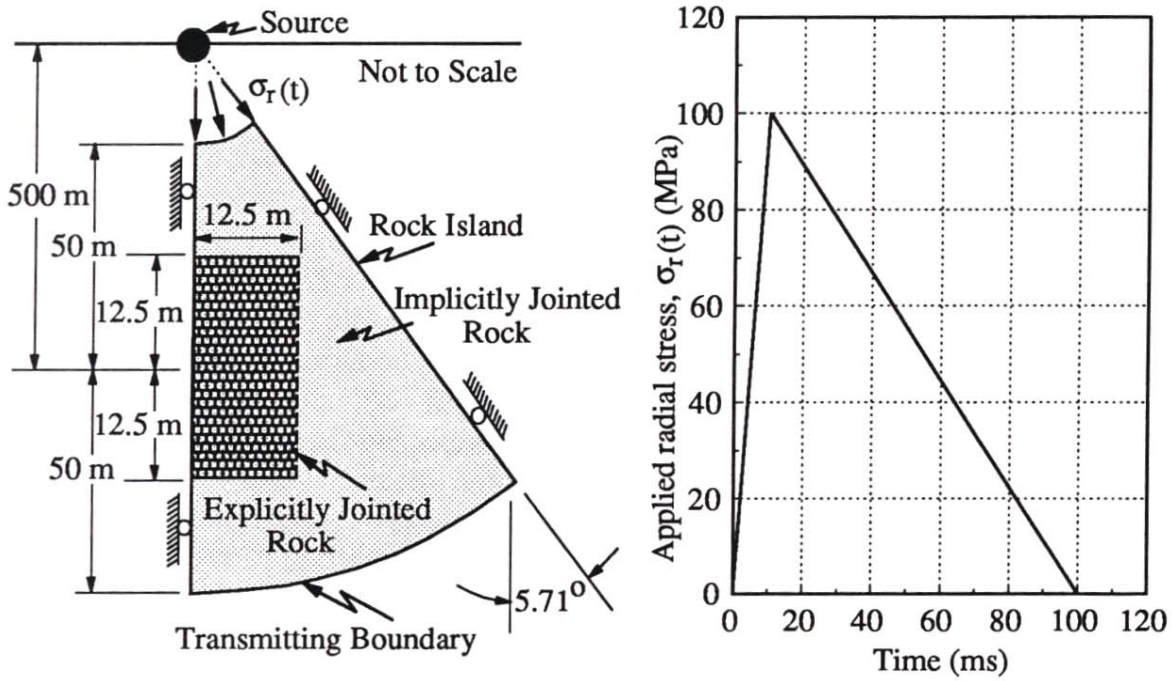

NOTE: The stress characteristics of the source are shown at right (Senseny 1993 [DIRS 162017]).

Figure 7-56. Problem Geometry of the Mechanical Response of a 5-m Diameter Tunnel in Jointed Rock Subjected to a Spherically Expanding Blasting Source

Table 7-1. Code-to-Code Comparison Problems

Problem Number	Description	Comments
1	Testing of intact rock sample to spherically divergent strain path in intact rock.	Quasi-static strain path that simulates passage of a shock front in intact rock (i.e., demonstrates the model accounts properly for propagation in intact media).
2	One-dimensional compression of a 5 m by 4 m sample of jointed rock, exercising the joints in normal deformation.	Tests that the model is able to produce proper pressure vs. volumetric strain response for jointed rock and for intact rock components.
3	Compression of a jointed block, joint in shear while maintaining a homogenous strain rate in the intact rock.	Tests ability of model to produce proper deformations on slipping joint in shear when subjected to complex deformation path.
4	Deformation and stress changes in a wedge-shaped jointed rock mass subjected to spherically divergent wave (same as Problem 5, but without tunnel present).	Ability to properly reproduce rock mass strains in the free field.
5	Deformation and yield of a tunnel in a jointed rock mass subjected to a spherically divergent blast wave. Prediction of stress in rock mass around tunnel.	Complex problem of a jointed rock mass subjected to a triangular blast wave. Highly non-linear response of tunnel as joints shear and large deformations of tunnel occur. No analytic solution – code to code comparison.

Source: Senseny 1993 [DIRS 162017].

These problems tested a number of aspects of the programs that are used in the current drift degradation work, including:

- Ability to represent wave transmission through intact and jointed rock
- Ability to represent the mechanical response of joints to normal and shear loading
- Ability to represent non-reflecting boundaries
- Ability to represent a non-linear, joint-controlled tunnel deformation mode under dynamic loading.

The numerical programs used to conduct the calculations covered a wide range of techniques and methodologies (Table 7-2). With the exception of the PRONTO code, the simulations were conducted by the organization that developed the programs, and thus, the issue of having ill-informed users was removed from the benchmark study. For each problem, the boundary and initial conditions and rock properties were provided and fully specified. The calculator then used their particular model to solve the problem and submit the solutions in a "blind" fashion.

Table 7-2. Programs and Modeling Participants in the Benchmark Study

Organization	Abbreviation	Code
California Research and Technology Division, the Titan Corporation	CRT	EXCALIBUR (Finite Element, Joints modeled explicitly or via constitutive model)
Itasca Consulting Group	Itasca	UDEC (Distinct Element/Finite Difference, joints modeled explicitly)
Lawrence Livermore National Laboratory	LLNL	DIBS (Distinct Element, Rigid Block Formulation)
RE/SPEC, Inc.	RE/SPEC	PRONTO (From Sandia National Laboratory, Finite Difference)
Weidlinger Associates	WA	FLEX (Finite Element, Joints modeled explicitly or via constitutive model)

Source: Senseny 1993 [DIRS 162017].

LLNL = Lawrence Livermore National Laboratory

Results–The UDEC program, as described in detail in Senseny (1993 [DIRS 162017]), provided good agreement to analytic solutions for problems 1 to 3. Only the results of Problems 4 and 5 are discussed in greater detail here. Figure 7-57 shows the comparative results of radial stress and radial velocity at the centroid of the tunnel (not yet excavated) in problem 4. As seen in Figure 7-57, the overall solution of the stress and velocity predictions are quite similar for the various methods, primarily because there is little variation in the stresses or velocities over the computational grid with the exception of temporal offsets in the input function which is consistent with the wavespeed. The distortion, evident in at least one of the models is a result of boundary reflection due to ineffective non-reflecting boundaries. The Lawrence Livermore National Laboratory modeling approach, which has no deformability of the intact material, was

found to perform poorly for the given source wavelength characteristics. UDEC was found to compare favorably with the finite element approaches, which appear to account properly for both non-reflecting boundaries, and free field straining and energy dissipation due to plastic yield.

The final problem of tunnel stability under the divergent wave loading provides a significant numerical test. As stated in Senseny (1993 [DIRS 162017]), the conventional wisdom assumes that after peak stressing, the radial outward motion causes a rapid tangential loading while resulting in a loss of radial confinement and a reduced failure strength than would be assumed for uniaxial loading of the tunnel. The UDEC program was found to provide a reasonable match to crown and invert tunnel closures with other numerical approaches (Figure 7-58) with the exception of the RE/SPEC and Lawrence Livermore National Laboratory models, which provided contrary results (and were later determined to not have provided credible solutions). The tangential and radial stresses for various radial lines around the tunnel at peak free field stress arrival time are given in Figures 7-59 and 7-60. The calculations are compared to the static analytic solution for an orthotropic elastic material. All of the programs show a relatively close agreement to one another, and demonstrate that the effect of the tunnel is to relieve the radial stress component and greatly increase the tangential stresses in comparison to the equivalent free field values. Radial stresses approaching about 8 MPa at the tunnel wall is the result of confinement provided by the steel tunnel liner. Comparison of tunnel deformation modes indicate that significant springline yield and closure (displacements exaggerated by a factor of 10), resulting from slip on joints and intact rock plastic failure occurs in the models with the exception of the Lawrence Livermore National Laboratory rigid block model, again illustrating the importance of internal block deformability and yield.

As concluded by Senseny (1993 [DIRS 162017]), "Three of the five participants (CRT, WA, Itasca) obtained numerical solutions which–where comparisons were possible–agree with each other in most practical respects. All of these solutions appear credible, based on the significant body of evidence available:

1. *Use of rational continuum models to represent the rock*
2. *Use of physically based models for the joints*
3. *Compatibility of results with basic understanding of wave propagation processes*
4. *Absence of obvious numerical artifacts such as spurious reflections*
5. *Comparison of stresses and strains with complete and partial analytic solutions in all the benchmark problems*."

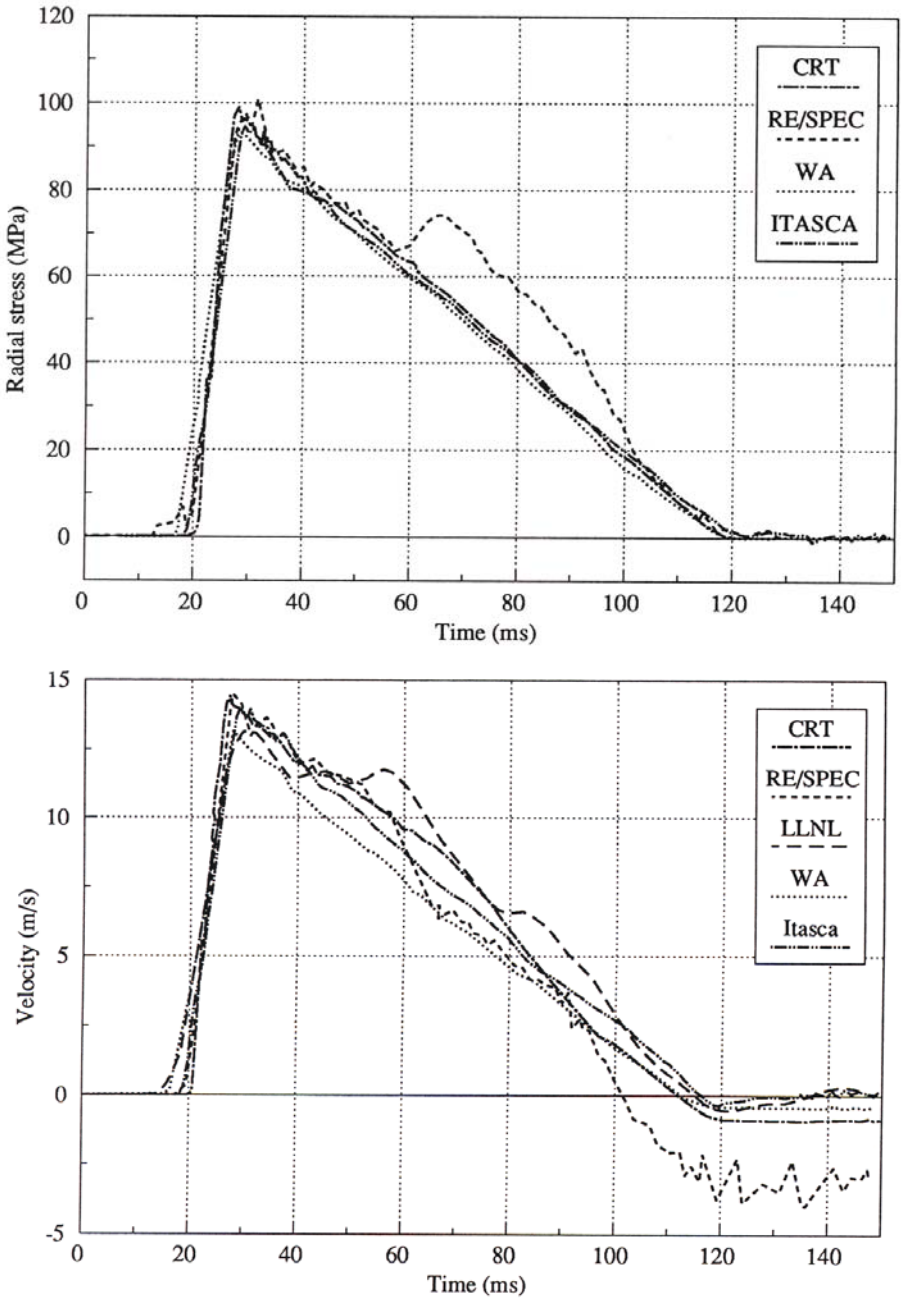

Source: Senseny 1993 [DIRS 162017].

Figure 7-57. Radial Stress (Top) and Radial Velocity (Bottom) at the Centroid of the Future Tunnel Location in Problem 4

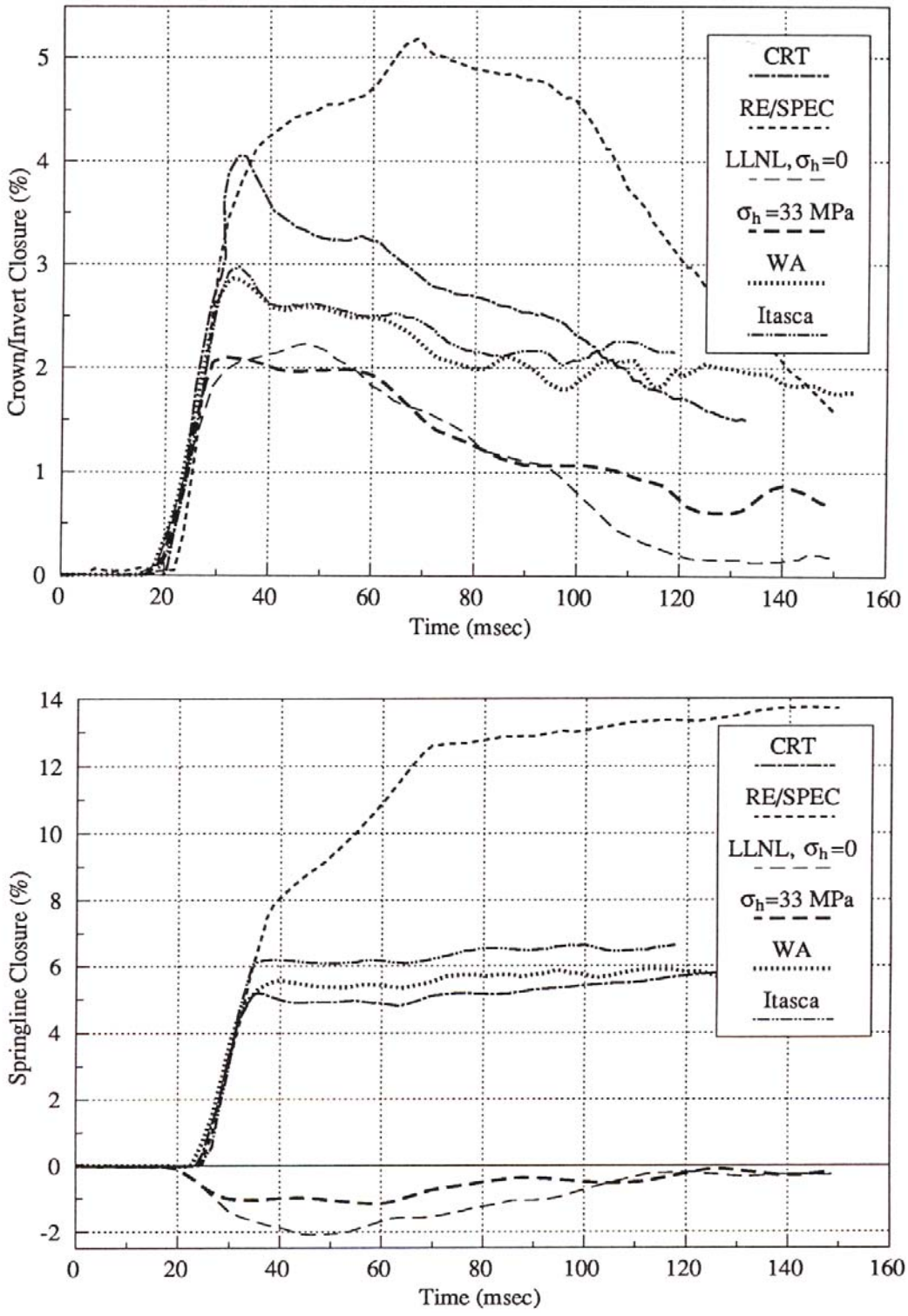

Source: Senseny 1993 [DIRS 162017].

Figure 7-58. Comparison of Predicted Tunnel Invert-Crown (Top) and Springline (Bottom) Closure for Problem 5

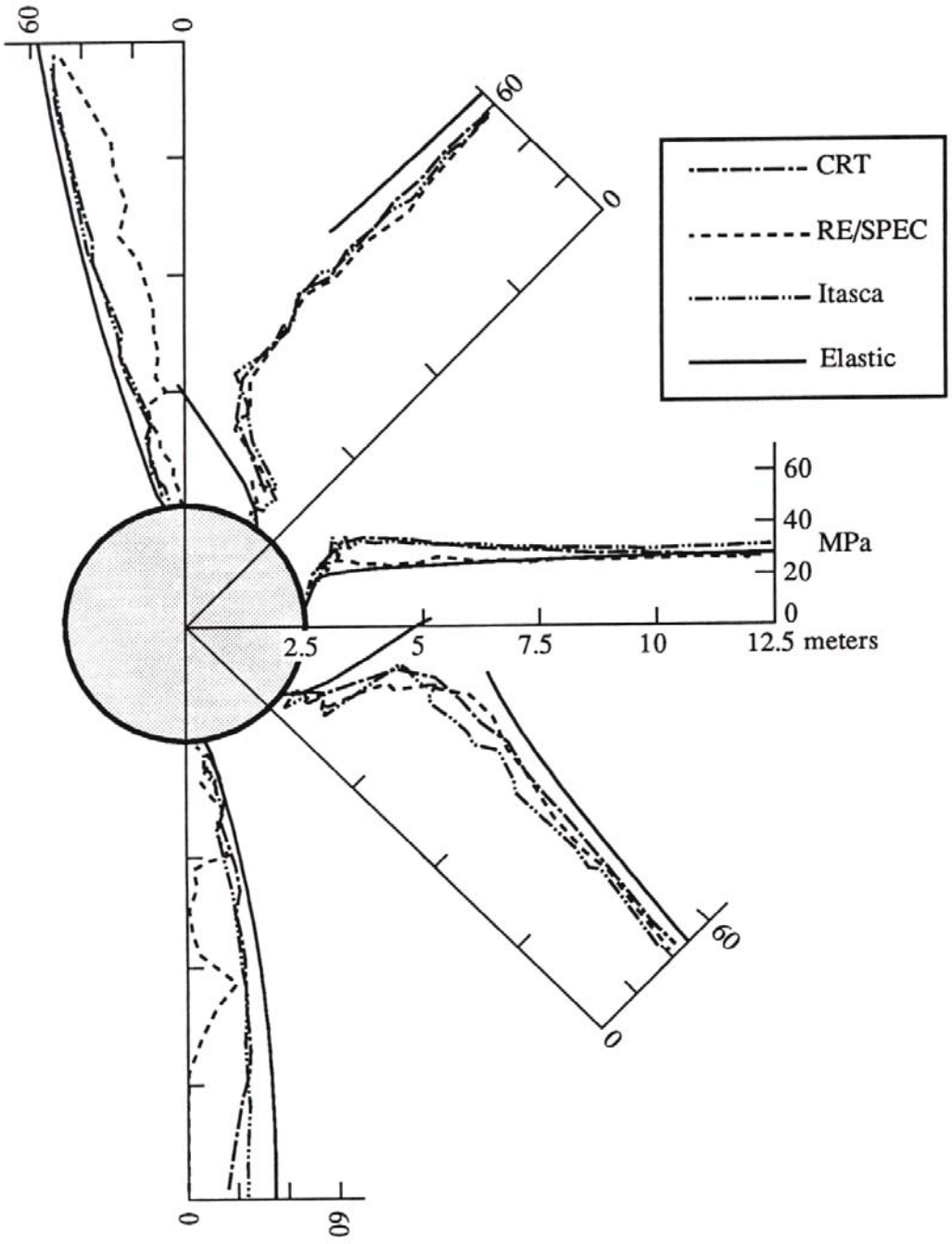

Source: Senseny 1993 [DIRS 162017].

Figure 7-59. Comparison of Radial Stress Along Radial Lines at Peak Free Field Stress Arrival Time, Problem 5

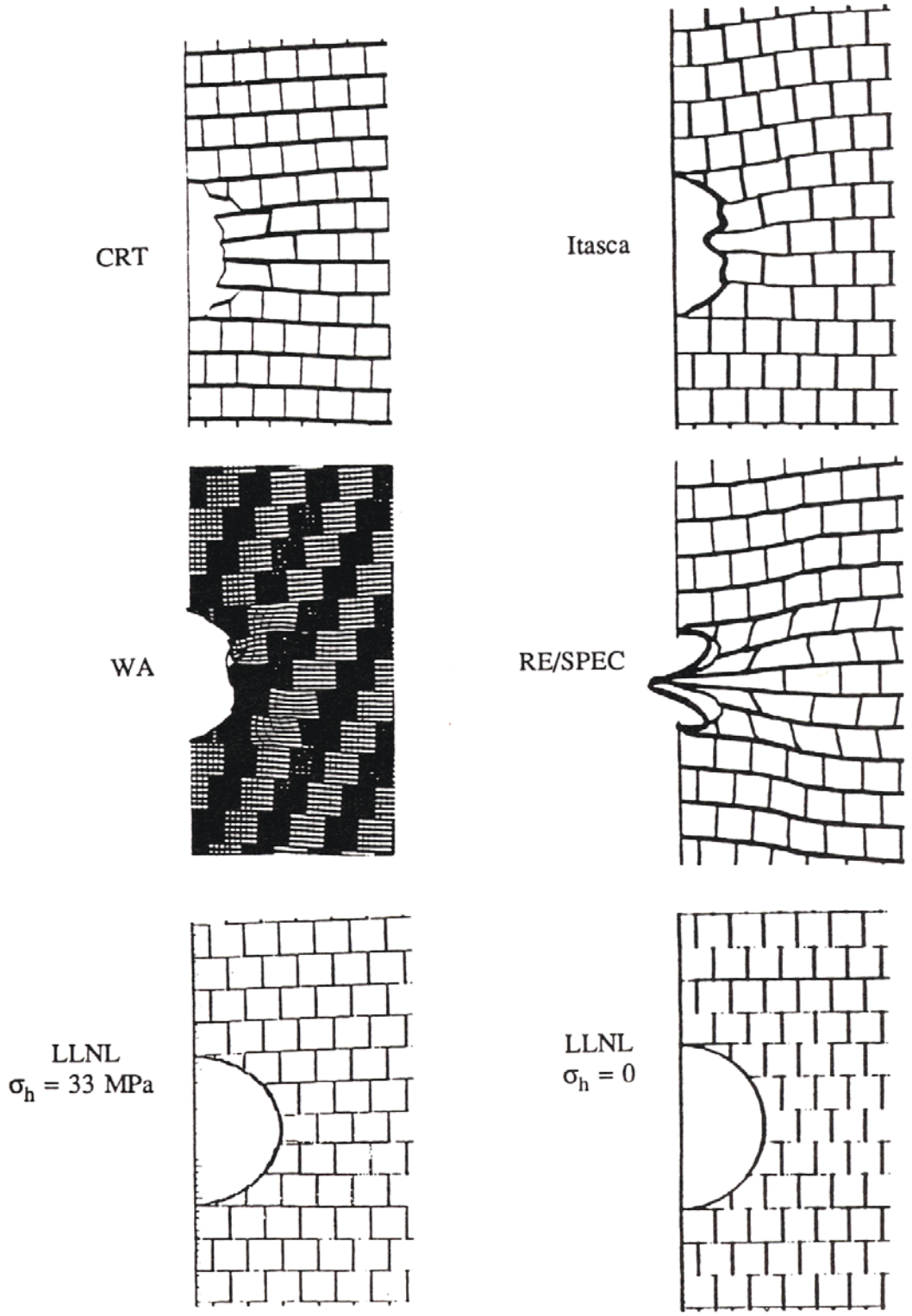

Source: Senseny 1993 [DIRS 162017].

Figure 7-60. Comparisons of Exaggerated Tunnel Shapes (×10) at Equilibrium, Problem 5

7.6.6 Conclusions from UDEC Lithophysal Rockfall Model Validation—Comparison to Criteria

Consistent with the stated level of confidence required for the model, the above validation problems satisfy the criteria for mechanical models of lithophysal rock (Section 7.2.3) and demonstrate the following:

A. The mechanical model, implemented within the UDEC program has been calibrated against laboratory compression tests to reproduce the basic deformability and strength properties of the lithophysal rock. To account for variability introduced by lithophysal porosity, the rock properties range has been subdivided into a number of categories that cover the entire deformability/strength range. This is done in lieu of a statistical treatment of the test data due to the relatively small number of large-core tests. The base model was calibrated to reproduce the moduli and strength for each of these categories.

B. The resulting model was applied to several boundary value problems to demonstrate reasonable ability to predict failure mode and failure extent. The first problem was use of the model to represent laboratory testing. The results show an ability to reproduce the basic failure mechanisms observed in the laboratory testing, which includes axial fracture development in uniaxial compression and localization of a single fracture plane normal to the core axis in uniaxial tension. The model was then applied to represent tunnel response of the ECRB Cross-Drift at various depths. Sidewall springline fracturing and yield occur in the model for the lower end of the calibrated strength range for depths of around 300 to 350 m. The model predicts sidewall fracturing, parallel to the tunnel surface developing at the springline region and extending less than 1 m into the sidewall. This agrees qualitatively to observations of springline fracturing in boreholes and alcoves observed in the lower lithophysal exposures in the ECRB Cross-Drift and ESF main loop, in the mid- to lower-portions of the tunnel. Observations show that wall-parallel fractures in the springline extend approximately 0.5 m in depth. The model and observation agree that no fracturing should exist in the Tptpul which, although of the same general strength range as the Tptpll, the shallower depth of burial results in stresses insufficient to fail the rock mass. Finally, a qualitative comparison of the modeling approach to predict thermally induced rock fracture was demonstrated through comparison of the model to field observation of the Drift Scale Heater Test in the Tptpmn. This validation showed that the general technique is able to reproduce, qualitatively, the development of roof-parallel spalling fractures induced by the thermally overdriven horizontal stresses in the immediate crown of the drift. The model is able to reproduce the timing (i.e., the stress level), extent and general mechanism of the failure (i.e., splitting parallel to the free surface).

C. The UDEC model has been shown to produce rock mass stress, displacement and yield around a heated emplacement drift that are quite similar to those produced from an alternative, continuum-based modeling approach for both elastic and inelastic rock mass constitutive models.

D. The ability of the model to properly represent complex dynamic boundary conditions is demonstrated in the UDEC User's Manual, but was further demonstrated in the validation exercise in which comparisons were made between UDEC and other numerical methods (Senseny 1993 [DIRS 162017]). In this work, conducted for the Defense Nuclear Agency, a rigorous code-to-code comparison was conducted in which test problems of increasing complexity were analyzed in a "blind" calculation and comparison exercise. The simplest of the problems involved problems that tested the code's ability to properly reproduce the mechanical response of the basic building blocks of the model (i.e., the fractures, the intact blocks, and the ability to properly account for boundary conditions and complex load paths). The final test was a full comparison of the models to a large scale field experiment of a lined tunnel in a fractured rock mass subjected to dynamic loading sufficient to fail the material and deform the tunnel lining. Of interest was that the "answer" was not known in advance; the predictions made were "blind" and the comparison of the results with various models was performed by an outside agency. The UDEC lithophysal rockfall model, as shown, compared very favorably with the problems and demonstrated the ability of the program to reasonably represent the dynamic response of a fractured media.

7.6.7 UDEC Lithophysal Rockfall Model Limitations

7.6.7.1 Impact of Block Discretization Level

As was discussed previously, the discretization of the UDEC lithophysal rockfall model into Voronoi blocks does not represent actual internal structure of the lithophysal material. The block structure is merely a device that allows the formation of potential fractures within the rock mass, thus allowing it to fail and form independent blocks when stressed. There are two important points regarding the level of discretization of the blocks:

- The block dimensions must be small enough that they do not have an overriding influence on the failure extent or mechanical behavior

- The block dimensions should be commensurate to or smaller than the size of the expected rock particles to be formed (see Section 6.4.1).

Therefore, it is necessary to show that the mechanical behavior of the synthetic material is independent of the block size. Selection of the block size for simulation is an optimization process. Very small block size (e.g., 100 times smaller than the drift diameter, the characteristic dimension of the problem) will certainly ensure that the problem solution would be practically independent of the block size, but would lead to very long calculation times. The block size was selected based on the criteria of small differences in rockfall prediction as the block size is reduced, and reasonable calculation time for problem solution. A comparison of the fracturing predictions due to drift excavation in rock mass Category 1 for 300 m overburden from two models considering average block edges of 0.3 m (5.4 percent of the drift diameter, or roughly 18 blocks across a drift diameter) and 0.2 m (3.6 percent) is shown in Figure 7-61. The in situ stress state is characterized with a vertical to horizontal stress ratio of 2:1. The results, shown in Figure 7-61, compare the failure (i.e., sidewall fracturing, for two different cases). As seen, the overall end-result of the calculation shows that mechanism of sidewall spalling is

roughly the same for both cases. There is some small difference in the amount and location of fracturing, depending on the block geometry. However, the cases show the same general behavior and the same general depth of damage in the sidewalls. Also, the effect of three different realizations of geometry of blocks (maintaining the same average block size of 0.3 m) was investigated and results (for Category 1 rock mass an 350 m overburden) are shown in Figure 7-62. Clearly, the realization of block geometry effects a particular realization of cracking. But more importantly, the general characterization of cracking (density, depth) is not affected by the particular geometry of blocks. If the block size is too large, the effect of a particular geometry of Voronoi blocks on the model results would be more pronounced. From parametric analyses of block size, a block size of 0.3 m produced satisfactory results while optimizing model run time.

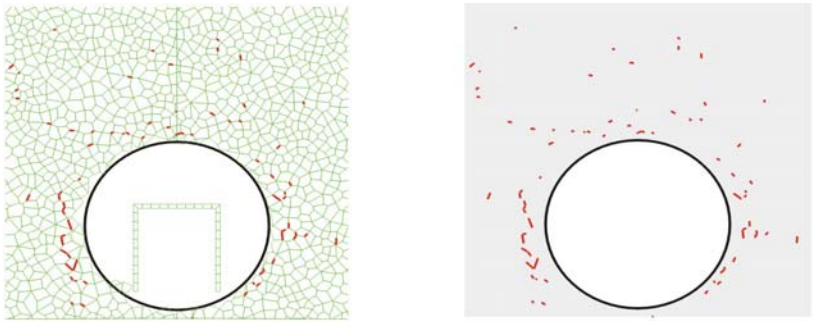

a) block size 0.3 m

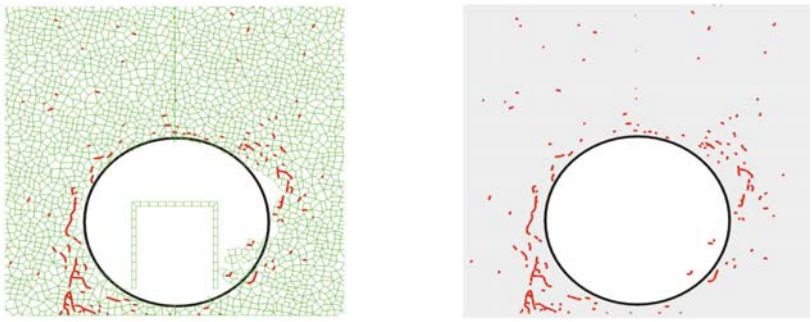

b) block size 0.2 m

NOTE: The general behavior of the drift is similar in each case. A small portion of the sidewalls fails to a depth of approximately 0.5 m, while the depth of fracturing is similar. Note that the failure response is not symmetric due to the random block patterns.

Figure 7-61. Block Size Effect: Behavior of the Rock Mass (Rock Mass Category 1, 300-m Overburden) Under Vertical and Horizontal Stress at Ratio of 2:1

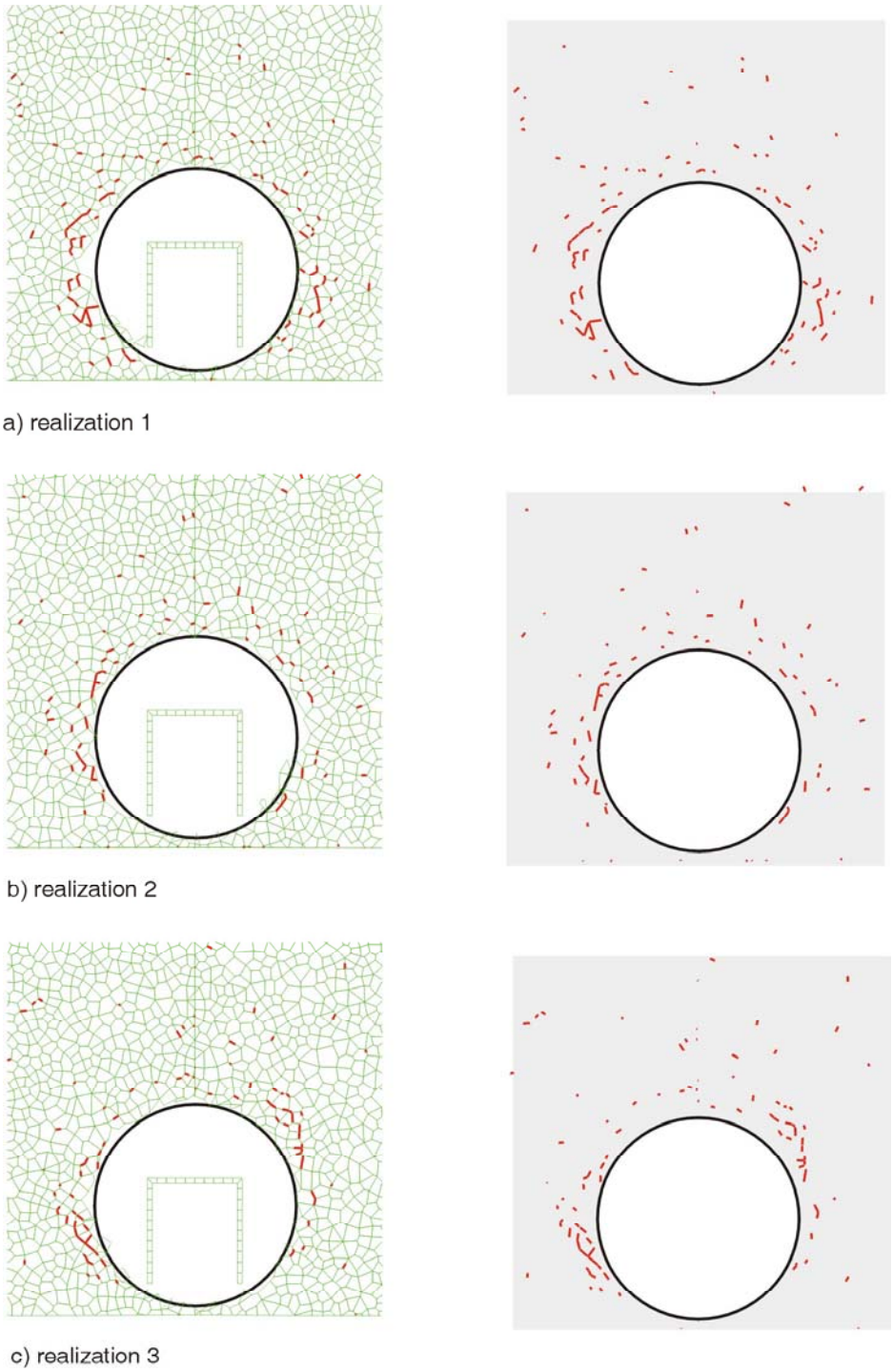

Figure 7-62. Effect of Voronoi Block Realization: Behavior of the Rock Mass (Rock Mass Category 1, 350-m Overburden) Under Vertical and Horizontal Stress at Ratio of 2:1

7.6.7.2 Impact of Inertial Forces in Quasi-Static Loading

The UDEC program uses an explicit finite difference method for solving Newton's Laws of Motion utilizing a fully dynamic formulation. A viscous damping scheme is used to remove energy from the model to achieve quasi-static equilibrium. When modeling quasi-static problems, such as thermal loading, it is important not to apply temperatures in too large an increment to avoid dynamic effects. In the modeling conducted in this study for the lithophysal rocks, temperatures are input from the NUFT program (see Section 3) to UDEC, which, in turn, calculates thermally induced expansions and stresses. Sensitivity studies indicated that the change in temperature applied to the UDEC program should be kept to less than 5°C to avoid dynamic effects.

7.6.7.3 Consideration of Homogenous and Isotropic Response of the Lithophysal Rock Mass

The modeling method employed for representing lithophysal rock considers that the rock mass is homogeneous and isotropic, and thus a two-dimensional, cross-sectional analysis is sufficient for model tunnel response to heating and dynamic stressing. Essentially, this consideration means that the region around the tunnel that could contribute to yielding has lithophysal porosity that is uniformly distributed. In other words, at any given location, a tunnel driven at any azimuth would encounter roughly the same lithophysal porosity variation. Data on lithophysal porosity variation from Section 6.1.4.2 and Appendix O indicate that lithophysal porosity varies over a range of perhaps 10 m.

7.6.7.4 Lack of Confined Compression Tests in the Lithophysal Rock

No experimental data are available for large diameter lithophysal rock under confined conditions. This is because it is very difficult to carry out triaxial tests on samples from the lithophysal rock mass, since the membrane used for application of the confinement on the sample would deform into the lithophysae exposed on the circumference of the cylinder and most likely be punctured. Additionally, very large triaxial pressure vessels are rare. To overcome this potential issue, the PFC and UDEC lithophysal rockfall models were used to model the lithophysal rock as a solid matrix with internal holes. These models were calibrated against laboratory data on large core unconfined compression tests to verify that that relationship of strength and modulus to lithophysal porosity, and failure mechanisms was reasonably reproduced.

As discussed in Section 9.2.3.2 of the *Subsurface Geotechnical Parameters Report* (BSC 2003 [DIRS 166660]), the calibrated PFC and UDEC lithophysal rockfall models were used to simulate triaxial compression tests on lithophysal rock "samples" of various porosity. The results of these numerical experiments were then used to construct expected failure envelopes for the lithophysal rock mass. Figure 7-63 and Table 7-3 provide a summary of the results of these analyses.

Model results show that damage (due to excavation, thermally induced stresses, seismically induced preclosure ground motion, or time-dependent effect) is mostly confined to the drift boundary, and takes place under almost uniaxial loading conditions. For these conditions,

correct behavior of the rock mass under confinement is not essential for proper simulation of damage and rockfall.

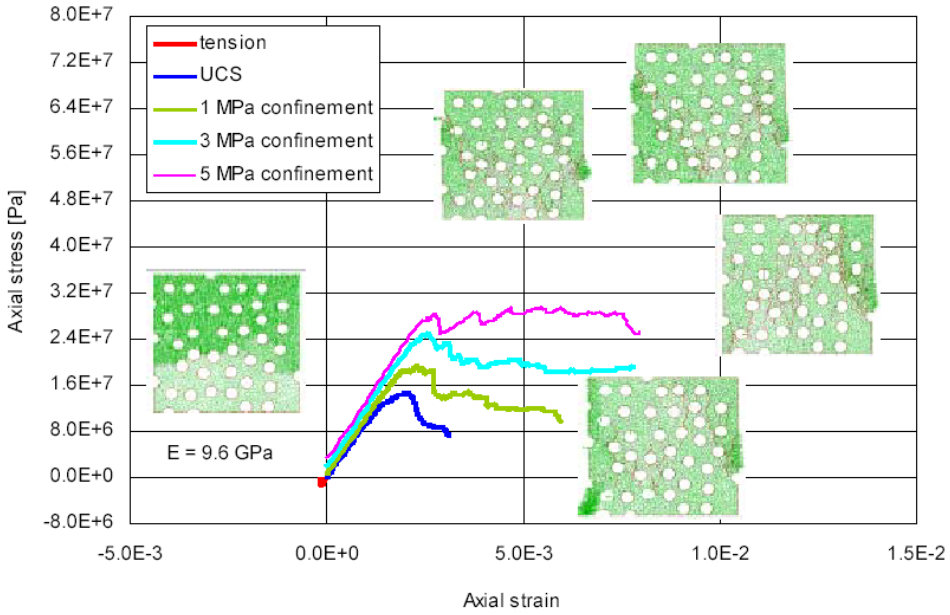

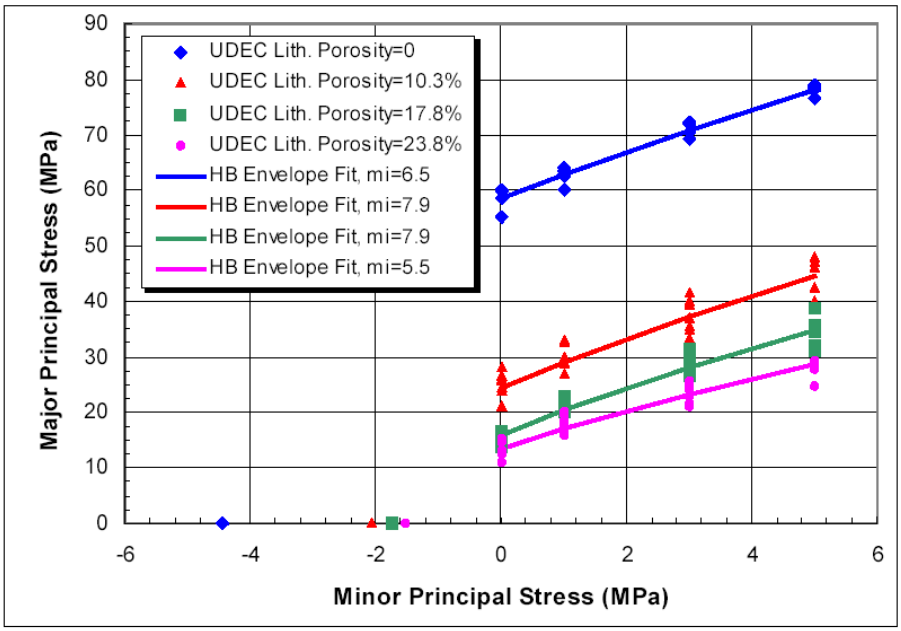

NOTE: Several realizations of UDEC analyses were conducted at each minor principal (confining) stress level. Non-linear Hoek-Brown failure envelopes have been fit to each dataset.

Figure 7-63. Sample UDEC Simulation of Triaxial Response for 23.8% Lithophysal Porosity (top) and Hoek-Brown Failure Criteria Fits for Lithophysal Rocks Determined from UDEC Lithophysal Rockfall model Triaxial Numerical Test Analysis

Table 7-3. Estimated Lithophysal Rock Mass Properties as Estimated from UDEC Triaxial Test Simulations

Lithophysal Porosity (%)	UCS (MPa)	Young's Modulus (GPa)	Friction Angle (degree)	Cohesion (MPa)	Tensile Strength (MPa)	Hoek-Brown σ_{ci} (MPa)	Hoek-Brown m_i
0	58.7	19.8	36	14.9	4.4	58.5	6.6
10	25.1	14.2	36	6.4	2.1	25.1	7.7
17	15.5	11.2	35	4.1	1.7	16.5	7.3
24	13.2	9.3	29	3.9	1.5	14	5.0

Source: Table 9-3, *Subsurface Geotechnical Parameters Report* (BSC 2003 [DIRS 166660], Table 9-3).
UCS = uniaxial compressive strength

The derived rock mass friction angles from the UDEC lithophysal rockfall models in this table can be compared to laboratory measurements of friction angles measured on small samples of nonlithophysal rock are more than 40° (Appendix E, Section E.3).

7.7 MODEL VALIDATION FOR REPRESENTATION OF NONLITHOPHYSAL ROCK

7.7.1 Introduction

As stated in Section 7.1, modeling of the nonlithophysal rock requires use of a three-dimensional, discontinuum modeling approach. A validation strategy was adopted based on demonstrating that the mechanical response of the fractures, which control the stability of the tunnel under shaking, function properly by corroboration with laboratory data. The rockfall component results from 3DEC are compared to an explosively loaded, scaled tunnel stability experiment in jointed rock. Additionally, results from the nonlithophysal rockfall model are compared to an alternative numerical model. Finally, an external expert technical review is used as a method for validation of the overall modeling approach for representation of nonlithophysal rock.

7.7.2 Verification of Initial Conditions and Dynamic Boundary Conditions (Confidence Building During Model Development)

Section 6.3.1.2 provides verification that the initial stress conditions and the dynamic boundary conditions were modeled properly within the 3DEC program. A test case was run in which the ground motion is applied at the base of the model and monitored at the mid-point of the model to ascertain that the method of ground motion application at the boundary (by applying equivalent stresses) properly converts the stress history to the velocity history. The test case also verified that no distortion of the waveform (which could result from insufficient model element discretization) occurred.

7.7.3 3DEC Post-Development Validation Exercise 1 – Validation of the Fracture Mechanical Representation – Comparison to Laboratory Direct Shear Testing (Corroboration with Laboratory Data)

7.7.3.1 Introduction

This validation example is given to demonstrate the ability of the 3DEC program, and the joint constitutive model used to reproduce the joint direct shear test data from large-scale testing of Tptpmn samples (DTN: GS030283114222.001 [DIRS 161913]).

7.7.3.2 Direct Shear Data

A number of direct shear tests were run on joints obtained from 11.5-in diameter core samples that were drilled at a low angle to either the smooth, sub-vertical cooling joints, or the rough, sub-horizontal vapor-phase alterations. The cores were obtained from the Tptpmn unit. The tests were run by setting (in hydrostone) the two halves of the core sample containing the fracture in opposing halves of a steel direct shear box. The opposing halves of the fracture are then reconstructed and placed in a large direct shear machine. A sequence of direct shear tests were then run by first applying a normal stress of 1 MPa to the sample which is then slowly sheared by applying a lateral stress to the upper half of the sample. The sample fracture surface is then cleaned by compressed air, reconstructed and the test run again with normal stresses of 4 MPa and 7 MPa (approximate) normal stresses. A final re-test at the initial 1 MPa normal stress level is run to document damage to the joint. One possible limitation of these tests is that successive damage is done to the joint surfaces by re-running the tests at increasing normal loads. However, with limited large sample availability, it was decided to get the greatest amount of information from each sample. From these tests, it is possible to plot the shear stress-shear displacement and normal stress-normal displacement behavior as well as the Coulomb slip envelope, from which the cohesion and friction angle can be calculated. The joint shear stiffness and dilation angle can be determined from the shear stress-shear displacement and normal displacement-shear displacement data, respectively. The test data for two representative tests are given in Figures 7-64 and 7-65 (DTN: GS030283114222.001 [DIRS 161913]). Figure 7-64 shows the test results for a typical sub-horizontal vapor-phase parting, and Figure 7-65 shows the test results for the sub-vertical cooling fracture. The plots superimpose the results from the normal stresses as well as the re-test at the 1 MPa stress level.

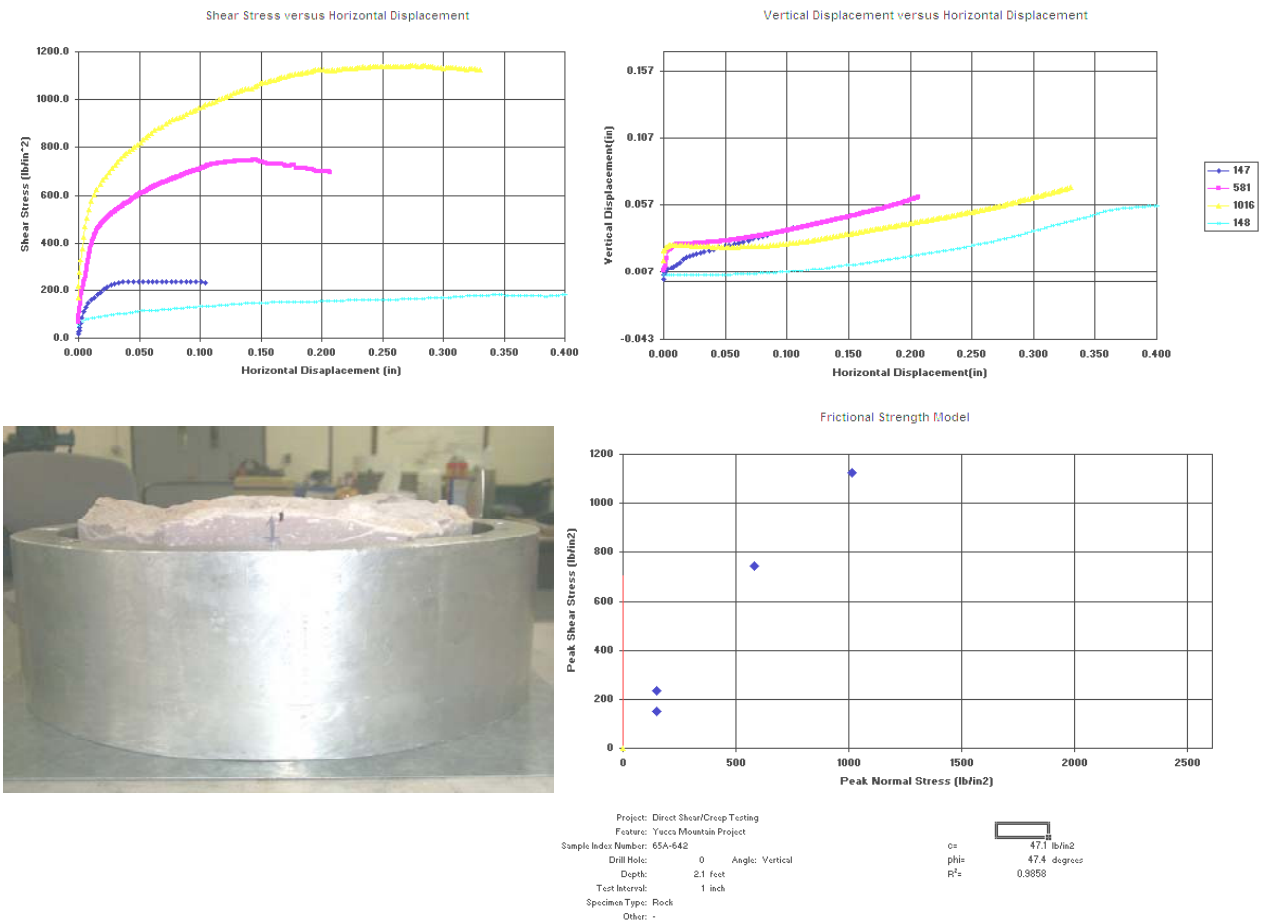

Source: DTN: GS030283114222.001 [DIRS 161913].

NOTES: Cohesion is 0.3 MPa, and friction angle of the surface is 47.4°. Legend shows normal stress (lbs/in^2). The data can be accessed through the Records Processing Center Package # MOY-030226-41-01 (MOL.20030226.0038, pp. 2-5) associated with the source DTN.

Figure 7-64. Direct Shear Test Results for a Rough, Sub-Horizontal Vapor-Phase Parting

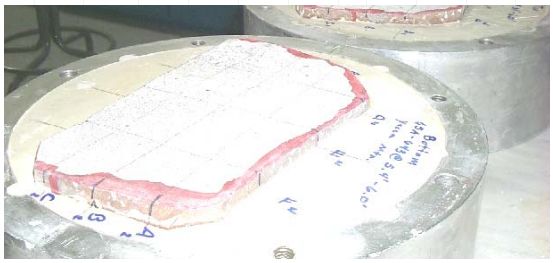

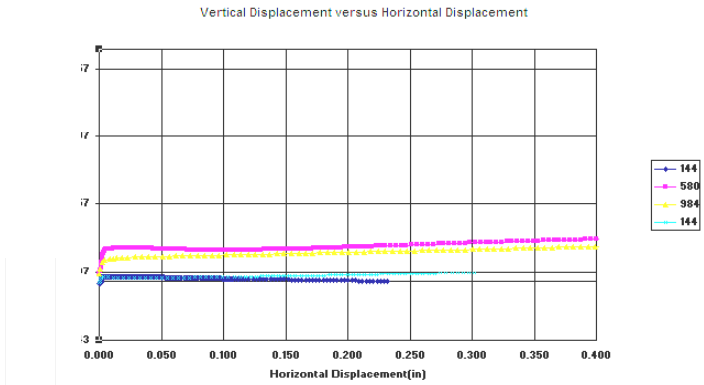

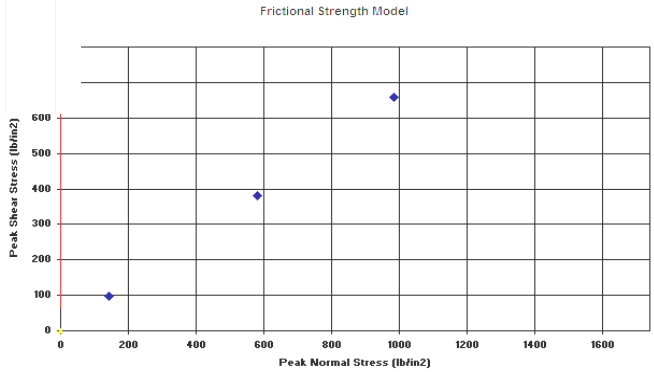

Project:	Direct Shear/Creep Testing				
Feature:	Yucca Mountain Project				
Sample Index Number:	65A-643			c=	-0.2 lb/in2
Drill Hole:	0	Angle:	Vertical	phi=	33.7 degrees
Depth:	5.4-6.0 feet			R^2=	0.9998
Test Interval:	1 inch				
Specimen Type:	Rock				
Other:	-				

Source: DTN: GS030283114222.001 [DIRS 161913].

NOTES: Cohesion is zero and friction angle of the surface is 33.6°. Legend shows normal stress (lbs/in2). The data can be accessed through the Records Processing Center Package # MOY-030226-41-01 (MOL.20030226.0039, pp. 2-6) associated with the source DTN.

Figure 7-65. Direct Shear Test Results for a Smooth, Sub-Vertical Cooling Joint

7.7.3.3 Analysis

In this validation, the 3DEC program is used to recreate the direct shear test numerically. The results of the model and test for the calculated surface friction angle and cohesion are compared. Figure 7-66 shows the 3DEC model with a horizontal fracture plane. The bottom block is fixed along its vertical and lower horizontal surfaces to represent the shear box. A vertical pressure is applied to the top of the upper block, while the lateral expansion is held fixed. A velocity is then applied to one of the vertical faces, forcing the top block to shear over the lower block. Figure 7-67 shows a cross-section through the block with superimposed shear slip vectors after it has begun slipping.

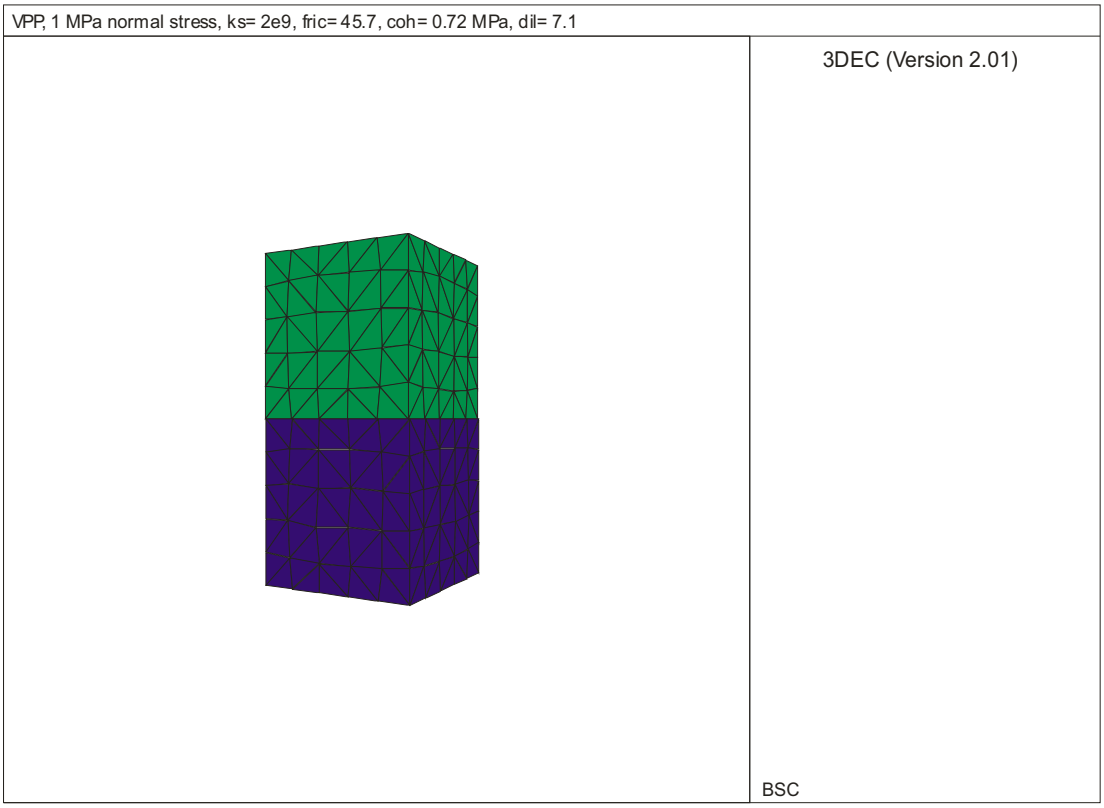

NOTE: Lower (blue) block has surface displacements fixed on the vertical and bottom faces to represent the fixed block of the direct shear test. The upper (green) block has two vertical faces fixed, one vertical face free and one vertical face with a prescribed horizontal velocity representing the shear displacement of the test machine. A constant stress is applied to the upper surface to provide the normal stress to the joint surface.

Figure 7-66. Perspective View of 3DEC Model of Direct Shear Test of Joint

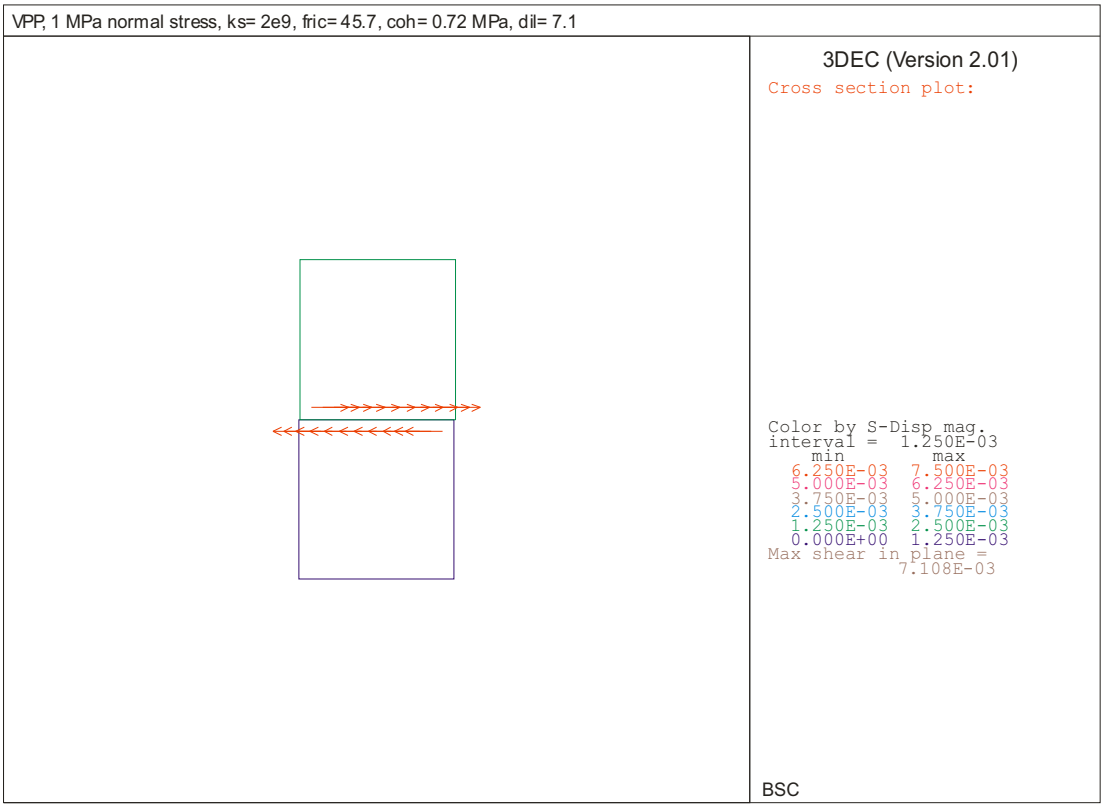

NOTE: Cross-section is taken parallel to shear movement applied by machine.

Figure 7-67. Cross-Sectional View Through Model Showing Relative Shear Displacement of Joint Surfaces

Analyses were performed for two cases: the sub-vertical, smooth cooling joint shown in Figure 7-65, and the sub-horizontal vapor-phase parting illustrated in Figure 7-64. Two basic types of joint shear constitutive models based on a standard Coulomb slip condition are available in the 3DEC program. The first model, the default in 3DEC (JCONS=1), considers that once slip is initiated, the cohesive strength of the joint is broken, and drops to zero. From that point, the joint reaches a residual strength based only on the friction and dilation angles of the surfaces. The second model (JCONS=2) considers that the cohesion of the surfaces remains constant, resulting in a typical elastic-perfectly plastic response. The seismic and thermal analyses discussed in Section 6.3 of this report use the default constitutive model.

The JCONS=1, or default, model is applicable to both the vapor-phase partings and the cooling fractures. First, the rough, vapor-phase partings (which are anastomosing structures) are cohesive structures that have surfaces weakly bonded in situ by minerals such as cristobalite and tridymite. Once this bond is broken, it is sensible that the surfaces reach a residual state of strength based primarily on friction. The cooling joints, however, have smooth surfaces with no apparent cohesion or tensile resistance. Therefore, there is no difference in JCONS 1 or 2. Figures 7-68 and 7-69 show a comparison of the 3DEC direct shear simulations to the laboratory tests. As seen in Figure 7-68, the comparison of model to laboratory is qualitatively quite reasonable, particularly for the first test conducted at 1 MPa normal stress, in which the joint is in an undamaged state. The comparison is still reasonable for the higher confinements,

but it must be realized that the model is using the average friction angle and dilation angle determined for the tests. The re-test at 1 MPa normal load shows virtually the same results as for the initial test, indicating that there is little surface damage from the previous testing. This makes sense since the joint has less than 2° dilation angle, and thus very little surface irregularity (roughness) that can be permanently damaged. The shear stiffness used in this simulation is determined from the tangent value (the initial loading slope). The stiffness departs from this approach only near its peak strength.

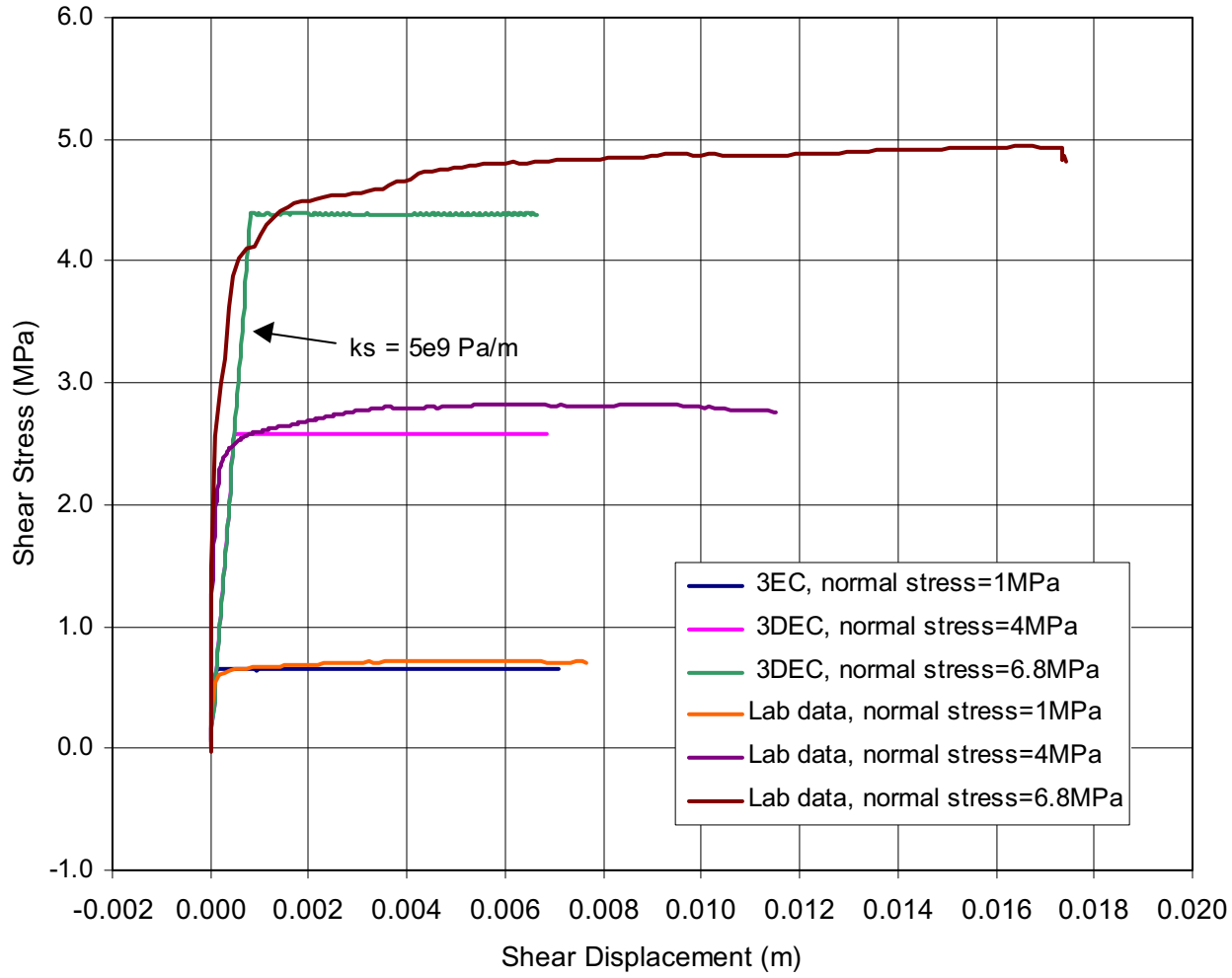

NOTE: Joint sample is a subvertical, smooth cooling joint (see Figure 7-65).

Figure 7-68. Comparison of 3DEC Mohr-Coulomb Joint Constitutive Model to Laboratory Direct Shear Testing for Sample 643, Hole ERCB-GTEC-CS1250-13

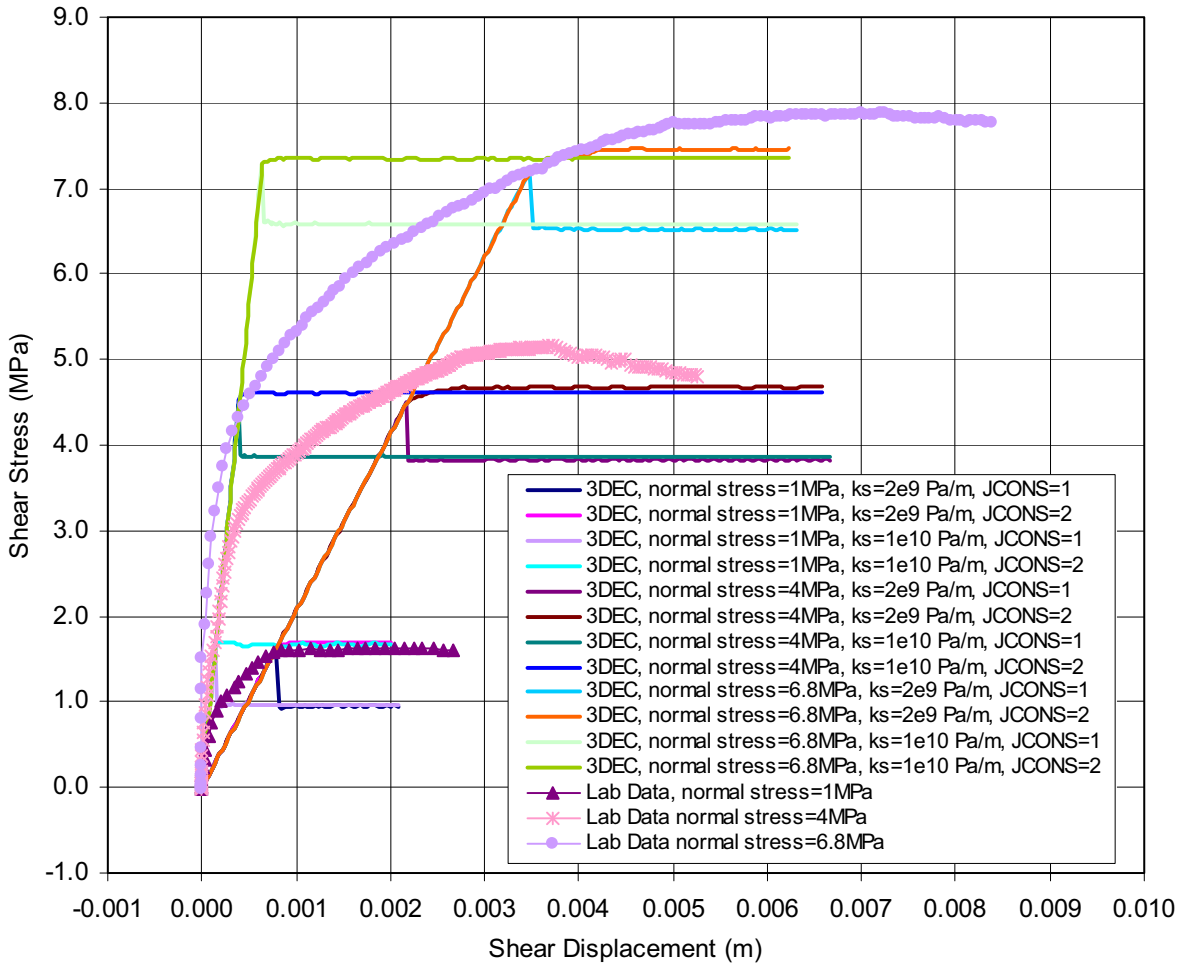

NOTE: The laboratory data are the plots displayed with symbols and the 3DEC results are shown as lines. Three tests are shown for three different normal stress levels. Each of these tests is compared to four different 3DEC results that use the same friction and dilation angles as calculated from laboratory test results. Since 3DEC uses a linear shear stiffness consideration, two different shear stiffness values have been used to bound the laboratory data: a tangent value (Ks=1e10 Pa/m) that represents the initial loading, and a secant value (Ks=2e9 Pa/m) that represents the shear displacement at peak strength.

Figure 7-69. Comparison of 3DEC Simulation of Direction Shear Testing of a Vapor-Phase Parting (see Figure 7-64)

In Figure 7-69, the comparison of the 3DEC results for both JCONS 1 and 2 shows the laboratory data. The vapor-phase partings, being very rough joints with high dilation angle (approximately 13°), show a non-linear shear stiffness that is seen as the curvature in the loading portion of the curve. This is contrasted to the largely linear loading slope for the previous smooth cooling joint case. The 3DEC joint model considers a simple, linear loading slope characterized by a constant shear stiffness. Therefore, the approach taken in the tunnel modeling discussed in Section 6.3 of this report is to examine the effect of variable shear (and normal) stiffness on the global response. The validation of the 3DEC model examines two shear stiffness values: the tangential slope defined by the initial loading prior to its departure from linearity, and the secant slope determined from the displacement at peak shear strength. For each of these shear stiffness values, simulations are run for the JCONS=1 (softening model) and for

JCONS=2 (elastic-perfectly plastic model with no strength loss). Thus, for each level of normal stress (1, 4, and 7 MPa), four simulations are conducted. Each of the simulations considers a constant friction angle and dilation angle derived from the laboratory test data.

As seen in Figure 7-69, the laboratory data are fit reasonably well with the selection of a secant shear stiffness and no post-peak softening of the material response. The tangent stiffness consideration, coupled with the post-peak softening model (JCONS=1) is conservative in that peak strength is reached after a smaller level of shear displacement, and that the strength drops to a slightly smaller residual value when cohesion of the surface is considered to be destroyed. The tunnel scale modeling is conducted with values of shear stiffness (1e10 Pa/m – default, and 2e9 Pa/m) that bound the prospective range. It was shown in Section 6.3.1.6.2 that sensitivity studies of shear stiffness have a minor effect on the calculation of rockfall.

7.7.4 3DEC Post-Development Validation Exercise 2 – Validation of the Nonlithophysal Rockfall Model Implemented in 3DEC by Comparison to an Explosively Loaded, Scaled Tunnel Stability Experiment in Jointed Rock (Corroboration with Information Published in the Literature)

In this example, data from a Defense Nuclear Agency-sponsored explosive tunnel stability field experiment conducted in a simulated jointed rock mass is used as a validation test for the 3DEC program. This problem tests a number of aspects of 3DEC that are used in the current drift degradation model, including:

- The ability of 3DEC for representation of wave transmission through intact and jointed rock
- The ability of 3DEC for representation of the mechanical response of joints to dynamic normal and shear loading
- The ability of 3DEC for representation of a non-linear, joint controlled tunnel deformation under dynamic loading.

Details of the physical experiment are described in detail in Senseny and Pucik (1999 [DIRS 168479]), and summarized here. The test involved blast-induced dynamic loading of a scaled, lined cylindrical tunnel in a simulated jointed rock, and was described in Section 7.6.5.5. The purpose of the test was to provide a realistic experiment at a relatively large scale for validation of and comparison of a number of numerical modeling programs capable of representing tunnel failure under dynamic loading.

The experiment consisted of a simulated rock mass composed of over 4000 limestone blocks, each being 51 mm square by 0.6 m or 1.2 m in length (Figure 7-70). The bricks were stacked into a nearly cubical specimen measuring 2.1 m square and 2.4 m in length with a central 0.4 m diameter cylindrical hole (the tunnel) that was lined with a thin aluminum tube. Instrumentation included 46 gauges for monitoring velocity, stress, joint slip and tunnel closure.

The entire “sample” was placed in a pit and covered with concrete. The midline of the concrete surface was formed in a half-cylinder to allow application of a cylindrically-diverging blast wave

generated by explosives. The resulting stress wave had a radius of 4.4 m, a rise time of about 500 μm, a peak stress of about 100 MPa and peak particle velocity of about 14 m/sec, a total radial displacement of about 25 mm, and peak circumferential strain of about 0.6 percent. This divergent dynamic environment was sufficient to cause joint slip, intact rock fracture and permanent deformation of the lined opening.

A number of calculators were presented with the model boundary and initial conditions, the block geometry and laboratory-measured rock and joint properties. A "blind" validation of a number of two-dimensional numerical models (including the UDEC program), which used different methods for simulating joint surfaces, was then conducted as discussed in Section 7.6.5.5. The term "blind" here refers to fact that the numerical analysts were asked to produce model predictions of the system response without knowledge of the experiment outcome. Analysts were provided the basic intact and joint material testing data, test geometry and boundary and initial conditions. They subsequently formulated the analysis methodology, conducted the numerical analyses and submitted the results to a separate group whose purpose was to perform code-to-experiment and code-to-code comparisons. Senseny and Pucik (1999 [DIRS 168479]) gathered the results of the simulations and performed code-to-experiment and code-to-code comparisons from the various calculators. Here, the results of the same experiment are compared to numerical predictions made by the 3DEC program.

7.7.4.1 Rock Properties Data

The rock chosen for this test was a porous limestone from the Salem formation. Intact specimens were tested in triaxial compression and triaxial extension. The reported data shown in Figure 7-71 indicate very little variation between tests, and the results were consistent between three different testing laboratories.

Seen in Figure 7-72, failure envelopes developed from the triaxial compression and triaxial extension tests. Tests also were conducted on joints to determine their shear strength and stiffness. Special specimen preparation procedures were employed to ensure that the joint surfaces in the laboratory tests were similar to those in the jointed-rock tests. The normal compressibility of the joint surfaces was determined by unconfined compression tests on specimens with a single joint oriented at 90^{o} to the specimen axis. Each specimen was loaded to approximately 75 percent of its unconfined strength and then unloaded. Figure 7-73(a) shows typical joint normal-direction compressibility data. Under normal loading, the joints are fully closed after approximately 0.05 mm displacement.

The shear strength of the joints was determined by a series of triaxial compression tests on cylindrical specimens, each containing a single joint oriented at 30^{o} to the specimen axis. The confining pressure in these tests ranged from 1 MPa to 35 MPa. At confining pressures up to 30 MPa, the specimens failed by sliding of the joints at approximately constant stress. When loaded at a confining pressure of 35 MPa, the intact portion of the test specimen failed without sliding along the joint. Figure 7-73(b) plots peak shear stress on the joint as a function of normal stress on the joint for tests performed at confining pressures up to 30 MPa. The joint strength data are well represented by a straight line passing through the origin with a 38.3^{o} friction angle.

7.7.4.2 Constitutive Models

Limestone Intact and Joint Constitutive Models–The constitutive model used for intact limestone in the 3DEC program is an elastic-plastic, strain-softening model (no cap on the yield surface) using a Mohr-Coulomb shear failure surface with tension cutoff. Greater detail on the Mohr-Coulomb strain-softening plasticity model can be found in the 3DEC User's Manual (Itasca Consulting Group 2002 [DIRS 160331]). The strains are subject to a non-associated flow with zero dilatancy in shear and associated flow in tension. The strain softening is controlled via isotropic softening of the intact material cohesion and tensile strength. No rate dependence of material properties is considered. The joint model used considered Coulomb slip with constant shear and normal stiffness based on the data shown in Figure 7-73, and given in Table 7-4. The constitutive model for the aluminum liner was an isotropic-hardening Tresca model with properties given in Table 7-4.

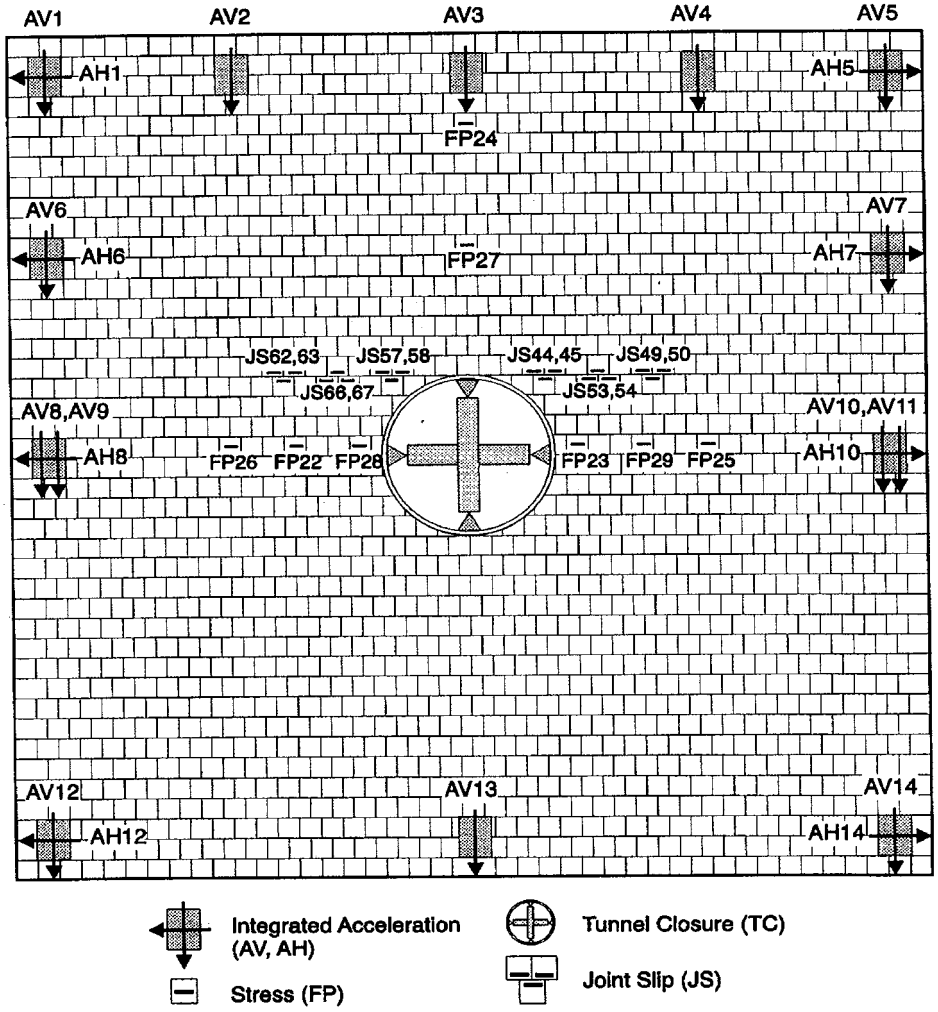

Source: Senseny and Pucik 1999 [DIRS 168479].

Figure 7-70. Geometry of the 2.1-m Square (2.4 m Long) Joint Rock Experiment Showing Internal Tunnel and Instrument Locations

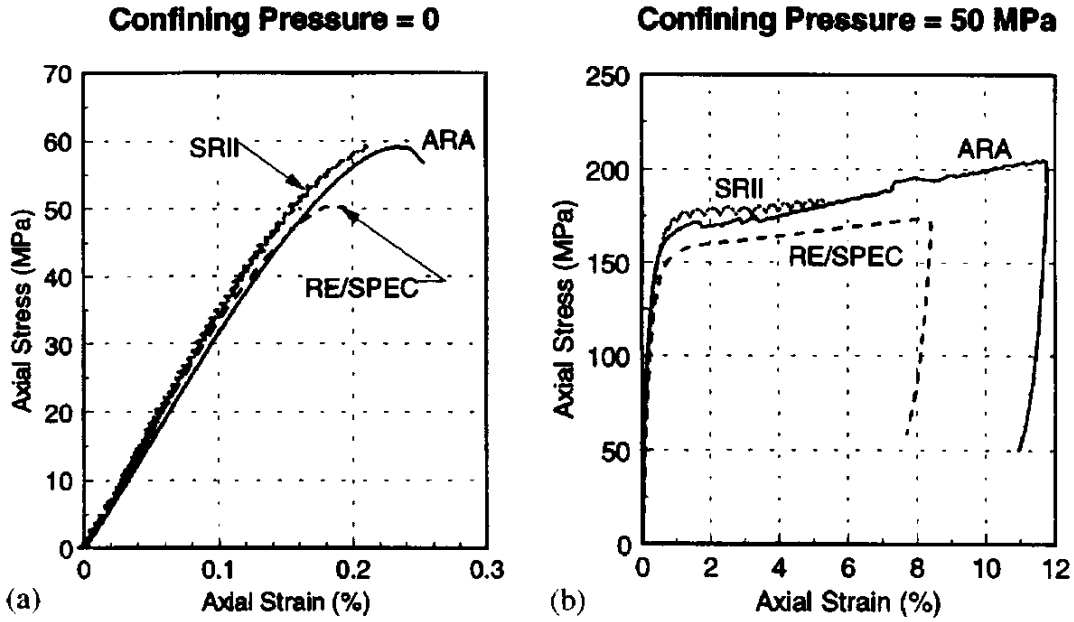

Source: Senseny and Pucik 1999 [DIRS 168479].

Figure 7-71. Stress Strain Curves for Salem Limestone: (a) Unconfined Compression and (b) Triaxial Compression

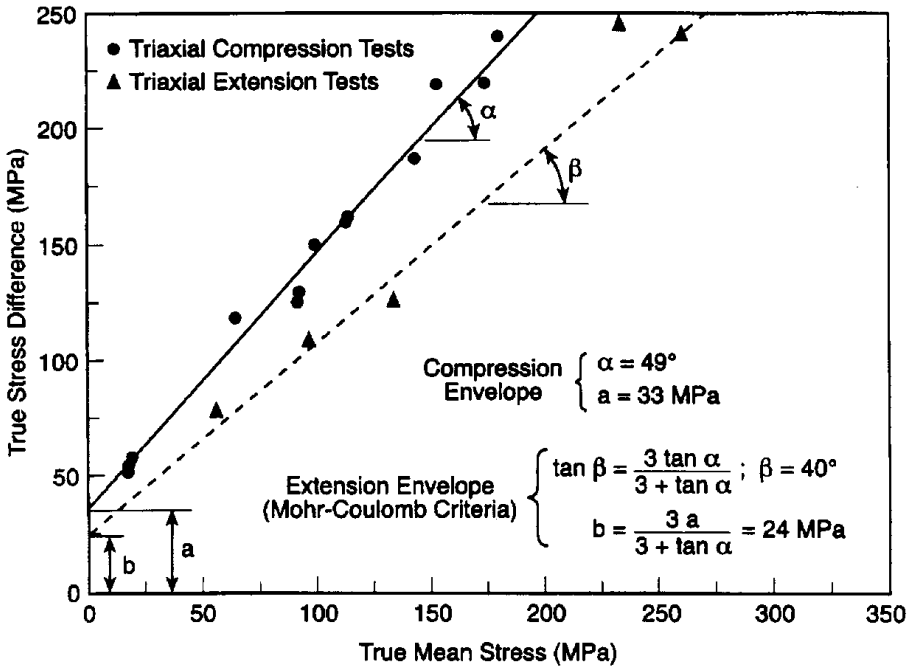

Source: Senseny and Pucik 1999 [DIRS 168479].

Figure 7-72. Comparison of Extension and Compression Strength Envelopes for Salem Limestone

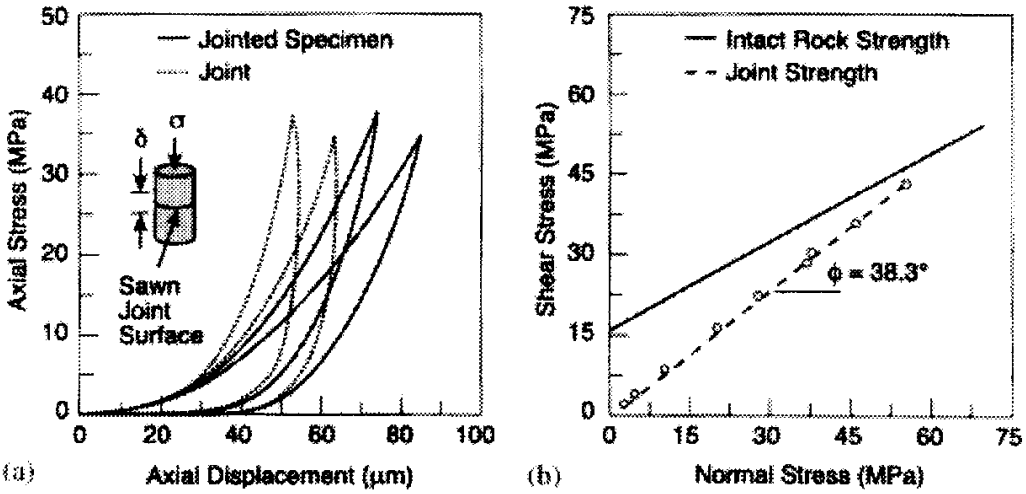

Source: Senseny and Pucik 1999 [DIRS 168479].

Figure 7-73. Compressibility and Strength in Salem Limestone: (a) Normal-Load Compressibility and (b) Shear Strength Envelope

Table 7-4. Properties of the Limestone Rock Mass and Aluminum Liner

Component	Bulk Modulus (GPa)	Shear Modulus (GPa)	Internal Angle of Friction (degrees)	Cohesion (MPa)	Tension Strength (MPa)	Density (kg/m^3)
Limestone Intact Rock Properties	21.5	12.3	56.7	8	5.4	2340
Limestone Joint Properties	500	100	38.3	0	0	N/A
Aluminum Liner	69.4	25.9	0	27.5	55	2700

Source: Senseny and Pucik 1999 [DIRS 168479].

NOTE: Limestone is considered to strain-soften via a post-peak reduction in cohesion and tensile strength. Cohesion is reduced linearly from 8 MPa to 3 MPa over 0.2 percent plastic strain. Tensile strength is reduced linearly from 5.4 MPa to 0 over 0.2 percent plastic strain. Aluminum is considered to behave as a strain-hardening material via a post-yield linear in cohesion and tensile strength. Cohesion increases linearly from 27.5 to 60 MPa over 2.9 percent plastic strain. Tensile strength increases linearly from 55 to 120 MPa over 2.9 percent plastic strain.

Block Model–The 3DEC model incorporated information about the effective vertical and horizontal gaps between the limestone bricks as measured in the actual experiment. The width of these gaps was determined using an indirect technique that relied on careful measurements of the overall dimensions of the stack of blocks in both directions. The contribution of the solid material to these measurements (i.e., the values that would be expected in the absence of gaps) was estimated by multiplying the number of bricks by the average brick thickness. The differences between these numbers and the actual measurements then provided an estimate of the total effective gap width. Dividing these differences by the number of joints then provides an estimate of the average effective gap thickness in each direction.

Since post-test measurements of the test specimen showed that the deformation was symmetric about a vertical plane through the tunnel mid-length and was nearly constant in the middle half of the specimen (Senseny and Pucik 1999 [DIRS 168479]), the problem can reasonably be represented using a two-dimensional, plane strain simulation. Therefore the 3DEC model (Figure 7-74) can be simplified to represent a thin slice parallel to the tunnel axis. The tunnel lies in the z-direction, with Figure 7-74 depicting the x-y plane. The boundary conditions applied include:

- Fixed displacements on the x-y plane outer surfaces to represent the plane-strain condition perpendicular to the tunnel axis
- A roller boundary along the left hand y-z surface to represent a symmetry plane
- Fixed displacements on the lower x-z and outer y-z surfaces
- Free upper surface with application of the input waveform above the symmetry line.

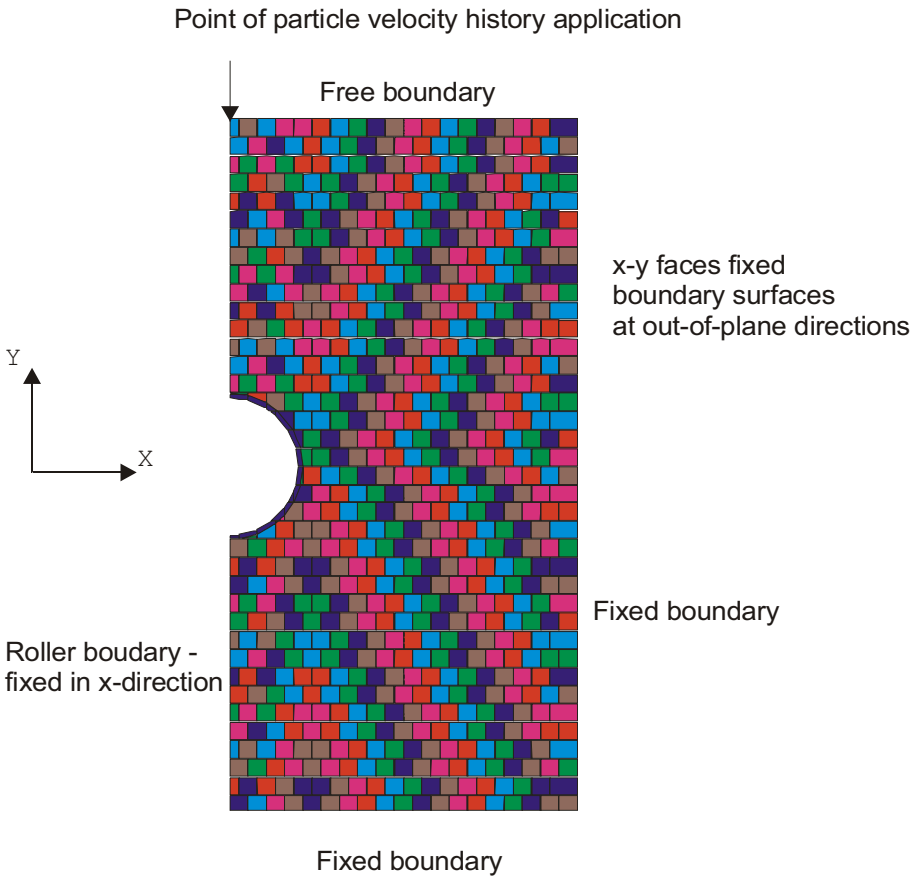

Figure 7-74. 3DEC Half-Symmetry Model Used in the Simulation Showing Boundary Conditions

The measured particle velocity time histories induced by the input blast at its application point were used as a time-dependent boundary condition at the symmetry line at the top of the model above the tunnel. The subsequent stress and deformation induced in the stack of blocks were monitored during the test at the gauge locations shown in Figure 7-70: the stress history measured at two locations above the crown and at three locations laterally from the springlines; deformation of the tunnel crown-invert; and springline diameters. The 3DEC model output is compared to the time histories of these measurements. 3DEC output is also compared to the deformed shape of the aluminum tunnel liner as determined by measurement after the test was completed. Data concerning slip at the joint slip meter gauges were not recorded in 3DEC, as the movements in the actual test were outside the resolution of the installed instrumentation.

Seen in Figure 7-75, the predicted deformation of the thin tunnel liner. In the experiment, the closure instrumentation that was to be used to measure the tunnel liner movements failed, and thus there is no time history of tunnel deformation available for model-test comparison. Therefore, Figure 7-75 shows only the final roof-to-floor and wall-to-wall closures of the liner (on the right edge of the figure) as measured after the test. The predicted and actual final displacements of the crown and springline displacements show close agreement.

Seen in Figure 7-76, the predicted and measured stresses at the two gauges located on the specimen centerline above the tunnel crown (FP 24 and 27). The 3DEC stresses were monitored in the blocks adjacent to the actual stress measurement locations, which were directly on the symmetry line. The adjacent block, was chosen for comparison purposes as the symmetry line boundary conditions in 3DEC impose a condition of no rotation of the half-blocks along this line. The symmetry condition simplifies the model and the associated computing time, but locally results in solution inaccuracy. Since this consideration will affect the modeled stresses at this location, the adjacent block, which is free to translate or rotate provides a better comparison point. As seen in Figure 7-76, the stresses in the blocks directly adjacent to the measurement show good correlation to the measured values.

As seen in Figure 7-77, the predicted and measured stresses at the six gauges are located adjacent to the springlines (FP 23, 25, 26, 28 and 29). Because of symmetry in the experiment, the gauges on each side of the tunnel measure similar stress histories and, therefore, provide a measure of precision. As the figure shows, the precision in these stress measurements is very good. 3DEC predicts the wave arrival time accurately. The magnitude of the 3DEC prediction at stress points FP23/28 and FP25/26 are lower than those measured in the experiment. At stress point FP29/22, the magnitude is similar to the measured stresses. In each case along the springline, there is a dip in the stresses after approximately 1.8 ms. This is a result of a wave reflection from the bottom of the model and could be avoided by using non-reflecting boundaries. However, this simulation was done using the same conditions as were prescribed for the numerical experiments as outlined in Senseny and Pucik (1999 [DIRS 168479]).

After the test, the tunnel liner was recovered and measured to determine more information than was obtained from the crown-invert and springline diameter changes alone. The shape of the liner was measure at three different locations.

As seen in Figure 7-78, the magnified, measured, and predicted shape shows the deformed aluminum liner. Over the entire perimeter, the liner displacements as predicted by 3DEC lie

within the variability of the actual measurements. 3DEC accurately predicts the diametral closure along the centerline and the diametric expansion along the springline.

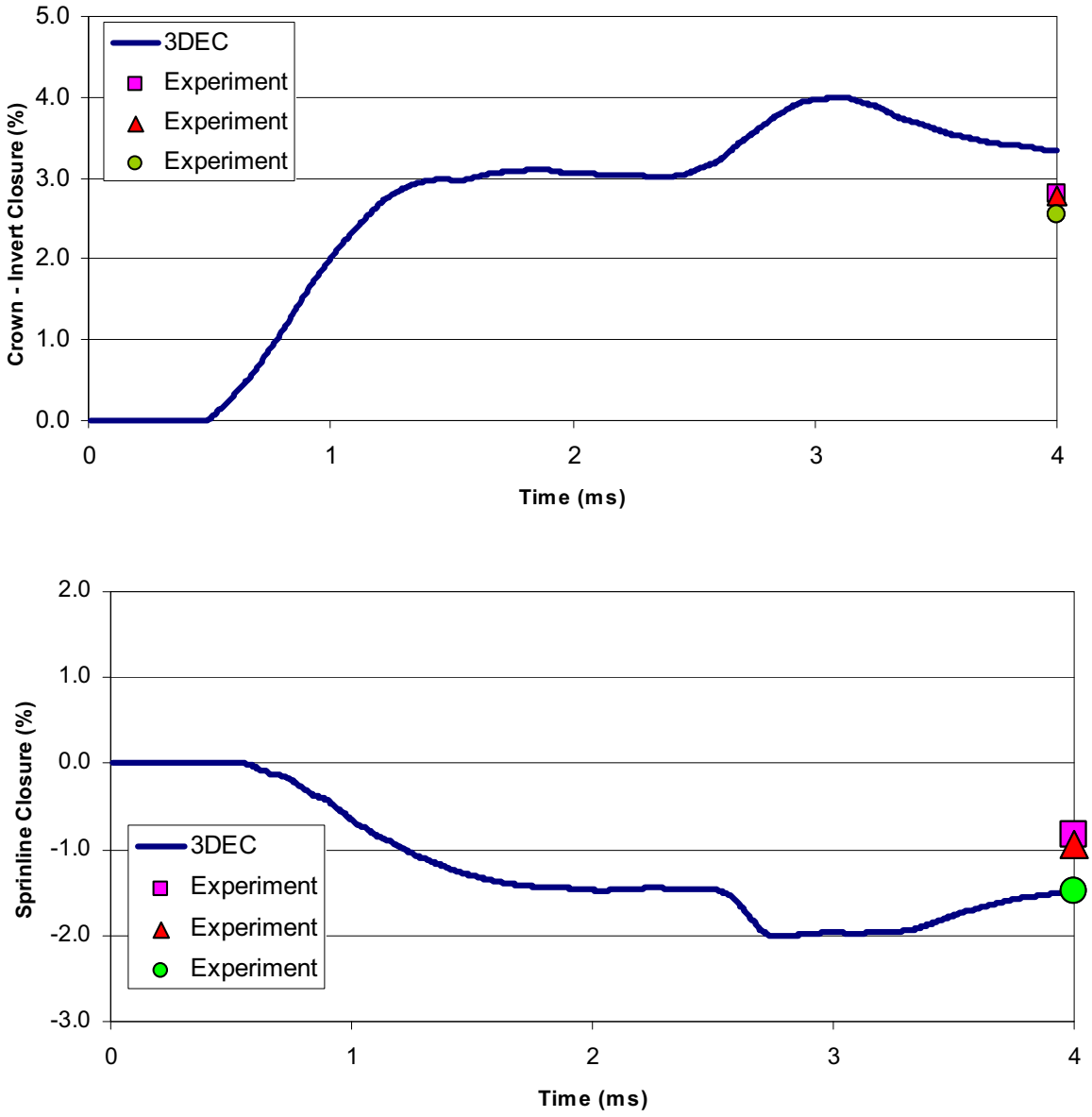

Source: DTN: MO0408MWDDDMIO.002, file *mighty_north_2.xls.*

Figure 7-75. Predicted (3DEC) and Measured Final Deformation (Exp) of the Crown-Invert and Springline Tunnel Diameters at Three Locations Along the Tunnel Length

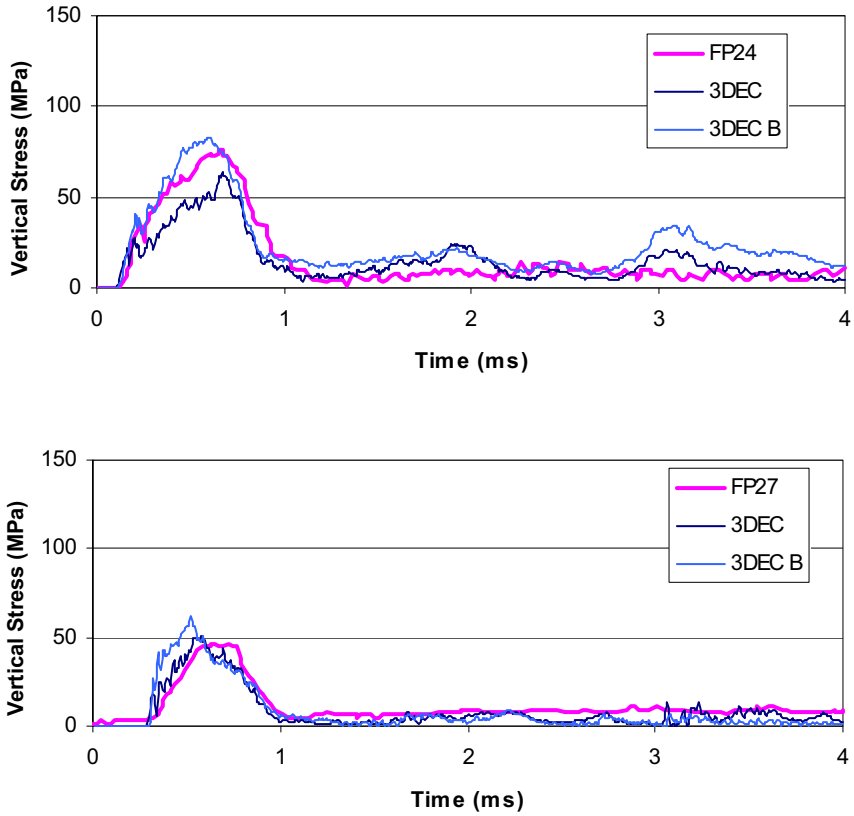

Source: DTN: MO0408MWDDDMIO.002, file *mighty_north_2.xls.*

NOTE: The points labeled "3DEC" are taken from the model at the exact reported stress gauge location, and "3DEC A" and "3DEC B" in the 3DEC blocks immediately to the left and right of the reported location, respectively.

Figure 7-76. Predicted Stresses in Block Adjacent to Measured Stresses (Gauges FP24 and FP27) Above the Tunnel Crown

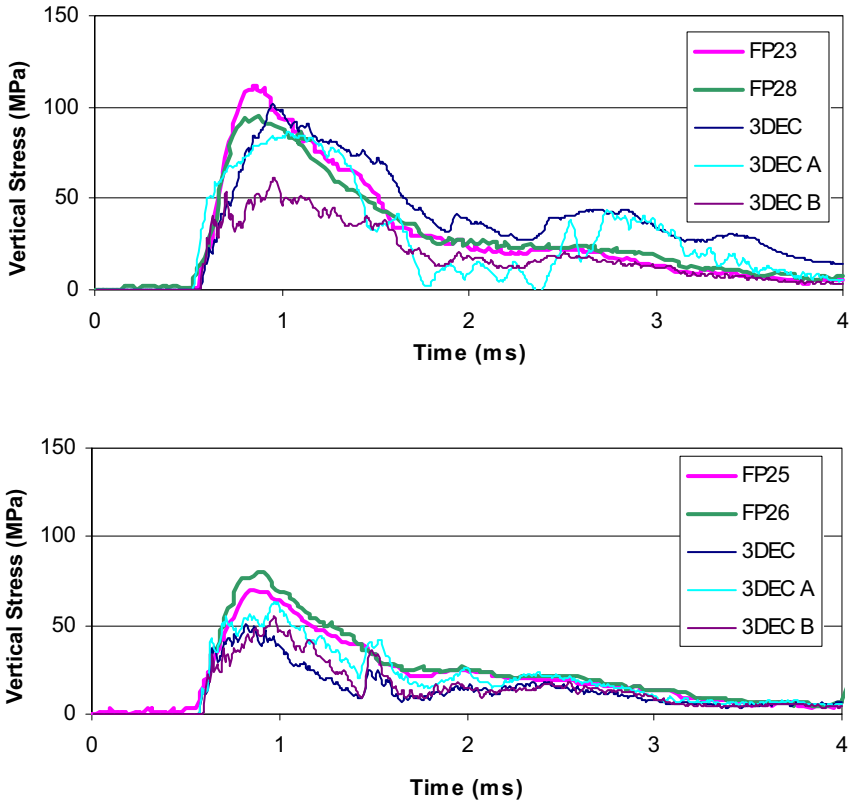

Source: DTN: MO0408MWDDDMIO.002, file *mighty_north_2.xls.*

NOTE: The points labeled "3DEC" are taken from the model at the exact reported stress gauge location, and "3DEC A" and "3DEC B" in the 3DEC blocks immediately to the left and right of the reported location, respectively.

Figure 7-77. Predicted and Measured Stresses Adjacent to the Tunnel Springline

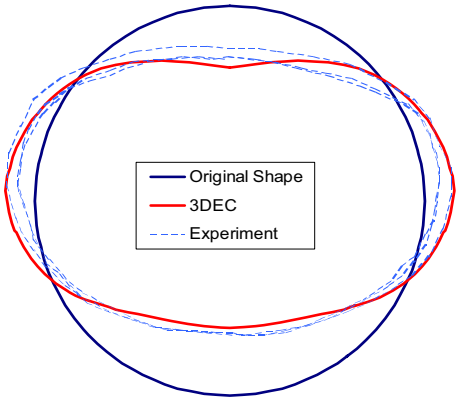

Source: DTN: MO0408MWDDDMIO.002, file *mighty_north_2.xls.*

Figure 7-78. Measured and Predicted Shape of the Deformed Aluminum Liner (Displacements are Magnified by 10)

7.7.5 3DEC Post-Development Validation Exercise 3 - Nonlithophysal Rockfall Model Validation by Corroboration with Alternative Numerical Model

The probabilistic key-block software DRKBA is used as an alternative numerical model to validate the 3DEC model results on block size distribution and rockfall frequency. The DRKBA code employs a numerical technique with Monte-Carlo simulation to account for the statistical variation of the joint system. A description of DRKBA approach and the input data for the probabilistic key-block analysis are provided in Appendix D.

The results of DRKBA analyses for the 1×10^{-4} seismic hazard are presented in Figure 7-79. Size distributions are compared with the 3DEC results, including both 1×10^{-4} and 1×10^{-7} seismic hazards. The frequency of blocks for both DRKBA and 3DEC is also provided in Figure 7-79. The size distribution curves show that the 3DEC results predict smaller size blocks for the same level of cumulative percentiles compared to the DRKBA results. The frequency of rockfall from the 3DEC results is much higher compared to the DRKBA results.

While both the DRKBA and 3DEC approaches have used the same fracture data inputs based on tunnel mapping in the ESF and ECRB Cross-Drift, the respective methods for developing synthetic fracture geometries are different. The DRKBA joint geometry generator produces larger joint planes concentrated about the center of the three-dimensional model space. The 3DEC joint generator (i.e., FracMan) develops a more realistic sizing of joint planes with an improved distribution throughout the model space, resulting in a higher frequency of smaller blocks compared to DRKBA.

The shape and range of the DRKBA and 3DEC rockfall distributions are generally similar. The DRKBA method resulted in a maximum block size of 34 tons, which is similar the 29 ton maximum block from the 3DEC results for the 1×10^{-7} seismic hazard.

7.7.6 3DEC Post-Development Validation Exercise 4 - Model Validation by Expert Technical Review

An outside expert technical review was conducted as a means of validation, as discussed in procedure AP-SIII.10Q, *Models*. Dr. John Tinucci of the PanTechnica Corporation in Minneapolis, Minnesota, was contracted for this purpose. Dr. Tinucci is a Professional Engineer and has a Ph.D. from the University of California, Berkeley, where his thesis research was in the area of analysis of the stability of blocky rock masses, and, in particular, in the development of key-block methods for tunnel stability assessment. He has extensive experience in the use of the 3DEC program for surface and underground stability assessment. Particularly valuable experience for the present application is his use of 3DEC to model dynamic stability of deep underground mine openings.

Dr. Tinucci was provided with a number of reports and presentations detailing the geology, laboratory properties, modeling methodology and preliminary results of the FracMan and 3DEC modeling work prior to visiting the site. A site visit of three days was then conducted in which discussions were held with YMP engineers and geologists regarding the FracMan and 3DEC work. A visit to the ESF main loop and ECRB Cross-Drift was conducted to view the rock mass conditions in situ.

Dr. Tinucci's review report is provided in Appendix N. In general, the technical review finds the 3DEC and FracMan approaches to be adequate for simulation of the rockfall problem in the nonlithophysal rocks. The model approach, data selection and ranges were found to be adequate. The model boundary conditions and methodology for application of the ground motions were also felt to be proper.

7.7.7 Conclusions and Comparison to Validation Criteria

The following discussion of comparison of validation criteria is given.

A. Analyses presented in Sections 6.3 and 7.7.4 indicate that the 3DEC program is able to represent dynamic boundary conditions and wave transmission through the material in an accurate fashion.

B. The comparison of the 3DEC program to the results of direct shear testing on fractures from the Tptpmn shows that 3DEC is able to adequately reproduce the shear constitutive response of the cooling and vapor-phase altered fractures. Use of sensitivity analyses to bound fracture shear stiffnesses in the vapor-phase altered fractures is warranted, although the analysis shown here indicates that the use of tangent stiffnesses and a softening joint mechanical model (the default used in Section 6.3 analyses) appears to be conservative in nature, resulting in more rockfall.

C. The ability of 3DEC to represent the complex problem of an explosively-loaded tunnel in jointed rock was tested via comparison to a scaled field experiment in limestone. The field experiment tested several capabilities of the program, including:

- The predictive capability of the nonlithophysal rockfall model as implemented in 3DEC for structures in jointed rock was demonstrated by comparing predictions with the results of a large jointed-rock precision test specimen that that involved dynamic loading and large strain of a lined cylindrical opening. Based on this validation case, 3DEC can reasonably simulate the wave transmission through the jointed rock, the stress change in the rock mass resulting from the dynamic excitation, and the large strain and permanent deformation of a tunnel in jointed rock and its internal support.

- 3DEC demonstrated the ability to represent complex dynamic boundary conditions.

- 3DEC accurately predicted the final shape of the deformed liner.

- 3DEC accurately predicted the arrival time of the stress waves, thus validating the wave transmission simulation through the jointed rock.

- 3DEC accurately predicted the stress magnitudes and wave shape at several of the monitoring points. Wave reflections disturbed this prediction in some locations. Note that the inclusion of random gaps in the model adds difficulty in matching the stresses at specific locations.

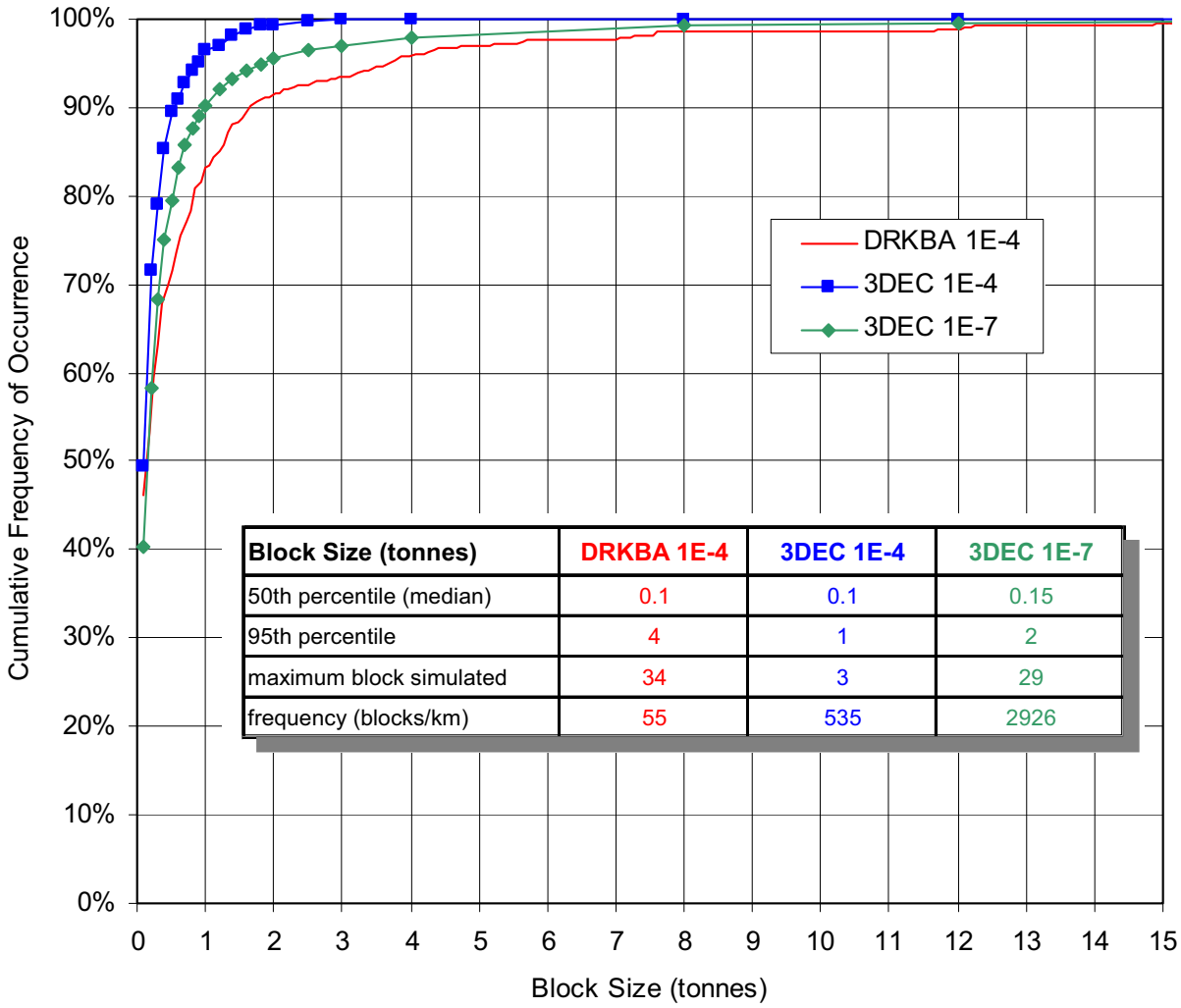

Block Size (tonnes)	DRKBA 1E-4	3DEC 1E-4	3DEC 1E-7
50th percentile (median)	0.1	0.1	0.15
95th percentile	4	1	2
maximum block simulated	34	3	29
frequency (blocks/km)	55	535	2926

Figure 7-79. Comparison of Rockfall Results from 3DEC and DRKBA

- The 3DEC model as shown compared very favorably with the physical experiment and demonstrated the ability to represent reasonably the dynamic response of a fractured media.

D. The overall adequacy of the modeling approach and the specification of property ranges have been validated by corroboration with the results of an alternative numerical model and by external technical review.

7.8 VALIDATION SUMMARY

The drift degradation models for lithophysal and nonlithophysal rocks have been validated by applying acceptance criteria based on an evaluation of the model's relative importance to the potential performance of the repository system. The validation requirements defined in the *Technical Work Plan for: Regulatory Integration Modeling of Drift Degradation, Waste Package*

and Drip Shield Vibratory Motion and Seismic Consequences (BSC 2004 [DIRS 171520], Section 2.2.1) have been fulfilled. This includes:

- Corroboration with laboratory measurements or relevant observations not previously used to develop or calibrate the models
- Corroboration of results with alternative mathematical models
- Corroboration with data published in referred journals or literature
- Technical review by reviewers independent of the model development, checking, and interdisciplinary review.

Requirements for confidence building during model development have also been satisfied. The model development activities and post-development validation activities described establish the scientific bases for the drift degradation models. Based on this, the drift degradation models are considered to be sufficiently accurate and adequate for the intended purpose and to the level of confidence required by the models' relative importance to the potential performance of the repository system.

INTENTIONALLY LEFT BLANK

8. CONCLUSIONS

8.1 SUMMARY

This report was developed to document the degradation of the rock mass surrounding the emplacement drifts of a geologic repository at Yucca Mountain. The factors leading to drift degradation include the stresses induced by the heat released by the emplaced waste, the stresses due to seismically related ground motions, and the strength loss of the rock mass due to time-dependent strength degradation. These factors have been modeled and analyzed, resulting in the prediction of the amount and size distribution of rockfall in the repository drifts during both the preclosure and postclosure regulatory periods. The data developed and documented in this model report have been entered into the Technical Data Management System (DTNs: MO0408MWDDDMIO.002, MO0408MWDRNLRA.002, MO0306MWDDPPDR.000, MO0404MWD3DRFA.000, MO0407MWDDSLCR.000, MO0407SPAMTSHR.000, and MO0403MWDRPNLR.000).

The following statements summarize the results from this drift degradation modeling and analysis activity and present the key conclusions:

- The rock mass at the repository host horizon has been geologically characterized to support the rockfall modeling activities presented in this report. Drift degradation models have been developed for both nonlithophysal and lithophysal rock. A detailed description of the rock mass characteristics of the repository host horizon is provided in Section 6.1. The available rock mass geotechnical data, including fracture geometry (Section 6.1.4.1, Section 6.1.6, and Appendix B), lithophysal abundance and geometric characteristics (Section 6.1.4.2 and Appendix O), and geotechnical rock properties (Section 6.1.3 and Appendix E), are sufficient to support detailed drift degradation analyses using both continuum and discontinuum approaches.

- The drift-scale temperature history was calculated throughout the preclosure and postclosure periods of the repository as documented in Section 6.2. The temperature history was used to calculate the thermal stress state that develops within the rock mass due to the heat energy released from the stored nuclear waste, and appropriate boundary conditions for thermal loading have been applied (Sections 6.2, 6.3.1.3, and 6.4.2.3). Appropriate thermal properties have been used in the thermal-mechanical calculation as provided in Section 4.1 and Appendix E (Section E5).

- A nonlithophysal rockfall model was developed using the three-dimensional discontinuum code, 3DEC, with the following features:

  - Appropriate boundary conditions are provided for thermal and seismic loading (Sections 6.3.1.2 and 6.3.1.3).

  - Critical fracture patterns are included from multiple sampling from a synthetic rock mass volume that contains a realistic fracture population based on field mapping data (Section 6.1.6).

  - Appropriate thermal and mechanical properties of rock blocks and joints are used (Appendix E).

  - Long-term degradation of joint strength parameters is considered (Section 6.3.1.5).

  - Site-specific ground motion time histories appropriate for both the preclosure (5×10^{-4} and 1×10^{-4} hazard levels) and postclosure (1×10^{-5}, 1×10^{-6}, and 1×10^{-7} hazard levels) time periods are included in the model (Section 4.1.5).

- A lithophysal rockfall model was developed using the two-dimensional discontinuum code, UDEC, with the following features:

  - Appropriate boundary conditions are provided for thermal and seismic loading (Sections 6.4.2.1 and 6.4.2.2).

  - The rock mass is represented as an assembly of polygonal, elastic blocks in which the bond strength of the blocks is calibrated such that the overall mechanical behavior of the mass is consistent with the material model developed for the lithophysal rock (Section 7.6.4).

  - The lithophysal rockfall model allows for the formation of stress-induced fractures between blocks (i.e., the formation of internal fracturing), separation and instability (under the action of gravity or seismic shaking) of the rock mass around the drift (Section 6.4.2).

  - Appropriate thermal and mechanical properties of rock blocks and joints are used (Appendix E).

  - Long-term degradation of rock mass strength is considered (Section 6.4.2.4).

  - Site-specific ground motion time histories appropriate for both the preclosure (5×10^{-4} and 1×10^{-4} hazard levels) and postclosure (1×10^{-5} and 1×10^{-6} hazard levels) time periods are included in the model (Section 4.1.5).

- Model validation activities include (1) validating the mechanical material models or representations for the two specific repository host rock types (i.e., lithophysal and nonlithophysal rocks), and (2) validating the implementation of these material models in general numerical modeling schemes (Section 7).

- The results for the nonlithophysal units are summarized as follows:

  - Preclosure ground motion results in minor drift damage due to rockfall.

  - Postclosure ground motion results in varying extent of drift damage due to rockfall, with localized areas of rock failure sufficient to cover the drip shield.

  - Thermal effects have a minor impact on rockfall.
  - Time-dependent strength degradation has a minor impact on rockfall.

- The results for the lithophysal units are summarized as follows:
  - Degradation is primarily controlled by stress conditions.
  - Preclosure ground motion results in minor drift damage due to rock failure.
  - Damage to the host rock is not significantly accumulating from multiple preclosure ground motions (Section S3.4.3). That is, a preclosure seismic event is shaking loose rock fragments that have already failed by strength degradation and thermal stress; no new fractures and failures are caused by this low amplitude ground motion.
  - Postclosure ground motion results in collapse of the drift, with fragmented rock particle sizes on the order of centimeters to decimeters.
  - Thermal and time-dependent effects can result in localized to significant areas of rock failure, depending on the selection of the degree of strength loss of the rock mass with time. The analyses of the available static-fatigue test data indicate that an approximate 40 percent reduction in cohesive strength occurs over a 20,000 year period. The nominal case for drift degradation (i.e., considering thermal and time-dependent effects, but excluding seismic effects) results in only partial collapse of the drift at 20,000 years, as depicted by Figures S-41 through S-44. The analyses of the available static-fatigue test data indicate that the lower bound quality rock mass can be represented as rock mass Category 2, which represents only about 10 percent of the total lithophysal rock mass in the emplacement drifts. A combination of the thermally induced stresses with time-dependent strength degradation results in a deterioration of the walls for Category 2. As rock mass quality increases, there is less rockfall from the walls and more rockfall from the drift roof. Preclosure seismic ground motion causes additional, but not significant, rockfall as a result of shaking down already loose, broken ground.

- The drift degradation models and analyses documented in this report address the requirements of NRC/DOE agreements items regarding rockfall and related issues to support the resolution of NRC's KTI on Repository Design and Thermal-Mechanical Effects (Section 6.8).

8.2 ASSESSMENT

The drift degradation and modeling activities presented in this report address the criteria identified in Section 4.2 as summarized in Table 8-1. The rockfall models have adequately captured the physical phenomena associated with the various components of rock mass behavior anticipated within the repository horizon. Appropriate boundary and initial conditions have been

applied, and the technical bases for the development of these rockfall models have been adequately documented. Sufficient data have been collected to adequately model the drift degradation processes. The technical bases and ranges of data used in the rockfall models are documented. Data uncertainty (Section 6.5) has been characterized through parameter sensitivity studies in the rockfall models. Model uncertainty has been characterized through an evaluation of alternative conceptual models, and the model results have been validated by comparison to field and laboratory data, alternative numerical approaches, and industry experience through external technical review. The most significant uncertainties impacting the results of the rockfall models are the uncertainties associated with the postclosure ground motion and time-dependent strength degradation. Some of the ground motions provided are larger than the largest ground motions observed and may not be physically realizable. Therefore, predictions of complete drift collapse with postclosure ground motion may be unrealistic. Without a technical basis to limit such ground motions to smaller values, these inputs represent the best available information to support this work. Prediction of time-dependent strength degradation for the duration of the regulatory period of 10,000 years is a highly approximate task. A significant program of static-fatigue testing of Tptpmn core specimens is currently being conducted. A part of this static-fatigue data has been included in this document (Section 6.4.2.4.2). This present work will be updated as additional long-term testing data are developed.

8.3 RECOMMENDATIONS

The drift degradation and modeling activities presented in this report are sufficient to support a license application. Specifically, the drift degradation results presented in Sections 6.3 and 6.4 are sufficient to provide input to drip shield and waste package design calculations, consequence models for the seismic scenario for TSPA-LA, and seepage abstraction models for TSPA-LA.

Table 8-1. Mapping of Yucca Mountain Review Plan Acceptance Criteria and Drift Degradation Analysis

Acceptance Criteria	Subcriteria	Paraphrase of Subcriteria	Sections Where Addressed
AC1: System description and model integration are adequate	1	Total system performance incorporates important aspects of model	1.1 – Background 6.3.1.2 – Rockfall in nonlithophysal units feed to SCA[a] 6.4.2 – Rockfall in lithophysal units and quasi-static drip shield loads – feed to SCA 6.4.2.2.4 – Drift profile change to DSA[b] 7.2 – Level of importance to TSPA for model validation 8 – Conclusions
	2	Description of geological and engineering aspects that may affect design, couplings, of mechanical disruption	1.1 – Background 6.1 – Rock mass characteristics and discussion of geologic parameters of importance 6.2 – Thermal mechanical calculations that provide thermal environment 6.3.1.2, 6.4.2 – Rockfall parameters for drip shield evaluation 6.4.2 – Drip shield loading parameters and drift profile change parameters for SCA[a] and DSA[b]
	3	Description of assumptions and technical bases consistent with other abstractions	4 – Inputs, includes data and parameters, criteria and codes and standards 5 – Assumptions 6.1 – Geology and rock mass characterization consistent with other abstractions
	4	Boundary and initial conditions propagated through abstractions	4 – Input – In situ stress, thermal loading and ground motion data 6.3, 6.4 – Boundary conditions specific to model described Appendix W – Thermal and mechanical boundary condition verification
	5	Sufficient data for assessment of FEPs	4 – Input data 5 – Assumptions 6.5 – Uncertainties and limitations 6.6 – FEPs discussion
	6	Criticality	Not relevant to this document
AC2: Data are sufficient for model justification	1	Geological and engineering values used are adequately justified	4 – Input data 5 – Assumptions 6.5 – Uncertainties and limitations 7.4, 7.5, 7.6 – Development and validation of material model and numerical model for lithophysal rock Appendix E – Rock properties

Table 8-1. Mapping of Yucca Mountain Review Plan Acceptance Criteria and Drift Degradation Analysis (Continued)

Acceptance Criteria	Subcriteria	Paraphrase of Subcriteria	Sections Where Addressed
AC2: Data are sufficient for model justification	2	Sufficient data has been collected to establish boundary conditions	4 – Input data Appendix C – Verification of topographic effects on thermal and stress initial and boundary conditions Appendix W – Thermal and mechanical boundary conditions verification
	3	Data on geology based on appropriate techniques	4 – Input 6.1 – Rock mass characteristics of the repository 6.3.1, 6.4.2 , 7.3, 7.4, 7.5, 7.6 – Methods for incorporation of geology into degradation models 6.5 – Uncertainties and limitations Appendix E – Rock properties Appendix O – Lithophysal characterization
	4	Engineered barrier mechanical failure models appropriate	6.3.1, 6.4.2 – Rockfall parameters for feed to drip shield stability modeling
AC3: Data uncertainty is characterized and propagated through the model abstraction	1	Models use parameter values, ranges, bounding assumptions that are technically defensible	4 – Input 6.1 – Describes variability of fractures and lithophysae upon which models are based 6.2 – Thermal analysis and range of thermal properties on temperature prediction 6.3 and 6.2 – Provide implementation of geologic variability into models via stochastic representation of fractures and bounding ranges for lithophysal rock properties Appendix E – Rock properties – Ranges of rock properties used in analyses
	2	Process models represent and do not underestimate mechanically disruptive events	6.2 – Thermal modeling – Determines thermal stress for range of thermal properties 6.3, 6.4 – Provides rockfall and drift degradation for seismic events derived from conservative PSHA[c] process; time-dependent drift degradation based on bounding of static fatigue behavior of welded tuff
	3	Uncertainty is adequately represented via sensitivity analyses or conservative limits	6.3, 6.4 – Rockfall in nonlithophysal units represented conducting many analyses of stochastically defined fracture conditions, rockfall in lithophysal units determined from bounding ranges of rock properties 6.5 – Uncertainties and limitations Appendix E – Development of rock properties ranges
	4	Use of expert elicitation	6.3, 6.4 – Ground motion inputs based on expert elicitation via PSHA[c] process

Table 8-1. Mapping of Yucca Mountain Review Plan Acceptance Criteria and Drift Degradation Analysis (Continued)

Acceptance Criteria	Subcriteria	Paraphrase of Subcriteria	Sections Where Addressed
AC4: Model uncertainty is characterized and propagated through the model abstraction	1	Alternative modeling approaches considered as well as uncertainties and limitations	6.3 – Alternative, conservative approach to defining fracture bridges used for rockfall in nonlithophysal 6.4 – Alternative numerical and analytical approaches used for estimation of drip shield static loading 6.5 – Uncertainties and limitations 7.7.5 – Alternative modeling approach (DRKBA) considered for rockfall in nonlithophysal units
	2	Conceptual model is consistent with available site characterization data including lab experiments and field measurements	1.1 – Background describes interrelationships between data, model development and validation 6.1 – Fracture and lithophysae field mapping consistent with model 6.3, 7.7, Appendix E – Nonlithophysal model development based on field geologic mapping 6.4, 7.3, 7.4, 7.5, 7.6, Appendix E, Appendix O – Lithophysal model is consistent with field mapping, laboratory data and field observations 6.5 – Uncertainties and limitations
	3	Alternative models used to assess uncertainties and limitations	6.4 – Alternative approaches for rock loading to drip shield in lithophysal rock 6.5 – Uncertainties and limitations 7.7.5 – DRKBA model used as alternative for rockfall in nonlithophysal rock
AC5: Model abstraction output is supported by objective comparison	1	Models used in TSPA are consistent with abstractions in current model	1.1– Background – Describes approach to providing information to TSPA 6.3.1.2 – Rockfall in nonlithophysal units feed to SCA[a] 6.4.2 - Rockfall in lithophysal units and quasi-static drip shield loads – Feed to SCA[a] 6.4.2.2.4 – Drift profile change to DSA[b] 7.2 – Level of importance to TSPA for model validation 8 – Conclusions
	2	Outputs of mechanical disruption of engineered barrier abstractions reasonably produce bound of process model abstractions	6.3.1.2 – Rockfall in nonlithophysal units feed to SCA[a] 6.4.2 – Rockfall in lithophysal units and quasi-static drip shield loads – Feed to SCA[a] 6.4.2.2.4 – Drift profile change to DSA[b] 7.2 – Level of importance to TSPA for model validation 8 – Conclusions

Table 8-1. Mapping of Yucca Mountain Review Plan Acceptance Criteria and Drift Degradation Analysis (Continued)

Acceptance Criteria	Subcriteria	Paraphrase of Subcriteria	Sections Where Addressed
AC5: Model abstraction output is supported by objective comparison	3	Well-documented, accepted procedures are provided to support TSPA abstractions	6.2, 6.3 and 6.4 – Use of industry standard acquired software in modeling analyses 7 – Validation of models includes documentation as per validation procedures, including outside expert technical review 9.2 – Describes codes, standards and procedures followed in development of this report
	4	Sensitivity analyses are used to support the TSPA abstraction that covers ranges of data obtained from field and laboratory measurements	1.1 – Background describes interrelationships between data, model development and validation 6.1 – Fracture and lithophysae field mapping consistent with model 6.3, 7.7, Appendix E – Nonlithophysal model development based on field geologic mapping 6.4, 7.3, 7.4, 7.5, 7.6, Appendix E, Appendix O – Lithophysal model is consistent with field mapping, laboratory data and field observations 6.5 – Uncertainties and limitations

[a] SCA = Seismic Consequence Abstraction
[b] DSA = Drift Seepage Abstraction
[c] PSHA = Probabilistic Seismic Hazard Assessment

9. INPUTS AND REFERENCES

9.1 DOCUMENTS CITED

Albin, A.L.; Singleton, W.L.; Moyer, T.C.; Lee, A.C.; Lung, R.C.; Eatman, G.L.W.; and Barr, D.L. 1997. *Geology of the Main Drift - Station 28+00 to 55+00, Exploratory Studies Facility, Yucca Mountain Project, Yucca Mountain, Nevada.* Milestone SPG42AM3. Denver, Colorado: Bureau of Reclamation and U.S. Geological Survey. ACC: MOL.19970625.0096. 101367

Anna, L.O. 1998. *Preliminary Three-Dimensional Discrete Fracture Model of the Topopah Spring Tuff in the Exploratory Studies Facility, Yucca Mountain Area, Nye County, Nevada.* Open-File Report 97-834. Denver, Colorado: U.S. Geological Survey. TIC: 236829. 138501

Anna, L.O. 1998. *Preliminary Three-Dimensional Discrete Fracture Model, Tiva Canyon Tuff, Yucca Mountain Area, Nye County, Nevada.* Open-File Report 97-833. Denver, Colorado: U.S. Geological Survey. TIC: 236723. 144421

Barr, D.L.; Moyer, T.C.; Singleton, W.L.; Albin, A.L.; Lung, R.C.; Lee, A.C.; Beason, S.C.; and Eatman, G.L.W. 1996. *Geology of the North Ramp — Stations 4+00 to 28+00, Exploratory Studies Facility, Yucca Mountain Project, Yucca Mountain, Nevada.* Denver, Colorado: U.S. Geological Survey. ACC: MOL.19970106.0496. 100029

Barton, N.; Lien, R.; and Lunde, J. 1974. "Engineering Classification of Rock Masses for the Design of Tunnel Support." *Rock Mechanics*, *6*, (4), 189-236. New York, New York: Springer-Verlag. TIC: 219995. 101541

Bauer, R.A.; Curry, B.B.; Graese, A.M.; Vaiden, R.C.; Su, W.J.; and Hasek, M.J. 1991. *Geotechnical Properties of Selected Pleistocene, Silurian, and Ordovician Deposits of Northeastern Illinois*. Environmental Geology 139. Champaign, Illinois: Illinois State Geological Survey. TIC: 253871. 161775

Bauer, S.J.; Hardy, M.P.; Goodrich R.; and Lin, M. 1992. "Fault Stress Analysis for the Yucca Mountain Site Characterization Project." *High Level Radioactive Waste Management, Proceedings of the Third International Conference, Las Vegas, Nevada, April 12-16, 1992*. 2, 2267-2277. La Grange Park, Illinois: American Nuclear Society. TIC: 204231. 162227

Beason, S.C.; Turlington, G.A.; Lung, R.C.; Eatman, G.L.W.; Ryter, D.; and Barr, D.L. 1996. *Geology of the North Ramp - Station 0+60 to 4+00, Exploratory Studies Facility, Yucca Mountain Project, Yucca Mountain, Nevada.* Denver, Colorado: U.S. Geological Survey. ACC: MOL.19970106.0449. 101191

Bieniawski, Z.T. 1989. *Engineering Rock Mass Classifications*. New York, New York: John Wiley & Sons. TIC: 226350. 101715

Board, M. 2003. *Resolution Strategy for Geomechanically-Related Repository Design and Thermal-Mechanical Effects (RDTME)*. REV 00. Las Vegas, Nevada: Bechtel SAIC Company. ACC: MOL.20030708.0153. 165036

Bolt, B.A. 1997. "World Earthquakes and Seismicity Rates." Appendix A of *Earthquakes*. Pages 270-274. New York, New York: W.H. Freeman and Company. TIC: 255644. 167798

Brace, W.F.; Paulding, B.W., Jr.; and Scholz, C.H. 1966. "Dilatancy in the Fracture of Crystalline Rocks." *Journal of Geophysical Research*, *71*, (16), 3939-3953. Washington, D.C.: American Geophysical Union. TIC: 226778. 101990

Brady, B.H.G. and Brown, E.T. 1985. *Rock Mechanics for Underground Mining*. London, United Kingdom: George Allen and Unwin. TIC: 226226. 126811

Brekke, T.L.; Cording, E.J.; Daemen, J.; Hart, R.D.; Hudson, J.A.; Kaiser, P.K.; and Pelizza, S. 1999. *Panel Report on the Drift Stability Workshop, Las Vegas, Nevada, December 9-11, 1998*. Las Vegas, Nevada: Management and Technical Support Services. ACC: MOL.19990331.0102. 119404

Brodsky, N.S.; Riggins, M.; Connolly, J.; and Ricci, P. 1997. *Thermal Expansion, Thermal Conductivity, and Heat Capacity Measurements for Boreholes UE25 NRG-4, UE25 NRG-5, USW NRG-6, and USW NRG-7/7A*. SAND95-1955. Albuquerque, New Mexico: Sandia National Laboratories. ACC: MOL.19980311.0316. 100653

Brown, E.T. 2003. *Block Caving Geomechanics. JKMRC Monograph Series in Mining and Mineral Processing 3*. Indooroopilly, Queensland, Australia: Julius Kruttschnitt Mineral Research Centre. TIC: 256115. 169527

Broxton, D.E.; Chipera, S.J.; Byers, F.M., Jr.; and Rautman, C.A. 1993. *Geologic Evaluation of Six Nonwelded Tuff Sites in the Vicinity of Yucca Mountain, Nevada for a Surface-Based Test Facility for the Yucca Mountain Project*. LA-12542-MS. Los Alamos, New Mexico: Los Alamos National Laboratory. ACC: NNA.19940224.0128. 107386

BSC (Bechtel SAIC Company) 2001. *Drift Degradation Analysis*. ANL-EBS-MD-000027 REV 01 ICN 01. Las Vegas, Nevada: Bechtel SAIC Company. ACC: MOL.20011029.0311. 156304

BSC 2001. *Ground Control for Emplacement Drifts for SR*. ANL-EBS-GE-000002 REV 00 ICN 01. Las Vegas, Nevada: Bechtel SAIC Company. ACC: MOL.20010627.0028. 155187

BSC 2002. *Subsurface General Construction, Specification Section 01501*. BAB000000-01717-6300-01501 REV 07. Las Vegas, Nevada: Bechtel SAIC Company. ACC: MOL.20021209.0164. 161707

BSC 2003. *Heat Capacity and Thermal Expansion Coefficients Analysis Report*. ANL-NBS-GS-000013 REV 00. Las Vegas, Nevada: Bechtel SAIC Company. ACC: DOC.20030820.0002. 164670

BSC 2003. *Scoping Analysis on Sensitivity and Uncertainty of Emplacement Drift Stability*. 800-K0C-TEG0-00600-000-000. Las Vegas, Nevada: Bechtel SAIC Company. ACC: ENG.20031125.0002. 166183

BSC 2003. *Subsurface Geotechnical Parameters Report*. 800-K0C-WIS0-00400-000-00A. Las Vegas, Nevada: Bechtel SAIC Company. ACC: ENG.20040108.0001. 166660

BSC 2003. *Underground Layout Configuration*. 800-P0C-MGR0-00100-000-00E. Las Vegas, Nevada: Bechtel SAIC Company. ACC: ENG.20031002.0007. 165572

BSC 2004. *Abstraction of Drift Seepage*. MDL-NBS-HS-000019 REV 01. Las Vegas, Nevada: Bechtel SAIC Company. 169131

BSC 2004. *D&E / PA/C IED Emplacement Drift Configuration and Environment*. 800-IED-MGR0-00201-000-00B. Las Vegas, Nevada: Bechtel SAIC Company. ACC: ENG.20040326.0001 168489

BSC 2004. *D&E / PA/C IED Interlocking Drip Shield and Emplacement Pallet*. 800-IED-WIS0-00401-000-00D. Las Vegas, Nevada: Bechtel SAIC Company. ACC: ENG.20040503.0018. 169220

BSC 2004. *D&E / PA/C IED Subsurface Facilities*. 800-IED-WIS0-00101-000-00A. Las Vegas, Nevada: Bechtel SAIC Company. ACC: ENG.20040309.0026. 164519

BSC 2004. *D&E / PA/C IED Typical Waste Package Components Assembly*. 800-IED-WIS0-00204-000-00B. Las Vegas, Nevada: Bechtel SAIC Company. ACC: ENG.20040202.0012. 167369

BSC 2004. *D&E/PA/C IED Typical Waste Package Components Assembly*. 800-IED-WIS0-00202-000-00C. Las Vegas, Nevada: Bechtel SAIC Company. ACC: ENG.20040517.0008. 169472

BSC 2004. *Development of Earthquake Ground Motion Input for Preclosure Seismic Design and Postclosure Performance Assessment of a Geologic Repository at Yucca Mountain, NV*. MDL-MGR-GS-000003 REV 01. Las Vegas, Nevada: Bechtel SAIC Company. 170027

BSC 2004. *Drip Shield Structural Response to Rock Fall*. 000-00C-SSE0-00300-000-00A. Las Vegas, Nevada: Bechtel SAIC Company. ACC: ENG.20040405.0019. 168993

BSC 2004. *Geologic Framework Model (GFM2000)*. MDL-NBS-GS-000002 REV 02. Las Vegas, Nevada: Bechtel SAIC Company. ACC: DOC.20040827.0008. 170029

BSC 2004. *Ground Control for Emplacement Drifts for LA.* 800-K0C-SSE0-00100-000-00A. Las Vegas, Nevada: Bechtel SAIC Company. ACC: ENG.20040712.0019. 170292

BSC 2004. *Lithophysal Rock Mass Mechanical Properties of the Repository Host Horizon*. 800-K0C-SS00-00200-000-00Aa. Las Vegas, Nevada: Bechtel SAIC Company. ACC: MOL.20040510.0200. TBV-5811. 168970

BSC 2004. *Multiscale Thermohydrologic Model*. ANL-EBS-MD-000049 REV 02. Las Vegas, Nevada: Bechtel SAIC Company. 169565

BSC 2004. *Peak Ground Velocities for Seismic Events at Yucca Mountain, Nevada*. ANL-MGR-GS-000004 REV 00. Las Vegas, Nevada: Bechtel SAIC Company. 170137

BSC 2004. *Q-List.* 000-30R-MGR0-00500-000-000 REV 00. Las Vegas, Nevada: Bechtel SAIC Company. ACC: ENG.20040721.0007. 168361

BSC 2004. *Repository Subsurface Emplacement Drifts Steel Invert Structure Plan & Elevation*. 800-SS0-SSE0-00101-000-00B. Las Vegas, Nevada: Bechtel SAIC Company. ACC: ENG.20040520.0004. 169503

BSC 2004. *Sampling of Stochastic Input Parameters for Rockfall Calculations and for Structural Response Calculations Under Vibratory Ground Motion.* ANL-EBS-PA-000009 REV 01. Las Vegas, Nevada: Bechtel SAIC Company. ACC: DOC.20040901.0004. 169999

BSC 2004. *Seismic Consequence Abstraction*. MDL-WIS-PA-000003 REV 01. Las Vegas, Nevada: Bechtel SAIC Company. 169183

BSC 2004. *Structural Calculations of Waste Package Exposed to Vibratory Ground Motion.* 000-00C-WIS0-01400-000-00A. Las Vegas, Nevada: Bechtel SAIC Company. ACC: ENG.20040217.0008. 167083

BSC 2004. *Technical Work Plan for: Regulatory Integration Modeling of Drift Degradation, Waste Package and Drip Shield Vibratory Motion and Seismic Consequences.* TWP-MGR-GS-000003 REV 00 ICN 01. Las Vegas, Nevada: Bechtel SAIC Company. ACC: DOC.20040810.0003. 171520

BSC 2004. *Thermal Conductivity of Non-Repository Lithostratigraphic Layers*. MDL-NBS-GS-000006 REV 01. Las Vegas, Nevada: Bechtel SAIC Company. 170033

BSC 2004. *Thermal Conductivity of the Potential Repository Horizon.* MDL-NBS-GS-000005 REV 01. Las Vegas, Nevada: Bechtel SAIC Company. 169854

BSC 2004. *UZ Flow Models and Submodels*. MDL-NBS-HS-000006 REV 02. Las Vegas, Nevada: Bechtel SAIC Company. 169861

BSC 2004. *Ventilation Model and Analysis Report*. ANL-EBS-MD-000030 REV 04. Las Vegas, Nevada: Bechtel SAIC Company. 169862

Buesch, D. 2003. "Fractures in Thin Sections with Rims as Cooling Joints in Tptpmn and Tptpll for AMR." E-mail from D. Buesch to D. Kicker, June 2, 2003. ACC: MOL.20030610.0067. 163729

Buesch, D. 2003. "Hydrogeologic Properties of Features in Crystallized Topopah Spring Tuff." E-mail from D. Buesch to D. Kicker and D. Rigby, March 10, 2003, with attachment. ACC: MOL.20030314.0188. 162271

Buesch, D.C. and Lung, R.C. 2003. "Tephrostratigraphic Relations and the Timing and Locations of Faulting Near Exile Hill at Yucca Mountain, Nevada." *Proceedings of the 10th International High-Level Radioactive Waste Management Conference (IHLRWM), March 30-April 2, 2003, Las Vegas, Nevada*. Pages 388–397. La Grange Park, Illinois: American Nuclear Society. TIC: 254559. 170297

Buesch, D.C. and Spengler, R.W. 1998. "Character of the Middle Nonlithophysal Zone of the Topopah Spring Tuff at Yucca Mountain." *High-Level Radioactive Waste Management, Proceedings of the Eighth International Conference, Las Vegas, Nevada, May 11-14, 1998*. Pages 16-23. La Grange Park, Illinois: American Nuclear Society. TIC: 237082. 101433

Buesch, D.C.; Beason, S.C.; and Spengler, R.W. 1999. "Relations Among Welding, Vapor-Phase Activity, Crystallization, and Fractures in the Tiva Canyon and Topopah Spring Tuffs, at Yucca Mountain, Nevada." *Abstracts with Programs - Geological Society of America, 31,* (7), A-476 - A-477. Boulder, Colorado: Geological Society of America. TIC: 254857. 165483

Buesch, D.C.; Nelson, J.E.; Dickerson, R.P.; Drake, R.M., II; Spengler, R.W.; Geslin, J.K.; Moyer, T.C.; and San Juan, C.A. 1996. *Distribution of Lithostratigraphic Units Within the Central Block of Yucca Mountain, Nevada: A Three-Dimensional Computer-Based Model, Version YMP.R2.0*. Open-File Report 95-124. Denver, Colorado: U.S. Geological Survey. ACC: MOL.19970618.0573. 101202

Buesch, D.C.; Spengler, R.W.; Moyer, T.C.; and Geslin, J.K. 1996. *Proposed Stratigraphic Nomenclature and Macroscopic Identification of Lithostratigraphic Units of the Paintbrush Group Exposed at Yucca Mountain, Nevada*. Open-File Report 94-469. Denver, Colorado: U.S. Geological Survey. ACC: MOL.19970205.0061. 100106

Byers, F.M., Jr.; Carr, W.J.; Orkild, P.P.; Quinlivan, W.D.; and Sargent, K.A. 1976. *Volcanic Suites and Related Cauldrons of Timber Mountain-Oasis Valley Caldera Complex, Southern Nevada*. Professional Paper 919. Washington, D.C.: U.S. Geological Survey. TIC: 201146. 104639

Byrne, P.M.; Srithar, T.; and Kern, C.B. 1990. "Field Measurements and Analysis of a Large Diameter Flexible Culvert." *Structural Performance of Flexible Pipes, Proceedings of the First National Conference on Flexible Pipes, Columbus, Ohio, 21-23 October, 1990*. Sargand, S.M; Mitchell, G.F.; and Hurd, J.O., eds. Pages 27-37. Brookfield, Vermont: A.A. Balkema. TIC: 255970. 168921

Canori, G.F. and Leitner, M.M. 2003. *Project Requirements Document*. TER-MGR-MD-000001 REV 02. Las Vegas, Nevada: Bechtel SAIC Company. ACC: DOC.20031222.0006. 166275

Carlos, B.A.; Chipera, S.J.; and Bish, D.L. 1995. *Distribution and Chemistry of Fracture-Lining Minerals at Yucca Mountain, Nevada*. LA-12977-MS. Los Alamos, New Mexico: Los Alamos National Laboratory. ACC: MOL.19960306.0564. 101326

Charles, R.J. 1959. "The Strength of Silicate Glasses and Some Crystalline Oxides." *Fracture, Proceedings of an International Conference on the Atomic Mechanisms of Fracture held in Swampscott, Massachusetts, April 12-16, 1959*. Averback, B.L.; Felbeck, D.K.; Hahn, G.T.; and Thomas, D.A., eds. Chapter 12, 225–249. New York, New York: John Wiley & Sons. TIC: 236240. 170308

Chen, E.P. 1987. *A Computational Model for Jointed Media with Orthogonal Sets of Joints*. SAND86-1122. Albuquerque, New Mexico: Sandia National Laboratories. ACC: MOL.19991116.0419. 101800

Christiansen, R.L.; Lipman, P.W.; Carr, W.J.; Byers, F.M., Jr.; Orkild, P.P.; and Sargent, K.A. 1977. "The Timber Mountain-Oasis Valley Caldera Complex of Southern Nevada." *Geological Society of America Bulletin*, *88*, (7), 943-959. [Boulder, Colorado]: Geological Society of America. TIC: 201802. 157236

CRWMS M&O 1997. *Data Transmittal Package (DTP) for "Hydraulic Fracturing Stress Measurements in Test Hole: ESF-AOD-HDFR#1, Thermal Test Facility, Exploratory Studies Facility at Yucca Mountain*. DTN: SNF37100195002.001, TDIF 305878. Las Vegas, Nevada: CRWMS M&O. ACC: MOL.19970717.0005; MOL.19970717.0006; MOL.19970717.0007; MOL.19970717.0008. 147458

CRWMS M&O 1997. *Yucca Mountain Site Geotechnical Report*. B00000000-01717-5705-00043 REV 01. Two volumes. Las Vegas, Nevada: CRWMS M&O. ACC: MOL.19971017.0736; MOL.19971017.0737. 103564

CRWMS M&O 1998. *Geology of the Exploratory Studies Facility Topopah Spring Loop*. BAB000000-01717-0200-00002 REV 01. Las Vegas, Nevada: CRWMS M&O. ACC: MOL.19980415.0283. 102679

CRWMS M&O 1998. *Preliminary Block Size Calculation*. BCAA00000-01717-0210-00001 REV 00. Las Vegas, Nevada: CRWMS M&O. ACC: MOL.19981106.0282. 102723

CRWMS M&O 1999. *South Ramp 3.01.X Area Ground Support Analysis*. BABEE0000-01717-0200-00023 REV 00. Las Vegas, Nevada: CRWMS M&O. ACC: MOL.19990908.0318. 108441

CRWMS M&O 2000. *Fracture Geometry Analysis for the Stratigraphic Units of the Repository Host Horizon*. ANL-EBS-GE-000006 REV 00. Las Vegas, Nevada: CRWMS M&O. ACC: MOL.20000918.0286. 152286

Cundall, P.A. and Strack, O.D.L. 1979. "A Discrete Numerical Model for Granular Assemblies." *Geotechnique*, *29*, (1), 47-65. [London, England: Thomas Telford]. TIC: 253962. 162194

Day, W.C.; Dickerson, R.P.; Potter, C.J.; Sweetkind, D.S.; San Juan, C.A.; Drake, R.M., II; and Fridrich, C.J. 1998. *Bedrock Geologic Map of the Yucca Mountain Area, Nye County, Nevada. Geologic Investigations Series I-2627*. Denver, Colorado: U.S. Geological Survey. ACC: MOL.19981014.0301. 100027

Derman, C.; Gleser, L.J.; and Olkin, I. 1973. *A Guide to Probability Theory and Application. New York, New York: Holt, Rinehart and Winston*. TIC: 242445. 108444

Dershowitz, W.S. and Herda, H.H. 1992. "Interpretation of Fracture Spacing and Intensity." *Rock Mechanics, Proceedings of the 33rd U.S. Symposium, Santa Fe, New Mexico, 3-5 June, 1992*. Tillerson, J.R. and Wawersik, W.R., eds. Pages 757-766. Rotterdam, The Netherlands: A.A. Balkema. TIC: 245647. 104893

DOE 2004. *Software Management Report for: CLUSTRAN V1.1, SMR REV. NO.: 00*. 11162-SMR-1.1-00. Las Vegas, Nevada: Bechtel SAIC Company. ACC: MOL.20040426.0368. 170474

Dowding, C.H. 1979. "Earthquake Stability of Rock Tunnels." *Tunnels & Tunnelling*, *11*, 15-20. London, England: Morgan-Grampian Publishing. TIC: 242115. 101977

Duan, F. 2003. "A White Paper by Nick Barton." E-mail from F. Duan to D. Kicker, May 28, 2003, with attachment. ACC: MOL.20030603.0132; MOL.20030219.0058. 163586

Duncan, J.M.; Byrne, P.; Wong, K.S.; and Mabry, P. 1980. *Strength, Stress-Strain and Bulk Modulus Parameters for Finite Element Analyses of Stresses and Movements in Soil Masses*. UCB/GT/80-01. Berkeley, California: University of California, College of Engineering, Office of Research Services. TIC: 253873. 161776

Eatman, G.L.W.; Singleton, W.L.; Moyer, T.C.; Barr, D.L.; Albin, A.L.; Lung, R.C.; and Beason, S.C. 1997. *Geology of the South Ramp - Station 55+00 to 78+77, Exploratory Studies Facility, Yucca Mountain Project, Yucca Mountain, Nevada*. Milestone SPG42CM3. Denver, Colorado: U.S. Geological Survey. ACC: MOL.19980216.0328. 101219

Eckel, E.B. 1970. *The Alaska Earthquake, March 27, 1964: Lessons and Conclusions*. Geological Survey Professional Paper 546. Washington, D.C.: U.S. Government Printing Office. TIC: 251802. 157493

Fisher, N.I.; Lewis, T.; and Embleton, B.J.J. 1987. *Statistical Analysis of Spherical Data*. New York, New York: Cambridge University Press. TIC: 208442. 108447

Flint, L.E. 1998. *Characterization of Hydrogeologic Units Using Matrix Properties, Yucca Mountain, Nevada*. Water-Resources Investigations Report 97-4243. Denver, Colorado: U.S. Geological Survey. ACC: MOL.19980429.0512. 100033

Freeze, G.A.; Brodsky, N.S.; and Swift, P.N. 2001. *The Development of Information Catalogued in REV00 of the YMP FEP Database*. TDR-WIS-MD-000003 REV 00 ICN 01. Las Vegas, Nevada: Bechtel SAIC Company. ACC: MOL.20010301.0237. 154365

Fruchtbaum, J. 1988. "Handling Special Materials." *Bulk Materials Handling Handbook*. Pages 327-375. New York, New York: Van Nostrand Reinhold. TIC: 253872. 161774

Gibson, J.D.; Shephard, L.E.; Swan, F.H.; Wesling, J.R.; and Kerl, F.A. 1990. "Synthesis of Studies for the Potential of Fault Rupture at the Proposed Surface Facilities, Yucca Mountain, Nevada." *High Level Radioactive Waste Management, Proceedings of the International Topical Meeting, Las Vegas, Nevada, April 8-12, 1990*. 1, 109-116. La Grange Park, Illinois: American Nuclear Society. TIC: 202058. 157245

Goodman, R.E. 1980. *Introduction to Rock Mechanics*. New York, New York: John Wiley & Sons. TIC: 218828. 101966

Goodman, R.E. and Shi, G-H. 1985. *Block Theory and Its Application to Rock Engineering*. Englewood Cliffs, New Jersey: Prentice-Hall. TIC: 241514. 150094

Hoek, E. 2000. *[Practical] Rock Engineering, [2000 Edition]*. Toronto, Ontario, Canada: RocScience. TIC: 253544. 160705

Hoek, E. and Brown, E.T. 1982. *Underground Excavations in Rock*. London, England: The Institution of Mining and Metallurgy. TIC: 217577. 120981

Hoek, E.; Carranza-Torres, C.; and Corkum, B. 2002. "Hoek-Brown Failure Criterion – 2002 Edition." *5th North American Rock Mechanics Symposium and 17th Tunnelling Association of Canada Conference: NARMS-TAC 2002, July 7-10, University of Toronto*. Toronto, Ontario, Canada: Rocscience. Accessed March 17, 2003. TIC: 253954. http://www.rocscience.com/Anon/ResearchPapers/NARMS.pdf 162204

Hoek, E.; Kaiser, P.K.; and Bawden, W.F. 2000. *Support of Underground Excavations in Hard Rock*. Rotterdam, The Netherlands: A.A. Balkema. TIC: 252991. 160539

Hoerger, S.F. and Young, D.S. 1990. "Probabilistic Prediction of Keyblock Occurrences." *Rock Mechanics Contributions and Challenges: Proceedings of the 31st U.S. Symposium, Golden, [Colorado], 18-20 June, 1990*. Hustrulid, W.A. and Johnson, G.A., eds. Pages 229-236. Brookfield, Vermont: A.A. Balkema. TIC: 245123. 151814

Hudson, J.A. and Priest, S.D. 1979. "Discontinuities and Rock Mass Geometry." *International Journal of Rock Mechanics and Mining Science & Geomechanics Abstracts*, *16*, ([6]), 339-362. [New York, New York]: Pergamon. TIC: 240802. 104915

Itasca Consulting Group 2002. *Itasca Software–Cutting Edge Tools for Computational Mechanics*. Minneapolis, Minnesota: Itasca Consulting Group. TIC: 252592. 160331

Jackson, J.A., ed. 1997. *Glossary of Geology.* 4th Edition. Alexandria, Virginia: American Geological Institute. TIC: 236393. 109119

Jaeger, J.C. and Cook, N.G.W. 1979. *Fundamentals of Rock Mechanics*. 3rd Edition. New York, New York: Chapman and Hall. TIC: 218325. 106219

Kaiser, P.K.; McCreath, D.R.; and Tannant, D.D. 1996. *Canadian Rockburst Support Handbook*. Ontario, Canada: Geomechanics Research Centre. TIC: 233844. 108453

Kanamori, H. 1977. "The Energy Release in Great Earthquakes." *Journal of Geophysical Research, 82,* (20), 2981-2987. Washington, D.C.: American Geophysical Union. TIC: 255672. 167797

Kemeny, J.M. 1991. "A Model for Non-Linear Rock Deformation Under Compression Due to Sub-Critical Crack Growth." *International Journal of Rock Mechanics and Mining Science & Geomechanics Abstracts*, *28*, (6), 459-467. [New York, New York]: Pergamon. TIC: 245750. 108455

Kemeny, J.M. and Cook, N.G.W. 1986. "Effective Moduli, Non-Linear Deformation and Strength of a Cracked Elastic Solid." *International Journal of Rock Mechanics and Mining Science & Geomechanics Abstracts*, 23, (2), 107-118. [New York, New York]: Pergamon. TIC: 245751. 108454

Kessler, J.; McGuire, R.; Vlasity, J.; Long, A.; Childs, S.; Ross, B.; Schwartz, F.; Bullen, D.; Apted, M.; Zhou, W.; Sudicky, E.; Smith, G.; Coppersmith, K.; Kemeny, J.; and Sheridan, M. 1996. *Yucca Mountain Total System Performance Assessment, Phase 3*. EPRI TR-107191. Palo Alto, California: Electric Power Research Institute. TIC: 238085. 100558

Konietzky, H. 2003. "Preface." *Numerical Modeling in Micromechanics via Particle Methods, Proceedings of the 1st International PFC Symposium, Gelsenkirchen, Germany, 6-8 November 2002*. Konietzky, H., ed. Page ix. Exton, Pennsylvania: A.A. Balkema. TIC: 253950. 162198

Kuszmaul, J.S. and Goodman, R.E. 1995. "An Analytical Model for Estimating Keyblock Sizes in Excavations in Jointed Rock Masses." *Fractured and Jointed Rock Masses, [Conference held at Lake Tahoe, California, June 3-5, 1992]*. Pages 19-26. Rotterdam, The Netherlands: A.A. Balkema. TIC: 240658. 151816

Lau, J.S.O.; Gorski, B.; Conlon, B.; and Anderson, T. 2000. *Long-Term Loading Tests on Saturated Granite and Granodiorite*. Report No. 06819-REP-01300-10016 R00. Toronto, Ontario, Canada: Ontario Power Generation, Nuclear Waste Management Division. TIC: 254970. 164769

Lefebvre, G.; Laliberté, M.; Lefebvre, L.M.; LaFleur, J.; and Fisher, C.L. 1976. "Measurement of Soil Arching Above a Large Diameter Flexible Culvert." *Canadian Geotechnical Journal*, *13*, 58-71. [Toronto, Ontario, Canada: National Research Council of Canada]. TIC: 255968. 168919

Lemos, J. and Damjanac, B. 2002. *New Developments in 3DEC Version 2.01*. Minneapolis, Minnesota: Itasca Consulting Group. TIC: 252778. 162058

Lipman, P.W.; Christiansen, R.L.; and O'Connor, J.T. 1966. *A Compositionally Zoned Ash-Flow Sheet in Southern Nevada*. Professional Paper 524-F. Washington, D.C.: U.S. Geological Survey. TIC: 219972. 100773

Martin, R.J., III 1972. "Time-Dependent Crack Growth in Quartz and its Application to the Creep of Rocks." *Journal of Geophysical Research*, *77*, (8), 1406-1419. [Washington, D.C.]: American Geophysical Union. TIC: 224770. 169721

Martin, R.J., III and Durham, W.B. 1975. "Mechanisms of Crack Growth in Quartz." *Journal of Geophysical Research*, *80*, (35), 4837-4844. Washington, D.C.: American Geophysical Union. TIC: 224771. 170301

Martin, R.J., III.; Price, R.H.; Boyd, P.J.; and Noel, J.S. 1993. "The Influence of Strain Rate and Sample Inhomogeneity on the Moduli and Strength of Welded Tuff." *International Journal of Rock Mechanics and Mining Science & Geomechanics Abstracts*, *30*, (7), 1507–1510. [New York, New York]: Pergamon. TIC: 254873. 164770

Martin, R.J., III; Price, R.H.; Boyd, P.J.; and Noel, J.S. 1995. *Creep in Topopah Spring Member Welded Tuff*. SAND94-2585. Albuquerque, New Mexico: Sandia National Laboratories. ACC: MOL.19950502.0006. 100159

Martin, R.J.; Noel, J.S.; Boyd, P.J.; and Price, R.H. 1997. "Creep and Static Fatigue of Welded Tuff from Yucca Mountain, Nevada." *International Journal of Rock Mechanics and Mining Sciences*, *34*, (3-4), Paper No. 190. [New York, New York]: Pergamon. TIC: 255298. 165960

Martin, R.J.; Noel, J.S.; Boyd, P.J.; and Price, R.H. 1997. *Creep Properties of the Paintbrush Tuff Recovered from Borehole USW NRG-7/7A: Data Report*. SAND95-1759. Albuquerque, New Mexico: Sandia National Laboratories. ACC: MOL.19971017.0661. 148875

Mongano, G.S.; Singleton, W.L.; Moyer, T.C.; Beason, S.C.; Eatman, G.L.W.; Albin, A.L.; and Lung, R.C. 1999. *Geology of the ECRB Cross Drift - Exploratory Studies Facility, Yucca Mountain Project, Yucca Mountain, Nevada*. [Deliverable SPG42GM3]. Denver, Colorado: U.S. Geological Survey. ACC: MOL.20000324.0614. 149850

MRD (Mining Research Directorate) 1995. *Rockburst Research Handbook, Canadian Rockburst Research Program 1990-1995*. Six volumes. Sudbury, Canada: Canadian Mining Industry Research Organization, Mining Division. TIC: 256095. 169719

Munsell Color Company 1994. *Munsell Soil Color Charts*. 1994 Revised Edition. New Windsor, New York: GretagMacbeth. TIC: 238646. 106399

Newmark, N.M. 1965. "Effects of Earthquakes on Dams and Embankments." *Geotechnique*, *XV*, (2), 139-160. London, England: Institution of Civil Engineers. TIC: 255743. 169515

Nimick, F.B. and Connolly, J.R. 1991. *Calculation of Heat Capacities for Tuffaceous Units from the Unsaturated Zone at Yucca Mountain, Nevada*. SAND88-3050. Albuquerque, New Mexico: Sandia National Laboratories. ACC: NNA.19910308.0017. 100690

NRC (U.S. Nuclear Regulatory Commission) 2002. *Integrated Issue Resolution Status Report*. NUREG-1762. Washington, D.C.: U.S. Nuclear Regulatory Commission, Office of Nuclear Material Safety and Safeguards. TIC: 253064. 159538

NRC (U.S. Nuclear Regulatory Commission) 2003. *Yucca Mountain Review Plan, Final Report*. NUREG-1804, Rev. 2. Washington, D.C.: U.S. Nuclear Regulatory Commission, Office of Nuclear Material Safety and Safeguards. TIC: 254568. 163274

Olsson, W.A. and Brown, S.R. 1997. *Mechanical Properties of Fractures from Drillholes UE25-NRG-4, USW-NRG-6, USW-NRG-7, USW-SD-9 at Yucca Mountain, Nevada*. SAND95-1736. Albuquerque, New Mexico: Sandia National Laboratories. ACC: MOL.19970224.0064. 106453

Ortiz, T.S.; Williams, R.L.; Nimick, F.B.; Whittet, B.C.; and South, D.L. 1985. *A Three-Dimensional Model of Reference Thermal/Mechanical and Hydrological Stratigraphy at Yucca Mountain, Southern Nevada*. SAND84-1076. Albuquerque, New Mexico: Sandia National Laboratories. ACC: MOL.19980602.0331. 101280

Otto, S.J. and Buesch, D.C. 2003. "Porosity, Bulk Density, and Rock-Particle Density of Lithostratigraphic Components in Lithophysal Rocks of the Topopah Spring Tuff at Yucca Mountain, Nevada." *Abstracts with Programs - Geological Society of America, 35,* (6), 434-435. Boulder, Colorado: Geological Society of America. TIC: 254862. 170727

Peterman, Z.E. and Cloke, P.L. 2002. "Geochemistry of Rock Units at the Potential Repository Level, Yucca Mountain, Nevada (includes Erratum)." *Applied Geochemistry*, *17*, (6, 7), 683-698, 955-958. New York, New York: Pergamon. TIC: 252516; 252517. 162576

Potyondy, D. and Cundall, P. 2001. *The PFC Model for Rock: Predicting Rock-Mass Damage at the Underground Research Laboratory*. Report No. 06819-REP-01200-10061-R00. Toronto, Ontario, Canada: Ontario Power Generation, Nuclear Waste Management Division. TIC: 253569. 156895

Potyondy, D.O. 2003. "PFC Stress Corrosion Model." Annex 11.4 of *Seismic Validation of 3-D Thermo-Mechanical Models for the Prediction of the Rock Damage Around Radioactive Spent Fuel Waste*. Project No. FIKW-2001-00200. Liverpool, England: University of Liverpool. TIC: 254978. 165550

Pratt, H.R.; Hustrulid, W.A.; and Stephenson, D.E. 1978. *Earthquake Damage to Underground Facilities*. DP-1513. Aiken, South Carolina: E.I. du Pont de Nemours and Company, Savannah River Laboratory. TIC: 210276. 151817

Price, R.H. 1986. *Effects of Sample Size on the Mechanical Behavior of Topopah Spring Tuff*. SAND85-0709. Albuquerque, New Mexico: Sandia National Laboratories. ACC: NNA.19891106.0125. 106589

Price, R.H.; Nimick, F.B.; Connolly, J.R.; Keil, K.; Schwartz, B.M.; and Spence, S.J. 1985. *Preliminary Characterization of the Petrologic, Bulk, and Mechanical Properties of a Lithophysal Zone Within the Topopah Spring Member of the Paintbrush Tuff*. SAND84-0860. Albuquerque, New Mexico: Sandia National Laboratories. ACC: NNA.19870406.0156. 106602

Raney, R.G. 1988. *Reported Effects of Selected Earthquakes in the Western North America Intermontane Region, 1852-1983, on Underground Workings and Local and Regional Hydrology: A Summary*. NRC FIN D1018. Spokane, Washington: U.S. Department of the Interior, Bureau of Mines. TIC: 217278. 147173

Reamer, C.W. and Williams, D.R. 2001. *Summary Highlights of NRC/DOE Technical Exchange and Management Meeting on Repository Design and Thermal-Mechanical Effects*. Meeting held February 6-8, 2001, Las Vegas, Nevada. Washington, D.C.: U.S. Nuclear Regulatory Commission. ACC: MOL.20010307.0511; MOL.20010307.0512; MOL.20010307.0513; MOL.20010307.0514; MOL.20010307.0515; MOL.20010307.0516; MOL.20010307.0517; MOL.20010307.0518; MOL.20010307.0519; MOL.20010307.0520; MOL.20010307.0521. 154348

Rowe, R. 1992. "Tunnelling in Seismic Zones." *Tunnels & Tunnelling*, *24*, (12), 41-44. London, England: Morgan-Grampian. TIC: 252094. 156898

Savino, J.M.; Smith, K.D.; Biasi, G.; Sullivan, T.; and Cline, M. 1999. "Earthquake Ground Motion Effects on Underground Structures/Tunnels." *Eos, Transactions (Supplement)*, *80*, (17), S10. Washington, D.C.: American Geophysical Union. TIC: 247757. 148612

Sawyer, D.A.; Fleck, R.J.; Lanphere, M.A.; Warren, R.G.; Broxton, D.E.; and Hudson, M.R. 1994. "Episodic Caldera Volcanism in the Miocene Southwestern Nevada Volcanic Field: Revised Stratigraphic Framework, $^{40}Ar/^{39}Ar$ Geochronology, and Implications for Magmatism and Extension." *Geological Society of America Bulletin*, *106*, (10), 1304-1318. Boulder, Colorado: Geological Society of America. TIC: 222523. 100075

Schmidtke, R.H. and Lajtai, E.Z. 1985. "The Long-Term Strength of Lac du Bonnet Granite." *International Journal of Rock Mechanics and Mining Science & Geomechanics Abstracts*, *22*, (6), 461-465. [New York, New York]: Pergamon. TIC: 254874. 164774

Scholz, C.H. 1972. "Static Fatigue of Quartz." *Journal of Geophysical Research*, *77*, (11), 2104-2114. [Washington, D.C.]: American Geophysical Union. TIC: 224772. 169724

Schuraytz, B.C.; Vogel, T.A.; and Younker, L.W. 1989. "Evidence for Dynamic Withdrawal from a Layered Magma Body: The Topopah Spring Tuff, Southwestern Nevada." Journal of Geophysical Research, *94*, (B5), 5925-5942. Washington, D.C.: American Geophysical Union. TIC: 225936. 107248

Scott, R.B. 1990. "Tectonic Setting of Yucca Mountain, Southwest Nevada." Chapter 12 of *Basin and Range Extensional Tectonics Near the Latitude of Las Vegas, Nevada*. Wernicke, B.P., ed. Memoir 176. Boulder, Colorado: Geological Society of America. TIC: 222540. 106751

Scott, R.B. and Bonk, J. 1984. *Preliminary Geologic Map of Yucca Mountain, Nye County, Nevada, with Geologic Sections*. Open-File Report 84-494. Denver, Colorado: U.S. Geological Survey. ACC: HQS.19880517.1443. 104181

Senseny, P.E. 1993. "Stress Wave Loading of a Tunnel: A Benchmark Study." *Dynamic Analysis and Design Considerations for High-Level Nuclear Waste Repositories, Proceedings of the Symposium Sponsored by the Nuclear Dynamic Analysis Committee of the Structural Division of the American Society of Civil Engineers and Co-sponsored by the U.S. Department of Energy, Office of Civilian Radioactive Waste Management, San Francisco, California, August 19-20, 1992*. Hossain, Q.A., ed. Pages 311-338. New York, New York: American Society of Civil Engineers. TIC: 206451. 162017

Senseny, P.E. and Pucik, T.A. 1999. "Development and Validation of Computer Models for Structures in Jointed Rock." *International Journal for Numerical and Analytical Methods in Geomechanics*, *23*, ([8]), 751-778. [New York, New York]: John Wiley & Sons. TIC: 253795. 168479

Shanley, R.J. and Mahtab, M.A. [1974]. *A Computer Program for Clustering Data Points on the Sphere. Information Circular 8624*. Washington, D.C.: U.S. Department of the Interior, Bureau of Mines. ACC: MOL.20040413.0435. 169199

Sharma, S. and Judd, W.R. 1991. "Underground Opening Damage from Earthquakes." *Engineering Geology*, *30*, (3/4), 263-276. Amsterdam, [The Netherlands]: Elsevier. TIC: 226268. 154505

Singleton, B. 1995. "Data Report Package, Supporting Information." Memorandum from B. Singleton (U.S. Bureau of Reclamation) to C. Miller-Corbett (U.S.Geological Survey), July 20, 1995, with attachments. ACC: MOL.19960731.0235. 107044

SNL (Sandia National Laboratories) 1996. *Mechanical Properties of Fractures in Specimens from Drillhole USW SD-9*. Albuquerque, New Mexico: Sandia National Laboratories. ACC: MOL.19961220.0133. 165408

SNL (Sandia National Laboratories) 1996. *Mechanical Properties of Fractures in Specimens from Drillholes USW NRG-7/7A and USW SD-12*. Albuquerque, New Mexico: Sandia National Laboratories. ACC: MOL.19961029.0087. 165410

Stevens, P.R. 1977. *A Review of the Effects of Earthquakes on Underground Mines*. Open-File Report 77-313. Reston, Virginia: U.S. Geological Survey. TIC: 211779. 154501

Stone, C.A.; Kuszmaul, J.S.; Boontun, A.; and Young, D. 1996. "Comparison of an Analytical and a Numerical Approach to Probabilistic Keyblock Analysis." *Rock Mechanics*, *2*, 1769-1775. Rotterdam, The Netherlands: [A.A.] Balkema. TIC: 240659. 150437

Terzaghi, K. 1943. *Theoretical Soil Mechanics*. New York, New York: John Wiley & Sons. TIC: 223837. 162180

Terzaghi, R.D. 1966. "Sources of Error in Joint Surveys." *Geotechnique*, *11* to *15*, 287-304. London, England: [Thomas Telford]. TIC: 239078. 105805

Tyler, D.B.; Trueman, R.; and Pine, R.J. 1991. "Rockbolt Support Design Using a Probabilistic Method of Key Block Analysis." *Rock Mechanics as a Multidisciplinary Science, Proceedings of the 32nd U.S. Symposium, the University of Oklahoma/Norman, July 10-12, 1991*. Roegiers, J-C., ed. Pages 1037-1046. Brookfield, Vermont: A.A. Balkema Publishers. TIC: 103533. 151818

USGS (U.S. Geological Survey) 1996. *Geotechnical Report for Station 4+00 to 8+00, North Ramp of the Exploratory Studies Facility (ESF) Rock Mass Quality Ratings*. Denver, Colorado: U.S. Geological Survey. ACC: MOL.19970610.0620. 169024

USGS 1996. *Geotechnical Report for Station 8+00 to 10+00, North Ramp of the Exploratory Studies Facility (ESF), Rock Mass Quality Ratings*. Denver, Colorado: U.S. Geological Survey. ACC: MOL.19970610.0598. 169025

USGS 1996. *Supplemental and Supporting Information for Rock Mass Quality Ratings, Main Drift of the Exploratory Studies Facility (ESF), Station 30+00 to 35+00.* Denver, Colorado: U.S. Geological Survey. ACC: MOL.19970106.0347. 169030

USGS 1996. *Supplemental and Supporting Information for Rock Mass Quality Ratings, Main Drift of the Exploratory Studies Facility (ESF), Station 35+00 to 40+00.* Denver, Colorado: U.S. Geological Survey. ACC: MOL.19970106.0348. 169031

USGS 1996. *Supplemental and Supporting Information for Rock Mass Quality Ratings, Main Drift of the Exploratory Studies Facility (ESF), Station 40+00 to 45+00.* Denver, Colorado: U.S. Geological Survey. ACC: MOL.19970106.0392. 169032

USGS 1996. *Supplemental and Supporting Information for Rock Mass Quality Ratings, Main Drift of the Exploratory Studies Facility (ESF), Station 45+00 to 50+00.* Denver, Colorado: U.S. Geological Survey. ACC: MOL.19970106.0393. 169033

USGS 1996. *Supplemental and Supporting Information for Rock Mass Quality Ratings, Main Drift of the Exploratory Studies Facility (ESF), Station 50+00 to 55+00.* Denver, Colorado: U.S. Geological Survey. ACC: MOL.19970106.0422. 169034

USGS 1996. *Supplemental and Supporting Information for Rock Mass Quality Ratings, Main Drift of the Exploratory Studies Facility (ESF), Station 55+00 to 60+00.* Denver, Colorado: U.S. Geological Survey. ACC: MOL.19970804.0153. 169035

USGS 1996. *Supplemental and Supporting Information for Rock Mass Quality Ratings, North Ramp and Main Drift of the Exploratory Studies Facility (ESF), Station 26+00 to 30+00*. Denver, Colorado: U.S. Geological Survey. ACC: MOL.19970106.0299. 169029

USGS 1996. *Supplemental and Supporting Information for Rock Mass Quality Ratings, North Ramp of the Exploratory Studies Facility (ESF), Station 10+00 to 18+00*. Denver, Colorado: U.S. Geological Survey. ACC: MOL.19970618.0552. 169026

USGS 1996. *Supplemental and Supporting Information for Rock Mass Quality Ratings, North Ramp of the Exploratory Studies Facility (ESF), Station 18+00 to 26+00*. Denver, Colorado: U.S. Geological Survey. ACC: MOL.19970106.0276. 169027

USGS 1997. *Supplemental and Supporting Information for Rock Mass Quality Ratings, Alcove #5, Cross Drift & Heated Drift of the Exploratory Studies Facility (ESF)*. Denver, Colorado: U.S. Geological Survey. ACC: MOL.19980203.0461. 169040

USGS 1997. *Supplemental and Supporting Information for Rock Mass Quality Ratings, South Ramp of the Exploratory Studies Facility (ESF), Station 60+00 to 65+00*. Denver, Colorado: U.S. Geological Survey. ACC: MOL.19970804.0164 169036

USGS 1997. *Supplemental and Supporting Information for Rock Mass Quality Ratings, South Ramp of the Exploratory Studies Facility (ESF), Station 65+00 to 70+00*. Denver, Colorado: U.S. Geological Survey. ACC: MOL.19980216.0348. 169037

USGS 1997. *Supplemental and Supporting Information for Rock Mass Quality Ratings, South Ramp of the Exploratory Studies Facility (ESF), Station 70+00 to 75+00*. Denver, Colorado: U.S. Geological Survey. ACC: MOL.19980216.0359. 169038

USGS 1997. *Supplemental and Supporting Information for Rock Mass Quality Ratings, South Ramp of the Exploratory Studies Facility (ESF), Station 75+00 to 78+77*. Denver, Colorado: U.S. Geological Survey. ACC: MOL.19980216.0299. 169039

USGS 1999. *Supplemental and Supporting Information for Rock Mass Quality Ratings, ECRB Cross Block Drift, Station 00+00 to 10+00*. Denver, Colorado: U.S. Geological Survey. ACC: MOL.20000209.0203. 169018

USGS 1999. *Supplemental and Supporting Information for Rock Mass Quality Ratings, ECRB Cross Block Drift, Station 10+00 to 15+00*. Denver, Colorado: U.S. Geological Survey. ACC: MOL.20000209.0212. 169019

USGS 1999. *Supplemental and Supporting Information for Rock Mass Quality Ratings, ECRB Cross Block Drift, Station 15+00 to 20+00*. Denver, Colorado: U.S. Geological Survey. ACC: MOL.20000209.0221. 169020

USGS 1999. *Supplemental and Supporting Information for Rock Mass Quality Ratings, ECRB Cross Block Drift, Station 20+00 to 26+65*. Denver, Colorado: U.S. Geological Survey. ACC: MOL.20000209.0231. 169021

Wang, J-M. 1985. "The Distribution of Earthquake Damage to Underground Facilities During the 1976 Tang-Shan Earthquake." *Earthquake Spectra*, *1*, (4), 741-757. [Berkeley, California]: Earthquake Engineering Research Institute. TIC: 226272. 151821

Warburton, P.M. 1981. "Vector Stability Analysis of an Arbitrary Polyhedral Rock Block with Any Number of Free Faces." *International Journal of Rock Mechanics and Mining Science & Geomechanics Abstracts*, *18*, (5), 415-427. New York, New York: Pergamon. TIC: 241134. 150093

Wiederhorn, S.M. 1968. "Moisture Assisted Crack Growth in Ceramics." *International Journal of Fracture Mechanics*, *4*, (2), 171-177. Groningen, The Netherlands: Wolters–Noordhoff Publishing. TIC: 256161. 170309

Williams, N.H. 2001. "Contract #: DE-AC08-01NV12101 - Drift Scale Test (DST) White Paper: Scaling Along the Roof of the Heated Drift." Letter from N.H. Williams (BSC) to S.P. Mellington (DOE/YMSCO), May 15, 2001, PROJ.05/01.033, with enclosure. ACC: MOL.20010622.0252. 159516

Williams, N.H. 2002. "Thermal Inputs for Evaluations Supporting TSPA-LA." Interoffice memorandum from N.H. Williams (BSC) to Distribution, September 16, 2002, 0911024159, with enclosures. ACC: MOL.20021008.0141. 159916

9.2 CODES, STANDARDS, REGULATIONS, AND PROCEDURES

10 CFR 63. Energy: Disposal of High-Level Radioactive Wastes in a Geologic Repository at Yucca Mountain, Nevada. Readily available. 156605

AP-2.22Q, Rev. 1, ICN 1. *Classification Analyses and Maintenance of the Q-List*. Washington, D.C.: U.S. Department of Energy, Office of Civilian Radioactive Waste Management. ACC: DOC.20040714.0002.

AP-3.15Q, Rev. 4, ICN 5. *Managing Technical Product Inputs*. Washington, D.C.: U.S. Department of Energy, Office of Civilian Radioactive Waste Management. ACC: DOC.20040812.0004.

AP-SIII.9Q, Rev. 1, ICN 6. *Scientific Analyses*. Washington, D.C.: U.S. Department of Energy, Office of Civilian Radioactive Waste Management. ACC: DOC.20040805.0003.

AP-SIII.10Q, Rev. 2, ICN 6. *Models*. Washington, D.C.: U.S. Department of Energy, Office of Civilian Radioactive Waste Management. ACC: DOC.20040805.0005.

AP-SIII.2Q, Rev. 1, ICN 2. *Qualification of Unqualified Data*. Washington, D.C.: U.S. Department of Energy, Office of Civilian Radioactive Waste Management. ACC: DOC.20040127.0008.

AP-SIII.3Q, Rev. 2, ICN 1. *Submittal and Incorporation of Data to the Technical Data Management System*. Washington, D.C.: U.S. Department of Energy, Office of Civilian Radioactive Waste Management. ACC: DOC.20040226.0001.

LP-SI.11Q-BSC, Rev. 0. *Software Management*. Washington, D.C.: U.S. Department of Energy, Office of Civilian Radioactive Waste Management. ACC: DOC.20040225.0007.

YMP-USGS-GP-20, Rev. 1. *Estimating Abundance of Fractures in Core and in Outcrops, Including Lithophysae, Spots, Clasts, and Fractures.* Denver, Colorado: U.S. Geological Survey. ACC: MOL.19960129.0372.

9.3 SOFTWARE

BSC 2002. Software Code: 3DEC. V2.01. PC WINDOWS 2000/NT 4.0. 10025-2.01-00. 161930

BSC 2002. Software Code: DRKBA. V3.31. PC WINDOWS 2000/NT 4.0. 10071-3.31-00. 161946

BSC 2002. Software Code: F LAC. V4.0. PC WINDOWS 2000/NT 4.0 10167-4.0-00. 161953

BSC 2002. Software Code: FLAC3D. V2.1. PC WINDOWS 2000/NT 4.0. 10502-2.1-00. 161947

BSC 2002. Software Code: PFC2D. V2.0. PC WINDOWS 2000/NT 4.0. 10828-2.0-00. 161950

BSC 2002. *Software Code: PFC3D*. V.2.0. PC. 10830-2.0-00. 160612

BSC 2002. *Software Code: UDEC*. V3.1. PC WINDOWS 2000/NT 4.0. 10173-3.1-00. 161949

BSC 2004. *Software Code: Clustran*. V. 1.1. PC, Windows 2000. 11162-1.1-00. 169203

BSC 2004. *Software Code: PFC2D*. V 2.0. PC, Windows 2000. 10828-2.0-01. 169930

BSC 2004. *Software Code: PFC3D*. V 2.0. PC, Windows 2000. 10830-2.0-01. 169931

BSC 2004. *Software Code: Read DXF*. V. 1.0. PC, Windows 2000. 11159-1.0-00. 169204

CRWMS M&O 1997. *Software Code: DIPS*. V4.03. 30017 V4.03. 149839

CRWMS M&O 1998. *Software Code: UNWEDGE* V2.3. V2.3. 30053 V2.3. 145366

Dynamic Graphics 2000. *Software Code: EARTHVISION*. 5.1. SGI/IRIX 6.5. 10174-5.1-00. 167994

LLNL (Lawrence Livermore National Laboratory) 2002. *Software Code: NUFT*. V3.0s. Sun, SunO.S. 5.6 & 5.7. 10088-3.0s-01. 157280

USGS 1999. *Software Code: FracMAN*. V.2.512. PC, Windows NT. 10114-2.511-00. 160577

9.4 SOURCE DATA, LISTED BY DATA TRACKING NUMBER

GS000608314224.004. Provisional Results: Geotechnical Data for Station 35+00 to Station 40+00, Main Drift of the ESF. Submittal date: 06/20/2000. 152573

GS000608314224.005. Provisional Results: Geotechnical Data - Full Periphery Maps for the North Ramp of the Exploratory Studies Facility, Stations 4+00 to 8+00. Submittal date: 06/28/2000. 166002

GS000608314224.006. Provisional Results: Geotechnical Data for Station 26+00 to 30+00, North Ramp and Main Drift of the ESF, Full-Periphery Geotechnical Maps (Drawings OA-46-222 through OA-46-226) and Rock Mass Quality Ratings Report. Submittal date: 06/28/2000. 152572

GS020908314224.001. Supplemental Fracture Study Traverses 1 through 16 at WT-11 Wash and Solitario Canyon Starting in WT-11 Wash along Iron Ridge. Submittal date: 10/23/2002. 171038

GS021008314224.002. Lithophysal Data Study from the Tptpll in the ECRB from Stations 14+44 to 23+26. Submittal date: 01/28/2003. 161910

GS030283114222.001. Direct Shear Data from Selected Samples of the Topopah Spring Tuff. Submittal date: 02/20/2003. 161913

GS030483351030.001. Bulk Density, Rock-Particle Density, Porosity Properties of Core Samples of Spot, Rim & Matrix-Groundmass from 17 Boreholes in the Upper & Lower Lithophysal Zones of the Topopah Spring Tuff from the ESF & ECRB Cross Drift. Submittal date: 04/24/2003. 163440

GS040108314224.001. Detailed Line Survey Data for Horizontal and Vertical Traverses, ECRB. Submittal date: 02/27/2004. 169591

GS040308314224.002. Supplemental Fracture Study Traverses 17 through 23 at Prow Pass in the Yucca and Windy Washes. Submittal date: 05/05/2004. 171039

GS040608314224.001. Large-Lithophysal Inventory Data from the Tptpll and Tptpln in the ECRB from Stations 14+44 to 25+35. Submittal date: 08/19/2004. 171367

GS950508314224.003. Provisional Results: Geotechnical Data - Full Periphery Map Data from North Ramp of the Exploratory Studies Facility, Stations 0+60 to 4+00. Submittal date: 05/24/1995. 107488

GS960408314224.001. Provisional Results: Geotechnical Data – Full Periphery Geotechnical Maps of the North Ramp, Exploratory Studies Facility, Station 8+00 to 10+00, Plots OA-46-201, -202, -203; Geotechnical Report – Rock Mass Quality Ratings. Submittal date: 06/24/1996. 168135

GS960408314224.003. Provisional Results: Geotechnical Data – Full-Periphery Geotechnical Maps (Drawing OA-46-204 through -212) and Rock Mass Quality Ratings from North Ramp of the Exploratory Studies Facility, Stations 10+00 to 18+00. Submittal date: 08/29/1996. 168136

GS960708314224.008. Provisional Results: Geotechnical Data for Station 30 + 00 to Station 35 + 00, Main Drift of the ESF. Submittal date: 08/05/1996. 105617

GS960708314224.009. Provisional Results: Geotechnical Data for Station 18+00 to 26+00, North Ramp of the ESF, Full-Periphery Geotechnical Maps and Rock Mass Quality Ratings Report. Submittal date: 09/09/1996. 168137

GS960708314224.010. Provisional Results: Geotechnical Data for Station 40+00 to Station 45+00, Main Drift of the ESF. Submittal date: 08/05/1996. 106031

GS960908314224.014. Provisional Results - ESF Main Drift, Station 50+00 to Station 55+00. Submittal date: 09/09/1996. 106033

GS960908314224.015. Provisional Results: Geotechnical Data for Stations 30+00 to 40+00, Main Drift of the ESF, Full-Periphery Geotechnical Maps and Rock Mass Quality Ratings Report. Submittal date: 09/09/1996. 108372

GS960908314224.016. Provisional Results: Geotechnical Data for Station 40+00 to 50+00, Main Drift of the ESF, Full-Periphery Geotechnical Maps and Rock Mass Quality Ratings Report. Submittal date: 09/09/1996. 108373

GS960908314224.017. Provisional Results: Geotechnical Data for Stations 50+00 to 55+00, Main Drift of the ESF, Full-Periphery Geotechnical Maps and Rock Mass Quality Ratings Report. Submittal date: 09/09/1996. 108376

GS960908314224.020. Analysis Report: Geology of the North Ramp - Stations 4+00 to 28+00 and Data: Detailed Line Survey and Full-Periphery Geotechnical Map - Alcoves 3 (UPCA) and 4 (LPCA), and Comparative Geologic Cross Section - Stations 0+60 to 28+00. Submittal date: 09/09/1996. 106059

GS970108314224.002. Geotechnical Data for Station 55+00 to Station 60+00, Main Drift of the ESF, Full Periphery Geotechnical Maps. Submittal date: 01/31/1997. 107490

GS970208314224.003. Geotechnical Data for Station 60+00 to Station 65+00, South Ramp of the ESF. Submittal date: 02/12/1997. 106048

GS970208314224.004. Geotechnical Data for Station 60+00 to Station 65+00, South Ramp of the ESF. Submittal date: 02/12/1997. 107492

GS970608314224.007. Provisional Results: Geotechnical Data for the Exploratory Studies Facility, Main Drift, Alcove 5 (DWFA): Heated Drift and Cross Drift Full Periphery Geotechnical Map (Drawing OA-46-300) and Rock Mass Quality Ratings Report. Submittal date: 06/24/1997. 158430

GS970808314224.009. Provisional Results: Geotechnical Data for Station 65+00 to Station 70+00, South Ramp of the ESF; Full-Periphery Geotechnical Maps (Drawings 0A-46-269 through 0A-46-274) and Rock Mass Quality Ratings Report. Submittal date: 08/18/1997. 107494

GS970808314224.010. Provisional Results: Geotechnical Data for Station 70+00 to Station 75+00, South Ramp of the ESF. Submittal date: 08/25/1997. 106050

GS970808314224.011. Provisional Results: Geotechnical Data for Station 70+00 to Station 75+00, South Ramp of the ESF. Submittal date: 08/25/1997. 107495

GS970808314224.013. Provisional Results: Geotechnical Data for Station 75+00 to Station 78+77, South Ramp of the ESF. Submittal date: 08/25/1997. 107497

GS971108314224.025. Revision 1 of Detailed Line Survey Data, Station 26+00 to Station 30+00, North Ramp and Main Drift, Exploratory Studies Facility. Submittal date: 12/03/1997. 106025

GS971108314224.028. Revision 1 of Detailed Line Survey Data, Station 55+00 to Station 60+00, Main Drift and South Ramp, Exploratory Studies Facility. Submittal date: 12/03/1997. 106047

GS990408314224.001. Detailed Line Survey Data for Stations 00+00.89 to 14+95.18, ECRB Cross Drift. Submittal date: 09/09/1999. 108396

GS990408314224.002. Detailed Line Survey Data for Stations 15+00.85 to 26+63.85, ECRB Cross Drift. Submittal date: 09/09/1999. 105625

GS990408314224.003. Full-Periphery Geologic Maps for Station -0+10 to 10+00, ECRB Cross Drift. Submittal date: 09/09/1999. 108404

GS990408314224.004. Full-Periphery Geologic Maps for Station 10+00 to 15+00, ECRB Cross Drift. Submittal date: 09/09/1999. 108405

GS990408314224.005. Full-Periphery Geologic Maps for Station 15+00 to 20+00, ECRB Cross Drift. Submittal date: 09/09/1999. 108408

GS990408314224.006. Full-Periphery Geologic Maps for Station 20+00 to 26+81, ECRB Cross Drift. Submittal date: 09/09/1999. 108409

LA000000000086.002. Mineralogic Variation in Drill Core UE-25 UZ#16 Yucca Mountain, Nevada. Submittal date: 03/28/1995. 107144

LA9912SL831151.001. Fracture Mineralogy of Drill Core ESF-HD-TEMP-2. Submittal date: 01/05/2000. 146447

LADB831321AN98.002. Revised Mineralogic Summary of Yucca Mountain, Nevada. Submittal date: 05/26/1998. 109003

LADV831321AQ97.001. Mineralogic Variation in Drill Holes. Submittal date: 05/28/1997. 107142

LADV831321AQ99.001. Quantitative XRD Results for the USW SD-6 and USW WT-24 Drill Core Samples. Submittal date: 04/16/1999. 109044

LB0205REVUZPRP.001. Fracture Properties for UZ Model Layers Developed from Field Data. Submittal date: 05/14/2002. 159525

LB0208UZDSCPMI.002. Drift-Scale Calibrated Property Sets: Mean Infiltration Data Summary. Submittal date: 08/26/2002. 161243

LL030808623122.036. Input and Output Files for NUFT MSTHM Sub-Models Supporting LA Multi-Scale Analyses. Submittal date: 09/11/2003. 165790

MO0001SEPDSTPC.000. Drift Scale Test (DST) Temperature, Power, Current, and Voltage Data for June 1, 1999 through October 31, 1999. Submittal date: 01/12/2000. 153836

MO0002ABBLSLDS.000. As-Built Borehole Locations and Sensor Locations for the Drift Scale Test Given in Local (DST) Coordinates. Submittal date: 02/01/2000. 147304

MO0004QGFMPICK.000. Lithostratigraphic Contacts from MO9811MWDGFM03.000 to be Qualified Under the Data Qualification Plan, TDP-NBS-GS-000001. Submittal date: 04/04/2000. 152554

MO0007SEPDSTPC.001. Drift Scale Test (DST) Temperature, Power, Current, and Voltage Data for November 1, 1999 through May 31, 2000. Submittal date: 07/13/2000. 153707

MO0012MWDGFM02.002. Geologic Framework Model (GFM2000). Submittal date: 12/18/2000. 153777

MO0107SEPDSTPC.003. Drift Scale Test (DST) Temperature, Power, Current, and Voltage Data for December 1, 2000 through May 31, 2001. Submittal date: 07/06/2001. 158321

MO0202SEPDSTTV.001. Drift Scale Test (DST) Temperature, Power, Current, and Voltage Data for June 1, 2001 through January 14, 2002. Submittal date: 02/28/2002. 158320

MO0301SPASIP27.004. Sampling of Stochastic Input Parameters for Rockfall Calculations and for Structural Response Calculations Under Vibratory Ground Motions. Submittal date: 01/15/2003. 161869

MO0301TMHIS106.001. Acceleration, Velocity, and Displacement Time Histories for the Repository Level at 10-6 Annual Exceedance Frequency. Submittal date: 01/28/2003. 161868

MO0306MWDALAFV.000. ANSYS-La-Fine Ventilation. Submittal date: 06/23/2003. 163961

MO0306MWDASLCV.001. ANSYS-LA-Coarse Ventilation. Submittal date: 07/01/2003. 165695

MO0306SDSAVDTH.000. Seismic Design Spectra and Acceleration, Velocity, and Displacement Time Histories for the Emplacement Level at 10-4 Annual Exceedance Frequency. Submittal date: 06/26/2003. 164033

MO0311RCKPRPCS.003. Intact Rock Properties Data on Uniaxial and Triaxial Compressive Strength. Submittal date: 11/04/2003. 166073

MO0401DQRIRPTS.003. Data Summary for Intact Rock Properties Data on Tensile Strength. Submittal date: 01/07/2004. 168905

MO0402AVDTM105.001. Acceleration, Velocity, and Displacement Time Histories for the Repository Level at 10-5 Annual Exceedance Frequency. Submittal date: 02/09/2004. 168890

MO0402DQRIRPPR.003. Intact Rock Properties Data on Poisson's Ratio and Young's Modulus. Submittal date: 02/19/2004. 168901

MO0403AVDSC106.001. Acceleration, Velocity, and Displacement Time Histories for the Repository Level at 10-6 Annual Exceedance Frequency. Submittal date: 03/09/2004. 168891

MO0403AVTMH107.003. Acceleration, Velocity, and Displacement Time Histories for the Repository Level at 10-7 Annual Exceedance Frequency. Submittal date: 03/22/2004. 168892

MO0407SEPFEPLA.000. LA FEP List. Submittal date: 07/20/2004. 170760

MO0407TMHIS104.003. Acceleration, Velocity and Displacement Time Histories for the Emplacement Level (Point B) at 5X10-4 Annual Exceedance Frequency. Submittal date: 07/15/2004. 170599

MO9807DSTSET01.000. Drift Scale Test (DST) Temperature, Power, Current, Voltage Data for November 7, 1997 through May 31, 1998. Submittal date: 07/09/1998. 113644

MO9906DSTSET03.000. Drift Scale Test (DST) Temperature, Power, Current, Voltage Data for September 1, 1998 through May 31, 1999. Submittal date: 06/08/1999. 113673

SN0108SD821723.001. Uniaxial and Triaxial Compression Test Data on Samples from USW G-1 (VA Supporting Data). Submittal date: 08/09/2001. 159959

SN0208F4102102.002. Rock Mass Mechanical Properties, Slot Test #1, Location 57+77 in the ESF. Submittal date: 08/27/2002. 161874

SN0208L0207502.001. Mechanical Properties of Lithophysal Tuff, Batch #1 (Test Dates: July 31, 2002 through August 16, 2002). Submittal date: 08/20/2002. 161871

SN0211L0207502.002. Mechanical Properties of Lithophysal Tuff, Batch #2 (Test Dates: October 22, 2002 through October 25, 2002). Submittal date: 11/13/2002. 161872

SN0212F4102102.004. Rock Mass Mechanical Properties, Slot Test #2, Location 63+83 in the ESF. Submittal date: 12/17/2002. 161875

SN0301F4102102.006. Rock Mass Mechanical Properties, Slot Test #3, Location 21+25 in the ECRB. Submittal date: 01/14/2003. 161876

SN0302L0207502.003. Mechanical Properties of Lithophysal Tuff, Room Temperature Batch #4, Set 1 (Test Dates: 01/21/03 through 01/23/03). Submittal date: 02/25/2003. 165014

SN0303T0503102.008. Revised Thermal Conductivity of the Non-Repository Layers of Yucca Mountain. Submittal date: 03/19/2003. 162401

SN0305L0207502.004. Mechanical Properties of Lithophysal Tuff, Batch #4, Set 2 (Test Dates: March 5, 2003 through March 13, 2003). Submittal date: 05/01/2003. 165013

SN0305L0207502.005. Material Abundances from Point Counts on Laboratory Mechanical Property Specimens for Batch #1 and Batch #2. Submittal date: 05/20/2003. 163373

SN0306L0207502.008. Revised Mechanical Properties of Welded Tuff from the Lower Lithophysal Zone of the Topopah Spring Tuff, Batch #3 (Test Dates: March 6, 2003 through April 18, 2003). Submittal date: 06/20/2003. 165015

SN0307T0510902.003. Updated Heat Capacity of Yucca Mountain Stratigraphic Units. Submittal date: 07/15/2003. 164196

SN0404T0503102.011. Thermal Conductivity of the Potential Repository Horizon Rev 3. Submittal date: 04/27/2004. 169129

SN0406L0212303.002. Static Fatigue Data from New England Research (NER) (Test Dates: 1/2/2004 through 2/25/2004. Submittal date: 06/08/2004.	170289
SNF37100195002.001. Hydraulic Fracturing Stress Measurements in Test Hole: ESF-AOD-HDFR1, Thermal Test Facility, Exploratory Studies Facility at Yucca Mountain. Submittal date: 12/18/1996.	131356
SNL01B05059301.006. Laboratory Thermal Expansion Data for Boreholes UE25 NRG-4, NRG-5; USW NRG-6 and NRG-7/7A. Submittal date: 02/07/1996.	129168
SNL02030193001.001. Mechanical Properties Data for Drillhole USW NRG-6 Samples from Depth 22.2 ft. to 328.7 ft. Submittal date: 05/17/1993.	120572
SNL02030193001.002. Mechanical Properties Data for Drillhole USW NRG-6 Samples from Depth 22.2 ft. to 427.0 ft. Submittal date: 06/25/1993.	120575
SNL02030193001.003. Mechanical Properties Data for Drillhole UE-25 NRG-2 Samples from Depth 150.5 ft. to 200.0 ft. Submittal date: 07/07/1993.	120578
SNL02030193001.004. Mechanical Properties Data for Drillhole USW NRG-6 Samples from Depth 462.3 ft. to 1085.0 ft. Submittal date: 08/05/1993	108415
SNL02030193001.005. Mechanical Properties Data for Drillhole UE-25 NRG#3 Samples from Depth 15.4 ft. to 297.1 ft. Submittal date: 09/23/1993.	122545
SNL02030193001.006. Mechanical Properties Data for Drill Hole UE-25 NRG#2A Samples from Depth 90.0 ft. to 254.5 ft. Submittal date: 10/13/1993.	120579
SNL02030193001.007. Mechanical Properties Data for Drill Hole UE-25 NRG#3 Samples from Depth 263.3 ft. to 265.7 ft. Submittal date: 10/20/1993.	120582
SNL02030193001.008. Mechanical Properties Data for Drill Hole USW NRG-6 Sample 416.0 ft. Submittal date: 10/20/1993.	120597
SNL02030193001.009. Mechanical Properties Data for Drillhole UE25 NRG-5 Samples from Depth 781.0 ft. to 991.9 ft. Submittal date: 11/18/1993.	109614
SNL02030193001.012. Mechanical Properties Data for Drillhole UE25 NRG-5 Samples from Depth 847.2 ft. to 896.5 ft. Submittal date: 12/02/1993.	108416
SNL02030193001.013. Mechanical Properties Data for Drillhole UE25 NRG-2B Samples from Depth 2.7 ft. to 87.6 ft. Submittal date: 12/02/1993.	120614
SNL02030193001.014. Mechanical Properties Data for Drillhole UE25 NRG-4 Samples from Depth 378.1 ft. to 695.8 ft. Submittal date: 01/31/1994.	109609
SNL02030193001.015. Mechanical Properties Data for Drillhole UE25 NRG-4 Samples from Depth 527.0 ft. Submittal date: 02/16/1994.	120617

SNL02030193001.016. Mechanical Properties Data for Drillhole USW NRG-7/7A Samples from Depth 18.0 ft. to 472.9 ft. Submittal date: 03/16/1994. 120619

SNL02030193001.018. Mechanical Properties Data for Drillhole USW NRG-7/7A Samples from Depth 344.4 ft. Submittal date: 04/11/1994. 109611

SNL02030193001.019. Mechanical Properties Data for Drillhole USW NRG-7/7A Samples from Depth 507.4 ft. to 881.0 ft. Submittal date: 06/29/1994. 108431

SNL02030193001.020. Mechanical Properties Data for Drillhole USW NRG-7/7A Samples from Depth 554.7 ft. to 1450.1 ft. Submittal date: 07/25/1994. 108432

SNL02030193001.021. Mechanical Properties Data (Ultrasonic Velocities, Static Elastic Properties, Triaxial Strength, Dry Bulk Density & Porosity) for Drillhole USW NRG-7/7A Samples from Depth 345.0 ft. to 1408.6 ft. Submittal date: 02/16/1995. 108433

SNL02030193001.022. Mechanical Properties Data for Drill Hole USW NRG-6 Samples from Depth 5.7 ft. to 1092.3 ft. Submittal date: 02/27/1995. 109613

SNL02030193001.023. Mechanical Properties Data (Ultrasonic Velocities, Static Elastic Properties, Unconfined Strength, Triaxial Strength, Dry Bulk Density & Porosity) for Drillhole USW SD-12 Samples from Depth 16.1 ft. to 1300.3 ft. Submittal date: 08/02/1995. 108435

SNL02030193001.026. Mechanical Properties Data (Ultrasonic Velocities, Elastic Moduli and Fracture Strength) for Borehole USW SD-9. Submittal date: 02/22/1996. 108436

SNL02030193001.027. Summary of Bulk Property Measurements Including Saturated Bulk Density for NRG-2, NRG-2A, NRG-2B, NRG-3, NRG-4, NRG-5, NRG-6, NRG-7/7A, SD-9, and SD12. Submittal date: 08/14/1996. 108410

SNL02112293001.003. Results from Shear Stress Experiments on Natural Fractures from NRG-4 & NRG-6. Submittal date: 03/13/1995. 108413 108412

SNL02112293001.005. Mechanical Properties of Fractures in Specimens from Drillhole USW SD-9. Submittal date: 07/15/1996. 108413

SNL02112293001.007. Mechanical Properties of Fractures in Specimens from Drillholes USW NRG-7/7A and USW SD-12. Submittal date: 08/08/1996. 108414

SNSAND83164600.000. Experimental Data of Fully Saturated and Wet Samples; Static Mechanical Properties of GU-3 760.9 Samples; Ultrasonic Velocity Data; and Dynamic Elastic Model of GU-3 760.9 Samples Compression Test. Submittal date: 04/24/1992. 160009

SNSAND84110100.000. Uniaxial and Triaxial Compression Test Series on Topopah Spring Tuff from USW G-4, Yucca Mountain, Nevada. Submittal date: 02/01/1986. 160016

SNSAND85070300.000. Uniaxial and Triaxial Compression Test Series on the Topopah Spring Member from USW G-2, Yucca Mountain, Nevada. Submittal date: 09/24/1987. 160020

SNSAND85070900.000. Effects of Sample Size on the Mechanical Behavior of the Topopah Spring Tuff. Submittal date: 12/16/1998. 160022

SNSAND85076200.000. Bulk, Thermal, and Mechanical Properties of the Topopah Spring Member of the Paintbrush Tuff, Yucca Mountain, Nevada. Submittal date: 10/17/1987. 160024

SNSAND86113100.000. Petrologic and Mechanical Properties of Outcrop Samples of the Welded, Devitrified Topopah Spring Member of the Paintbrush Tuff. Submittal date: 06/11/1987. 159594

9.5 DEVELOPED DATA, LISTED BY DATA TRACKING NUMBER

MO0306MWDDPPDR.000. Drift Profile Prediction and Degraded Rock Mass Characteristics in Lithophysal Units. Submittal date: 06/18/2003.

MO0403MWDRPNLR.000. Rock Properties for Nonlithophysal Rock. Submittal date: 03/31/2004.

MO0404MWD3DRFA.000. Input and Output file for 3DEC Rockfall Analyses with 1E-4 Ground Motion. Submittal date: 04/08/2004.

MO0407MWDDSLCR.000. Drip Shield Load in Collapsed Lithophysal Rock. Submittal date: 07/21/2004.

MO0407SPAMTSHR.000. Modeled Thermal Stresses Within the Host Rock at Three Graduated Points in Time. Submittal date: 07/20/2004.

MO0408MWDRNLRA.002. Results from Nonlithophysal Rockfall Analyses for Emplacement Drifts with 1E-4 Ground Motion. Submittal date: 08/19/2004.

MO0408MWDDDMIO.002. Drift Degradation Model Inputs and Outputs. Submittal date: 08/31/2004.

INTENTIONALLY LEFT BLANK